SURFACE FOOTINGS ON SAND

UNDER GENERAL PLANAR LOADS

A Thesis submitted for the degree of
DOCTOR OF PHILOSOPHY
in the Faculty of Engineering and
Applied Science, University of
Southampton

by

John Ticof

November 1977

UNIVERSITY OF SOUTHAMPTON

ABSTRACT

FACULTY OF ENGINEERING AND APPLIED SCIENCE

CIVIL ENGINEERING

Doctor of Philosophy

SURFACE FOOTINGS ON SAND UNDER GENERAL PLANAR LOADS

by John Ticof

The thesis is concerned with the behaviour of rigid surface strip footings on sand when subjected to eccentric and/or inclined loads.

Experiments have been performed in two apparatuses, the one having a three times greater sand-bed width than the other, together with a preliminary investigation in a smaller apparatus.

The bearing capacity predictions from various published theoretical and semi-empirical solutions are compared with the experimental results. Contact stress distributions which were measured in each case are also presented.

The effect of the tank to footing width ratio on the bearing capacity and the contact stress distribution is examined by means of comparative results from nominally identical tests.

The deformation of the sand mass has been measured by both X-ray and Stereophotogrammetric techniques and representative results obtained by each method are presented and discussed. The effect of the sand-glass friction on the photogrammetrically measured displacement fields has been investigated by comparing results obtained from identical load increments in identical tests using each of the techniques.

A new rational approach to the bearing capacity problem, based upon concepts from plasticity theory, and supported by the author's experimental evidence, has been advanced. This analysis, which utilises the concept of the plastic potential, describes the planar translation of a footing in a very satisfactory way under inclined central loads both qualitatively and even quantitatively in tests carried out so far.

Finally, a generalization of the analysis has been devised to cover the case of footings under general loading, its potentialities have been discussed with particular reference to offshore oil platforms and areas recommended for future research in this field.

ACKNOWLEDGEMENTS

The work described in this thesis has been conducted at both the Universities of Cambridge and Southampton and many people have been involved in it, either directly or indirectly. Their contributions are greatly appreciated.

I am deeply grateful to my present supervisor, Dr. R. Butterfield, for his continuous help and enthusiasm throughout. His interest and criticism helped me to clarify my ideas and strengthen my arguments.

I would like to express my gratitude to my previous supervisor at Cambridge University, Dr. R.G. James, who initiated the project, for his help in the design of the apparatus at Cambridge and for his contribution through many fruitful discussions.

Many thanks are also due to the members of the Soil Mechanics group at Cambridge University and especially to Prof. A.N. Schofield for his permission to use the techniques developed at that University.

Special thanks are due to Mr. R.M. Harkness for many stimulating discussions and to Dr. A. Lock who, together with the former, provided me with the examples of the new data analysis method which they developed and are presented in the thesis.

My fellow research students, both at Cambridge and Southampton, have helped me through many discussions, and their contribution is much appreciated.

I would also like to express my thanks to the following people:
To Messrs D. Orchard, A. Rogerson, R. Bell of the Civil Engineering Workshops, Mr. T. Pickett of the Soil Mechanics Laboratory and Mr. E. Meech for their help throughout the work at Southampton. I am particularly grateful to Mr. K. Yeates to whose craftsmanship the efficient operation of the footing apparatus at Southampton is largely due, and who has contributed immeasurably throughout the experimental work at Southampton.
To Messrs R.E. Ward, B. Balodis, J. Doherty, C. Hodgson, W. Gwizdala, T. Overall and Mrs. V.E. Johnson of the technical staff of the Soil Mechanics Group at Cambridge who have helped in many ways with their skill and cheerfulness.
To Mr. M. Julian and his staff Messrs B. Hauttot and J. Filby of the Engineering Laboratory Workshops for the construction of the footing apparatus at Cambridge.

To Mr. P.K. Clarkson and the staff of the Engineering Computing Service at Cambridge for their help in the involved computations.
To the staff of both the Libraries of Southampton University and of the Engineering Department of Cambridge University for their help throughout the work.
To Mr. N. Lindsay of the City University, London for his kind offer to assist with stereophotogrammetic measurements and to Mr. A. Kenney who measured the photographs.
To Mrs. A. Lampard for her neat typing of the thesis.

The partial financial support of the Soil Mechanics Group and Sidney Sussex College while at Cambridge University, and of the University of Southampton while at Southampton University is also gratefully acknowledged.

Finally I would like to express my thanks to my parents, and especially to my wife for her continuous support throughout the work and for her constant encouragement and assistance in preparing the manuscript.

CONTENTS

LIST OF FIGURES

6.7 Moment-rotation relationships for a footing under a vertical eccentric load

6.8 Vertical component of the load-vertical displacement relationships under an inclined central load

6.9 Vertical component of the load-horizontal displacement relationships under an inclined central load

6.10 Contact stress load cells arrangement (a) Positive contact stresses (b) FAC (c) FAS

6.11 Normalized stress distribution measured in test D ($\alpha_o = 0$, $E_o = 0$, FAC) (a) Mean normal stress (b) Normal stress at stage $P/P_f = 0.90$ (c) Mean shear stress

6.12 Normalized mean stress distribution measured in test DS ($\alpha_o = 0$, $E_o = 0$, FAS) (a) Normal stress-centre section (C.F.) (b) Normal stress-side section (S.F.) (c) Shear stress

6.13 Normalized mean stress distribution measured in test A ($\alpha_o = 0$, $E_o = 0.167$, FAC) (a) Normal stress (b) Shear stress

6.14 Normalized mean stress distribution measured in test H ($\alpha_o = 0$, $E_o = 0.167$, FAC) (a) Normal stress (b) Shear stress

6.15 Normalized mean stress distribution measured in test HS ($\alpha_o = 0$, $E_o = 0.167$, FAS) (a) Normal stress - centra section (C.F.) (b) Normal stress - side section (S.F.) (c) Shear stress

6.16 Total load recorded by each section of the footing in test HS ($\alpha_o = 0$, $E_o = 0.167$, FAS)

6.17 Normalized mean stress distribution measured in the FAC (a) Normal stress and (b) shear stress - test B ($\alpha_o = 12^o$, $E_o = 0$)

(c) Normal stress and (d) shear stress - test GB ($\alpha_o = 20^o$, $E_o = 0$)

(e) Normal stress and (f) shear stress - test E ($\alpha_o = 30^o$, $E_o = 0$)

6.18 Normalized mean stress distribution measured in the FAS (a) Normal stress - centre section, (b) Normal stress - side section and (c) shear stress: Test BS ($\alpha_o = 12^o$, $E_o = 0$)

(d) Normal stress - centre section, (e) Normal stress - side section and (f) shear stress : Test RS ($\alpha_o = 5^o$, $E_o = 0$)

6.19 The normal stresses recorded by the 'normalizing' load cell during tests D,A,H,DS,AS,HS.

6.20 The shear stresses recorded by the 'normalizing' load cell during tests D,A,H,DS,AS,HS.

6.21 The normal stresses recorded by the'normalizing' load cell during tests B,GB,E,BS,RS.

6.22 The shear stresses recorded by the 'normalizing' load cell during tests B,GB,E,BS,RS.

7.9 The zero extension line directions from test D(e_o=0.52,α_o=0,E_o=0) at stages: (a) 0.74 and (b) 0.93 of the failure load.

7.10 Total displacement fields from test A(e_o=0.52,α_o=0,E_o=0.167) at stages (a) 0.72 and (b) 0.91 of the failure load (c) Horizontal and (d) Vertical displacements at stage 0.91 of the failure load.

7.11 The major principal compressive strain directions from test A(e_o=0.52,α_o=0,E_o=0.167) at stages: (a) 0.72 and (b) 0.91 of the failure load.
The major principal compressive strain rate directions between stages: (c) 0.72-0.91 and (d) 0.91-after failure.

7.12 The total maximum shear strain fields from test A(e_o=0.52,α_o=0, E_o=0.167) at stages: (a) 0.72 and (b) 0.91 of the failure load. (c) The shear strain pattern from test A.

7.13 Maximum shear stress contours in an elastic plate under a normal concentrated load (Frocht,1948).

7.14 Total volumetric strains from test A(e_o=0.52,α_o=0,E_o=0) at stages: (a) 0.72 and (b) 0.91 of the failure load.

7.15 The zero extension line directions from test A(e_o=0.52,α_o=0, E_o=0.167) at stages: (a) 0.72 and (b) 0.91 of the failure load.

7.16 Total displacement fields from test B(e_o=0.52, α_o=12°,E_o=0) at stages (a) 0.70 and (b) 0.86 of the failure load.

7.17 Total displacement fields (units in 0.1mm) from test B(e_o=0.52, α_o=12°,E_o=0) at stage 0.70 of the failure load (a) Horizontal (b) vertical displacements. At stage 0.86 of the failure load (c) Horizontal (d) vertical displacements.

7.18 The major principal compressive strain directions from test B(e_o=0.52,α_o12°,E_o=0) at stages (a) 0.70 and (b) 0.86 of the failure load.
The major principal compressive strain rate directions between stages: (c) 0.70-0.86 and (d) 0.0-0.53 of the failure load.

7.19 The major principal compressive strain directions from test B(e_o=0.52,α_o=12°, E_o=0) between stages (a) 0.86-failure (b) 0.0-failure.

7.20 The total maximum shear strain fields from test B(e_o=0.52,α_o=12°, E_o=0) at stages (a) 0.70 and (b) 0.86 of the failure load.

7.21 The volumetric strains from test B(e_o=0.52,α_o=12°,E_o=0) at stages (a) 0.70 and (b) 0.86 of the failure load.

7.22 The zero extension line directions from test B(e_o=0.52,α_o=12°, E_o=0) at stages (a) 0.70 and (b) 0.86 of the failure load.

7.23 The average volumetric-maximum shear strain relationships and the standard deviations of Δ from tests:
(a) D(e_o=0.52,α_o=0,E_o=0) (b) A(e_o=0.52,α_o=0,E_o=0.167)
(c) B(e_o=0.52,α_o=12°,E_o=0) and (d) C(e_o=0.52,α_o=12°,E_o=-0.167).

7.24 The distribution of the number of readings used in the calculation of the average Δ-γ_M relationships from tests (a) D (b) A (c) B, (d) C, shown in fig. 7.23.

7.25 The average Δ-γ_M relationship from all the tests in the FAC - Comparison with results from the SSA (Stroud,1970).

NOTATION

The following symbols have been used throughout the text. Any deviations or additions are defined locally.

e = eccentricity (in mm)

E = eccentricity ratio (= e/B)

e_o = initial voids ratio

V = vertical component of the load

v = vertical displacement

u = horizontal displacement

H = horizontal component of the load

R = applied load

M = applied moment

N_γ, N_c, N_q = bearing capacity factors with respect to soil weight, cohesion, surcharge

p = bearing capacity

D = depth of embedment

c = cohesion

c_u = undrained shear strength

$i_\gamma = V/V_{max}$ = inclination factor

B' = B-2e = effective width

B = width, L = length } of footings

P/P_f = ratio of the currently applied normal pressure to the average normal pressure at failure

ϵ = Base of natural logarithms

Δ = volumetric strain

γ_m = maximum shear strain

ω = rotation footing (^{o})

δ = angle of base friction (^{o})

τ = shear stress (contact)

σ = normal stress (contact)

γ = unit weight of soil

α_o = inclination of load R to the vertical (initial)

ϕ = angle of internal friction

μ = Poisson's ratio

ν = angle of dilatancy

ξ = inclination of the principal compressive strain directions to the x-axis

α,β = the inclinations of the directions of the zero extension lines to the x-axis

$\dot{\varepsilon}_1,\dot{\varepsilon}_3$ = major and minor principal strain increments

CHAPTER 1

INTRODUCTION - GENERAL LITERATURE REVIEW

1.1 Introduction

Most civil engineering structures transmit their loads to the earth through foundations, and an engineer is required to predict the response that can be expected due to the imposed loadings. However, the precise prediction of the subsequent performance of these structures is still difficult, despite the rapid development of the science of soil mechanics and there-by the better understanding of the main constituent 'soil'.

Advanced scientific and technological development, together with the more restricted access to natural resources has led to new types of structures for which past experience is at least limited if not altogether absent. Heavy structures of immense size and height are built, sometimes in areas in which, previously, the supporting strength of the soil would have been considered quite inadequate. The new era of offshore oil exploration has created the need for vast structures subjected to immense loads to be founded on the bottom of the sea. Empirical rules, are therefore, increasingly left aside and rational methods of design, tempered as ever by indispensible engineering judgement, are sought.

The development of any rational method requires the correct postulation of the problem, its theoretical solution being subsequently checked by experimental investigation. It has, however, often been the case that consideration of existing experimental evidence has led to the formulation of basic ideas from which a rational analytical approach has been developed.

The problem that was chosen for investigation is the behaviour of a surface footing on sand under general planar loads. This project followed a preliminary investigation on submerged footings on sand under cyclic loads (Ticof, 1974) which, rather surprisingly, revealed our present limited knowledge about the behaviour of such footings even when statically loaded (and under drained conditions). As will become evident in subsequent sections, there is limited experimental information about the contact stress distribution, almost no information

on the deformation of the soil mass under eccentric and/or inclined loads, and, perhaps as a consequence, lack of any truly rational approach. The lack of such information becomes even more startling when one considers that structures like the Ekofisk and Condeep oil platforms are already installed in the North Sea (ICE, 1974).

The project is not oriented towards predicting the behaviour of such structures by conducting laboratory tests applying the principles of similarity. These experiments are idealized model tests and may be used to either check theoretical analyses or even provide a basis for quite new approaches.

1.2 A review of previous work on the bearing capacity of shallow footings

In this section, a review of previous work on the subject is presented. In view of the amount of literature, especially on the subject of central vertical loading, (an extensive review of this topic was made by Roscoe (1956), Roberts (1961) and Vesic (1973)), the review is intended to be brief and selective. However, the previous work on both eccentric and/or inclined loading conditions will be looked at in much more detail, in an effort to summarize all the published major contributions on this field.

Three main categories will be considered; one dealing with the vertical central load case, the second with eccentric loadssand the third with inclined loads.

1.2.1 Theoretical approach

1.2.1.1 Vertical central load

The bearing capacity of footings is one of the fundamental classical stability problems and various methods, basically utilising the concepts of perfect plasticity, are used to assess the collapse load. These techniques may be divided into three principal groups (Chen, 1975):

(a) Limit analysis
(b) Slip-line methods
(c) Limit equilibrium methods

(a) Limit analysis provides bounding estimates of the collapse load for an ideal soil, replacing the actual one, which possesses the following properties:

(I) The soil behaves as a perfectly plastic solid i.e. neither work hardening nor work softening occurs (the stress increment vector always lies tangent to the yield surface, whenever plastic strain increments occur).

(2) The yield surface is convex enveloping the origin and the plastic strain increment vectors are normal to it (consequently $\dot{\sigma}_{ij}\ \dot{\varepsilon}^{p}_{ij} = 0$)

(3) Changes in geometry of the soil system at the limit load are neglected (thus the virtual work equations may be applied).

The limit load for this ideal soil usually gives a good approximation to the actual plastic collapse load for the real soil, and the bounding estimates for the ideal soil limit load serve as upper and lower bounds to the actual collapse load. These upper and lower bounds may be obtained by using the plastic limit theorems of Drucker et al (1951) which may be stated essentially as follows:

(1) If a distribution of stress satisfies the equilibrium equations, the stress boundary conditions and does not violate the yield criterion anywhere within the region, then the load determined from such a distribution will be a lower bound to the actual collapse load.

(2) If a kinematically admissible field (a velocity field which satisfies the velocity boundary conditions and the strain and velocity compatibility conditions) can be found, then the load determined by equating the external rate of work to the internal rate of energy dissipation within this field serves as an upper bound to the actual collapse load.

(b) When ultimate failure (unrestricted plastic flow) is imminent, then both the equilibrium and failure conditions within the region are satisfied. If the two equations of stress equilibrium, namely

$$\frac{\partial \sigma_x}{\partial x} + \frac{\partial \tau_{xy}}{\partial y} = 0 \qquad (1.1)$$

$$\frac{\partial \sigma_y}{\partial y} + \frac{\partial \tau_{xy}}{\partial x} = 0 \qquad (1.2)$$

are combined with the Coulomb failure criterion - mainly used as the yield criterion for soils - namely

$$\sqrt{\frac{(\sigma_x - \sigma_y)^2}{4} + \tau_{xy}^2} - \frac{\sigma_x + \sigma_y}{2} = c \cos \phi \qquad (1.3)$$

they form a set of hyperbolic differential equations for the determina-

tion of the stresses σ_x, σ_y, τ_{xy}.

For a particular set of known boundary stress conditions, these equations may be used to determine the stresses within the region of impending plastic flow (and therefore everywhere beneath the footing), by proceeding along the slip-line network, which consists of a family of lines the directions of the tangents of which, at every point in the region, coincide with the directions of the failure planes, on which $\tau_f = c + \sigma_f \tan \phi$.

If the weight of the soil is taken into account, then eq. (1.2) with y along gravity axis, becomes

$$\frac{\partial \sigma_y}{\partial y} + \frac{\partial \tau_{yx}}{\partial x} = \gamma \qquad (1.2')$$

and the system of equations (1.1), (1.2'), (1.3) is nonlinear and cannot, in general, be integrated in closed form (Scott, 1963). Sokolovskii (1965) has developed a finite difference technique to integrate approximately the basic differential equations along the slip lines, when the soil weight is considered.

(c) If the limit equilibrium method is adopted to obtain a solution for a stability problem (eg. a footing), then a failure surface is assumed and the position for which this surface will produce the minimum stable load is sought. This failure surface is usually chosen such that the stress distribution along it is conveniently included in the overall equilibrium equation, which usually requires only simple statics for the solution of various problems (Fellenius method for stability of slopes, (for $\phi = 0$ or $\phi \neq 0$) Terzaghi,1943).

The comparative power and limitations of these three methods are discussed by Chen (1975), and the versatility and relative simplicity of the limit analysis emphasised. However, the method most widely used in calculating the bearing capacity of shallow foundations is the approximate'superposition' method as expressed by the well-known formula of Terzaghi (1943) (see fig. 1.1a) for a shallow strip foundation:

$$p = \tfrac{1}{2}\gamma N_\gamma B + c N_c + q N_q \qquad (1.4)$$

where γ is the unit weight of the soil, B is the foundation width, c is

the cohesion of the soil, q is the surcharge on the surface of the soil outside the footing, N_c N_q N_γ are dimensionless factors depending only on the angle of internal friction ϕ, and p is the ultimate bearing pressure. These factors represent the resistance due to soil cohesion, surcharge and soil weight respectively, and Terzaghi (1943) suggested the superposition of these three separate cases. A similar approach to the subject has been attributed to Caquot (1934) and Buisman (1935) (Vesic (1963)).

Meyerhof (1951) adopted Terzaghi's technique and obtained approximate solutions to the problem of shallow (and deep) footings by assuming failure mechanisms for the footing and taking into account the shear strength of the overburden, unlike Terzaghi who considered its weight only as an equivalent surcharge (q) (see fig. 1.1b). Like Terzaghi, Meyerhof presented results in form of bearing capacity factors N. Even though the soil behaviour in the plastic range is definitely nonlinear, therefore, any superposition does not hold for the bearing capacity of a c, ϕ, γ soil (soil possessing cohesion, friction and weight), the mathematical difficulties encountered when the conventional limit equilibrium method is used for nonlinear problems provide some justification, at least for practical purposes, for using this semi-empirical method.

The effect of the shape and of the relative embedment of the footing have been taken into account subsequently by introducing shape and depth factors respectively (Meyerhof, 1951, 1963; De Beer 1965a, 1970; Hansen, 1970) in the equation (1.4), even though the relative importance of the latter in most cases of embedded footings was found to be negligible (Vesic, 1963). Equation (1.4) now becomes

$$p = \tfrac{1}{2}\gamma N_\gamma B s_\gamma d_\gamma + \gamma D N_q s_q d_q + c N_c s_c d_c \qquad (1.5)$$

where s and d are the shape and depth factors related to self-weight (γ), surcharge (q) and cohesion (c).

Considering the case of surface strip footings on sand, the bearing equation becomes simply:

$$p = \tfrac{1}{2}\gamma N_\gamma B \qquad (1.6)$$

The major problem in applying equation (1.6) is the correct estima-

tion of the angle of internal friction ϕ, since the N_γ factor is a function of ϕ. It is well established that the angle of internal friction for a sand of the same density is stress level dependent (and therefore scale effects are inherent) (Bishop, 1966; Stroud, 1971; Berezantzev et al, 1969; Vesic and Clough, 1968; Meyerhof, 1948; De Beer, 1961, 1965a) and that it varies considerably with varying test conditions particularly in dense state (plane strain versus triaxial) (Bishop, 1957, 1966; Meyerhof, 1963;Cornforth, 1964). Furthermore, due to the fact that the maximum shear strength of the soil is not fully mobilized simultaneously throughout the failure surface, but progressively from the edge of the footing (depending on the shear strain the soil has experienced at that instant) (fig. 1.2), the angle of internal friction ϕ also varies along the slip surface (De Beer, 1965a, 1965b; Roscoe, 1970).

Meyerhof (1948) suggested that the mean normal value of the normal stress along the slip surface was 1/10 of the ultimate bearing capacity and that this mean value should be used for the determination of the appropriate angle of friction. De Beer (1965a) found this assumption quite acceptable and suggested a formula to calculate the average normal stress as a function of ϕ, bearing capacity p and surcharge q. Graham and Stuart (1971) showed that such an assumption would result in a scale effect. To conform with the plane strain conditions that prevail in the case of a strip footing, Meyerhof (1963), following remarks by Bishop (1957), suggested that the angle of internal friction ϕ used in the bearing capacity calculations should be 10% higher than that obtained from a triaxial test. This suggestion, which was subsequently confirmed by Conforth (1964) and Bishop (1966), was also adopted by Brinch Hansen (1970). However, as was pointed out by Roscoe (1970) it is a very crude approximation to assume that ϕ is constant throughout the deforming region because of strain propagation, and such findings were reported by a number of research workers (Arthur, James and Roscoe, 1964; James, 1965; Bransby, 1968; Tennekoon, 1970). Modified Sokolovskii type analyses, incoprorating variable ϕ, have been developed by Tennekoon (1970), Graham and Pollock (1972).

1.2.1.2 The eccentricity of the load

The 'effective width' concept for the calculation of the bearing capacity of footings under eccentric loads was introduced by Meyerhof

(1953), even though it is claimed that it was suggested and used almost a decade earlier (De Beer, 1965, 1949). The eccentric load is assumed acting centrally on a footing of width (fig. 1.3)

$$B' = B - 2e \tag{1.7}$$

while the remaining width is not considered. This assumption, which is somewhat conservative, seems to have been generally accepted as a valid one, and in a number of cases agrees well with the experimental results (see chapter 2).

The conventional method often adopted for the design of eccentrically loaded footings (for example Peck et al, 1973) is based on the allowable earth pressure concept. A straight line normal contact stress distribution is assumed (derived by precisely the same equilibrium analysis as used for struts and beams in elementary structural analysis). The maximum pressure at the corner of the footing must then not exceed the average ultimate pressure under a vertical central load. This implies that the whole footing width may be considered as "effective" for eccentricities up to B/6, while a reduced width is considered for higher eccentricities (dependent on the stress distribution diagram). As it will be discussed in chapter 2, the predictions from this method are unsafe for eccentricities larger than B/6 and lie on the safe side for a load eccentricity within the "middle third".

Based on experimental observations, Giraudet (1965) suggested the following experimental expression for the bearing capacity reduction, namely

$$\frac{V}{V_{max}} = \varepsilon^{-12E^2} \tag{1.8}$$

where $\varepsilon = 2.7183$, E is the eccentricity ratio e/B, B is the width of the footing and V_{max} is the ultimate vertical central load. The predictions from this formula grossly overestimate the bearing capacity of surface footings (see chapter 2) but, it appears to give reasonable predictions for the embedded footings used by Giraudet.

Assuming one-sided failure surface (forming on the same side as the eccentric load) Prakash et al (1971) developed an analytical solution based on the limit equilibrium approach. Following Terzaghi, they assumed that superposition holds and, in addition, that the footing

partially loses contact with the soil with increasing load eccentricity. Good agreement with published experimental results was reported; however, apart from the superposition shortcomings already discussed, the actual "effective" width, established theoretically, was estimated from the relative tilt and the settlement of the footing. This method cannot provide a correct measure of the contact area, which should be more accurately indicated by monitoring the contact stress distribution.

Recently, Purkayastha et al (1977) presented a stability analysis for eccentrically loaded footings based on an assumed failure surface derived from experimental results. Again a linear distribution of contact stresses was assumed and the one-sided failure zone (which consisted, as usual, of two triangular Rankine zones and one logarithmic spiral) was considered to contract with increasing eccentricity. They obtained a rather good agreement with the "effective width" concept, apart from eccentricity ratios E between 0.2 and 0.3 where a 10% difference was observed.

1.2.1.3 Inclination of the load

The case of a strip footing on sand under an inclined central load was considered by Meyerhof (1953) who suggested that the vertical component V of the load (fig. 1.4) could be expressed as

$$V = \tfrac{1}{2}\gamma\ B\ N_{\gamma q}(BL) \qquad (1.9)$$

where the bearing capacity factor $N_{\gamma q}$ depends on ϕ,α (angle of load inclination) and depth of embedment (the length of the footing, $L \geq 6B$). V is seen to decrease rapidly with greater inclination and becomes zero for $\alpha = \phi$, when simple sliding of the footing occurs. Later, Meyerhof (1963) suggested that the vertical component of the load could be expressed in the form of reduction factors (with respect to the ultimate vertical centreline load bearing capacity V_{max}) known as 'inclination factors' which, for the case of surface footings on sand, take the following form:

$$\frac{V}{V_{max}} = \left(1 - \frac{\alpha}{\phi}\right)^2 \qquad (1.10)$$

Semi-empirical relationships of the form

$$\frac{V}{V_{max}} = \left(1 - \beta_1 \frac{H}{V}\right)^{\beta_2} \qquad (1.11)$$

have been suggested by Brinch Hansen, with $\beta_1 = 1.5$, $\beta_2 = 2$ (Hansen, 1957), $\beta_1 = 1$, $\beta_2 = 4$(Hansen, 1961), and $\beta_1 = 0.7$, $\beta_2 = 5$ (Hansen, 1970), the last one being an approximate expression of a slip-line solution by Odgaard and Christensen for $\phi = 30^{\circ}$ and 45° (Hansen, 1970). Muhs and Weiss (1973), from large scale field tests, suggested a reduction factor of the same form as equation (1.11) with $\beta_1 = 1$ and $\beta_2 = 2$ (see section 1.2.2.3). All the above expressions will be compared with the current experimental results in Chapter 2.

Janbu (1957) suggested that the reduction bearing capacity due to an inclined load could be predicted by the following equation:

$$\frac{V}{V_{max}} = \frac{1}{1 + N_h \left(\frac{H}{V}\right)} \qquad (1.12)$$

The factor N_h is a monotonically increasing factor of the angle of internal friction for which he provided graphical information, while $H/V \leq \tan \phi$. Considering the case $\phi = 45^{\circ}$ and $\alpha = 45^{\circ}$, $N_h = 4$ (from fig. 6, Janbu (1957)) and $V/V_{max} = 0.20$ which is an unsafe prediction, since the footing fails by sliding and $V = 0$ (angle of basal friction $\leq$ angle of internal friction for a rough footing). In fact, the predictions from this equation are rather unsafe as may be easily seen from its form: for decreasing angles of internal friction, the relative bearing capacity increases, while the opposite would be expected to occur.

Reflecting on all these solutions it becomes very evident that the stability of a footing under an inclined load is a nonlinear problem of general shear failure and therefore the effect of both, the vertical and horizontal load components cannot be evaluated separately and superimposed. This will become even more obvious in the next chapter, where results from various experiments are presented and discussed.

1.2.1.4 Inclined-eccentric load

Based on the same argument, that the various components of the applied load on a footing should not be considered separately, the following relationship was suggested (Hansen, (1957,1970); Meyerhof (1963))

$$p = \frac{V}{A'} = \tfrac{1}{2}\gamma\, N_\gamma\, B'\, i_\gamma\, s_\gamma \qquad (1.13)$$

where p is the vertical stress component of the bearing capacity, A' is the effective area A' = B' × L' (B' is the effective width, B' = B - 2e, and L' is the effective length calculated similarly), N_γ is the corresponding bearing capacity factor and i_γ, s_γ are the inclination and shape factors respectively.

Expressions for the inclination factor have already been presented in the previous section, and various empirical relationships for the shape factor have been suggested by Meyerhof (1963), De Beer (1970) to which reference should be made for details. Each of the factors of equation (1.13) is established from the consideration of simpler individual cases, in which each effect is investigated separately. This clearly leads to an approximate solution utilising the method of superposition again. Nevertheless, this procedure provides a rather conservative solution to the general bearing capacity problem.

1.2.2 Experimental studies

The problem of the bearing capacity of footings on sand has been the subject of experimental investigation by a number of research workers, in an effort to evaluate various prediction techniques. Large scale or field tests on either prepared beds or on the actual soil are obviously the most advantageous, since, in particular, scale effects are thereby eliminated. However, the high cost due to the unavoidably expensive instrumentation, as well as the number of variables involved when in-situ soil is tested with inadequate control (e.g. permafrost, non-homogeneity of the soil, correct assessment of its mean density etc.), make comparison between predicted and observed behaviour rather difficult and the conclusions dubious. These have been the main reasons for the wide use of laboratory scale model tests, in which, under carefully controlled conditions the soil behaviour may be examined in greater detail. Even though direct prediction of the prototype behaviour needs careful consideration, the information that may be gained from model tests can be invaluable in understanding, at least, the general principles governing the problem under investigation. Consequently, it is not surprising that the bulk of the experimental studies has been

conducted at laboratory scale and relatively few at large scale.

In the following, the principal experimental contributions will be presented but the detailed results will be discussed and compared with the results of the present work in a later chapter. After a brief review of cases involving vertical symmetric load, a detailed account of experimental studies involving load eccentricity and/or inclination will be given.

1.2.2.1 Vertical central load

Small scale laboratory tests on sand have been reported by Golder (1941), Meyerhof (1948, 1951), Dhillon (1958, 1961), Hansen Bent (1961), Feda (1961), De Beer (1961, 1965, 1970), De Beer - Ladanyi (1961), L' Herminier et al (1961, 1965), Selig and McKee (1961), Vesic (1963), Ko and Davidson (1973), Tennekoon (1970), Graham and Stuart (1971), Yamaguchi (1976). These studies concerned surface or shallow rigid footings, of rectangular, square and circular shape, whose width (diameter) varied from 12.7 mm to 300 mm.

Two dimensional soil analogues (stacked cylindrical rods made from steel, dural, brass) have also been used instead of sand beds, by Schneebeli (1957), Biarez (1962), Biarez et al (1961), Giraudet (1965), Andrawes (1970). Their main advantages are the plane strain simulation free from the lateral wall-effects, the elimination (due to their structure) of the stresses (along their length), the quick preparation of the model after each test and the fact that the model's high density results in relatively high forces which can be measured easily.

Large scale tests (to the writer's knowledge) have been mainly performed at Degebo and were reported by Muhs (1965) - rectangular footings 0.6 × 1.2 m - Muhs (1959, 1961 from Milovic 1961) - Muhs (1952, 1953 from De Beer 1961) - square 1.0 × 1.0 m and rectangular 0.5 × 1.0 m - Muhs (1963) (from De Beer 1965a) - square 1.0 × 1.0 m. Similar scale tests were also performed by Giraudet (1965) and Milovic (1961).

All these experimental studies aimed at investigating the influence of various factors on the shallow footing problem such as the shape of footings (Meyerhof (1951), De Beer and Ladanyi (1961), De Beer (1965a, 1970), L'Herminier et al (1961), Vesic (1963)), size of the footing (Golder (1941), Eastwood (1951), De Beer (1961, 1965b), Feda (1961), Dhillon (1958), Tennekoon (1970), L'Herminier et al (1961)),

the relative density of the sand (Golder (1941), Meyerhof (1948), Hansen Bent (1961), De Beer (1961), Vesic (1963), L'Herminier et al (1965), Selig and McKee (1961)), as well as at the determination of the bearing capacity factors N (Meyerhof (1948, 1951), De Beer and Ladanyi (1961), Vesic (1963), De Beer (1970)). As a result, a number of correction factors have been suggested for each case, and some of them have been used in design, even though a rigorous theoretical (and large scale experimental) verification is not available as yet (Hansen, 1970; Bjerrum, 1973).

Experimental results from these studies tend to confirm, in general, that Terzaghi's bearing capacity solution gives too conservative results, even though there is a marked discrepancy on the proposed relationship between the selected angle of internal friction used for this prediction and the N_γ factor (fig. 1.5). If, however, the appropriate (plane strain) ϕ is employed, then both the Terzaghi and the Meyerhof bearing capacity equations overestimate the bearing capacity of a long footing (Ko and Scott, 1973).

This very bfief reference to the experimental side of the bearing capacity problem is by no means complete, the writer's intention being to show the extent of the experimental work so far undertaken in relation to the complication of the problem even in its simplest form (vertical symmetric load). The cases of the eccentric and/or inclined load will now be considered.

1.2.2.2 Eccentric load

Probably the earliest experimental study on eccentric loads was reported by Ramelot and Vandeperre (1950), in order to investigate the behaviour of electricity transmission tower footings subjected to large overturning moments. Square and circular footings of 200 and 300 mm width (diameter), tested on compact sand under various vertical load eccentricities, indicated a rapid decrease of the ultimate load with increasing eccentricity. This decrease could be safely predicted by the conventional theory for eccentricity to width ratios of up to 0.17 only ('middle third'), the prediction becoming unsafe for larger eccentricities (Meyerhof, 1953).

Following the results of an extensive experimental series, Meyerhof (1953) suggested that a safe prediction of the ultimate load could be obtained if the load was assumed to act in the centre of a fictitious footing of reduced width B' (= B-2e). Footings of 25.4 mm (1 in) width

and of various shapes were tested on loose and dense medium river sand ($\phi = 36^{o}$ and $\phi = 48^{o}$ respectively), and the average bearing capacity was found to decrease approximately parabolically with increasing eccentricity (along the axis parallel to the width of the footing).

Eastwood (1955) and Dhillon (1958, 1961) indicated that Meyerhof's - De Beer suggestion produced unsafe predictions for eccentricities within the 'middle third'. The former performed tests applying loads within the 'middle third' area only on rectangular footings with dimensions 152 × 457, 203 × 457, 254 × 457 mm on dense coarse sand contained in a wooden box braced with steel (3.0 × 1.5 × 0.9 m deep). Lateral movements of the footings were restrained in a number of tests and this produced approximately 8% higher failure loads than for the cases of a freely moving footing. A possible explanation may be that the failure surface during a 'restrained' loading was formed at the footing side away from the eccentricity and was deeper and longer than the surface formed during a 'non-restrained' loading, which developed on the same side as the load eccentricity.

The same loading system, but without lateral restraints, and with a more rigid tank (2.4 × 1.2 × 1.2 m made from steel supported plates) was used by Dhillon (1958); he undertook an extensive experimental study on the effect of load eccentricity on square and rectangular footings with width ranging from 152 mm (6 in) to 300 mm (12 in) and length over width ratio (L/B) varying from 1 to 4, and suggested some empirical formulae for the load-displacement, moment-tilt relationships and for the contact stress distribution (which, however, he did not measure). He also pointed out that Meyerhof's hypothesis gave too unsafe predictions. There is, however, some doubt on the applicability and validity of his strip footing results (L/B = 4), due to the relatively small thickness of the footings (12.7 mm becoming only 6.35 mm underneath the grooves where the load was applied by means of a knife edge), the relatively small length of the knife edge (0.40 of the length footing) and the rather inconsistent bed preparation (removal of only 0.5 m of sand, crude compaction of 150 mm layers, approximate levelling with a wooden screen).

Experiments performed by Biarez (1962) using a 2-dimensional analogue, consisting of duraluminium cylinders of 3 and 5 mm diameter ($\phi = 26^{o}$) and 60 mm length, indicated that the failure load underneath

a wooden footing of 300 mm width and 120 mm length loaded eccentrically was underestimated by the effective width concept.

Small scale, two-dimensional footing tests on loose sand ($\phi = 37^{o}$ from shear box) were reported by Zaharescu (1961a, 1961b). The maximum load eccentricity applied on the 72 mm wide footing (with rough base) was B/6, the load being applied by a knife edge sitting in grooves provided on the upper face of the model. Even though photographs were taken during the experiments, they were used only for the determination of the footing movement (fixed camera position) as well as for the determination of the elastic core (camera solidly fixed to the model). Despite the small number of experiments, very good agreement with the ' B' = B-2e ' concept was obtained and it was also shown that the apex of the elastic core triangle was formed in the direction of the eccentricity.

Experiments with varying footing widths were also carried out by Krivorotov (1965), Lee (1965), Prakash et al (1971). During the plane strain model tests, with steel plates of 100 to 300 mm width (and constant length of 760 mm) on dry medium dense sand ($\phi = 40^{o}$ from shear box tests), Krivorotov observed successive failure surfaces (2-4) subsequent to the initial one. This was also observed by Eastwood (1955) and similarly, on retaining walls, by James (1965), Bransby (1968) and on wedged footings on sand by Andrawes (1970). Lee (1965) applied pure moment and vertical central load independently on the 300 mm wide footing (L/B ranging from 1 to 3), but restricted any lateral movement. He also used buried earth pressure transducers to assess the normal contact stress distribution (see later section). His results (even though there is a possibility of side effects from the container) indicated an average rotation of 1^{o} at failure and were in good agreement with conventional theory and Meyerhof's concept for eccentricities up to B/6; for higher values, it seemed that the effective width concept overestimated the moment ratio (the peak moment for any specific vertical load over the maximum moment the soil can withstand), but the data was too limited for any firm conclusions to be drawn.

Both plane strain and three dimensional experiments were performed by Prakash et al (1971) with square and rectangular footings with widths ranging from 50 mm to 150 mm (on dry sand). Good agreement was obtained with the effective width concept as well as with the limit

equilibrium approach they developed, even though the actual contact width of the footing, could not be accurately determined since no contact stresses were measured.

The only large scale tests reported are those performed by Giraudet (1965), Muhs and Weiss (1969). Giraudet performed tests with a 0.4 m wide × 1.4 m long steel footing on two different sands, a coarse one (particle size 0.3 to 5 mm diameter, $\phi = 46^{o}$ from triaxial tests) and a fine one (0.1 - 0.5 mm diameter, $\phi = 40^{o}$ from triaxial tests), contained in a 6.5 m diameter and 4.4 m deep pit. Despite some scatter, the results seem to compare well with Meyerhof's suggestion for surface footings; a new coefficient of reduction was proposed as a better fit to the results, which, however, does not seem to give satisfactory predictions when compared with other people's experimental results (see chapter 2.3.1).

Muhs and Weiss (1969) and Weiss (1969) presented some experimental results from large footing tests on prepared sand gravel mixed fill of 150 m area ($\phi = 40^{o}$ to 42^{o} from triaxial tests). The footing, 2.0 m × 0.5 m × 0.8 thick/deep, made of concrete, was instrumented so that contact stresses could be measured (see section 1.4.3), and was loaded by a hydraulic jack. From the performed tests with vertical eccentric load along the axis parallel to the longest side, they concluded (supported by further experimental data, Muhs and Weiss, 1969) that the reduction in bearing capacity could be predicted by the 'fictional equivalent area' method suggested by De Beer (1949) (or 'effective width' method as it is also known, after Meyerhof (1953)). They also indicated that the failure surface started very near to the edge of the 'effective width'.

As a general conclusion, one might say that the 'effective width' method predictions lie well on the safe side, especially when foundations with large moments are considered, and its use in practical design seems to be justified.

1.2.2.3 Inclined load

The earliest investigation of this subject is reported by Meyerhof (1953), who performed tests with steel, rough based footings of 25.4 mm (1 in) width on dense sand ($\phi = 45^{o}$ from direct shear box) under a combination of vertical and horizontal loads (measured by proving rings). The bearing capacity was found to decrease rapidly with increasing angle

of inclination α of the resultant and approached zero when α was almost equal to ϕ.

A similar loading arrangement was used by Jumikis (1961), who carried out two-dimensional experiments using wooden footings of various widths (50, 75, 100, 125, 150 mm). The purpose of this investigation was to study the shape of the rupture surface and the effect of the width on it, and the use of black-stained horizontal sand layers enabled him to establish a logarithmic spiral as its best approximation, with the pole lying along the edge of the footing. However, no indication was given on the relationship between vertical and horizontal load, which was studied by Zaharescu (1961a, 1961b) employing a similar apparatus (already described in the previous section). He found (as may also be deduced from Meyerhof's results), that there is a maximum horizontal load which a footing can withstand (fig. 1.6) and that, from a state of stress of a point A away from the envelope $H = f(V)$, failure may occur by either increasing or decreasing the applied vertical load V. The slope of the tangent at a point of the envelope approaching $V = 0$ defines the angle of the base friction which was approximately 24^{o}, as it may be deduced from his experimental results (while $\phi = 37^{o}$). Field tests on gravel-sand (Kezdi, 1961) indicated similar behaviour (the angle of surface friction (33^{o}) approached the angle of internal friction (36.5^{o})),while Mencl (1961) reported tests performed with concrete blocks on rock which exhibited distinctly similar variation with α for a 'c,ϕ' soil (fig. 1.6 dotted line).

It is of interest to note here the similarity between footings under inclined loads and large scale field "plate-shear" tests (such as the ones referred to by Mencl (1961) and others reported by Evdokimov et al (1973))(see fig. 1.7). These tests were conducted at the base of foundation excavations for hydraulic structures in order to determine the shear strength parameters of the soil, which were found to differ considerably from those obtained from laboratory direct shear box tests. However, as they rightly pointed out, soil strength parameters obtained from such tests characterize the integral strength of foundations, while the corresponding laboratory values at best define the shear strength of the soil at the particular sampling point and under a stress state usually different from the actual one experienced in situ. In addition, invaluable information about the displacement of the foundation under combined loading may be obtained from the field

tests the behaviour of which cannot be realistically simulated by conventional laboratory procedures.

Kananyan (1970) carried out two-dimensional experiments with rough footings of various widths (up to 300 mm) on a finite thickness sand bed (maximum layer thickness 300 mm) under vertical and inclined loads, and showed that, for the same load inclination, the relative decrease of the bearing capacity (with respect to the vertical central load case) is smaller with increasing foundation width. However, his results were directly affected by the relatively small thickness of the sand sample and their applicability is rather questionable.

Tests under directly applied inclined loads (the ratio of the horizontal to the vertical load remaining constant) with small footings (B = 100 mm, L/B = 1,2,4) on dry uniform dense sand ($\phi = 42^{o}$ from triaxial tests) were reported by Saran et al (1971). The 20% difference between predicted (Meyerhof, 1953) and observed ultimate loads was claimed to have been due to the use of the ϕ value from triaxial tests instead of the appropriate plane strain one. It is, however, of interest to note the 13% average overprediction for the vertical symmetric case using the triaxial value for the angle of internal friction.

The effect of load inclination was studied experimentally on a large scale by Giraudet (1965) and Muhs and Weiss (1969, 1973). The former used the set up already described in the previous section with the two 50 ton hydraulic jacks inclined at 12.5^{o} and 22.5^{o} to the vertical and from tests on both surface and embedded footings he concluded that there was very good agreement with the inclination factors proposed by Meyerhof (1963). The test area and loading arrangements used by the latter are described in sections 1.2.2.1 and 1.4.3. In the first experimental series (Muhs and Weiss, 1969; Weiss, 1969) the inclined load acted parallel to the longer side of the 2.0 × 0.5 m rectangular concrete footing. From test results using 10^{o}, 20^{o} and 30^{o} angles of inclination, they suggested that the bearing capacity under an inclined load amounted to $1 - \tan \alpha$ of the bearing capacity under vertical load (α being the angle of inclination). One of the reasons for this reduction was attributed to the observed flatter form of the failure zone, which lay mainly in soil regions with lower normal stresses.

The case of a strip footing of 1.0 × 3.0 m under inclined load (parallel to the short edge) was studied during the second test series (Muhs and Weiss, 1973). The bearing capacity was found to decrease more rapidly with α than in the previous case, and, they suggested a reduction factor on the basis of a general form,

$$i = (1 - \beta_1 \tan \alpha)^{\beta_2}$$

where $\beta_1 = 1$ and $\beta_2 = 2$. This semi-empirical form had been proposed by Hansen (1957) with $\beta_1 = 1.5$ and $\beta_2 = 2$ and by Hansen (1970) with $\beta_1 = 0.7$ and $\beta_2 = 5$. They also pointed out that the length of the failure zone became smaller with increasing load inclination, implying a direct dependence of the ultimate bearing capacity on the size of the zone.

In summary, it has become evident that the effect of a horizontal load cannot be studied separately, adopting safety against sliding only and that it must be tackled in conjunction with the vertical load as a problem of general shear failure. This can be clearly demonstrated with the help of fig. 1.8: Designing a footing on the basis of bearing capacity under vertical load on the one hand and providing safety against sliding with $H < V \tan \delta$ for the horizontal load on the other, the combined (H,V) load may legitimately be anywhere inside area II, while the footing can withstand any load combination within the area I only, as has been already pointed out.

1.2.2.4 Eccentric-inclined load

The effect of an eccentric-inclined load on a footing has been studied experimentally by Meyerhof (1953) and Zaharescu (1961a,b) at small scale and by Muhs and Weiss (1969) and Weiss (1969) at large scale. Meyerhof distinguished between 'positive' and 'negative' eccentricity (fig. 1.9) and reported test results with 'positive' eccentricity only, whilst only referring to a preliminary study with 'negative' eccentricity.

The very distinct difference between the two cases was pointed out by Zaharescu who demonstrated, from a limited number of experimental results on sand (for details on experimental set up see previous section), that for the same vertical load × eccentricity, a higher horizontal load can be sustained by the footing, if the eccentricity is 'negative'. This difference diminishes for very low pressures as would be expected from the independence of the angle of base friction on the position of the

eccentric load. From the observed failure patterns, Zaharescu (1961a) suggested, as a qualitative explanation, that this relative increase in strength against horizontal loads was due to the different failure mechanisms which are observed when each case (eccentric or inclined) is considered on its own, and which, in the case of 'negative' eccentricity, they oppose each other. This will be further discussed in Chapter 2.3.3.

Muhs and Weiss (1969) performed tests with 'positive' eccentricity only and found that the bearing capacity under inclined eccentric load, as a proportion of the vertical central load case, can be determined by the product of the corresponding reduction factors when the effect of each component is taken into account separately.

1.3 Displacement of footings: A brief outline

The design of a foundation in sand is usually governed by maximum acceptable displacements rather than by an ultimate (bearing capacity) failure criterion. Indeed, bearing capacity corresponds to the load which will cause infinite displacements, while working load conditions correspond to the load which will cause acceptable ones. Thus, even though it is necessary to design footings against ultimate failure with a sufficient safety margin, the prediction of their relative displacements is still a major concern of the designer.

The prediction of displacements of footings on sand is clearly dependent upon one's knowledge of the engineering properties of such materials. These properties may be determined by either laboratory tests or in situ testing. Sampling of sands, however, is particularly difficult and undisturbed samples are virtually impossible to obtain. In situ tests are, therefore, the most common method of determining these properties. Of these, the small plate bearing load test (despite its major shortcomings of the difficulty in extrapolating the results to predict the behaviour of a prototype footing (Bjerrum and Eggestad, 1963) plus, in cases involving heterogeneous deposits, the considerable time and money required) provides values of subgrade moduli and shear strength for the sand which can be used to predict load-displacement relationships.

A less expensive but equally reliable method, the self-boring pressuremeter test, has been recently developed (see, for example, Windle (1976)). This provides direct measurements of moduli and shear strength as well as an estimate of the in situ horizontal stresses.

However, settlement analysis methods in sand are usually based upon two widely used in situ tests, the dynamic Standard Penetration Test (SPT) and the quasistatic Dutch cone test. They are relatively inexpensive and simple to perform and many methods have been developed which purport to establish the correlation between the blow count of the SPT, or the cone resistance of the Dutch cone, with the settlement of footings.

Many authors have reviewed and discussed these methods (Schmertmann 1970; Sanglerat, 1972; Sutherland, 1974; Jorden, 1977), and it is of interest to note that the predictions can vary by factors ranging from 5 (Simons et al, 1975) to even 14 (Bratchell et al, 1974). This is not really surprising since the determination of soil compressibility depends on many factors such as the stress history of the sand deposit and the position of the water table, which will not be indicated by the results of either of the tests. Furthermore, both tests subject the soil to large strains and thus the behaviour of the sand at small strains is difficult to assess. Plate bearing tests, however, do appear to be potentially more relevant involving as they do stress paths more similar to prototype structures and these may, therefore, finally lead to more reliable settlement predictions.

The above is by no means an exhaustive account of the methods used to predict displacements of footings on sand, nor of tests they are based upon. It merely illustrates some of the difficulties involved in providing sound predictions, difficulties which become even greater, when planar translation of the footing under an inclined load is to be considered. Intuitively, one might assume that a footing would move in the direction of the applied load. This does apply approximately to the two extreme cases, the vertical central load acting alone (H = 0), and the horizontal load under zero (or very small) vertical load (fig. 1.10), even though it is highly unlikely that an actual footing would move along either the v or the u axis alone (due, for example, to either structural constraints or local non-uniformities). However, as will be discussed in chapters 2, 6 and 8, there are indications, based on experimental evidence, that isolated footings do move along a displacement path inclined at an angle to the loading direction, the angle remaining practically constant for almost the entire loading sequence.

The various methods referred to above are mainly used to predict

only the vertical displacement (settlement) of a footing under a vertical centric force. Milovic et al (1970), using an elastic finite element analysis, calculated horizontal and vertical displacements, and rotation of a rigid perfectly rough footing under inclined and/or eccentric loads. They assumed that the footing rests on an elastic homogeneous isotropic layer of varying thickness (1,2,3B, B being the footing breadth) and limited by a rigid base, and that the soil properties are defined by the two elastic constants, a Young's modulus and a Poisson's ratio. Their solution shows that the displacement vector is always inclined at a constant angle with the loading vector, according to the relationship

$$\frac{u}{v} = K \tan \alpha \qquad (1.14)$$

where u is the horizontal displacement, v is the vertical displacement, α is the angle of the inclination of the load and K is a constant which depends on both the Poisson's ratio and the thickness of the layer, and is given in table form. When $\alpha = 0^{o}$ (H = 0) the displacement vector becomes coaxial with the V axis, while for no vertical load (V = 0) its direction coincides with the H axis (fig. 1.11). This is not an unexpected result, being similar to the 'sidesway' behaviour of structural frameworks under eccentric vertical load.

Since sand is fundamentally an inelastic material, it is not at all surprising that the elastic model used in the above analysis does not agree quantitatively with the behaviour of real footings. Nevertheless, when one considers the measurements made on real footings, the elastic result does imply that not all of the non-coaxiality of load and displacement vectors will be due to plastic response of the sand alone. Although, see chapters 2 and 6, the horizontal displacement recovery (elastic rebound) on unloading is quite negligible, this is not so for recovery under a purely vertical load and unload cycle. Therefore a precise analysis of the experimental data would need to separate the vertical displacement components due to non-linear elastic behaviour from the remaining entirely irrecoverable 'plastic' displacements.

1.4 Contact stress distribution

1.4.1 Introduction

It was pointed out in the preceding sections that knowledge of the load-displacement relationship, as well as of the bearing capacity of the foundation soil, is of high practical importance for an engineer. An immediate consequence, is that the contact stress distribution (hereafter abbreviated as c.s.d.) must be known, if a rational design of the foundation is to be made. The knowledge of both the normal and shear c.s.d. will help to establish the inclination (δ) of the resultant reaction stress vector at any point across the foundation. This inclination (δ) of the vector to the normal on the foundation base, referred to as the angle of base friction, is used in most earth pressure calculations, with the assumption that it is constant across the contact area (extreme methods, Brinch Hansen 1953). Experimental evidence, however, has shown this not to be valid (James, 1965; Bransby, 1968; Tennekoon, 1970). The same assumption is maintained in the Sokolovskii (1965) analysis, where the earth pressure coefficients are assumed constant with depth, as also is δ. Furthermore, the c.d.s. is often used as input in calculating load-displacement relationships, as well as for the determination of stresses and displacements in the soil, if an elastic approach is adopted.

In the following sections an account of the previous work on stress distribution will be presented.

1.4.2 Theoretically predicted c.s.d. - Literature review

The c.s.d. on an elastic foundation, depends upon the elastic properties of the supporting soil and the flexural rigidity of the foundation. For a perfectly flexible footing the stress distribution is uniform, since the footing follows the deflection of the ground. For an infinitely rigid circular foundation on an elastic medium, Boussinesq has shown that the pressure distribution has a minimum of $p_m/2$ under the centre of the plate and increases to infinity at the edges (Terzaghi, 1943), according to the relationship

$$p_{zz} = \frac{p_m}{2\sqrt{1-\left(\frac{\rho}{r}\right)^2}} \qquad (1.15)$$

where p_{zz} is the normal stress component on the interface (z is the

vertical axis), p_m is the mean applied pressure per unit area of the base, r is the radius of the foundation and ρ is the distance from the centre of the base to a given point ($\rho \leq r$). (see fig. 1.12). The basic assumptions of the Boussinesq analysis are, in addition to those of linear elasticity (a) there is no friction at the plane of contact and (b) the plane of contact is horizontal.

Most foundations, however, possess a definite rigidity, and it is of importance to estimate the effect of the rigidity on the c.s.d.. Borowicka (1936) analysed the normal c.s.d. on circular footings under a vertical central load. The footings considered had finite rigidities, ranging from perfectly flexible to perfectly rigid, and were assumed to lie on a semi-infinite elastic isotropic mass. As may be seen from figure 1.13, where the c.s.d. for different rigidities are presented, the stiffer the footing the less uniform is the stress distribution. It is of interest to note that even for quite small footing stiffnesses the distribution of contact stresses is very different from uniform. Again, Barden (1962), proposed an approximate method of obtaining the c.s.d. underneath a plate of varying rigidity and resting on an elastic soil, either isotropic or anisotropic, based on De Beer's method (Bo-Göran Hellers and Olle Orrje, 1969). In his analysis, as in the ones mentioned above, the effect of the shear stresses on the contact area was not considered; indeed, Barden commented - on the same lines as Terzaghi (1943) - that the shear effect was not much understood, but was taken to be of secondary importance in comparison with the vertical normal stresses.

An attempt to examine the effect of the relative roughness of the base of an elastic raft, resting on elastic soil, on the c.s.d. had already been presented by Parkes (1956). By varying the Poisson ratio of the medium, he showed that when the footing is perfectly rough, the c.s.d. is slightly greater than that of a smooth one - for Poisson ratio less than 0.5 - but that there was no difference when the Poisson ratio was taken as 0.5.

So far only the effect of a vertical load acting at the centre of the foundation has been presented. The shear and normal c.s.d. resulting from the application of an inclined and/or eccentric force on an infinitely rigid strip footing have been calculated by Milovic et al (1970) using the finite element method. (The various assumptions made

by the authors have been already presented in section 1.3). They presented both the normal and shear stress distributions with varying values of μ, depth of layer, eccentricity and inclination of the load, in table form. Again, the normal stress distribution is of an inverted parabolic shape with infinite values at the edges. This shape, which is obtained in the case of a soil with linear law of deformation and constant E, becomes more uniform in the case of E increasing with depth. This effect of heterogeneity and non-linearity of deformation of the foundation soil on the normal c.s.d. across the width of a rigid footing (loaded vertically either centrally or eccentrically) was considered by Zaretsky and Tsytovich (1965). (E = Young's modulus)

It has been shown, according to the elastic analysis, that the normal c.s.d. underneath an infinitely rigid slab on an elastic soil is a minimum at the centre and infinite at the edges of the foundation (fig. 1.12), the latter being a direct consequence of the assumption that Hooke's law is valid at all stress levels. This, however, is not a realistic assumption, since the stresses at the edges cannot be higher than the strength of the soil.

Considering, now, a soil in a state of limiting equilibrium, and assuming that it possesses no cohesion, the normal c.s.d. underneath a footing (with no surcharge) has to be zero at the edges (since no lateral support exists there) and, by analogy to the passive earth-pressure problem, to increase with distance from the edge. If it is assumed that the limiting stress increases linearly with distance, from zero at the edges, the triangular distribution shown in figure 1.14a will be obtained (Prandtl distribution). Adding the effect of the cohesion and surcharge (uniform distribution), the normal c.s.d. becomes the one shown in figure 1.14b. Schultze (1961) combined the plastic state solution, outlined above, with the elastic state one, which follows Boussinesq, to suggest a probable normal c.s.d. The elastic part is governed by the equation (based on a solution by M. Sadovsky (Tsytovich, 1961)):

$$p_s(x) = \frac{2p}{\pi B} \frac{1}{\sqrt{1 - \left(\frac{2x}{B}\right)^2}} \qquad (1.16)$$

where B is the width of the foundation and p is the axial pressure on the foundation. The normal c.s.d. for the ultimate load (plastic state)

is given by the equation:

$$p_s(x) = cN_c + \gamma_1 N_q D + 2B \gamma_2 N_\gamma (1 - \frac{2x}{B}) \qquad (1.17)$$

where γ_1, γ_2 is the unit weight of the soil above and below the level of the foundation, D is the foundation depth, and N_γ, N_c, N_q are factors depending on the angle of internal friction (fig. 1.15). The combined solution is shown in figure 1.15 by the continuous lines, and is based on the assumption that in the middle regions under the footing, Boussinesq's distribution is valid, but that at the edges the bearing capacity cannot be exceeded, thus attaining limiting stress values. A number of field measurements, reported by Schultze (1961), shows a qualitative agreement with the c.s.d. proposed.

Gorbunov-Possadov (1961,1965), considering the stability of a dense sand bed under a rigid, rough, vertically centrally loaded shallow strip footing, predicted both the normal and shear c.s.d. using an elastic analysis and assuming the soil underneath the footing to be in an elastic state and that the stresses at the corners are zero. The derived shape of the normal c.s.d. is that of a 'saddle' with a smooth dip in the centre of the footing, whereas the shape of the shear c.s.d. is skew-symmetric (fig. 1.16). This is a distinct improvement over the classical Boussinesq solution and has, qualitatively at least, been verified by experimental results (an account of the experimentally obtained c.s.d. will be presented in the next section). It is worth noting that the saddle-type normal stress distribution was suggested as a probable shape for a rigid foundation resting on a sand bed by Taylor, as early as 1938!

Considering sand as a particulate body rather than an elastic medium, Smoltczyk (1967) used a statistical theory to obtain the normal stress distribution on a rigid footing resting on sand. A not so pronounced saddle-type distribution (as the one predicted by Gorbunov-Posadov) at small external loads is followed by an almost parabolic one (the stresses at the corners being zero), when the applied load approaches the bearing capacity of the soil.

More recently Biernatowski (1973) presented a solution for the c.s.d. underneath an infinitely rigid foundation, based on the assumption that the stresses and deformations in the contact area are characterised by an elastic-plastic state. The distribution he suggested agrees qualitatively

with that of Schultze (1961) (see fig. 1.15). Graham and Stuart (1971) used a modified Sokolovski analysis involving constant angle of internal friction condition and a linear variation of the base angle of friction δ from zero at the centre to its maximum at the edge of the footing ($\delta = \phi$). The calculated normal c.s.d., shown in figure 1.17, has a fairly sharp dip on the axis of symmetry of the foundation, compared with the saddle-shaped distribution predicted by Gorbunov-Posadov, but becomes less sharp and tends to a parabolic shape as the footing width increases. Finally Snarskii (1974) combined the elastic theory with the theory of limiting equilibrium, for the case of a rigid circular footing with surcharge, to obtain a c.s.d. similar to that derived from the elastic theory (Boussinesq type) but with finite values at the edges.

Soil, as is well known, is a material neither purely elastic nor purely plastic, and any simple theoretical attempt to predict the exact c.s.d. under footings resting on soil is bound to be invalidated by the many known and unknown factors not included in the analysis. A theoretical approach may be directed more reliably, if it is assisted by experimental and field evidence. In view of this fact, many workers have performed a variety of experiments either small or large scale ones, including tests in laboratories, as well as field tests. A review of their work will be attempted in the next section.

1.4.3 Experimental work on c.s.d.

1.4.3.1 Stress distribution under a vertical-central load

The earliest report on experimentally measured stress distributions comes from Koegler and Scheidig (1927 - 1929) (Tschebotarioff, 1951). They performed tests on sand using footings with different widths (340, 450, 630 and 1000 mm) and with special pressure measuring cells, embedded on the lower face of the foundation, in order to measure the variation of the reaction forces across the contact area. A pronounced parabolic distribution was obtained for a vertical central load acting on the narrower width used, becoming considerably flatter as the width increased (fig. 1.18). In 1933, O. Faber used a 300 mm (12 in.) diameter footing which was composed of six equal area concentric rings, each of which was connected to a rigid top plate by three 6.35 mm (0.25 in) diameter steel

rods. The average pressure acting on each of those rings was obtained by measuring the compression of the steel rods using an extensometer on the extensometer gauge holes provided on them. Tests were performed by applying a vertical central load to the footing resting either on Leighton-Buzzard sand or London clay, contained in a tank approximately 700 mm diameter and 500 mm depth. The results from tests on sand indicated an approximately parabolic shape of c.s.d. which became more pronounced with increasing load (fig. 1.13).

The development of a small earth pressure cell by Arthur and Roscoe (1961), which could be built into the sides and base of the foundation to measure local contact stresses, initiated an extensive research programme on retaining walls at Cambridge (Roscoe, 1970). Since that time a variety of load cells has been designed and used in various apparatuses, one of which is the footing used by the author. Similar load cells were also developed at Southampton (Andrawes, 1970; Tanner, 1972), which were used for the investigation of earth pressure problems. A number of these load cells was also used by the author in his experiments.

Large scale tests on instrumented footings were reported by Leussink and Schweickert (1963). Tests results from a 1.0 m square concrete block under a vertical central load on dense sand, indicated that the c.s.d., measured with the help of 98 gauges on the footing base, had an almost uniform shape at low stress levels, became a saddle type one at intermediate stages and reached a 'flattened' triangular shape with zero stresses at the edges, for loads approaching the ultimate bearing capacity (fig. 1.20).

Faber's idea formed the basis of the design of an apparatus by Chae, Richart and Hall (1965). They investigated mainly the dynamic pressure distribution beneath a vibrating footing but for the static case the distribution then obtained was very similar to Faber's (1933)., It is worth noting that the saddle-shaped distribution, predicted by the elastic analysis of Gorbunov-Possadov and the similar shape one predicted by Schultze and Smoltzyk, was not observed by Koegler and Scheidig, Faber and Chae et al, whereas it was observed during the experiments of many other workers whose work will be outlined below (Leussink and Schweickert, Murzenko, Krivorotov, Skormin and Malyshev, Ho and Lopes,

Muhs, Hartikainen, Lasebnik, Tennekoon, Zangl). This difference appears to be due mainly to the relative rigidity of the footings used.

Field tests involving a concrete footing (0.6 × 1.2 m) lying on sand of different densities and supporting a vertical central load, were reported by Muhs (1965). Specially designed gauges, capable of measuring both the normal and shear contact forces, were placed into the base of a concrete block, which was eventually positioned on the sand surface. The water level was always at the sand surface level, so as to eliminate any apparent cohesion in the sand. The results, shown in figure 1.21, indicate a distinct saddle-shaped c.s.d. for intermediate loading stages, after an almost uniform one during initial loading. As the load approaches the ultimate bearing capacity, the c.s.d. changes over to a parabolic form. The shear stress distribution, on the other hand, follows an approximately skew-symmetric pattern with the maximum stresses concentrated near the footing edges decreasing rapidly to zero at the centre. This shear stress pattern is to be expected since the sand particles try to move away from the centre towards the edges of the foundation.

Experimental data from Berezantsev (1952), Malyshev (1953), and Kananyan (1954), on the saddle-shaped normal c.s.d. were reported by Gorbunov-Possadov (1965). A number of research workers have since then reported similar experimental observations. Murzenko (1965) used steel, slightly roughened, square footings of dimensions 500 × 500 mm, 700 × 700 mm, and special dynamometers, which were embedded in the sand before the footing was placed, in order to measure the local reaction forces. His tests on dense sand showed that the well-marked saddle-like c.s.d., which was observed at low stress levels, changed to a less-pronounced one with stresses at the centre increasing faster, and stresses near the edges decreasing.

A similar technique for the measurement of the contact forces was employed by Krivorotov (1969). Small electrical pressure cells embedded in the sand at various inclinations (horizontal, 45^{o} to the vertical, vertical) enabled him to measure the normal c.s.d. and to calculate the shear c.s.d. from the measured pressures at different inclinations. The mainly uniform normal stress distribution, at initial stages, became a saddle-type one for the total applied loads up to 85% of the ultimate one; the shear stresses, necessarily zero at the centre, reach their maximum at points approximately 0.4 × B away from the centre (where B is the width of the footing, in this case 300 mm). The unbalanced shear

stress diagram probably implies a non-symmetric settlement and, eventually, a one-sided failure. This is also implied by the non-symmetrical 'saddle' of the normal c.s.d. (A similar case was reported by Muhs (1965)).

The concavity of the normal c.s.d. was also observed by Hueckel et al (1965) on an embedded fully instrumented square vertical plate. The plate itself consisted of load cells which were capable of measuring the normal contact forces, and was driven horizontally into a sand bed. It is of interest that this concave shape is maintained even in the case of buried foundations, and since, to the author's knowledge, there is no other experimental evidence of c.s.d. on embedded footings, the observed shape is currently accepted as the actual one.

A rigid circular reinforced concrete slab, 600 mm diameter, with a sand-coated metal base was used by Skormin and Malyshev (1970) in their tests on medium dense sand. Hydraulic dynamometers were embedded in the sand near the footing base in the 4.0 × 4.0 m pit. The normal c.s.d., derived from readings from 21 diametrically arranged dynamometers showed that from an initial slightly saddle-type shape, it became slightly parabolic at intermediate stages; this was followed by a well-marked concave shape at its middle, before obtaining an approximately parabolic form near the failure condition. A similar pattern was observed by Ho and Lopes (1969), from tests performed on dense sand, using a 150 mm diameter circular footing with pressure transducers mounted on it: the initially parabolic curve changed to a concave one, which was maintained throughout the rest of the first cycle as well as for the next two cycles performed. Such a stress redistribution effect had been also observed by Murzenko (1965), who stressed additionally that this was still the case when many more cycles were executed, the more pronounced redistribution occurring after the second cycle (providing that the same limit load for each cycle was maintained).

Hartikainen (1973) followed Faber's idea again for the design of his 300 mm square footing. Equal area square steel blocks composed the active face and were connected to the top rigid plate each by a steel rod, their compression being measured by strain gauges bonded to them. A thin aluminium sheet with strain gauges bonded to both faces of it, and located between the rods in parallel with the contact face, was used to measure the horizontal forces acting on the footing. At the

initial stages, the normal stresses were higher at the edges and lower at the centre, changing over to completely the opposite shape for higher load values. The shear stresses followed the expected pattern of higher values near the edges and decreasing to zero at the centre. It is of interest to notice the dip of the normal c.s.d. at the centre of the footing, despite the fact that the basic idea is the same one used by Faber and Chae et al. This is probably due to the very short length of the steel rods used which therefore produced a higher rigidity footing. This, too, seems to be the case in the experiments by Lasebnik (1973); a saddle-like distribution was observed underneath a reinforced concrete foundation, resting on sand, with pressures measured by pressure cells mounted in the face of the footing.

To round off the presentation of the experimental work by various workers on the c.s.d. produced by a vertical central load acting on a footing resting on sand, the work at Cambridge will now be presented briefly. Tests on dense Leighton-Buzzard sand were performed by Tennekoon (1970) using a fully instrumented footing (description and performance of the footing is discussed in chapters 3,4,6). Results from his tests were in good agreement with the experimental findings of the other research workers so far reported. The initial, almost uniform, distribution of normal stresses, is followed by a not very pronounced saddle-like one, ending up as an almost parabolic (or curved triangular) shape for load levels approaching failure. An expected skew - symmetric shear c.s.d. was also observed, which was maintained throughout the test duration, the highest values being recorded at approximately $0.25 \times B$ from the centre of the footing (except for the very initial stages, where the maximum values were recorded near the edges). Results from a basically similar experimental set up at Karlsruhe, reported by Zangl (1977), provide a further experimental support for a similar c.s.d. underneath a rigid footing on sand, as that observed in most test results discussed so far, which implies that it may represent the actual c.s.d. for a rigid foundation on sand under vertical central load.

1.4.3.2 Stress distribution under eccentric and/or inclined loads

A much more limited amount of experimental evidence is available to support the c.s.d. for cases with load inclination and eccentricity. Lee's report on eccentrically loaded footings (1965) and Muhs and Weiss' report on inclined and/or eccentric loads on large foundations (1969,1973)

seem to be, to the author's knowledge, the only reported works on the subject.

Lee (1965) designed a controlled-deformation and rotation mechanism to apply moment and central vertical force independently to 38 mm-thick steel model footings of varying plan dimensions (300 × 300, 300 × 600, 300 × 900 and 325 × 900 mm). The tests were performed on dry dense sand contained in a tank of plan dimensions 1.8 × 1.8 m and 1.5 m deep. Two different types of pressure cells were used to record the contact normal stresses, both embedded in the sand underneath the model footings. One type of cell used, the vibrating wire boundary type (Trollope and Lee, 1961), was placed in the sand so that its active face would be in direct contact with the base of the footing. Test results indicated that for small eccentricities ($e/B \leq 0.083$) a non-symmetric saddle-shaped distribution was observed, with zero at the edges, its highest value appearing underneath the side of the footing, where the eccentric load acted. (fig. 1.22a). (Unfortunately, no indication was given of which stage of the test the distribution represented). For larger eccentricities ($e/B = 0.17$), a curved triangular shape was observed, again with zero stress at the edges and highest value towards the side where the eccentricity of the load lies (fig. 1.22b). For eccentricities of the order of $e/B = 0.33$, the c.s.d. indicated that part of the footing was not in contact with the sand (for a particular stage of the test which seemed to be close to the failure load), (fig. 1.22c). Some scatter of results occurred, the reasons for which will be discussed at the end of this section.

Large scale field tests with prefabricated concrete footings were performed by Muhs and Weiss (1969, 1973). A test area of 150 m^2 was used to prepare a 5 m deep sand-gravel mixture fill, the water level reaching the surface of the ground. Two series of tests were performed: during the first series, (Muhs and Weiss, 1969; Weiss, 1969), a 0.5 × 2.0 m footing was loaded along its long axis (2.0 m) by vertical or inclined central loads. The load was applied via a hydraulic jack, the initial load inclination being maintained with the help of a smaller horizontally placed hydraulic jack. The eccentricity of the vertically applied load produced an approximately triangular reaction of normal stresses (as expected), which was measured by four pressure gauges built into the base of the footing (Muhs, 1965). No indication was given of the shear c.s.d. An inclined central load produced a normal c.s.d. with

slightly higher stresses near the sides rather than at the centre, whereas the shear c.s.d. was reported to be of triangular shape with its maximum underneath one edge of the footing. The same patterns were maintained until failure occurred.

The second series of tests (Muhs and Weiss, 1973) was carried out with the intention of simulating a plane strain condition, at least underneath the centre of the foundation. For that purpose a new footing was constructed, with plan dimensions 1.0 × 3.0 m and the applied inclined central load acted along the short axis (1.0 m). First indications deriving from an unfinished (then) analysis of the data, showed that the normal c.s.d. reached a parabolic shape along the centre cross-section during failure, the distribution which may be expected from the vertical component of the applied load. An increase of the maximum (mobilised) angle of base friction with increasing load inclination was observed, but the detailed description of the measured shear stress distribution was not presented. It is of interest to notice that the normal (and shear) c.s.d. were not affected by the presence of the horizontal hydraulic jack which, whilst maintaining the initial load inclination, would appear to impose restrictions on the footing movements.

This lack of experimental information on the c.s.d. problem in cases of general planar loads, was one of the reasons that prompted the research undertaken by the author.

1.4.4 Discussion of experimental techniques

The various experimental techniques used by research workers to investigate the c.s.d. problem may be divided into two categories: In the first pressure cells are embedded in the sand fairly near the base of the footing and, in all probability, the stresses recorded by those devices will also represent the actual stresses acting upon the foundation base. (Koegler and Scheidig,(1927-29), Lee (1965), Murzenko (1965) Krivorotov (1969), Skormin and Malyshev (1970)). The second one seems to employ special devices (namely, load cells) which may be either mounted on the contact face of the footing, or themselves comprise the base of the foundation. (Faber (19), Chae et al (1965), Sutherland and Lindsay (1961), Authur and Roscoe (1961), Muhs (1965), Ho and Lopes (1969), Hueckel et al (1965), James (1965), Roscoe (1970), Tennekoon (1970), Zangl (1977)).

Results using the former technique become more reliable if the actual size of the earth pressure cell is small even though they cannot be too small, since their minimum side should be at least 50 grain diameters, and the number of the cells underneath the foundation is sufficient to provide a distinct c.s.d. But, however small the cells may be, - and their sizes, up to now, are considerable (see Krivorotov (1969), Trollope and Lee (1961), Prange (1971)) - they do interfere with the soil; firstly, because the cell's behaviour differs from that of the soil, and, secondly, because of the cable connections, employed to carry out of the soil the measuring signals. This latter disadvantage may be avoided completely by the use of telemetry (transmission of data by radio - Prange (1971)). A further reason limiting the use of the embedded cells to large scale tests only and away from the surface, is that the zone in which stress redistribution within the soil may occur, following the cell's diaphragm movement, is restricted to that of a cone having the cell diaphragm as its base, and side slopes of approximately 60^{o} (Trollope and Lee, 1961). This indicates that the minimum depth for a cell of 40 mm diameter diaphragm (usual diaphragm dimension) is approximately 35 mm. A similar observation was made by Prange (1971), where rigid cones were formed around the telemetric cells he had embedded in sand, and traced via X-ray photography. Consequently, it is reasonable to suggest that this technique is justified in large laboratory or field experiments, where the dimensions of the embedded cells may be relatively small (Lee, 1961). However, the roughness of the base and its effect on the shear and normal c.s.d. is not easily obtained (Krivorotov, 1969).

The latter technique may be subdivided into two smaller sections: In the first section the devices are mounted on the already made base of the footing (Muhs, 1965), whereas in the second section the load cells comprise the footing itself, or part of it (Tennekoon, 1970). Depending on the sophistication of the design of such a cell, the normal force, the shear force and the eccentricity of the normal force in either one or both axes of the contact area may be measured (Bransby, 1973). If part of the contact face is composed of such devices then care must be taken that the deflection characteristics of both the solid part and the load cell part are the same. The cells, also, must deflect freely, without any interference from neighbouring parts. The relative imponderables of the former technique are not met in the latter. However, the

size of the load cells must also be relatively small, if they are to be used in small scale experiments (Larsen, 1977). Furthermore, their location is independent of the soil movement, so that they may record any redistribution of stresses (their relative position not being affected), unlike the embedded devices of the first category. Finally, they may be used for the investigation of the dynamic pressure distribution beneath cyclically loaded or vibrating foundations, where the use of embedded measuring devices is rather inappropriate.

1.5 Conclusions - Scope of the present work

It is hoped that the summary of previously published theoretical and extensive experimental investigations of surface footings under general planar loads presented in the preceding sections demonstrates, in contrast to the usual design method assumptions, the complexity of the problem in a simple but clear manner. It also becomes apparent that, surprisingly, there is still a lack of carefully controlled experiments, for failure loads and even more so for displacements, especially when eccentric and/or inclined loads are considered; that no data are available on displacement and strain patterns within the soil for cases with non-symmetric loads and that only little, low accuracy, information can be found on the contact stress distribution under these loading conditions.

When one considers the enormous structures involved in the North Sea Oil adventure and follows the basic principles behind the design of their foundation (Bjerrum, 1973), one is immediately aware of the lack of a rational solution to such problems and the very great need for comprehensive and precise experimental results against which improved analytical and design methods can be checked, although, even if the model scale footing problem could be understood adequately, the extrapolation to prototype scale structures and stress levels would still remain as a major problem.

Therefore the problem selected for investigation by the author is the behaviour of surface footings on sand under general planar loads. This choice was further encouraged by the existence of sophisticated experimental 'tools' at both Cambridge University (contact load cell and radiographic technique) and Southampton University (stereophotogrammetric technique and normal contact stress cell). Such 'tools'

have enabled a very accurate investigation to be conducted and reliable detailed information to be obtained, in addition to comparisons between nominally identical experiments on geometrically different apparatuses.

The main objectives of this research work have been the following:

1) To obtain reliable data from a number of carefully controlled and instrumented model tests concerning the planar displacements, contact stress distribution and soil deformation characteristics of a rigid surface strip footing on sand under general planar loads. The tests were performed under plane strain conditions and three different apparatuses were employed during the research project.

2) To investigate the effect of the width of a narrow tank on the results from model tests by conducting nominally identical tests in both narrow and wide sand beds.

3) To investigate the effect of the glass-side friction on the displacement fields obtained by the Stereophotogrammetric technique, by employing both this and the X-ray techniques at the same tests and at the same load intervals.

Finally, it is hoped that some of the simple analytical approaches presented contain the nucleus of ideas which can be extended to provide a basis for more rational analytical and design methods for such footings.

CHAPTER 2

EXPERIMENTAL WORK PART I - PRELIMINARY INVESTIGATION

2.1 Introduction

A preliminary experimental investigation was carried out by the author at Cambridge, in order to elucidate the most important areas for the main research programme. A large number of tests was performed with strip footings under various load combinations. The same sand was used in all of the three experimental series, so that the test results from this preliminary study could be used for planning of the experiments in the main apparatuses. As it will be seen, however, the experimental results helped to generate some very interesting ideas and to initiate a simple analytical approach which promises areas of fruitful future expansion.

2.2 The apparatus - Small footing rig

A small glass sided tank 970 × 290 × 215 mm deep, raised at about 1.0 m above the floor and supported by a steel framework was used for the experiments. The footings used were of stainless steel, with constant thickness of 5 mm and length of 250 mm in a variety of widths from 10 to 50 mm, in steps of 10 mm. In some cases, the steel base was covered with 2S grade sandpaper, in order to obtain a relatively rough surface. A hook was attached on the long side of each footing, so that a direct horizontal load could be applied. This small apparatus, which was designed by Dr. R.G. James, provided facilities for applying independently both vertical and horizontal loads. The vertical load was applied by means of weights on a steel hanger, which in its turn applied the load to the footing via a stainless steel pointed rod, sitting in one of the indentations in the top surface. The horizontal load was applied by weights attached to a cable running over a pulley through a hole to the hook (fig. 2.1).

The 14-25 BS Leighton-Buzzard sand was in most cases poured from a hopper hanging over the tank area to obtain medium density samples (voids ratio ranging from 0.5 to 0.6). This average density could also be obtained by vibrating the base of the tank with an electric hammer, but

that method was used in few cases only. In almost all the experiments performed, the sand surface was levelled accurately (see chapter 3.6) so that the volume of the sand mass could be determined, and, therefore, the density of the fill estimated.

Planar translation of the footing was recorded by a set of two mechanical dial gauges (0.01 mm/division) with magnetic bases attached to the rigid frame. A third dial gauge was also used when the in plane rotation was to be recorded.

2.3 Presentation and discussion of the experimental results

2.3.1 Vertical eccentric load

A series of tests with varying .eccentricities was conducted under vertical load. As expected, a pronounced decrease of the failure load with increasing eccentricity was observed, as shown in fig. 2.2, where the failure load ratio $V/V_{e=o} = V/V_{max}$ (the ratio of the failure load at a particular eccentricity over the ultimate failure load with zero eccentricity), is plotted against the 'eccentricity ratio' e/ B (the ratio of the eccentricity over the width of the footing). The results (fig. 2.2, the best fit curve $(1 - 1.9E)^2$ correlation coefficient 0.989) compare favourably with both the De Beer-Meyerhof 'effective width' concept (curve $(1-2E)^2$) and, for eccentricities up to B/6 (E = 0.167), with the conventional theory (i.e. assumed straight line contact pressure distribution with the maximum pressure at the corner equal to the average pressure under a vertical central load). However, for larger eccentricities, the predictions of the latter theory are unsafe by approximately 50%.

Published experimental results by several research workers together with results from the author's various experiments are plotted in fig. 2.3. The mean curve, calculated by a least squares method, is also drawn, together with the curves derived from the effective width idea, the exponential suggestion by Giraudet (1965) and the conventional theory, which are expressed by the following relationships respectively :
Mean curve of the experimental data:

$$\frac{V}{V_{max}} = 0.976 - 3.13E + 2.38(E)^2 \qquad (2.1)$$

'Effective width' concept:

$$\frac{V}{V_{max}} = (1 - 2E)^2 \qquad (2.2)$$

Suggestion by Giraudet (1965):

$$\frac{V}{V_{max}} = \epsilon^{-12E} \qquad (2.3)$$

where $\epsilon = 2.7183$.

Conventional theory:

$$\frac{V}{V_{max}} = \frac{1}{1 + 6E} \quad \text{for } 0 \leq E \leq \frac{1}{6}$$

$$\frac{V}{V_{max}} = \frac{3}{2}\left(\tfrac{1}{2} - E\right) \quad \text{for } \frac{1}{6} \leq E \leq \tfrac{1}{2} \qquad (2.4)$$

The exponential expression seems to give the least safe predictions, while the 'effective width' concept serves as a lower boundary to the experimental results, especially for eccentricity ratios greater than 0.10, where the effect of the conservative assumptions becomes rather distinct. Predictions from the conventional theory lie on the safe side for eccentricities within the 'middle third', but become unsafe for greater eccentricities.

A footing under a vertical eccentric load V may be considered as subjected to a vertical load V and a moment M, which is equal to the load V times its distance from the centre. The effect of a moment acting on a footing resting on sand is shown in figs 2.4 and 2.5, where the experimental results from fig. 2.3 are used again, but plotted in the $\frac{V}{V_{e=o}} = \frac{V}{V_{max}}$ versus $\frac{M}{V_{max}B} = \frac{Ve}{V_{max}B}$ plane in fig. 2.4, while fig. 2.5 is a normalized diagram on the V - M plane with respect to V_{max} and M_{max} respectively. There is a maximum moment, which the footing can withstand, and this is attained when approximately half of the ultimate vertical central load is acting on it. In fact, a mean value of 0.492 (s.d. =

± 0.066) for the V/V_{max} ratio, corresponds to a mean value of 0.091 (s.d. = ± 0.011) for the $M/V_{max}B$ ratio,both these values being derived from the test points of fig. 2.4. This mean value of the maximum dimensionless moment implies an eccentricity of the applied vertical eccentric load $V = V_{max}/2$ of 0.185 B, which is a little over the one third of the footing width. The 'effective width' concept, on the other hand, predicts that maximum moment is obtained at $V/V_{max} = 0.44$ when this eccentric load acts at the middle third of the footing, the maximum moment being 17% smaller than the experimental average ($M_{max}/V_{max}B$ = 0.0741).

Considering the results presented above, it seems reasonable to infer that a surface footing can withstand a maximum moment of 1/10 of the product $V_m \times B$, when the vertical load acting on it is one half of the ultimate load.

2.3.2 Inclined central load

The effect of a horizontal load acting on a centrally vertically loaded footing has been investigated by a series of tests with 30 mm and 50 mm width footings, the results from which are shown in figs. 2.6, 2.7a. The sharp decrease in bearing capacity with increasing inclination of the applied load is evident from fig. 2.6 (in which the normalized bearing capacity (V/V_{max}) is plotted against the load inclination); a small load inclination, say 0.1 ($\simeq 5^o$), causes as much as 20% reduction to the bearing capacity. It is of interest to note that for quite a wide range of load inclinations, the relative bearing capacity is not greatly affected by the angle of internal friction of the sand, as may be seen from fig. 2.6, where tests at various sand densities are presented (the angles on internal friction are obtained from Stroud's tests in the Simple Shear Apparatus (1971)). The size of the footing, too, does not seem to affect the relative bearing capacity decrease at any load inclination (compare B = 30 mm, e_o = 0.53 mm, B = 76.2 mm (L = 190.5 mm), e_o = 0.52 mm, B = 76.2 mm (L = 584 mm), e_o = 0.54). However, it is well established that scale effects do exist because of the stress level dependence of the angle of internal friction (see chapter 1.2.1.1) and this probably implies that only the N_γ factor is influenced by these effects.

To a first approximation, the inclination factor ($V/V_{H=o}$) could be expressed by two straight lines, the first relating $V/V_{H=o}$ and tan α for inclinations up to about 20^o, and the second for higher inclinations, the slope of the latter being furnished by the angle of basal friction ($V/V_{H=o}$ for tan α = tan δ) (see fig. 2.6). A better correlation is obtained for inclinations up to 30^o, with a second degree curve (fig. 2.6) of the form $\frac{V}{V_{H=o}} = \frac{V}{V_{max}} = (1 - \beta_1 \frac{H}{V})^2$, and a regression analysis of the results gave $\beta_1 = 1.36$ (with $r^2 = 0.942$) which is similar to the relationship proposed by Hansen (1957) ($\beta_1 = 1.5$). For inclinations bigger than 30^o a straight line relationship seems to give a safe estimate of the vertical component of the load.

A normalised diagram (with respect to V_{max}) of the results is shown in fig. 2.7a. Between the ultimate bearing capacity ($V/V_{max} = 1$, $H/V_{max} = 0$) and the zero bearing strength ($V/V_{max} = 0$) $H/V_{max} = 0$) there exists an optimum vertical component to resist a maximum horizontal load. Indeed, at about half the ultimate bearing capacity, the horizontal load to be withstood attains its maximum value (approximately $0.12V_{max}$). This behaviour is to be expected: At low values of vertical load, the applied horizontal load is the predominant component for the soil failure. After a certain optimum value of the vertical load, where the horizontal load becomes maximum, the vertical component becomes predominant and as it approaches the ultimate bearing capacity (under H = 0), a small perturbation caused by another factor (horizontal load or moment) is sufficient to induce failure, since the footing-soil system approaches a state of instability (see fig. 2.7b).

It was pointed out in the previous chapter, that the slope of the tangent to the envelope, when H tends to zero, defines the angle of base friction δ. This, for surface footings, will generally be lower than ϕ, as obtained from either triaxial or simple shear tests, and full shear strength cannot be obtained in practice unless the footing is embedded. Hvorslev (1965) argued that full horizontal shear strength ($\delta = \phi$) may be attained for values of V/V_{max} smaller than 0.1, when the depth/width ratio is greater than 5, whilst Kezdi (1961) showed, from field tests on gravel, that the slope of the tangent to the envelope was smaller than tan ϕ. The experimental results in fig. 2.7a support the above argument

($\delta \approx 40^{o}$ while $\phi = 50^{o}$ see chapter 6) which suggests that sliding of a rough footing on the soil surface will occur, when $\tan \alpha = \tan \delta$ (angle of load inclination is equal to the angle of base friction).

The various relationships that have been suggested for the inclination factor have been drawn in both figs 2.6 and 2.7a. The relationships drawn are the following:

Meyerhof (1963):

$$\frac{V}{V_{max}} = \left(1 - \frac{\alpha}{\phi}\right)^2 \qquad (2.5a)$$

or

$$\frac{H}{V_{max}} = \left(1 - \frac{\alpha}{\phi}\right)^2 (\tan \alpha) \qquad (2.5b)$$

where α is the load inclination.

Hansen (1957):

$$\frac{V}{V_{max}} = \left(1 - 1.5\,\frac{H}{V}\right)^2 \qquad (2.6)$$

Hansen (1961):

$$\frac{V}{V_{max}} = \left(1 - \frac{H}{V}\right)^4 \qquad (2.7)$$

Hansen (1970):

$$\frac{V}{V_{max}} = \left(1 - 0.7\,\frac{H}{V}\right)^5 \qquad (2.8a)$$

or

$$\frac{H}{V_{max}} = 1.43\,\frac{V}{V_{max}}\left(1 - \left(\frac{V}{V_{max}}\right)^{0.2}\right) \qquad (2.8b)$$

Mean curve through the experimental results obtained by the author:

$$\frac{V}{V_{max}} = \left(1 - 1.36\,\frac{H}{V}\right)^2 \qquad (2.9a)$$

or

$$\frac{H}{V_{max}} = 0.735\,\frac{V}{V_{max}}\left(1 - \left(\frac{V}{V_{max}}\right)^{0.5}\right) \qquad (2.9b)$$

Meyerhof's formula (1963), which is based on ϕ, overestimates the bearing capacity for load inclinations higher than approximately 15^{o} but gives a good estimate for $\alpha < 15^{o}$. Hansen's suggested relationships (1957, 1961, 1970) give a rather safe estimate of the bearing capacity values, the last one, $V/V_m = (1 - 0.7 \frac{H}{V})^5$ providing a good correlation with the experimental data.

In figs 2.8 and 2.9, the results from experimental studies by various authors are shown, together with the relationships proposed by Meyerhof (1963), Hansen (1957, 1960, 1970), Muhs and Weiss (1973) and the author (a brief outline of each study has already been presented in chapter 1.2.2.3). In general, an overall agreement on the effect of the horizontal load on the bearing capacity is observed, but there is appreciable scatter, so that a formula which gives safe predictions for the results of one experimental study, lies on the unsafe side of another. However, these discrepancies can probably be attributed to differences in the particular experimental set up used by each investigator. Muhs and Weiss (1973) and Saran et al(1971) used apparatuses which imposed kinematic restraints on the footings: they were allowed to translate along the loading path only, which was fixed at the required angle. A similar arrangement was followed by Giraudet (1965) even though his own results show a considerable scatter within themselves. Such kinematic constraints result in much higher failure loads than in cases where the footing is free to translate and rotate, as this was established experimentally by the author (see chapter 6). Thus it is believed that the 'expanded' failure load envelopes, defined by these results (shown in fig. 2.9) are mainly due to inconsistencies in the test arrangements. However, there is no obvious explanation of the quite high horizontal loads obtained by Zaharescu (1961b) for $V/V_{max} > 0.7$, although there is good agreement for $V/V_{max} < 0.7$.

As may be seen from figs 2.8 and 2.9, both Hansen's (1970) and the author's suggestions compare favourably with the test data. The maximum horizontal load obtained by the former formula is $0.096\ V_{max}$ (s.d. = 0.030) for $V/V_{max} = 0.52$ (s.d. = 0.067). However, if the cases with kinematic constraints are excluded, then $H_{max} \approx 0.11 V_{max}$ and $V/V_{max} \approx 0.50$ and the relationship proposed by the author gives a rather better approximation.

2.3.3 Inclined - eccentric loads

The combined effect of an eccentric and an inclined load on the bearing capacity of the footing has received relatively little experimental attention, probably the most significant investigation being one conducted by Zaharescu (1961a,b). A number of tests were carried out by the author to investigate this combination of loads, as well as the effect of a 'positive' and a 'negative' eccentricity (terms already defined in fig. 1.6).

Results from tests with B = 50 mm and with both 'positive' and 'negative' eccentricity are shown in fig. 2.10. Two interesting observations may be made: (i) Higher horizontal loads can be carried by the footing under the same vertical load, when the latter is acting eccentrically on the opposite rather than on the same direction to the horizontal load ("negative eccentricity"). (ii) The bearing capacity under these conditions may be increased (by approximately 15%) compared with the case when no horizontal load is applied. The former observation was also indicated by Zaharescu (1961a,b) see fig. 2.10, but he could not obtain the increased bearing capacity under 'negative eccentricity' observed by the author, mainly due to the loading procedure he followed: A vertical load was first applied followed by the application of the horizontal force, until failure occurred (path OAB, fig. 2.11), consequently vertical eccentric loads higher than the one obtained under zero horizontal load could not be reached. However, it is clear from fig. 2.10, that a similar behaviour to the one obtained experimentally by the author may have been found, if an alternative load path had been followed (e.g. OACD, OE fig. 2.11).

The capability of the footing to sustain relatively higher horizontal forces under vertical load with 'negative' eccentricity than with zero eccentricity, is also implied in fig. 2.12, where the two cases are compared. Even though the differences are distinctly smaller than between 'positive' and 'negative' eccentricities (fig. 2.10), the relative 'strengthening' of the footing in relation to horizontal forces, when under vertical load with -E is again clearly demonstrated.

This behaviour could be attributed in the first instance, to the following observations on the failure modes:
At low values of V^e/V_{max}, the horizontal load is dominant causing shallow shear failure of the soil (Region I, fig. 2.13); at relatively high

values of V^e/V_{max} (at values of V^e approaching the value $V^e_{(H=o)}$ which is the bearing capacity under eccentricity e and zero horizontal load), the shear failure took place again in the same direction as the horizontal load, the latter attaining its highest relative values (region II, fig. 2.13). For load combinations within region IIIa, where the vertical eccentric load V^e is dominant, the failure surface was developed with movements in the opposite direction to the horizontal load, but either type of failure surface (type IIIa, or II) could be observed for loads within the region IIIb (fig. 2.13). Considering, now, the case of a 'positive' eccentricity (fig. 2.13b and 2.13a, dotted line), the failure surface was always developed along the direction of the horizontal load. If these failure modes are compared with the corresponding ones of a vertical eccentric load and of an inclined central load case separately, an explanation of the increased 'strength' of a footing against horizontal forces may be derived: When the eccentricity of the vertical load is 'positive', the failure surface, due to the vertical load acting on its own, would have been located on the same side of the footing as the slip surface due to the horizontal load acting alone, thus contributing to the loss of strength of the soil mass. However, if the eccentricity of the load is 'negative', the two slip surfaces would have been developed in opposite directions (if the loads were considered acting separately), and the vertical eccentric load would contribute to the increase of strength of the sand mass, by stressing a larger region of the soil to the limiting state. This very simple explanation is basically a qualitative one, because the effects of the eccentricity and inclination of the load cannot be superimposed precisely at failure in such a non-linear situation.

The comparison between some experimental results and the 'effective' width concept combined with the author's suggestion, expressed as $H/V_{max} = 0.735(1-2E-\sqrt{V/V_{max}})V/V_{max}$ is shown in fig. 2.10 (dotted line). The predictions lie well on the safe side of the 'positive' eccentricity envelope (case compared: B = 50 mm, E = ± 0.2), grossly underestimating the load capacity of the footing under 'negative' eccentricity conditions.

The effect of the initial sand density on the failure load envelopes is shown in fig. 2.14, where the relative expansion of their shape is directly combined with the bearing capacity increase due to reduced voids ratio.

The few published results by Zaharescu (1961a) and Meyerhof (1953) are plotted in fig. 2.15, together with some of the author's own experimental data. The failure load envelopes contract as they approach the limit E = 0.5, where V/V_{max} and H/V_{max} are zero. The expression $H/V_{max} = 0.735V/V_{max}(1 - 2E - \sqrt{V/V_{max}})$ is also plotted (dotted lines) at the corresponding eccentricities, whilst an alternative 3-D presentation of this expression is shown in fig. 2.16, where the three planar loads (vertical, horizontal, moment) are normalised with respect to V_{max}. The latter has more theoretical potential as a diagram, since the generalised forces on the footing are related and hence a 'plasticity' approach would lead to plotting the related generalised displacement increments in the same axes. A direct implication from both of these diagrams is that once V_{max} is known (either through a plate bearing test or through some reliable estimation), then the behaviour of the footing at failure under any planar load combination may be safely predicted. Furthermore, as will be shown in a later chapter, the knowledge of the load-settlement relationship of the vertical central load case may provide an approximate prediction of the load-settlement and load-horizontal displacement relationships at any load inclination.

2.3.4 Related displacements

Both the vertical and horizontal displacements (and, in some cases, the rotation) of the footing were monitored in a series of tests, and the following observations were made:

The dimensionless load-settlement curves for footings on both dense and medium dense sand under vertical central load are plotted on fig. 2.17. As may be seen from the tests on sand with initial voids ratio 0.55 and 0.65, the higher density of the sand results in a stiffer response of the footing (as expected), and, naturally, in higher bearing capacity. It is of interest to note that a loading cycle up to V/V_{max} = 0.4 (load-unload-reload) produces a vertical displacement recovery of the order of 20% which must be mainly due to the elastic recovery of the volumetric strains, since, as shown in fig. 2.18, a horizontal load cycle does not produce any significant horizontal displacement recovery, implying that the induced shear strains are practically irrecoverable. The same behaviour was observed by Head (1977), who carried out similar footing tests in the same sand, and by the author (see chapter 6).

Another interesting point from fig. 2.17 is the load 'plateaux' observed in the load-displacement relationship of a footing on medium dense sand under vertical central load. These 'plateaux', which were also observed by Head (1977), are a reflection of the changing yield mechanism which may be illustrated by the diagram shown in fig. 2.19. The load 'plateaux' correspond to the successive yield surfaces f_i (i = 1,2, ... n) while ultimate failure is defined by the failure envelope F.

The incremental displacement vectors are plotted on the corresponding V- H diagram axes in fig. 2.20. For a given vertical load V, the incremental displacement vector rotates with increasing horizontal load from being approximately co-linear with the V axis to a maximum angle (with respect to the V axis), depending on the ratio V/V_{max}. The relative inclination of the vector, which is rather unaffected by the load path followed (Head, 1977), was found to remain practically constant along any constant slope load paths from the origin throughout a load sequence (see, for example, the 7^{o} constant load path of fig. 2.20). The constant angle between the radial load-path and the resultant incremental displacement vector ranges from approximately zero (vertical central load) to a maximum of 90-δ, where the actual displacement vector becomes horizontal (failure by sliding of the footing). This becomes even more significant when the potential similarities with the non-associated flow rule material of the plasticity theory are considered. The consequences of these observations will be discussed in the next section and analysed in chapter 8.

2.4 Conclusions and some further implications

This preliminary study has lead to the following conclusions:

(a) The 'effective width' concept provides rather conservative predictions when compared with experimental results, which, however, are quite acceptable for all practical purposes. Considering, on the other hand, the presented experimental results, it is suggested that a surface footing on sand can withstand a maximum moment of V_{max} B/10.

(b) The reduction factor for the cases of an inclined load

$$\frac{V}{V_{max}} = (1 - 0.7 \frac{H}{V})^5$$

suggested by Hansen (1970) compares well with the experimental results, even though it gives a somewhat conservative prediction for the maximum horizontal load that can be carried by a surface footing. A better correlation is shown by the relationship proposed by the author

$$\frac{V}{V_{max}} = (1 - 3.6 \frac{H}{V})^2$$

for inclinations up to 30^o (for bigger inclinations the relationship is furnished by a straight line with $H/V = \tan \delta$ for $V/V_{max} = 0$).

(c) An increase in the 'strength' of a surface footing against horizontal loads, when the eccentricity of the vertical load is 'negative', was established experimentally and a schematic qualitative explanation is given, based on failure modes observations (also supported by results from tests to be discussed in chapters 6 and 7). These findings confirm the only available observations by Zaharescu (1961a,b), but, in addition, indicate the possibility of obtaining higher bearing capacity under certain load combinations (see fig. 2.13a) than under the action of a vertical eccentric load only. Finally, the effect of a general planar load on a surface footing on sand is presented in a unified manner in figs 2.15 and 2.16 where the accurate knowledge of the ultimate bearing capacity is sufficient to describe safely the behaviour of the footing under any planar load combination.

(d) The associated incremental displacement vectors of a footing under inclined central load remain practically parallel throughout the test for a constant slope load path from the origin. The angle between the incremental displacement vectors and the constant load path varies from approximately 0^o (vertical central load case) to a maximum of $90 - \delta$, where the footing slides horizontally. Finally, it may prove to be useful to consider the load-displacement relationship of a footing on medium dense or loose sand (fig. 2.17) as a plastic work hardening system as illustrated in fig. 2.19, with hardening yield surfaces (f) within a failure envelope (F).

When considering the failure envelopes for the cases of combined loading under vertical and horizontal load, one's mind leaps to the structural interaction diagrams like the one shown in fig. 2.21b for the fixed foot portal frame of fig. 2.21a loaded by a vertical load V

and a horizontal load H. Collapse of the portal frame will not occur for any load combination within the locus defined by the three-straight-lines envelope. Loaded by a vertical load only (H = 0), the frame will collapse when $V = 8M_p/\ell$ (locus 1, fig. 2.21b). A horizontal load (under V = 0) will cause collapse when $H = 4M_p/h$ (locus 2). The combined action of H and V is furnished by locus 3, where $V\ell + 2Hh = 12M_p$ (see, for example, Palmer, 1976).

A similar behaviour could be exhibited by a rough footing on a saturated clay bed under undrained loading and a central vertical load V and a horizontal load H (fig. 2.22a,b). The footing will fail under a vertical load intensity (H = 0) when $p = V/BL = c\,N_c \approx 6c$ say (locus 1, fig. 2.22b) while for the case when V = 0, the horizontal load intensity must be equal to c (Meyerhof, 1953) - the base adhesion being assumed equal to the undrained shear strength of the soil c_u - (locus 2). When an inclined load is acting on the footing (i.e. combined V and H loading) the actual failure envelope will (see fig. 2.21b) cut off the corner of the area outlined by 1,2, possibly elliptically as at 3 in fig. 2.22b. This general pattern of behaviour was, in fact, pointed out by Hvorslev (1965); the full horizontal shear strength can be developed when the normal stress is less than half the bearing capacity for normal loads. The available horizontal shear strength decreases rapidly for vertical loads exceeding $V_{max}/2$ and becomes zero for $V = V_{max}$.

If we now consider the case of a rough footing on sand under an inclined load (fig. 2.23a,b), line 1 again serves as a failure locus for the case H = 0 but when V = 0, the available horizontal load capacity is also zero. Thus locus 2 has the position shown in fig. 2.23b where the slope of the line will be at the soil-footing friction angle (δ) and kinematically the footing is merely sliding along the soil surface. However, as has been shown experimentally (for example fig. 2.20) the effect of the combined V and H loading is described by the curved locus 3, lying within 1 and 2 and the major part of the (1,2) region envelopes inadmissible loading states.

Let us now return to the portal frame of fig. 2.21a and consider the associated displacement increments for each of the three cases described by the three-line interaction diagram. When H is applied (V = 0), the horizontal movement is $h.\theta$ (where θ is the rotation of the column AB about A) and its direction coincides with that of the horizon-

tal load (fig. 2.21d). Similarly, the horizontal beam deflects along the direction of V (when H = 0) by $\ell\theta/2$ (fig. 2.21c), while the combined effect of H and V results in both horizontal movement by h and vertical deflection by $\ell\theta/2$ respectively (fig. 2.21e). If the associated displacement increments are plotted on the V,H axes (fig. 2.21b), then the displacement vectors for the two cases shown in figs 2.21c and 2.21d are coaxial. Therefore they are perpendicular to the loci 1 and 2. The combined application of V and H defines the locus 3 (fig. 2.21b) which is given by the equation

$$V\ell + 2Hh - 12M_p = 0 \qquad (2.10)$$

The equation of the displacement vector is given by the equation

$$h\theta\dot{v}^p - \frac{\ell\theta}{2}\dot{u}^p = 0 \qquad (2.11)$$

where $\dot{v}^p$ and $\dot{u}^p$ are the incremental plastic vertical and horizontal displacements. Since V,$\dot{v}$ and H,$\dot{u}$ axes coincide respectively, the two lines defined by equations (2.10) and (2.11) intersect each other at right angles. Consequently the incremental plastic displacement vectors are normal to the yield surface (Wroth, 1976).

The portal frame case (for a classical rigid plastic material) is of course an example of the application of plasticity theory utilising the concepts of a yield surface (f) and a plastic potential (g). In this case f and g are identical and plastic displacement increment vectors are necessarily normal to f (i.e. associated 'flow'). The behaviour of rough footings on both clay and sand under inclined loads exhibits strong similarities with the portal frame. The suggested 'work hardening' behaviour shown in fig. 2.19 and the related displacement increment vectors, discussed in section 2.3.4, however, imply the existence of successive yield surfaces and non-associated 'flow' so that the plastic potentials and yield surfaces will not coincide. These ideas will be pursued in more detail in chapter 8, where the implications following from the above discussion will be examined and the possibility of their practical application considered.

Considering the effect of a moment on a surface footing on sand (for example, see fig. 2.4), again a similarity with the portal frame case may be observed. This case, however, was not investigated any further.

CHAPTER 3

EXPERIMENTAL WORK - PART II

3.1 The footing apparatus at Cambridge

3.1.1 The footing apparatus

The apparatus used for conducting the major part of the experimental work was originally designed by James (1965) in order to investigate the behaviour of a sand mass adjacent to a retaining wall, which could rotate about either its top or its toe. The footing apparatus, from now on referred to as F.A.C. (Footing Apparatus Cambridge) is, essentially, a large glass-sided tank, 2.4 m long, 1.5 m high and 190.5 mm (7.5 in) wide. The two glass sides, the rear one 19.05 mm (0.75 in) thick and the front one 15.88 mm (0.625 in) thick, are mounted in peripheral steel frames. The constant width is maintained by two 190.5 mm (7.5 in) wide channel sections. The main frame consists of heavy channel sections, which are bolted to a heavy concrete slab, isolated from the rest of the laboratory. A large number of rubber faced round pads, supported via 9.52 mm (0.375 in) diameter threaded studs by the channel framework, supports the glass sides (fig. 3.1). This arrangement proved to be fairly successful, since the allowable glass deflection was small enough for essentially plane strain conditions to prevail.

The original frame was modified by Tennekoon (1970) to allow for the higher stresses, generated by surface footing indentation into dense sand. Two extra wide channel sections were used to reduce the opening of the tank, so that the glass-sides could be supported more effectively. The round rubber faced pads, running along the centre channels, were replaced by 12.7 mm (0.5 in) wide rubber faced metal strips so that interference with the X-rays was kept down to a minimum.

The inability of the X-rays to penetrate thick samples, was the reason for the use of a 19.05 mm (7.5 in) wide tank. The reasons for using glass-sides, are: (James, 1965) i) Low absorption coefficient for X-rays, ii) the glass is a very hard material, not easily scratched by sand particles, iii) the high Young modulus (approx. equal to that of aluminium), iv) the relative small angle of friction between

glass-sand grains. An approximate value of 6^{o} for the angle of friction between sand and polished glass (previously cleaned by acetone) obtained from direct shear tests, was reported by James and Bransby (1970). Andrawes (1970) distinguished between the static and kinematic angles of friction, the former corresponding to the maximum value of the frictional force, for a given normal load during a direct shear test, and the latter corresponding to the minimum constant value of the frictional force, again for a given normal load. He also distinguished between dense and loose sand, and suggested the following angles for the two different sand densities (the sand he used was Leighton Buzzard, with particle size ranging from 0.4 to 0.85 mm, a little finer than the one used by the author):

Initial voids ratio	δ_g static	δ_g kinematic
0.77	7.7^{o}	5.9^{o}
0.55	12.8^{o}	11.4^{o}

Cole (1967) and Basset (1967) estimated a coefficient of friction between sand and glass of approximately 0.1 ($\delta_g = 5.7^{o}$). Stroud (1971) measured $\delta_g = 5.1^{o} - 6.3^{o}$, from direct shear box results. Arthur and Roscoe (1965) quoted $\delta_g = 6.3^{o}$, whereas James (1965) quoted $\delta_g = 4.6^{o}$. From the afore-mentioned values, the relative friction between sand grains and a glass surface may be assumed to be acceptably low.

The retaining wall was used as a rigid boundary and, for that reason, it was clamped in its vertical position, which reduced the effective length of the tank to 1.45 m.

3.1.2 The footing

The footing used by the author, was originally designed by Tennekoon (1970) for the investigation of the bearing capacity of a model strip footing on dense sand under vertical central load. It was built up from the three rows of load cells, (fig. 3.2) each of dimensions 25.4 × 12.7 × 63.5 mm (1.0 × 0.5 × 2.5 in) with respect to height × width × length, and each capable of measuring the normal force acting on its active face, its eccentricity, and the shear force acting parallel to the shortest face of the cell. Three successive plates, the two outer ones made from steel and the in-between one made from dural, were used as backing plates for the cells. A series of carefully located

holes allowed for the cables emerging from the load cells, to come out freely. The dural plate, as well as one of the steel plates (the one immediately backing the cells) were maintained unaltered, but the top steel plate was completely reconstructed, to allow for the new loading conditions to be imposed.

The main objective was the application of a variety of load inclinations and/or eccentricities, including, of course, the case of the vertical central load, throughout which the footing was to be maintained free to move on the plane through the applied load and the vertical axis through the centre of the width. This was achieved by the use of two parallel slotted bars SLO (fig. 3.3), of dimensions 202 × 50.8 ×31.75 mm, which were bolted, via 12.7 mm (0.5 in) diameter Whitworth G.N.K. (high tensile steel) bolts, down on the 14 mm thick top backing plate TBP (fig. 3.3). The load was transmitted to the top backing plate of the footing via a bracket on a 12 mm shaft, which was fitted in the inner race of two INA - Na 4901RS, 24 mm outside diameter needle bearings, each carried by one slotted bar. The free plane movement of the footing was achieved with the use of the afore-mentioned needle bearings, as well as with the freely rotating loading system (see section 3.1.3).

A disadvantage was already noticed at this stage, in so far as the axis of relative rotation of the footing was too high from its base; a small movement or rotation of the foundation would result to a different boun-dary loading condition from the initial one. That was reckoned to be a minor disadvantage, mainly because the movements and/or rotations on dense sand prior to failure were not expected to be so large, as to affect dramatically the overall initial geometry of the set up (provided that the initial eccentricity and inclination were not excessive). On the other hand, the dimensions of the load cells and their necessary backing plates, made this configuration unavoidable.

The two SLO bars were kept together flat and parallel via two end plates, screwed and dowelled on them. The rear end plate carried two 9.5 mm (0.375 in) diameter BSF Allen bolts ABO (fig. 3.3), which 'locked' the footing at the initial relative position. That facility enabled the footing to be lowered gently to test on the sand surface, with its bottom face always kept parallel to the levelled surface. After the first load increment, it was 'unlocked' and then it was free to rotate through the bearing axis BA (fig. 3.3).

3.1.3 The loading system

A double-action hydraulic jack was used to apply the load on the model footing. Its maximum tested capacity was over 2 tons (2,000 kg), and the maximum travel of the ram 150 mm (fig. 3.4, 'J'). Its main body was made from aluminium alloy, and it was used originally on the under-carriage of a Spitfire aeroplane! The pressure system consisted of an oil pressure vessel (V) mounted on one of the vertical wide channels of the apparatus, at the rear of it, pressurised by a nitrogen gas cylinder (N), of maximum gas pressure 140 kg/cm^2 (≃ 2,000 psi) (fig. 3.4). The oil reservoir pressure was monitored by a Bourdon Gauge G, of range 0 - 14,000 KN/m^2 (0 - 2,000 psi) and sensitivity 70 KN/m^2 (10 psi), the pressure being stabilized for each load increment by a reducing valve located between the nitrogen gas cylinder and the oil reservoir, just after the 'on - off' valve of the cylinder. Two small air pressure gauges were connected directly with the reducing valve VAL, (range 1 - 7,000 KN/m^2 (1 - 1,000 psi)), one monitoring the current pressure of the nitrogen cylinder, while the other monitoring the applied gas pressure on the oil reservoir, but much less accurately. (The 1 - 7,000 KN/m^2 (1 - 1,000 psi) reducing valve replaced a 1 -14,000 KN/m^2 (1 - 2,000 psi) one, before the beginning of the experimental work, in order to increase the sensitivity in performing the required load steps). Two special high pressure steel reinforced pipes were used to connect the cylinder with the oil vessel and that with the jack itself (P1 and P2, fig. 3.4). The return action inlet RE was connected via a reinforced pipe to screw pump SP (fig. 3.4). This set up was used to retract the footing from the tank after each test, and to accelerate the oil drainage from the jack back to the pressure vessel. During loading the return action line was left open, so that the oil drained freely into the screw pump. A third valve VAL3 was inserted between the pressure vessel and the jack, which helped to stop any movement of the footing when the latter started failing; it was, thus, made possible to follow, with X-radiographs, the development of the failure surface and the probable appearance of new ones during post peak penetration, as it will be described later on.

One of the main requirements of the loading frame was that it should be easy to set the frame up and dismantle it quickly since it had to be removed for the sand to be poured into the tank, as well as to allow the X-ray equipment to enter the compound. The loading frame con-

sisted of two 76.2 mm (3 in) square section steel columns, 3 mm wall thickness, each welded on a 165.1 × 114.3 × 12.7 mm (6.5 × 4.5 × 0.5 in) steel plate, each plate being bolted down on the top channel section of the apparatus via four 12.7 mm (0.5 in) diameter bolts (fig. 3.3). Four 25.4 mm (1 in) steel spacers were used between the steel plates and the apparatus, so that the minimum initial length of the whole system could be accommodated. A 100 × 9 mm (4 × 0.375 in) equal angle cross-beam, bolted on the two uprights (fig. 3.3), carried the upper bracket UB, where the jack was suspended from. Two INA-NKI 12/20, 24 mm outside diameter, 20 mm width, 12 mm shaft needle bearing were built in the upper bracket, the pin running through the top side of the jack. This configuration allowed the jack to rotate about this practically friction-less joint, so that any desired inclination of the resultant load could be applied; on the other hand, the footing was free to move in the same plane as that in which the jack was operating. A small protractor PR (fig. 3.3) was placed on the rear side of the bracket, which helped to adjust, at first approximation, the initial inclination of the applied resultant load. A dial gauge, reading 0.01 mm per division, located on the equal angle cross-beam and pointing on the rear of the jack, helped to set the initial angle much more accurately. A 12.7 mm (0.5 in) diameter BSF stud, connected through a pin and a steel collar to the lower part of the jack (fig. 3.3) and running through a slotted steel plate supported by the two basic upright columns, helped to maintain the initial position of the jack for the first one or two small load increments. After this stage the locking nut of the stud on the slotted plate was released and the jack-footing system was completely free to translate and rotate in the above mentioned plane.

The footing was connected to the hydraulic jack via a similar to the upper bracket frictionless joint (as already described), the shaft of the needle bearings being a push-fit one to the jack bracket. This lower bracker LB (fig. 3.3), carrying the shaft, was screwed into a specially made load cell TLC1, which, in its turn, was screwed into the 28.6 mm outside diameter stainless steel ram (inside diameter 19.05 mm, wall thickness 4.0 mm). The axially applied load (along the axis through the two frictional joints), was recorded by this load cell,which was made from dural HE15, of circular cross-section (fig. 3.5). The top part consisted of a (male) threaded shaft 17 BSF, 19.05 mm (0.75 in) diameter,

which was screwed into the steel ram of the jack. The bottom part consisted of a similarly threaded hole, 19.05 mm (0.75 in) 17 BSF, where the lower bracket was screwed in. The centre hollow 20 mm long part, was maintained free from threading, and a set of electrical foil strain gauges was glued around its accurately machined surface (± 0.025 mm tolerances). The resultant circuit (fig. 3.6) enabled the axially applied load to be recorded, with the maximum sensitivity of a Wheatstone bridge, at the same time compensating for any moment applied on the load cell. A similar circuit was built on the jack rod itself TLCR (fig. 3.3), with a much less sensitive output (since the material was stainless steel), mainly to be used as an extra independent source of information of the axially applied load. This 'load cell' was not operative for some period, since part of the gauge wiring was disturbed during the retraction of the footing from the tank.

3.1.4 The attachment for horizontal load

One part of the experimental work was to investigate the effect on the bearing capacity of a directly applied horizontal load either on the footing base or at some distance from the sand level, thus imposing a moment to the foundation. A special bracket was built for that purpose, which could be bolted on the top plate of the footing (fig. 3.7). It consisted of two annealed-steel (EN 24) plates STP, 100 × 65 × 14.5 mm (fig. 3.7), bolted on an anchor post AP 70 × 37 × 80 mm by 7.94 mm (0.3125 in) diameter bolts and clamping a stainless steel wedge shaped probe PAB 165 × 35 × 15 mm between them. The anchor post was bolted on the top plate of the footing by one 12.7 mm (0.5 in) BSW bolt and two 9.5 mm (0.375 in) BSW bolts. The steel probe was wedge shaped at the bottom, so that it provided the least obstruction during penetration, when the horizontal load line of action was to lie on the sand surface. The horizontal load was applied by dead weights on a hanger via a Bowden cable running through a pulley system and connected with the probe by a turn-buckle. The turn-buckle could be bolted in any of the six tapped holes 6.3 mm (0.25 in UNF - 28 threads/in), in the front face of the probe. Therefore a variety of applied moments could be achieved by clamping the probe at different positions.

After the bracket was constructed, it was found that the bolts

keeping the plates and the post together (fig. 3.7) were obstructing the free relative position of the slotted bars, and they were replaced by counter-bored Allen screws.

The load, as mentioned above, was applied by dead weights, but it was reckoned that a load cell should be employed to record the actually applied load on the footing, thus overcoming the friction influence of the pulley system. For that purpose a cylindrical dural (HE 15) load cell was designed, 90 mm long and 10 mm diameter, with two flat ends, each end with 5.1 mm clearance hole to connect with the turn-buckle. Two dural (HE 15) rings were glued near the flat ends by two-tube Araldite epoxy resin. A four arm Wheatstone Bridge was formed by four active strain gauges bonded to the cylindrical part of the load cell and at 45° to the axis of symmetry (fig. 3.8a), each pair creating a 90° rosette (the gauges bonded diametrically opposite one another), and four dummy ones bonded on one of the two rings, which carried the top strip as well. The circuit shown in fig. 3.8b was used and, as it may be seen, the output is independent of both torque and moment. A three-volt (3 V) DC power supply was employed The maximum design working load was 5 KN.

In order to increase the accuracy of measurement of the horizontal load at low levels, a new load cell was designed (fig. 3.9). A full Wheatstone bridge was used, for the two T-shape pairs of strain gauges (width 3 mm, length 10 mm, R = 120 Ohm± F = 2.09), which were bonded to the thin neck of the cell. The cell was made out of mild steel and the dimensions are given in fig. 3.9 (together with the circuit details). The circuit used did not compensate for bending or torque, but it was felt that it was not very critical, since the Bowden cable was replaced by a thin nylon line, and it was unlikely that it would impose any torque or bending on the cell. (Breaking strength of the line approx. 0.7 KN (70 kg)). The load cell was located between the turn-buckle and the line.

Pulley system: In order to enable the horizontal load to be applied at any required initial position either at or above the sand level, a small frame carrying a pulley was designed. It consisted (fig. 3.10) of two mild steel equal angles ANG 76.2 × 9.53 mm (3 × 0.375 in), joined together via a rectangular mild steel plate B 203.2 × 50.8 × 9.53 mm (8 × 2 × 0.375 in) and carrying two slotted mild steel equal angles C

50.8 × 6.35 mm (2 × 0.25 in) with the 89 mm diameter pulley D1 (9.53 mm shaft), located at the one end of them. The angles ANG were bolted directly on the top channels of the footing apparatus (fig. 3.10), whereas the angles C slid along the bolts E through the slots until the required position of the pulley D1 was obtained. Then the angles C were bolted and the whole system could withstand the maximum design horizontal load without excessive deflection. This small frame was located at about 300 mm from the end of the rig, where another small pulley D2 was located (fig. 3.10). The Bowden cable (or the nylon line in some cases) ran through the first pulley D1, over the second pulley D2 down to the specially made lever arm, where it was connected via a shackle. This lever was a mild steel plate of dimensions 603 mm × 63 mm × 12.7 mm with a load ratio of 10:1. A small hanger was attached to the end of the plate.

3.1.5 Displacement recording equipment

The planar movement of the footing was recorded by a system of 6 Baty dial gauges, with 50.8 mm (2 in) stroke and 0.01 mm/division, mounted on a Dexion frame and fitted on the top channels of the footing apparatus. Their relative position is shown in fig. 3.11. This arrangement allowed the rotation of the footing to be deduced as well as the displacements along the x and y axes of any point of it in the plane of the action of the load, and recorded any potential relative tilt across the tank width (it was found that the resultant tilt was negligible). The relative position of the dial gauges was carefully measured with a vernier calliper to the nearest 0.05 mm, and the frame was set up so that the line XX was horizontal (checked with a spirit level) and the line YY was vertical. Thus the footing base was initially parallel to the XX line.

3.1.6 Sand sample preparation

The initial density of the sand samples prepared, ranged from 0.51 voids ratio to 0.64. This range was obtained by using two different hoppers, the hopper S (designed by Schofield (1959)), and the hopper J (designed by James (1965)).

Hopper S consisted of a cylindrical section with a truncated cone shaped base. The rate of discharge was adjusted by a gate valve which controlled the size of the base opening, a 50.8 mm (2 in) diameter hole, with a long flexible hose attached to it, used to direct the sand flow in the tank. The hopper was suspended by a manually operated crane and it travelled along the whole length of the F.A.C., with the opening fixed for the required flow rate. Its capacity being only 0.081 m^3, it had to be refilled at least three times for the preparation of a complete sample (approximately 0.33 m^3). The total tank capacity was approximately 0.372 m^3 (assuming a relative height of the sample of 1.38 m), but after the first dense sample was poured into the tank, it was only partially removed for every subsequent test. The first sample had a voids ratio of approximately 0.50, which implies a fairly dense state. In order to achieve that, the slowest possible flow rate was maintained (usually interrupted by arching across the tiny discharge hole). With such a flow rate, the pouring would take almost a week, and the whole arrangement was slightly modified: A long flexible hose with spiral wire reinforcement was attached to the opening of the hopper, and both were placed over the centre of the tank opening. A string, connected at approximately the mid-height of the hose, and running over a pulley, was attached to an arm fixed on a motor shaft (fig. 3.12). This arrangement helped to pour the most of the sample, avoiding the tedious job of moving the hopper by the crane along the length of the tank. Since it was reckoned that below a depth of about 10 times the width of the footing there was no detectable movement in the sand mass, it was decided that after the end of each test, the sand that was to be removed would not be less than 0.80 m depth.

The hopper just described was used for the preparation of dense sand beds. For medium dense samples the J hopper was used. It consisted of a large container with two perforated plates as its base which can slide relative to each other with the help of a handle. The base was designed to fit the top of the F.A.C. and stood at over 0.60 m above the final surface of the sand mass. This requirement being fulfilled, the variation of voids ratio with depth would be very small and the pouring could take place simultaneously over the entire area of the tank. The required size of the aperture could be adjusted by a stop screw.

After the end of pouring, the final surface of the sample was levelled up using a device shown in fig. 3.13. A 6.35 mm (0.25 in) brass

tube T, locked at the required height via a screw S in the circular brass block B, which was bolted on the long machined dural plate D, was connected via a plastic pipe with a small container C, where vacuum may be applied with the suction pressure provided by a vacuum cleaner. The dural plate could slide on two Dexion equal angles DE, and with a relatively small suction, a levelled sand surface was obtained.

3.1.7 Tank assembly

Before the beginning of the test series, the tank was emptied and cleaned. It was then noticed that the front glass had a permanent inwards deflection due to continuous prestressing of the top glass side over a long period of time (unknown to the author), by careless assembly. After some modifications the tank width was arranged at 190.5 mm (7.5 in) at its central position (with respect to its length), being about 198 mm at the side opposite the clamped retaining wall (which, together with specially made rigid channel frame covering the gap between the wall and the bottom of the tank, were used as a rigid boundary).

The glass sides were cleaned with Inhibisol and the tank dimensions were measured. The length was measured with a 3 m steel tape as well as with a 1 m steel ruler with 0. 5 mm/division at three different depths, on both sides of the tank. The width was measured at 16 different points along the whole length and the whole depth, using a device designed by Bransby (1968), carrying a dial gauge of 0.025 mm/division (0.001 in/div.), and the mean value was taken. The height of the lower sand surface was measured with a 1000 mm steel ruler (0.5 mm/division) and of the final one with a 150 mm steel ruler (0.5 mm/division). The long brass tube, used for levelling the lower sand surface, was lowered carefully until it touched the tops of the sand grains. Locked at this position on the brass block on the dural bar, it was taken out of the tank and the length of the brass tube was measured with the 1000 mm steel ruler. This procedure was repeated at 6 chosen positions along and across the tank. When the sand was poured in and levelled up, the same procedure was repeated, and the mean value of the differences of the corresponding readings gave the average height of the poured sample. The weight of the sand was obtained via a 200 kg × 0.5 kg (± 0.25 kg) spring weigher when the S hopper was used, and via a proving ring (1500 × 1 kg (3200 × 2 lbs)) when the J hopper was used. The initial

voids ratio of the sand was calculated using the expression

$$e_o = \frac{V \times \gamma_s}{W} - 1 \qquad (3.1)$$

where γ_s is the unit weight of the sand grains, W is the weight of sand, V is the average occupied volume by the sand sample ($V = \ell_{av} \times w_{av} \times h_{av}$, length × width × height). (Leighton-Buzzard sand has a specific gravity of 2.66 (Cole 1967)).

3.1.8 Test procedure

After the end of each test, the main footing was disconnected from the slotted bars and the main loading frame was removed from the tank area with the help of the crane. The first, approximately, 0.60 mm of sand was shovelled out with a small scoop. Then, using a similar levelling system to the one described earlier on, but with a hose of 50 mm diameter and using the vacuum cleaner described by James (1965), a further 10 mm of sand was removed. The sand surface was, finally, levelled with the system described in the previous section, but with a 1000 mm long brass tube. The glass sides were cleaned with Inhibisol, in order to reduce the sand-glass friction. After having measured the relative depth of the sand surface at six different points, sand was poured either from the S or the J hopper. A 300 mm high cardboard frame and slightly larger in area than the plan view of the sample was placed on the top side channels of the F.A.C. during the preparation of the sand bed, in order to prevent sand spilling outside the tank area. Lead shot was used only with dense samples, which were prepared using the S hopper, and covered the whole length of the tank, but only 280 mm depth from the final surface. The lead shot was placed on the temporary sand surface via a specially made Perspex template similar to that described by James (1965) and using a similar technique. The length of the tank being approximately 1400 mm, the template had to be used twice to obtain a complete lead shot layer. The grid formed was a rectangular shaped one with 12.7 mm (0.5 in) both horizontal and vertical spacing, and was located 35 mm away from the rear glass of the tank, (fig. 3.14). Tracing paper with coloured straight lines of 12.7 mm spacing was placed behind the rear glass, which helped to adjust the temporary sand surface for each lead shot layer to be placed. This was repeated until the sample space was filled. Sand was poured over the required final level and was

eventually removed using the afore-mentioned levelling device, until the sand surface was level and at the correct height. This relative depth was carefully measured at the same six points, and the last lead shot layer was then placed.

For the first few tests, a levelling technique of the footing contact area described by Stroud (1971) and used by Tennekoon (1970) was applied, which consisted of lowering a greased Perspex flat plate carefully on the sand surface already levelled by the vacuum cleaner, in order to pick up the top grains from that area. This was repeated for a few times until no grains were picked up. However, since a reasonably level surface could be obtained, if the area in use was repeatedly levelled by the vacuum cleaner, there was no need for the Perspex plate to be employed, and the technique was subsequently abandoned.

Having finished the sample preparation, the loading frame was lifted, with the help of the overhead crane, to the required position and bolted on the top channels. Then the footing was assembled, its relative position being adjusted with the help of a vernier calliper. The initial position of the jack being adjusted, the initial readings of the load cells were scanned and the footing was 'locked' at the horizontal position with the adjusting screw ABO (fig. 3.3). A very small oil pressure was applied to lower the footing just above the top layer of lead shot (the jack was maintained at its initial position with the help of the two lock-nuts of the stud S, fig. 3.4), where the valves were shut off and the footing remained motionless. The dial gauge frame was then installed and bolted on the top channels of the rig. To avoid any influence from the reverse action of the jack, the screw-pump valve was opened and the screw-pump was adjusted so that the oil could drain freely out of the piston. The first radiograph was then taken (the footing was now just touching the lead shot), and it was developed and fixed before any further loading took place. Initial readings of the dial gauges, together with another scan of the load cells, were recorded, with the footing resting on the sand surface. A range of 5 to 15 load increments were performed during each test, the dial gauge readings being the guides of the amount of load increment. The footing was allowed to rest for about 10 minutes before the dial gauges and load cells readings were recorded. In some cases the next increment was not applied before 1 or even 2 hours later, and a subsequent recording of the above devices made.

This procedure would help to discover any major leak in the system as well as to give evidence of any possible stress redistribution with time. In general, however, the next increment was applied at approximately 30 minutes after the previous one, when a X-ray photograph was to be taken. The load steps became distinctly smaller as the applied load approached the failure condition. When failure occurred, the valve VAL3 (fig. 3.4) was immediately shut off, and the movement of the footing ceased. This helped to capture the development of the failure surface at increasing amounts of penetration, something which could have been more easily obtained by a strain-controlled system. When the test was over, the oil pressure was released and the footing was retracted with the help of the screw-pump, the load cells being scanned again. (A list of the performed tests is given in table 1).

3.2 Measurement of boundary stresses

3.2.1 Introduction

The footing, as mentioned in the previous chapter, consisted of load cells similar to those used for the last fifteen years at Cambridge, and whose features are described by Arthur and Roscoe (1961) and Bransby (1973). Essentially, the applied load is carried by thin metal webs with electrical strain gauges bonded to them. The strain gauges are wired up into three circuits, used to determine the normal load, the shear load and the eccentricity of the normal load respectively. The load cells used were originally designed by Tennekoon (1970), following the design of some very similar ones by Hambly (1969).

3.2.2 Description of the load cells

A comprehensive description of the load cells and their function is given by Tennekoon (1970) and only a brief outline of the main features of their construction and operation is presented here.

A typical cell may be seen in fig. 3.2; it has dimensions 63.5 × 12.7 × 25.4 mm (2.5 × 0.5 × 2 in) with respect to length, width and height respectively, the width being parallel to the shear load direction - it is constructed out of aluminium alloy HE15. The two relatively rigid blocks B1 and B2 (fig. 3.2) are connected together with thin vertical and sloping webs, W_i (i = 1,2,...,7), which have strain gauges bonded to both

of their faces. The four vertical webs are wired up into two circuits, the outputs from which may be used to obtain the normal load acting on the active face as well as its eccentricity; the three sloping webs, the central one being twice the width of the other two and of opposite inclination, are wired up into one circuit the output from which can be used to obtain the shear load acting on the load cell. The maximum design normal stress is 700 KN/m^2 (100 psi) whereas the maximum shear is 350 KN/m^2 (50 psi), (under the maximum normal load, the developed stresses in the vertical webs would be approximately 1/5 of the yield stress of this alloy (Tennekoon 1970)). The two tapped holes on the active face are used to bolt the calibration plate down by small dural studs which are screwed in when the cell is in operation. Two tapped holes on the rear face of the cell are used to bolt it on the mild steel backing plate, and a central clearance hole, allows the nine-core miniature wire cable to pass through.

3.2.3 Wiring of strain gauges

A total of twenty foil strain gauges, of nominally 120 ohms resistance and 2.09 gauge factor, are bonded to each load cell, four of them being dummies. Three independent circuits are formed, shown in fig. 3.15a; the normal load circuit (N), the shear load circuit (S) and the eccentricity of the normal load circuit (M). A common input line is used, supplying each Wheatstone bridge with three volts D.C. (± 1%). The dummy strain gauges (D in fig. 3.15a) of the normal circuit are bonded to the underside of the active face, a non-deforming location, to compensate for any temperature variations. The position of the strain gauges on the webs is shown in figs. 3.15b,c and a brief description of their function is given below.

3.2.3.1 Normal circuit

For a normal load applied on the cell face, all the vertical webs will be in compression and, therefore, the net result from the bridge will be (A + B) + (C + E) − (4D) = (A + B) + (C + E). The effect from a shear load application, as well as from a moment is eliminated, since two of the vertical webs are compressed and two are in tension (for example, if B,E in tension, then A,C in compression, and the net output should be zero). (fig. 3.15a).

3.2.3.2 Shear circuit

Two of the sloping webs are stressed in tension, while the other two in compression when a shear load is acting. The wiring shown in fig. 3.15a provides the maximum sensitivity for the applied load, whereas, at the same time, it compensates against any normal load applied on the active face, which compresses the four sloping webs. Any moment applied on the active face of the cell does not produce any strain at these webs (Tennekoon 1970) and this may be shown from the moments taken with respect to the centre of the back face of the cell. Nevertheless it was found out during calibration that the shear circuit output was quite substantial, when a moment was applied.

3.2.3.3 Moment circuit

From the four active arms of the Wheatstone bridge for the (M) circuit, shown in fig. 3.15a, two opposite arms will be in compression and two in tension, when a moment is applied. The normal load is eliminated by the wiring order since all of the webs are in compression, and, therefore, the net output will be zero. The shear load produces, however, an output of the same order as the moment one, since it applies a moment on the base of the load cell.

3.2.4 Footing assembly

When the load cells are bolted on the backing plates, a clearance of not more than 0.5 mm (0.020 in) was maintained, to ensure both the independent performance of each load cell and that no sand grain would wedge between two adjacent load cells (see Arthur and Roscoe, 1961). The active face of each cell was covered by 2S grade sand paper which was glued on it using a thin film of Evostic, thus making it possible to remove it, whenever a recalibration of one of the cells was needed: this was the case with the No. 4 load cell, which had one strain gauge replaced after it was damaged accidentally. Ideally, in order to form a rough base, sand grains should be glued on the cell face, using some epoxy resin, so that a fairly strong bond could be attained (Andrawes, 1970). However, it was reckoned that the bond between the sand paper and the cell face was strong enough for all test purposes and the use of this material was eventually adopted. The first footing used by the author was a 50.8 mm (2 in) wide one; that was mainly due to the fact that there

were only twelve load cells available at the time when tests started. Such a width, however, was thought to be too narrow for the test arrangements. As it was mentioned in the previous chapter, a major disadvantage of the load transfer to the footing, was the distance between the load application point and the active face of the footing, which is approximately 90 mm. In addition to that, any information from the load cells would not be sufficient to obtain a clear idea of the stress distribution, since there would be only four stress points from the four cells of the footing. Two new load cells were constructed and some more were recovered from another experimental apparatus, where they had been used for a time. Unfortunately, their active face was machined so that they were less thick by about 0.254 mm (0.010 in), and it was decided to use them after some modification as dummy ones, to complete the intended 76.2 mm (3 in) footing. A further 0.508 mm (0.030 in) thin HE15 dural plate was machined and bonded to the active cell face, using IS12 component. The result proved to be satisfactory for the intended purpose. The 76.2 mm (3 in) width was accepted as a constant width for all the tests that followed and there were two main reasons for selecting it. Firstly, it was calculated that it would be desirable to reach failure for all required tests, so that the limiting values of the applied loads could be obtained for different load combinations. Secondly, some three or four extra load cells would need to be constructed and wired up, and this would take an unacceptably long time. Out of three rows of load cells, only the centre one was used to record stresses, the other two rows being used as dummy ones. This decision was supported by the fact that Tennekoon (1970) did not encounter any significant difference in readings between the centre row and the rows adjacent to the glass sides. All the active load cells used by the author were calibrated by a method described subsequently.

3.2.5 Recording equipment

All the voltages from the different electrical devices used, that is load cells and voltage sources, were recorded by a Solatron 100 channel data-logging system and punched on paper tape by a Facit paper tape punch for processing on an IBM 1130 digital computer.

The most sensitive range of the data-logging system was selected, 0 - 20 mV, and all the voltage outputs were scaled down to operate within

that range. In this mode of operation, one digit was equivalent to 2.5 μV. Metal oxide resistors were used for the scaling down as well as for the zero balancing of the circuits, which were found to give less drift than carbon resistors. A schematic diagram (fig. 3.16) shows the general layout of the electrical connections: All the load cell cables were connected with the balancing box, which contained all the balancing resistors. The input voltage was also scaled down to the 0.20 mV range, so that it was recorded at every data-logging scan. A correction to each load cell output was then applied, in proportion to the ratio of the calibration voltage to the current supplied voltage, thus eliminating the error of any likely variation of the supplied voltage, over the period of an experiment.

3.2.6 Calibration of load cells

A brief outline of the main points of the method to calculate the applied loads through the measured voltage outputs will be presented together with the calibration procedure deriving from this method.

The general form of the equation relating the output voltage $\Delta V_i = V_i - V_o$ (V_i is the current voltage output, V_o the initial voltage output) for a circuit to the applied normal load N, shear load S and moment M, is

$$\frac{\Delta V_i}{V_{in}} = \frac{V_i - V_o}{V_{in}} = a_1 N + a_2 S + a_3 M \qquad (3.2)$$

where V_{in} is the voltage supply for the circuit and a_1, a_2, a_3 are constants. If all three circuits are combined together, a set of three linear equations are obtained.

$$\frac{(V_i - V_o)_N}{V_{in}} = a_{11} N + a_{12} S + a_{13} M$$

$$\frac{(V_i - V_o)_S}{V_{in}} = a_{21} N + a_{22} S + a_{23} M \qquad (3.3)$$

$$\frac{(V_i - V_o)_M}{V_{in}} = a_{31} N + a_{32} S + a_{33} M$$

where a_{ij} ($i = 1,2,3$, $j = 1,2,3$) are calibration constants and $\frac{(V_i - V_o)_N}{V_{in}}$,

$\frac{(V_i-V_o)_S}{V_{in}}$, $\frac{(V_i-V_o)_M}{V_{in}}$ are the outputs from the three circuits (normal, shear and moment respectively) per input volt. Equations (3.3), written in matrix form, give:

$$\begin{bmatrix} \frac{\Delta V_N}{V_{in}} \\ \frac{\Delta V_S}{V_{in}} \\ \frac{\Delta V_M}{V_{in}} \end{bmatrix} = [a] \times \begin{bmatrix} N \\ S \\ M \end{bmatrix} \qquad (3.4)$$

where

$$[a] = \begin{bmatrix} a_{11} & a_{12} & a_{13} \\ a_{21} & a_{22} & a_{23} \\ a_{31} & a_{32} & a_{33} \end{bmatrix}$$

or:

$$\{V\} = [a] \times \{P\} \qquad (3.5)$$

where

$$\{V\} = \begin{bmatrix} \frac{\Delta V_N}{V_{in}} \\ \frac{\Delta V_S}{V_{in}} \\ \frac{\Delta V_M}{V_{in}} \end{bmatrix} \quad \text{and} \quad \{P\} = \begin{bmatrix} N \\ S \\ M \end{bmatrix}$$

Solving equation (3.5) for the unknown vector {P}, we obtain

$$\{P\} = [a]^{-1} \times \{V\} \qquad (3.6)$$

Equation (3.6) implies that, once the matrix [a] is known, the three loads acting on the cell may be determined from the three voltage outputs.

The matrix [a] was obtained by using a calibration technique outlined by Hambly (1969) and Tennekoon (1970). Various combinations of normal, shear and moment loads were applied on the load cell by means of dead weights. The steel plate, attached to the active face of the cell, by means of countersunk bolts, carried four hooks, which were used for the application of the shear load (fig. 3.17). The normal load and the moment were applied by two different hangers H1, H2 shown in fig. 3.17; dead weights were added at the lower part of the H1 hanger, which rested on a point in a recess in the centre of the calibration plate (P). A small vane, placed underneath the dead weight plate, was submerged into a bucket of water; this helped to accelerate the calibration procedure. The H2 hanger could rest in any of the additional equidistant recesses of the arm of the calibration plate P, and moment was applied by adding smaller dead weights on the hanger. Two thin steel wires, attached to two of the four hooks of the plate, were connected, via a steel rod, with a third wire attached to the steel rod mid-way between the other two wires. The third wire ran over a pulley (PU) which was adjusted so that all the wires lay on the same plane as the load cell contact face. The shear load was applied by adding weights in a hanger attached to the third wire.

During calibration, the load cell was firmly screwed to a plate similar to the footing back plate which itself was rigidly bolted to the calibration frame, and all the connections used were the same ones used later on for the actual experiments. Furthermore, the input voltage was continuously monitored, so that small variations of the power supply could be taken into account in the calibration constants.

As it was mentioned earlier on, all the cells were subjected to a cyclic loading of approximately 120% of the maximum normal design working load, so that any hysteresis effect would be eliminated. The combination of normal, shear and moment loads were:

NORMAL	SHEAR	MOMENT
increasing	0	0
constant	increasing	0
constant	0	increasing

The effect of bolting the calibration plate on the cell face was also investigated by resting the plate accurately and carefully on the active face without bolting the counter-sunk bolts and by applying a normal load. Keeping this load constant, small shear and moment loads were applied, and the calibration lines were found to lie parallel to the ones obtained when using the calibration plate bolted to the cell. Similar findings had been reported by Tennekoon (1970).

It was also found that the moment circuit was sensitive to the applied normal load. This was mainly due to the fact that the centre recess of the calibration plate, as well as the pointed rod of the hanger resting on it, were found to be flattened and this made it difficult to ensure an accurate position of the hanger to the centre of the cell face. In order to establish the above mentioned effect on the calibration constants as well as to simulate the applied load on the footing during testing, another calibration procedure was adopted. The load cells were attached to the back plate and a small steel box was constructed, which fitted the total area of the footing. A rubber bag was then inserted in the box and a uniform load was applied on the footing inflating the bag with air pressure. The 350 KN/m^2 (50 psi) maximum applied pressure, with 35 KN/m^2 (5 psi) increments, was monitored by a BOURDON gauge. An approximately 10% higher output for the normal and shear circuits was recorded and it was decided to use the calibration coefficients from the rubber bag calibration, because it was felt that it simulated, as mentioned above, the normal load conditions during testing in a better way.

The load cells were calibrated both before and after the test first series, and the variation of the calibration coefficients was found to be insignificant.

3.2.7 Accuracy of load cell measurements

The accuracy of the results obtained from the load cells is controlled by the following factors:

(a) Accuracy of the recording system

(b) Zero drift of the bridge circuit

(c) Calibration errors

(d) Power supply instability (fluctuation)

(a) The accuracy of the measurement of the data logging system was specified by the manufacturer, Solatron, to be ± 1 digit on all ranges, which corresponds to ± 0.0025 mV on the 0-20 mV range (x4) used for the load cells. This error should not be considered separately, since it is present in the calibration errors below.

(b) Small temperature fluctuations caused small drifts on the voltage outputs, the maximum ones being ± 0.010 mV (≈ 4 digits) for the normal and shear circuits, and ± 0.015 mV (6 digits) for the moment circuit. Those values were obtained by leaving the load cells without any load for a 4 hour period. Load cell readings taken over one day (24 hours) period during rubber bag calibration, indicated that the temperature fluctuations were much smaller, amounting to an average of ± 0.005 mV (2 digits) for all the normal, shear and moment circuits. The same drift was noticed for a period of one hour with a constant pressure applied on the cells. It is thought that, the maximum fluctuation to be encountered during testing would be ± 0.005 mV for all circuits. (The temperature in the X-ray compound of the Soils Laboratory was kept constant at 20 degrees C (within ± 1°C)). A large drift was noticed when the air-conditioning system of the compound ceased working, the temperature becoming much higher than the required one. Nevertheless, during the whole experimental series, no significant change of temperature was encountered, and, in all probability, the above quoted error applies to all the performed tests.

(c) The maximum deviation from the assumed straight line during calibration was, for each circuit:

i. for the normal circuit ± 0.006 mV
ii. for the shear circuit ± 0.012 mV
iii. for the moment circuit ± 0.050 mV

(d) The energising the bridges voltage was supplied from an essentially constant stabilized power supply. Nevertheless, any likely small variations were taken into account by monitoring the supplied voltage during every data logging scan and the corresponding correction to each cell reading was applied as a proportion to the ratio of the calibration supplied voltage to the current one. Therefore, no error was expected from this source.

Assuming, now, that the errors mentioned above are normally distributed and that the maximum likely error and the standard deviation

are in a fixed ratio (Stroud,1970; Paradine and Rivett, 1960), the maximum likely error in each of the circuit readings is given by the square root of the sum of the squares of the individual maximum likely errors (Paradine and Rivett, 1960). Thus, the maximum likely error in each circuit is:

$$\text{Normal circuit:} \quad \pm \sqrt{(0.010)^2 + (0.006)^2} = \pm 0.012 \text{ mV}$$

$$\text{Shear circuit:} \quad \pm \sqrt{(0.010)^2 + (0.012)^2} = \pm 0.016 \text{ mV}$$

$$\text{Moment circuit:} \quad \pm \sqrt{(0.015)^2 + (0.050)^2} = \pm 0.052 \text{ mV}$$

Considering the case of the rubber bag calibration, the maximum likely error in each circuit is:

$$\text{Normal shear circuits:} \quad \pm\sqrt{(0.010)^2 + (0.005)^2} = \pm 0.011 \text{ mV}$$

$$\text{Moment circuit:} \quad \pm\sqrt{(0.015)^2 + (0.005)^2} = \pm 0.016 \text{ mV}$$

In order to find out the maximum likely error in the measured forces, we will use the calibration constants of one load cell. The [a] matrix of a load cell, which may be considered as typical, is given below (Cell No. 1):

$$[a] = \begin{bmatrix} +0.6121 & +0.3465 & -6.6769 \\ +0.1507 & +3.4409 & +11.5902 \\ +0.4070 & -6.2137 & +406.5138 \end{bmatrix}$$

The units for the first two columns (i.e. for the coefficients a_{11}, a_{12}, a_{21}, a_{22}, a_{31}, a_{32}) are given in mV/(N × V × 1000), whereas the third column coefficients (a_{13}, a_{23}, a_{33}) are given in mV/(N × m × V × 1000).

Following eq. (3.6) and using the inverse matrix $|a|^{-1}$, we obtain:

$$\frac{N}{1000} = 15.7215 \frac{\Delta V_N}{V_{in}} - 1.0673 \frac{\Delta V_S}{V_{in}} + 0.2884 \frac{\Delta V_M}{V_{in}}$$

$$\frac{S}{1000} = -0.6043 \frac{\Delta V_N}{V_{in}} + 2.6889 \frac{\Delta V_S}{V_{in}} - 0.8683 \frac{\Delta V_M}{V_{in}} \qquad (3.7)$$

$$\frac{M}{1000} = -0.02498 \frac{\Delta V_N}{V_{in}} + 0.04216 \frac{\Delta V_S}{V_{in}} + 0.02195 \frac{\Delta V_M}{V_{in}}$$

where N, S are the Normal and Shear loads respectively in Newtons, M is the resultant moment (M = N.e, where e is the eccentricity of the normal load) in Newtons × metres. V_{in} is the input voltage in Volts, and ΔV_N, ΔV_S, ΔV_M are the changes in output of the normal, shear and moment circuits respectively, in mV. For an approximate value of 3.00 Volts, the above equation becomes:

$$\frac{N}{1000} = +5.4205\ \Delta V_N - 0.3561\ \Delta V_S + 0.0961\ \Delta V_M$$

$$\frac{S}{1000} = -0.2011\ \Delta V_N + 0.8966\ \Delta V_S - 0.0284\ \Delta V_M$$

$$\frac{M}{1000} = -0.00833\ \Delta V_N + 0.01406\ \Delta V_S + 0.00732\ \Delta V_M$$

Substituting ΔV_N, ΔV_S, ΔV_M with the corresponding likely errors for the three circuits, we get:

$N = \pm 5.9N$ (± 1.32 lbs) $\quad \sigma_N = \pm 7.32\ KN/m^2$ ($= \pm 1.06$ psi)

$S = \pm 0.99N$ ($= \pm 0.22$ lbs) $\quad \sigma_S = 1.22\ KN/m^2$ ($= \pm 0.18$ psi)

$M = \pm 0.049$ Nm ($= \pm 0.43$ lbs × in)

These are therefore the maximum values of any errors in N, S and M.

CHAPTER 4

EXPERIMENTAL WORK PART III

4.1 The footing apparatus at Southampton

4.1.1 Introduction

In the following chapter, the footing apparatus used at Southampton University (hereafter called F.A.S.) will be described. The F.A.S. was designed and constructed in order to achieve the following aims:

(a) The investigation of the effect of the tank width on both the contact stress distribution and the bearing capacity.

(b) The comparison of the boundary displacements and displacement and strain fields between narrow and wide tank.

To avoid the introduction of a large number of parameters, (i) the same sand, used in the F.A.C. experiments, was employed for the tests in the F.A.S., (ii) Tests would be performed with the same initial boundary conditions as far as possible. (iii) The footing, used in the F.A.C. tests, would be the centre section of the almost three times larger footing designed for the F.A.S. tests.

4.1.2 Test requirements

Following the experimental work performed at F.A.C., the design and construction of the F.A.S. was constrained, in that,

(a) The sand bed had to be uniform and of similar, if not quite identical, porosity, so that the tests to be performed could be compared with these carried out on the F.A.C. This was achieved by using the air activated sand spreader, described below (section 4.1.6).

(b) The tank had to be large enough, so that end effects could be kept to a minimum, Furthermore, the allowable deflection of the sides under maximum load should be very small, in order to preserve plane strain conditions.

(c) The footing, which was to be made of three separate sections, had to be rigid enough, so as to be considered infinitely rigid. Two of these sections would record both the total applied load and the contact

reaction forces, whereas the third one would record the total applied load only. Any load transfer from the one section to the other would be recorded by two small load cells, described in section 4.2.3.
(d) Both the footing and the loading jack should be free to move in the plane of the action of the load, and the footing had to translate and rotate in the same plane.
(e) The dead weight of the jack-footing system had to be balanced, so that its effect on the initial boundary conditions (especially in cases with inclined loads) could be kept to a minimum.
(f) A loading machine, which could maintain the applied load constant for a sufficient period of time to take both readings of the load cells and dial gauges and photographs was required.
(g) The jack-footing system should be easily removed away from the tank area, so that the sand bed could be prepared using the sand spreader.

4.1.3 The footing apparatus (F.A.S.)

The main frame, originally designed by Andrawes (1970), was used after extensive modifications, to overcome the space limitations which it imposed (these will be discussed below). This frame was used for the following reason: the time required to construct a new frame from the very beginning would have been considerably longer and bearing in mind that the sand spreader was already fitted on that frame, it was hoped that the modified sections and the new tank would be constructed over a shorter period. Furthermore, the frame fulfilled, in general, the rigidity requirements for the footing experiments, and the construction cost of the remaining parts could be kept to a low level.

The apparatus was originally designed so that constant penetration of either wedges or footings could be achieved (Andrawes, 1970). The main frame consisted of 152.4 mm × 152.4 mm (6 × 6 in) steel joists SJ (see fig. 4.1) leaving an internal space of 2.62 m × 1.52 m (103 × 60 in). At about 1.60 m (60 in) from the base of the main frame, a horizontal frame, consisting of four 152.4 mm × 76.2 mm (6 × 3 in) steel channels SCH1 (fig. 4.1) was fitted, with four steel columns SCO fixed to its corners, which rested on the floor. This frame was originally used to transmit the load reaction from the penetrating wedge to the main frame, as well as to serve as transverse rails for the sand spreader SS.

Three 101.6 × 50.8 mm (4 × 2 in) channel sections CS, with adjustable feet, were welded on the bottom steel joist, to provide lateral stability. The four 152.4 × 76.2 mm (6 × 3 in) steel channels SCH2, running along the bottom joist and carrying a 9.53 mm (0.375 in) mild steel plate welded on them, which were used to carry the sand tank upwards at constant rate for the wedge penetration tests, were clamped at their lowest position on the three bottom channel sections CS. To improve the rigidity of the main frame, two 12.7 mm (0.5 in) thick mild steel plates were bolted at the two column joints J1 and J2 (fig. 4.1).

A smaller frame, composed of steel channel sections, was fixed at the top joist of the main apparatus, and carried the sand storage tank TS (fig. 4.1) (121.9 × 610 × 610 mm (48 × 24 × 24 in)). A trap door, operated by a handle, and fitted at the base of this tank, was used to discharge the required amount of sand in the sand spreader. Since the angle of repose for dry Leighton-Buzzard sand in loose state is, approximately, 32^{o} (from infinite slope experiments), a large amount of sand, placed between the trap door and the tank sides, would remain in the tank. To avoid that 'hopper' effect, an approximately 30^{o} slope from hardboard was constructed in the storage bin, extending from the sides to the opening, which helped to maintain the sand flow during discharge.

4.1.4 The loading frame

One main requirement for the construction of the loading system was that it should be easily removable, to allow the sand spreader to operate over the tank area. To facilitate close alignment of the footing with the tank, it was decided to maintain the position of the tank adjustable, and a 'rail-guide' system was adopted for the main cross-beam, which will be discussed in the following section.

The main loading system consisted of an AVERY 4.5 ton (10,000 lbs) maximum load hydraulic jack J, with 57 mm (2.26 in) piston, the oil pressure being supplied by an Avery pump, with varying ranges of maximum load for higher sensitivity and of maximum supplied pressure 207,000 KN/m^2 (3000 psi). The jack was suspended from a 1500 mm long Universal

Column with Parallel Flanges UC 203 × 203 × 0.93 mm (8 × 8 × 0.375 in), which in turn was bolted on the two main vertical steel joists SJ (fig. 4.1). The calculated maximum vertical deflection of the UC beam under the maximum expected vertical load was dy_m = 0.46 mm; however, the maximum recorded deflection for the case of a vertical central load acting on the footing was dy_m = 0.17 mm, which amounted to 3% of the maximum recorded footing settlement, and, therefore, the loading frame could be regarded as being perfectly rigid.

Two 12.7 mm (0.5 in) thick steel plates, welded on the beam ends, were used to bolt the cross-beam with 12.7 mm (0.5 in) diam. BSW bolts on the steel joists. In addition, it rested on two equal angles 102 × 9.5 mm (4 × 0.375 in) EQ (fig. 4.1) which were both dowelled and bolted on the steel joists and used as a 'rail-guide' system. The beam could be placed at the edges of the 'rails', which were located just above the 'rail'frame of the sand spreader, and then slid easily to the final position. The two angles were levelled in both directions before the cross-beam rested on them, so that they were used as 'guides' as well as 'rails'. The length of the UC being equal to the inside distance of the steel joists, the main frame SJ had to be 'sprung' laterally slightly (using a removable thick-wall tube section fitted just above the beam, with a nut welded at one end and a 25 mm (1.0 in) diameter BSW bolt, which was free relatively to the nut), so that the UC could slide easily on the prelevelled 'rails'to the required position. To vary the initial angles of inclination of the applied load, two easily removable channel sections CHS with steel plates welded at the end of their legs (fig. 4.1) were located between the beam ends and the equal angles EQ: therefore, the jack, with a maximum travel of 150 mm, could operate at various inclinations (up to 40°), by adjusting the relative position of the cross-beam.

The jack was connected to the beam via a practically frictionless joint, RI, consisting of two tapered roller bearings 30303, with 39 mm shaft diameter, and capable of carrying a maximum working load of 4000 kg, which were housed in two steel blocks SBL1, bolted on a 19.05 mm (0.75 in) thick steel plate, which, in its turn, could be bolted at various positions on the bottom machined face of the cross-beam. A 6.35 × 12.7 mm (0.25 × 0.5 in) cross-section machined steel SB bar

(fig. 4.1) bolted near the one edge of the bottom face of the beam, served as guide for the plate carrying the bearings. The shaft was housed in three separate steel blocks SEL2 which were bolted on a 12.7 mm (0.5 in) thick steel plate fixed on the top face of the jack. The combination of taper-roller bearings and the steel blocks produced a system free from sideways (across the width of the tank) movement. A pulley system, located at both sides of the main frame (PS1, PS2, PS3 fig. 4.1), helped to counterbalance the dead weight of the loading device (i.e. jack, footing). Since the basic hydraulic jack was only single acting, a spring system was designed to help retract the footing from the tank after each test. Two identical stiffness (1.95 kg/mm) coil springs were located over the PL1 plate at the end of ram, with a 12.7 mm (0.5 in) long stud, bolted on the channel, running through the spring. A nut, supplied with a handle, was used to compress the spring, and thereby apply the necessary load to pull the three sections from the tank.

The whole footing assembly was fixed on a 12.7 mm (0.5 in) thick steel plate, which was bolted to the end of the ram of the jack. A 101.6 × 76.2 mm (4 × 3 in) steel channel CHAN carried the three-section footing, was mounted on this plate via a 12.7 mm (0.5 in) thick steel plate, welded at the recessed channel centre (fig. 4.2b). In order to increase the rigidity of the channel section, reinforcement was welded along its length.

4.1.5 The footing assembly

As mentioned in the beginning of this chapter, the footing consisted of three separate sections, mounted directly onto the channel CHAN (figs. 4.2a, 4.2b) and connected to each other by specially made connectors SC, which will be described in a later section. The section near the front glass side (hereafter referred to as SOUTHAMPTON FOOTING, SF) was equipped with 12.7 mm wide load cells, originally designed by Tanner (1972) as part of a model wall for passive earth pressure experiments. The centre section (hereafter referred to as CAMBRIDGE FOOTING, C.F.) was the same footing used during the first series of experiments at Cambridge. The third section, close to the rear side of the tank, was used as a dummy section, (hereafter referred to as DUMMY FOOTING,

D.F.), since there were no boundary force measurements obtained from it.

The main requirements for the design of the footing were: (i) The three sections should perform as a single rigid strip footing.
(ii) They should be able to record independently the applied and reaction forces acting on them as well as any transfer of load from one section to the other when they were constrained to move monolithically.
(iii) The footing should be able to rotate as well as translate in the plane of load application.

In order to fulfill the third requirement, the basic idea underlying the design of the C.F. was adopted for the whole footing. The final design will be briefly described below:
Using the same two slotted bars with the housed-in needle bearings for the C.F., four similar slotted bars were made up from mild steel, each pair to be fitted on the S.F. and D.F. respectively. A 30302 taper-roller bearing with 15 mm shaft diameter was housed in each bar, so that all six bearings through axes were at the same distance with respect to the fotting base. Three identical brackets, each including a load transducer were constructed to connect the footing with the channel CHAN (fig. 4.2b). The top of the bracket contained a 19.05 mm (0.75 in) diameter BSF tapped hole, and an allen bolt was used to connect the channel with each bracket. Each one carried the shaft for the corresponding pair of bearings, so that the axis through the shafts was parallel to the channel CHAN. Thus, when the whole footing was assembled together, the three sections could rotate independently about the same axis. (The clearance between the footing bases was approximately 0.25 mm (0.010 in), so that no sand grain would wedge between two sections and affect the boundary forces readings).

To fulfill the first two requirements, small shear connectors were designed which were located at the front side of the top plate of the three sections. These connectors, apart from forcing the sections to move as a unit, were instrumented with foil strain gauges so that they could record any load transfer between the individual footings.

A more detailed account of the electrical devices involved in monitoring loads and movements will be presented in a later section.

A detailed description of the C.F. has already been presented in chapter 3; a brief description of the other two sections will be outlined hereafter:

The six load cells, which composed the actual base of the S.F., were capable of measuring only the normal reaction forces, and were mounted on a 6.35 mm (0.25 in) thick mild steel plate B (figs 4.2a, 4.2b). This plate was bolted on a 12.7 mm (0.5 in) thick mild steel plate, which carried 12.7 mm (0.5 in) BSW tapped holes, where 12.7 mm (0.5 in) GNK high tensile bolts were used to clamp the slotted bars on it.

The dummy footing consisted of a 76.2 × 50.8 mm (3 × 2 in) channel section, welded on a 9.54 mm (0.375 in) thick mild steel plate mounted together on a 12.7 mm (0.5 in) thick mild steel top plate. The whole assembly was carefully constructed and when complete, the distance between the machined bottom face of the channel CHAN and the base of all the sections was the same within ± 0.05 mm (± 0.003 in). It is worth mentioning that the two outer pairs of the slotted bars (i.e. the S.F. and the D.F. ones) were checked to be parallel within ± 0.012 mm (± 0.0005 in).

The plan dimensions of each side footing were 76.2 × 196.85 mm (3 × 7.75 in) that is slightly longer than the centre section, a limitation imposed by the length of the S.F. load cells. Grade 2S sand paper was bonded to the load cell active faces in order to increase the roughness of the footing base.

4.1.6 Preparation of uniform sand samples

The sand spreader originally designed by Butterfield and Andrawes (1970) was used to prepare the required uniform dense sand bed. The air control system was slightly modified and a water (pink coloured glycerine) manometer was attached on the rear side of the sand spreader, inclined at 20° to the horizontal for increased resolution, and connected via a pipe to the air chamber of the spreader. It was hoped that by this means the actual average air pressure in the chamber could be recorded. Furthermore, an aluminium channel (see fig. 4.3) was attached to the front side above the opening; two small screws helped to adjust the opening and break up arching occurring at its centre under very low air-pressures, so that the sand flow was uniform. Since the densest packing was required, the minimum air-pressure resulting in sand flow was adopted. The uniformity of the sample was determined by measuring the positions at different parts of the deposited sand, using cylindrical perspex density pots, 8.89 cm (3.5 in) diameter and 8.89 cm (3.5 in)

high, with knife edge upper rims. The weights of both the water used to measure their volume, and the sand, were measured on a weigher with maximum load 4000 ± 0.2 gramms. The minimum voids ratio obtained with the minimum air-pressure necessary to produce uniform flow was 0.52 (the minimum density e_{min} for Leighton-Buzzard sand BS sieves 14-25 was measured to be 0.50). However, since the spreader was traversing on the side channels of the rig and not along any specially made rails, the movement, not being free of random vibrations, would affect the intensity of the flow under such a low air-pressure. Furthermore the areas where the direction of the spreader movement was reversed, were marked by change of sand uniformity because of inertia effects. Therefore, it was decided to use a higher air-pressure and the resulted voids ratio 0.53 - 0.54 was maintained throughout the test series. The density variation of the sand sample was checked using density pots, which were placed at various positions both across the width and along the height of the tank and was found to be negligible; thus, there was no need for continuous adjustment of the height of fall, as it was shown by Andrawes (1970). In addition, the final sand surface was well over 600 mm from the opening, the minimum required height of fall to produce uniform sand beds with small variation in voids ratio with depth (James, 1965). An attempt to eliminate the reversal effect proved to give satisfactory results, without, though, eliminating the resulting local non-uniformity; the tank length was adjusted to be some 50 mm shorter than the fixed spreader travel, so that the reversal would take place outside the main tank. An inclined steel channel and a small framed cardboard box (fig. 4.1) were placed at either ends of the tank, to collect the sand poured at the change of direction. It was reckoned, however, that an extra 300 mm length of spreader travel either side was necessary, in order to eliminate completely the afore-mentioned effects. Unfortunately, this could not be accommodated because of the limitation imposed by the existing main frame. Nevertheless this small modification improved the performance of the sand spreader and it was felt that the local non-uniformity occurring at the two ends of the tank would hardly affect the results of the experiment.

Even though approximately the same air-pressure was used for the preparation of all the sand samples, density pots were used to check

the resulting voids ratio after the end of the pouring; the whole tank covered by a plate and the density pots, placed on it, were filled with sand. As a final corroboration of the initial average voids ratio, the weight of the sand was weighed after each test, before filling up the container above the sand spreader. The dimensions of the tank having been measured accurately with a 1000 mm × 0.5 mm steel ruler, the voids ratio was calculated using the formula shown in chapter 3.1.7.

4.1.7 The tank

A new tank, in which the experiments were to be performed, was designed and built, according to the following requirements:

(i) The friction between sand particles and tank sides should be kept to a minimum.

(ii) The container sides should be rigid enough so that the maximum deflection under the maximum load should not be excessive if plane strain conditions were to be satisfied.

(iii) The tank width should be adjustable, and it should allow a sufficient sand sample height to be formed.

(iv) Photographic recording of the sand particles movements should be possible.

The second requirement was the main reason for not using the then existing sand container, because it was reckoned that the sides were not and could not be modified to be sufficiently rigid for the high stress-level experiments to be performed. Furthermore, its width should be increased to accommodate the footing length. The new sand container frame (fig. 4.1) consisted of three horizontal rectangular frames made of 50.8 × 6.35 mm (2 × 0.25 in) equal angles mild steel and kept at their relative position by four similar angle sections welded at the four corners of the overall framework. At the front large side, where photography was to be used, a 38.1 mm (1.5 in) thick toughened glass plate was used, with overall plan dimensions 1270 × 430 mm. This plate rested on 25.4 mm (1.0 in) thick hard wood, with a 6.35 mm (0.25 in) thick glass plate covering its inner face. The rear large side consisted of a 35.0 mm thick flat plywood plate, with a 6.35 mm (0.25 in) thick glass plate attached to its entire inner side. The two smaller

adjustable sides were made of 12.7 mm (0.5 in) hardwood plates, with thin hard rubber strips glued on the edge facing the rear glass side. A 25.4 mm (1.0 in) square tube section, with a similar thin hard rubber strip attached to the face supporting the front glass plate, was placed between the hardwood plate and the toughened glass side. Four 76.2 × 50.8 × 6.35 mm (3 × 2 × 0.25 in) steel angle sections were placed upright at the four corners of the container, inside the main steel frame, their inner faces covered with similar hard rubber strips, and their position adjusted with the help of 9.35 mm (0.375 in) diameter set screws by the angles section of the main frame. This arrangement provided the facility for altering the width of the tank by choosing the appropriate dimensions for the hardwood plates. The length of the tank could also be adjusted by using an extra plate at the required position, and supported via wooden and steel spacers by the main plate.

A diagrammatic plan view of the tank is given in fig. 4.4, and an overall view of it in fig. 4.1. The four sides were supported at various points by adjustable rubber faced steel pads which were held in position by 12.7 mm (0.5 in) diameter bolts screwed into the main framework of the tank. In addition to that, two 6.35 mm (0.25 in) thick steel strips, running across the tank width, were bolted on the top angles. This arrangement increased the load carrying capacity of the sides and helped to minimize their deflection during testing. The whole frame, bolted on a 20 mm wood flat plate, was clamped on the steel plate welded on the four channels SCH2 (fig. 4.1), and adjustable steel sections, resting on the vertical steel joists of the main apparatus, supported the shorter sides of it.

The effective dimensions of the container were 1230 × 584 × 610 mm with respect to length × width × depth. The overall dimensions of the apparatus did not allow a greater effective depth, but it was reckoned that the rigid plate at the bottom would not affect the experimental results. However, the effective length of the tank had to be reduced to 1055 mm, the sand spreader maximum travel being approximately 1000 mm.

4.1.8 Settlement recording

Two different systems of recording the footing displacements were used; one electrical and one mechanical. The former employed three linear

variable differential transducers mounted on a 500 × 50.8 × 6.35 mm machined mild steel plate. Two of them, having 76.2 mm (3 in) maximum travel were fixed at right angles to the plate, whereas the third one, with 114.3 mm (4.5 in) maximum travel, was fixed at right angles to the other two and along the long side of the plate. A similar arrangement was adopted for the latter system (the mechanical one), which consisted of three mechanical dial gauges reading to 0.01 mm accuracy; two of them had 50.8 mm (2 in) travel and the third 25.4 mm (1.0 in) travel. The whole arrangement was similar to the one used at Cambridge, with the steel plate replacing the Dexion frame. Each system operated at either end of the footing, and the two plates were clamped (with G clamps) on two 9.35 mm (0.375 in) thick steel plates which, lying either side of the footing and running across the tank width, were clamped on the top angle sections of the frame. The whole set up was levelled up, so that the two plates carrying the dial gauges and the LVDTs were parallel to the initially horizontal position of the footing. The linear transducers were calibrated with a barrel micrometer, and a constant 10 V D.C. power was supplied to them. Fig. 4.1 shows the relative position of both the dial gauges and the linear transducers with respect to the footing.

4.1.9 Test procedure

After the end of an experiment, the settlement measuring frames were removed from the test area, and the footing was retracted from the tank. The jack was then rotated to its maximum inclination with respect to the vertical (approximately 50^{o}), by applying dead weights on the hanger, H1 of the PS2, PS3 pulley system (fig. 4.1), and the plate carrying the bearings was disconnected from the UC cross-beam. The jack-footing system was carefully lowered on a 12.7 mm (0.5 in) thick hardwood plate resting on the top angles of the tank frame and the four pipes, supplying the oil pressure from the Avery pump, were disconnected. An electrical crane was used to carry the wooden plate away from the tank. The sand was, then, removed from the tank into plastic containers, where it was weighed with a 180 × 0.5 kg (400 × 1 lbs) spring weigher before it was poured into the storage tank. A special frame was constructed to lift the plastic containers with the use of the crane. The UC cross-beam was then disconnected from the vertical joists and was pushed to the side of the apparatus on the 'fail-guide' angles, where it

was picked up by the crane. One of these angles was also removed from the rig, to allow the sand spreader to operate at its maximum permissible travel. Having removed the main loading frame from the test area, the sand spreader was placed on the trailer which travelled at constant velocity on the horizontal channel rails SCH1 (fig. 4.1) and the air-pressure system was connected. Before the sand pouring, the inside faces of the glass sides of the tank were cleaned with Tricon (Trichloro-ethylene) to ensure a consistent low friction coefficient surface. This was followed by measuring both the width and the length of the tank at various sections, and the setting up of polythene sheets around the pouring area which served to minimize sand grain spillage outside the tank.

The sand sample was then set up, as described in section 1.6, and the final surface was levelled with a device similar to that used for the Cambridge experiments. Before levelling the final surface, the density pots were used (see section 4.1.6) to check the uniformity of the obtained sample. The test area was subsequently covered with wooden plates, after measuring the height of the final sand surface, to avoid any accidental disturbance of the sand sample. Driving the trailer to its furthest position before reversing (near the air-pressure controls) the sand spreader was removed and the angle 'rail-guide' was put back into position. After levelling up, the UC cross-beam, carried with the crane, was placed on the two angles EQ (fig. 4.1). The beam was easily pushed into the required position (the steel joists having been previously sprung slightly using the device described in section 4.1.3) the latter being ensured by special guides clamped at both flat ends of the beam. After connecting the beam with the steel joists, the jack-footing system was brought to the tank area, and the plate carrying the top bearings was bolted at the bottom of the UC beam. The initial readings of the load cells were then recorded (the load cells were not disconnected from the power supply after the completion of the preceding experiment and were scanned at various intervals during test preparation to establish any major drifts), and both the oil pipes and the pulley systems were connected with the jack. Before setting the jack to its initial position, the footings were adjusted to the required relative position with respect to the slotted bars, with the help of slip gauges,

and then, they were bolted firmly together. A 127 mm (5 in) sin-bar, in conjunction with an accurate spirit level, helped to set up the jack at the initial position, where it was held by the dead weights of the balancing systems. The subsequent movements of the jack were monitored by a dial gauge, clamped at the bottom face of the UC beam via a magnetic base and pointing at the rear of the jack, as well as by the sin-bar, which was used as an 'on spot' indication of the current position of the jack.

Two dial gauges monitored the deflections of the glass sides, and an extra dial gauge monitored the deflection of the UC beam. After setting the jack to its initial position, the footing was levelled with the help of spirit levels and was locked at the horizontal position while a very small oil pressure was used to lower it carefully and gently onto the sand surface. The two reinforced steel strips were then bolted onto the top angles of the tank and the LVDTs and dial gauges frames were assembled.

Having completed the main preparation, the plate camera, its heavy tripod being fixed onto a specially constructed wooden frame (see chapter 5.3.3), was adjusted so that two 500 W flood lights were placed at the necessary position (where they remained until the end of the test). A number of cassettes were loaded up, and the first photograph was taken. This was developed and fixed before starting loading up the footing, and having recorded both dial gauges and electrical devices, the first increment was applied. The magnitude of a load increment was determined by the recorded settlement and it became distinctly smaller as the failure condition was approached. Photographs were taken at various intervals (the load was kept constant during both scanning and taking photographs), but they were not developed before the end of the test. Usually, at least ten load increments were performed with the exception of the last test (initial load inclination 5^{o}) where a total of twenty four increments were performed, (mainly due to unload-reload steps). A list of the performed tests is given in table 1. All tests were carried up to ultimate failure, and a final photograph was then taken. The average ultimate load was monitored at the Avery pump, as well as at any one of the three digital voltmeters, each monitoring one of the three total load cells.

The average duration of the test was approximately three hours, and the experiments were carried out during the early afternoon, when the temperature would be constant for that period. Furthermore, large polythene sheets covered the whole apparatus, in order to maintain the constant temperature conditions required during the testing. After the end of an experiment, the footing was retracted from the tank, and the paper-tape output was processed at the ICL - 1907 University Computer.

4.2 Load and boundary stress measurements

4.2.1 Introduction

During every experiment, both the reaction forces on the footing contact area as well as the overall applied loads on each section of the footing were measured by load cells. The main features concerning their design and operation will be described in this section. The footing, already described in section 4.1.5 consisted of three sections, two active (with respect to boundary stress measurements) and one dummy (fig. 4.2b). The axially applied total load on each section was recorded by proving ring type load cells fitted between the slotted bars and the rigid channel, carrying the three units. The forces transferred between the footings were recorded by specially made load cells, which were fitted on the top plates of the three sections. In the following, a more detailed description of the load cells measuring the contact forces on the S.F. section, together with the proving rings and the shear connectors will be presented. Then, a brief discussion of their performance and accuracy of measurement together with a description of the calibration procedure and the recording equipment, will be described. The centre section of the footing consisted of the C.F., the same footing used for the Part I experiments, and its load cells are described in more detail in chapter 3.2.2.

4.2.2 Normal load cells of the S.F.

4.2.2.1 Description of the load cell

The actual base of the S.F. section consisted of six load cells, 196.85 mm (7.75 in) long, 12.70 mm (0.50 in) wide and 46.99 mm (1.85 in) high each. A typical load cell is shown in fig. 4.5. The main

characteristic of this design was the two arms AB and A'B', which, under the applied load on the active face CC', worked as cantilevers with their fixed ends at A and A'. A detailed description of the design, construction and operation of the load cells has been presented by Tanner (1971), and a brief presentation of their main features will be outlined below.

Constructed out of mild steel, the cell consisted mainly of two parts: The main body EABDD'B'A'E' and the active face plate CC'D'D. The main body, machined out of a single piece of steel, provided extra space S and S'' (fig. 4.5) which was necessary to enable the bonding of the strain gauges b and b'. The minimum space between the two main blocks of the cell was 3.175 mm (0.125 in), becoming 8.89 mm (0.35 in) at S and S'. The AA'E'E backing block was machined to be 12.7 mm (0.5 in) wide, whereas the active face 6.35 mm (0.25 in) thick and 196.85 mm (7.75 in) long steel plate was 12.60 mm (0.496 in) wide, so that when all the load cells were bolted together on a common rigid backing plate, with the AA'E'E backing blocks of neighbouring cells in contact, the required 0.010 mm (0.004 in) gap between each cell would be obtained. Three counter-sunk screws held the CC'D'D plate on the main cell body, and the cell was bolted on the 6.35 mm (0.25 in) thick mild steel plate via two 6.35 mm (0.25 in) diameter allen bolts.

4.2.2.2 Circuit

Four 120 Ohms, 2.10 gauge factor 'SHOWA' foil strain gauges were bonded to both sides of the two cantilevers, at a,b,a',b' (fig. 4.5). A terminal strip, mounted on one of the cantilevers, was used to connect the gauges of each cell to a four-core miniature cable, which carried the electrical signal to the balancing box via an eight-way square pin Plessey plug (every such plug carried the signals of three cells; two of the pins used for the common power supply and the other three pairs for the three output signals). To achieve higher load-output sensitivity, a fully active four arm Wheatstone bridge was used. This arrangement had the extra advantage of self temperature compensation, since all active gauges, being bonded to the roots of the two cantilevers, would experience the same variation in temperature or humidity.

The circuit used, is shown in fig. 4.6. Two gauges being in tension

(b,b') and two in compression (a,a'), the net result would be the sum of the changes in resistance of the four gauges, as is shown below:

$$V_{out} = V_{input} \times \frac{F}{4} \times \varepsilon_{net}$$

where $\varepsilon_{net} = \varepsilon_b + \varepsilon_{b'} - (\varepsilon_a + \varepsilon_{a'})$. But since $R_a = R_b = R_{a'} = R_{b'} = R$ and $\varepsilon_b = -\varepsilon_a = \varepsilon_{b'} = -\varepsilon_{a'}$, then $\varepsilon_{net} = 4\varepsilon$ and the above equation becomes:

$$V_{out} = V_{input} \times F \times \varepsilon$$

An at least two times higher sensitivity could be achieved by using two full active four arm bridges under a higher common power supply than the one used by Tanner (1972). Since the maximum width of a 8 mm foil strain gauge is only 3 mm, pairs of gauges could be bonded to the position where a single gauge was used, their axes being parallel to the cantilever length (fig. 4.7a). Thus, each cantilever would create a full four arm Wheatstone bridge and the sum of the two bridges' outputs would provide the total applied load on the cell face. Furthermore this configuration would monitor any non-central load (along the length of the cell face). Such a loading condition, however, did not affect the cell performance, as found by Tanner (and confirmed, during calibration, by the author) and it was decided that the cells should be used with the existing circuits.

Nevertheless, an increased input voltage of 3 Volts D.C. was used, providing 1.5 times higher output for the same applied load, since it was felt that the cantilever was thick enough to allow for a quick and safe heat dissipation, without affecting the gauge performance.

4.2.2.3 Calibration

Even though the maximum design load to cause yield at the cantilever roots was approximately 90 kg (200 lbs), the included factor of safety together with the simplified assumption of the cell operation underestimated the load cell capability to resist linearly higher loads than this. The cells were tested on an Instron Universal testing machine at the Model Structures laboratory, where they were loaded many times

up to 182 kg (400 lbs). Both the load-strain curve and the load-millivolt curve obtained were found to be linear, thus justifying the intended use of 160 kg (350 lbs) maximum load per cell for the experiments. Having established this linearity in high loads, the cells were recalibrated under dead weights up to 130 kg (300 lbs). A mild steel plate CP was used to transfer the load, applied by a hanger via a ball bearing BB (fig. 4.8), on the active cell face. Two silver steel rollers SR, located in symmetrical positions with respect to the cell axis by two recesses on the underside face of the plate, were used to transfer the load from the beam to the cell. A constant 3.0 volt power supply was used and the voltage was continuously monitored and recorded by a Solatron portable multimeter, whereas the cell output was monitored by a Dynamco digital voltmeter with a D6 module. The cell was firmly clamped on a rigid calibration frame consisting mainly of channel sections. The calibration procedure did not start before at least 2 hours after energising the cell circuit, thus allowing sufficient time for the strain gauges to warm up and to stabilize (the power supply was kept on for the whole calibratoon period), and, therefore, minimize the drift due to increasing temperature. No shear loads were applied during calibration, since Tanner (1972) had found out that the cell output was not affected by the application of such loads.

Before calibrating the load cells, the sand grains, glued on their active face to increase their relative roughness, were removed and both the active CC' and backing EE' faces (fig. 4.5) were carefully machined. After calibration was finished, 2S grade sand paper was glued on the active faces in order to obtain the same relative roughness with the centre C.F. section.

4.2.3 The shear connectors

4.2.3.1 Description

Two of the main requirements for the design of the footing were that the three sections should perform as a rigid strip, and that, on the same time, they should record independently both the applied and the reaction forces. To fulfill these requirements and, since the three sections were made in such a way that they could rotate through the same axis, suspended through load cells from the same channel CHAN

(fig. 4.2) special attachments were necessary to restrict rotation relative to each other. However, these connectors would interfere with the measurement of loads and, in view of this, it was decided to design special load cells, which apart from restricting relative rotation, would be able to record any potential load transfer from one section to another. The requirements, therefore, for the design of these load cells, as imposed by the nature of the problem, were:

(i) They should be rigid enough to ensure that the three footing sections formed a rigid strip.

(ii) They should be sensitive to small loads, (approximately 0.5 kg). and they should be capable of measuring loads up to 100 kg (220 lbs).

(iii) They should be made out of a single piece of mild steel.

(iv) They should be unaffected by normal loads or moments.

(v) The circuit employed should be temperature compensating.

(vi) The load sensitive part of the cells should be thin enough to establish the line of the action of the transferred load, and, therefore, to evaluate the resulting moment with respect to the rotation axis.

Two sections of the load cell designed are shown in fig. 4.9. The two relatively symmetrical rigid blocks, connected together via the thin web (16 mm × 15 mm × 3 mm with respect to length × height × thickness) were bolted on the top backing plates of the footing sections using two 6.35 mm (0.25 in) diameter BSF allen bolts on each side. Two 3 mm diameter dowel pins on each block, ensured a firm location of each block on the plate, and a cable clamp on one of the blocks safeguarded the cable carrying the signal from the terminal strip to the balancing box. Both load cells were bolted at the furthest possible location from the rotation axis, so that a higher output could be ensured. The rear face of one of the blocks carried accurately located punch marks with 5 mm spacing, which were used to apply loads during calibration.

4.2.3.2 Circuit

Two 'SHOWA' rosettes each consisting of two 120 Ohms, 2.06 gauge factor foil strain gauges, with their filament inclined at 45^{o} to the axis of the rosette, were bonded each on either side of the web face and at its mid-height, the rosette axis being parallel to the web length.

The full four active arm Wheatstone bridge resulted from the two rosettes provided both high sensitivity and self temperature compensation and the use of dummy strain gauges was avoided. The circuit used, shown in fig. 4.10b, provided maximum sensitivity for shear loads S (fig. 4.10a) acting on the web, whereas compensated against any moment M and normal load N. It also compensated against moments applied on planes perpendicular to the one defined by the web face.

4.2.3.3 Calibration

One of these cells was first constructed and calibrated to explore its performance. The calibration loads were applied by means of dead weights on an aluminium hanger, which in turn applied the load to a specially made 6.35 mm (0.25 in) thick steel plate, bolted on one side of the cell, via a stainless steel prong sitting in any of the indentations in the top surface of the plate (fig. 4.11). The other rigid side of the cell was bolted on the calibration frame. A constant 3.0 Volts D.C. was supplied to the circuit and was monitored continuously by a Solatron Schulberger multimeter, whereas the cell output was monitored on the Dynamco digital voltmeter with D6 module. During calibration it was found, as expected, that the relative position of the hanger on the plate did not affect at all the output voltage. The cell was then clamped on the calibration frame with the rear side facing upwards and a number of load cycles performed with the prong of the hanger sitting in any one of the indentations of the cell face; no change of the cell output was again recorded. The approximately 12 μ volts per 10N (12 μV per kg (for 3 volts D.C. power supply)) sensitivity was quite satisfactory, since the intended minimum 5 N (0.5 kg) detectable load corresponded to 6 μV, which was above the resolution of the recording equipment (a detailed account of the accuracy of measurements will be discussed in section 4.2.6).

The second load cell was, therefore, constructed in exactly the same way and after wiring it up, it was calibrated with the same method, producing an almost identical calibration curve (compare 11.2 μV/ 10N (11.2 μV/kg) of the first cell with 11.5 μV/ 10N (11.5 μV/kg) for the second one, for the same constant 3.0 Volts D.C. supply.

Before these cells were calibrated, they were loaded cyclically

up to 120% of the maximum load a number of times, to remove any initial hysteresis. The aluminium hanger was loaded by dead weights and then it was lifted slightly with the help of a lever. This was repeated approximately 40 times, which was sufficient to produce the same load cell output for zero applied load.

4.2.4 Total load cells

4.2.4.1 Description

The applied load on each section of the footing was recorded by three proving ring type load cells, two commercially made ones and another manufactured at the University workshops. The cell is essentially a flat proving ring and its deflection due to externally applied load is measured by a LVDT displacement transducer, housed at its centre (fig. 4.12). The two commercial ones, one Boulton Paul Aircraft LTD and the other SANGAMO LTD (identical cells), were of the 1140 kg (2500 lbs) range working load and were fitted at the C.F. and S.F. sections respectively. The third one, made out of a solid piece of mild steel, was tested and calibrated satisfactorily up to 900 kg (2000 lbs) and was fitted at the dummy section. A Sangamo DC/DC displacement transducer replaced the AC/AC one used by Andrawes (1970) and Tanner (1972) and a 10 Volt DC power energized the circuit. The other two load cells, fitted with AC/AC displacement transducers, were coupled with two transducer meters, which were used for both energizing the transducers and transforming the AC signal to a DC one, so that it could be monitored by the data-logging system.

4.2.4.2 Calibration

Each of the three load cells were calibrated at the Instron Universal testing machine up to 900 kg (2000 lbs) as well as by dead weights up to 100 kg (220 lbs). The machine was operated manually and many load steps were performed at different load ranges up to the maximum 900 kg (2000 lbs) one. The DC output was monitored on the Dynamco digital voltmeter. The performance and linearity of the load cells was proved to be quite satisfactory.

4.2.5 Recording system

The equipment used for supplying the power to the load cells, measuring the output voltages and recording the readings will be briefly described in the following section.

A general layout of the recording system is shown diagrammatically in fig. 4.13. The input voltage to the C.F. and S.F. section load cells and to the two shear connectors was supplied by two stabilized voltage supply units P1, P2 (fig. 4.13), made by Coutant Electronics Ltd. Energized by 240 volts mains, they produced an adjustable stabilized DC output from 1 to 4 volts with maximum load 1 amps; they also provided a feedback system in order to compensate for any fluctuation of the voltage. The 3 volts DC supplies were monitored during every scan of the data logging system. A third unit, P3, made by the same company, supplied a 10 volt DC to energize the three transducers recording the footing movement and the total load cell of the dummy section. Again, the power supply was monitored at every scan. Two Boulton Paul C.52 transducer meters T.M.1, T.M.2 (fig. 4.13) provided the power supply to the total load cells of the C.F. and S.F. sections. Energized by 200 - 250 volts mains, they provided 5 volts r.m.s. 5 kc/s for the AC transducers of the load cells and a filtered DC output of the AC transducer signal.

The electrical signals were transferred by screened cables to two balancing boxes BB1 and BB2 where balancing ocide resistors were used to scale the voltage outputs down to the most sensitive scale on the digital voltmeter of the Data logger. From these boxes the signals were transferred via eight screened cables attached to four 36-way Amphenol plugs to a transfer box (T.B.) and then to the Data logging system. The data logger unit, made by Dynamco, incorporated a DM2006 digital voltmeter using a D6 module, where 1 μV could be recorded (with an accuracy of ± 1 μV' on its most sensitive range, the 10 mV one, which was used for the experiments. Finally the data from the 35 channels were punched on a Data Dynamics 110 high speed tape punch and the paper tape output was processed on an ICL 1907 Computer.

4.2.6 Accuracy of measurements

The accuracy of measurements of the load cells outputs is mainly

controlled as was mentioned in chapter 3.2.7, by the following factors:

(a) Accuracy of the recording equipment.

(b) Zero drift of the bridge circuit (as well as under constant load).

(c) Calibration errors.

(d) Power supply instability.

Since the centre section was instrumented with the same load cells used at the Part I experiments with the Cambridge footing apparatus, the likely errors of the load cells readings due to calibration errors and power supply instability are identical to the ones discussed in chapter 3.2.7. As far as the accuracy of the data logger and the drift of the bridges is concerned, it will be seen that it mounts to approximately similar magnitudes. Therefore, in all probability, the same maximum likely errors will prevail the measurements of the cells during the experiments at the Southampton footing apparatus.

(a) The accuracy of the data logger unit, as stated by the manufacturers, Dynamco, on the most sensitive range used (0-10 mV) is ± 1 digit, which corresponds to ± 1 μV. However, it was noticed that all the circuits could not be measured with a better than ± 2 digits (± 2 μV) accuracy. This was found to be due to the drift of the digital voltmeter rather than to the drift of the load cell bridges (this error is included in the calibration errors, since the same D.V.M. was used for the recording of the cells outputs during calibration).

(b) The zero drift of the bridge circuit will be considered for each set of load cells used in the experiments.

1. Normal load cells (S.F. section)

An average zero drift of 3.5μ V was observed from a series of readings of the normal load cell circuits, for a 6 hours period with no load applied on the load cells. An average test lasted approximately three hours and, therefore, the maximum expected fluctuations (with the inherent drift of the recording equipment) would be ± 3.5 μV. This drift represented an error in measurement of the normal load of ± 2.5 N (± 0.25 kg (± 0.5 lbs)) for the least sensitive cell (the cells varied in sensitivity, and this was mainly due to the variations in the gauge positions, as well as to slight dimensional variations between cells (Tanner 1972)).

2. C.F. section load cells

The average drift of the normal and shear circuit of a load cell was ± 6 μV for the above mentioned 6 hours period, whereas the moment circuit fluctuation was ± 3 μV in average. Compared with the average ± 5 μV drift for all circuits encountered during the Part I experiments, no significant difference was noticed during the Part II experiments, and, therefore, the same errors in measurements of the load cell outputs was expected.

3. 'Shear connectors'

The maximum drift observed for both the 'shear' connectors was ± 2 μV, which corresponded to ± 3.5 N (± 0.35 kg (± 0.8 lbs)) (for the same period of 6 hours). This drift was the same with the inherent fluctuation of the voltmeter.

4. Total load cells

For the two load cells fitted at the C.F. and S.F. sections a maximum ± 3 μV fluctuation was noticed during the 6 hours period. The only constant applied load was the dead weight of the footing. This fluctuation corresponded to ± 3 N (± 0.3 kg (± 0.63 lbs)) for both load cells. The drift of the dummy section load cell was noticed to be ± 4 μV corresponding to an error in load measurement of about ± 4.5 N (± 0.45 kg (± 1 lbs)).

(c) Again, the cases in individual groups will be presented.

(1) The C.F. section load cells calibration errors have been already discussed in chapter 3.2.7.

(2) The maximum deviation from the calibration curves, appeared on the least sensitive load cell, was ± 3 μV, which corresponded to ± 2 N (± 0.2 kg (+ 0.44 lbs)).

(3) The maximum deviation from the calibration curves of the shear connectors was ± 2 μV, but the drift observed during calibration amounted to ± 3 μV, corresponding to shear load of ± 3 N (± 0.28 kg (± 0.6 lbs)).

(4) The deviation from linearity at the 1135 kg (2500 lbs) range is stated by the manufacturers to be ± 1% which implies a maximum expected error, if maximum used load is 1135 kg (2500 lbs), of ± 110 N (± 11 kg (± 25 lbs)). From the calibration curves, however, the maximum observed

deviation was ± 40 μV, which represented ± 40N (± 3.8 kg (± 8.4 lbs)). For the dummy section load cell, the maximum deviation was ± 4 μV corresponding to ± 5 N (± 0.45 kg (± 1.0 lbs)).

(d) Power supply instability.

The accuracy of the three DC stabilized power supplies, as stated by the manufacturers, is ± 0.001% for ± 10% mains change and 0.005%/°C. During an experiment, the maximum recorded fluctuation of the output voltage was less than ± 0.005%. Nevertheless, the voltage supply of the circuits was monitored during every data logging scan and the corresponding correction (if any) with respect to the calibration input voltage was applied.

The power supply to the two total load cells measuring the total load of the C.F. and S.F. sections was provided from two Boulton Paul Aircraft Ltd. C52 transducer meters. The frequency variation is stated by the manufacturers to be less than 0.1%. An excessive drift was observed from the DC passive filtered outputs, probably due to the incomplete filtering of the AC signal; two 125 μFarad capacitors were used to stabilize the output, including some unavoidable small time lag in the load cell response, but without any particular consequence, since the load cell readings were scanned 10 mins after each load increment was applied. During testing, two 500 Watt photoflood lamps were used to illuminate the sand model for photography (close to the S.F. section), and the radiated heat could cause the load cells to drift. However, this was avoided by switching the lights on and off every time a photograph was to be taken. This procedure lasted approximately 2 seconds, and it was thought that no appreciable heat could be generated to cause output fluctuation.

Adopting the same assumptions as in chapter 3.2.7, the maximum likely error for each group is:

(a) Normal load cells (S.F. section)

$$\pm \sqrt{(0.0035)^2 + (0.003)^2} = \pm 0.0046 \text{ mV} = \pm 4.6 \text{ μV}$$

which corresponds to ± 3 N (± 0.31 kg (± 0.7 lbs)).

(b) 'Shear' connectors

$$\pm \sqrt{(0.002)^2 + (0.003)^2} = \pm 0.0036 \text{ mV} = \pm 3.6 \ \mu V$$

which corresponds to ± 3 N (± 0.33 kg (± 0.72 lbs))

(c) Total load cells

(1) C.F. and S.F. sections

$$\pm \sqrt{(0.003)^2 + (0.040)^2} = \pm 0.0401 \text{ mV} = \pm 40.1 \ \mu V$$

which corresponds to ± 40N (± 3.8 kg (± 8.4 lbs))

(2) D.F. section (proving ring type)

$$\pm \sqrt{(0.004)^2 + (0.004)^2} = \pm 0.0057 \text{ mV} = \pm 05.7 \ \mu V$$

which corresponds to ± 6 N (± 0.6 kg (± 1.4 lbs))

CHAPTER 5

MEASUREMENT OF THE DEFORMATION OF THE SAND MASS

5.1 Introduction

The influence of the deformation within a soil element upon its shear resistance has been long realized by research workers, but, owing to difficulties in measuring such deformations, few attempts were made to study this problem. However, in the last fifteen years, the re-introduction of non-destructive X-rays (Roscoe, Arthur, James, 1963) and the extended application of stereophotogrammetry (Butterfield et al., 1970) and of the Moiré method (Nikitin-Nesmelov, 1973) have provided the means to measure, fairly accurately, displacement fields within (X-rays) or on the boundary (photography) of a deforming soil mass.

The various techniques used for measuring displacements may be divided into four groups, depending on the method employed for recording the soil movements: (a) Techniques involving transducers embedded in the soil (b) Techniques involving the use of X-rays (c) Techniques involving the use of photography (d) Other techniques.

Both X-rays and photography were employed by the author for the displacement recording of the sand mass; but, before describing the methods used in detail, a brief account of the techniques in each of the four groups will be presented.

(a) This technique involves displacement transducers embedded in the soil mass, which are able to record directly the local displacement. Eggestad (1964), for example, has used specially made variable inductance transducers in model tests of footings on sand. The fact, however, that the transducer embedded in the material is a foreign body, and hence introduced interference is unavoidable, reduces the reliability of the measurements. Furthermore, a large number of transducers are necessary in order to obtain representative information on a displacement field, but this will inevitably result in a substantial alteration of the material properties. The use of telemetric settlement gauges (Prange 1971) minimizes the influence introduced by the connections carrying the signal out of the sample; their present relative size and precision,

however, make them suitable for large scale tests or field work only, where their application (especially in earth-dams) has been successful (Prange, 1971).

(b) This technique involves radiographic recording of embedded load markers. As early as 1929, Gerber (Tschebotarioff 1951) pioneering this method, used X-rays to observe the total movements of embedded small lead spheres in his tests on footings on sand, taking two radiographs on the same film, one before and one after the application of the load to the footing. In 1949, Davis and Woodward (Roscoe, Arthur, James, 1963) measured relatively small incremental displacements using a refined version of the same technique. Again, Bergfelt (1956) used X-rays to determine, mainly qualitatively, the movements resulting from loading tests in clay. Basically the same idea was adopted and two square grids of lead shot were placed in the 300 mm thick clay sample. However, dimensionless deformation (strain) fields derived from the observed displacement fields were first calculated by Roscoe, Arthur and James (1963), using essentially the same experimental technique: A lead shot network was placed near the centre plane of the model, and the relative position of the markers, after successive load increments was recorded by X-rays. The power of this approach lies on the fact that the distribution of strains within a soil mass is not influenced by the boundaries of the container of the soil, and provided boundary stresses are measured, some form of a stress-strain relationship may result for the particular boundary value problem studied. In addition to that, the failure surface, in medium dense to dense sands is visible on the film as a dark band, which may be compared directly with respect to shape and depth, etc. with analytically predicted surfaces.

However,the limitation of the sample thickness in plane strain or axisymmetric conditions, due to the penetrating power of the X-rays, raises doubts on the overall influence of the narrow sand container on both the stresses and strains measured. An attempt by Arthur and Roscoe (1965) to investigate the difference between strain patterns obtained by the X-ray method and those obtained by photography of discrete nylon markers on the sand-glass interface, showed that the difference was very small. Furthermore, Tennekoon (1970) measured almost identical stresses underneath a footing near the glass sides of the 190.5 mm (7.5 in) wide sand container as at the centre. Rowe and Peaker (1965) however, using

a 1.80 m wide retaining wall in plain strain conditions, divided into three parts, found out that the horizontal load recorded from the central part of the passively translating wall was 33% less than that recorded from a side section. Even though the first two investigations imply that the sides do not interfere with the measured strains, there is a strong possibility that the effect of friction is spread uniformly across the width of the tank which cannot be ruled out.

An answer to this problem may be provided if a wide tank is used in plane strain conditions, where displacement fields are measured near the centre section of the sample (by X-rays) and at the glass-soil interface (photography) and boundary stresses recorded at different sections across the width. The first requirement implies the use of a very powerful X-ray unit and consequently the existence of a very specialized laboratory with adequate safety facilities. The second requirement may be met by proper boundary instrumentation which was provided for the second series of tests carried out by the author in the F.A.S. The major hurdle imposed by the first requirement, however, may be partially overcome by performing identical tests in two tanks of different width, and using X-rays and photography to determine the displacement fields for the narrow one, with only photography for the wide one, when its validity has been established from the narrow tank experiments. The comparison of the displacement and strain fields obtained will therefore show whether significant difference exists between X-rays and photography on the one hand, and between narrow and wide tanks on the other. This is the approach that was adopted by the author.

(c) The use of photography in model studies is claimed to have been introduced to soil mechanics by Kurdyumov in 1891 (Malyshev, 1971). The method involved time exposure photographs of the indentation by a model footing in a sand bed contained in a glass sided tank, where the actual slip surfaces in the sand mass could be defined as the boundary between the sharp (in focus) and the blurred (out of focus) parts of the photograph. Since that time, a number of different methods have been developed involving photography coupled with various measuring techniques; Bekker (1948) attached a camera rigidly to the extension of a wooden model footing (secured to a solid base), the footing being located behind the glass plate of a sand container, which was subsequently lifted up by means of a hydraulic jack; the photographs taken during

upward movement, helped to define the 'elastic' soil core developed underneath the footing during penetration.

Both the above mentioned methods have been widely used by many research workers (Peynircioglu, 1948; Malyshev, 1953; Biarez, 1962; Biarez, Burel and Wack, 1961; Zaharescu,1961; Gorbunov-Possadov,1965). Qualitative information about the displacement patterns may be obtained from these techniques, but no quantitative analysis is possible. The use of coloured sand layers (De Beer-Ladanyi, 1961; Jumikis, 1961) helped to determine the shape, depth and length of the failure surface, but accurate displacement measurements could not be made. Superposition of successive photographs of discrete markers placed at the sand-glass interface (Arthur and Roscoe, 1965; Avgherinos and Schofield, 1969; Andrawes, 1970) enabled accurate measurements to be made of their location and hence the calculation of displacement and strain fields. A major requirement for the successful application of this method is the accuracy of the measurement of the marker coordinates. However, a general disadvantage of the techniques involving measurement at discrete points is the relatively wide spacing of the markers, which is required. A very close marker spacing would yield detailed information in areas where high displacement gradients occur, but this would result in altering the soil properties. This difficulty was completely overcome by the development of a stereo-photogrammetric method (Butterfield, Harkness & Andrawes, 1970; Andrawes, 1970; Andrawes, 1976). Planar displacements at every point on the model-glass interface may be measured by employing conventional stereo-photogrammetric principles and using standard equipment and techniques available.

Another technique, applying an extended use of the Moiré method on irregular gratings has been recently presented, for the investigation of the strain state in foundation beds (Nikitin & Nesmelov, 1973). The positive of the initial photograph (before loading) superimposed to the negatives of the successive photographs at different stages of the tests, produced a Moiré pattern in transmitted light. The accuracy of the method using irregular gratings is claimed to be approximately the same as in the use of regular gratings (10^{-4} for a spacing of 0.02 mm).

All the afore mentioned applications of photography have as a common restriction the unknown influence of the glass friction on the model's behaviour. The investigation of this problem was part of the author's

research programme.

(d) A very crude method used by Airhorn in 1931 (Tschebotarioff, 1951), consisted of embedding small wooden spheres in a sand fill and measuring their relative coordinates before testing. The sand was then 'carefully' removed after the test and the position of the spheres were measured again, thus producing a total displacement pattern of the sample.

Another recent method consists of repeated resin impregnation and subsequent sectioning at different stages of deformation (Oda, 1972, see Arthur, 1977).

All groups of displacement measurements (except, possibly, the first one) have been mainly applied in plane strain conditions. However, the trace of the 3-D movements of individual particles within a three dimensional soil has been recently attempted (Arthur, 1977) but no data have been published as yet.

5.2 The radiographic technique

5.2.1 An outline of the method

Details of the method have been fully documented by James (1965) and Tennekoon (1970) and, therefore, only a brief description will be given.

During the formation of the sand bed, a regular lead shot grid was placed into the sample by means of a specially made perspex template, as has already been described in chapter 3. The 12.7 mm (0.5 in) spacing square network lay in a plane parallel to the X-ray film, which was located at the rear of the apparatus. Successive radiographs at different stages of the test monitored the relative position of the lead shot with respect to the same reference axis. Subsequent measurement of the shot coordinates enabled the calculation of the displacement and, hence, of the strain field.

The X-ray equipment used was an industrial type Müeller H.G. 150 KV with a coarse focal spot of 4 mm and a fine one of 1.5 mm. Three steel pedestals, each in front of one opening of the tank (see fig. 3.1) and bolted firmly on the laboratory floor, were used to locate accurately the X-ray. Three dowel pins on the top flat steel plate helped to ensure

reliable repositioning of the head. The height of the pedestal was adjusted so that the central ray of the X-ray beam passed through the horizontal centre line of the lead shot grid. The focal spot-to-film distance was 115 cm, the same one used by Bransby (1968) and Tennekoon (1970). In the majority of the tests, the centre section (where the footing lay) was covered by radiography, and only in a limited number of tests either the 'left' or the 'right' radiograph was taken. (This was mainly due to the fact that in most of the cases, the failure surface was included within the central section, and hence, no appreciable movement was expected at the other sections).

In all the tests involving X-ray recording, lead shot of 2.54 mm (0.100 in) diameter were placed in a single vertical plane perpendicular to the central ray of the X-ray beam and parallel to the film, and at 35 mm away from the inner face of the rear glass side. Before the start of the test series, a large number of lead shot was carefully sorted. Each shot was checked for sphericity by rolling it along the inside of a brass equal angle; any pronounced lack of sphericity would give rise to a non-uniform rolling. The diameter of a number of shot was measured and they were used as guides for the rest. The 2.54 mm (0.100 in) diameter was adopted because an average of 35 points of contact could be established between each shot and the sand grains, thus the shot movement representing the average soil movement rather than the random movement of individual grains (Tennekoon, 1970). Furthermore, a smaller diameter shot, even though it might have provided a better definition because of decreased 'penumbra' effect, it would have made their recovery from the sand more difficult. About 1200 shot were selected and some 800 used for each test.

The films were placed in cassettes, which were positioned securely behind the rear glass of the rig in a specially made aluminium holder, which held the cassette 12.7 cm (0.5 in) away from the glass face. The bottom part of the cassette was located in an aluminium channel, with steel springs, attached to it, ensuring film positioning whereas the top part was held in place by spring loaded adjustable aluminium holders (see fig. 5.1). This arrangement enabled the cassette to be replaced quickly for the next radiograph to be taken.

A number of reference shots were bonded to the outside face of the rear glass side and their relative position accurately measured.

The film used throughout the test series was Kodak Industrex D,

305 mm (12 in) × 381 mm (15 in) for the centre section and 356 mm (14 in) × 432 mm (17 in) for the other two sections, with exposure time of approximately 10 minutes, at 150 KV with coarse focal spot and with a tube current of 12 mA. These values were adopted after many trials with various combinations.

The quality of the radiographs improved dramatically with the use of a 'lead tunnel', which, located in front of each section, reduced the effect of scattered radiation from the steel skeleton. Furthermore, the use of a copper wedged plate helped to improve the definition of the lead shot at the top layer, which could not have been achieved even by special weakening baths for these portions of the film (Bergfelt, 1956). Nevertheless, even though identical procedure was followed in processing each film, the quality of the radiographs was not always of the high standard achieved for the majority of them; this was found to be partially due to the developer and fixer, even though they were renewed regularly, since either heavy use or accidental intermixing (of either fixer or developer), could decrease their efficiency.

5.2.2 The measurement of the radiographs

All the X-ray films were measured by the author, using the Film Measuring Machine (F.M.M.) described by Tennekoon (1970) and James (1973). The x,y coordinates of each lead shot were measured manually (with ± 1 μm resolution) with this computer controlled machine, and each film measurement took approximately 2½ hours.

The paper tape produced was processed on the Cambridge University Computer IBM 370/165, using a programme originally developed by Smith (1972) but now extensively modified (Orr, 1975).

Where the definition of the shot was not very good, repeated measurements of its location ensured a better accuracy. In general, each shot was measured at least twice and no more than two films per day were used, in order to decrease the influence of the human error.

Since it was impossible to place two successive films in exactly the same position, the FMM shot coordinates (normal right handed axis system) were related, for every film, to the same real space system, via the coordinates of the fiducial markers which were known in both the FMM and real space system. The latter was related to the geometry of the footing apparatus. The basic relationship for the transformation of the

coordinates between the two right-handed axis systems, is (see fig. 5.2):

$$x = c + au + bv$$
$$y = d - bu + av \qquad (5.1)$$

where (x,y) is the real space coordinate system (u,v) is the FMM space coordinate system and a,b,c,d, are constants for each film. Considering the known coordinates of the reference markers, 1 and 2, the corresponding relationship(5.1)becomes respectively:

$$x_1 = c + au_1 + bv_1$$
$$y_1 = d - bu_1 + av_1$$
$$x_2 = c + au_2 + bv_2 \qquad (5.2)$$
$$y_2 = d - bu_2 + av_2$$

From equation(5.2)the a,b,c,d, constants, may be calculated and thus, by using eq.(5.1), the real space coordinates of every lead shot may be found. The displacement field between successive films can now be calculated since the coordinates of the lead shot images of each film are transferred to the same real space coordinate system.

5.2.3 Calculation of strains

Before strains in the sand mass may be calculated from the already calculated displacement field, the following assumptions (James, 1965) must be made:

(a) The element of sand defined by a single mesh of lead shot network strains uniformly.

(b) The shot do not interfere with the behaviour of the soil element they define.

(c) Displacement of the shot represents displacements of the corners of the soil elements defined by them.

(d) The shot lie in and remain in a single vertical plane to which the calculated strains apply.

(e) Geometry changes of the system during testing have negligible effect on the calculated results.

The whole lead shot network is divided up into a series of triangles, and a typical one is shown in fig. 5.3, where for convenience, the origin of coordinates is taken at corner 1. Assuming that the uniform strain within the triangular element is caused by a linear displacement field, then for any point:

$$u = u_1 + K_1 x + K_2 y$$
$$v = v_1 + K_3 x + K_4 y \qquad (5.3)$$

where u,v, are the displacements along x and y directions respectively, and K_1, K_2, K_3, K_4, are constants for the triangle which may be determined from eq.(5.3)by substituting the measured dimensions of the triangle and the measured displacements of the corners 1,2,3. Thus,

$$u_2 = u_1 + K_1 x_2 + K_2 y_2$$
$$v_2 = v_1 + K_3 x_2 + K_4 y_2$$
$$u_3 = u_1 + K_1 x_3 + K_2 y_3 \qquad (5.4)$$
$$v_3 = v_1 + K_3 x_3 + K_4 y_3$$

The four constants are derived from the solution of these four equations. Consequently, the associated strain increments may be determined (taking compressive strains positive) as:

$$\delta\epsilon_x = -\frac{\partial u}{\partial x} = -K_1$$
$$\delta\epsilon_y = -\frac{\partial v}{\partial y} = -K_4 \qquad (5.5)$$
$$\delta\epsilon_{xy} = -\tfrac{1}{2}\left(\frac{\partial v}{\partial x} + \frac{\partial u}{\partial y}\right) = -\tfrac{1}{2}(K_2 + K_3)$$

The above equations apply, strictly speaking, for very small strain increments. If larger strain increments are considered, then the strains are calculated using both the initial and final configurations of the triangle and an average taken. From the three calculated strain parameters, the following parameters may be derived (see Mohr circle of strain, fig. 5.4a).

(a) the principle strain increment

$$\begin{matrix}\delta\varepsilon_1 \\ \delta\varepsilon_3\end{matrix} = \tfrac{1}{2}(\delta\varepsilon_x + \delta\varepsilon_y) \pm \sqrt{(\delta\varepsilon_x - \delta\varepsilon_y)^2 + 4\delta\varepsilon_{xy}^2} \quad (5.6)$$

(b) the inclination of the principal compressive strain increment direction to the X-axis (ξ is taken positive in anticlockwise direction) (fig. 5.4b)

$$\xi = \tfrac{1}{2}\tan^{-1}\frac{2\delta\varepsilon_{xy}}{\delta\varepsilon_x - \delta\varepsilon_y} \quad (5.7)$$

(c) the maximum shear strain increment

$$\delta\gamma = \delta\varepsilon_1 - \delta\varepsilon_3 = \sqrt{(\delta\varepsilon_x - \delta\varepsilon_y)^2 + 4\delta\varepsilon_{xy}^2} \quad (5.8)$$

(d) the volumetric strain increment

$$\dot{\Delta} = \delta\varepsilon_1 + \delta\varepsilon_3 = \delta\varepsilon_x + \delta\varepsilon_y \quad (5.9)$$

(e) the angle of dilation ν (see fig. 5.4b)

$$\nu = \sin^{-1}\left(-\frac{\dot{\Delta}}{\delta\gamma}\right) \quad (5.10)$$

(f) from the angle of dilation, the inclination of the direction of the zero extension lines to the X-axis (fig. 5.4b)

$$a = \xi + \frac{\pi}{4} - \frac{\nu}{2} \quad (5.11)$$

$$b = \xi - \frac{\pi}{4} + \frac{\nu}{2}$$

Cumulative strains are calculated by summing the incremental strains, i.e.

$$\varepsilon_x = \sum \delta\varepsilon_x$$

$$\varepsilon_y = \sum \delta\varepsilon_y$$

$$\varepsilon_{xy} = \sum \delta\varepsilon_{xy}$$

5.2.4 Errors in the calculation of strain

A detailed account of the errors in the calculation strain has been presented by James (1973), and the main points will be considered here.

The major sources of error that affect the accuracy of the calculated strain components are:

(1) The measurement of the position of the lead shot images
(2) The repositioning of the X-ray tube and the cassette between successive exposures
(3) Distortions of the X-ray films
(4) Departure of lead shot from the vertical plane of the network
(5) Geometry changes the apparatus during testing.

Considering the last error source, the observed overall deflection of the glass sides under maximum load of the footing apparatus was very small (≃ 0.3 mm for the highest recorded load), and, therefore, the error resulting from the likely relative movement of the fiducial marks due to glass deflection was negligible. Departure of lead shot from the vertical plane during placing was reckoned to be very small (a magnitude of approximately 1 mm (0.039 in) was anticipated). Such a departure would result in a negligible error in the calculated strains.

An estimate of the error in the calculated strains was obtained by producing a pair of radiographs of the same lead shot network (without having undergone any strain) - where the X-ray tube was removed and replaced on the pedestal (Bransby, 1968) - and by calculating the resultant apparent strains for every triangle (as described in the previous section). The standard deviation for the distribution of the ε_x, ε_y was 0.0028 and 0.0037 respectively whereas for the ε_{xy} was 0.0039; similarly, the standard deviation for the maximum shear strain about a false mean of zero was 0.0035.

Those accuracies are in agreement with the 0.3% average accuracy achieved by a variety of workers at Cambridge (James, 1973). Nevertheless, it is worth mentioning that the overall accuracy in determination of strains may be greatly increased with high quality radiographs and careful measurement.

5.3 The stereo-photogrammetric method

5.3.1 Description of the method

If an object is photographed from two different camera positions, then a three-dimensional image of this object is obtained, when the two photographs are viewed stereoscopically, for example with the aid of a stereo-projector. A minor modification of this standard photogrammetric principle is involved in the method to be presented. This method, which was developed at the University of Southampton, has been described in detail by Andrawes (1970), Butterfield et al (1970) and Andrawes (1976), and an outline of the technique will be given below, followed by a detailed account of its application to the footing problem.

If two photographs of a displaced object, taken from a fixed camera position, (the first before and the second after the object was displaced), are projected simultaneously then a stereoscopic image can be obtained, the object appearing at a different elevation from the immovable background field. This height, when properly scaled, is proportional to the displacement component of the object parallel to the viewing eye base. This basically simple idea is used in measuring displacement fields. Two photographs of a displacement field, when viewed stereoscopically, will yield a three dimensional optical model where, all points which have undergone similar displacements relative to the fixed position camera, will be seen to lie on the same level. It should be noted that the height of the apparent elevation of the various points of the displaced field is proportional to the displacement component which is parallel to the viewing line and displacements in other directions may be viewed by rotating the photographic plates through similar angles. Thus, considering the case of a surface footing resting on sand, with the horizontal and vertical displacements occurring along the x and y axes, respectively, the horizontal components of the soil displacement will be obtained when the x-axis is set parallel to the viewing line, while the vertical components will be obtained if the two photographs of the displaced field are turned through 90^{o}. A set of undisplaced points will appear on the so called reference plane, from which the relative displacement of the various points of the sand mass are measured.

5.3.2 Experimental set-up - Part II (Cambridge footing apparatus

Photography, in conjunction with X-rays, was used in a number of tests performed at the F.A.C. During these experiments, photographs were usually taken at the same intervals between load increments as the X-rays, with the aim to obtain information on the displacement field using both methods at identical load stages.

The camera used was a Swiss made ARCA plate camera equipped with bellows and a Schneider normal lens of 150 mm focal length, its main body consisting of two plates working on a rail, one carrying the lens and the other a spring loaded cassette holder with a focusing glass plate mounted on it. These plates were adjusted at their vertical position with the help of small spirit levels, mounted on the frame of the plates. The camera was securely mounted on the pedestal via a 9.53 mm (0.375 in) thick accurately machined mild steel plate. This plate, which provided a stable holder for the camera rail, was clamped on the top flat of the pedestal always at the same position, with the help of three small steel blocks bolted at its sides. In its final position the horizontal axis through the lens centre almost coincided with the horizontal centre ray of the X-ray, the focal distance being 680mm.

Fine grain high speed (ASA 160 - DIN 23) 102 × 102 × 1.3 mm (4 × 4 × 0.051 in) thick ILFORD FP4 glass plates were used throughout the experimental series. Lighting was provided by four 500 Watt photo floods (two at each opening) which gave even illumination of the sand, and which remained at the same position throughout the test (so as to maintain the same relative angle of illumination). In order to avoid any likely drifting of the load cells, due to radiated heat from the lamps, the two photo floods were only switched on during the photograph exposure time of approximately 2 seconds.

Since the main aim in using photography was the direct comparison of the stereophotogrammetry and the X-ray techniques, it was felt that it would be desirable to use the same computer programme for analysing the results (the consequences of this will be discussed in chapter 7). This requirement imposed a restriction in the format of the stereo measurements, which had to follow the same pattern as those for the X-ray films. After consultation with the operator who measured the photographic plates, it was decided to draw a 10 mm square grid on the inside of the glass, which would provide both locations for the measure-

ments in an array form and ample reference marks. The grid was drawn with a ruling pen (with indian ink) attached to 0.02 mm division height gauge, which operated on the flat faces of a wooden frame. This frame, consisting of two perpendicular faces, was wedged via six adjustable pads, in the inside area of the tank, so that one of the faces was horizontal (adjusted with the help of a spirit level). The accuracy of the drawn grid was checked by a travelling microscope (for the vertical lines) and by a cathetometer (for the horizontal lines) and the anticipated error was found to be less than 1%. In order to minimize any increase in glass friction due to the grid, the inner faces of the glass sides were cleaned with Inhibisol, which had been found not to affect the ink grid.

Before beginning a test, the sand mass was brought into focus and the two camera plates were locked at this position, while the camera itself was locked on the rail and clamped on the steel plate. Since the same pedestals were used for both the X-ray tube and the camera, precise repositioning of the camera was ensured by the three 'guides' bolted on the steel plate as mentioned earlier. The time required to take a photograph, including the necessary preparation and camera repositioning, was negligible (approximately 2 minutes) compared with at least 15 minutes required for an X-ray. Therefore no appreciable time was added to the average duration of a test by including the photography.

5.3.3 Experimental set-up - Part III (Southampton footing apparatus)

A similar arrangement was used for the Part III experimental work. The same camera was employed and similar procedure was followed. A brief description of the camera set-up will now be presented.

The camera was mounted on a very stable tripod and positioned about 700 mm (focal distance approximately 900 mm) away from the front glass side of the tank. At that position, almost the entire displacement field was included in the photograph. The camera axis was adjusted perpendicular to the plane of the displacement field with the help of the spirit levels provided, a 1 m (0.5 mm/division) steel ruler and a steel set square. To improve the overall stability of the set up and to protect it from any accidental disturbances during testing, the tripod was mounted on a wooden plate, which in turn was clamped on the laboratory

floor (fig. 4.1). Two 500 watt photo-floods, positioned at either side of the camera, provided ample and even illumination.

A number of fiducial marks were drawn on the inner face of the front glass side, and their relative distance was measured with a 0.5 mm/ division steel ruler. For reasons discussed in the next section, no square grid was drawn.

The same type of film was used for the part III experiments, and the plates were developed and fixed using the same chemicals (ILFORD ID - 11 developer and ILFORD ILFOFIX fixer).

5.3.4 Measurement of the displacement field

Measurements of planar displacements (parallaxes) can be made using any one of the following apparatuses:
(a) Mirror stereoscope (b) Stereoplotter (c) Stereocomparator
The mirror stereoscope provides the least accurate measurements, and it was used for qualitative viewing of the photographs. The most accurate measurements of photograph coordinates and parallaxes are produced by using a stereo-comparator. The photographs are viewed stereoscopically and with the aid of a floating light point, measurements of the x and y parallaxes are possible. One of the main advantages of the stereo-comparator is that relative plate orientation procedure is much simpler than with the other devices. All the photographic plates from both experimental series were measured using a Carl Zeiss Jena stereo-comparator (stecometer) which was equipped with automatic recording unit for both x and y parallaxes and the corresponding coordinates of the location of measurement with respect to a preset arbitrary right-handed coordinate system. The accuracy of measurement of coordinates quoted by the manufacturers is ± 2 μm, and, in order to gain full advantage of the facilities provided and precision of the apparatus (and taking into account also the limited time available for the author to practice) the plates were measured by the already experienced and well-equipped Photogrammetry Department of the City University London.

Measurement of the plates followed the same format as that of the X-ray films, and the coordinates for the 1st (left-hand-side viewed) plate were formed by adding the y parallaxes to the corresponding y coordinates, while for the second by adding the x parallaxes to the x coordinates.

One of the limitations of the method lies in the restriction of the human eye to accommodate accurately too big parallaxes. Therefore, by employing the square grid for the part II experimental work, it was hoped that measurements could be performed at almost the same locations (within a few microns) for successive pairs of plates, thus making it possible to produce a cumulative information about displacement and strain fields: The x and y parallaxes of the subsequent pairs of photographs would be added algebraically to the corresponding x and y coordinates of the first pair and the total movement which occurred at the area of measurement could be obtained, therefore, overcoming the limitation of direct measurement of big parallaxes. This particular format for the measurements was dictated by the requirements of the computer program, which accepted data from discrete points measured with respect to a fixed reference axis. However, it was eventually realized that the grid interfered with the stereoscopic viewing of the area, and that, for accurate assessment of the parallaxes, the area of measurement should be well away from the grid lines. Thus it was decided to measure at approximately the centres of the squares formed by the grid, being aware that the cumulative displacement and strain information would not be of the same high accuracy as the incremental one. At the same time, in order to investigate the upper limit of parallax magnitude that could be measured, one pair of photographs involving almost the entire displacement history of a test was measured and the results were analysed, to be compared with the corresponding identical information from X-ray films. A detailed discussion of both X-ray and photogrammetry results will be presented in chapter 7.

This interference was the main reason for not employing a similar grid for the part III tests. Instead, it was decided to produce incremental information only for comparison with nominally identical experiments of the part II series. It is worth mentioning here that a new way of analysing the results from measured photographic plates has been devised by Harkness (1977) and the computer program written for this enables contours of x and y displacements, shear and volumetric strains to be generated with high precision, whilst at the same time overcoming the previous limitations on producing cumulative information. In addition to that, any relative tilt of the plate or the camera is taken

into account from the fiducial mark parallaxes, and the necessary corrections applied.

5.3.5 Errors and accuracy

The main sources of error in calculating strain fields from the photographic plates are:

(1) Repositioning of the photographic film and the camera for successive photographs.
(2) Measurement of the parallaxes with the stereocomparator.
(3) Distortions of the photographic films.
(4) Camera lens distortion.
(5) Geometry changes of the apparatus during testing, glass refraction

(1) For the part-II series, the camera was mounted on a machined plate and was subsequently clamped on the top flat faces of the pedestals (see section 5.2), the accurate repositioning being secured by the three 'guides' of the steel plate. Therefore no error was anticipated from this source. Regarding the repositioning of the cassettes, it was noticed that the spring loaded holder did not apply sufficient pressure on the cassette, and, taking into account that the recesses on the rear camera plate were ill-defined, it was expected that this would cause some relative tilt. For the plate size and the focal length used, a tilt of about 2^{o} would produce an error of approximately ± 1%. The relative tilt was determined by the apparent parallaxes of the reference marks and was found to be less than 0.10^{o} ($\simeq 1.7 \times 10^{-3}$ radians) in the worst case, which implied an error in the measured linear strain of approximately 9×10^{-4}.

(2) As it was mentioned in the previous section, the measuring accuracy of the stereocomparator is stated to be ± 2 μm which can be achieved when measuring photographs of displaced objects with well-defined corners (for example the translating footing). However the maximum likely expected error is stated to be ± 5 μm. The accuracy, on the prototype, is therefore approximately ± 25 μm, for 1/5 scale reduction on the photographic plates and it was anticipated that this was maintained for all the measured pairs.

(3) No significant error was expected from the film distortions, since glass plates were used.

(4) The use of a high quality lens is not of prime importance, since any slight distortion of the image will occur in the same part of the field for each successive photograph and, provided a sharp image is maintained throughout, the resulting error will be the same for each.
(5) The observed deflection of the front glass side amounted to less than 0.1 mm, while that of the rear one was measured to be 0.25 mm, and thus the error resulting from the likely relative movement of the fiducial marks due to glass deflection was negligible. Errors from non uniformity of the glass, resulting in glass refraction effects, were reckoned to be of minor significance (second order correction).

CHAPTER 6

MEASURED LOAD-DISPLACEMENT BEHAVIOUR AND CONTACT STRESSES

6.1 Introduction

The importance of the knowledge of the load-displacement relationship, together with the contact stress distribution, has already been demonstrated in chapters 1 and 2. In this chapter the footing displacements and the c.s.d. measured during various experiments performed in the two apparatuses will be presented.

Non-dimensional parameters will be used in general, so that all results may be directly compared. When stresses are presented, the stress parameter $P/\gamma B$ will be used, where P is the average stress underneath the footing, γ the soil unit weight and B the width of the footing. As far as displacements are concerned, the well known non-dimensional parameters v/B and u/B will be used, where v and u are the vertical and the horizontal displacements of the footing respectively. The dimensionless parameters H/V_{max}, V/V_{max} and $M/B\ V_{max}$ (which were used in chapter 2) will be used again here.

Results from the contact load cells will be presented with the simple assumption of a constant normal and shear stress distribution across the face of each load cell even though the eccentricity of the normal load on the cell face was also calculated. Nevertheless it is thought that the presentation adopted will help to demonstrate the shape of the c.s.d. for each case and will assist in comparing results from tests with different initial boundary conditions.

A list of the tests performed, together with the various measurements made during each experiment is given in Table 1. Apart from test D ($e_o = 0.52$, $\alpha_o = 0$, $E_o = 0$) all tests were taken to failure, the failure load being monitored by both the total load cell readings and the jack oil pressure (see chapters 3 and 4). However, the ultimate load for test D was extrapolated from both the corresponding load-displacement curve and a reload cycle (see section 6.2.1) and was compared with the ultimate load from a similar test performed by Tennekoon (test H, B = 76.2mm, $e_o = 0.525$), their difference being approximately 10%.

The presentation of the experimental bearing capacity and the load-displacement relationships will be followed by the c.s.d. results.

6.2 Bearing capacity

6.2.1 Vertical central load

Two tests were performed with vertical symmetric loads, one at the F.A.C. (test D, e_o = 0.52) and one at the F.A.S. (test DS, e_o = 0.53). As was mentioned in the introduction to this chapter, test D was not brought to failure during first loading, because it was feared that the glass sides could not sustain such a high stress level. After the footing had been retracted from the sand surface, a layer of sand of approximately 10 mm thickness was removed from the free surface area around the footing by the suction method described in chapter 3. The footing was then put back in position and reloaded up to failure, which occurred at approximately 10 KN (1000 kg). This load was accepted as an indicative rather than as an absolute one, since between the first and the second loading the footing had been removed completely from the sand surface, and this might have altered the contact area appreciably. Nevertheless, if the effect of the removed soil is taken into account as a surcharge $\gamma h N_q$ (h is the sand layer thickness) and is added to the observed failure load, then this compares favourably with the extrapolated value from the load-vertical displacement curve, shown in fig. 6.1.

It was pointed out in chapter 1, that the selection of the correct angle of internal friction is of major importance, since a 10% difference in its value (for dense sand, $\phi \geq 45^o$) will result in an at least three-fold increase in the N_γ value. The footing experiments were performed under plane strain conditions and the corresponding plane strain value for the internal friction angle was obtained from test results in the Simple Shear Apparatus (hereafter abbreviated as SSA), performed by Stroud (1971). As will be shown in the next chapter, the volumetric-maximum shear strain relationship obtained from the SSA is very similar to that measured during the various experiments at the F.A.C. carried out by the author. The marked difference in the stress level between tests at the two apparatuses would seem to contradict the fact that the angle of internal friction is stress level dependent. However, the greatest part of sand mass under consideration (i.e. where measurement of Δ and γ_m were made) is not highly stressed, high stresses occurring in regions near the footing only (Tennekoon, 1970).

To take into account the stress variation along the slip surface, Meyerhof (1948) suggested that the mean normal stress along a possible failure surface is equal to 1/10 of the ultimate bearing capacity. Considering test D, this assumption would lead to a mean normal stress of approximately 70 KN/m^2 (10 psi), which is identical to the average vertical pressure used at low stress level test in the SSA, where the angle of internal friction was obtained from ($\phi = 49.5^o$ for $e_o = 0.53$ and $P_{av} = 70$ KN/m^2 (10 psi), Stroud, 1971 fig. 6.11). Almost all the tests in the F.A.C. were performed on sand beds with initial voids ratio approximately 0.52 and the value $\phi = 50^o$ was adopted as the corresponding peak angle of internal friction.

The experimentally obtained bearing capacity is compared with test results from various research workers in fig. 1.5 (the results from Kezdi (1952) and Varga (1962) are taken from Balla (1962)) and agrees rather well with them. The observed close agreement between the experimentally obtained N_γ values by the Author and Tennekoon (1970) seems to suggest consistency of results from the F.A.C. However, one should be careful in drawing firm conclusions, since the N_γ values are plotted on a logarithmic rather than a natural scale, where any major discrepancies would show up more distinctly.

The dimensionless bearing capacity $2P_v/\gamma B$ predicted by various formulae suggested is shown in fig. 6.2 and ranges from 569 (Hansen, 1970) to 1120 (Balla, 1962). As may be seen, the best predictions are given by Chen (1975) and Balla (1962). The striking point about these predictions is that the highest bearing capacity is approximately double the lowest one; this implies that, depending upon the formula one uses for the design of a strip footing on dense sand one might have already included a factor of safety of about 2 (if for instance Hansen's formula is adopted).

It should be noted that the effect of the surcharge, which results from the settlement of the footing, was not considered in the calculated bearing capacity values. If it was taken into account, then the corresponding values would increase by 9% on average. (In fact,considering the two extreme cases, the bearing capacity predicted by Hansen (1970) would increase by 11% while the one predicted by Balla (1962) would increase by 6%).

The load-vertical displacement relationship obtained from test DS ($e_o = 0.53$) at the F.A.S. is shown in fig. 6.1. The dimensionless

ultimate load $p_v/\gamma B$ was lower than that of test D by about 20%. Even though there was a small difference in the initial density of the two sand beds, this can only partly explain the reduced bearing capacity value, and the effect of the larger tank width seems to have influenced the observed drop of the failure load. However, no firm conclusions may be drawn at this stage, and the effect of the tank width will be discussed in a later section, in the light of the results from other experiments.

6.2.2 Vertical-Eccentric load

Four tests were performed with vertical-eccentric load; two at the F.A.C. (test A, $e_o = 0.52$ and test H, $e_o = 0.52$, both with $E_o = e/B = 0.167$) and two at the F.A.S. (test AS, $e_o = 0.54$ and test HS, $e_o = 0.53$, both with $E_o = 0.167$). Both tests A and H resulted in almost identical ultimate loads and the relative reduction of the applied vertical load due to its eccentricity is shown in fig. 6.3 where the load ratio V/V_{max} is plotted against the eccentricity ratio E. The 'effective width' curve, which is also drawn (solid line), seems to give a rather unsafe prediction.

It was pointed out in chapter 3 that one unavoidable disadvantage of the footing apparatus was the relatively high position of the friction-less joint with respect to the footing base (see fig. 3.3). Therefore even a small rotation of the footing resulted in a considerable increase of the initial load eccentricity. If, therefore, the load eccentricity at failure is used (E = 0.210) in fig. 6.3, then the 'effective width' concept provides a safe estimate for the reduction in bearing capacity.

It is of interest to note the almost identical failure loads for both tests A and H, indicating the repeatability of tests in the F.A.C. This will be further examined in view of the load-displacement relation-ships, which will be discussed in a later section.

In all the cases referred to above, the footing was quite free to move in the plane of the load. (Even though this is not a model study of the behaviour of an actual footing, the investigated case may be related to a footing at the bottom of a relatively slender column or to the foundation of a tall chimney, where there may be little or no restraint against lateral movement). However, the structure may be so

stiffened that lateral movement is insignificant; in such a case, the footing may rotate and displace vertically, but cannot translate horizontally.

The effect of such constraints has been investigated by the author (Ticof, 1978) using the same experimental set up (F.A.C.). The 76.2 mm (3 in) footing was again free to rotate about a frictionless joint (fig. 3.3), but the jack was 'locked' at its initial position by means of the lock-nuts of the stud S, (fig. 3.4). Results from tests (FA, e_o = 0.52, E_o = 0.167 and FB, e_o = 0.52, E_o = 0.334) with similar initial voids ratio are shown in fig. 6.3. The observed ultimate loads were much higher than the ones obtained from the freely translating and rotating system. This very important observation implies that, by restraining the footing against lateral movement, the bearing capacity is increased by a factor of about 2, even though (as will be discussed in a later section), the footing rotation at failure is very similar in both cases.

Lee (1965) stated that moments causing failure would have been much smaller than the ones observed, if the model footings he used in his tests on sand were not restrained from moving sideways. However, his remarks were only qualitative, since he did not perform any tests with completely unrestrained footings. Eastwood (1955) reported tests from both unrestrained and 'partially' restrained against lateral movement footing tests on sand. As was already discussed in chapter 1, he observed an 8% increase in the failure loads of the 'partially' restrained footings (the footing was allowed to move laterally approximately 1/10 of the corresponding movement in a completely restrained case). This relatively small increase in the ultimate loads might have been possibly due to the 'partial' restraint.

The ultimate load ratios V/V_{max} obtained experimentally from tests AS and HS are shown in fig. 6.3. Attention is drawn to the fact that V_{max} is considered as the failure load observed at test DS. As expected, the slightly higher initial voids ratio of test AS has resulted in a lower bearing capacity than the one obtained from test HS. Furthermore, the relative reduction in bearing capacity obtained from test HS compares favourably with that obtained from tests A and H. The significance of this observation will become apparent later in this section.

It may be seen from fig. 6.3 that the 'effective width' curve again seems to overpredict the ultimate loads obtained from both test AS and HS. However, as will be discussed later on, the footing, during both these tests, developed similar rotation to that observed during tests A and H. Therefore, the eccentricity ratio at failure was larger than the initial one (for reasons discussed earlier in this section), and if the former is used in fig. 6.3, rather good agreement is obtained with this empirical assumption of the 'fictitious width'.

The dimensionless bearing capacity $P_v/\gamma B$ obtained from test HS (e_o = 0.53) was about 20% lower than the one observed during tests A and H (e_o = 0.52). A similar reduction was noticed between tests DS and D with the same difference in initial voids ratio (see previous section), which suggests again that this might be due to effects from the relative widths of the tanks.

6.2.3 Inclined central load

Five tests were performed with inclined central loads: Tests B, GB and E, with angle of load inclination 12°, 20° and 30° respectively, were performed at the F.A.C. and tests RS and BS (α_o = 5° and 12° respectively) at the F.A.S. All tests were carried up to failure, since developed glass deflection in both apparatuses was very small (the maximum recorded deflection was of the order of 0.3 mm). An additional test was attempted, with 40° angle of load inclination, but the available ram travel of the jack was exhausted after the first increment (before the jack was 'unlocked' from the lock-nuts of the stud S, fig. 3.4), and the test was stopped. Nevertheless, it was anticipated (from the failure locus shown in fig. 6.4) that the attained load at that stage was close to the failure one and it was adopted as the ultimate load for 40° load inclination.

The results from tests B, GB and E are presented in fig. 6.4 in dimensionless form (P_H is the average horizontal pressure at failure). As may be seen, the maximum horizontal load ($H/V_{max} \simeq 0.12$) is attained at $V/V_{max} \simeq 0.50$, which is in good agreement with the other test data presented in chapter 2.

Some of the suggested relationships for the inclination factors,

discussed in chapter 1, are plotted in fig. 6.4. For the assumed angle of internal friction ($\phi = 50^o$), Meyerhof's inclination factor

$$i_\gamma = (1 - \frac{\alpha}{\phi})^2 \qquad (6.1)$$

combined with the N_γ value proposed by Meyerhof (1963), provides conservative predictions for load inclinations up to approximately 15^o, whilst the predictions are unsafe for greater inclinations. If the same factor is used, but with the experimentally obtained N_γ value, then, apart from values of α within 0^o and 10^o, where a rather good agreement is observed, the predicted failure loads for larger inclinations overestimate the experimental ones by as much as 35% (approximately) (compare test GB, $\alpha_o = 20^o$, $P_v/\gamma B = 146$ with the predicted value of 196).

The inclination factors suggested by Hansen (1970) and the proposed one by the author (see chapter 2) are also compared and the corresponding curves are drawn in fig. 6.4. It was shown in section 6.2.1 that the N_γ value derived from Hansen's empirical formula $N_\gamma = 1.5(N_q-1)\tan\phi$ (which corresponds closely to the N_γ values calculated by Lundgren and Mortensen (1953)) is approximately half the experimentally obtained one. Therefore, the grossly conservative results obtained from the expression

$$\frac{P_v}{\gamma B} = \frac{N_\gamma}{2}(1 - 0.7\tan\alpha)^5 \qquad (6.2)$$

where $N_\gamma = 1.5(N_q-1)\tan\phi$, are hardly surprising.

The same expression was again used, but this time the N_γ factor was set equal to the experimental one (1086) (see fig. 6.4). The test results curve envelopes the one produced by the above expression and this implies that Hansen's inclination factor, unlike Meyerhof's, provides safe predictions for any load inclination.

Finally, the expression proposed by the author

$$\frac{P_v}{\gamma B} = \frac{N_\gamma}{2}(1 - 1.36\tan\alpha)^2 \qquad (6.3)$$

gives rather better predictions, again on the safe side (fig. 6.4).

The test results from the F.A.S. are also shown in fig. 6.4. The

observed failure load of test BS (e_o = 0.53) is 29% smaller than the corresponding test B (e_o = 0.52) and a similar comment may be made for test RS (e_o = 0.54) when compared with the extrapolated $P_v/\gamma B$ value from the F.A.C. test curve. In fact, the RS ultimate load lies well within the experimental failure envelope (through the points DS and BS), demonstrating once more the effect of the initial voids ratio on the bearing capacity (fig. 6.4).

In view of the results from the other tests in the F.A.S, discussed in the previous sections, the lower bearing capacity observed when compared with tests from the F.A.C. implies that, in all probability, the use of a narrow width tank (≈ 200 mm) resulted in higher failure loads than the use of a wider one (≈ 600 mm). The slightly higher initial voids ratio of the sand beds in the F.A.S. (e_o = 0.52 for tests in the F.A.C. while e_o = 0.53 and 0.54 for tests in the F.A.S.) will have definitely contributed to the reduction of the bearing capacity, however, such difference in density would justify a decrease of 10-15% at the most and this may be shown by considering, for example, the N_γ factor suggested by Meyerhof (1963): For e_o = 0.52, $\phi = 50^o$ (from Stroud, 1971) and $N_\gamma^M = (N_q - 1)\tan(1.4\phi) = 874$, while for e_o = 0.53, $\phi = 49.5^o$ and $N_\gamma^M = 773$ which is 12% lower. Therefore part of the typically 20% observed difference can be attributed to the tank width effects (approximately 5-10%).

The observations mentioned above will be considered again at the end of this chapter together with the loadxdisplacements and contact stress distribution results.

6.2.4 Eccentric - Inclined loads

Tests with an eccentric-inclined load acting on the footing were conducted at the F.A.C. only: Test C was performed with initial eccentricity ratio E_o = -0.167 and constant load inclination 12^o (e_o = 0.52), while for both tests K and F (e_o = 0.52) the vertical load was maintained constant and the horizontal load was gradually increased up to failure. The main features of the last two tests, K,F, were the 'positive' and'negative' sense of the load eccentricity (defined in fig. 1.9): The vertical load at test K was acting with 'negative' eccentricity, and the line of action of the horizontal load was along the base of the

footing. In test F, the constant vertical centreline load was combined with an increasing horizontal one acting at 100 mm from the footing base, thus resulting in a 'positive' eccentricity effect.

The non-dimensional failure loads are shown in fig. 6.5, where the scale of the $P_H/\gamma B$ axis is double that of the $P_v/\gamma B$ axis for clarity. The results from tests A and H ($e_o = 0.52$, $\alpha_o = 0$, $E_o = 0.167$) are also included. It is evident that higher horizontal loads can be carried by the footing under the same vertical load, when the load eccentricity is 'negative' rather than 'positive' (compare tests C, K ($E = -0.167$) and F ($E = +0.151$)). This finding confirms similar observations made during the preliminary investigation in the small footing rig, described in chapter 2.

The other major finding of the preliminary tests, the increase of the bearing capacity of an eccentrically loaded footing under small horizontal loads with respect to the case under zero horizontal load, was not directly observed. However, the available experimental points shown in fig. 6.5 imply that, if an appropriate load sequence was followed, results on the dashed curve could possibly have been obtained.

The schematic explanation suggested in chapter 2, will be again discussed in the next chapter, where results from the deformation of the sand mass will be presented.

6.3 Load-displacement relationships

6.3.1 Vertical central load

The dimensionless load-vertical displacement relationships obtained by the author for tests D ($e_o = 0.52$) and DS ($e_o = 0.53$) with a vertical load are shown in fig. 6.1. The vertical displacement at failure of test D is shown to be approximately 12% of the footing width. Vesic (1963) measured 0.11B vertical displacement at failure during tests with 50 mm wide rectangular footings (L = 300 mm) on dense sand ($\phi \approx 44^o$), while similar results were reported by De Beer (1961) on small scale footing tests.

It must be emphasized here, that apart from moving vertically, the footing may also displace horizontally and rotate under a symmetric load, unless it is restrained by the superstructure from doing so. Thus the

catastrophic failure occurring in dense sand, may be also accompanied by substantial tilting of the foundation, as was pointed out by Vesic (1973). Results by Eastwood (1955) and Dhillon (1958, 1961) indicated that surface footings on sand under vertical central loads tilted and moved sideways while displacing vertically. The former reported that the average angle of rotation at failure was 1^{o}, while the latter measured an average value of 0.8^{o}, the maximum recorded one being 1.9^{o}. Head (1977) measured the rotation at peak to be 0.8^{o}.

The possible tilt and sideways movement of a footing loaded by a vertical symmetric load is not unexpected. In fact, perfect symmetry is highly unlikely to prevail throughout the loading sequence, since the sand sample is not a homogeneous isotropic medium. Local nonuniformities underneath the footing will cause the development of nonsymmetrical strains in the sand mass resulting in rotating the footings. Tennekoon (1970) observed non-symmetrical strain distribution underneath his footing which was not allowed either to rotate or to move sideways. He subsequently attributed to this lack of symmetry the development first of a single failure surface to the side showing larger strains, and then the formation of the second failure surface to the other side.(Similarly Andrawes (1970) observed that, when a wedge is driven into a dense sand bed and is not allowed either to rotate or to displace horizontally the successive failure surfaces did not occur simultaneously at both sides of the model, and this behaviour was reflected in measuring different forces at each side of the wedge). Therefore, if the footing was free to rotate, it would have tilted at failure, which would have occurred along a one-sided failure zone.

The angle of rotation measured at stage $P/P_f \simeq 0.95$ (the ratio of the current average pressure to the average pressure at failure) of test D was 0.25^{o}, while the horizontal displacement was 0.005B, which is approximately 5% of the recorded vertical displacement. In fact, the footing exhibited negligible tilt up to $P/P_f = 0.88$ (only 0.09^{o}), the angle of 0.25^{o} being developed during the last stages of loading. In addition, the horizontal displacement recorded at that stage ($P/P_f = 0.95$) was a result of the relative tilt of the footing only, since the horizontal movement of its rotation axis was measured to be zero. This is somewhat surprising, because the rotation axis translated horizontally

with increasing load up to P/P_f = 0.85, when it started to move towards its initial position, while it was expected to continue to move horizontally up to failure.

The non-dimensional load-vertical displacement relationship for test F (e_o = 0.52, α = 0, e = 0) is also shown in fig. 6.1. Even though the vertical load was kept constant after it reached 30% of its ultimate value, the quite good agreement between the load-displacement curves of tests F and D implies repeatability of test results in the F.A.C.

Considering now test DS (e_o = 0.53), it may be seen from fig. 6.1 that the vertical displacement at failure was approximately 0.07B. However, the remarkable agreement between the load-displacement curves of tests D and DS (performed in different apparatuses) would suggest that almost the same bearing capacity would have been obtained from both tests and at similar relative vertical displacements.

The rotation of the footing at P/P_f = 0.98 (P_f is the average pressure at failure of test DS) was 0.82^o, over three times that observed at test D, and the horizontal displacement was 0.1 × B, which is 15% of the vertical displacement at the same stage and approximately twice that of test D. Furthermore, a well-defined one-sided rupture surface was formed in the opposite direction to that in which the horizontal translation occurred. It is, therefore, likely that the reduced bearing capacity may have been caused by the development of this non-symmetrical behaviour. In addition, as was pointed out in an earlier section, the slightly higher voids ratio of test DS may have contributed to this reduction, even though such claim would have been coupled with a distinct deviation between the two load-displacement curves, due to the softer response in the case of a less dense sand bed.

Finally, it is of interest to note the 11% vertical displacement recovery during unloading which started at P/P_f = 0.95. This supports a similar observation made during the preliminary experimental series (see chapter 2).

6.3.2 Vertical eccentric load

The load-vertical displacement relationships obtained from tests A and H under vertical eccentric load are shown in fig. 6.6 (it should be

noted here, that both the vertical and horizontal displacements of the footing refer to the translation of the centre of its base). The remarkable agreement between these two tests implies again that test results in the F.A.C. may be considered as repeatable. This may be also shown from fig. 6.7 where the dimensionless moment versus rotation relationship is shown.

The vertical displacement at failure of test A was approximately 0.03B which is about 1/4 of the corresponding displacement under a vertical centreline load, while the angle of rotation of the footing at peak load (or moment) was 1.67^{o}. Similar values were obtained from test H ($v/B = 0.03$, $\omega = 1.50^{o}$). Lee (1965) stated that in all his tests peak moment capacity was developed at rotations between 0.75^{o} and 1.5^{o}, while Eastwood (1955) had argued that, generally, the rotation at failure would increase with increasing eccentricity and may reach 8^{o}, although he did not suggest at which specific eccentricity ratio such high rotation of the footing is attained. It is nevertheless of interest to note the narrow range of the rotation at failure observed by Lee (1965) as compared to the much wider one reported by Eastwood (1955). Since both test series were carried out in dense sand, it is probable that this difference may be due to the kinematic constraints imposed during Lee's experiments (see chapter 1.2.2.2), as discussed in the following section.

The load-vertical displacement relationship of test FA ($e_o = 0.52$, $E_o = 0.167$), which was restrained from displacing horizontally, is shown in fig. 6.6, while the moment rotation relationship for the same test is shown in fig. 6.7. The striking feature is that the kinematic constraints imposed to the footing did not affect its moment-rotation response when compared with the completely free footing, and the rotation at failure (1.8^{o}) was very nearly the same to that obtained from both tests A and H. Furthermore, the load vertical displacement relationship was almost identical to those from A and H (see fig. 6.6).

Results from tests AS and HS ($e_o = 0.54$, and 0.53 respectively, $E_o = 0.167$) performed at the FAS are shown in figs 6.6 and 6.7. The slightly softer response exhibited by the footing during test AS and shown in fig. 6.6 was expected, since the initial voids ratio was a little higher than that for test HS. The difference in the moment-rotation relationships was more distinct as may be seen in fig. 6.7, and peak

moment was developed at 1.6° rotation for test HS and at 2.1° for test AS.

Both the load-vertical displacement and moment rotation relationships obtained from test HS (e_o = 0.53), shown in figs. 6.6 and 6.7 respectively, compare rather well with the corresponding ones from tests A and H (e_o = 0.52). The obtained vertical displacements and rotations obtained at failure were 0.33B and 1.66° respectively, which are almost identical to those obtained from tests A and H. The above again indicate that the 20% lower bearing capacity obtained from test HS may be partly due to the three times larger tank width of the FAS, compared to that of the FAC.

6.3.3 Inclined central load

The dimensionless load-vertical displacement relationships obtained from tests B (α_o = 12°, e_o = 0.52), GB (α_o = 20°, e_o = 0.52) and E (α_o = 30°, e_o = 0.52) performed at the FAC, are shown in fig. 6.8. These relationships indicate that the greater the inclination of the load, the smaller the relative vertical displacement at failure. In fact, there is a close similarity of the slope of all these curves with that of the vertical central load, which is replotted in fig. 6.8.

A good approximation may be obtained if the load-displacement relationships of fig. 6.8 are expressed in a bilinear form (drawn with continuous lines. The first part of the curve is identical for all inclinations, while the second part forms a constant angle with the displacement axis, the particular inclination being defined by its intercept with the axis of the vertical component of the load. As may be seen from fig. 6.8, the form of the load-displacement curve of test E (α = 30°) implies that for higher inclinations, the vertical displacement is very small and that for α = 40°, the footing will move horizontally (i.e. the motion becomes predominantly one of horizontal sliding along the footing base).

This bilinear approximation, which is a rather good approximation to the test results, is particularly convenient. It implies that the knowledge of the load-vertical displacement relationship for the vertical centreline load case, provides sufficient information to predict the load-vertical displacement relationship for any load inclination (up to,

of course, 40^{o}). These relationships will again be discussed and used in chapter 8.

The dimensionless vertical load-horizontal displacement relationships obtained from tests B ($\alpha_o = 12^{o}$), GB ($\alpha_o = 20^{o}$) and E ($\alpha_o = 30^{o}$) are shown in fig. 6.9. These results again indicate that the greater the angle of load inclination the smaller the relative horizontal displacement at failure.

It was noticed that the footing remained practically horizontal throughout the loading sequence in almost all the tests. In addition, the angle of load inclination remained practically constant (in test B ($\alpha_o = 12^{o}$) the load inclination at stage $P/P_f = 0.97$ was 12.2^{o}, in test GB ($\alpha_o = 20^{o}$) it was 20.11^{o} ($P/P_f = 0.35$), test E ($\alpha_o = 30^{o}$) it was 30.17^{o} ($P/P_f = 0.83$), in test BS ($\alpha_o = 12^{o}$) it was 12.5^{o} ($P/P_f = 0.8$) and in test RS ($\alpha_o = 5^{o}$) it was 5.20^{o} ($P/P_f = 0.98$)). In particular, during test B ($\alpha_o = 12^{o}$) the maximum absolute recorded rotation before failure ($P/P_f = 0.93$) was 0.17^{o}, but the average tilt did not exceed 0.04^{o}, and during test E ($\alpha_o = 30^{o}$) the maximum absolute monitored tilt was 0.26^{o}. Saran et al (1971) stated that the observed rotation of the model footings in all their experiments under inclined centric load was negligible. This behaviour seems to suggest that the failure loads obtained from tests where the footing did not rotate at all may serve as an upper bound to the actual collapse load, whilst ultimate loads from corresponding tests where the footing tilted may provide a lower bound.

The load-displacement relationships obtained from tests RS ($\alpha_o = 5^{o}$) and BS ($\alpha_o = 12^{o}$) performed in the F.A.S. are shown in figs 6.8 (vertical component of the load versus vertical displacement) and 6.9 (vertical component of the load versus horizontal displacement). The results from test BS ($\alpha_o = 12^{o}$, $e_o = 0.53$) compare rather well with those from test B ($\alpha_o = 12^{o}$, $e_o = 0.52$) and such an agreement might suggest that the bearing capacity obtained from both tests should be similar. This is further supported by the fact that the maximum observed rotation of the footing during test BS was only 0.03^{o}. However, as was already mentioned, the experimentally obtained bearing capacity was 29% lower than that of test B, and that the slightly higher initial voids ratio of test BS could count for approximately 15% reduction. Thus it may be argued again that the difference in the tank width has affected the bearing capacity obtained from each test.

As may be seen from both figs 6.8 and 6.9, the load-displacement relationships obtained from test RS do not compare very well with the rest of the results. Furthermore, the footing rotated by as much as 0.60^{o} (at $P/P_f = 0.99$), and this observation, combined with the higher initial voids ratio, may explain this deviation.

Experimental evidence from the preliminary investigation indicated that the horizontal displacement recovery (elastic rebound) on unloading was negligible (see fig. 2.18) whilst there was a considerable recovery of the vertical displacement under a purely vertical load. The latter was also observed in test D ($e_o = 0.52$, $\alpha_o = 0$, $E_o = 0$), see fig. 6.1. It was felt, therefore, necessary to try to separate the non-recoverable displacement vector from the recoverable one by performing two load cycles during the 5^{o} load inclination test RS ($e_o = 0.54$, $\alpha_o = 5^{o}$, $E_o = 0$). The first cycle was performed well within the working load range (1st load cycle, P/P_f : 0.38 - 0.10 - 0.38) while the unloading for the second cycle started at a stage 0.77 of the failure load (2nd load cycle, P/P_f : 0.77 - 0.58 - 0.77). The footing was, finally, loaded up to failure.

The load-displacement curves obtained from these two cycles are shown in figs 6.8 and 6.9. Both the vertical and horizontal displacement recovery obtained from either load cycles was rather negligible and for all practical purposes the total displacement vector at stages corresponding to P/P_f values of 0.38 and 0.77 may be considered as non-recoverable. The consequences of this observation will become evident in chapter 8.

6.4 Contact stress distribution

6.4.1 Introduction

The contact stress distribution obtained from tests performed in both the FAC and the FAS will be presented in this section. The arrangement of the load cells on the footing at each apparatus is shown in figs 6.10b and c, while the positive direction of the reactive loads on the footing is shown in fig. 6.10a. As was mentioned in chapter 3, only the centre row of load cells (numbered 1-6) were monitored during tests at the FAC. This followed earlier experimental evidence that the measured

stresses on the centre row load cells of the footing were almost the same as those measured on the side ones (Tennekoon, 1970). Furthermore, experimental evidence from various earth pressure problems investigated in the FAC by a number of research workers indicated that the three rows of load cells did not differ by more than 10% at any stress level, when stress exceeded 70 KN/m^2 (0.7 kg/cm^2, 10 psi) (Roscoe, 1970).

Both the centre section and one side section of the footing in the FAS were instrumented by load cells, so that any difference in the stress distribution across the width of the tank could be detected. The centre section comprised the FAC footing, while the instrumented side section was composed of load cells (labelled R,S,T,M,N,O) capable of measuring the normal reaction only (see chapter 4).

Results from all load cells will be presented mainly in a form normalized with respect to the load cell recording the highest load for the greater part of the test. A visual inspection of the computer plotted stress distribution indicated that the shape of the contact stress distribution diagrams remained practically invariant for the greater part of almost every performed test which validated this approach. Furthermore, this presentation aids the comparison of stress distributions from tests with similar initial boundary conditions.

6.4.2 Vertical central load

The mean normal stress distribution measured during test D (e_o = 0.52, α_o = 0, E_o = 0) in the FAC is shown in fig. 6.11a. The diagram shown is the mean distribution (from stage P/P_f = 0.20 to 0.90) "normalized" with respect to load cell 3 which recorded the maximum normal stress throughout the test (the corresponding standard deviations are also shown). The variation of the normal stress recorded by cell 3 during the test is shown in fig. 6.19.

As may be seen there is a slight "dip" at approximately the centre of the footing (cell 4) which is qualitatively similar to the "saddle" type stress distribution predicted by Gorbunov-Possadov (1961, 1965) and shown in fig. 1.16, but distinctly less pronounced. This decrease in stresses in the middle of the footing width disappears for load stages approaching failure as may be seen in fig. 6.11b where the normalized stress distribution at 0.90 of the failure load is shown. Similar

observations were reported by Tennekoon (1970) from tests on dense sand using the same footing, and by many more research workers (see chapter 1.4).

The striking feature about the normal stress distribution is that its shape remains approximately constant for the greater part of the test and that it expands geometrically, as is indicated by the reasonably small standard deviations (fig. 6.11a) and from the linear increase of the normal stresses recorded by the No.3 cell with increasing total load on the footing (fig. 6.19). In fact the stresses of both edges of the footing increase somewhat more slowly, than those near its centre as may be seen from figs 6.11a and b. This is to be expected since the sand starts yielding at the footing edges where the maximum stress ratio is attained at the very start of loading. This will become more evident in the next section where the deformations of the sand mass will be presented.

The mean shear stress distribution measured during the same test is shown in fig. 6.11c, where the variation of stresses measured by each individual load cell is also indicated. (The arrows indicate increasing total applied load). This diagram is normalized with respect to the highest shear stress (recorded by the load cell 6). The shear stresses recorded by that cell at any stage of the test are shown in fig. 6.20. The pattern shown in fig. 6.11c is as expected; the sand particles try to move away from the centre towards the edges of the footing and thus introduce opposite sign shear stresses on the footing base. It may be seen that the maximum shear stresses are recorded by the end load cells 1 and 6 over the greater part of the test but, as failure is approached, the shear stresses at cells 2 and 5 build up faster and at around 0.90 of the failure load, the maximum shear stresses are then measured at cells 2 and 6, those at cell 5 being 0.94 of the stresses measured at cell 6. The shear stresses, which become zero at the centre, must be zero at the edges of the footing too, since the footing is not embedded.

Similar patterns have been measured experimentally by Muhs (1965), Krivorotov (1969), Tennekoon (1970) and Zangl (1977). The shear stress distribution presented agrees, at least qualitatively, with the skew symmetric one predicted by Gorbunov-Possadov (1961, 1965), discussed in chapter 1.4.

The mean normal stress distributions (between stages P/P_f = 0.28 and 0.94) measured by the load cells of the centre and side section of the footing during test DS (e_o = 0.53, α_o = 0, E_o = 0) in the FAS are shown in figs 6.12a and b respectively. These diagrams are again normalized with respect to the cell recording the highest normal stresses at every stage of the test. (Cell 3 of the centre section and cell M of the side section). The normal stresses measured at either of these cells during the test are shown in fig. 6.19. A visual inspection indicates that the normal c.s.d. (contact stress distribution) measured underneath the side section appears to be more uniform than that measured underneath the centre section, and furthermore, that the ill-defined 'saddle', observed during test D in the FAC does not appear in test DS.(In fact a slight 'dip' was observed at a very early stage of test DS underneath the side section (P/P_f = 0.07) but disappeared subsequently). The 'smoothing' of the normal c.s.d. observed underneath the S.F. (Southampton footing, side section - see chapter 4) may well be due to the fact that the load cells of the C.F. (Cambridge footing, centre section) are twice as stiff as these of the S.F., although both sets of cells were extremely stiff deflecting approximately 0.01 of their width under full rated load. However, the effect of the glass sides cannot be ruled out. In general, both the C.F. and S.F. normal contact stresses measured during test DS (e_o = 0.53, α_o = 0, E_o = 0) performed in the FAS appear to be more uniformly distributed than those measured in test D (e_o = 0.52, α_o = 0, E_o = 0) performed in the FAC, but are very similar to those measured at stage 0.90 of the failure load of the latter test.

It is of interest and importance to note that the normal c.s.d. measured underneath both the centre and the side section do not alter appreciably throughout the major part of the test (notice the consistently small standard deviations) and that they expand geometrically with increasing total load.

The average normal stress measured at a stage 0.98 of the failure load by the centre section in test DS was found to be approximately 8% lower than that measured at either of the side sections (the S.F. and the D.F., the dummy footing). This slight decrease was noticed for stages higher than 0.50 of the failure load, where the C.F. measured about 3% lower stresses than the side footings. Up to that stage there was no

difference in the measured stresses, and in the very initial stages (up to $P/P_f \simeq 0.20$), the centre section recorded slightly higher ones. It is, therefore, suggested that the average strains recorded underneath the three sections of the footing in test DS did not practically differ (within experimental error), even though, as will be seen later on, there is an approximately 5-10% decrease in the stresses measured by the centre section at relatively high stress levels (over 40 KN/m^2).

The mean shear c.s.d. measured underneath the centre section of the footing in test DS is shown in fig. 6.12c. The pattern obtained is similar to that observed during test D in the FAC (see fig. 6.11c); the maximum shear stresses were measured at the end load cells 1 and 6 initially, while near failure, the maximum stresses occurred at cells 1 and 5. The slight non-symmetry of the distribution is caused by the small horizontal component induced by the footing rotation (see section 6.3.1).

6.4.3 Vertical eccentric load

The mean normal stress distribution (between stages 0.10 - 0.90 of the peak load) obtained from test A ($e_o = 0.52$, $\alpha_o = 0$, $E_o = 0.167$), performed in the FAC, is shown in fig. 6.13a again normalized with respect to load cell 5. (The variation of normal stresses recorded by cell 5 during loading is shown in fig. 6.19). It should be noted here that the applied vertical load was initially acting between cells 4 and 5 (see fig. 6.13c). It may be seen from fig. 6.13a that the distribution is of triangular shape, its apex being formed near the "point of application of the load". The stresses at the edges of the footing are initially zero but, due to subsequent vertical displacement, they become of a small finite value. The exact variation of the stress distribution at areas of stress jumps cannot be obtained in any more detail, because the load cell widths were relatively large with respect to the footing width. However, it is rather evident that the end load cell (cell 1) on the side opposite to the load eccentricity recorded extremely low stresses, which implies that, at some stage, it partially lost contact with the sand. This was a consequence of the footing rotation, coupled with the relatively high position of the frictionless joints with respect to the footing base (see section 6.2.2).

Lee (1965) measured the normal c.s.d. underneath a 300 mm wide footing subjected to moments by means of embedded load cells (see chapter 1.4), and some representative results are shown in fig. 1.22a to c. Despite the shortcomings of embedded load cells, there is good agremeent between the normal c.s.d. shown in fig. 6.13a obtained by the author for initial eccentricity ratio of 0.167 and that shown in fig. 1.22b obtained for an identical eccentricity ratio. It should be remembered here that, due to the footing rotation, the eccentricity ratio at failure to test A (e_o = 0.52, α_o = 0, E_o = 0.167) was 0.21 (see section 6.2.2). It was therefore, expected that a larger part of the footing base would have lost contact with the soil than that shown in fig. 1.22b.

Muhs and Weiss (1969) reported a triangular distribution of the measured normal stresses underneath a concrete footing subjected to an eccentric vertical load but no actual results were presented.

The mean shear stress distribution normalized with respect to the shear stresses recorded by load cell 6 is presented in fig. 6.13b for test A (e_o = 0.52, α_o = 0, E_o = 0.167). The shear stresses recorded by cell 6 at any stage of the test are shown in fig. 6.20. As may be seen from fig. 6.13b, the distribution of shear stresses changes sign at approximately where the line of action of the load cuts the footing soil interface. Even though the exact position of the change of sign cannot be traced due to the relatively large width of the load cell, it is evident that it occurs at the load cell 5. The highest shear stresses were recorded at cell 6, whereas relatively low shear stresses were measured at all other load cells, those measured at cell 1 being almost zero. For reasons of equilibrium, the shear stresses underneath the footing must add up to the small horizontal load component arising from the fact that the footing has tilted and therefore the contact stresses are no longer horizontal and vertical. Thus the high shear stresses measured at cell 6 were rather expected since they counterbalance those measured by the other load cells. Furthermore, as was mentioned above, cell 1 merely touches the sand surface beyond some stage during the test and, therefore, the shear stresses recorded by that cell were expected to be very small.

It is of interest to note that both the normal and shear c.s.d.

showed little change throughout the greater part of the test, as is indicated by the relatively small standard deviations from the mean value of the readings of each load cell (see fig. 6.13a and b). This is somewhat surprising since the footing tilted with increasing total load and this would be expected to have affected the c.s.d. The relative rotation at failure (1.8^{o}) was relatively small with respect to the width of the cell (12.7 mm) and, therefore, the changes in orientation would not justify any appreciable alteration of the stress distribution. If load cells of narrower width had been used, small local variations in the c.s.d. would have occurred. However, it does seem highly probable that the shape of c.s.d. underneath a footing remains practically invariant throughout any particular test.

It was mentioned in section 6.2.2 that both tests A and H were carried out under almost identical conditions, and it was shown in section 6.3.2 that there was very good agreement between the corresponding load-displacement and moment-rotation relationships. The same seems to apply for the corresponding c.s.d., as may be seen in figs 6.13a,b and 6.14a,b where the mean normalized normal and shear stress distribution obtained from tests A and H respectively are presented. The apparent small differences are probably due to local non-uniformities of the sand. The author is not aware of any other published results on experimentally measured shear c.s.d. under footings loaded by moments, and the limited experimental evidence available on the normal c.s.d. (Lee, 1965) is in good agreement with the author's results.

The mean normalized contact stress distributions (between stages P/P_f = 0.15 - 0.95) measured during test HS (e_o = 0.53, α_o = 0, E_o=0.167) in the FAS, are shown in figs 6.15a (normal c.s.d, centre section), 6.15b (normal c.s.d, side section) and 6.15c (shear c.s.d, centre section). The stresses on the cells with respect to which these diagrams have been normalized, are shown in figs 6.19 (normal stresses) and 6.20 (shear stresses) for each stage of the test. At first sight, the normal c.s.d. measured underneath both the C.F. and the S.F. are of a triangular shape similar to those measured in test A in the FAC (see fig. 6.13a).

The maximum stresses were consistently measured at cell N of the side section (corresponding to cell 5 of the C.F. in test A), whereas

the highest stresses in the centre section appeared to have been recorded by cell 4. In fact this was the case for early stages of the test, but at 0.75 of the peak load, cell 5 started to record the highest stresses, in agreement with the corresponding cell N of the side section (note the relatively high standard deviation at cell 5). The maximum stress recorded by cell 5 at 0.96 of the failure load is indicated by a dotted line in fig. 6.15a. In general there are no appreciable differences between the c.s.d. measured in either the FAS or the FAC. The apparently relatively high shear stress recorded by cell 1 becomes almost zero when failure is approached, due to the rotation of the footing, as is indicated in fig. 6.15c.

The average normal stresses measured underneath each section of the footing at any stage of test HS (e_o = 0.53, α_o = 0, E_o = 0.167) are shown in fig. 6.16. As may be seen there is no appreciable difference between them for stages approaching failure, but the centre section seems to have picked up slightly higher stresses (of the order of 5-8%) during the initial stages of the test. It should be noted here that failure occurred at an average normal pressure of approximately 20 KN/m^2 and that the normal stresses at the side sections become higher than at the centre one for higher stress levels (over 40 KN/m^2), as indicated in the previous section.

6.4.4 Inclined central load

The mean normalized normal stress distributions obtained from tests B ($\alpha_o = 12^o$, P/P_f = 0.25 - 0.86), GB ($\alpha_o = 20^o$, P/P_f = 0.35 - 0.95) and E ($\alpha_o = 30^o$, P/P_f = 0.47 - 0.87) performed in the FAC are shown in figs 6.17a,c and e respectively. The variation throughout the test of the normal stresses recorded by the cell, with respect to which these diagrams have been normalized (cell 3 for test B, cell 5 for tests GB and E), is shown in fig. 6.21. An interesting point is that the form of normal stress distribution does not alter appreciably with increasing load inclination, and that it is similar to the normal c.s.d. of a rigid footing loaded by a vertical central load (see fig. 6.11a). This could be expected as a result of the vertical component of the applied load. It should be remembered that the footing did not rotate appreciably

throughout the loading sequence of any test (see section 6.3.3) and, therefore, the line of action of the applied load always passed practically through the middle of the footing base.

Similar findings were reported by Muhs and Weiss (1973) who stated that the normal stress distribution underneath a concrete footing was of parabolic shape and that it was independent of the load inclination (see chapter 1.3.4.2). However no results were presented.

It is of interest to note that the same basic pattern is maintained (for stages of the test corresponding to P/P_f values of 0.30 to 0.90 approx.) which expands with increasing load. This is supported by the relatively small standard deviations of the readings of each load cell from their mean value (see figs 6.17a, c and e).

For equilibrium, the shear stresses must counterbalance the horizontal component of the load. It was pointed out in section 6.4.2 that, in the case of vertical central loads, the soil moves almost symmetrically towards the footing edges, and, therefore, the shear stresses must be equal and of opposite sign (on either side of the centre line). In the case of inclined loads, the soil particles move, relatively to the footing, in a direction opposite to that of the horizontal component of the load and the shear stresses are therefore expected to be of the same sign.

The mean normalized shear stress distributions obtained from tests B ($\alpha_o = 12^o$), GB ($\alpha_o = 20^o$) and E ($\alpha_o = 30^o$) are shown in figs 6.17b, d and f respectively. The highest shear stresses were measured at cell 5 in all three tests and their magnitudes throughout the test are shown in fig. 6.22. As may be seen from figs 6.17b, d and f, the shear stresses are basically of the same sign and it may be assumed that, to a reasonable approximation, their distribution remains invariant throughout a large part of the test. However, it is evident that for small load inclinations the shear stress distribution is not entirely of the same sign which implies that some of the sand particles move towards the same direction with the horizontal component of the load. This could be expected since, in such cases, the vertical component of the load is predominant and the soil particles will move towards both the footing edges. As the load inclination increases (see figs 6.17d and f), the whole contact shear stress diagram becomes of one sign only.

The contact stress distributions obtained from tests BS (e_o = 0.53, α_o = 12°, E_o = 0) and RS (e_o = 0.54, α_o = 5°, E_o = 0), performed in the FAS, are shown in fig. 6.18a to f in a normalized form similar to that of figs 6.17. The diagrams shown are the mean distributions between stages corresponding to P/P_f values of approximately 0.35 and 0.95. The normal c.s.d. measured underneath the S.F. (side section), shown in figs 6.18b and e, appears to be more uniform than that measured underneath the C.F. (centre section), shown in figs 6.18a and d (for tests BS (α_o = 12°) and RS (α_o = 5°) respectively). A similar observation was made for the vertical central load case (see section 6.4.2) and it is anticipated that either the effect of glass friction or the difference in stiffness between the load cells of the centre and side sections, or both, might have affected the distribution of normal stresses measured underneath the S.F. (side section).

The shear stress distributions obtained from tests BS (α_o = 12°) and RS (α_o = 5°) are shown in figs 6.18c and f respectively. The pattern is similar to that observed during tests in the FAC (shown in figs 6.17). In fact, as may be seen from the shear c.s.d. of test RS (α_o = 5°), the shear stresses become zero at a point between cell 3 and cell 2, which implies that the sand underneath cells 2 and 1 is moving in the same direction (relative to the footing) as the horizontal component of the applied load. Such behaviour must be mainly influenced by the vertical component of the applied load, which, in this case (α_o = 5°) plays a dominant part.

The variation of the average pressure measured underneath each section of the footing during tests BS (α_o = 12°) and RS (α_o = 5°) in the FAS, is shown in figs 6.23 and 6.24 respectively. It may be argued that, within experimental error, the three sections recorded the same average pressure. However, it is evident that for relatively high stress levels (average pressure over 20 KN/m^2) the centre section measured consistently 4 to 7% lower stresses than those measured by the side sections (see also section 6.4.2). The interesting point is that, in both tests, the Dummy section measured relatively higher stresses than the other two did. Nevertheless, the differences between the side sections were of the order of 2 to 4% only.

It should be noted here that the loads recorded by the "shear connectors" which interconnected the three sections of the footing in the

FAS (see chapter 4), amounted to 2% at the most of the total load recorded by each section, usually being even smaller. Therefore, the loads transferred from one section to another were of negligible magnitude.

6.4.5 Inclined-eccentric loads

The normal and shear c.s.d. obtained at stages very near failure from tests F ($e_o = 0.52$, $\alpha_o = 0$, $E_o = 0$, independent horizontal load at 100 mm from the footing base) and C ($e_o = 0.52$, $\alpha_o = 12^o$, $E_o = -0.167$), performed in the FAC, are shown in figs 6.25a, b and 6.26a, b respectively. As may be seen, the normal stress distribution from both tests is similar to that of an eccentric vertical load (see figs 6.13, 6.14, 6.15) as was anticipated. However, the shear stresses in test C do not show a similar pattern to those of an eccentric vertical load (whereas those in test F do), which implies a significant influence of the horizontal component of the load.

6.4.6 Angle of base friction

The measured angle of base friction in tests D ($e_o = 0.52$, $\alpha_o = 0$, $E_o = 0$), B ($e_o = 0.52$, $\alpha_o = 12^o$, $E_o = 0$), GB ($e_o = 0.52$, $\alpha_o = 20^o$, $E_o = 0$) and E ($e_o = 0.52$, $\alpha_o = 30^o$, $E_o = 0$), in the FAC, is shown in figs 6.27a,b,c and d respectively, while that measured during tests BS ($e_o = 0.53$, $\alpha_o = 12^o$, $E_o = 0$) and RS ($e_o = 0.54$, $\alpha_o = 5^o$, $E_o = 0$), in the FAS, is shown in fig. 6.28a and b. The distributions shown correspond to stages at approximately 0.90 of the failure load.

The maximum angle (δ) measured during a vertical central load test, test D, was about 32^o (fig. 6.27a) while the maximum angle (δ) measured underneath the footing was 43.3^o recorded during test E ($\alpha_o = 30^o$). As may be seen from figs 6.27 and 6.28, the angle of base friction increases with increasing load inclination. This implies that δ is a function of stress level and, therefore, inclined loads (and lower average pressure) will produce higher δ values. However, δ will not become equal to ϕ (here assumed 50^o approximately, see section 6.2 and chapter 7.5) for reasons explained in chapter 2, and sliding of the footing will occur, when $\alpha = \delta$.

Similar findings were also reported by Muhs and Weiss (1973) who

observed that with increasing load inclination (α = 10°, 20° and 30°) the angle of base friction also increased (δ = 10°, 19° and 25° respectively). However, they stated that the maximum δ amounted to approximately 38° which is very near the angle of internal friction of the fill they used (ϕ = 39° to 40°).

A summary of the experimentally measured angle of friction between different types of footing and soil has been reported by Schultze and Horn (1969). For concrete footings, either smooth or rough (prefabricated or cast in place), and for rough steel footings, both resting on sand, δ seems to vary between 0.7 to 1.0 ϕ.

Considering the values of the angle δ measured from a number of tests performed by the author, an average value of 40° was adopted as the angle of base friction, and this will be discussed again in chapter 8.

6.4.7 Conclusions and some further implications

The following are the main conclusions drawn from this chapter.

1) The experimentally obtained bearing capacity of a vertical central load case was found to be in general agreement with experimental results from other research workers. However, the predicted bearing capacity of strip footings on dense sand may vary by a factor of 2, depending upon the formula one uses for its estimation.

2) The 'effective' width concept provides a safe estimate of the bearing capacity reduction of vertically eccentrically loaded footings.

3) The inclination factors proposed by Hansen (1970) and by the author provide safe predictions of the bearing capacity reduction for any load inclination in the case of a strip footing on sand under inclined central load. It should however be emphasized here again that N_γ for a vertically centrally loaded footing is the dominant parameter in designing a strip footing on sand under general planar loads and, therefore, accurate prediction of N_γ is of prime importance.

4) One of the findings of the preliminary investigation, that higher horizontal loads can be carried by the footing under the same vertical eccentric load when E < 0, was confirmed by the experimental results in the FAC.

5) The footing was found to rotate and displace horizontally when under a vertical central load. This non-symmetrical behaviour (which will be discussed again in the next chapter) caused a one-sided failure (see, for example, the failure surface of test DS (e_o = 0.53, α_o = 0, E_o = 0) shown in fig. 7.53). The rotation at failure,when under an eccentric vertical load,was found to be approximately 2^o, whereas the footing remained practically horizontal throughout almost the whole test under an inclined central load. An 11% vertical displacement recovery was also observed during complete unloading from a stage P/P_f = 0.95 in test D (e_o = 0.52, α_o = 0, E_o = 0) which supported a similar observation made during the preliminary investigation. However, both the vertical and horizontal displacements recovery, observed from two load cycles in test RS (e_o = 0.54, α_o = 5^o, E_o = 0), were negligibly small. This confirms the finding of the part I experimental series that the horizontal displacements are practically irrecoverable, but the 'irrecoverable' vertical displacements here do not agree with the previous experimental results.

6) It was demonstrated that kinematic constraints on the lateral motion resulted in an increase of the bearing capacity of an eccentrically vertically loaded footing by a factor of about 2, when compared to the case with no constraints. However, both the dimensionless load-displacement and moment-rotation relationships obtained for both the above cases were almost identical.

7) It was suggested that the vertical load component-vertical displacement relationship for any load inclination may be described by a bilinear approximation. This will be used in chapter 8.

8) For almost identical initial boundary conditions, both the load-displacement relationships and the ultimate loads obtained from tests A

(e_o = 0.52, α_o = 0, E_o = 0.167) and H (e_o = 0.52, α_o = 0, E_o = 0.167) were found to be identical, which establishes the repeatability of the experimental results. This is further supported by the almost identical contact stress distributions measured underneath the footing on both tests.

9) The contact stress distribution (both normal and shear) under a vertical central load was found to be similar to that reported by an earlier investigation (Tennekoon, 1970). For an eccentric vertical load acting on the footing, the normal stress distribution at failure was approximately triangular, as expected, with the apex of the triangle located close to the line of action of the applied load. For inclined central loads, the normal c.s.d. was found to be similar to that for a vertical central load and independent of the inclination of the applied load. It was also observed that, for a considerable part of the test (P/P_f = 0.30 to 0.90), the normal c.s.d. under any planar load do not change appreciably and expanded geometrically with increasing total load.

10) The angle of base friction was found to increase with increasing load inclination, and a value of 40^o was adopted as an average δ from the many values measured, see figs 6.27, 6.28.

11) The average pressure recorded by the centre section of the footing in the FAS near failure was found to be 7% lower on average than that recorded by either side sections, even though the opposite was found to be the case at early stages of the test. Rowe and Peaker (1965) reported that the load recorded by the centre section of an articulated wall (Height/Width = 0.25) was about $\frac{2}{3}$ of the load recorded by the side sections. It was also suggested (Rowe, 1972) that the stresses measured on a wall (even in the centre section) in a narrow tank (say Height/Width $\approx$ 1) must be greater than those obtained if there had been no side friction. The author performed tests with two different height to width ratios, 0.4 in the FAC and 0.13 in the FAS, but a reduction of only 7% was observed in tests in the FAS. From an earlier investigation (Tennekoon, 1970) it was shown that the stresses recorded by the centre

section were usually slightly higher than those recorded by the side ones even though the reverse was true in many instances, which suggested that either the effect from the glass friction was negligible or that it was uniformly distributed across the width of the tank.

It was also observed that the ultimate loads obtained from tests in the FAS (tank width=584mm) were lower (≈ 20%) than those obtained from nominally identical tests in the FAC (tank width = 190.5 mm). Part of this reduction was very likely due to the small difference in the initial density of the sand bed. However, the remarkable agreement between the load-displacement relationships obtained from either apparatus implied that the relative width of the tank must have affected, at least partially, the observed difference in the failure loads. It is, therefore, suggested that the reducing bearing capacity due to the larger tank width is of the order of 5 - 10% only.

CHAPTER 7

DEFORMATIONS MEASURED IN THE SAND MASS

7.1 Introduction

The various bearing capacity theories discussed in chapter 1 assume, amongst other things, that the soil fails at constant yield stress along a simultaneously developed failure surface. The deformation prior to failure is not considered; instead, it is assumed that the soil behaves like a rigid plastic material (e.g. limit equilibrium method). The validity of these assumptions may be checked by actually performing stress and displacement measurements.

The methods used for measuring soil movements have been summarized in chapter 5. The author used both the X-ray and the Stereophotogrammetric techniques to measure displacement fields in the sand mass. In doing so, he had two objectives: Firstly, to obtain reliable displacement fields of the deforming sand mass for various footing loading conditions and secondly to attempt a direct comparison of these two techniques, in order to reveal the effect of the glass side friction on the measured displacements. In addition, after having established the difference (if any) between the displacement fields obtained by these two methods from tests in the FAC, the author used the Stereophotogrammetric technique to obtain displacement fields from nominally identical tests in a three times wider tank (FAS)(in which the X-rays technique cannot be used). These measurements, combined with the measured boundary stresses (no internal stresses were measured in this project), would be used to investigate the effect of the tank width on the results from model tests in narrow tanks.

It should be noted here that this extensive experimental commitment did not allow the author to undertake any theoretical analysis to predict analytically the experimentally obtained displacement fields. It was thought, however, that the fulfillment of the above objectives would improve our understanding on soil deformation underneath footings when subjected to eccentric and/or inclined loads, and would be valuable in shedding some more light in the effect of the tank width on the model test results, as well as in providing high quality experimental data

against which future analyses could be checked.

The strain parameters that may be calculated from a measured displacement field have already been presented in chapter 5. The data manipulation was carried out by the 'STRAINS' program (Orr, 1975) from which the output consisted of printed and/or plotted displays. The following information could be provided, if requested:

a) Printed displays at the centroids of the triangular elements (see chapter 5) of the

   a_i) X-displacements in tenths of a millimetre

   a_{ii}) Y-displacements in tenths of a millimetre

   a_{iii}) Shear strain in % (γ_m)

   a_{iv}) Volumetric strain in % (Δ)

   a_v) The angle of dilatation in degrees (defined as $\sin \nu = - \dot{\Delta}/\dot{\gamma}_m$)

b) Plotted information of the following at the centroid of each triangular element:

   b_i) The position of each centroid

   b_{ii}) The principal strains

   b_{iii}) The direction of the maximum principal compressive strain

   b_{iv}) The displacements of either the centroids or the lead shot (plotted as vectors)

   b_v) The zero-extension line directions (plotted as straight line segments, their magnitude being a function of the corresponding maximum γ).

The above information could be also listed in much more detail in tabular form.

Displacement fields will be mainly used when comparing the two techniques, since the strain fields within the sand mass are calculated from them, and therefore any difference between these techniques may be best established from consideration of the former.

The importance of the various strain parameters referred to above will now be briefly discussed. Information about the amount of strain the sand sample has experienced is provided by the shear and volumetric strains. It is well known that in the theory of elasticity the principal axes of stress increments and strain increments coincide whereas in the theory of plasticity it is usually assumed that the principal axes of strain increments and stress coincide. The Cambridge S.S.A was designed

so that it would cause the principal axes to rotate during the test; hence, the relationship between these sets of axes could be investigated. It is therefore important to examine whether the directions of the principal axes of strain increment of a soil element rotate when subjected to loads from the footing.

The 'zero extension' line directions (so named by James (1965)), are directions of lines along which the linear strain is zero. Hansen (1958) had suggested that failure in sands takes place when the Mohr-Coulomb failure criterion is satisfied on the stress characteristics but along a plane which is parallel to the direction of a zero extension line rather than along a plane where the maximum stress ratio has been reached. This was first established experimentally with Leighton-Buzzard sand by James (1965) and confirmed subsequently by almost all the tests in the earth pressure models and in the S.S.A with the same sand (Roscoe, 1970).

Results from tests performed at the FAC will be presented first and the X-rays and Stereophotogrammetric techniques compared. Results from tests in the FAS will follow and they will be compared with those from similar tests in the FAC. All failure surfaces from tests in the FAC were photographed by X-rays and some of their major characteristics (like shape, depth, etc.) are also presented and discussed.

7.2 Displacement and strain fields from tests D ($e_o = 0.52$, $\alpha_o = 0$, $E_o = 0$)

Sixteen load increments were performed during test D, carried out at the FAC, before unloading (see chapter 6), and radiographs were taken at stages which correspond to the following P/P_f values: 0.46, 0.59, 0.74, 0.93.

The total displacement field at the end of each increment is shown successively in figs 7.1a,b,c,d, where the computer plotted vectors denote the displacement of the lead markers. As may be seen, the penetration of the footing causes the sand to displace both downwards and sideways and it is of interest to note that displacements of the order of 30% of the footing movement are recorded at a depth well over three times the footing width (76.2 mm) (see for example, fig. 7.1d). It will be shown later in this section that shear strains of the order of 3% were calculated at that depth. The relative position of the rigid boundary,here at 1400 mm depth, can have, therefore, a considerable effect on experimental results from model studies.

An important feature of the general displacement pattern shown in fig. 7.1 is that it remains almost the same throughout the test: There is a main sand core which moves practically vertically (zone 1), two nearly symmetrical zones (zones 2) where the displacement vectors rotate to become almost horizontal near zone 3, and two zones (zones 3) where the sand is moving primarily sideways and upwards. This regular pattern was also observed by Tennekoon (1970) in all his tests under vertical central load, and by Zangl (1977) in similar tests with an 84 mm wide footing in a similar apparatus.

A visual examination of the displacement fields (fig. 7.1) indicates that they may be considered to be symmetrical with respect to the vertical through the centre of the footing base. However, a closer examination (with the help, for instance, of the total displacement field contours at the end of stage $P/P_f = 0.93$, shown in figs 7.2a,b) reveals that the x displacements underneath the 'right' edge of the footing are slightly higher than those underneath the 'left' edge. This will be further discussed when the strain results are presented.

The directions of the maximum principal compressive strain at the end of each loading stage ($P/P_f = 0.46, 0.59, 0.74, 0.93$) are shown in figs 7.3a,b,c,d. A pattern similar to that of the lead shot displacement is observed, which, in fact, is maintained unaltered throughout the loading sequence. This implies that the principal axes of strain do not rotate to any great extent, and, in addition, that the principal axes of strain rate show a similar pattern. The latter point is further supported by the corresponding incremental results shown in figs 7.4a,b,c, d, despite some scatter especially in the increments 0.46-0.59, 0.59-0.74, due mainly to the relatively small strains which occurred during these increments. Therefore, the axes of principal compressive strain and strain rate coincide to a reasonable approximation.

Nearly all the strain data presented is based on the total strains rather than the incremental ones. (The total strains are derived from the total displacements that have been measured from the beginning of a test). This procedure is justified only if the principal axes of strain and of strain rate do not rotate throughout the loading sequence which has been found to be the case. As will be shown later in this chapter, the angle of dilatancy remains approximately constant over a considerable range of shear strain. Thus, the use of total strains in calculating the

zero extension line directions (which are inclined to the principal compressive strain rate at an angle ($45^o - \nu/2$)) should not induce any significant error. Furthermore, the total strains rather than the cumulative ones will be used since, as was pointed out by Tennekoon (1970), the errors involved in the former are due only to those arising from the measurement of the two X-rays films (The cumulative strains are obtained by adding "vectorially" the strains calculated in all previous increments). However, as will be shown, the difference between total and cumulative strains is generally very small.

The total shear strain fields at the end of the increments corresponding to P/P_f 0.46, 0.59, 0.74 and 0.93 are shown in figs 7.5a,b,c,d. Contours of equal shear strain are also drawn in these figures. It is evident that during the first increment (7.5a) the maximum shear strains develop at the edges of the footing which is to be expected since the sand starts yielding at the footing edge. They begin, then, to spread downwards both towards the centre and the sides. This deformation pattern, which is basically maintained throughout the test, may be represented by two bulbs of shear strain, each beginning and ending near either of the footing edges and decreasing with depth, enveloped by another bulb of shear strain, again decreasing with depth, which begins from one edge and ends at the other (see fig. 7.5b). A fourth bulb of shear strains increasing with depth is located between the first two and runs from one corner of the footing to the other.

This pattern of sand deformation was observed by Tennekoon (1970) (see, for example, his fig. 5.12c, reproduced here in fig. 7.7), who suggested this kind of subdivision of the shear strain fields. It is of interest to note the striking similarities between these patterns and the equal stress contours observed experimentally by Mesmer (1930) (from Nadai, 1963), Frocht (1948), Tockhov (1961), from a photoelastic pattern of a rigid foundation on an elastic base (see fig. 7.6). Such a similarity indicates that, despite the fact that sand is not intrinsically an elastic medium, the use of the theory of elasticity may provide qualitative description of the deformation patterns within the sand mass.

The maximum shear strains at stage $P/P_f = 0.93$ of test D ($e_o = 0.52$, B = 76.2 mm), shown in fig. 7.5d, seem to be very similar to those shown in fig. 7.7 which were obtained from a similar test performed by Tennekoon (1970) (test H, $e_o = 0.525$, B = 76.2 mm) at approximately the

same loading stage (PEP_f = 0.955) (it should be noted here that at least the top two layers of lead shot do not seem to have been measured by Tennekoon). In fact, he showed that the strain distribution he obtained was reproducible and the relatively good agreement between these two tests implies that this also applies to the corresponding results from tests performed by the author.

The cumulative shear strains at stage P/P_f = 0.93 obtained from test D are shown in fig. 7.8aand are almost identical to the total shear strains at the same stage (shown in fig. 7.5b). The maximum differences are of the order of 1% of strain which may be considered as insignificant.

It was pointed out earlier in this section that the displacement field is not as symmetrical as anticipated from visual inspection of the lead shot displacement vectors in fig. 7.1. The strain field of fig. 7.5d shows that strains as high as 30% are observed underneath the left edge of the footing while they do not exceed 20% underneath the right edge. This non-symmetrical strain field caused the footing to rotate by 0.16°. Similar observations were made by Tennekoon (1970); the footing he used could not either rotate or displace horizontally and he attributed to this non-symmetry the order of the formation of the failure surfaces (as already discussed in chapter 6.3.1). In addition Andrawes (1970) observed similar non-symmetrical behaviour in dense sand when indented by a rigid wedge (not allowed either to rotate or displace horizontally).

The volumetric strains at stage 0.93 are shown in fig. 7.8b. Despite some scatter of the results, which is noticeably greater than that of the shear strains, they follow the same general pattern as the shear strains, which suggests that a relationship may exist between the volumetric and maximum shear strains in dense sand. This will be later discussed after the results from the other tests are presented.

The direction of the zero extension lines at stages P/P_f=0.74 and 0.93 are shown in figs 7.9a and b. As may be seen, the sand immediately underneath the footing decreases in volume (the angle between the zero extension lines is greater than 90°) while it dilates almost in all other areas.

A closer examination of fig. 7.9b reveals that the angle between these two directions (average value 70°) remains practically the same within a wide area of the deforming sand mass. The constancy of this angle implies that the sand dilates at constant rate over a wide range

of shear strains. It will be later shown that the angle of dilatancy ν remains practically constant at about 20^{o} for shear strains between 0.02 and 0.15.

The zero extension line directions will be discussed again, when the failure surface patterns are presented.

7.3 Displacement and strain fields from test A ($e_o = 0.52$, $\alpha_o = 0^{o}$, $E_o = 0.167$)

Test A was performed in the FAC. The footing was taken to failure after 20 increments, and radiographs were taken at stages 0.72, 0.91 of the peak load and just after peak load was attained.

The total displacements at stages 0.72 and 0.91 are shown in figs 7.10a,b where the vectors represent the total movements of the lead shot. The displacement pattern remains practically the same and is of similar type to that obtained from test D (see figs 7.1a and d). However, higher displacements occur underneath the footing edge near the eccentric load, as may be seen from figs 7.10c,d, where horizontal and vertical displacements of the sand mass at stage 0.91 are displayed in a map form. This rather expected pattern is mainly due to the non-symmetry of the applied load.

Figures 7.11a and b show the directions of the maximum principal compressive strains at the end of the loading stages 0.72 and 0.91. Despite some scatter, which appears in areas where the sand mass has experienced relatively small strains compared to those at which peak stress ratio is reached, the overall pattern remains essentially invariant with increasing load. It may therefore be argued again, that the principal strain axes did not rotate throughout the test, and that the axes of principal strain and of principal strain rate coincide. The latter is further supported by the directions of the incremental maximum principal compressive strain between stages 0.72 and 0.91 (shown in fig. 7.11c), despite the considerable scatter which is again due to the development of very small strains. It is also of interest to note that the pattern remains basically unaltered after the failure load has been reached (see fig. 7.11d).

The shear strain fields obtained from test A at stages 0.72 and 0.91 of the failure load are shown in figs 7.12a and b; equal shear strain

contours have also been drawn. Contrary to the strain fields obtained from test D (e_o = 0.52, α_o = 0, E_o = 0), which are shown in figs 7.5a to d, the shear strains become very small at a relative depth twice the footing width, their magnitudes being less than 1%. This implies that the areas affected by an eccentric vertical load are considerably smaller than the corresponding ones under a vertical central one. In fact, as may be seen from figures 7.12 and 7.5, smaller shear strains were developed during test A (e_o = 0.52, α_o = 0, E_o = 0.167) rather than during test D (e_o = 0.52, α_o = 0, E_o = 0) at similar stages of the test. . Stroud (1971) showed from tests in the SSA that, in dense Leighton-Buzzard sand, the shear strain at which the peak stress ratio occurs depends on the stress level: The higher the stress level, the larger the shear strain the sand element must experience for the maximum ratio of shear stress to normal stress to be obtained. It was demonstrated in chapter 6 that the failure load for test A was approximately 40% of that for test D. Therefore, the development of relatively lower shear strains during test A may be attributed to the relatively lower stress level.

As may be seen from fig. 7.12a, the maximum shear strains developed mainly underneath the 'left' edge of the footing, while the sand mass immediately underneath the 'right' edge does not seem to experience any significant strain. This implies that only part of the footing is 'effective' and this has been already demonstrated by the contact stress distribution in chapter 6. Subsequently, the strains spread downwards from that edge at the same time expanding laterally (see figs 7.12a,b). The essence of this deformation pattern may be represented by a single bulb of shear strains which begin and end near the 'left' edge of the footing (on the same side with the load eccentricity) (see fig. 7.12c) and which decrease with increasing depth. In fact, a second shear strain bulb may be observed near the 'right' edge of the footing (see fig. 7.12b), but its size is substantially smaller than that formed underneath the 'left' edge. This second bulb appears to cease expanding after stage 0.72 (compare figs 7.12a and b), which implies that the footing is tilting towards the side where higher shear strains have been developed. It must be remembered that due to the experimental set up already discussed in chapter 3, even a small rotation of the footing increases the eccentricity of the load so that the 'effective' footing

breadth indenting the sand mass decreases continuously.

Figure 7.13 shows contours of principal stress difference and therefore maximum shear stress in a semi-infinite elastic plate under a normal concentrated load (obtained photoelastically by Frocht, 1948). These are surprisingly similar in shape to the maximum shear strain bulb of figs 7.12a and b (the second bulb of shear strains being negligibly small, by comparison).

The volumetric strains obtained at stage 0.72 and 0.91 of test A are shown in figs 7.14a and b. The distribution is again similar to that of the single shear strain bulb shown in figs 7.12a and b, but is not so well defined due to the very small magnitudes of the volumetric strains. No volumetric strains were developed underneath the right hand edge of the footing.

The zero extension line directions at the end of the same load increments are shown in figs 7.15a and b. The sand is seen to dilate underneath the 'left' edge of the footing, while it contracts in areas near the centre immediately underneath the base. This is indicated by the zero-extension line included angle being less than 90^{o} or more than 90^{o} respectively (see chapter 5). The pattern is well defined near the 'left' corner of the footing but becomes considerably scattered in other areas. This is mainly due to the very small volumetric strains (see figs 7.14a and b). The zero extension lines will be again discussed after the failure surfaces from the various tests in the FAC have been presented.

7.4 Displacement and strain fields from test B ($e_o = 0.52$, $\alpha_o = 12^{o}$, $E_o = 0$)

Test B was performed in the FAC and was taken to failure after twenty load increments. Radiographs were taken at stages $P/P_f = 0.25$, 0.70 add 0.86 and just after peak load was attained.

The total displacement fields at the end of load increments 0.70 and 0.86 are shown in figs 7.16 a and b.(Results from the $P/P_f = 0.25$ stage were unfortunately lost due to erroneous measurements of lead shot coordinates). As may be seen, the sand mass is mainly moving in the direction of the load inclination, while the observed displacements on the other side (outside the 'left' edge of the footing) are relatively very small. This is more clearly demonstrated in figs 7.17a,b,c,d, where the x and y displacements at the end of the same increments are presented

separately in map form.

An interesting feature of the displacement fields shown in figs 7.16a and b (and in figs 7.17a and c), is the direction of the movement of the sand mass underneath the footing, which is inclined at approximately 35^{o} to the vertical. In fact, the footing, too, was found to displace (from the dial gauge measurements) along a direction inclined at approximately the same angle to the vertical almost throughout the test. This indicates that the footing does not move along the direction of the applied load (here $\alpha = 12^{o}$), but along a direction,the inclination to the vertical of which remains practically constant throughout the loading sequence. The consequences of this important finding will be discussed in chapter 8.

It would be expected that the top lead shot layer, immediately underneath the footing base,would have also moved along the same direction. Nevertheless, as may be seen from both figs 7.16a and b, each of the lead shot marker displacement vectors is inclined at a different angle to the vertical. This is thought to be due to errors in measurement of their coordinates in the FMM caused by poor definition of their image on the radiograph. The main reason for the poor definition is the interference of the duraluminium of the load cells. Furthermore, the X-rays hitting the top lead shot row penetrate a relatively thinner sand sample (due to the relative position of the X-ray tube at the mid-height of the lead marker network), and this results in overexposure of these areas. The latter hazard was partially overcome by using a wedge shaped copper plate placed at the front glass side, just beneath the sand surface (see chapter 5). However, the definition of the image of the lead shot only outside the footing area was improved, whilst that in touch with the footing base still remained ill-defined. Therefore, it is almost certain that the variation of the inclination angles to the vertical of the displacement vectors of these lead markers is due to erroneous measurements rather than to some strange behaviour of the sand mass in contact with the footing.

The directions of the principal compressive strain at stages P/P_f= 0.70 and 0.86 are shown in figs 7.18a and b respectively, while the same directions obtained from the load increment 0.70 - 0.86 are shown in fig. 7.18c. It is evident that the principal strain axes do not rotate to any great extent during at least the late stages of the test (P/P_f =

0.70 onwards) and that, for these stages, the axes of principal compressive strain and principal compressive strain rate coincide. In fact the same behaviour is exhibited even after failure, as may be seen from figs 7.19a and b, where the directions of the principal compressive strain and strain rate presented at a stage just after peak load was reached; the directions of fig. 7.19b are calculated from the measured displacement field corresponding to the load increment P/P_f = 0.86 to 1.0, whilst those of fig. 7.19a are calculated from the total displacement field measured at the latter stage.

Figure 7.18d shows the major principal compressive strain directions at the end of a stage at 0.53 of the failure load, as calculated from the measured displacement field using the Stereophotogrammetric technique (which will be compared to the X-ray technique in section 7.7). It is interesting to note that the directions shown in that figure and in figures 7.18a,b,c, 7.19a,b, are almost identical, implying that the principal compressive strain axes do not show any appreciable rotation for load increments after stage P/P_f = 0.50.

Perhaps the most striking feature of the principal strain directions is the distinct similarity (if not identity) of the patterns obtained from the three tests so far presented. The directions of the principal compressive strain throughout the deforming sand mass seem to remain invariant with the imposed boundary conditions (compare figs 7.3, 7.11, 7.18, 7.19) for load increments after stage $P/P_f \simeq 0.45$, which may be considered as the upper working load level. It is unfortunate that information from earlier stages is not available. However, considering the various strain fields presented, it may be argued that the developed strains at stage say 0.25 of the failure load will be generally very small (high strains mainly concentrated around the footing edges), with the errors in their measurement approaching the magnitude of the strains. Hence, it would not be surprising if the apparent patterns detected proved to be highly irregular showing considerable scatter. It should be remembered here that in all these tests (that is D, A and B) the vertical load was dominant.

The maximum shear strains obtained at stages 0.70 and 0.86 of the failure load are shown in figs 7.20a and b, where the continuous lines are contours of equal strain. It should be noted here that the relatively high shear strains observed immediately underneath the footing are suspect and are probably in error due to imprecise measurements of the

corresponding lead shot coordinates as pointed out earlier in this section. However, concentration of high shear strains near both footing edges is as expected, since it is there that the sand starts yielding. As may be seen, the shear strains develop at both edges A and B of the footing; then begin to spread downwards, from A along a radius at an angle of about 40^{o} to the vertical and from B along a radius at an angle of approximately 30^{o} to the vertical. It is of interest to note that this pattern (four bulbs of shear strain) is basically similar to that developed in the sand mass under a footing loaded with a vertical central load (test D, see figs 7.5a and d), but now expanding along a direction inclined at an angle to the vertical.

The volumetric strains at stages corresponding to P/P_f values of 0.70 and 0.86 are shown in figs 7.21a and b; contours of equal volumetric strain are also drawn. Again attention is drawn to the fact that the relatively high contraction rate of the sand mass observed at areas immediately underneath the footing is rather exaggerated because of errors in measurement. However, despite some scatter, it is evident that the observed pattern is like that of the maximum shear strains (figs 7.20a and b) which suggests that volumetric and maximum shear strains may be interrelated uniquely. This will be discussed in detail in the next section.

The directions of the zero extension lines calculated from the total strain fields at stages $P/P_f = 0.70$ and 0.86 are shown in figs 7.22a and b. As may be seen from the angle of intersection of these directions the sand contracts in areas underneath the footing base and away from the edges, while it dilates at approximately constant rate in other relatively highly strained areas. The α-zero extension lines starting near the left edge of the footing are inclined to the vertical at an angle of approximately 40^{o}. It will be shown in a later section that the failure surface at the same position makes a similar angle to the vertical which suggests that the failure surfaces lie along lines of zero-extension. A detailed discussion of this observation will be presented in section 7.6,together with information about the various characteristics of the failure patterns obtained from the various tests.

7.5 The relationship between volumetric strain and maximum shear strain in dense sand

It was pointed out in the previous section that the angle of intersection of the α and β-zero extension line directions remains practically constant throughout the deforming zones in all the tests so far presented. Furthermore, the patterns of both the volumetric and the maximum shear strain were shown to be similar. These preliminary observations imply that there may be a unique relationship between these two strain parameters. Similar observations were made by other research workers on various earth pressure problems using the same Leighton-Buzzard sand (James(1965), Bransby (1968) and Lord (1969) on model retaining walls and Tennekoon (1970) on model strip footings under vertical symmetric load). It was, therefore, thought that it would be interesting to investigate the above indications in the light of the strain data from tests D (e_o = 0.52, α_o = 0, E_o = 0), B (e_o = 0.52, α_o = 12°, E_o = 0), A (e_o = 0.52, α_o = 0, E_o = 0.167) and C (e_o = 0.52, α_o = 12°, E_o = -0.167).

The procedure adopted was suggested by James (1965) and consisted of calculating the mean value of the volumetric strain from all triangles of the lead shot network which lay within a small interval of maximum shear strain (say 0.01) and then plotting the mean volumetric-maximum shear strain curve for all triangles in the mesh. While the fixed maximum shear strain interval used in most cases was 0.01, it was increased to 0.02 or even to 0.03 when the number of triangles with 0.01 interval was too small (less than 10) to give statistically significant results. Furthermore, since the strain data from these tests were not stored in the computer, it was reckoned that it would be quicker to perform the calculation with a pocket calculator. The choice of larger shear strain increments, therefore, made the whole exercise less tedious but equally reliable.

The mean volumetric-maximum shear strain curves obtained from each of the four tests, are plotted in figures 7.23a to d, while the distribution of the number of readings used in the calculation of each of the above curves are shown in figs 7.24a to d. The standard deviation of the volumetric strains at each fixed maximum shear strain interval is also shown as dashed lines on either side of each curve. It should be noted

that each of the mean curves of figs 7.23 have been calculated from the total strain fields obtained at the end of the last recorded increment before failure occurred.

A common characteristic of the four curves shown in figs 7.23a to d is that they can be well approximated by straight lines, which implies that the sand dilates at a constant rate for a considerable range of shear strain. In fact all curves do not go through the origin, but remain basically straight from shear strains greater than approximately 0.02. The shape of this transition line suggests that as the sand begins shearing (i.e. as maximum shear strain γ_m increases from zero), the dilatation rate increases rapidly from zero to attain its peak value at a γ_m value of about 0.02.

The individual data points have been replotted in fig. 7.25 and the mean curve has been drawn. This mean curve may be expressed by a straight line with correlation coefficient 0.986. The slope of this curve is $|0.3600|$ which corresponds to a constant angle of dilatation of $\nu = 21.1^{o}$. Similar volumetric-shear strain relationships obtained by James (1965) Bransby (1968) and Tennekoon (1970) have been also drawn in the same figure. The excellent agreement between their relationships and that obtained by the author is quite remarkable,despite the considerable difference of the boundary conditions in the earth pressure problems investigated by each of them. Furthermore, the stress levels attained were distinctly different: James (1965) measured maximum stresses of 150 KN/m^2 (23 psi) on a retaining wall when rotated about its toe; Tennekoon measured maximum stresses of 800 KN/m^2 (120 psi) underneath a strip footing under vertical central load which are very similar to those measured by the author. However, as already shown in chapter 6, the maximum stresses attained during each test performed by the author depended upon the initial boundary conditions, so that, for example, the maximum recorded stress during test A (e_o = 0.52, α_o = 0, E_o = 0.167) was 550 KN/m^2 (80 psi).

The results from four tests with dense sand samples (e_o = 0.53) in the SSA (Stroud, 1971) are also drawn in fig. 7.25. It is evident that the rate of dilatation is dependent on the stress level and decreases with increasing stress level. Similar findings were reported by Cole (1967). This would seem to contradict the observed agreement between the volumetric-shear strain relationships obtained from different

earth pressure problems with distinctly different measured maximum stresses. However, as pointed out by Tennekoon (1970), high stresses occur only in small areas neighbouring the footing, and the stresses in the greatest part of the sand mass (which was used for the $\Delta-\gamma_m$ calculation) will not differ from those in the problem investigated by Bransby (1968), for instance, by as much as 400 KN/m^2.

Even though only strains within the sand mass were calculated from the lead shot displacement fields (no stresses were measured within the sand mass) the similar dilatation rates measured at the SSA and the FAC suggest that the stress-strain relationship followed by the sand in both apparatuses is similar. Both Cole (1967) and Stroud (1970) found that the Stress Dilatancy theory suggested by Rowe (1962) gave the best agreement with the experimental results from the SSA. This flow rule was used here to predict the stress ratio t/s from the calculated $\Delta - \gamma_m$ relationship, and can be expressed as:

$$R = D\,K \qquad (7.1)$$

where $R = \sigma_1/\sigma_3$ is the principal stress ratio, $D = \dot{\varepsilon}_3/\dot{\varepsilon}_1$ is the dilatancy factor, and $K = \tan^2(45 + {}^{\phi}f/2)$. For plane strain ϕ_f is taken equal to the angle of internal friction $\phi_{c.v.}$ when the sand has reached the critical state and deformation continues under constant volume; for Leighton-Buzzard sand in the SSA, $\phi_{c.v.} = 35^o$ (Stroud (1971)).

For plane strain conditions, Rowe's flow rule may be expressed as:

$$\frac{t}{s} = \frac{KD^* - 1}{KD^* + 1} \qquad (7.2)$$

where $t/s = \sin\phi$, $D^* = \frac{1 + \sin\ \nu}{1 - \sin\ \nu}$ and $\sin\nu = \frac{-\dot{\Delta}}{\dot{\gamma}_m}$

(the dot above each strain parameter indicates a small increment). For $\phi_{c.v.} = \phi_f = 35^o$, K = 3.68. From the observed dilatation rate $\sin\nu = 0.36008$, $D^* = 2.1254$ and, therefore, from equation (7.2) $\sin\phi = t/s = 0.7733$ or $\phi = 50.6^o$. This value of the angle of internal friction agrees remarkably well with the adopted mean value of 50^o (see chapter 6). In fact, this could be expected from the reported good agreement between this flow rule and the experimental results from the SSA from which the angle of internal friction was extrapolated (see chapter 6).

7.6 Failure surfaces in the sand mass

7.6.1 Introduction

One of the major attractions of the X-rays technique is that failure surfaces in dense sand are visible on the radiograph as dark bands; the sand apparently dilates along these surfaces and, by becoming looser than the rest of the soil mass, the radiograph gets overexposed around those areas. Nevertheless, the rupture surfaces may equally well be detected by the Stereophotogrammetric technique, as was shown by Butterfield et al (1970) and Andrawes (1970) (see chapter 5): A pair of photographs, one taken before and the other after failure has occurred, when viewed stereoscopically (e.g. through a mirror stereoscope), will yield an optical model where the failure surface will be seen as a very steep hill-slope. This 'cliff' can be easily traced , therefore, information about its shape, relative depth and length may be obtained equally accurately. Both techniques were used to record the failure surfaces developed and the major features of which will be presented herein.

7.6.2 Failure surfaces under vertically centrally loaded footings

It was mentioned in chapter 6 that, in test D (e_o = 0.52, α_o = 0, E_o = 0) the footing was not loaded to failure during the first loading, but only after it was retracted and then replaced on the sand surface. Even though the peak load attained was similar to that obtained during a similar test (test H) in almost identical initial sand density (e_o = 0.525) performed by Tennekoon (1970), the failure surface developed in the former was considerably different from that in the latter, as may be seen in figs 7.26 and 7.27. The failure surface formed in test D is shown in fig. 7.26 (the small white spots are the images of the lead shot), while fig. 7.27 is reproduced from fig. 5.29 (Tennekoon, 1970). Perhaps the most striking difference is the relatively shallow position of the rupture surface of test D (≈ 1.3 B) and the short length of its outcrop (≈ 2.4 B) measured from the nearest edge of the footing, compared with those observed by Tennekoon (1.9B to 2.4B and 5.5B to 6.5B respectively). As may be seen in fig. 7.26, a second failure surface had begun to form which is much deeper (≈ 2.4B) (and, therefore, would have been longer) and it is very likely that this would have been developed first instead of the former, provided that the footing was restrained from both

rotating and displacing horizontally. An ill defined dilated zone may be seen underneath the 'right' edge of the footing which, together with the initial part of the developed failure surface form a soil 'wedge', the inclination of the side of the wedge to the footing base (the latter assumed horizontal) being approximately 60^{o}. (This will be further discussed later in this section).

The failure surface formed in the sand mass by a 50.8 mm (2 in) wide footing loaded vertically and at the centre of its base is shown in fig. 7.28. (It should be mentioned here that the white rectangular blocks separated by straight dark lines, which may be seen in all photographs from radiographs, are the images of the load cells of the footing). This figure shows the part of the failure surface that was obtained from the 'centre' radiograph (see chapters 3 and 5); the remaining section of the rupture surface together with its outcrop, were recorded on the 'right' radiograph (not shown here). As can be seen from fig. 7.28, a single failure surface was formed towards one side of the footing, while a second one, probably symmetric to the former, had begun to develop, but was not fully formed. The sand mass has dilated along the main failure surface much more than along the second one (compare the wide dark band defining the former with the less well-defined one defining the latter), which indicates that sliding took place along the former.

The formation of two failure surfaces, one to each side of the footing (fig. 7.27) was considered highly improbable, if not impossible, during tests under vertical symmetric load performed by the author, because 'perfect' symmetry in the sand mass deformation is more of an assumption rather than a reality. Thus the development of slightly larger shear strains on one side of the footing (as was the case with test D, for example) will result in a single failure surface forming initially to that side, along which the footing will move. Subsequent failure surfaces on the other side will not be formed, unless the footing is forced to displace vertically only and is restricted from rotating, as was the case with test H by Tennekoon (1970). Similar findings were reported by Andrawes (1970) from the penetration of a rigid wedge in dense sand.

The length of the rupture surface outcrop was approximately 5B (measured from the nearest edge of the footing) while its deepest position was measured to be at 1.2B. The former compares well with that

obtained by Tennekoon (5.5 to 6.5B for 76.2 mm wide footing) and suggests that a similar surface would have been expected to be formed in test D as well. Therefore, the formation of a relatively short and shallow failure surface during test D (e_o = 0.52, α_o = 0, E_o = 0) is very likely to have been initiated by the disturbance of the sand mass at the contact area between the first and the second load cycle (see chapter 6.2.1).

It has been shown experimentally (James (1965), Roscoe (1970)), that failure surfaces (which are zones where velocity discontinuity occurs) lie along lines of zero extension. This would imply that the outcrop would intersect the unloaded horizontal sand surface at an angle 45 - $\nu/2$, since the principal compressive strain direction is approximately horizontal at the sand surface (see, for example, fig. 7.3d). The corresponding angle measured from both tests D and that with 50.8 mm wide footing was approximately 35°. The angle of internal friction was taken as 50° (see chapter 6.2) while the angle of dilatancy was calculated 21.1° (see section 7.5). Therefore the measured angles compare favourably with the assumed 34.5°, which suggests that the above hypothesis may be valid.

Fig. 7.28 shows a well-defined 'wedge' being formed underneath the footing and it is interesting to note that its 'right' side is inclined at 54° to the footing base (the latter assumed horizontal), while its 'left' side is inclined at 72°. Such a non-symmetry has been probably caused by the footing which, as well as displacing vertically, both rotated and displaced horizontally after failure. Nevertheless, the fact that the failure surface makes an angle 36° to the vertical immediately underneath the footing, together with the experimental evidence that the principal compressive strain directions are almost vertical at that area (see fig. 7.3d), comes as a further support to the hypothesis stated above.

Finally it should be noticed that the main failure surfaces formed in both these tests did not start from the very edge of the footing but at approximately 0.15B from it. A similar observation was reported by Tennekoon (1970).

7.6.3 Failure surfaces under centrally inclined loading footings

The failure surfaces formed in tests B (e_o = 0.52, α_o = 30°, E_o = 0) are shown in figs 7.29, 7.30 and 7.31 respectively. All of them were developed on the same side of the footing towards which the load was

inclined and the footing remained practically horizontal even after failure in both tests B ($\alpha_o = 12^o$) and GB ($\alpha_o = 20^o$). In fact this behaviour was exhibited throughout each of these three tests (see chapter 6.3.3) and the small rotation of the footing after failure during test E ($\alpha_o = 30^o$) was probably due to the influence of the weight of the jack in relation to the relatively low failure load.

As may be seen from figs 7.29 to 7.31, the failure surfaces become shorter and shallower with increasing load inclination. The failure load was also found to decrease with higher load inclinations, as was indicated in chapter 6.

It is of interest to note that a 'wedge', similar to that of fig. 7.28, is formed underneath the footing in all three tests, but with its apex displaced towards the same side as the load inclination. The greater the angle of the applied load to the vertical the further the 'wedge' apex is displaced, the apex angle remaining practically constant ($\approx 50^o$) (In test E ($\alpha_o = 30^o$), fig. 7.31, the 'right' side of the 'wedge' is not very clearly defined probably because the main failure surface is very shallow). Similar findings were reported by Zacharescu (1961a), who used time exposure photographs taken from a camera solidly fixed to the model footing.

The appearance of this 'wedge' underneath the footing indicates that, during failure, the enveloped soil moves essentially as a rigid body together with the footing. However, as may be seen from figs 7.32a and b, where the incremental displacement and strain fields obtained from the last increment of test B ($\alpha_o = 12^o$) (increment from $P/P_f = 0.86$ to failure) are shown, the sand mass within the wedge did deform, but relatively little in comparison to the large strains occurring along the failure zones. Therefore it is rather evident that the soil within the wedge does not remain entirely 'rigid' during failure, as assumed in the conventional bearing capacity theories (e.g. Terzaghi, 1943).

The average angle the 'left' side of the wedge makes with the vertical is 40^o for test B ($\alpha_o = 12^o$), 56^o for test GB ($\alpha_o = 20^o$) and 70^o for test E ($\alpha_o = 30^o$). These angles are very similar to the inclinations to the vertical of the incremental displacement vectors of the footing itself obtained from each of the above tests. Such a similarity implies that the incremental displacement vector, the direction of which remained practically constant almost throughout the loading sequence (see chapter 6), did not rotate significantly during failure. This will be discussed

in greater detail in chapter 8.

Another interesting point observed from fig. 7.29 is that, together with the formation of the main failure surface, secondary ones were also formed. These either spread from the main rupture surface or start developing from the footing base, and they seem to have dilated less than the main failure surface. Similar findings were reported by James (1965), Tennekoon (1970) and Andrawes (1970). It is also worth noticing (see figs 7.29 to 7.31 inclusive) that the main failure surfaces do not start from the footing edge, but approximately 0.15B from it, and that they are slightly curved (downwards concavity) near these areas. Similar observations were also made by Zaharescu (1961a).

It should be mentioned here, that a valve located between the pressure vessel and the jack (VAL 3, fig. 3.4) made it possible to control the movement of the footing even after failure, so that at least one radiograph could be taken before the lead shot grid was excessively distorted. This made it possible to obtain information about the behaviour of the sand mass during failure.

The zero extension line directions obtained from the last increment of test B ($\alpha_o = 12^o$) (from P/P_f value of 0.86 to just after peak load was attained) are superposed on the failure surface of the same test, shown in fig. 7.29. It can be seen that there is good agreement between the α-zero extension lines and the rupture surfaces, which seems to confirm experimentally the concept suggested by Hansen (1958). A similar agreement is also observed from the comparison of the failure surfaces shown in fig. 7.29 with the zero extension line directions calculated from the total strain fields at stages 0.70 and 0.86 of the same test and shown in figs 7.22a and b respectively.

The angle the rupture surface outcrop makes with the horizontal in test B ($\alpha_o = 12^o$) is 32^o approximately while similar values were measured for both tests GB($\alpha_o = 20^o$) and E ($\alpha_o = 30^o$) (33^oapproximately). This is similar to the angle the α-zero extension line directions make with the horizontal (with $\nu = 21.1^o$, see section 7.5), since the principal compressive strain directions were found to be practically horizontal at the sand surface. Thus the data tend to confirm the experimental finding of James (1965) (which has, also, been confirmed by Bransby (1968), and Tennekoon (1970)), that the rupture surfaces coincide with the directions of zero extension.

The failure surfaces obtained from large field tests performed by Muhs and Weiss (1973) are shown in figs 7.33a to c. The 1.0 × 3.0 m concrete footing embedded at 0.2 m, was loaded by an inclined load along the short side at 10^{o}, 20^{o} and 30^{o} (for details see chapter 1.2 and 1.4). As may be seen, there are some interesting similarities between the failure surfaces from tests performed at the FAC (figs 7.29 to 7.31) and those from large field tests (fig. 7.33): Their size decreases with increasing load inclination, while the angle of the rupture surface outcrop remains practically constant ($\simeq 30^{o}$) for all load inclination (figs 7.33a to c). (The angle of internal friction of the fill was reported as 39^{o}). In addition, the failure surfaces immediately underneath the footing are inclined at about 40^{o}, 68^{o} and 74^{o} to the vertical (for load inclinations 10^{o}, 20^{o} and 30^{o} respectively). The 'wedge' observed observed during tests in the FAC was not visible in the large scale tests. A number of secondary failure surfaces may be seen to have developed from the main one, (fig. 7.33) especially in the case of a 10^{o} load inclination, which bears a striking similarity to the failure pattern shown in fig. 7.29. Another interesting point is the relative depth and length (measured from the nearest edge of the footing) of the rupture surface outcrop. For the large scale field tests the corresponding values were approximately 1.5B and 4B (10^{o} load inclination), 0.8B and 2.2B (20^{o} load inclination) and 0.6B and 1.5B (30^{o} load inclination). These can be compared with those observed from tests in the FAC: 1.3B and 3.5B ($\alpha_o = 12^{o}$), 0.9B and 2.8B ($\alpha_o = 20^{o}$), and 0.5B and 1.6B ($\alpha_o = 30^{o}$). This rather close agreement would seem to suggest that the narrow tank width in the model tests in the FAC did not affect the formation of the failure surface to any great extent. This will be further discussed in a later section, after the presentation of the experimental results from the FAS.

7.6.4 Failure surfaces under eccentrically vertical loaded footings

The failure surfaces formed in tests A ($e_o = 0.52$, $\alpha_o = 0$, $E_o = 0.167$) and H ($e_o = 0.52$, $\alpha_o = 0$, $E_o = 0.167$) are shown in figs 7.34 and 7.35 respectively. Test H was, in fact, a repeat of test A, the main aim being to establish the repeatability of test results in the FAC. As has been already shown in chapter 6, the various measurements performed on the footing (ultimate load, load-displacement and moment-rotation relationships, contact stress distribution) were almost identical, and

the same seems to apply to the corresponding failure surfaces.

As may be seen from both figs 7.34 and 7.35, a very small 'wedge' has been formed near the 'left' wedge of the footing and the main failure surface has been developed towards the same side as the load eccentricity. The part of the footing width defined by the 'wedge' is half of the 'effective' width, the fictitious width where the applied load acts vertically and at its centre (see chapter 1) (here B' = 101.6 mm with respect to initial loading conditions). As already discussed in chapter 6, the eccentricity of the load increased with increasing load due to the continuous rotation of the footing and, therefore, the 'effective' width at failure became narrower, even though both the load cell readings and the footing rotation at a stage $P/P_f = 0.92$ of test ($e_o = 0.52$, $\alpha_o = 0$, $E_o = 0.167$) indicated that the 'effective' width was larger than that implied by the 'wedge' of fig. 7.34. However, the conditions at failure, ($P/P_f = 0.99$ say) were not recorded, and there is a possibility that during the last stages the footing rotated substantially before peak load was attained.

Secondary failure surfaces were observed in both tests A and H (see figs 7.34 and 7.35) which were mainly formed along the same direction as the main rupture surface. (It should be noted here that the horizontal 'white' strip at the top of all photographs from X-rays, which reaches the footing base, has been caused by the wedge shaped copper plate, see chapter 5). Another failure surface, which begun to form towards the opposite side to the load eccentricity and at an angle to the vertical of about 35^o, was not completely developed probably due to kinematic requirements. The formation of successive failure surfaces due to an eccentric vertical load has been also reported by Eastwood (1955), Dhillon (1958, 1961), Lee (1961) and Krivorotov (1965).

Fig. 7.36 shows diagrammatically the failure surface formed in test FA ($e_o = 0.52$, $\alpha_o = 0$, $E_o = 0.167$), where the footing was restrained from displacing horizontally. It is an intriguing fact that the imposed kinematic constrained resulted in the formation of a longer (5.3B total length) and deeper (2B) rupture surface than the ones obtained in tests A and H (1.7B and 0.6B respectively) and on the opposite side from the load eccentricity. The interesting point is that the initial part of the rupture surface (near the 'left' side of the footing) is inclined at about 34^o to the vertical, which is very similar to the angle formed

by the partially developed secondary failure surface in both tests A and H (see figs 7.34 and 7.35). Such a similarity implies that this failure surface would have been fully formed had the footing been restrained from displacing horizontally.

The zero extension line directions, obtained from the incremental strain field between the stages $P/P_f = 0.0$ and just after failure load was attained during test A ($E_o = 0.167$), are superposed on the failure surfaces of fig. 7.34. There is a rather good agreement between the directions of the failure surfaces and the zero extension line directions which supports a similar observation made in fig. 7.29. Furthermore the failure surface outcrop of test FA (fig. 7.36) is inclined to the horizontal at about 34^o, while these of tests A and H are inclined at about 36^o and 30^o respectively.

7.6.5 Failure surfaces underneath footings loaded by eccentric-inclined loads

The failure surfaces formed in tests F ($e_o = 0.52$, $\alpha_o = 0$, $E_o = 0$, independent load acting at 100 mm from the footing base) and C ($e_o = 0.52$, $\alpha_o = 12^o$, $E_o = -0.167$) are shown in figs 7.37 and 7.38 (a and b) respectively. The former case corresponds to the 'positive' eccentricity sense of the vertical load, whilst the latter to the 'negative' sense (see fig. 7.38c).

One major feature of these failure surfaces is that they are always formed in the horizontal load direction, (as for an inclined central load, see, for example fig. 7.29) despite the 'opposite' action of the applied moment in test C (fig. 7.38). In fact, as was indicated by the preliminary investigation (see chapter 2.3.3), in cases of 'negative' eccentricity (see fig. 7.38c) failure occurs towards the load eccentricity when the inclination of the applied load is small (of the order of 5^o or less). The formation of such a rupture surface was not observed in either of the tests with 'negative' eccentricity test C ($e_o = 0.52$, $\alpha_o = 12^o$, $E_o = -0.167$) and test K ($e_o = 0.52$, $E_o = -0.167$, independent horizontal load acting along the footing base and in the opposite direction to the eccentricity of the vertical load). However, it may be seen from the maximum shear strain field obtained in test K and at a stage where $V = 0.7\ V_{max}$ (where V_{max} is the failure load in test A) and $H/H_F = 0.53$ (V and H are the current vertical and horizontal loads respectively and the subscript 'F' indicates conditions at failure) shown in fig.

7.39a, that the pattern is very similar to that developed during test A (e_o = 0.52, α_o = 0, E_o = 0.167) shown in fig. 7.12b. Therefore, if the horizontal load was kept constant and the vertical load increased, the failure surface would have been formed on the same side as the eccentricity of the load.

It may be noticed that while the whole footing width was'effective' at failure in test C (figs 7.38a and b), the failure surfaces of fig. 7.37 indicate that only part of the footing base was in contact at failure in test F, which could account for the lower bearing capacity obtained.

The zero extension line directions obtained from the incremental strain fields between an increment from P/P_f = 0.96 to 1.0 and a second one just after failure are shown in figs 7.38a and b, where they are superposed to the observed failure surface. As may be seen,there is good agreement between the α-zero extension lines and the failure surfaces (fig. 7.38b). However, the directions of the zero extension lines indicated that another failure surface was to be developed (fig. 7.38a), which would be deeper than the one formed as may be seen from the dotted line drawn. In fact, this rupture surface started to spread (see fig. 7.38a, continuous line and 7.38b) but was not eventually formed. The failure surface outcrop in tests F and C was inclined to the horizontal at 34^o and 37^o respectively. This can be compared with the 34.5^o angle the α-zero extension lines make with the horizontal at the sand surface (for a constant $\nu = 21.1^o$, see section 7.5), where the principal compressive strain increment directions (obtained from the increment P/P_f = 0.96 to 1.0 in test C) are approximately horizontal, as may be seen in fig. 7.39b.

7.6.6 The shape of the failure surface outcrops

A typical shape of the failure surface outcrop formed during testing in the FAC is shown in fig. 7.45. The small curvature near the tank sides was due to the glass friction, and this shape was consistently observed throughout the Part II experimental series. In section 7.8, the shape of the rupture surface outcrops obtained from tests in the FAS will be presented and the effect of the tank width on its shape discussed in more detail.

7.7 Comparison of results from the X-ray and the Stereophotogrammetric Techniques

As was mentioned in the beginning of this chapter, one of the objectives of the project was to investigate the effect of the glass sides on the measurement of displacements by employing both the X-ray and the Stereophotogrammetric techniques to record the movements of the soil mass within identical increments in the same test. Even though both X-rays and photographs were used almost throughout the Part II experimental series performed in the F.A.C., the results from test D (e_o = 0.52, α_o = 0, E_o = 0) will be mainly utilized, because the footing under vertical central load affected much larger soil areas than in any other test performed by the author (as shown in the previous sections).

The x and y total displacement fields obtained at the end of stage 0.74 of the peak load in test D (e_o = 0.52, α_o = 0, E_o = 0), using the X-ray technique, are shown in figs 7.41a and b respectively, while those obtained by using the Stereophotogrammetric technique (at the same stage of the same test) are shown in figs 7.41c and d respectively. Contours of equal x and y displacement in intervals of 100 μm (0.1 mm) are also drawn. A visual examination of the x-displacement fields (figs 7.41a and c) shows, in the first instance, that the displacements obtained by the X-rays technique (hereafter referred to as XRT) are slightly higher than those obtained by the Stereophotogrammetric technique (hereafter abbreviated as SP). The maximum difference seems to be of the order of 100 to 200 μm, but the patterns are almost identical.

Let us now consider the y-displacement fields, shown in figs 7.41b and d. An immediate observation is the considerable difference noticed underneath the footing and within approximately 0.4B downwards from its base. (It should be mentioned here that, due to the footing penetration, measurements on the photographs started at approximately 10 mm from the sand surface). The vertical displacement (recorded by the dial gauge system) of the centre of the footing base at that stage was 4.93 mm which agrees with the results from the XRT but the measurements by the SP underneath the footing base are seen to be 17% lower than the actual ones. In fact, the relative movement of the footing at that stage was found to be identical to that recorded by the dial gauges. Therefore it is almost certain that the apparent errors in measurement of these

areas were due to the relatively big parallaxes, which the human eye cannot easily accommodate. Nevertheless, the agreement between the two measured y-displacement fields in all other areas is remarkable, and it is rather difficult to find out by simple visual inspection their average difference.

To enable a quantitative comparison to be performed, cross-sections of the displacement fields obtained from both techniques at identical positions of the 'topography' shown in figs 7.41a to d were measured and the results are plotted in figs 7.42 and 7.43 for the x and y displacements respectively (each contour is 100 μm). Considering the x-displacements first (shown in figs 7.42a to c) it may be said that, in the first instance, there is a good agreement between the results from the two techniques and that, in some cases, the two curves literally coincide (see, for example, figs 7.42a and c). A closer examination indicates that there is an average absolute difference of about 100 μm, which approaches 200 μm in areas of relatively high x-displacements. However, if the error in measurements is taken into account, the average difference of the x-displacements measured by XRT and SP amounts to ± 50 μm approximately, which is about ±2%.

Similar remarks may be made about the y-displacement results, shown in figs 7.43a,b: The agreement between the two curves obtained from the 45^{o} to the horizontal cross-sections is remarkable and the average difference is again seen to be ± 50 μm. However, there appear to be some major deviations along the vertical cross-section through the footing base centre and especially in areas neighbouring the footing itself. The observed difference is almost constant 200 μm for areas between 0.4B and B from the base of the footing whereas it becomes approximately 800 μm immediately underneath it. The latter discrepancy has been discussed earlier in this section and the relatively big parallaxes were considered to be the reason for the inaccurate measurements. Some excessive parallax was expected from the deliberate operation at the maximum in order to minimise measuring time even though there is a well understood limitation on the parallax which human eyes can accommodate. The 200 μm difference observed at a greater depth (up to about B below the footing) is likely to have been due to the same cause. This is further supported by the fact that for all other areas (up to about 4B from the footing

base, where the last measurements were made) the maximum difference is 100 μm approximately, which agrees with the rest of the results presented in figs 7.42 and 7.43. Therefore, it may be argued that, in all probability, the difference between displacements measured within the sand mass (X-rays) and on the glass-sand interface (Stereophotogrammetry) does not exceed about ± 2%. Another interesting observation is that the slopes of the two curves are almost the same in figs 7.42 and 7.43 throughout, which indicates that the calculated strains from both techniques should be virtually identical. The strain fields obtained by the XRT and the SP are shown in figs 7.44a and b respectively, and appear to confirm the above indication.

Arthur and Roscoe (1965) compared the strains calculated from the displacement fields observed by radiography on the centreline of a sand sample with those calculated from the displacement fields observed by photography at the glass-sand interface in passive earth pressure tests. A network of nylon hemispheres, similar to the lead shot one placed within the sample, was positioned with the flat surfaces against the glass sides of the tank. They demonstrated, with the help of the maximum shear strain contours and the directions of the major principal compressive strains, that the strain patterns were almost the same, and they concluded that the glass side friction did not influence the determination of the strain fields of the surface to any great extent. However, they did not establish any quantitative difference between the two measured fields. These findings are in general agreement with the results presented in figs 7.44a to d. Fig. 7.44c shows the major compressive principal strain directions obtained by the SP at stage 0.74 of the peak load in test D, which compare favourably to those obtained by the XRT shown in fig. 7.44d. The author, however, is of the opinion that a proper comparison may be performed by adopting the method used for comparing the displacement fields. It should be remembered that, after all, strains are displacement gradients and, furthermore, it is the displacements that are measured and not the strains.

In order to use the method outlined in the beginning of this section to compare strain fields, the maximum shear strain contours should be accurately drawn which is a rather difficult task in view of the output provided by the computer program used so far (see, for example, fig. 7.44). Furthermore, this program is based upon measurements made at discrete

points, which form an equally spaced network. Recently, Harkness and Lock (1977) developed a new method of analysing data from measurements made by the Stereophotogrammetric technique. In fact, the main advantage of the SP is the ability to make measurements at actual grain size intervals in areas of high displacement gradient and this may be fully utilized with this analysis. Basically, splines are fitted through the data points (parallaxes) and two surfaces are defined from the corresponding measurements (parallaxes), one for the x and one for the y displacements, and the strain parameters at any point are calculated from the directional gradients of these surfaces. Consequently, cumulative results may be obtained from the incremental information provided by the measurement of pairs of photographs.

Perhaps the most important feature of the above method is the output format of the results, as may be seen in figs 7.45, 7.46 and 7.47, where the x and y displacement fields obtained from the increment $P/P_f = 0.74$ to 0.93 in test D ($e_o = 0.52$, $\alpha_o = 0$, $E_o = 0$) are shown. The displacement fields shown in figs 7.45 and 7.46 were obtained by the SP and that shown in fig. 7.47 by the XRT. Each contour consists of dots printed at very close spacing, so that they form a continuous line, and the red coloured ones are of opposite sign to the brown ones (red and black superposed), the black ones used for easier definition. The program is still under development so that shear strain and volumetric strain contours will be plotted in a similar fashion to the displacement fields. From such plots the produced shear strain fields could be compared along identical cross-sections of the exhibited 'topography'.

To round off, it may be argued that the difference in displacements between the XRT and the SP is very small and that *each* technique has its own merits. However both are dependent upon the operator which makes them equally reliable, and, at the same time, equally vulnerable, although professional photogrammetry technicians can contribute an expertise not necessarily available in the student. It should be noted here that the accuracy of the measurements by the SP shows to advantage when the parallaxes are relatively small. This is clearly demonstrated by the incremental y-displacement fields obtained from an increment $P/P_f = 0.59$ to 0.74 in test D ($e_o = 0.52$, $\alpha_o = 0$, $E_o = 0$) shown in figs 7.48a and b (results from XRT and SP respectively). Nevertheless, measuring displacement fields on a sand surface, is like measuring the topography of a

granular 'desert' and that monotonous view may result in erroneous readings. Similar remarks apply to the measurement of the lead shot coordinates from the radiograph. Therefore, the accuracies referred to in chapter 5 are the optimum ones, the actual errors being usually twice as high.

7.8 Displacement and strain fields from tests in the FAS

The movement of the soil mass during all five tests in the FAS were recorded by photographs. However, due to time restrictions, the displacements from only three increments of test DS (e_o = 0.53, α_o = 0, E_o = 0) were measured and the corresponding strain fields calculated. Information about cumulative (or total) displacement and strain fields could not be obtained, as explained in chapter 5.3.4.

The incremental displacement field at 0.67 of the peak load in test DS (α_o = 0, E_o = 0) is shown in fig. 7.49a where the computer plotted vectors denote the displacement of the sand mass at the point of measurement. It should be noted here that the measurements were made at approximately 20 mm intervals both horizontally and vertically instead of the preferred 10 mm ones. Despite the wide spacing of the network, the observed general pattern is similar to that shown in figs 7.1a to d obtained from test D (e_o = 0.52, α_o = 0, E_o = 0) performed at the FAC. As may be seen from fig. 7.49a, higher displacements occur underneath the 'right' edge of the footing than underneath the 'left' one , which indicates that the deformation of the sand mass is not symmetric with respect to the vertical through the centre of the footing base. The same displacement pattern was maintained throughout the test, as may be seen from the incremental displacement fields (P/P_f = 0.67 - 0.86, 0.86 - 0.98) shown in figs 7.49b and c.

The incremental maximum principal compressive strain directions obtained from increments corresponding to P/P_f values 0.0 - 0.67, 0.67 - 0.86 and 0.86 - 0.98 are shown in figs 7.50a to c. It may be seen that the principal strain rate axes do not rotate appreciably throughout the test and that the pattern remains invariant with increasing load. This was also shown to be the case with test D (see figs 7.3a to d) and it can be seen that the two patterns (that from test DS and that from test D) compare favourably, as would be expected.

The incremental maximum shear strain fields obtained from the above increments in test DS (e_o = 0.53, α_o = 0, E_o = 0) are shown in figs 7.51a to c. The contours of equal shear strain drawn show a similar pattern to that described in section 7.2 for test D, as anticipated. Since no cumulative information could be produced at that stage, the incremental shear strain fields obtained from similar increments in both tests DS and D (performed in the FAS and FAC respectively) were compared. Such a shear strain field for test D is shown in fig. 7.51d, obtained from a load increment of $P_v/\gamma B$ = 82 (from stage P/P_f = 0.59 to 0.74) which can be compared with that of test DS shown in fig. 7.51b, which was obtained from a similar load increment ($P_v/\gamma B$ = 85, from stage P/P_f = 0.67 to 0.86). As may be seen, slightly higher shear strains are developed underneath the footing in test D (FAC) which may probably be due to the higher actual stress level at the end of that increment (compare $P_v/\gamma B$ = 401 at stage 0.74 for test D, with $P_v/\gamma B$ = 369 at stage 0.86 for test DS). In addition, the use of a "double spaced" grid will naturally smooth the strain field (i.e. remove any small peaks in the distribution) as shown in fig. 7.51b, therefore local high displacement gradients can only be picked up by a much finer mesh size.

A major advantage of the SP against the XRT is the independence of the former from measurements only made at discrete points (markers) so that a much more detailed and accurate information can be obtained within highly strained areas. In fact, measurements at grain size intervals may be performed (Andrawes and Butterfield, 1973, Harkness, 1977).

The incremental volumetric strains of test DS obtained at the end of stage P/P_f = 0.67 are shown in fig. 7.52. Their general pattern is similar to that of the maximum shear strains (fig. 7.51a), which suggests that there may be a unique relationship between $\dot{\Delta}$ and $\dot{\gamma}_M$. The same method, as described in section 7.5, was used again here to investigate this observation and the results are plotted in fig. 7.25 together with the results from tests in the FAC. It may be seen that the mean curve through test DS shows higher dilatation ($\nu \approx 25.9^o$) than the mean curve through all tests from FAC (21.1^o). Nevertheless no firm conclusion may be drawn from this comparison, because the range of maximum shear strain investigated was relatively narrow (there were only 18 readings for the fixed maximum strain interval 0.03 - 0.04).

As may be seen from figs 7.51a to c, the distribution of maximum shear strains is not symmetrical with respect to a vertical axis through

the footing base, but higher shear strains were developed underneath the 'right' edge of the footing. These caused the footing to rotate by 0.82^{o} (at stage $P/P_f = 0.98$ of the peak load) and fail eventually along a single rupture surface, whose average length (from the nearest footing edge to the outcrop) was 4.9B and average depth 1.6B. These could be compared with the corresponding average values of 6B and 2.2B observed at the FAC by Tennekoon (1970) from a test with the same footing width (see section 7.6.2).

The failure surfaces formed during tests DS ($e_o = 0.53$, $\alpha_o = 0$, $E_o = 0$), RS ($e_o = 0.54$, $\alpha_o = 5^{o}$, $E_o = 0$) BS ($e_o = 0.53$, $\alpha_o = 12^{o}$, $E_o = 0$), AS ($e_o = 0.54$, $\alpha_o = 0$, $E_o = 0.167$) and HS ($e_o = 0.53$, $\alpha_o = 0$, $E_o = 0.167$) are shown diagrammatically in figs 7.53 to 7.57 respectively. It may be seen that the failure surface outcrop in all five tests is inclined at about 30^{o} to the horizontal. This average value is a little smaller than the values observed at the failure surfaces from tests with the same sand in the FAC (range from 30^{o} to 37^{o}, average value 34^{o}), although it is unlikely that the small variation in the initial density of the sand sample would cause such difference.

The relative depth (0.6B) and length (1.4B from the nearest footing edge) of the rupture surface formed in test HS ($E_o = 0.167$, FAS) compare favourably with those obtained during tests A and H ($E_o = 0.167$) performed at the FAC (0.6B and 1.4 to 1.7B respectively). However, the failure surface formed in test BS ($e_o = 0.53$, $\alpha_o = 12^{o}$, $E_o = 0$) performed in the FAS was both deeper and longer than the corresponding one formed in test B ($e_o = 0.52$, $\alpha_o = 12^{o}$, $E_o = 0$) performed in the FAC (compare 1.6B and 5B of the former with 1.3B and 3.5B of the latter respectively). This is rather surprising, because the peak load obtained for test BS was 29% smaller than that of test B (see chapter 6.2.3). Furthermore, the rupture surface in test RS ($e_o = 0.54$, $\alpha_o = 5^{o}$, $E_o = 0$) was very similar to that formed in test BS ($e_o = 0.53$, $\alpha_o = 12^{o}$, $E_o = 0$), both performed in the FAS, even though the failure load of the former was 46% higher than that of the latter.

The shape of the failure surface outcrop for the three tests DS ($\alpha_o = 0$, $E_o = 0$), BS ($\alpha_o = 12^{o}$, $E_o = 0$) and RS ($\alpha_o = 5^{o}$, $E_o = 0$) followed the same general pattern shown in fig. 7.58. The glass sides seem to have retarded the sand and to have prevented it from moving the same distance at the sides as in the centre of the tank. A distinct 'dip' at approximately the middle of the tank width may be seen, which was also

observed by Andrawes (1970) during the penetration of a wedge in dense sand (see his plate 5.9c). In fact, Andrawes obtained almost identically shaped slip surface outcrops to that shown in fig. 7.58. This 'dip' in the middle may be related to the lower boundary stresses recorded by the load cells of the centre footing section at failure (see chapter 6.4).

From a number of tests with a rigid wall 102 mm high translating horizontally into a Leighton-Buzzard sand bed and with varying the tank width from 50 mm to 406 mm, Beasley (1970) reported that there was no apparent connection between the rupture surfaces and the width of the tank. Furthermore, from the five different outcrop configurations observed he suggested that the shape of the failure surface did not follow a particular pattern which depended upon the tank width. Contrary to these observations, consistent results from both the FAC and the FAS, with a tank width ratio of approximately 1:3, indicate that the shape of the rupture surface outcrop is influenced by the tank width (see figs 7.40 and 7.58).

7.9 Conclusions and some further implications

The following are the main conclusions of this chapter.

1. The directions of the principal strain rate do not rotate to any great extent during each test for load increments after the stage $P/P_f \approx 0.45$ (i.e. approximately the upper working load level) up to failure. In fact, this was found to hold for early post failure stages as well. Such an observation implies that a non-rotating stress field accompanying the non-rotating strain field for a range of tests, is a plausible expectation, with the principal stress increment axis either coinciding with the principal strain increment axis (material obeying an associated flow rule) or inclined at a constant angle to it (non-associated flow with geometrically expanding yield and plastic potential surfaces).

2. The directions of the principal strain rate were found to be almost identical for the four different cases considered, regardless of the completely different initial boundary conditions. This rather unexpected result was confirmed by the results from tests D ($e_o = 0.52$, $\alpha_o = 0$, $E_o = 0$), A($e_o = 0.52$, $\alpha_o = 0$, $E_o = 0.167$), B ($e_o = 0$, $\alpha_o = 12^o$, $E_o = 0$),

C (e_o = 0.52, α_o = 12°, E_o = -0.167) and DS (e_o = 0.52, α_o = 0, E_o = 0). It should be noted that, in all the cases considered, the vertical load is the dominant one. Nevertheless, it is most remarkable that the principal axes of strain are similarly oriented throughout the sand mass over an appreciable range of load inclinations and eccentricities, as this is again even more convincingly demonstrated in figs 7.59a to d.

3. The strain distribution patterns obtained from tests D (α_o = 0, E_o = 0), and A (α_o = 0, E_o = 0.167) are surprisingly similar to the maximum shear stress distribution obtained from the indentation of a rigid punch and a vertical point load respectively into a semi-infinite elastic medium.

4. The maximum shear strain distribution was not symmetrical with respect to the vertical through the footing base in both tests D (e_o = 0.52, α_o = 0, E_o = 0) and DS (e_o = 0.53, α_o = 0, E_o = 0), and this non-symmetry resulted in the rotation of the footing and, in the case of test DS, in its failure along a single rupture surface towards the side where relatively larger shear strains were developed.

5. The distribution of the volumetric strains for each test in the FAC was similar to that of the maximum shear strains, and a unique empirical relationship was established between these two strain parameters for all the different loading conditions considered. This relationship was almost identical to that obtained by other research workers investigating various earth pressure problems with different boundary conditions from those investigated by the author (James (1965), Bransby (1968), Tennekoon (1970)) and very similar to that obtained from tests in the SSA by Stroud (1970). Such a similarity suggests that the stress-strain relationship followed by the sand in both apparatuses is similar.
The Δ-γ_M relationship for test DS (e_o = 0.53, α_o = 0, E_o = 0) performed in the FAS was also investigated and, despite the narrow range of maximum shear strains considered, it was found to be well approximated as a straight line. However, no firm conclusion could be drawn in this particular case.

6. The angle of dilatancy for dense Leighton-Buzzard sand was found to be approximately constant at $\nu = 21.1^{o}$ for a considerable range of maximum shear strain (i.e. $0.02 < \gamma < 0.15$).

7. The Stress dilatancy flow rule suggested by Rowe (1962) was used with $\nu = 21.1^{o}$ and the calculated angle of internal friction $\phi = 50.6^{o}$ agrees well with the adopted one from tests in the SSA performed by Stroud (1970).

8. The failure surfaces developed in the cases investigated seem to lie along lines of zero extension, as was observed from tests A ($\alpha_o = 0$, $E_o = 0.167$), B ($\alpha_o = 12^{o}$, $E_o = 0$) and C ($\alpha_o = 12^{o}$, $E_o = -0.167$). This was further supported by the evidence that all failure surface outcrops from tests performed at the FAC were inclined to the horizontal at an angle ranging from 30^{o} to 37^{o}, which is similar to 34.5^{o} which the α-zero extension line directions make with the horizontal at the free of load sand surface (for constant $\nu = 21.1^{o}$). The latter is a consequence of the fact that the principal compressive strain directions are horizontal (to a close approximation) near the sand surface away from the footing. However it should be mentioned here that other workers have argued,and quite convincingly so, that failure surfaces lie along stress characteristics (see, for example, Vesic (1973) on footings on sand under vertical central loads, Milligan (1974) and Milligan et al (1976) on retaining walls in sand rotating about an axis within their height).

9. In most cases a 'wedge' was defined by the failure surfaces immediately underneath the footing. The sand within this 'wedge' deformed throughout the loading sequence, but moved approximately as a rigid body together with the footing at failure. The apex of this 'wedge' was displaced towards the same side as the direction of the load increasing with increasing inclination of the applied load, but its apex angle was found to remain approximately constant ($\approx 50^{o}$). The side of the 'wedge' (from where the main failure surface was developed) was found to be inclined at an angle 50^{o} to 55^{o} for tests A and H ($\alpha_o = 0$, $E_o = 0.167$) B ($\alpha_o = 12^{o}$, $E_o = 0$) and the test with the 50 mm wide footing under vertical central load. This is similar to the 55.5^{o} angle the α-zero extension line directions form with the horizontal underneath the footing

(the major principal strain directions were found to be vertical at that area). However this angle decreases with increasing load inclination, as was found to be the case with tests GB ($\alpha_o = 20^o$) and E ($\alpha_o = 30^o$) Therefore, if coincidence of failure surfaces and zero extensions line direction is assumed, then the major compressive principal strain directions will not be vertical underneath the footing for load inclinations higher than 12^o, which supports an earlier suggestion in this section.

10. The failure surfaces under increasing load inclination became both shallower and shorter.

11. Secondary failure surfaces were observed in a number of tests. Some of these branched off the main failure surface while some were developed from the footing base. It was also noticed that the main failure surfaces did not start from the footing edge but at approximately 0.15B from it, whereas the secondary failure surfaces (whenever formed) started from the very edge of the footing. Finally, the failure surfaces obtained from tests with inclined loads were slightly concave with a downwards concavity, immediately underneath the footing.

12. The inclination to the vertical of the displacement vector of the footing for tests with inclined loads was found to be similar to the corresponding angle formed by the failure surfaces underneath the footing base. This observation, combined with the observation (from chapter 6) that the footing remained practically horizontal throughout the test, suggests that the displacement vector of the footing did not rotate singificantly at failure. This important conclusion will be used in the next chapter.

13. The observed failure surfaces obtained from tests in the FAC under inclined central load ($\alpha_o = 12^o$, 20^o, 30^o) showed some striking similarities with rupture surfaces obtained from large scale field tests (Muhs and Weiss, 1973), which suggests that the formation of the failure surfaces was not affected by the narrow tank width to any great extent.

14. It was demonstrated that by restraining the lateral motion (i.e. imposing a kinematic constraint) on a vertical eccentric load test, a

longer and deeper failure surface on the opposite side to the load eccentricity was formed than in the case with no kinematic constraints (tests A and H). In addition, the failure load achieved in the former case was almost double that of the latter (see, also, chapter 6).

15. The maximum shear strain fields obtained from test DS (e_o = 0.53, α_o = 0, E_o = 0) performed in the FAS were found to be similar to these obtained from test D (e_o = 0.52, α_o = 0, E_o = 0) performed in the FAC. Even though more experiments need to be performed, it can be argued already that the displacement fields obtained by either narrow or wide tank (at the sand-glass interface) are similar for the footing and tank geometries used here (B = 76.2 mm, W_{narrow} = 190.5 mm, W_{wide} = 584.0 mm. B/W_n = 0.4, B/W_w = 0.13).

16. The failure surface outcrop shape was found to be influenced to some extent by the relative tank width, and a consistent 'dip' at approximately the middle of the tank width was observed in tests in the FAS (and, also, by Andrawes (1970)).

17. The repeatability of results from the FAC was demonstrated by the comparison of the failure surfaces of tests A and H, performed under almost identical conditions (see, also, chapter 6) and by comparing the strain fields obtained from test D (e_o = 0.52, α_o = 0, E_o = 0) with those obtained from a similar test performed by Tennekoon (1970) (test H, e_o = 0.525, α_o = 0, E_o = 0).

18. The X-rays and the Stereophotogrammetric techniques were compared and it was found out that there was typically a difference of only about ± 2% on the measured displacement fields of identical increments of the same test (test D). Provided that the maximum parallax, which can be accommodated by the human eyes, is not exceeded, then displacement fields can be measured equally accurately by both the SP and the XRT. Nevertheless, areas of high local displacement gradient can only be traced by the SP, since this technique is independent of discrete point measurement, unlike the XRT, where a minimum space between the lead shot is required. Finally, it could be said that (from the author's experience) a profess-

ional photogrammetry technician, with adequate experience and guidance, can produce high quality measurements. However, it should always be born in mind that both the SP and the XRT are largely dependent upon the operator, and, therefore, his experience is of primary importance if high precision measurements are to be made.

CHAPTER 8

AN ANALYTICAL CONTRIBUTION TO THE PROBLEM OF FOOTINGS UNDER INCLINED LOADS

8.1 Introduction

In this chapter an essentially new analytical approach to the footing load-displacement problem will be presented, based upon ideas derived from the theory of plasticity. Although a detailed experimental investigation is needed to verify the general applicability of the proposed analysis, the available data do support it and provide at least a useful practical guide to the behaviour of footings under inclined central loads. It will be shown that a knowledge of the vertical load-vertical displacement relationship for a symmetrical footing, obtained either experimentally or analytically, combined with an assumed value of the angle of base friction for the footing can be used to assess the load-displacement behaviour of the footing under loads at any inclination. The main experimental evidence, which is incorporated in this approach is the constancy of the direction of the incremental displacement vector for the footing virtually throughout any test when the latter is loaded by an inclined central load (see chapters 2, 6 and 7). It was suggested in chapter 2 that the failure envelopes of a rough strip footing on sand under inclined central loads could be interpreted in precisely the same way as the conventional interaction diagram of a fixed-foot steel portal frame loaded by vertical and horizontal loads. The consequence of these observations will now be discussed together with the notion of a possible plastic potential relevant to the footing system. We first present a brief review of some important features of the theory of plasticity, which will be used in the analysis.

8.2 Some general features of plasticity theory

When a material is subjected to stresses, the resulting deformation may usually be divided into a recoverable component (elastic) and an irrecoverable one (plastic). Initially, as stresses are increased, the deformation of any system is frequently elastic and the material may

even obey Hooke's linear law. At some loading stage, the deformation becomes not entirely recoverable and some plastic strains develop. This takes place when the applied stresses reach a "yield" point. The condition which characterizes such a transition in a material under a complex stress state is called the yield criterion and the system is then in a "yield state" (Kachanov, 1971). The yield criterion may be represented in a stress space by a yield surface. For stresses within the yield surface, the material is in an elastic state and the resulting strains are reversible. If the material is perf ectly plastic, then plastic flow is associated with stresses corresponding to points on this surface and unlimited plastic strains may occur under constant stress. If, however, the material is work-hardening, then the stresses have to be increased to sustain yielding. The elastic limit of the system is, therefore, increased in the latter case by yielding, a new yield surface is defined and the system "hardens ". A hardening law is then required to relate the position of the yield surface to a hardening parameter (which is commonly some measure of the total shear distortion experienced by the material (Hill, 1950)). For an ideal strain hardening plastic body, the yield loci do not change in shape, but expand steadily maintaining geometrical similarity during continued loading (isotropic hardening).

Since the elastic strains are governed by either Hooke's law, or some non-linear elastic law, a complete stress-strain record requires the specification of some form of relationship between the plastic strains and the applied stresses. In plasticity we think in terms of strain increments (or strain rates) and stress increments, these being linearly related for our idealised plastic materials. In order to provide the complete stress-strain record for any potential loading path on such a system we need a "flow rule", which relates strain increments to the current stress state together with the yield surface and the hardening law. The "flow rule" can be furnished by a "plastic potential", a scalar function of stress, from which the plastic strain increments can be obtained by partial differentiation with respect to the stresses. The plastic potential may also be represented in stress space by a surface or surfaces, which, we shall refer to as the "g-surfaces", to differentiate them from the yield surfaces whose geometric representation in stress

space will be called the "f-surfaces".

By plotting plastic strain increments on the same axes as the corresponding stresses, the resultant plastic strain-increments may be represented in this space by a free vector. We may also work in terms of forces and related displacement increments for plastic systems generally and define f and g surfaces similarly. A key feature which follows from the definition of the plastic potential is that the vector representing the plastic strain increment is normal to the g-surface passing through the stress point from which yield is occurring. It should be noted here that a plastic potential has to be convex to the origin and enclose it, and that, if the g surface has corners, the plastic strain increment vector is indeterminate to the extent that it may have any direction within the fan defined by the normals of the contiguous surfaces.

In the simplest forms of plasticity theory it is usually assumed that the yield surface and the plastic potential coincide, and, therefore, the plastic strain increment vector is normal to the yield surface as well. This assumption is the backbone of the limit theorems postulated by Drucker et al (1951), and materials which obey this normality condition on f are called materials with an associated flow rule. However, in general, the plastic potential (g) and the yield surface (f) do not coincide and materials which belong to this more general class are referred to as having non-associated flow rules. In this case the plastic strain increment vector at a point on the yield surface is not in general normal to it but is normal to g (Chen, 1975).

The basic features of the theory of plasticity outlined above will now be used in the next section to formulate the analytical framework for a new look at the footing problem. Here the stresses and the strain increments will be directly analogous to the applied loads (vertical and horizontal) and the corresponding displacement increments of the footing respectively, for which generalised loads and displacements all the foregoing statements also apply (Prager, 1959).

8.3 The derivation of the plastic potential

It was pointed out in chapter 6 that the footing did not rotate significantly when loaded by an inclined central load (tests B ($\alpha_o = 12^o$),

GB ($\alpha_o = 20^o$), E ($\alpha_o = 30^o$)). Furthermore it was observed that the ratio of the horizontal displacement increment to the vertical one remained practically constant along such constant load ratio paths. It was also demonstrated in both the preliminary and the main experimental investigation that the horizontal displacements are practically irrecoverable (plastic) whereas the vertical ones do have a small recoverable part. These latter observations are strikingly similar to those postulated for the Cam-Clay model (see, for example, Schofield and Wroth (1968), Wroth (1976)). It was, therefore, thought interesting to develop a plastic potential equation following essentially the same reasoning as that used by Burland (1965). It should be noted here that both the vertical and the horizontal displacement increments measured during testing will be assumed to be totally irrecoverable, even though a partial elastic response of the former was established experimentally. This assumption is necessary since the exact amount of elastic recovery at various stages of a test was not established experimentally. Nevertheless it is thought that this is not a major shortcoming since the recoverable displacements were all relatively small.

Let us consider a footing on sand subjected to a vertical load V and a horizontal load H (fig. 8.1) and denote with $\dot{v}$ and $\dot{u}$ the vertical and horizontal displacement increments respectively. The superscripts p and e will denote plastic (non-recoverable) and elastic (recoverable) displacements respectively. The incremental work dissipated during deformation may be expressed as:

$$\delta W = V\,\dot{v}^p + H\,\dot{u}^p \tag{8.1}$$

Under the action of the vertical central load only (H = 0) the incremental work dissipated becomes (from eq. (8.1)):

$$\delta W = V\,\dot{v}^p \tag{8.2}$$

When a horizontal load H is also applied, the footing slides horizontally under $H/V = \tan\delta$, where δ is the angle of base friction, and the incremental work dissipation for this loading condition will be (from eq. (8.1)):

$$\delta W = (V \tan\delta)\dot{u}^p \tag{8.3}$$

No vertical displacement occurs at that stage, therefore $\dot{v}^p = 0$.

A generalisation of these two particular conditions would be (Burland, 1965):

$$\delta W = \sqrt{(V\ \dot{v}^p)^2 + (V \tan \delta)^2\ (\dot{u}^p)^2} \qquad (8.4)$$

Combining equations (8.1) and (8.4) the following expression may be derived:

$$\frac{\dot{u}^p}{\dot{v}^p} = \frac{2(\frac{H}{V})}{(\tan \delta)^2 - (\frac{H}{V})^2} \qquad (8.5)$$

It was stated in the previous section that any plastic strain increment vector is to be normal to the g-surface (plastic potential) and considering our analogous situation, the equation of the plastic potential for the footing system can be obtained from equation (8.5) by applying the normality condition and solving the resulting first order differential equation. The normality condition requires:

$$\frac{\dot{u}^p}{\dot{v}^p} = -\frac{dV}{dH} \qquad (8.6)$$

and equation (8.5) becomes:

$$\frac{dV}{dH} = \frac{2(\frac{H}{V})}{(\frac{H}{V})^2 - (\tan \delta)^2} \qquad (8.7)$$

The solution of this differential equation gives the equation of the plastic potential as:

$$\frac{V}{V_{max}} = \frac{t^2}{m^2 + t^2} \qquad (8.8)$$

where $m = \frac{H}{V}$ and $t = \tan \delta$.

This is the equation to an ellipse with its centre on the V axis and at $V_{max}/2$ from the origin (V_{max} is the ultimate load in the vertical symmetric case). The small principal semi-axis of this ellipse is $(V_{max}/2)\tan \delta$ (see fig. 8.2). The shaded area will not be accessible of course, since

the footing will always slide horizontally under $H = V \tan \delta$.

8.4 Comparison with the experimental results

The relationship of the predicted displacement increment directions predicted by this analysis to the experimental data will now be investigated. In chapter 6 it was shown that the angle of base friction is approximately 40°. From equation (8.6) and with $t = \tan \delta = 0.839^{\circ}$, the associated displacement increment vectors for 12°, 20° and 30° constant load ratio paths are inclined to the $\dot{v}$ axis at 33°, 52° and 72° respectively. These angles can be compared with the experimental ones 35° to 40° ($m = \tan 12^{\circ}$) 55° to 65° ($m = \tan 20^{\circ}$) and 71° to 76° ($m = \tan 30^{\circ}$). In fact, if δ is assumed to be 38.5° (which might equally well be the case), the corresponding predicted angles are 36°, 56° and 76° which compare remarkably well with the experimental results. This is now seen to be very important, since, by knowing the ultimate load under vertically symmetric conditions together with the angle of base friction, we can predict, to a surprisingly good approximation, the ratios of the displacement increments under any combination of V and H, over the greater part of the loading range from zero to failure.

If we can now determine some relationship between the vertical component of the applied load and the vertical displacement for any value of m then the foregoing analysis will provide the horizontal displacement increment magnitude also. The most optimistic expectation would be that the vertical load-displacement relationship might be independent of m. This was, unfortunately, not the case but a simple relationship was found to give a reasonable first approximation of the vertical load-vertical displacement for any load inclination. In chapter 6 it was shown that this load-displacement relationship could be approximated by a bilinear expression. The first straight line segment passes through the origin and is the same for all load inclinations. The second segment meets the load axis at a point $(P_v/\gamma B)_o$, fig. 8.4, the value of which decreases with increasing load inclination. A very good approximation to the variation of the $(P_v/\gamma B)_o$ with the load inclination angle α was found to be given by

$$\frac{\left(\frac{P_v}{\gamma B}\right)_o}{\left(\frac{P_v}{\gamma B}\right)_o^{max}} = (1 - 0.85 \tan \alpha)^5 \qquad (8.9)$$

where $(P_v/\gamma B)_o^{max}$ corresponds to the vertical central load case. The expressions for the two straight line segments are (see fig. 8.4) then given by

$$\left(\frac{P_v}{\gamma B}\right)^{(1)} = 7200 \frac{v}{B} \qquad (8.10)$$

and

$$\left(\frac{P_v}{\gamma B}\right)^{(2)} = \left(\frac{P_v}{\gamma B}\right)_o + 4050 \frac{v}{B} \qquad (8.11)$$

Therefore, if the vertical load–vertical displacement relationship of a footing is known either analytically or experimentally, then the corresponding relationships for any load inclination may well be predicted to a reasonable approximation by equation (8.9).

These equations, together with the plastic potential derived above, were used to predict the horizontal displacement of the footing when subjected to inclined central loads with $\alpha_o = 12^o$, 20^o and 30^o. The results are compared with the experimentally obtained ones in fig. 8.5, where the vertical component of the load versus the horizontal displacement, both in dimensionless form ($P_v/\gamma B$ and u/B respectively), is shown. The continuous lines were calculated with $\delta = 38.5^o$ whereas the dashed ones used $\delta = 40^o$. The agreement with the 12^o load inclination is rather good, while the predictions for either the 20^o or the 30^o are somewhat conservative. Nevertheless, the behaviour of the footing is described quite adequately in all three cases and the observed deviations are mainly due to the simple bilinear approximation adopted which could undoubtedly be improved by more sophisticated curve fitting and to the fact that the incremental displacement vector direction of the footing does rotate slightly throughout the test. It must be emphasized, however,

that the overall agreement, from the practical point of view, is quite remarkable and the author is not aware of any comparable, simple rational method of predicting horizontal displacements of footings when subjected to inclined central loads.

Unfortunately, the author was unable to find any other comprehensive data from either small scale laboratory tests or large scale field tests to test this analysis. The only available information was from a limited number of tests suggested by the author and performed by Head (1977) and from a number of experiments performed by Yip (1977). Head used a 63 mm wide footing under plane strain conditions on medium dense Leighton Buzzard sand (as the one used by the author), and loaded it in a similar manner to that described in chapter 2, whereas Yip used a 100 mm wide footing on a brass rod model and applied combinations of either vertical and horizontal loads or vertical load and pure moment. Results from Head (1977) indicated that the direction of the incremental displacement vector of the footing was approximately the same along a constant load ratio path from the origin, and a similar plastic potential surface (an ellipse) could be fitted through the experimental data.

The experimental results obtained by Yip (1977) are quite interesting. He, too, observed that the directions of the incremental displacement vector of the footing did not change appreciably along a constant load ratio path from the origin. However, whereas both the author and Head (1977) observed that the angle between the displacement vector and the load path increased with increasing inclination of the load, Yip's results indicated that this angle remained approximately constant ($\approx 70^{o} \pm 4^{o}$), for all load inclinations (see fig. 8.6) from a large number of tests (50). This finding implies that the incremental displacement vectors are normal to a logarithmic spiral which therefore serves as a plastic potential surface in his case. A similar observation was made for the case with vertical loads and pure moments applied to the footing (fig. 8.7). The angle between the displacement increment vector(consisting of two components, the B and the $\dot{v}$) and the constant load ratio path from the origin was found to be about 70^{o} and remained approximately invariant for any moment applied at the footing. This is quite remarkable, because it implies that a similar shape plastic potential surface (logarithmic spiral) applies to this case as well. Therefore, if the load displacement

relationship is known, then the rotation of the footing can be predicted for any moment applied. The implication of these findings in relation to the experimental results from the sand models will now be discussed.

It was pointed out earlier in this chapter that the vertical component of the displacement increment would be assumed as fully irreversible even though it was established experimentally that part of it was recoverable. In view of the results from the rod model, let us assume that the actual g-surface is a logarithmic spiral. This assumption, when applied to the results from the inclined central load cases referred to in this section, will require that the plastic displacement increment vector will form a constant angle with the radius from the pole at the origin, which coincides with a constant load ratio path from the origin. This angle must, therefore, be about 50^{o} (which is closely similar to the angle of internal friction) since the incremental displacement vector is parallel to the $(H,\dot{u})$ axis (see fig. 8.2) when $m = \tan 40^{o}$. If this is combined with the experimental results of fig. 8.3, then it is implied that a significant part of the assumed irrecoverable displacement increment is, in fact, elastic, and since the horizontal displacement increments are practically irrecoverable, the elastic part is related entirely to the vertical displacements (see fig. 8.8). The magnitude of the elastic vertical displacement increment (with respect to the total vertical displacement increment) decreases with increasing load inclination (or increasing m) but is nevertheless relatively high ($\dot{v}^{p} = 0.46\dot{v}^{T}$, where $\dot{v}^{T}$ is the total vertical displacement increment) for $m = \tan 20^{o}$, for example (compare, also $\dot{v}^{p} = 0.80\ \dot{v}^{T}$ for $m = \tan 5^{o}$). Therefore, even though the elastic part of the vertical displacement would be expected to decrease with increasing m, the experimental results indicate that the actual magnitude of the elastic recovery is significantly smaller. Furthermore, such an assumption would imply that the elastic response of the rod model is essentially zero which is questioned in view of the results from the tests performed by Yip (1977), who found as much as 30% recovery of the vertical displacement occurred during a vertical load cycle.

The results presented so far are, of course, few in number and a considerable experimental effort will be required to explore the fascinating potentialities of this new approach. Nevertheless it has been quite

clearly demonstrated already that such a rational approach is of immediate practical interest and could rapidly become a very useful tool for the engineers.

8.5 Some further implications of the proposed approach

Let us consider more closely the particular features of the experimental results in conjunction with the proposed model. At first the direction of the displacement increment vectors were seen to remain practically constant along a constant load ratio path through the origin almost throughout the test (from about 20% to 80% of the failure load at least). In addition it was established that the horizontal displacement increment is irrecoverable, whereas the vertical one is partly recoverable. These two main features, together with the fact that the footing rotated barely at all throughout the loading sequence, suggest that the response of a footing on dense sand under inclined central load may be described by a plastic work hardening system, shown in fig. 8.9, with geometrically expanding plastic potentials g, and yield surfaces f. The'hardening' is furnished by the vertical displacements, and for a load cycle from B to A to B, the vertical displacement increment is purely elastic.

The experimentally obtained failure envelope F is seen not to coincide with the predicted plastic potential (and, indeed, it was not expected to do so from the direction of the related displacement increment vectors). However, we cannot say the same for the suggested successive yield surfaces f. These surfaces may or may not coincide with the similarly expanding g-surfaces (i.e. flow may or may not be "associated"). There are, nevertheless, some indications that the f-surfaces do not, after all, coincide with the g-surfaces. Consider, for example, the case where the current yield surface corresponds to point B on the V axis (see fig. 8.9). The corresponding g-surface for that load point will be an ellipse going through C so that (OD) = (OB)/2. If the f and g surfaces do coincide, then there will be an inaccessible load area included within the yield locus (shown shaded). Furthermore, Yip (1977) obtained experimentally some yield surfaces which indicated very tenuously that they are similar to ellipses (fig. 8.6) and, therefore,

different from the g-surfaces (logarithmic spirals). Therefore it is likely that the f and g surfaces do not, after all, coincide, but no firm conclusions may be drawn at this stage. It is, however, quite clear that there is a need to establish experimentally the shape of these successive yield surfaces, and it is hoped that this will be investigated in the next experimental programme.

8.6 Conclusions

Based upon some features of the plasticity theory on plastic potentials and from experimental evidence presented in chapters 2, 6 and 7, a simple rational approach has been put forward to explain the behaviour of a rough strip footing on sand under inclined central loads. It has been demonstrated that a knowledge of the angle of base friction may be sufficient information to derive a plastic potential which will provide the ratios of the displacement increment components for footings loaded by any combination of V and H. Furthermore, a knowledge of the vertical load-vertical displacement relationship of the footing then enables us to predict, with reasonable accuracy, the load-horizontal displacement relationship for various load inclinations. Due to lack of comprehensive data from field or laboratory tests the universality of the proposed model could not be established conclusively. Nevertheless, additional experimental evidence from Head (1977) and Yip (1977) does lend strong support to the proposed analysis.

It is quite obvious that there are some assumptions in the development of these ideas which need to be explored further, for example, the determination of the elastic part $\dot{v}^e$ of the vertical displacement increment at any load inclination, the investigation of the dependence of the displacement increment vector upon the load path, the determination of the yield surfaces f, the determination of the g surfaces and the investigation of their coincidence with the f-surfaces, and, of course, similarly for the moment-vertical load space. Indeed, all this represents a recommendation for further research contribution and, as has been demonstrated, there is much scope in future expansion of the basic principles set in this chapter.

CHAPTER 9

CONCLUDING REMARKS

A review of the literature on surface footings on sand revealed that there was scarcely any high quality records of failure loads and displacements for cases with eccentric and/or inclined loads. Furthermore, no data were available at all on displacement and strain fields within the soil for the aforementioned cases and only a little, low precision information could be found on the contact stress distribution under these loading conditions.

A preliminary investigation was conducted to establish guidelines for the main research "route" and the following conclusions were drawn both from experiments in a small footing apparatus and from consideration of the results of other research workers:

1. The "effective" idea, proposed by De Beer (1949) and Meyerhof (1953) gave safe predictions for the reduction of the applied eccentric vertical load capacity in relation to the vertical central load ultimate bearing capacity V_{max}.

2. A rigid surface strip footing on sand can withstand a maximum moment of about $V_{max}B/10$

3. In the case of an inclined central load acting on a surface footing on sand, the reduction factor suggested by Hansen (1970) and another suggested by the author from his experimental results were found to give good predictions (on the safe side). On average it was established that the maximum horizontal load a surface footing can withstand is approximately $0.10\ V_{max}$.

4. It was established experimentally that higher horizontal loads of approximately 50% can be carried by the footing under the same vertical load, when the latter is acting eccentrically on the opposite rather than on the same direction to the horizontal load ('negative' and 'positive' eccentricity respectively). Furthermore it was indicated that a slightly higher bearing capacity ($\simeq$ 15%) could be obtained in the case

of 'negative' eccentricity of the applied vertical load and under certain load combinations than that under the vertical eccentric load alone.

The failure load envelope of the footing corresponding to general planar loads has been also presented. A direct implication from this diagram is that once V_{max} is known (either through a plate bearing test or through some reliable estimation), then the behaviour of the footing at failure under any planar load combination may be safely predicted.

5. The incremental displacement vectors of a footing under inclined central loads, when plotted on the corresponding V-H diagram axes, were found to remain practically parallel throughout the test for a constant slope load path from the origin and inclined at an angle to the load path. This angle ranges from approximately zero (vertical central load) to a maximum of $90-\delta$, where the footing 'slides' horizontally under $H = V \tan \delta$ (δ = angle of base friction).

Following the above observations, an analogy was drawn between the 'collapse' of strip footings on clay and sand under combinations of V, H and M and a fixed-foot steel portal frame and it was suggested that the failure envelopes of the former could be interpreted in precisely the same way as the conventional interaction diagram of the latter.

Two apparatuses were constructed, one at Cambridge (FAC) and the other at Southampton (FAS), the latter tank being approximately three times wider than the former. A list of the tests performed in both apparatuses is given in table 1. The total loads, contact stresses and the planar translation and rotation of the footing were recorded, while both X-ray and the Stereophotogrammetric techniques were used to obtain displacement fields of the deforming sand bed. The most important features of the experimental results obtained, are listed below:

1. The measured bearing capacity in the vertical central load case agreed, in general, with experimental results obtained by other research workers. Nevertheless it was thought worth emphasising that the current formulae in use to predict bearing capacities do produce a wide range of values (especially for footings on very dense sand, i.e. $\phi \geq 45^{o}$).

2. The findings of the preliminary investigation on the 'effective' width concept and the semi-empirical inclination factor proposed by Hansen (1970) were confirmed. The capacity of the footing to withstand

approximately 50% higher horizontal loads when subjected to a vertical eccentric load with 'negative' eccentricity was also confirmed.

3. The footing was found to tilt and displace horizontally even under vertical symmetric loads, due to the development of a non-symmetric strain field within the deforming sand mass. An eccentric vertical load $(E_o = e/B)_o = 0.167)$ caused the footing to rotate about 2^o by failure while under an inclined central load the footing remained essentially horizontal throughout the test. The footing was found to move along an approximately constant direction (in the latter case) inclined at an angle to the constant load ratio path through the origin, which again confirmed a similar finding of the preliminary investigation. A simple bilinear expression was suggested as an approximation to the vertical load component-vertical displacement relationship for any load inclination. Finally the vertical component of the footing displacement was found to consist of both an 'elastic' and a 'plastic' part (i.e. recoverable and irrecoverable respectively), whereas the horizontal displacements were found to be irrecoverable (i.e. 'plastic').

4. It was demonstrated that, if the lateral motion of the footing was restrained, this resulted in an increase of the bearing capacity of an eccentrically vertically loaded footing by a factor of about 2 and the formation of a longer and deeper failure surface on the opposite side to the load eccentricity, in comparison to the unrestrained case. However, the dimensionless moment-rotation and vertical load-vertical displacement relationships obtained for both the above cases were almost identical.

5. The repeatability of the experimental results was established from the almost identical load-displacement and moment-rotation relationships obtained from tests A ($e_o = 0.52$, $\alpha_o = 0$, $E_o = 0.167$) and H ($e_o = 0.52$, $\alpha_o = 0$, $E_o = 0.167$), their identical failure loads, the almost identical contact stress distributions underneath the footing and the almost identical failure surfaces which developed.

6. The shape of the normal (and, in some cases, the shear) contact stress distributions (c.s.d) were found to remain essentially the same for the greater part of the test for almost all the cases

considered and to expand geometrically with increasing total load (from stages $P/P_f \approx 0.30$ to 0.90).

The normal c.s.d. underneath a footing loaded with an eccentric vertical load was found to be triangular throughout the loading sequence. In the case of an inclined central load the shape of the normal c.s.d. was found to be similar to that for a vertical central load.

7. The angle of base friction (δ) increased with increasing load inclination (and, consequently, decreasing stress levels). A value of 40° was adopted as typical from the values measured in the 15 tests performed.

8. The mean pressure recorded by the centre section of the footing in the FAS near failure was found to be 7% lower on average than that recorded by either of the side sections, even though the opposite effect was found at early stages of the test. The ultimate loads obtained from tests in the FAS (tank width = 584 mm) were lower (* 20%) than those obtained from nominally identical tests in the FAC (tank width = 190.5 mm) Part of this reduction was very likely due to the small difference (≈ 4%) in the initial voids ratio of the very dense sand beds. However, the quite remarkable agreement between the load-displacement relationships obtained from both apparatuses implied that the relative width of the tank must have affected, at least partially, the observed difference in the failure loads. It is, therefore, suggested that the reduced bearing capacity due to the larger tank width can be of the order of 5-10% only. (In the cases investigated: Height/width = 0.4 in the FAC, 0.13 in the FAS).

9. The principal strain rate axes do not rotate significantly during each test for load increments beyond the stage $P/P_f \approx 0.45$ up to failure. It was suggested that a non-rotating stress field is the most probable consequence of a non-rotating strain field, with the principal stress increment axes either coinciding with the principal strain increment axes ('associated' flow) or inclined at a constant angle to them (one form of 'non-associated' flow). Furthermore, the principal strain rate directions were found to be almost identical for the four different

loading conditions ($\alpha_o = 0$ and $E_o = 0$, $\alpha_o \neq 0$ and $E_o = 0$, $\alpha_o = 0$ and $E_o \neq 0$, $\alpha_o \neq 0$ and $E_o \neq 0$). However it should be noted that the vertical component of the load in all these cases was the dominant one. Nevertheless it is most remarkable that the principal strain directions are similarly oriented throughout the sand mass over an appreciable range of load inclinations and eccentricities.

10. The maximum shear strain pattern for the vertical central load case was found to be surprisingly similar to the maximum shear stress distribution obtained from the indentation of a rigid punch into a semi-infinite elastic medium. (Similar observations were reported by Tannekoon (1970)). It would be interesting to compare analytical solutions of equal displacement contours for elastic solutions with those measured experimentally.

11. A unique empirical relationship was established between the volumetric and the maximum shear strains for all the different loading conditions considered in the FAC, and it was found to be almost identical to that obtained by other research workers investigating various earth pressure problems all with entirely different boundary conditions. This relationship, which may be approximated quite well by a straight line, implies that the very dense Leighton-Buzzard sand used in the experiments dilates at approximately constant rate ($\nu = 21.1^o$) over a considerable range of maximum shear strains ($0.02 < \gamma_m < 0.15$). This constant angle of dilatancy was used with the Stress dilatancy flow rule suggested by Rowe (1962) to predict the angle of internal friction ($\phi = 50.6^o$) which was found to agree well with the adopted one ($\phi = 50^o$) from tests in the SSA performed by Stroud (1970).

12. The failure surfaces developed in the cases considered seem to lie along lines of zero extension. This was further indicated from the angle the rupture surface outcrop makes with the free sand surface and the angle the sides of the "rigid wedge", formed underneath the footing, make with the vertical. However, the view that rupture surfaces must coincide with stress characteristics (i.e. directions at $\pm(45 - \frac{\phi}{2})$ to the direction of the major principal stress) is still widely held (e.g. Butterfield and Harkness, 1972; Vesic, 1973).

13. The failure surfaces under increasing load inclination became both shallower and shorter whereas secondary failure surfaces were observed in a number of tests which either branched off the main rupture surface or developed from the footing base. The main failure surfaces obtained from tests under inclined central load showed some striking similarities with rupture surfaces obtained from large scale field tests under similar loading conditions (Muhs and Weiss, 1973) which suggested that the formation of the failure surfaces was not greatly affected by either the narrow tank or the model scale.

14. The maximum shear strain fields obtained from tests in the FAS were found to be similar to these obtained from nominally identical ones in the FAC. It was, therefore, suggested that, even though further experimental evidence was required, the displacement fields obtained by either narrow or wide tank (at the sand-glass interface) are similar for the footing and tank geometries used.

15. The results obtained by X-ray and the Stereophotogrammetric techniques were compared and it was found out that there was typically a difference of only about ± 2% on the measured displacement fields from identical increments in the same test recorded simultaneously. Even though measurements of the same precision can be made by both techniques, one basic feature of the Stereophotogrammetric method (i.e. independence of discrete point measurement) make it very powerful and versatile (e.g. Harkness, 1977).

A simple rational approach, based upon some ideas in incremental plasticity theory, plastic potentials etc., has been developed to explain the behaviour of a rough strip footing on sand under inclined central planar loads. It was demonstrated that a knowledge of the angle of base friction may be sufficient (together with the load-displacement response for the vertical central load case) to derive a plastic potential which will provide the ratios (and magnitudes) of the displacement increment components for footings loaded by any combination of V and H.

It is also suggested tentatively from the experimental evidence of Yip (1977) that a similar analysis might be applicable to footings under

moments as well. Indeed, the results from the four vertical eccentric load tests performed by the author indicate that the ratio $B\dot{\omega}/\dot{v}$ (where $\dot{\omega}$ is the incremental tilt of the footing) remains approximately constant for a considerable part of the test. However, it should be noted here that, because the footing tilted continuously with increasing load, the eccentricity ratio (which is equal to the angle the "constant load ratio" path makes with the V axis, see fig. 8.7), increased, and at failure E was approximately 0.21 whereas E_o was only 0.167. Therefore, in order to establish the constancy of the direction of the displacement increment vectors, further experiments should be conducted with a pure moment acting on the footing (together with a vertical central load). Since the implications of these results are, at least, exciting, they will be discussed briefly below.

If it is assumed that at least to a first approximation a similarly shaped plastic potential can be derived for V-M space as for the V-H space (i.e. an ellipse), then the plastic potential surface for the V-H-M space would be an ellipsoid (see fig. 9.1). Furthermore, as was shown in chapter 2, the maximum values of both H and M/B which a surface footing can carry is approximately 0.10 V_{max}. If then the V-H-M/B failure surface is a surface of revolution this means that the generalized load component (say, for example, $F = \sqrt{(H)^2 + (M/B)^2}$) versus V becomes the key parameter.

In this context, it is interesting to examine the relevance of these ideas (and, indeed, of the results from the experimental work undertaken) to the design of oil production platforms for the North Sea.

An experimental wave force measuring tower with a circular base was built by the Building Research Establishment and the National Physics Laboratory (Penman et al, 1976) and placed on the sea bed in Christchurch Bay, the top 3 m layer of which consists of medium dense sand. The dimensions and design loads are shown in fig. 9.2 taken from a paper detailing the design and performance of the tower, published by Penman and Gallagher (1976). We will use our results to investigate the factor of safety against failure under this V-H-M load combination.

The failure load calculated by classical theory (Terzaghi, 1943) was found to be 41.1×10^3 KN (Penman et al, 1976). Considering, now, the design loads it may be seen that the vertical load is extremely small with respect to the failure one ($V \approx \frac{1}{33} V_{max}$). This suggests that the

case considered lies very close to the origin in fig. 9.1, and the load point (V-H-M) lies certainly on the conical,"sliding", region of the failure surface. Since the failure surfaces drawn in fig. 9.1 refer to strip footings, we will consider a square footing of equivalent area under the same loading conditions. We will assume that $\delta = 35^{o}$ ($\phi = 35$ to 38^{o}) (Penman et al, 1976), which, as was discussed in chapter 6, is a reasonable assumption. The following simple calculations are made:

The equivalent width of a square footing is

$$B^2 = \frac{(10.5)^2 \cdot \pi}{4}$$

$$B \simeq 9.3 \text{ m}$$

The generalized load component consists of H = 490 KN and M/B = 346 KN, and, therefore,

$$F = \sqrt{490^2 + 346^2} = 600 \text{ KN}$$

The resistance of the footing against sliding is given by

$$H_f = V \tan \delta$$

and

$$H_f = 1250 \times 0.7 = 875 \text{ KN}$$

Hence, the implied factor of safety against failure of the tower is

$$\text{F.S.} = \frac{875}{600} = 1.46$$

This value is almost identical (1.5) to that assumed for the design of the tower (Penman et al), by using Meyerhof's (1953) and Hansen's (1970) semi-empirical relationships for an eccentric-inclined load. The attraction of the procedure followed here is that an engineer has an immediate 'grasp' of the problem when considering fig. 9.1, and his judgement can be applied in a way which is just not possible with conventional bearing capacity formulae.

It does appear that the potentialities of the generalized failure surface and plastic potential as described are enormous. Thus, a knowledge of the load-displacement curve for the vertical symmetric case,

plus analogous information about the moment-rotation behaviour of the footing, combined with the plastic potential and failure envelope ideas, could describe the entire behaviour of the Christchurch Bay tower. If, furthermore, it is assumed that all tower loads were increased monotonically (in a manner similar to that used by the author), then the displacement and rotation of the tower could be also predicted.

The example presented above indicates that there is much scope for the future expansion of the basic ideas set out in chapter 8. Other recommendations for future research are listed below.

a) Experimental investigation of buried and deep footings in sand under general planar loads; measurement of the contact stresses and the deformation pattern of the sand mass and comparison with those obtained for surface footings.

b) Analytical investigation to predict the measured displacement fields for all three cases (surface, buried, deep footings). (e.g. associated field method (Roscoe, 1970), velocity hodograph (Butterfield and Harkness 1972)etc.).

c) Development of the basic ideas set in chapter 8 on plastic potentials and work hardening yield surfaces (a list of recommended areas for further relevant experimental work is given in chapter 8.6). Investigation of the possibility of applying similar ideas to footings on clay under general planar loads, and indeed to foundation systems, pile groups etc. generally.

REFERENCES

AICHORN, W. (1931) "Veber die Zusammendrueckung des bodens infolge oertlicher belastung", dissertation, Freiberg, Saxony.

ANDRAWES, K.Z. (1970) "A contribution to plane strain model testing of granular materials" Ph.D. Thesis, University of Southampton.

ANDRAWES, K.Z. (1976) "The use of stereo-photogrammetry for measuring displacement fields". Report submitted to SRC.

ARTHUR, J.R.F. (1977) 'Industrial Radiography in soil mechanics research.' British Journal of N.D.T., pp.9-13.

ARTHUR, J.R.F., JAMES, R.G. & ROSCOE, K.H, (1964) 'The determination of stress fields during plane strain of a sand mass' Géotechnique, 14, pp.283-308.

ARTHUR, J.R.F. & ROSCOE, K.H. (1961) "An earth pressure cell for the measurement of normal and shear stresses" Civ. Engng. Publ. Wks. Rev. 56, No.659, 765-770.

ARTHUR, J.R.F. & ROSCOE, K.H. (1965) "An examination of the edge effects in plane-strain model earth pressure tests", Proc. 6th ICSMFE, Montreal, Vol.2, 363-367.

AVGHERINOS, P.J. & SCHOFIELD, A.N. (1969) "Drawdown failures of centrifuged models", 7th ICSMFE, Vol.II, pp.497-505.

BALLA, A. (1962) "Bearing capacity of foundations" J. Soil Mech. Found. Div., ASCE, Vol.88 (SM5), pp.13-34.

BARDEN, L. (1962) "Distribution of contact pressure under foundations", Géotechnique 12, (3), pp.181-198.

BEKKER, M.G. (1948) "Photographic method for determining the soil action beneath footings" Proc. 2nd ICSMFE, Vol.3, pp.193-194.

BERGFELT, A. (1956) "Loading tests on clay" Géotechnique 6, pp.15-31.

BEASLEY, D.H. (1970) "An investigation of the effects of friction between sand and glass on results obtained in experiments on the model earth pressure apparatus" Mechanical Sciences Tripos Pt IIA, Cambridge University.

BIAREZ, J. (1962) "Contribution à l'étude des propriétés mécaniques des sols et des mãtéraux pulvérulents" These de Doctorat es Sciences, University of Grenoble.

BIAREZ, J., BUREL, M. & WACK, B. (1961) "Contribution to the study of the bearing capacity of foundations" Proc. 5th ICSMFE, Vol.1, pp.603-609.

BIERNATOWSKI, K. (1973) "The state of stress and displacement in the contact surface between a rigid foundation and subsoil" Proc. 8th ICSMFE Moscow, 1.3, pp.15-17.

BISHOP, A.W. (1957) "Discussion" Proc. 4th ICSMFE, London, Vol.III, pp.100.

BISHOP, A.W. (1966) "The strength of soil as engineering materials' Géotechnique, Vol.16(2) pp.91-128.

BJERRUM, L. (1973) Geotechnical problems involved in foundations of structures in the North Sea", Géotechnique, 23, (3), pp.319-358. -358.

BJERRUM, L. & EGGESTAD, A. (1963) "Interpretation of loading tests on sand" Proc. Euro. CSMFE, Vol.I, pp.199-204.

BO-GORAN HELLERS & OLLE ORRJE (1969) "Centrically loaded infinite strip on a single-layer elastic foundation - solution in closed form according to the Boussinesq theory" Swedish Geotechnical Institute, No.43.

BOROWICHA, H. (1936) "The influence of rigidity of a circular foundation slab on the distribution of pressures over the contact surface" Proc. 1st ICSMFE, vol.II, pp.144-149.

BRANSBY, P.L. (1968) "Stress and strain in sand caused by the rotation of a model wall" Ph.D. thesis, University of Cambridge.

BRANSBY, P.L. (1973) "Cambridge contact stress transducers" Internal report Cambridge University Engineering Department.

BRATCHELL, G.E., LEGGATT, A.J. & SIMONS, N.E. (1974) "The performance of two large oil tanks founded on compacted gravel at Fawley, Southampton, Hampshire" Proc. of Conf. on Settlement Structures, Cambridge, pp.3-9.

BUISMAN, A.S.K. (1935) "De weerstand van paalpunten in sand" De Ingenieur, 50, pp.25-28, 31-35.

BURLAND, J.B. (1965) Correspondence. Géot. 15, pp.211-215.

BUTTERFIELD, R. & ANDRAWES, K.Z. (1970) "An air activated sand spreader for forming uniform sand beds" Géotechnique 20, No.1, 97-100.

BUTTERFIELD, R. & HARKNESS, R.M. (1972) "The kinematics of Mohr-Coulomb materials" Proc. Roscoe Memorial Symp. pp.220-233, Foulis.

BUTTERFIELD, R., HARKNESS, R.M. & ANDRAWES, K.Z. (1970) "A stereophotogrammetric method for measuring displacement fields" Géotechnique 20, No.3, pp.308-314.

CAQUOT, A. (1934) "Equalibre des massifs a frottement interne" Gauthier-Villars, Paris.

Chen, W.F. (1975) "Limit analysis and soil plasticity" North-Holland-Elsevier.

CHAE, J.R., RICHART, F.E. & HALL, J.R. (1965) "Dynamic pressure distribution beneath a vibrating footing" Proc. 6th ISCMFE, Vol.II, pp.22-26.

COLE, E.R. (1967) "The behaviour of soils in the simple-shear apparatus" Ph.D. thesis, University of Cambridge.

CORNFORTH, D.H. (1964) "Some experiments on the influence of strain conditions on the strength of sand" Géotechnique, 14, pp.143-167.

DAVIS, H.E. & WOODWARD, R.J. (1949) "Some laboratory studies of factors pertaining to the bearing capacity of soils" Proc. Highways Res. Bd., Vol.29, pp.467-476.

DE BEER, E.E. (1949) "Grondmechanica", Antwerp, Belgium.

DE BEER, E.E. (1961) "Discussion" Proc. 5th ICSMFE, Paris, Vol.III, pp.205-208.

DE BEER, E.E. (1965a) "Bearing capacity and settlement of shallow foundations on sand" Symp. Bearing Capacity and Settlement of Foundations, Duhrain, N.C., pp.15-33.

DE BEER, E.E. (1965b) "The scale effect on the phenomenon of progressive rupture in cohesionless soils" Proc. 6th ICSMFE, Vol.II, pp.13-17.

DE BEER, E.E. (1970) "Experimental determination of the shape factors and the bearing capacity factors of sand" Géotechnique 20, No.4 pp.387-411.

DE BEER, E.E. & LADANYI, B. (1961) "Étude experimentale de la capacité portante du sable sous les foundations circulaires etablies en surface" Proc. 5th ICSMFE, Vol.1, pp.577-585.

DHILLON, G.S. (1958) "The settlement, tilt and bearing capacity of footings on sand under central and eccentric loads" Ph.D. thesis, University of Sheffield.

DHILLON, G.S. (1961) "The settlement, tilt and bearing capacity of footings on sand under central and eccentric loads" Journ. National Build. Org. Vol.1 (1961) pp.66-78.

DRUCKER, D.C., PRAGER, W. & GREENBERG, H.J. (1951) "Extended limit theorems for continuous media" Q. Appl. Math., 9, pp.381-389.

EASTWOOD, W. (1951) "A comparison of the bearing power of footings on dry and inundated sand" The Structural Engineer Vol.29, pp.1-11.

EASTWOOD, W. (1955) "The bearing capacity of eccentrically loaded foundations on sandy soils" The Structural Engineer, Vol.33, pp.181-187.

EGGESTAD, A. (1964) "Deformation measurements below a model footing on the surface of dry sand" Norwegian Géotechnical Institute, Publ. No.58, pp.29-35.

EVDOKIMOV, P.D., APTEKAR, L.D., BUSHKANETS, S.S. & LJPOVETSKAYA, T.E. (1973) "Shear resistance of soil foundations of structures" Proc. 8th ICSMFE, Vol.1.1, pp.117-122.

FABER, OSCAR (1933) "Pressure distribution under bases and stability of foundations", Struct. Engr.

FEDA, J. (1961) "Research on the bearing capacity of loose soil" Proc. 5th ICSMFE, Vol.I, pp.635-642.

FROCHT, M.M. (1948) "Photoelasticity" John Wiley & Sons.

GERBER, E. (1929) "Untersuchungen ueber die druckverteilung in Oertlich belasteten sand" Dissertation, Technische Hochschule, Zurich.

GIRAUDET, P. (1965) "Recherches experimentales sur les foundations soumises a des efforts inclines ou excentrés" Annales des Ponts et Chaussées, Vol.III, pp.168-193.

GIROUD, J.P., TRAN-VO-NHIEM & OBIN, J.P. (1973) "Tables pour le calcul des foundations" Vol.3, Dunod.

GOLDER, H.Q. (1941) "The ultimate bearing pressure of rectangular footings" Journ. Inst. Civil Eng., Vol.17, p.161.

GORBUNOV-POSSADOV, M.I. (1961) "Discussion" Proc. 5th ICSMFE, Vol.III, pp.224-225.

GORBUNOV-POSSADOV, M.I. (1965) "Calculation for the stability of a sand bed by a solution combining the theories of elasticity and plasticity" Proc. 6th ICSMFE, Vol.II, pp.51-55.

GRAHAM, J. & POLLOCK, D.J. (1972) "Scale-dependent plasticity analysis for sand" Civil Eng. and Publ. Works Rev., Vol.67, pp.245-251.

GRAHAM, J. & STUART, J.G. (1971) "Scale and boundary effects in foundation analysis" J. Soil Mech. Found. Div., ASCE, 97 (SM11) pp.1533-1548.

HAMBLY, E.C. (1969) "Plane strain behaviour of soft clay" Ph.D. thesis University of Cambridge.

HANSEN, BENT (1958) "Line ruptures regarded as narrow rupture zones. Basic equations based on kinematic considerations" Proc. Brussels Conf. on Earth Pressure Problems, Vol.I, pp.39-42.

HANSEN, BENT (1961) "The bearing capacity of sand tested by loading circular plates" Proc. 5th ICSMFE Vol.I, pp.659-664.

HANSEN, J.B. (1953) "Earth pressure calculation" The Danish Technical Press, Copenhagen.

HANSEN, J.B. (1957) "General report" Proc. 4th ICSMFE, Vol.II, pp.441-447.

HANSEN, J.B. (1961) "A general formula for bearing capacity" Bulletin 8, Danish Geotechnical Institute.

HANSEN, J.B. (1970) "A revised and extended formula for bearing capacity" Bull. Dan. Geotechn. Institute, 28, pp.5-11.

HARKNESS, R.M. (1977) Private Communication.

HARKNESS, R.M. & LOCK, A. (1977) Private Communication.

HARTIKAINEN, J. (1973) "On the distribution of the vertical and horizontal contact pressure components under a rigid foundation" Proc. 8th ICSMFE, Vol.1.3, pp.99-105.

HEAD, M.C. (1977) "The bearing capacity of long footings on sand under the influence of combined vertical and horizontal loads" Undergraduate project report, Southampton University.

HILL, R. (1950) "THe mathematical theory of plasticity" Oxford.

HO, M.M.K. & LOPES, R. (1969) "Contact pressure of a rigid circular foundation" J. Soil Mech. Found. Div., ASCE, (SM3) pp.791-802.

HUECKEL, S., KWASNIEWSKI, J., & BARAN, L. (1965) "Distribution of passive earth pressure on the surface of a square vertical plate embedded in soil" Proc. 6th ICSMFE, Vol.II, pp.381-385.

HVORSLEV, M.J. (1965) "Discussion" Proc. Bearing capacity and settlement of foundations, Duke Univ. pp.93-99.

ICE (1974) "Offshore Structures" Proc. Conf., London.

JAMES, R.G. (1965) "Stress and strain fields in sand" Ph.D. Thesis, University of Cambridge.

JAMES, R.G. (1973) "Determination of strains in soils by radiography" Cambridge University Engineering Department, Internal Report, Soils/LN1(a).

JAMES, R.G. AND BRANSBY, P.L. (1970) "Experimental and theoretical investigations of a passive earth pressure problem" Geotechnique 20, No.1, 17-37.

JANBU, N. (1957) "Earth pressures and bearinv capacity calculations by generalized procedure of slices" Proc. 4th ICSMFE, Vol.II, pp.207-212.

JORDEN, E.E. (1977) "Settlement in sand-methods of calculating and factors affecting" Ground Engineering Jan. 1977, Vol.10, No.1.

JUMIKIS, A.R. (1961) "The shape of rupture surface in dry sand" Proc. 5th ICSMFE, Vol.I, pp.693-698.

KANANYAN, A.S. (1970) "Experimental investigation of the stability of foundation beds of finite thickness" Soil Mech. Found. Eng., Transl., 5, pp.303-307.

KATCHANOV, L.M. (1974) "Foundations of the theory of plasticity" MIR Publications, Moscow.

KEZDI, M.A. (1961) "Discussion" Proc. 5th ICSMFE, Vol.III, p.209.

KO, H.Y. & SCOTT, R.F. (1973) "Bearing capacities by plasticity theory" J. Soil. Mech. Found. Div., ASCE, 99 (SM1) pp.25-43.

KO, H.Y. & DAVIDSON, L.W. (1973) "Bearing capacity of footings in plane strain" J. Soil Mech. Found. Div., ASCE, 99 (SM1) pp.1-23.

KÖEGLER, F. & SCHEIDIG, A. (1929) "Druckverteilung im baugrunde", Bautechnik, Berlin.

KRIVOROTOV, A.P. (1965) "Service conditions of a sand foundation bed under the base of a vertically loaded plate" Soil Mech. Found. Eng. Transl. No.3 pp.139-142.

KRIVOROTOV, A.P. (1969) "State of stress of a sand mass under a plate lying at shallow depth" Sol. Mech. Found. Eng., Transl. 1, pp.20-24.

LARSEN, H. (1977) "Centrifugal model tests of buried rigid pipes" Forthcoming Ph.D. thesis, University of Cambridge.

LASEBNIK, G. (1973) "Discussion" Proc. 8th ICSMFE, Moscow, Vol.4.3, pp.19-20.

LEE, I.K. (1965) "Foundation subject to moment" Proc. 6th ICSMFE, Vol. II, pp.108-112.

L'HERMINIER, R., TCHENG, Y. & LEBEGUE, Y. (1965) "Expérimentation en laboratoire de la capacité portante des sols" Proc. 6th ICSMFE Vol.II, pp.1171-121.

LEUSSINK, H. and SCHWEICKERT, K. (1963) "Versuche über setzungsverhalten und sohldruckverteilung am übergang vom elastichen zum plastischen zustand einer sehr dicht gelagerten sandunterlage pei belastung durch ein starres fundament." Proc. ECSMFE, Vol.I, pp.279-284.

LORD, J.A. (1969) "Stresses and strains in an earth pressure problem" Ph.D. thesis, University of Cambridge.

MALYSHEV, M.V. (1971) "Slip lines and displacement paths of particles in a cohesionless medium" Soil Mech. and Found. Eng. (Transl), 6, pp.379-386.

MARINAKIS, K. (1972) "Discussion" Proc. Europ. C.S.M.F.E. Madrid, pp.146-150.

MENCL, M.V. (1961) "Discussion" 5th ICSMFE, Paris, Vol.III, pp.165-167 and pp.214.

MESMER, G. (1930) "Vergleichende spannungsoptische untersuchungen und fliess-versuche unter konzentricrtem druck" Z.f. tech. Mech. u. Thermodyn., Vol.I, Nos 2 & 3, V.D.I., Berlin.

MEYERHOF, G.G. (1948) "An investigation of the bearing capacity of shallow foundations on dry sand' Proc. 2nd ICSMFE, Rotterdam, Vol.I, pp.237-243

MEYERHOF, G.G. (1951) "The ultimate bearing capacity of foundations" Géotechnique, 2(4), pp.301-332.

MEYERHOF, G.G. (1953) "The bearing capacity of foundations under eccentric and inclined loads" Proc. 3rd ICSMFE, Vol.I, pp.440-445.

MEYERHOF, G.G. (1963) "Some recent research on the bearing capacity of foundations" Can. Geotechn. J., 1(1), pp.16-26.

MILLIGAN, G.W.E. (1974) "The behaviour of rigid and flexible retaining walls in sand" Ph.D. thesis, University of Cambridge.

MILLIGAN, G.W.E. & BRANSBY, P.L. (1976) "Combined active and passive rotational failure of a retaining wall in sand" Géotechnique, 26, 3, pp.473-494.

MILOVIC, D.M. (1965) "Comparison between the calculated and experimental values of the ultimate bearing capacity" Proc. 6th ICSMFE Vol. II, pp.142-144.

MILOVIC, D.M., TOUZOT, G. & TOURNIER, J.P. (1970) "Stresses and displacements in an elastic layer due to inclined and eccentric load over a rigid strip" Géotechnique 20, No.3, pp.231-252.

MUHS, H. (1965) "Discussion" Proc. 6th ICSMFE, Vol.III, pp.436-440.

MUHS, H. & WEISS, K. (1969) "The influence of the load inclination on the bearing capacity of shallow footings" Proc. 7th ICSMFE, Vol. I, pp.187-194.

MUHS, H. & WEISS, K. (1973) "Inclined load tests on shallow strip footings" Proc. 8th ICSMFE, Moscow, Vol.1.3, pp.173-179.

MURZENKO, Yu.N. (1965) "Experimental results on the distribution of normal contact pressure on the base of a rigid foundation resting on sand" Soil Mech. Found. Eng. Transl., 2, pp.69-73.

NADAI, A. (1963) "Theory of flow and fracture of solids" Vol.II, McGraw-Hill Book Co.

NIKITIN, V.M. & NESMELOV, N.S. (1973) "Experimental investigation of the strain state of foundation beds by the Moire Method" Soil Mech. and Found. Eng. (Transl.), 3, pp.187-191.

ODA, M. (1972) "The Mechanism of fabric changes during compressional deformation of sand" Soils and Foundations, 12, pp.1-36.

ORR, T.L.L. (1975) "A user's guide to the soils strain calculating program" Cambridge University Engineering Department.

PALMER, A.C. (1976) "Structural mechanics" Oxford Eng. Science Texts.

PARADINE, C.G. & RIVETT, B.H.P. (1960) "Statistical methods for technologists" English University Press, London.

PARKES, E.W. (1956) "Comparison of the contact pressure beneath rough and smooth rafts on an elastic medium" Geotechnique, 6, pp.183-189.

PECK, R.B., HANSON, W.E. & THORNBURN, T.H. (1974) "Foundation Engineering" John Wiley & Sons (Second Edition)

PENMAN, A.D.M. & GALLAGHER, K.A. (1976) "Preliminary study of a gravity foundation failure" Ground Engineering, May, pp.15-20 and 44.

PEYNIRCIOGLU, H. (1948) "Tests on bearing capacity of shallow foundations on horizontal top surfaces of sand fills and the behaviour of soils under such foundations" Proc. 2nd ICSMFE, Vol.3, pp.194-205.

PRAKASH, S. & SARAN, S. (1971) "Bearing capacity of eccentrically loaded footings" J. Soil Mech. Found. Div., ASCE, 97, (SM1) pp.95-117.

PRANGE, B. (1971) "The state of telemetry in soil mechanics" Proc. Roscoe Memorial Symposium, Cambridge, pp.476-488.

PURKAYASTHA, R.D. & CHAR, R.A.N. (1977) "Stability analysis for eccentrically loaded footings" Geotechnical Div., ASCE, GT6, pp.647-651.

RAMELOT, C. & VANDEPERRE, L. (1950) "Travaux de la commission d'etude des foundations de pylones." Compt. Rend. Rech. IRSIA, Brussels, No.2.

ROBERTS, J.E. (1961) "Small scale footing studies: a review of the litarature" M.I.T., Department of Civil and Sanitary Eng., Soil Eng. Division, Public. 108.

ROSCOE, K.H. (1967) "Current concepts of the bearing capacity of foundations" Unpublished report, C.U.E.D.

ROSCOE, K.H. (1970) "The influence of strains in soil mechanics" Geotechnique, 20, pp.129-170.

ROSCOE, K.H., ARTHUR, J.R.F. & JAMES, R.G. (1963) "The determination of strains in soils by an X-ray method" Civ. Engng. publ. Wks. Rev. 58, No.684, 876 and 59, No. 685, 1009-1012.

ROWE, P.W. (1962) "The stress-dilatancy relation for static equilibrium of an assembly of particles in contact" Proc. Roy. Soc. A,269 pp.500-527.

ROWE, P.W. & PEAKER, K. (1965) "Passive earth pressure measurements" Géotechnique 15, No.1, pp.57-78.

SANGLERAT, G. (1972) "The penetrometer and soil exploration" Elsevier Publishing Comp.,

SARAN, S. & PRAKASH, S. (1971) "Bearing capacity of footings under inclined loads" Soils and Foundations, Vol-11, 1, pp.47-52.

SCHMERTMANN, J.H. (1970) "Static cone to compute static settlement over sand" J. Soil Mech. Found. Div., ASCE, 96, (SM3), p.1011.

SCHNEEBELI, G. (1957) "Une analogie méchanique pour l'étude de la stabilité des ouvrages en terre à deux dimensions" Proc. 4th ICSMFE, Vol.II, pp.228-232.

SCHOFIELD, A.N. (1959) "The development of lateral force during the displacement of sand by the vertical face of a rotating model foundation" Ph.D. thesis, University of Cambridge.

SCHULTZE, E. (1961) "Distribution of stress beneath a rigid foundation" Proc. 5th ICSMFE, Vol. I, pp.807-813.

SCOTT, R.F. (1963) "Principles of soil mechanics" Addison-Wesley.

SELIG, E.T. & McKEE, K.G. (1961) "Static and dynamic behaviour of small footings" Soil Mech. Found. Div., ASCE, 87, (SM6), pp.29-47.

SIMONS, N.E. and MENZIES, B.K. (1975) "A short course in foundation engineering" IPC Science and Technology Press Ltd., England.

SKORMIN, G.A. & MALYSHEV, M.V. (1970) "Experimental investigation of the stress distribution in sandy foundation beds beneath a circular foundation with increasing load" Soil Mech. Found. Eng., Transl. 5, pp.297-302.

SMITH, I.A.A. (1972) "Stress and strain in a sand mass adjacent to a modal wall" Ph.D. thesis, University of Cambridge.

SMOLTCZYK, H.U. (1967) "Stress computation in soil media" J. Soil Mech. Found. Div., ASCE, 93 (SM2) pp.101-124.

SNARSKII, A.S. (1974) "Stresses and displacements in the soil under a circular foundation" Transl. from Osnovaniya, Fundamenty i Mekhanika Gruntov, No.5, pp.38-40, Sept.-Oct.

SOKOLOVSKII, V.V. (1965) "Statics of granular media" Pergamon Press, New York.

STROUD, M.A. (1971) "The behaviour of sand at low stress levels in the simple shear apparatus" Ph.D. thesis, University of Cambridge.

SUTHERLAND, H.B. (1974) "Granular materials" (Review Paper), Proc. Conf. on the Settlement of Structures, Cambridge.

SCHOFIELD, A.N. & WROTH, C.P. (1968) "Critical state soil mechanics' McGraw-Hill.

SUTHERLAND, H.B. & LINDSAY (1961) "Measurement of load distribution under two adjacent column footings" Proc. 5th ICSMFE, Vol.I, pp.829

TANNER, A. (1971) "The design and development of a model system for passive earth pressure tests" M.Sc. thesis, University of Southampton.

TANNER, A. (1971) "The design and development of a model system for passive earth pressure tests" M.Sc. thesis, University of Southampton.

TAYLOR, D.W. (1938) "Discussion" Trans. ASCE, Vol.103, pp.852.

TENNEKOON, B.L. (1970) "Stresses and strains induced by a strip footing on sand" Ph.D. thesis, University of Cambridge.

TERZAGHI, K. (1943) "Theoretical soil mechanics" Wiley, New York.

TICOF, J. (1974) "Liquefaction phenomena in sands" Research Report - Cambridge University Engineering Department.

TROLLOPE, D.H. and LEE, I.K. (1961) "The measurement of soil pressures" Proc. 5th ICSMFE, Vol.II, pp.493-499.

TSCHEBOTARIOFF, G.P. (1951) "Soil mechanics- foundations and earth structures" New York, McGraw-Hill.

TSYTOVICH, N.A. (1961) "General report" Proc. 5th ICSMFE, Vol.II, pp.824-835.

VESIC, A.S. (1963) "Bearing capacity of deep foundations in sand" Highw. Research Record. 39, pp.112-153.

VESIC, A.S. (1973) "Analysis of ultimate loads of shallow foundations" J. Soil Mech. Found. Div., ASCE, 99 (SM1), pp.45-73.

VESIC, A.S. (1973) "Discussion" J. Soil Mech. Found. Div. ASCE, 99 (SM7) pp.575-577.

VESIC, A.S. & CLOUGH, G.W. (1968) "Behaviour of granular materials under high stresses" J. Soil Mech. Found. Div., ASCE, 94 (SM3), pp.661-688.

WEISS, K. (1969) "Discussion" 7th ICSMFE, Vol. III, pp.273-275.

WROTH, C.P. (1976) "Lectures on CSSM" Cambridge University.

YIP, S.F. (1977) Forthcoming M.Sc. thesis, University of Southampton.

ZAHARESCU, E. (1961a) "The eccentricity sense influence of the inclined load on the bearing capacity of rigid foundations" Journal of National Building Organization, Vol.2, pp.283-293.

TICOF, J. (1978) Dissertation to be submitted at Cambridge University.

WINDLE, D. (1976) Ph.D. thesis, University of Cambridge

ZAHARESCU, E. (1961b) "Sur la stabilite des fondations rigides" 5th ICSMFE, Vol.I, pp.867-871.

ZANGL, L.W. (1977) "Experimentelle und numerische untersuchungen eines ebenen verformungsproblems bei trockenem sand" Ph.D. thesis University of Karlsruhe.

ZARETSKY, Yu. K. AND TSYTOVICH, N.A. (1965) "Consideration of heterogeneity and non-linear deformation of the base in the design of rigid foundations" Proc. 6th ICSMFE, Vol.II, pp.222-225.

ANDRAWES, K.Z. & BUTTERFIELD, R. (1973) "The measurements of planar displacements of sand grains, Géot. 23, pp.571-575.

TABLE 1

TESTS IN THE FOOTING APPARATUS - CAMBRIDGE

TEST	INITIAL VOIDS RATIO e_o	INITIAL ECCENTR. RATIO E_o	INITIAL LOAD INCLINATION α_o(°)	MEASUREMENTS
A	0.52	0.167	0	L-D,C.S,XRT^M,SP^M
B	0.52	0	12°	L-D,C.S,XRT^M,SP^M
C	0.52	-0.167	12°	L-D,C.S,XRT^M,SP^M
D	0.52	0	0	L-D,C.S,XRT^M,SP
E	0.52	0	30°	L-D,C.S,SP
F	0.52	0	Independent H at 100 mm from footing base	L-D,C.S,SP
G	0.52	0	40°	C.S.
GB	0.52	0	20°	L-D,C.S.
H	0.52	0.167	0	L-D,C.S,S.P
K	0.52	-0.167	Independent H	L-D,C.S,XRT^M
FA	0.52	0.167	0	L-D,C.S,XRT^M

TESTS IN THE FOOTING APPARATUS - SOUTHAMPTON

AS	0.54	0.167	0	L-D,C.S,SP
BS	0.53	0	12°	L-D,C.S,SP
HS	0.53	0.167	0	L-D,C.S,SP
DS	0.53	0	0	L-D,C.S,SP^M
RS	0.54	0	5°	L-D,C.S,SP

L-D = Load-displacement relationships

XRT,SP = X-rays, Stereophotogrammetry (XRT^M,SP^M = Displacement fields measured)

C.S. = Contact stresses

H = Horizontal load

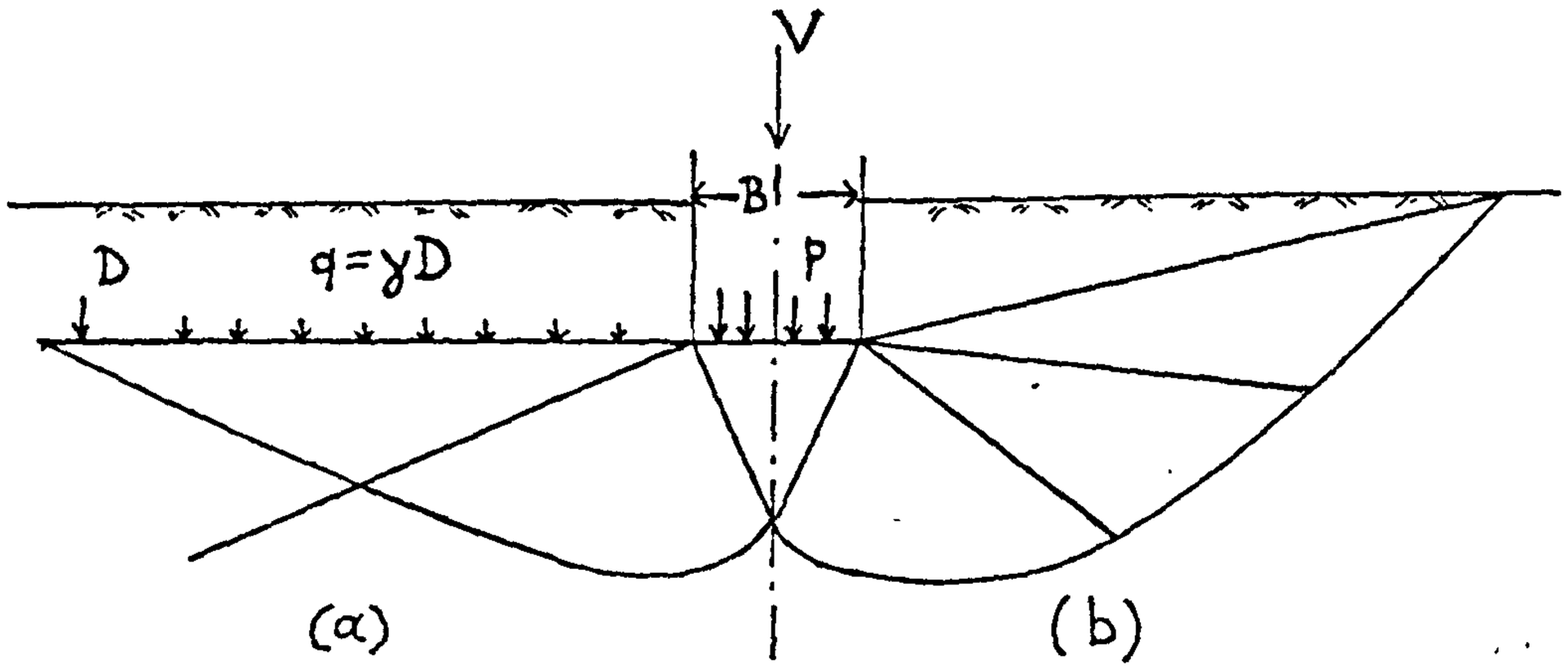

Fig. 1.1 Bearing capacity of a shallow strip footing
(a) Terzaghi's assumption (b) Meyerhof's assumption.

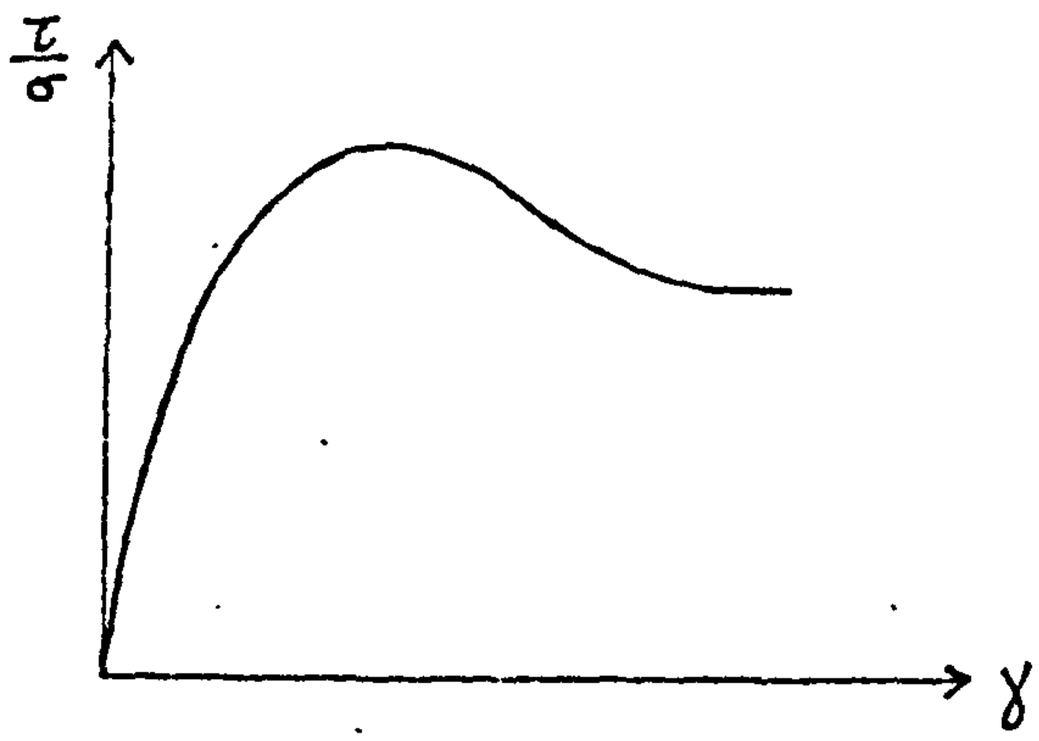

Fig. 1.2 Typical stress ratio-strain relationship for dense Leighton-Buzzard sand.

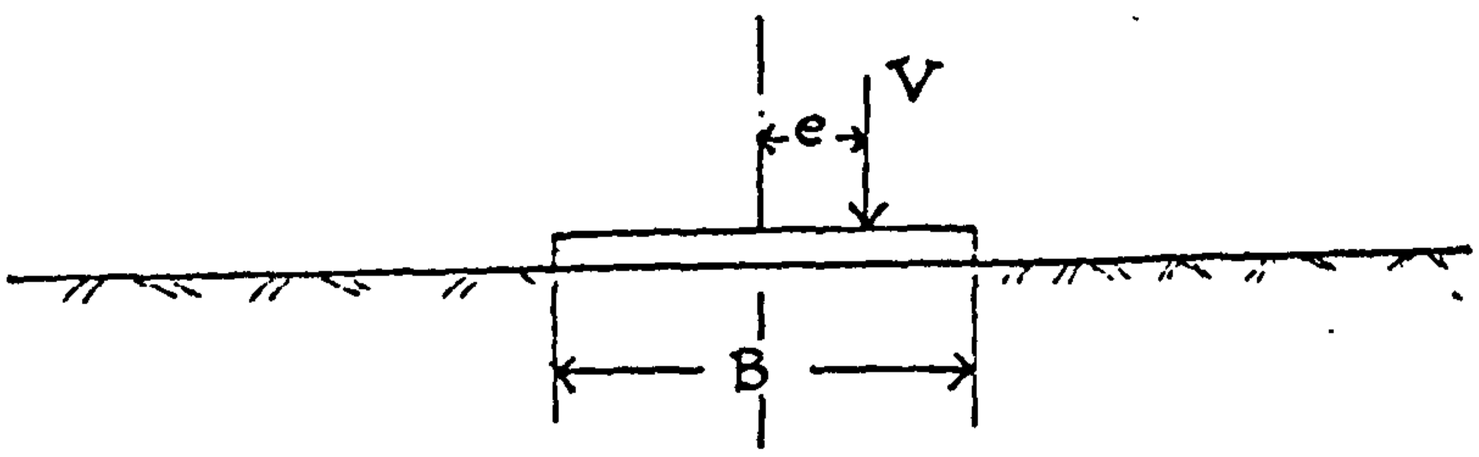

Fig. 1.3 Surface strip footing under a vertical eccentric load.

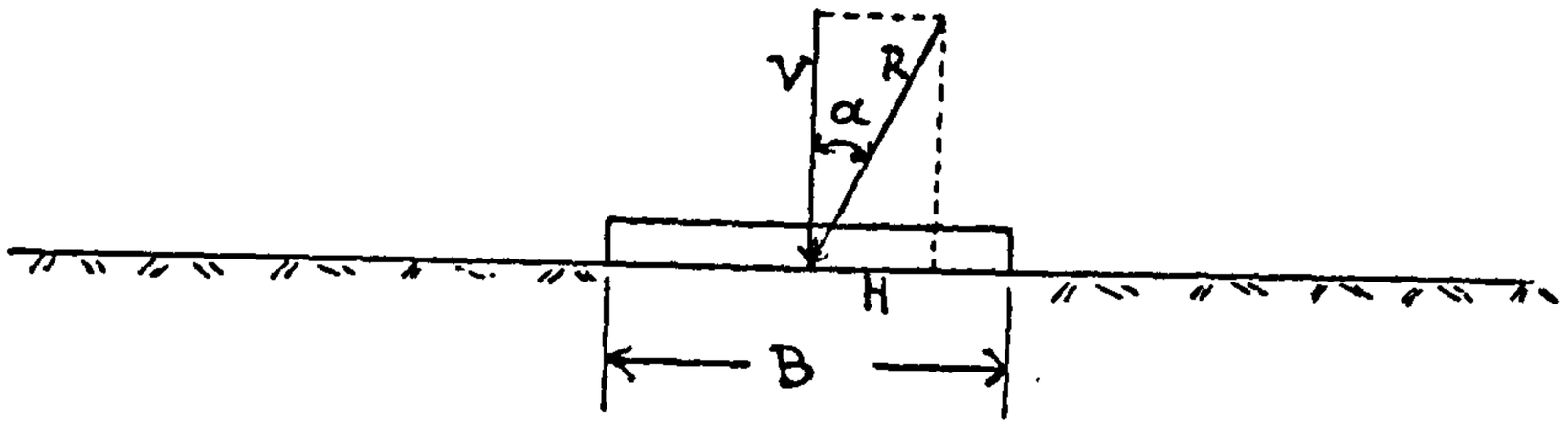

Fig. 1.4 Surface strip footing under an inclined central load.

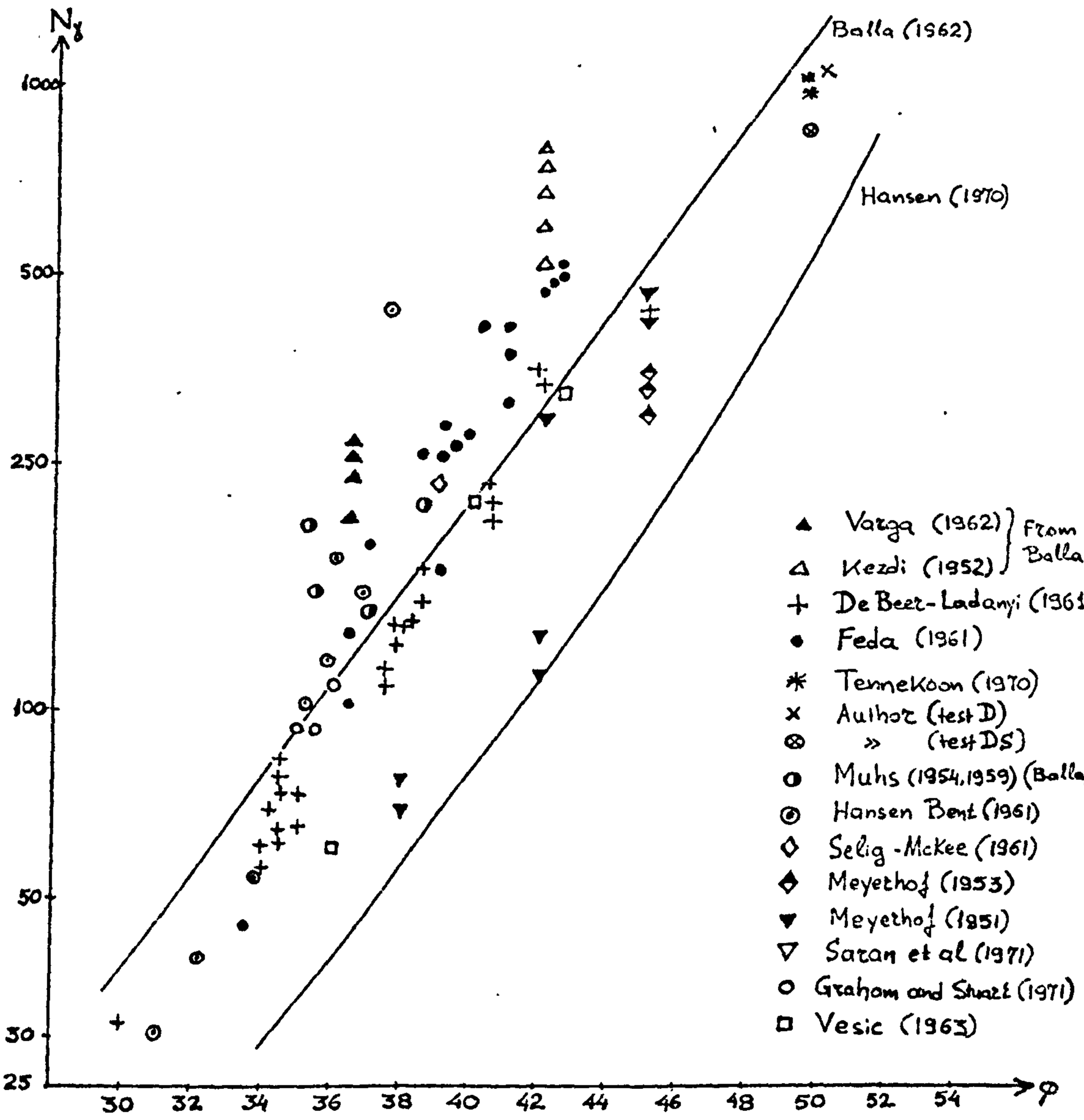

Fig. 1.5 Experimental results ($N_\gamma - \phi$) from various research workers and the Author.

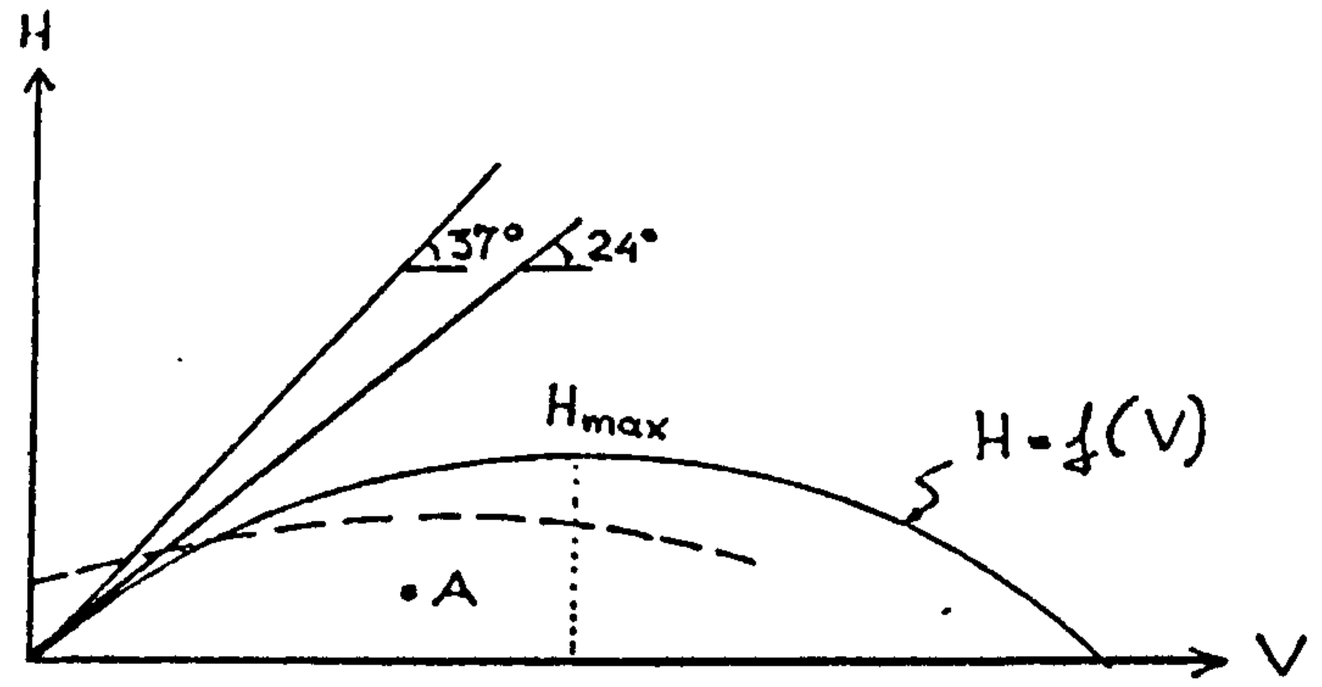

Fig. 1.6 The failure envelope for a combined V and H loading condition.

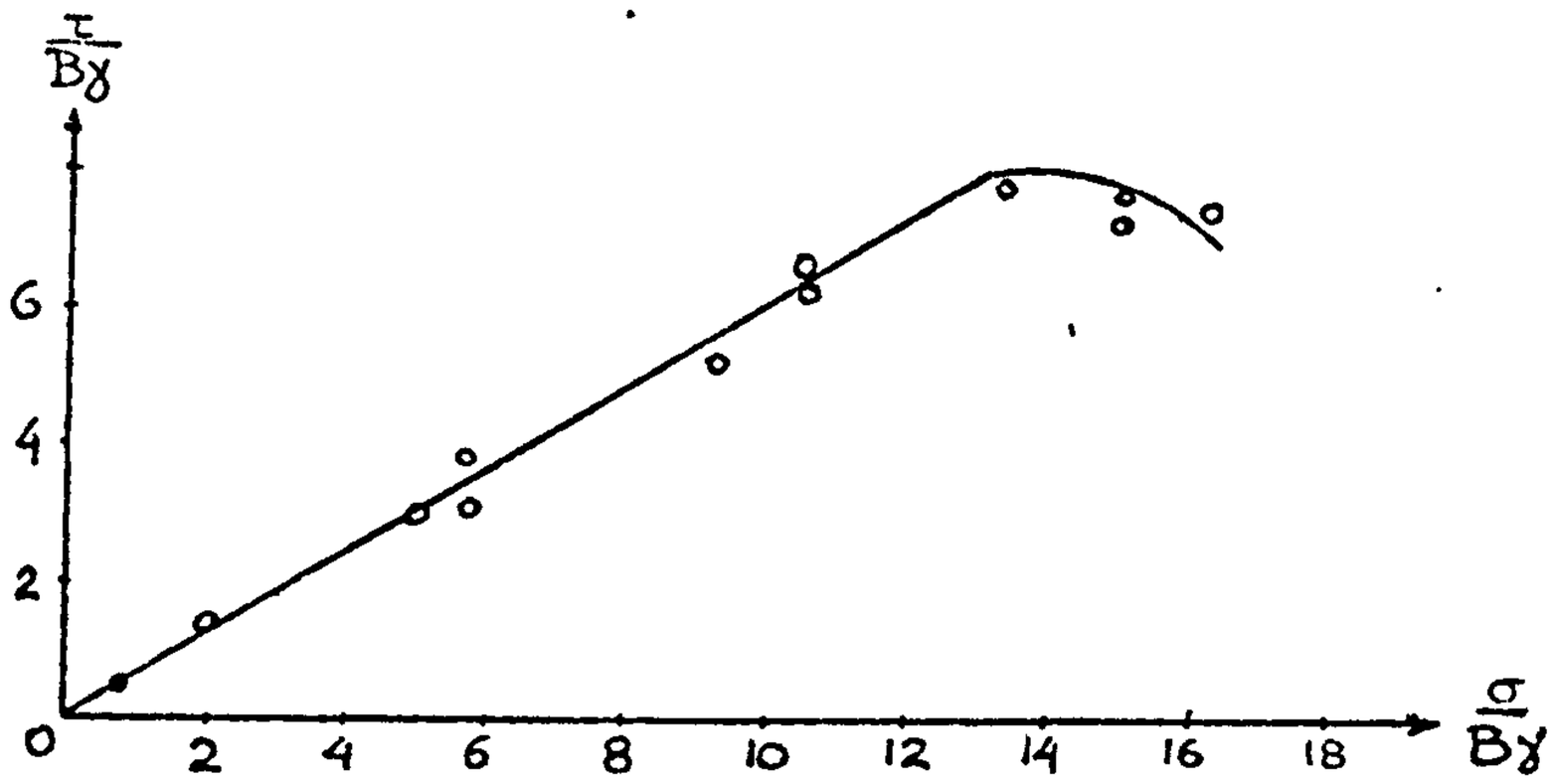

Fig. 1.7 Plate shear tests (Evdokimov et al, 1973)- B=1.25m and 2.5m.

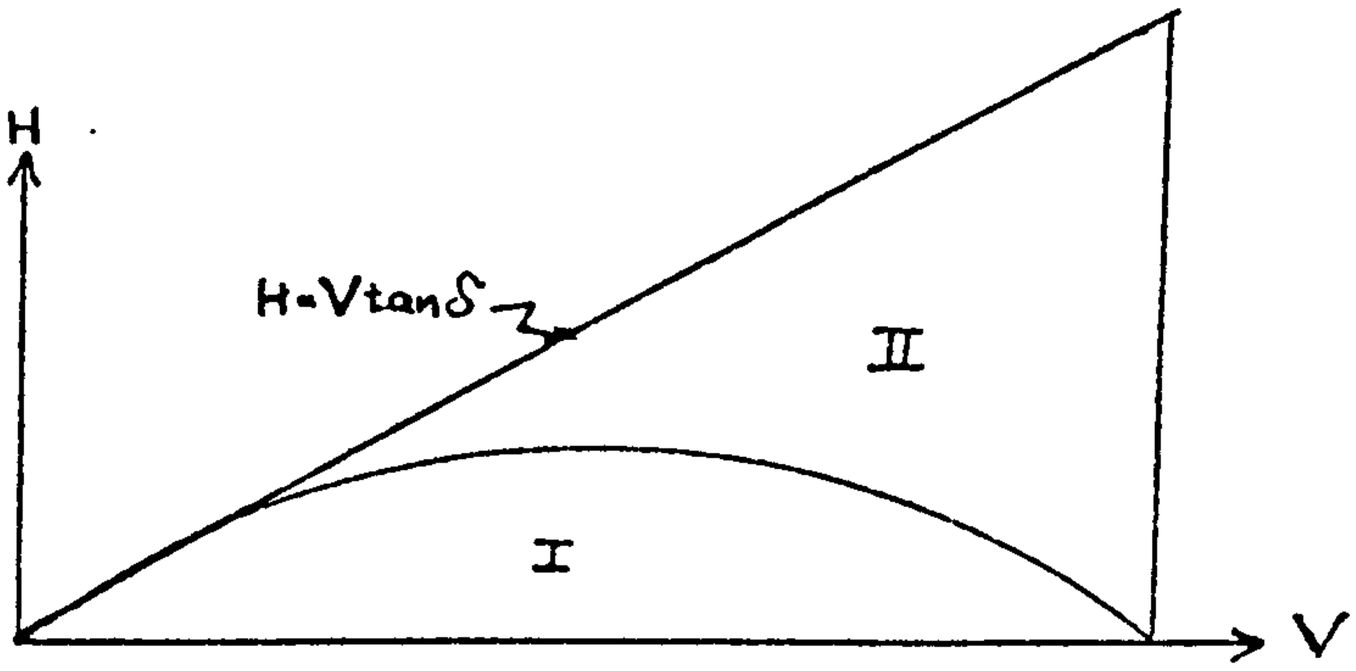

Fig. 1.8 V-H failure envelope and H=Vtanδ design curve against sliding.

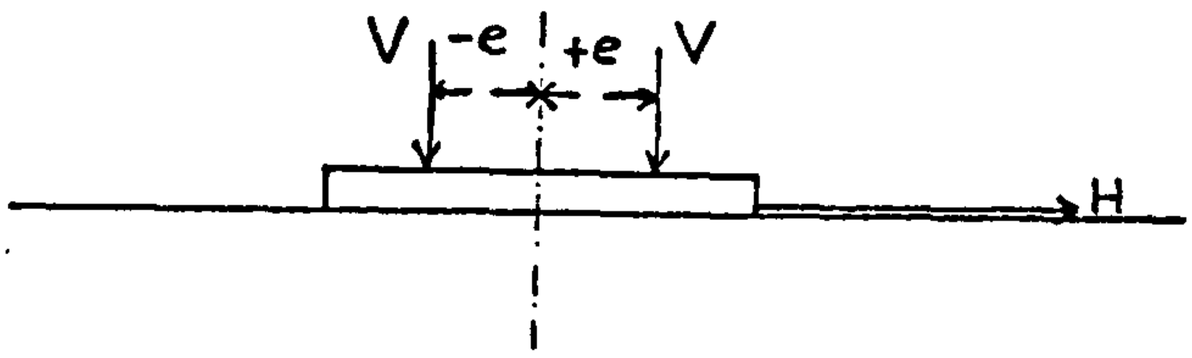

Fig. 1.9 'Positive' and 'Negative' eccentricity of the applied load.

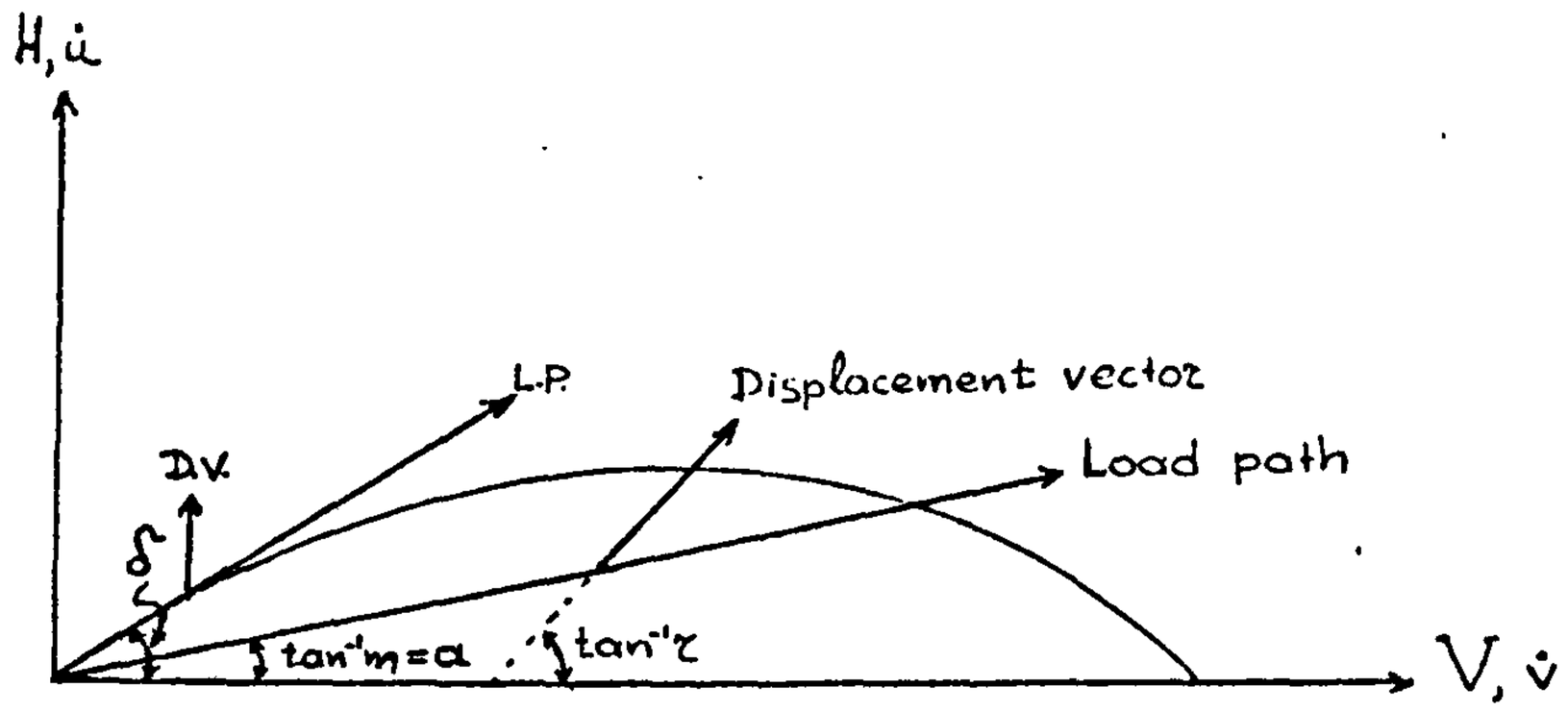

Fig. 1.10 Related displacements of a footing on sand under an inclined central load.

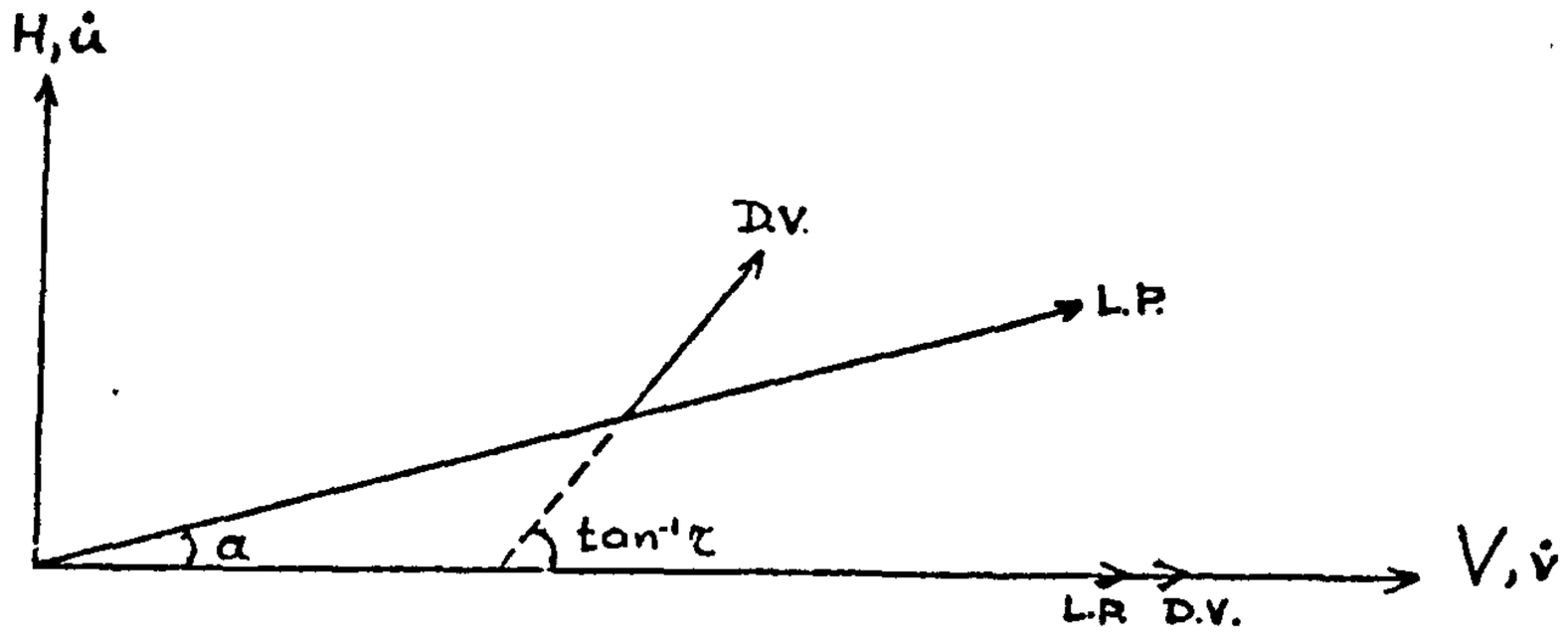

Fig. 1.11 Related displacements of a footing on a semi-infinite elastic medium under an inclined central load.

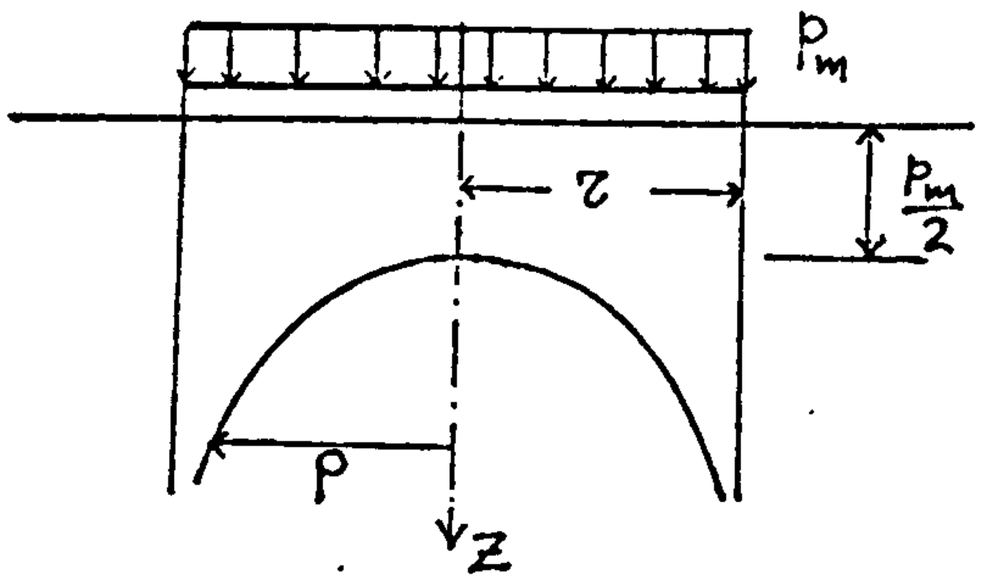

Fig. 1.12 Normal stress distribution under a uniformly loaded rigid circular footing resting on a semi-infinite elastic medium.

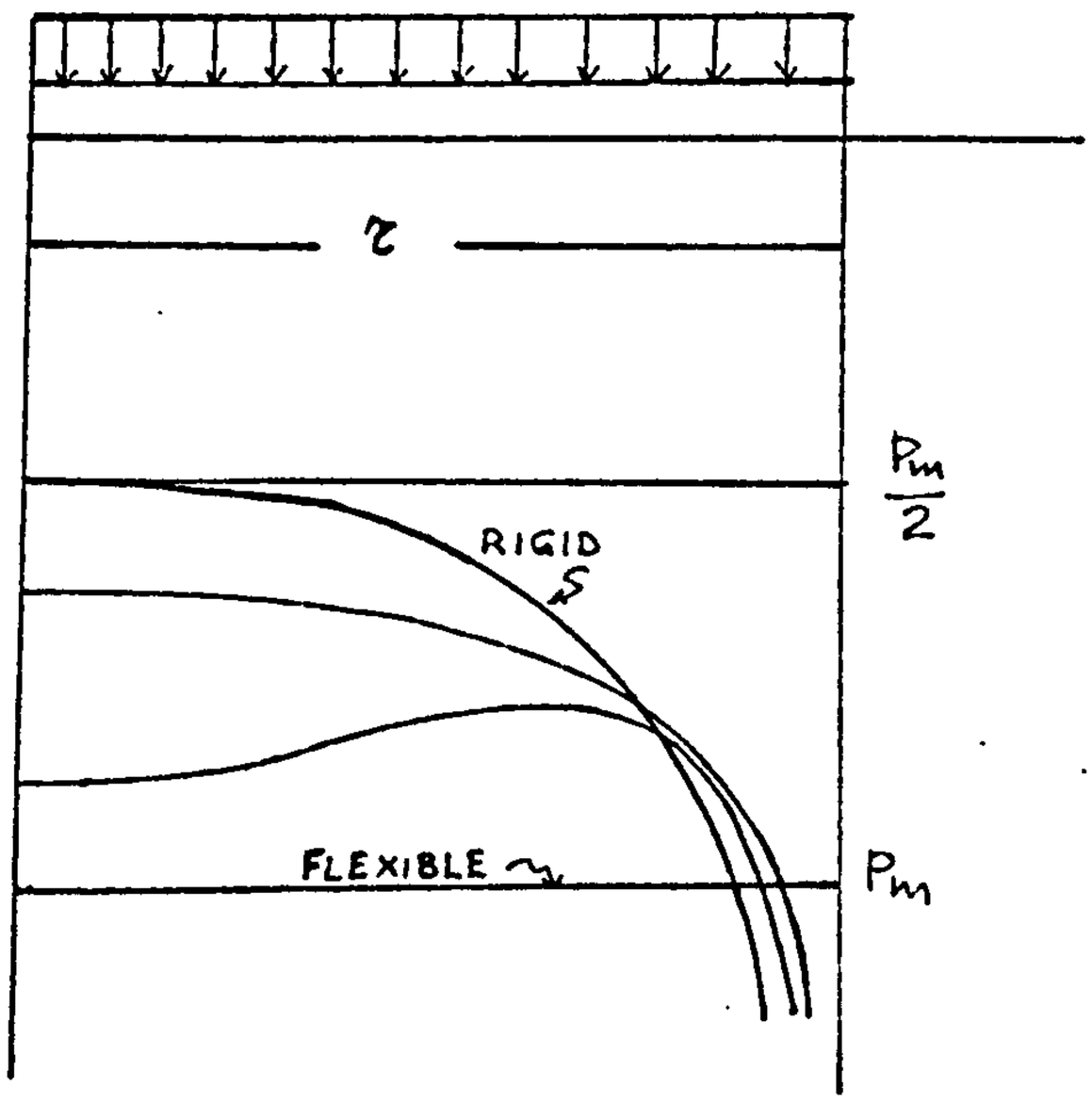

Fig. 1.13 Normal stress distribution under a uniformly loaded circular footing of varying stiffness resting on a semi-infinite elastic medium (Brówicka,1936).

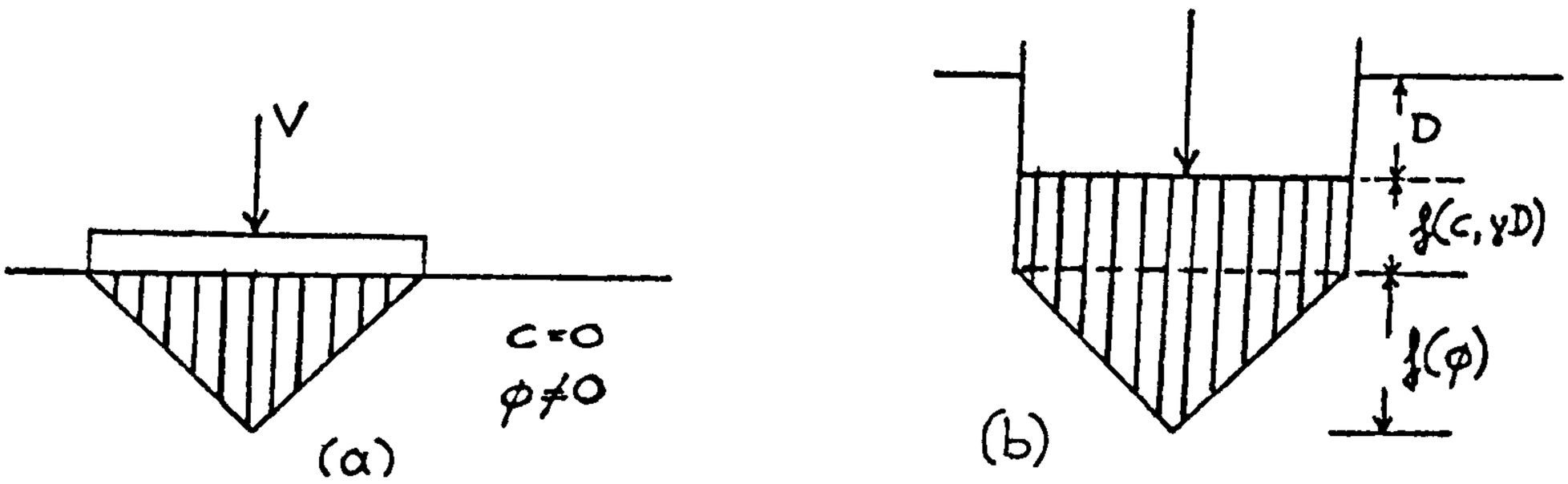

Fig. 1.14 Normal stress distribution under a rigid strip footing (a) For soil with c=0, $\phi \neq 0$ (b) For soil with c, ϕ, $\gamma \neq 0$.

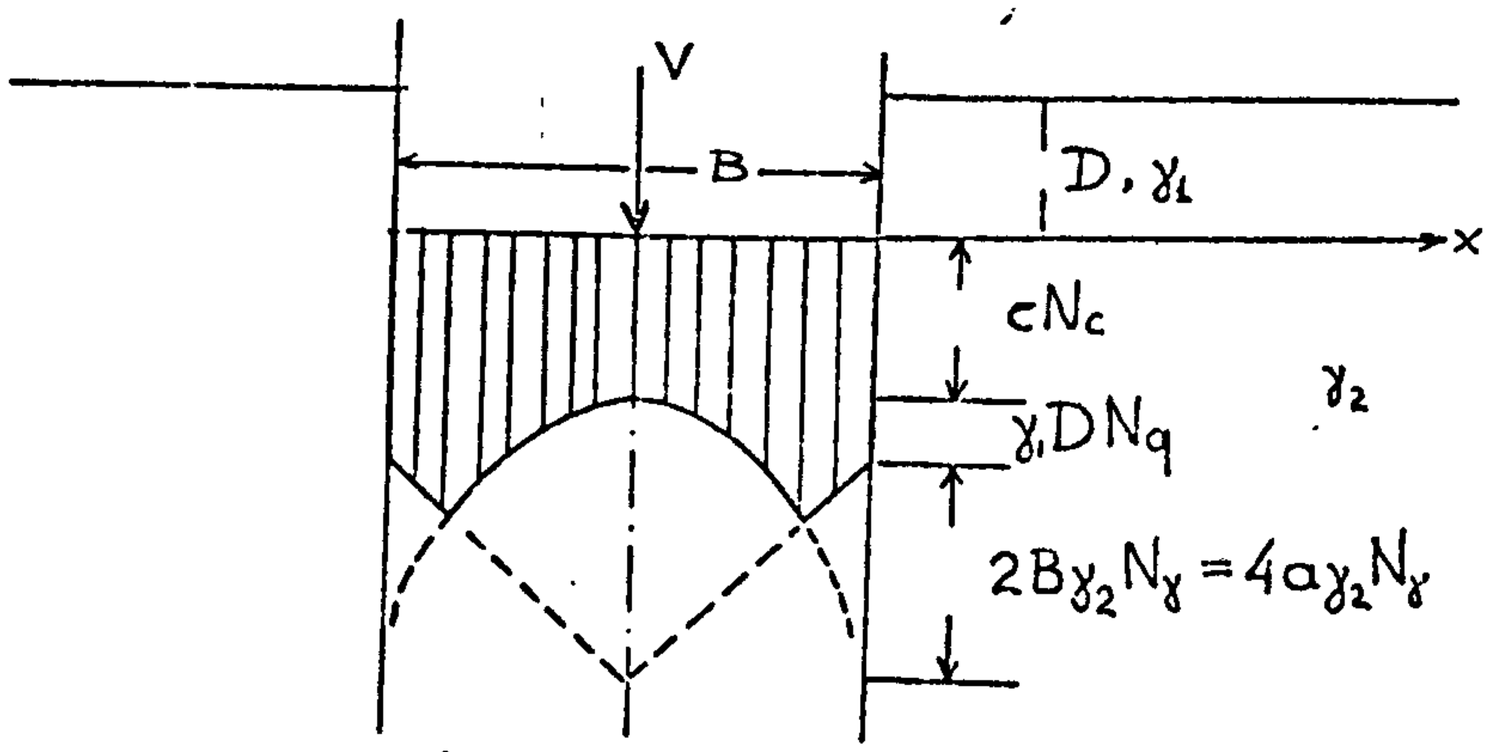

Fig. 1.15 Normal stress distribution predicted (Schultze,1961).

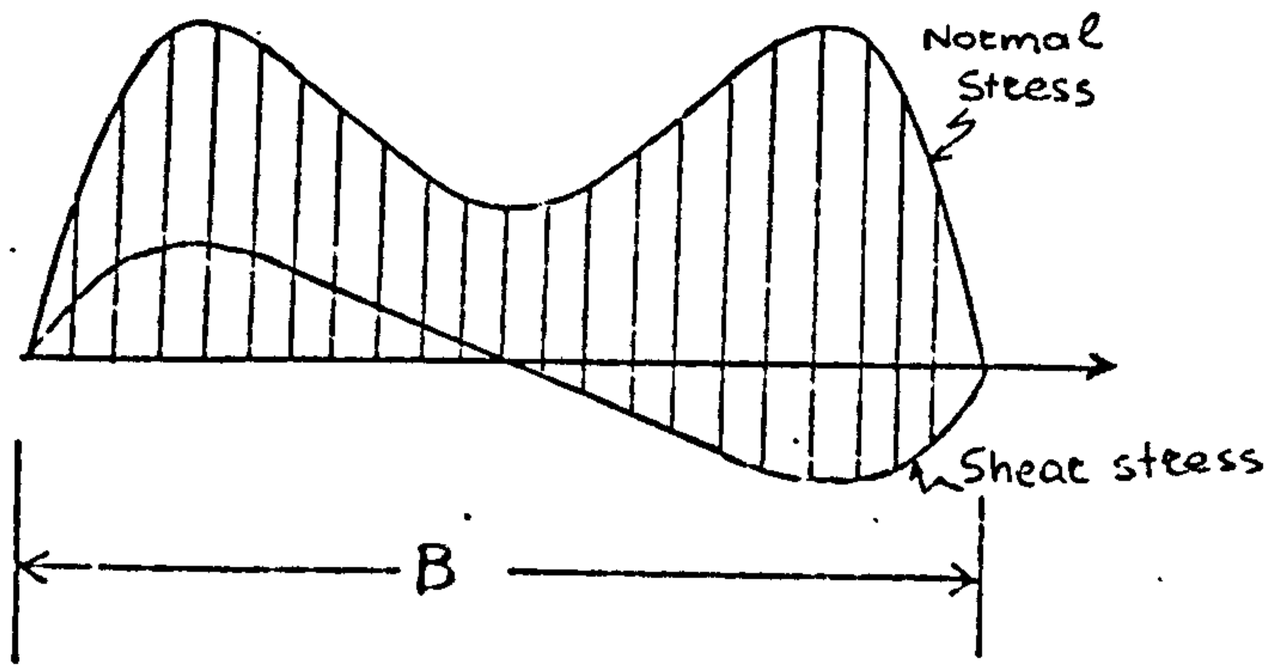

Fig. 1.16 Normal and shear stress distribution predicted (Gorbunov-Possadov (1961)).

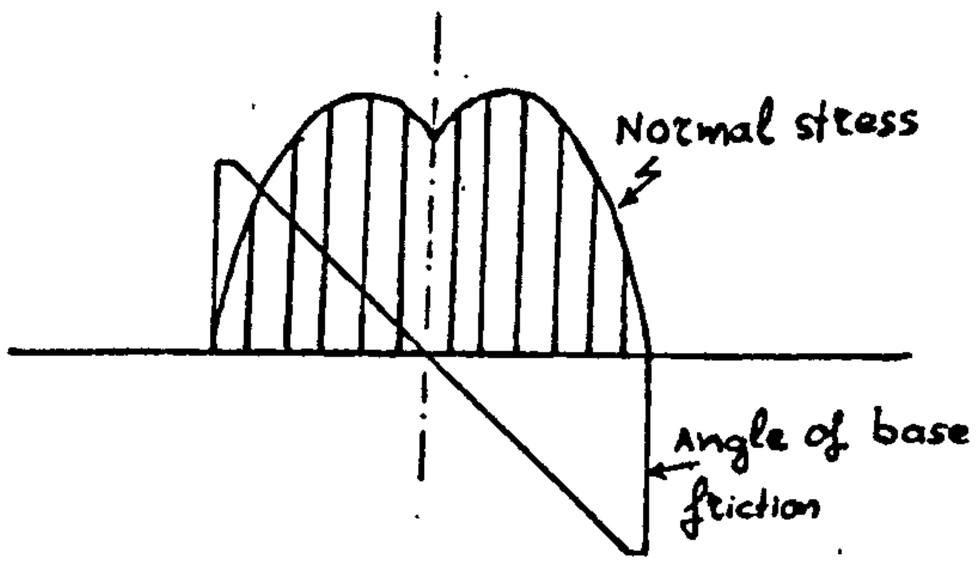

Fig. 1.17 Normal stress distribution predicted (Graham and Stuart,1971).

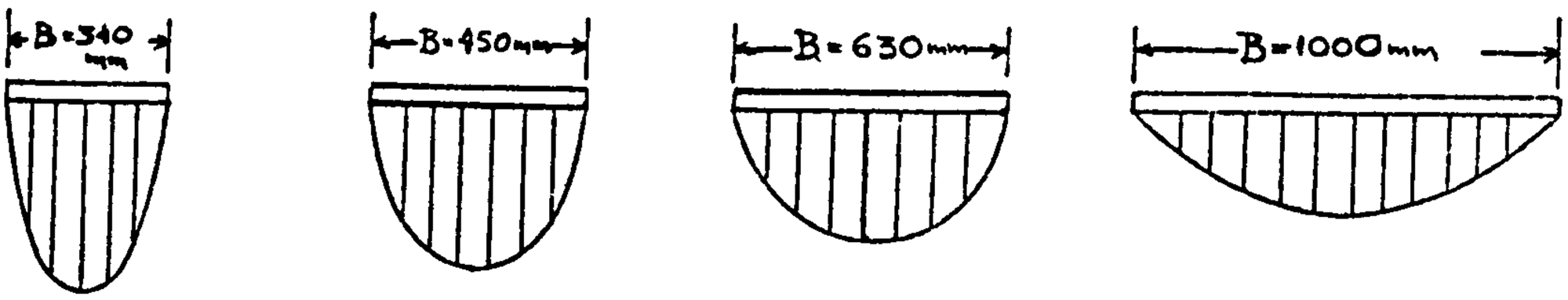

Fig. 1.18 Normal stress distribution measured (Köegler and Scheidig, 1929).

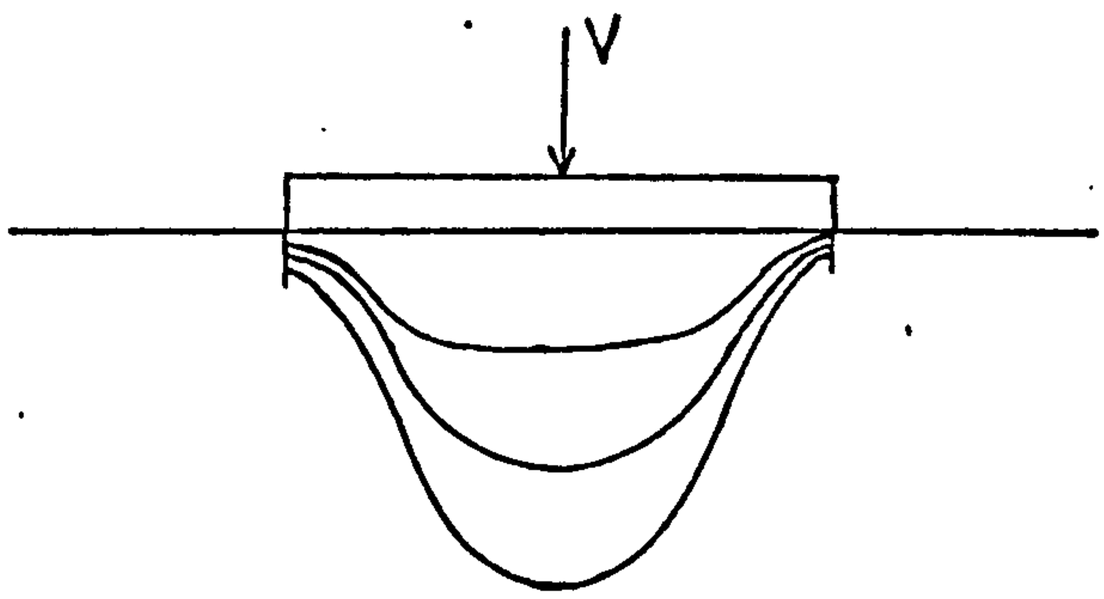

Fig. 1.19 Normal stress distribution measured (Faber, 1933).

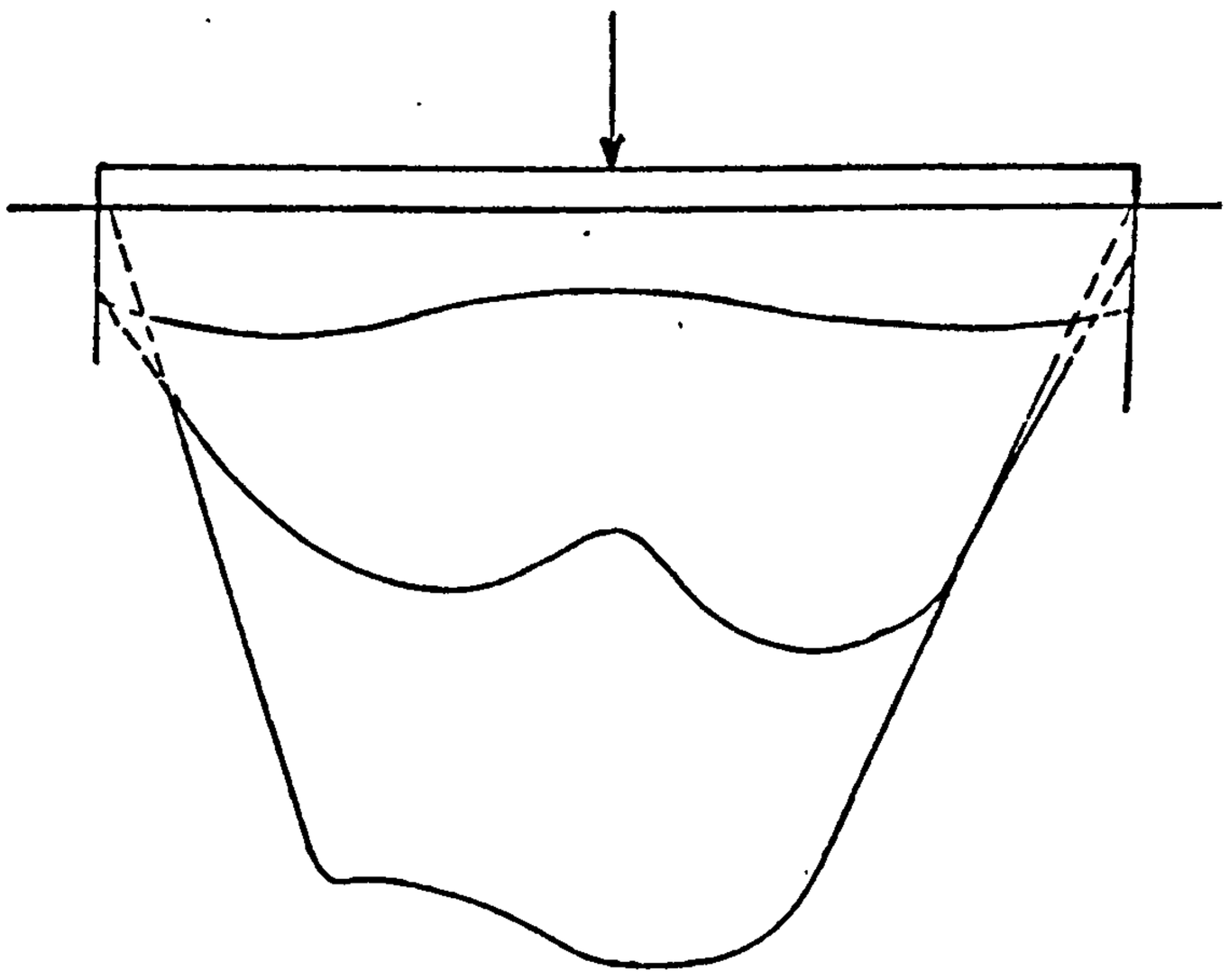

Fig. 1.20 Normal stress distribution measured (Leussink and Schweickert,1963).

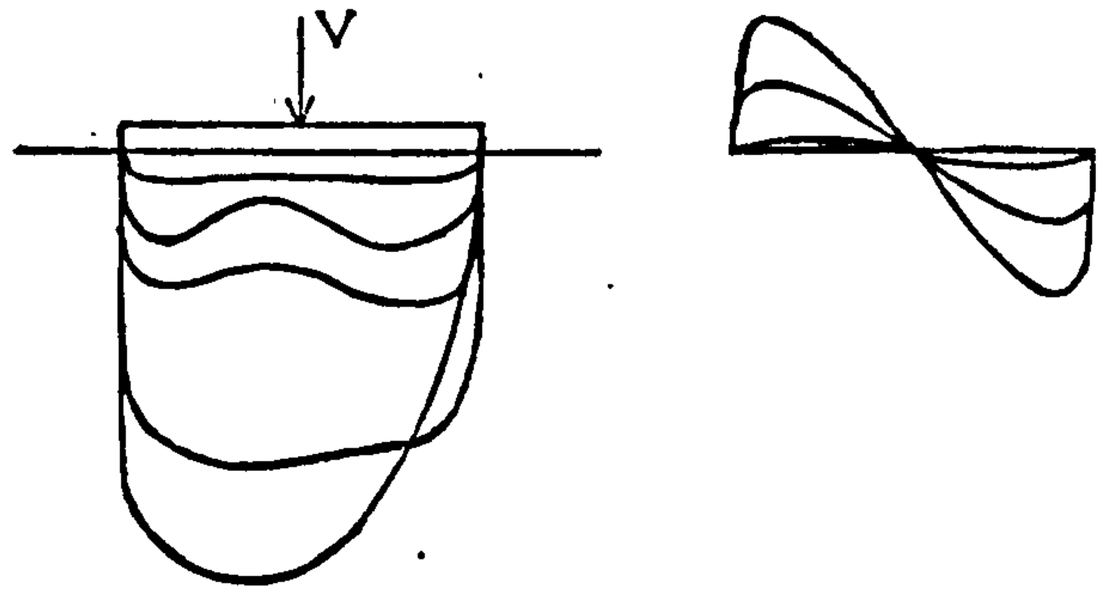

Fig. 1.21 Normal and Shear stress distribution measured (Muhs,1965).

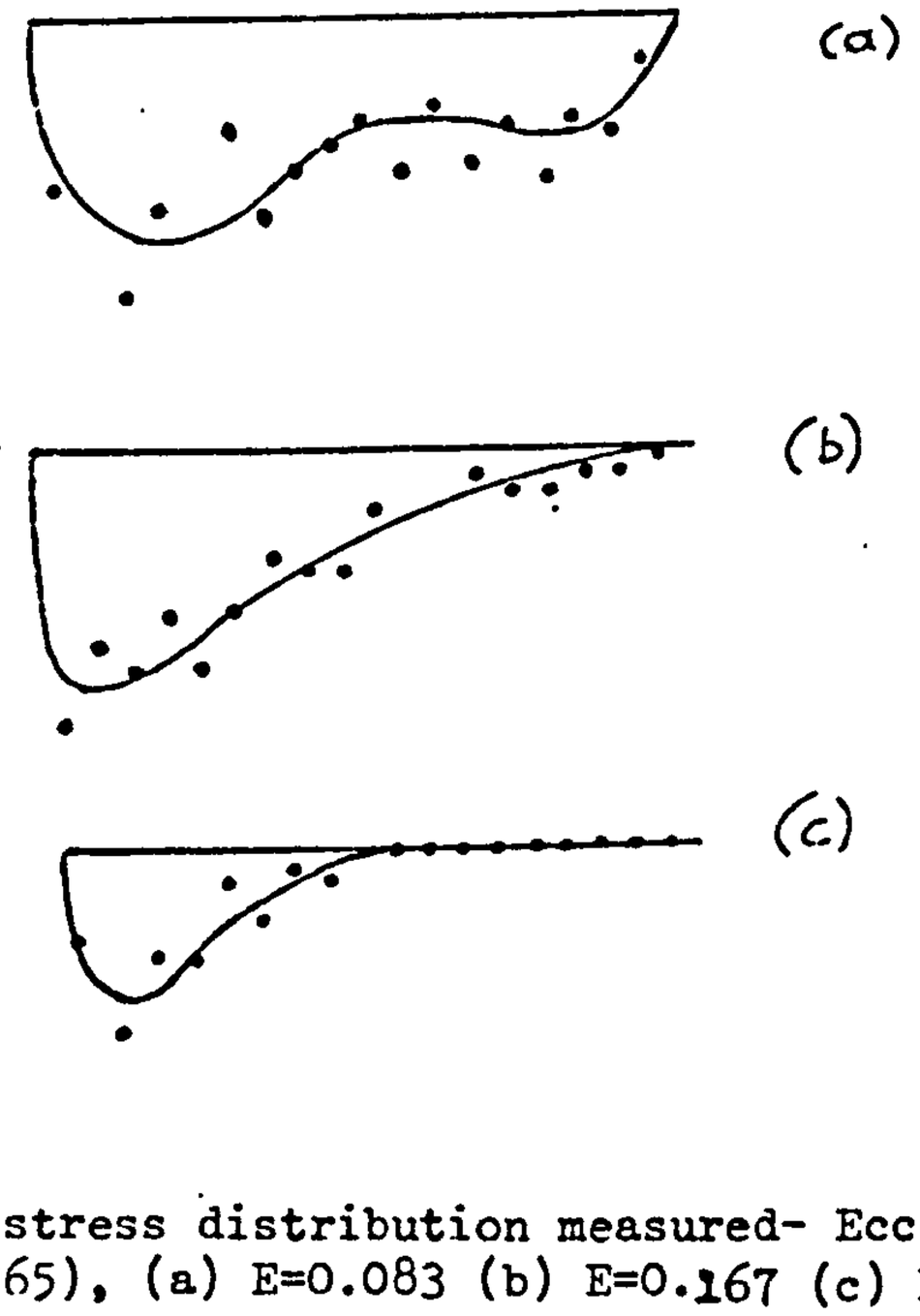

Fig. 1.22 Normal stress distribution measured- Eccentric vertical load (Lee,1965), (a) E=0.083 (b) E=0.167 (c) E=0.333.

Fig. 2.1 The small footing rig

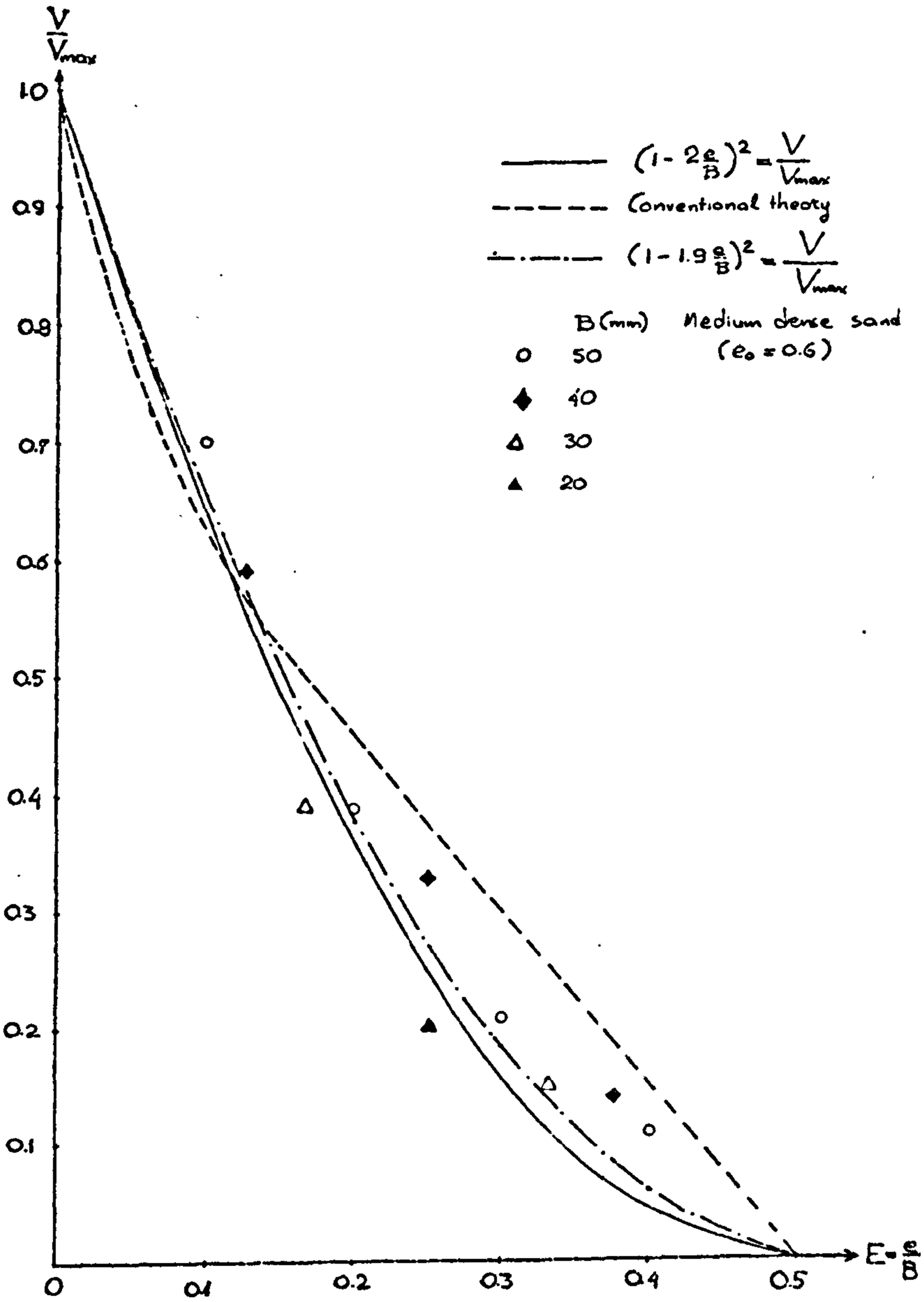

Fig. 2.2 V/V_{max} versus E=e/B. Results obtained by the Author.

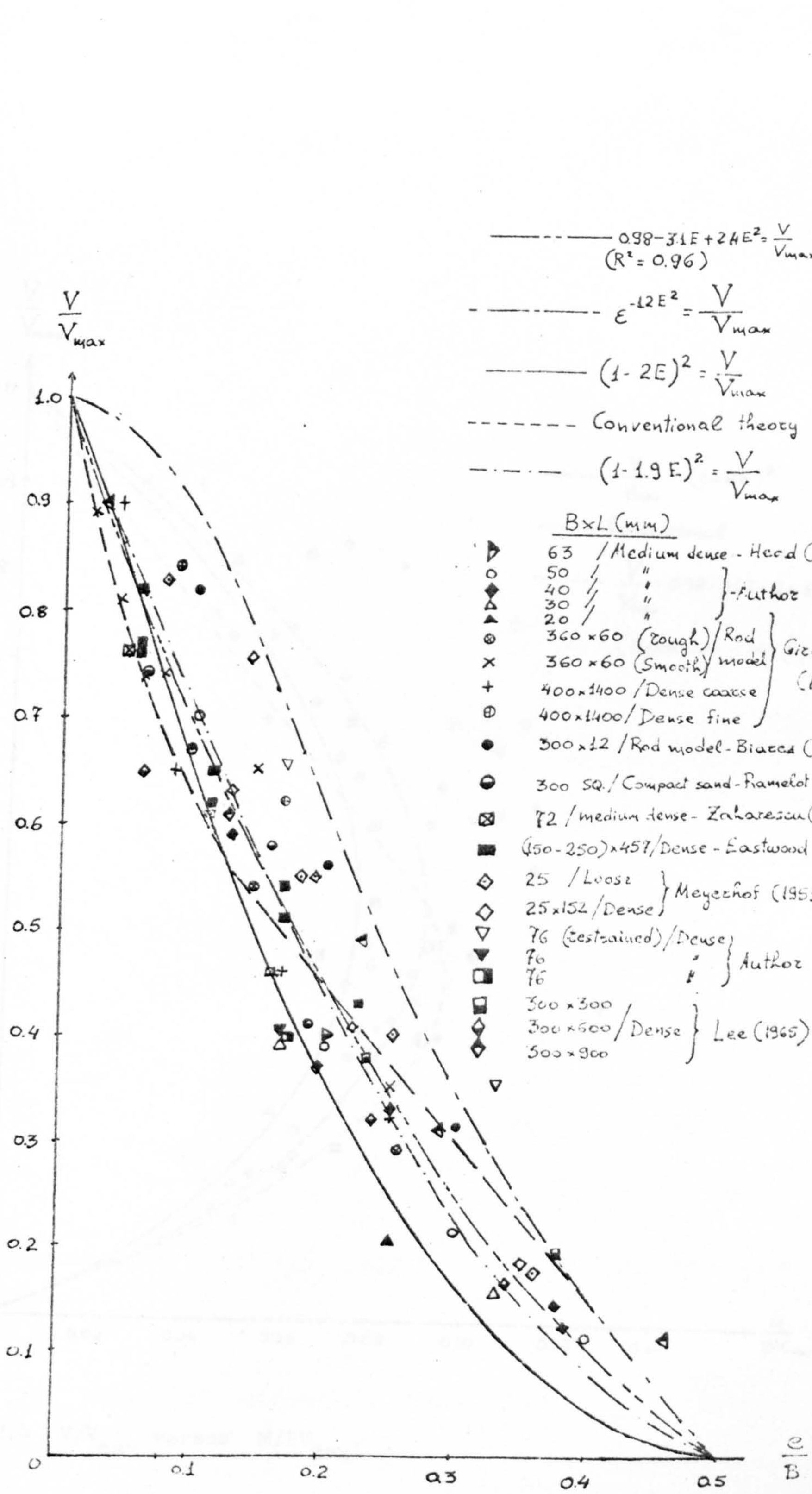

Fig. 2.3 V/V_{max} versus E=e/B. Results obtained by many research workers.

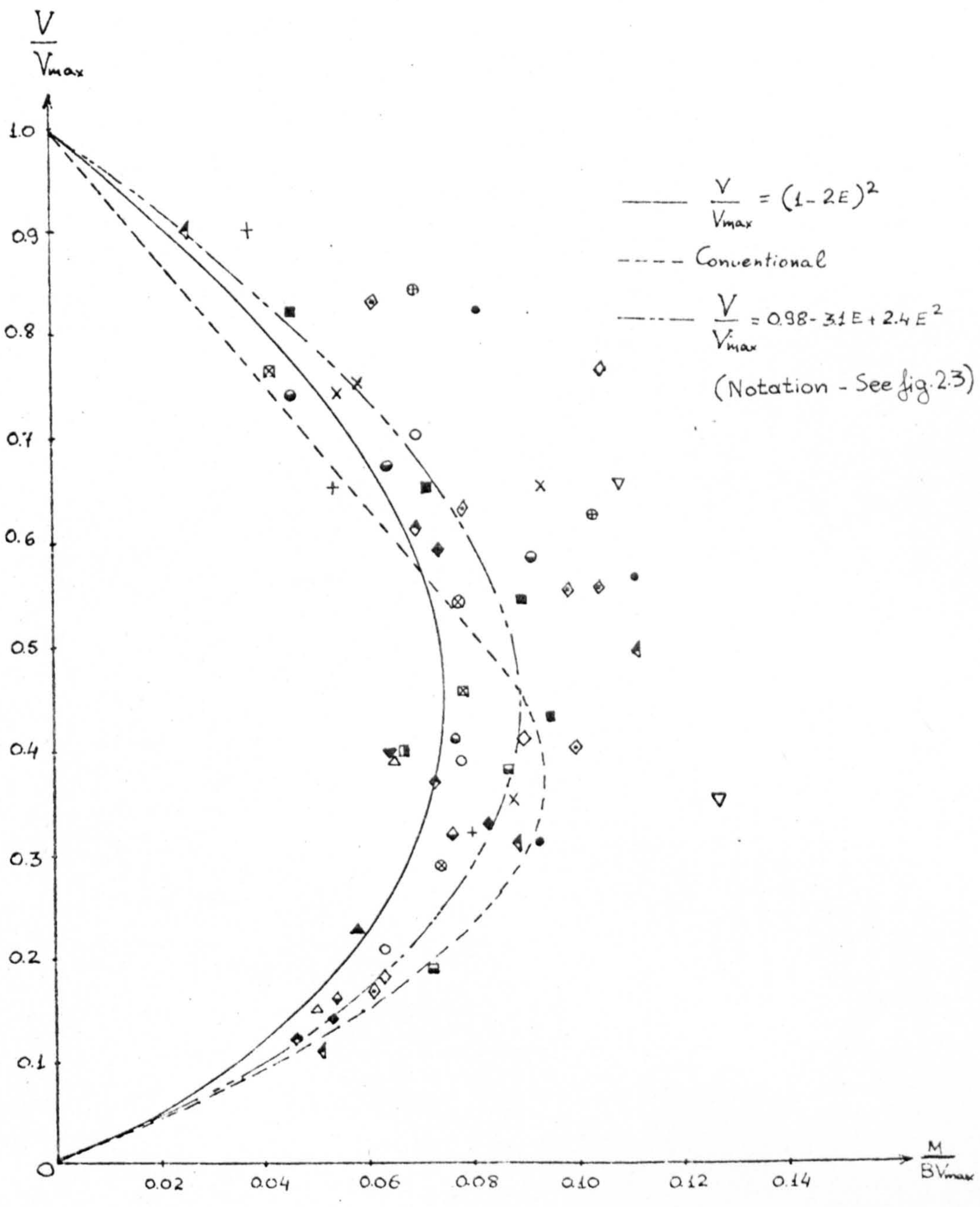

Fig. 2.4 V/V_{max} versus M/BV_{max}.

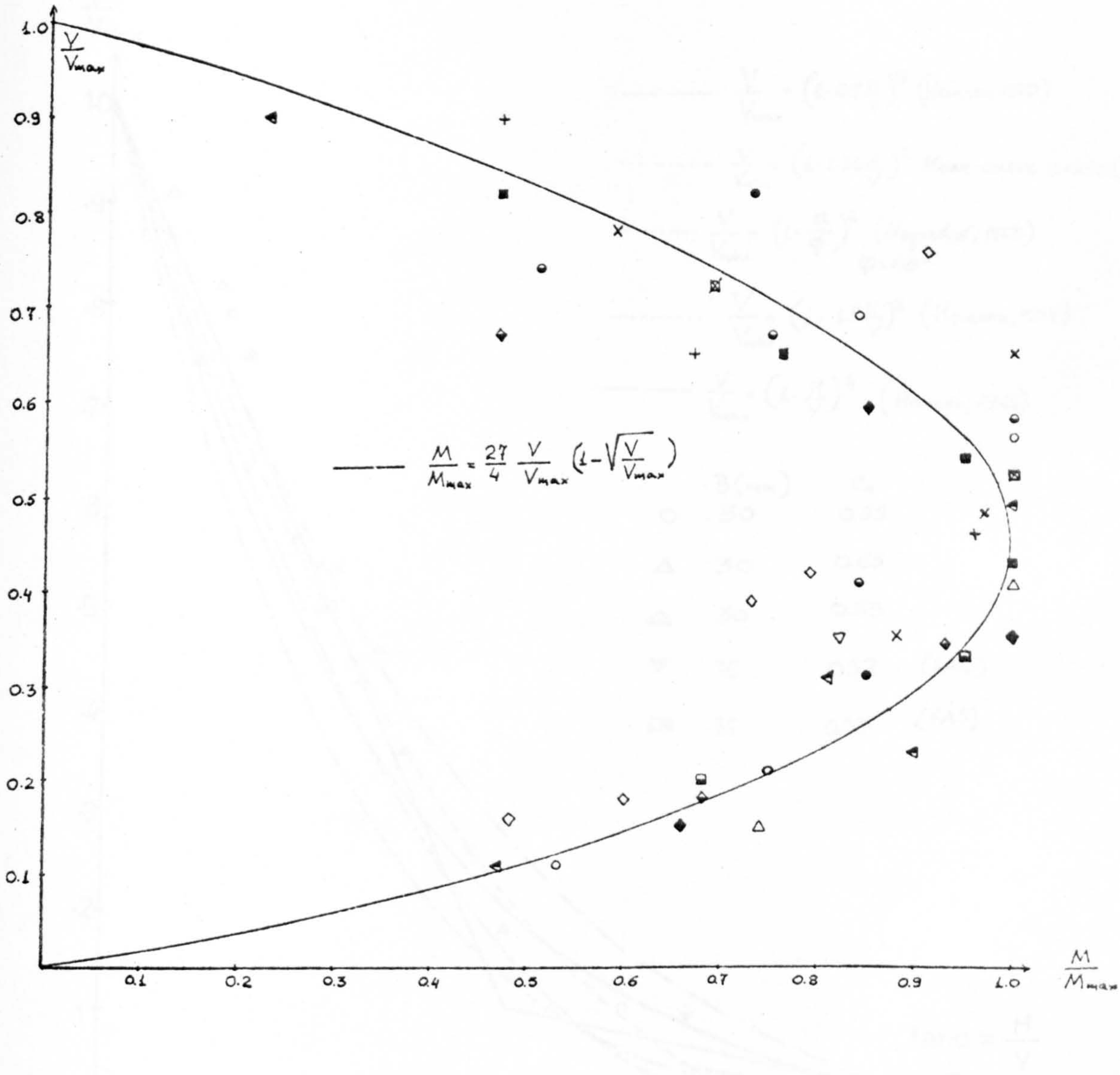

Fig. 2.5 Normalized Load-moment relationship (V/V_{max} versus M/M_{max}).

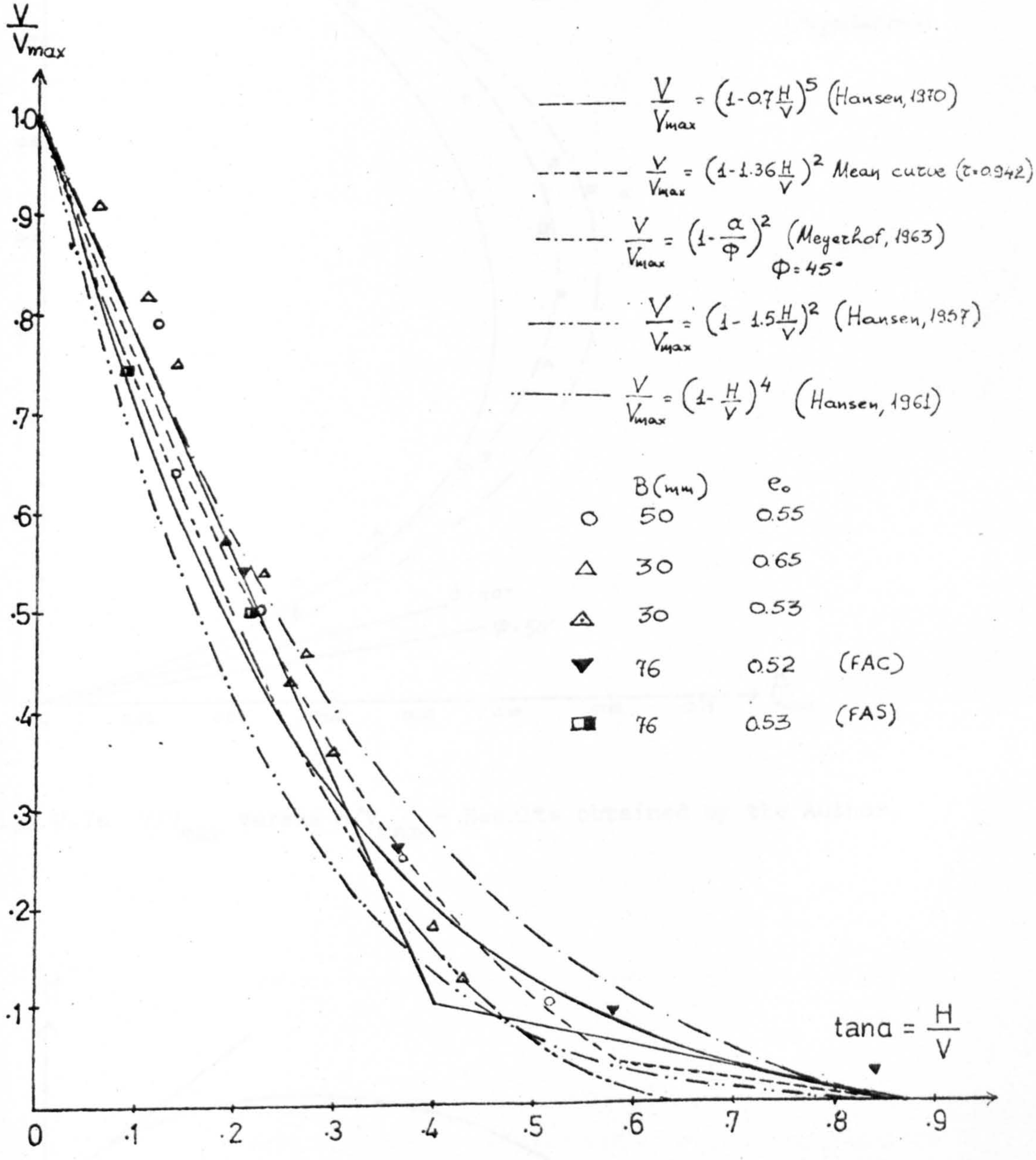

Fig. 2.6 V/V_{max} versus $\tan\alpha = H/V$ - Results obtained by the Author.

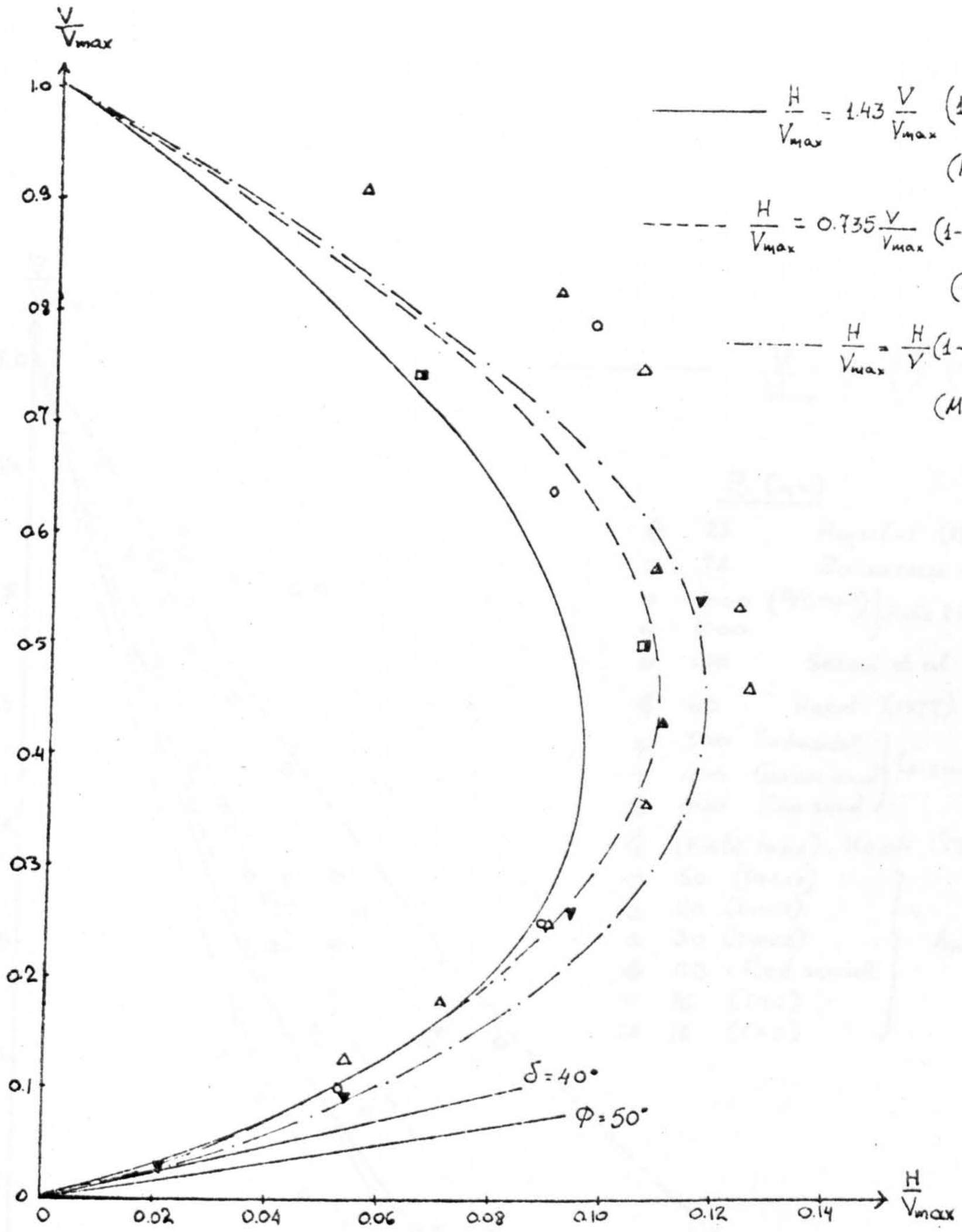

Fig. 2.7a V/V_{max} versus H/V_{max} - Results obtained by the Author.

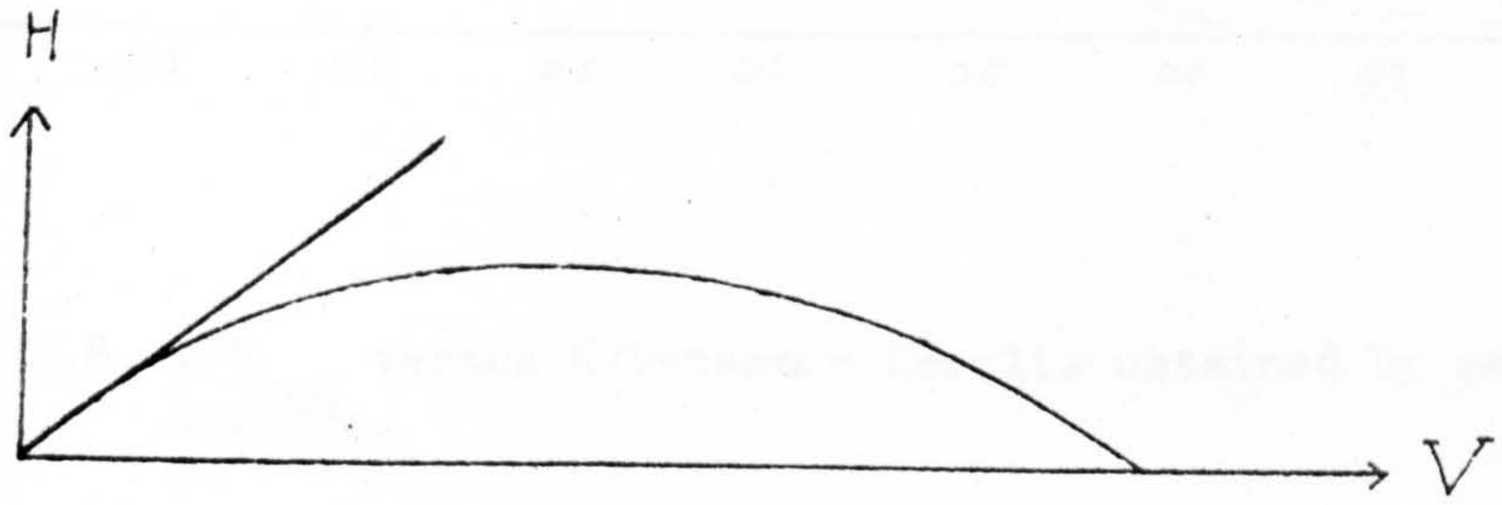

Fig. 2.7b V-H failure envelope.

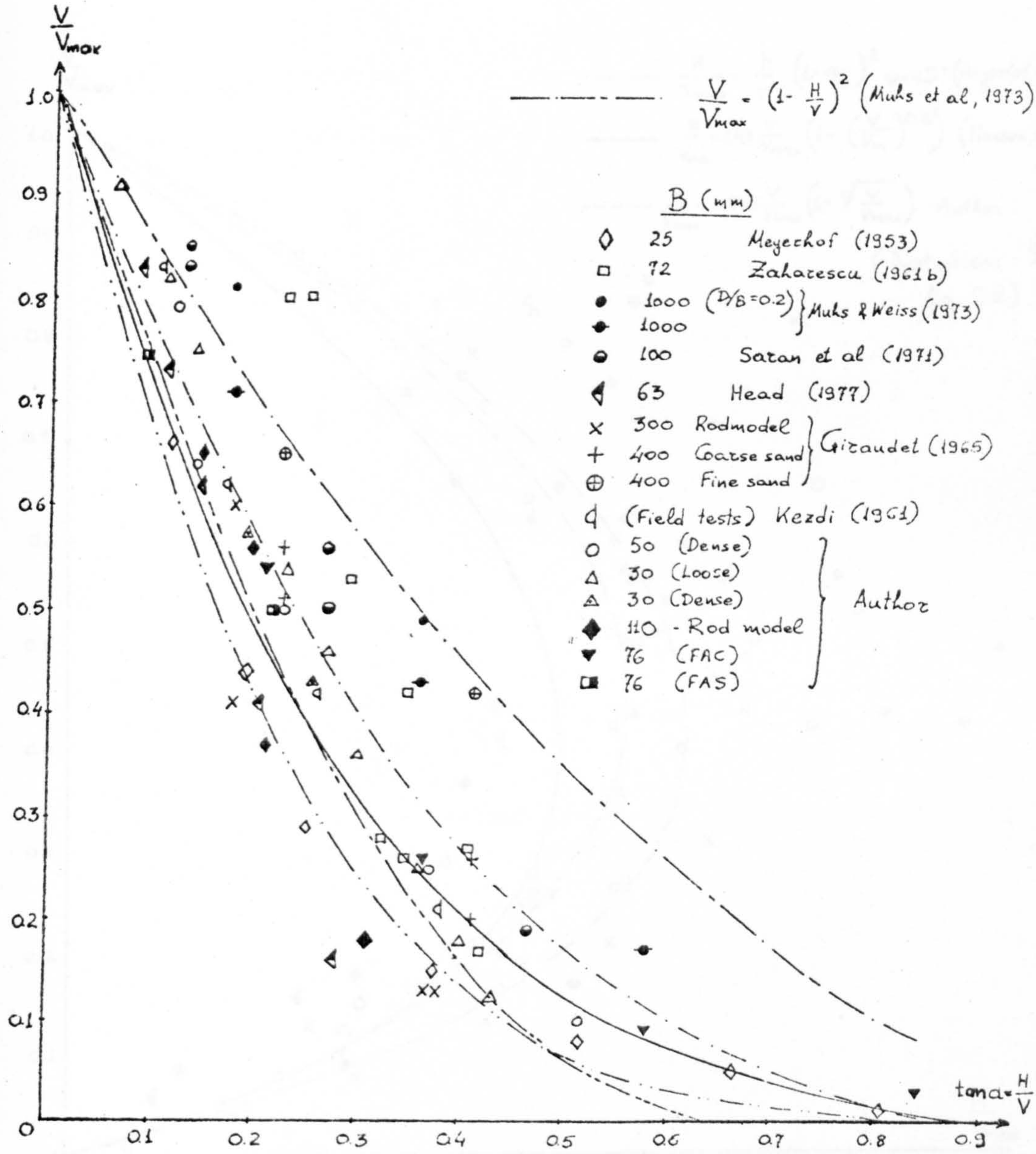

Fig. 2.8 V/V_{max} versus $H/V=\tan\alpha$ - Results obtained by many research workers.

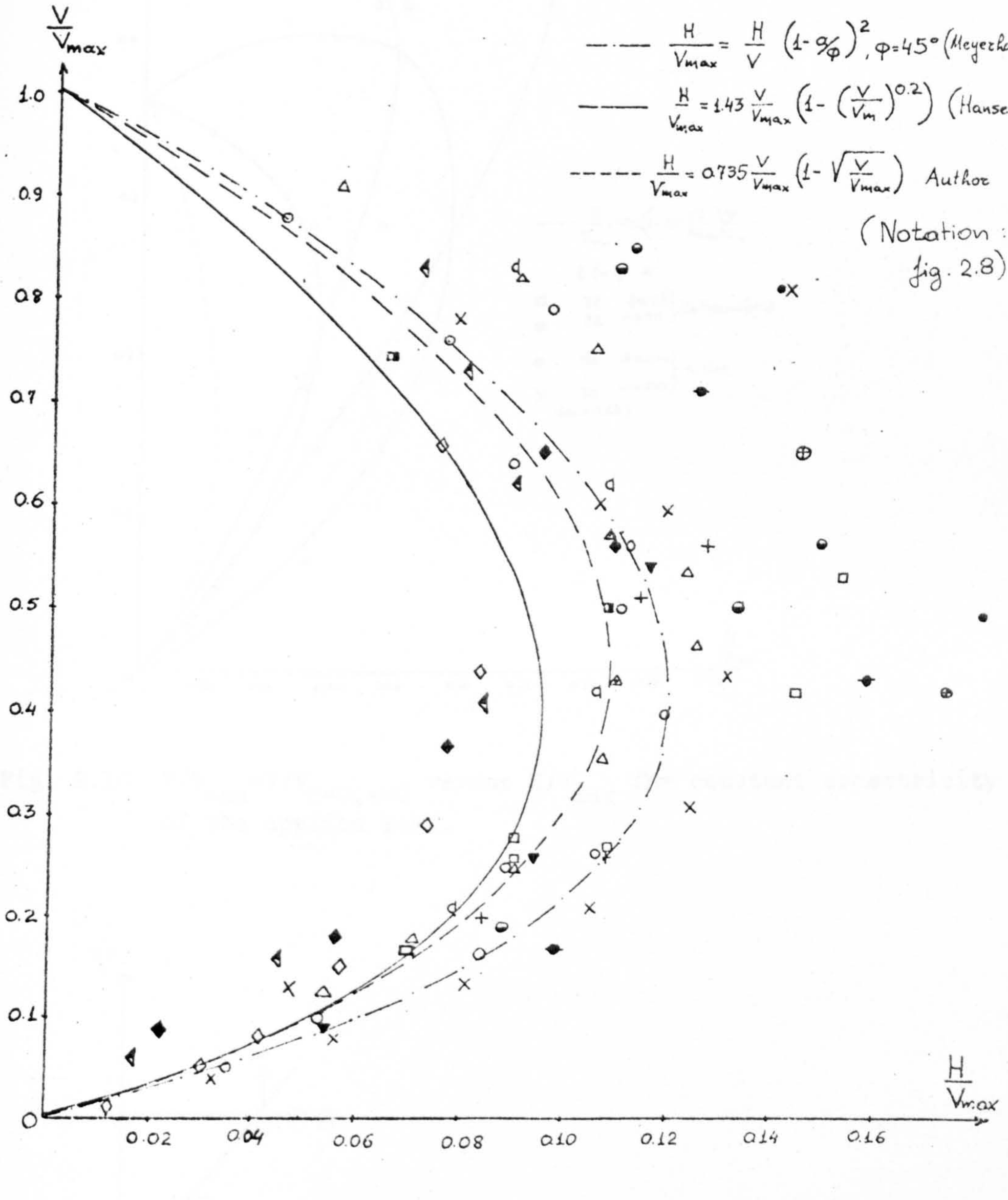

Fig. 2.9 V/V_{max} versus H/V_{max} - Results obtained by many research workers.

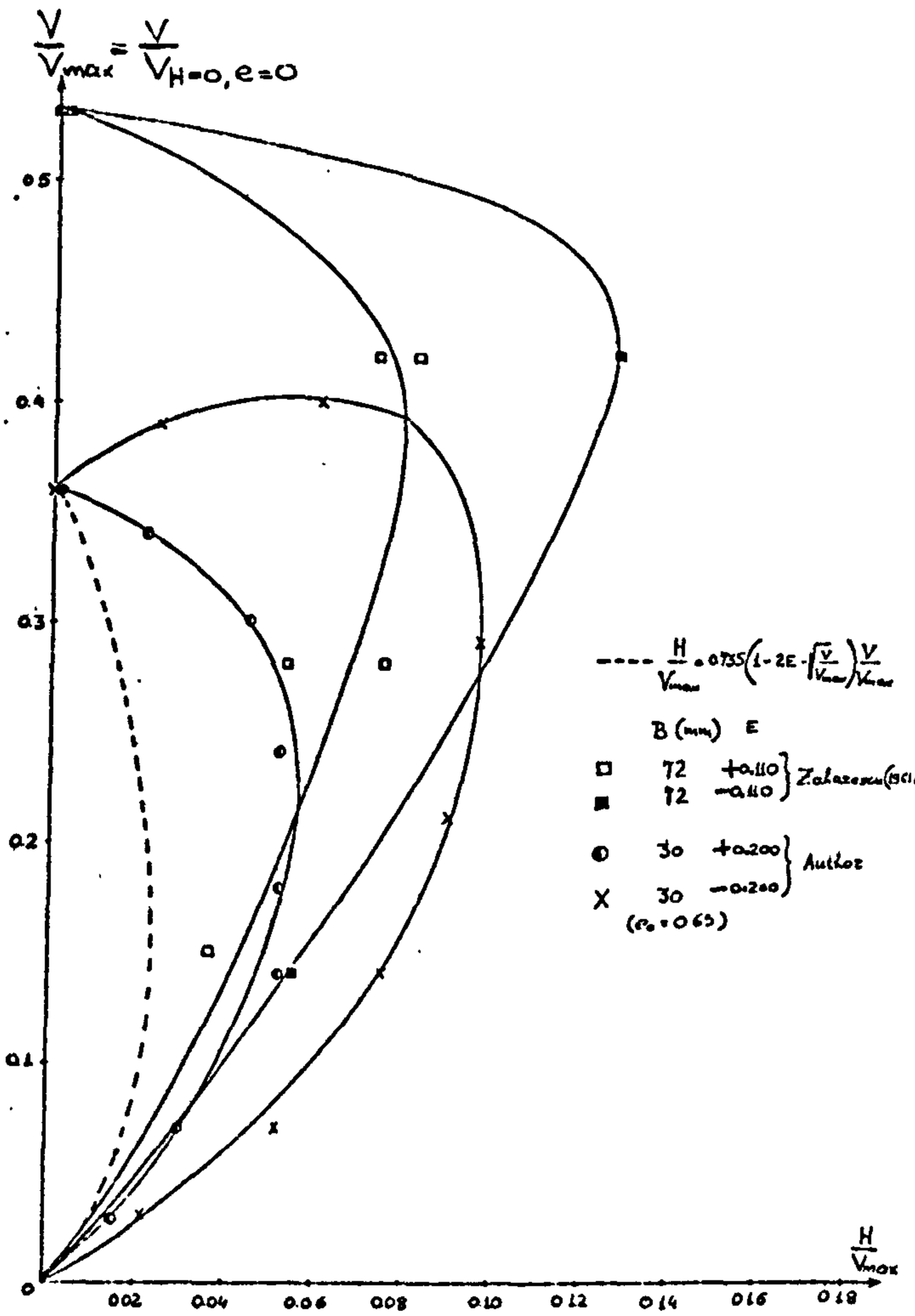

Fig. 2.10 $V/V_{max}=V/V_{H=0,e=0}$ versus H/V_{max} for constant eccentricity of the applied load.

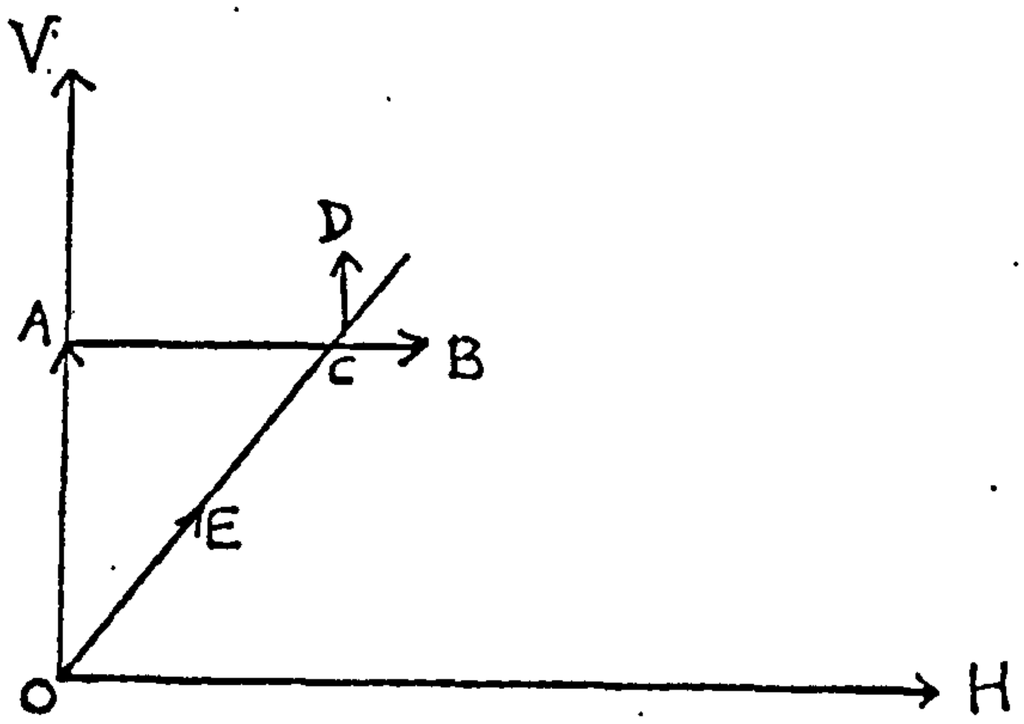

Fig. 2.11 V-H load paths.

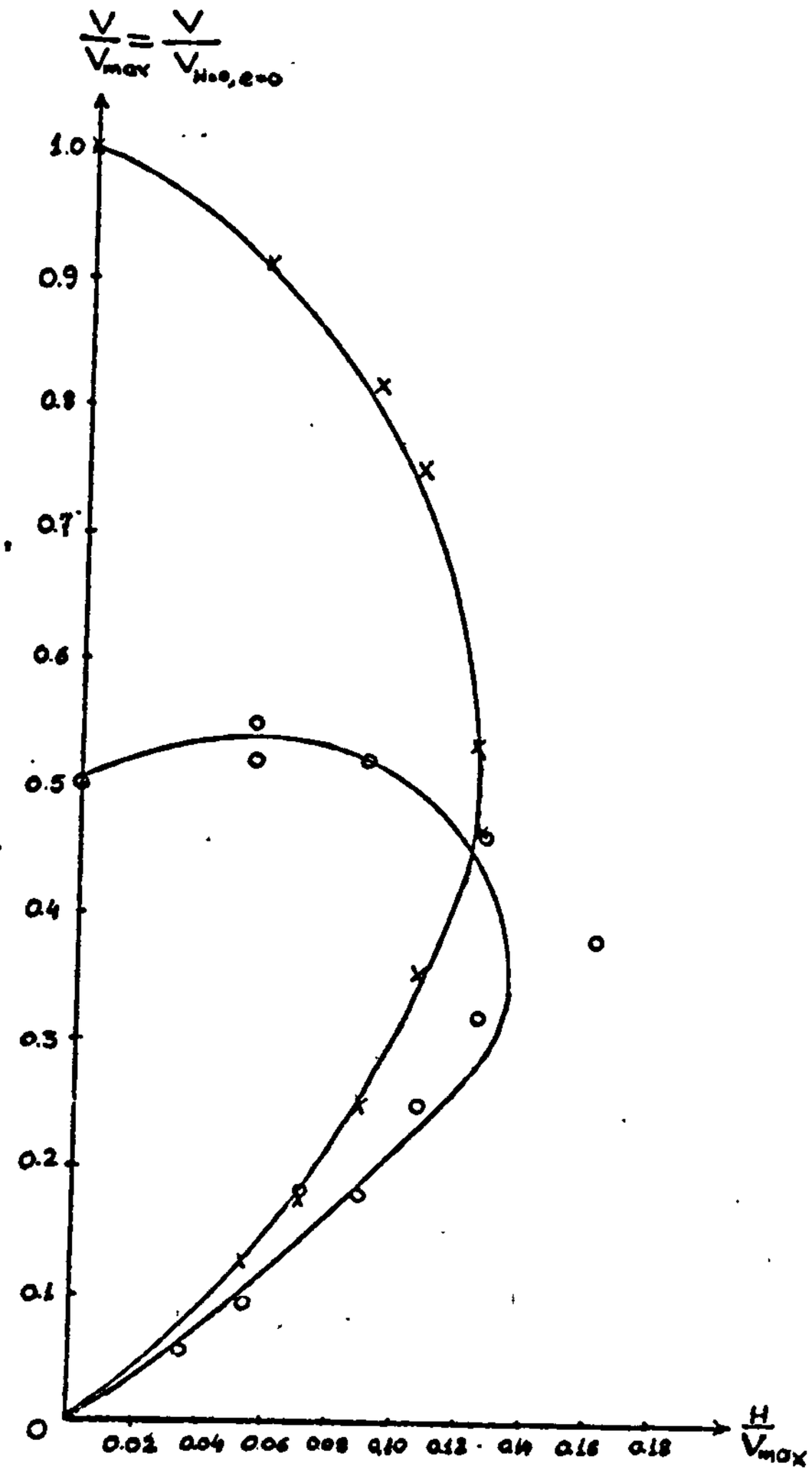

Fig. 2.12 $V/V_{max}=V/V_{H=0,e=0}$ versus H/V_{max} for constant eccentricity of the applied load.

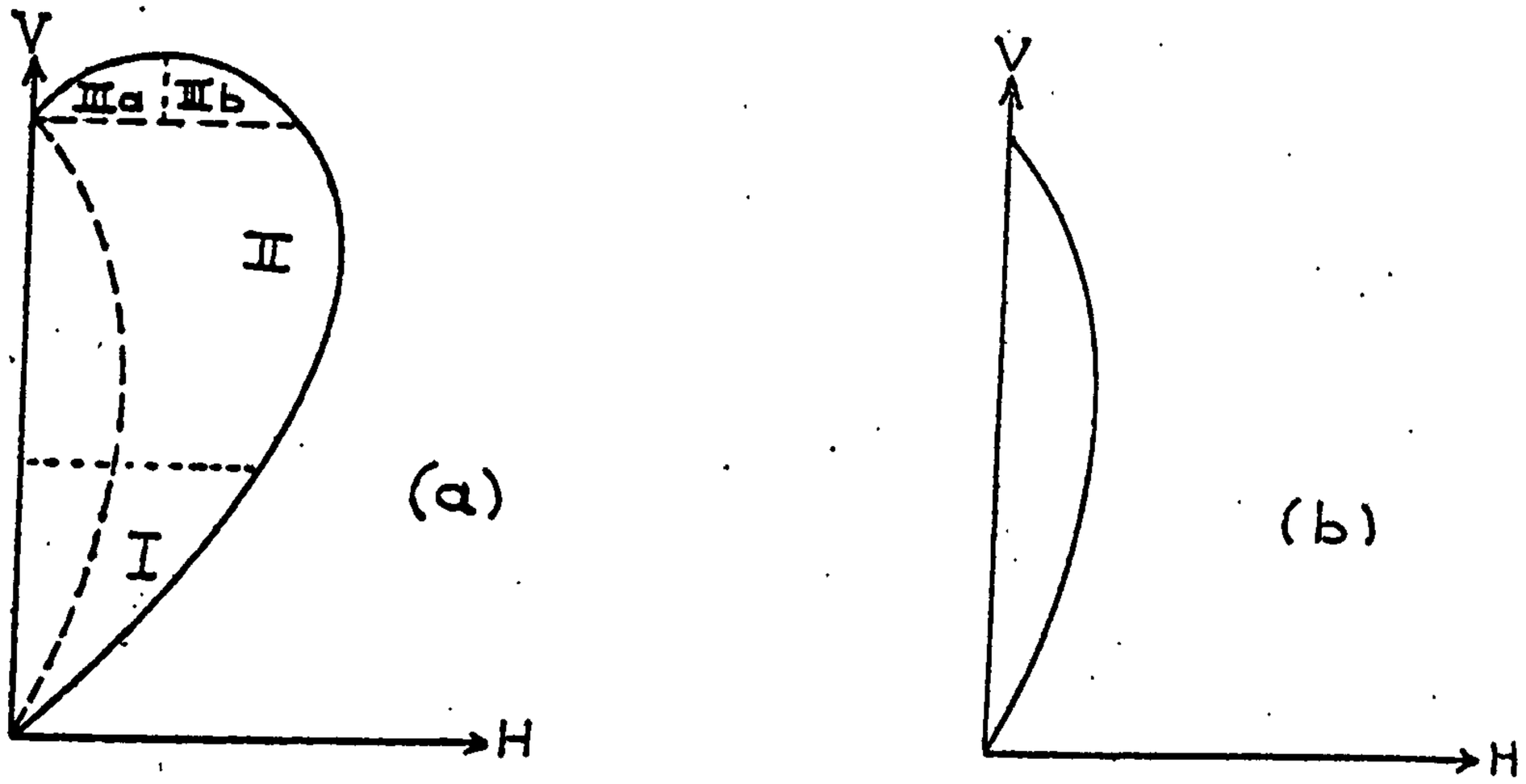

Fig. 2.13 Failure envelopes in the V-H space
(a) 'Negative' eccentricity (b) 'Positive' eccentricity of the vertical load.

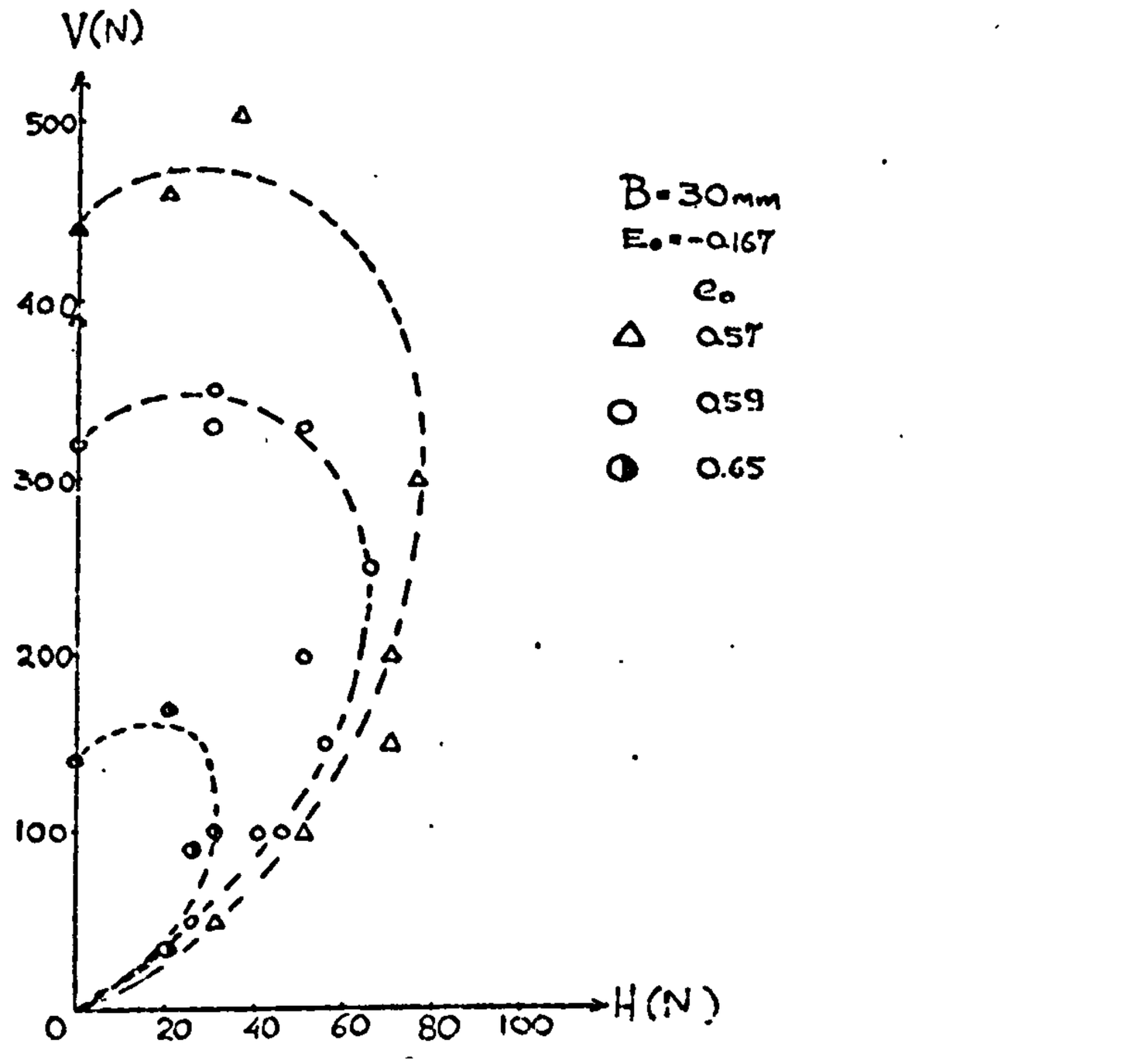

Fig.2.14 Failure envelopes in the V-H space for different initial voids ratios.

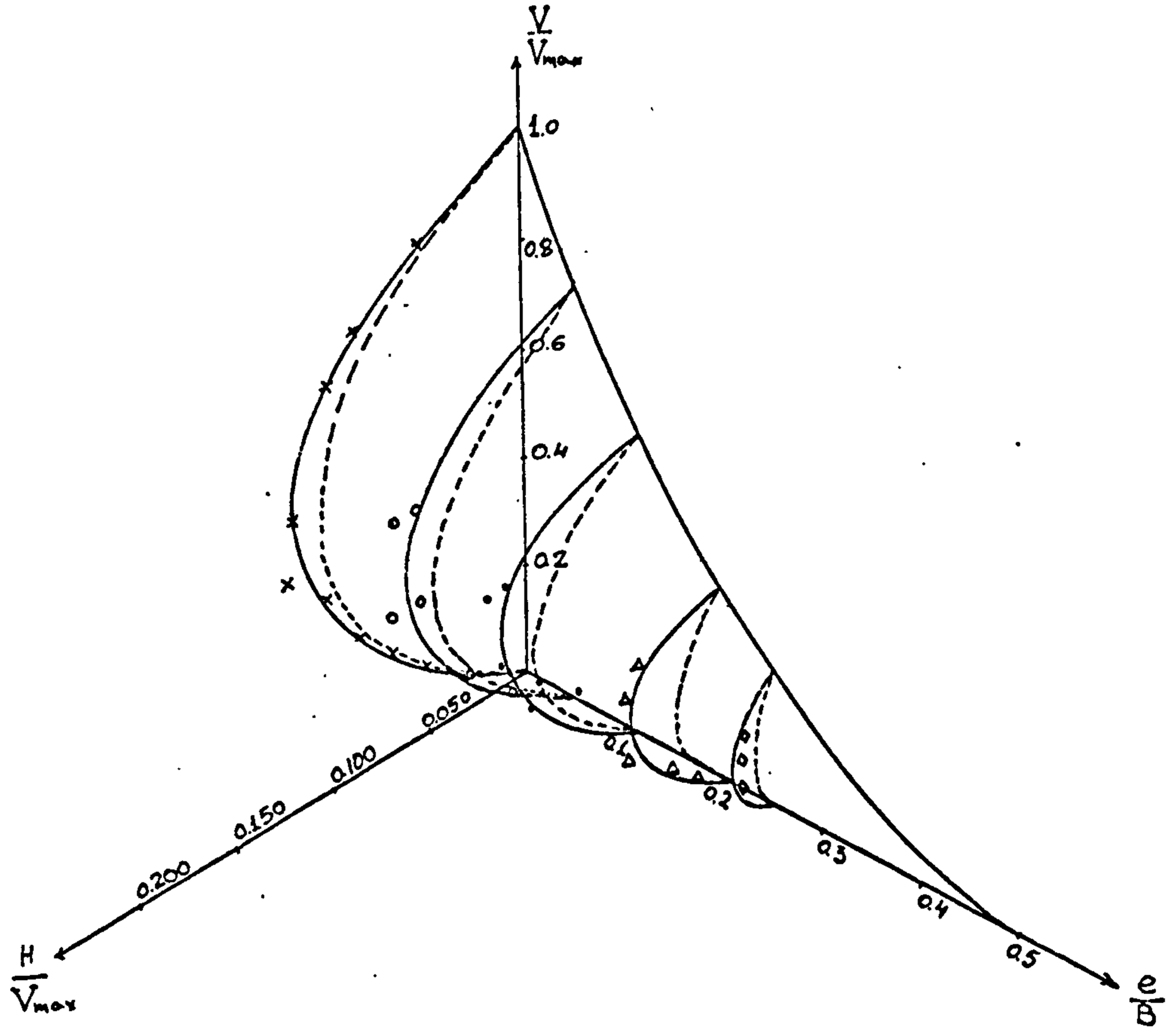

Fig. 2.15 Failure envelopes in the V/V_{max}- H/V_{max}- $E=e/B$ space.

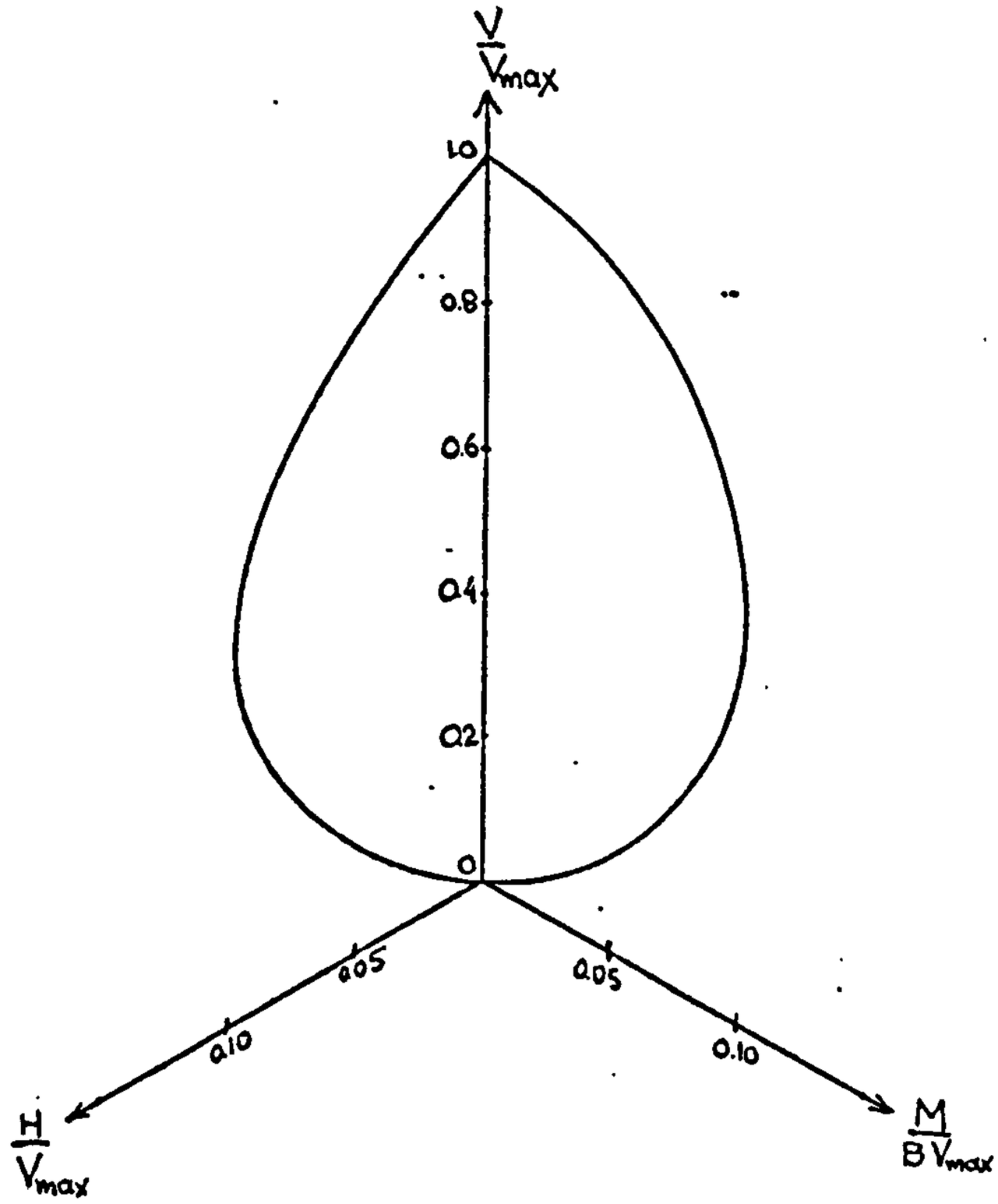

Fig. 2.16 Failure envelopes in the V/V_{max}-H/V_{max}-M/BV_{max} space.

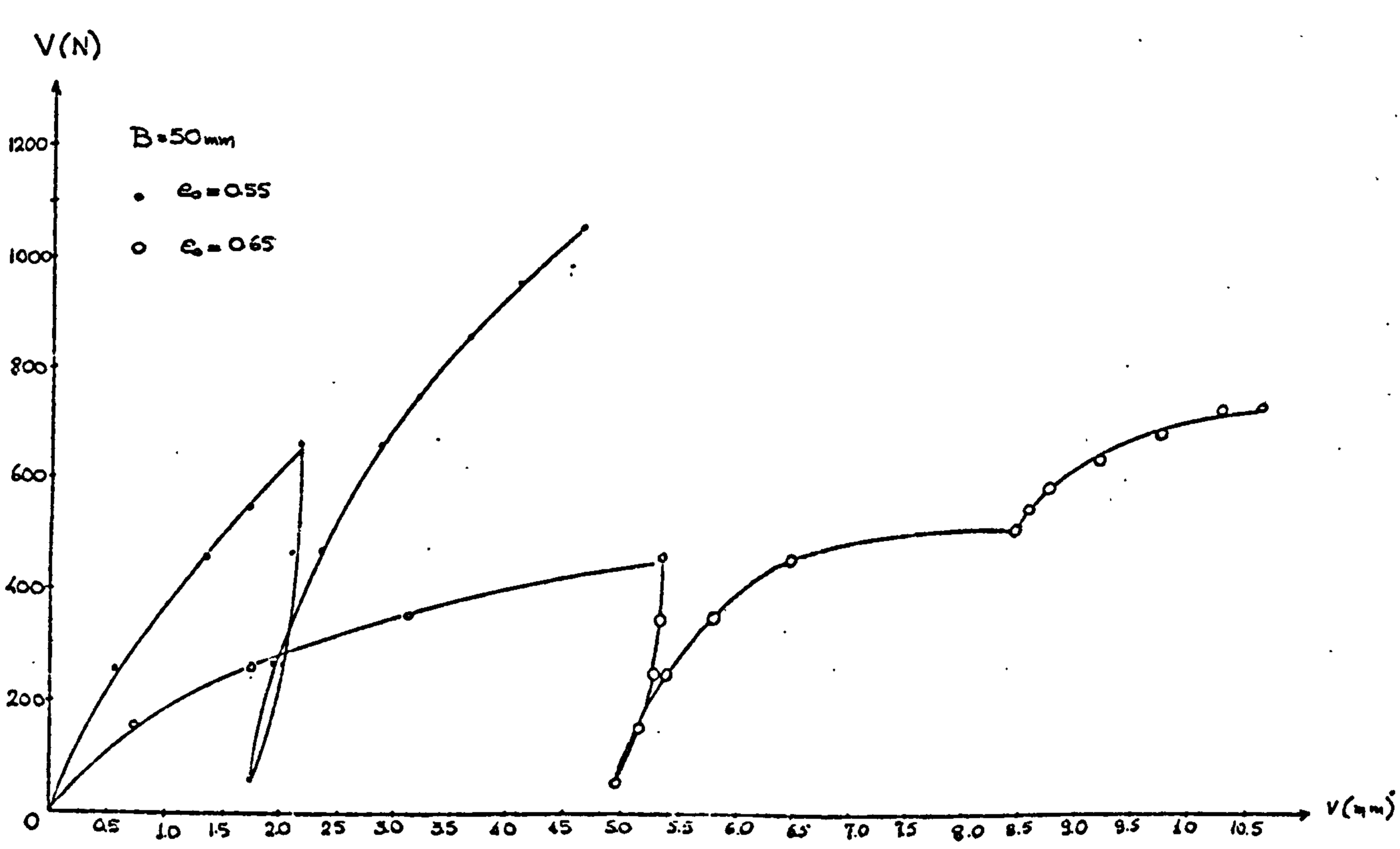

Fig. 2.17 Vertical load-vertical displacement relationships for footings on dense and loose sand.

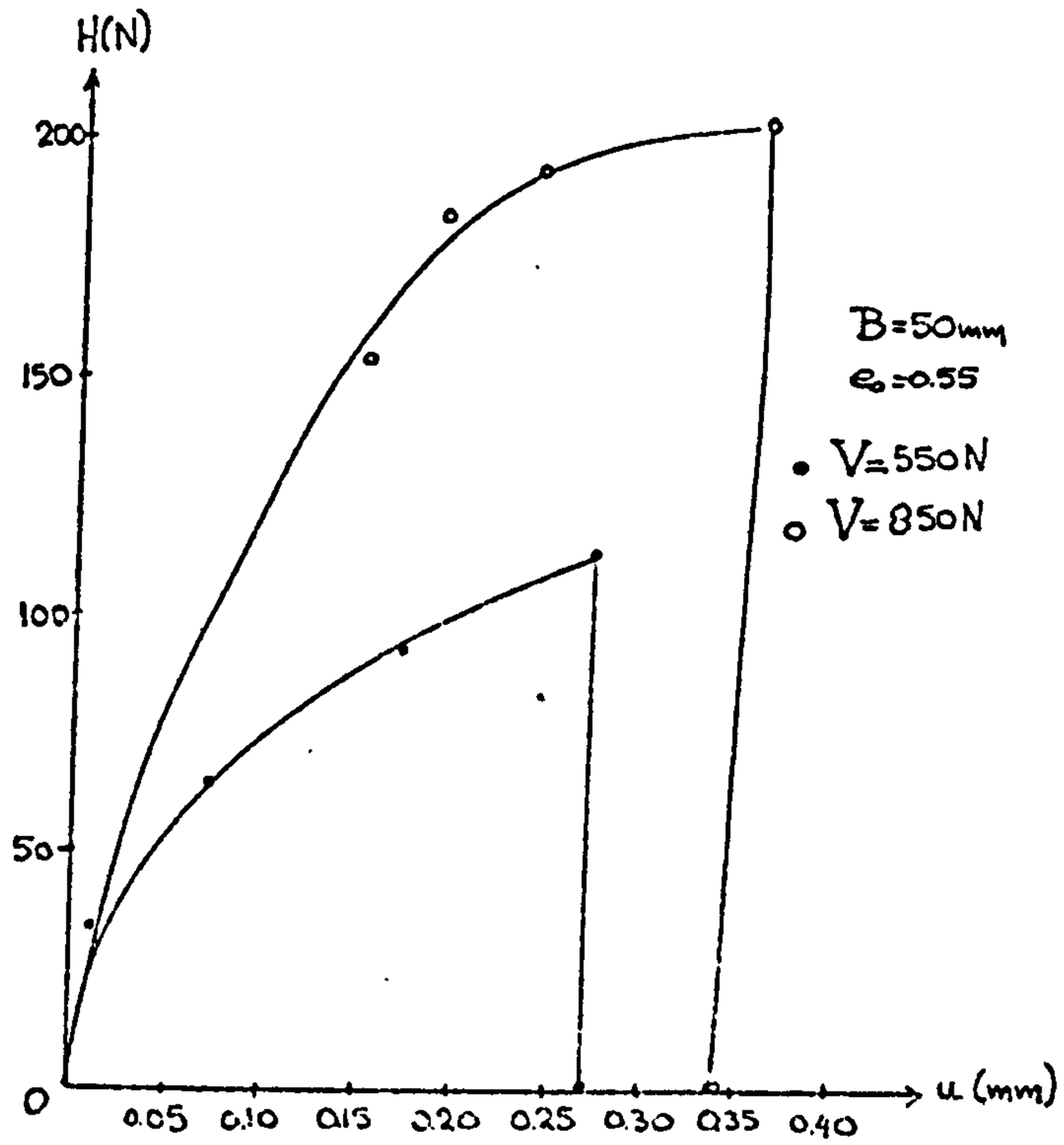

Fig. 2.18 Horizontal load-horizontal displacement relationships for footings on sand.

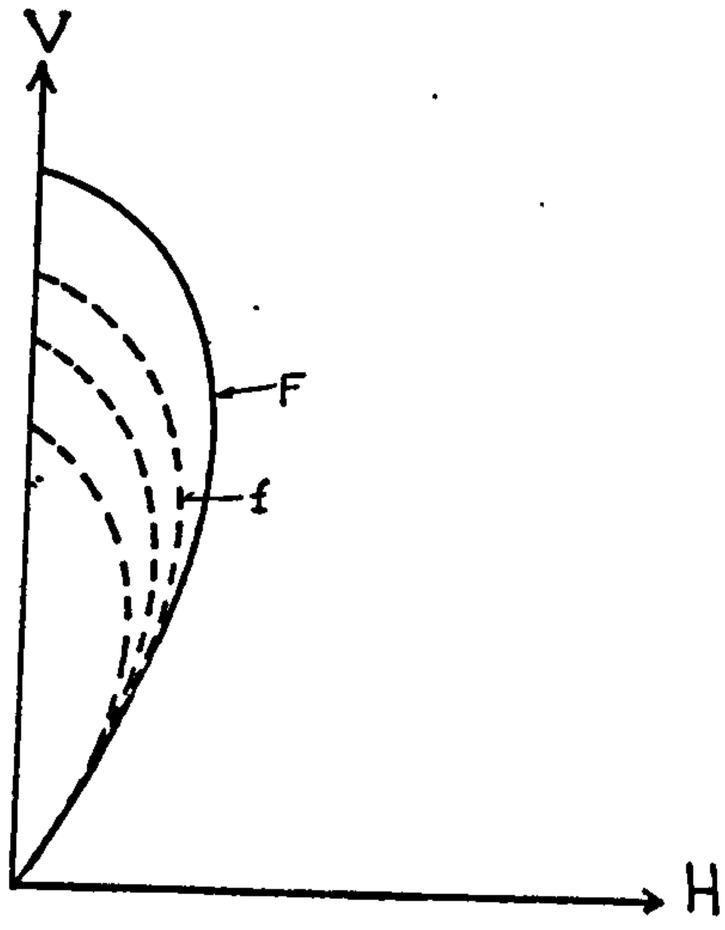

Fig. 2.19 Yield surfaces and failure envelope of a plastic work hardening system.

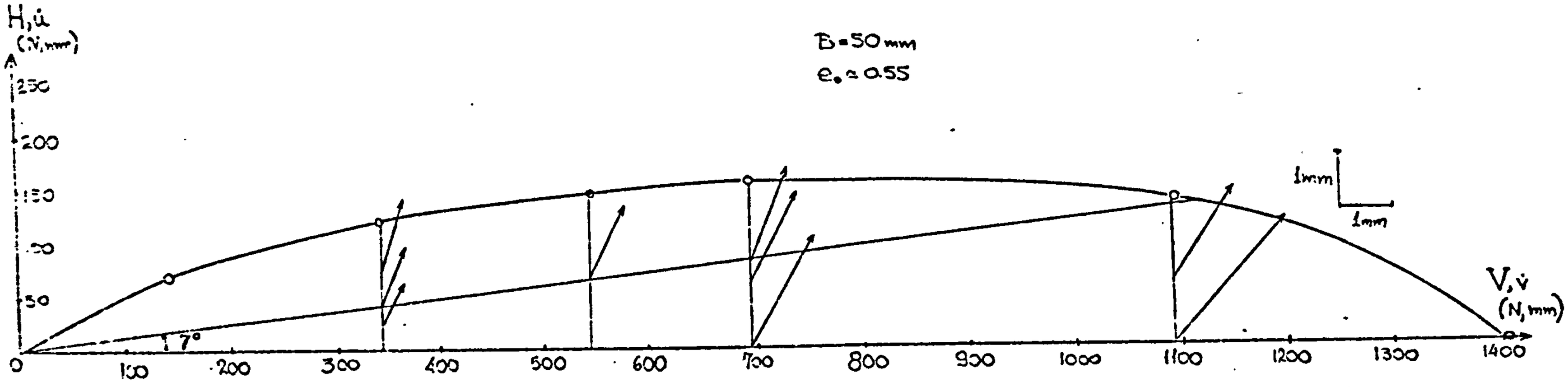

Fig. 2.20 V-H failure envelope and related displacements for a footing on dense sand.

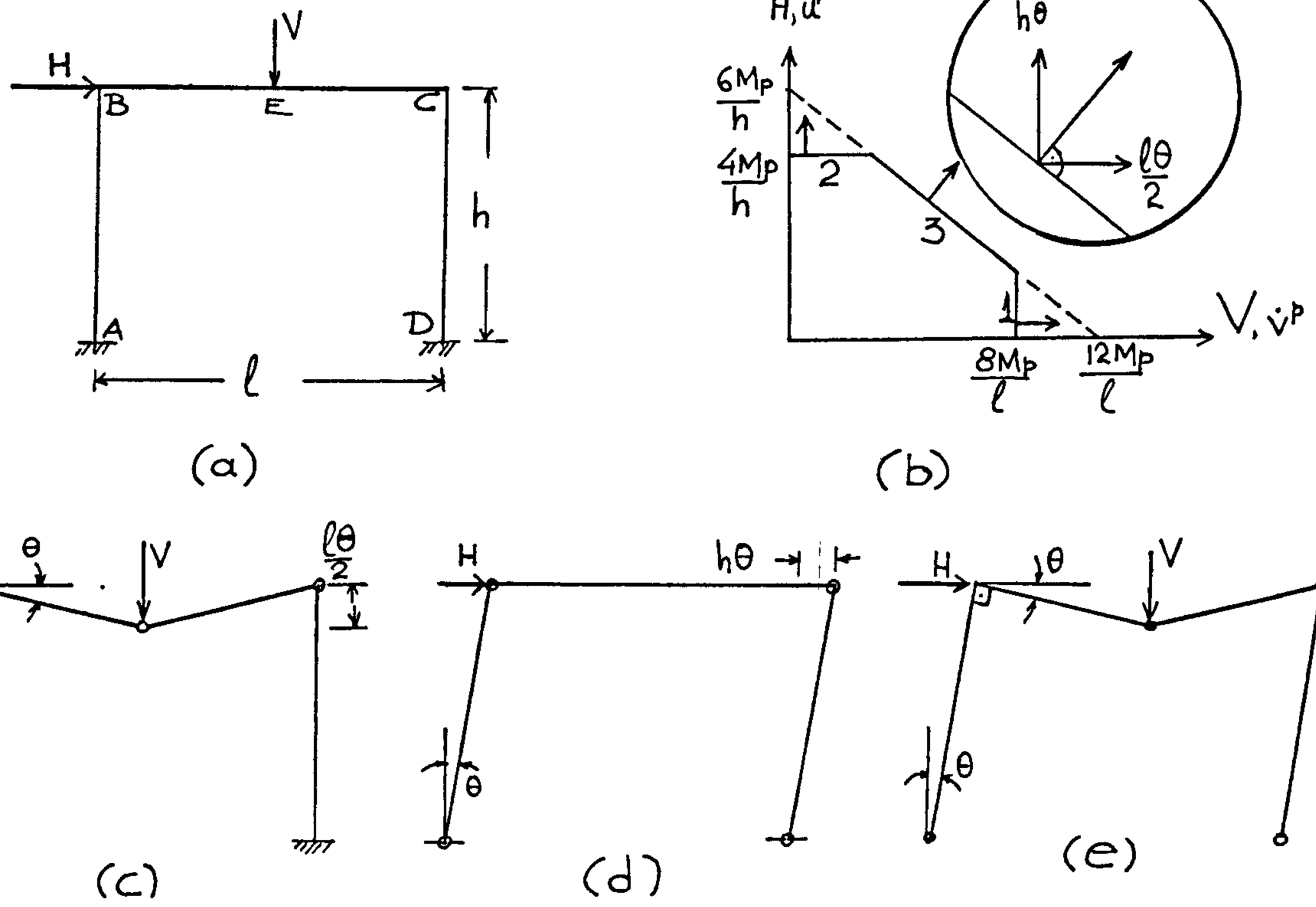

Fig. 2.21 Structural interaction diagrams and collapse mechanisms for a fixed-foot portal frame.

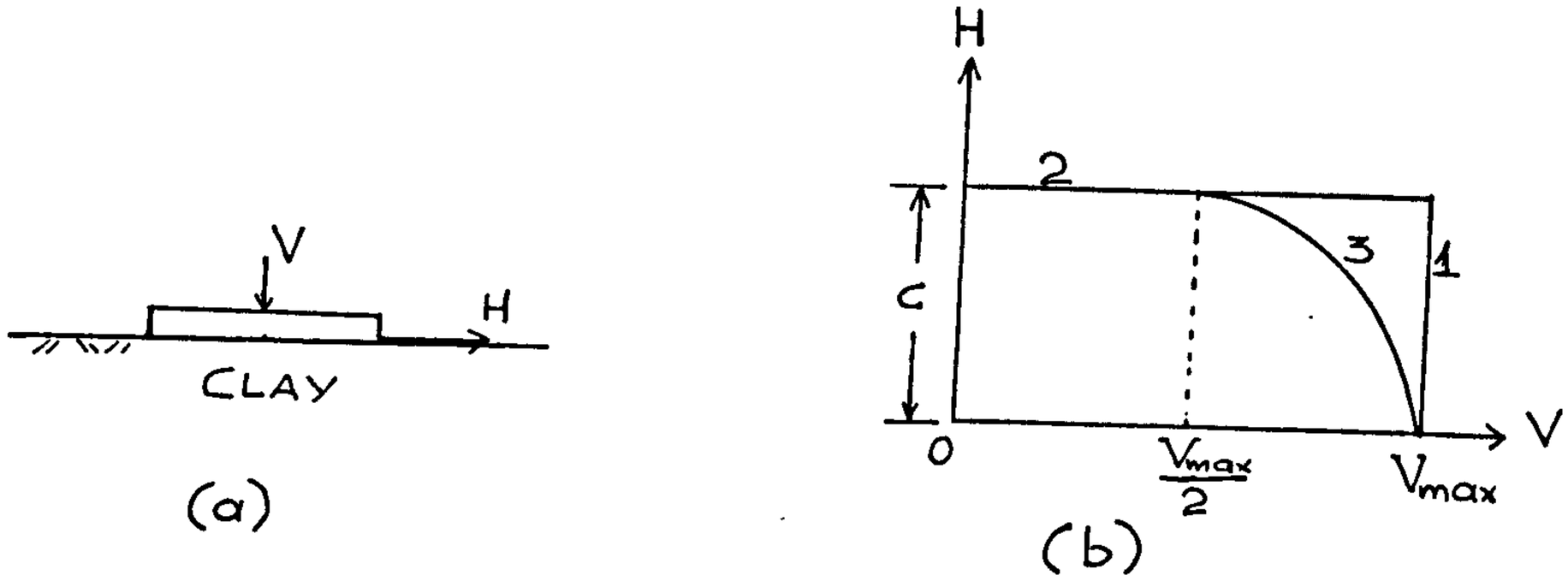

Fig. 2.22 V-H failure envelope for a rough footing on saturated clay.

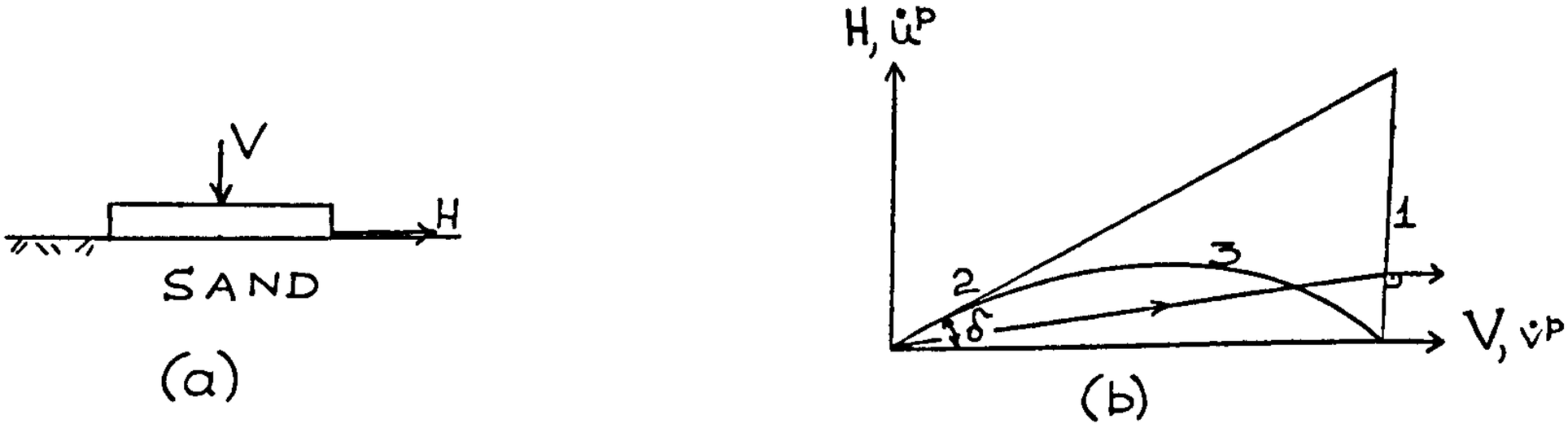

Fig. 2.23 V-H failure envelope for a rough footing on sand.

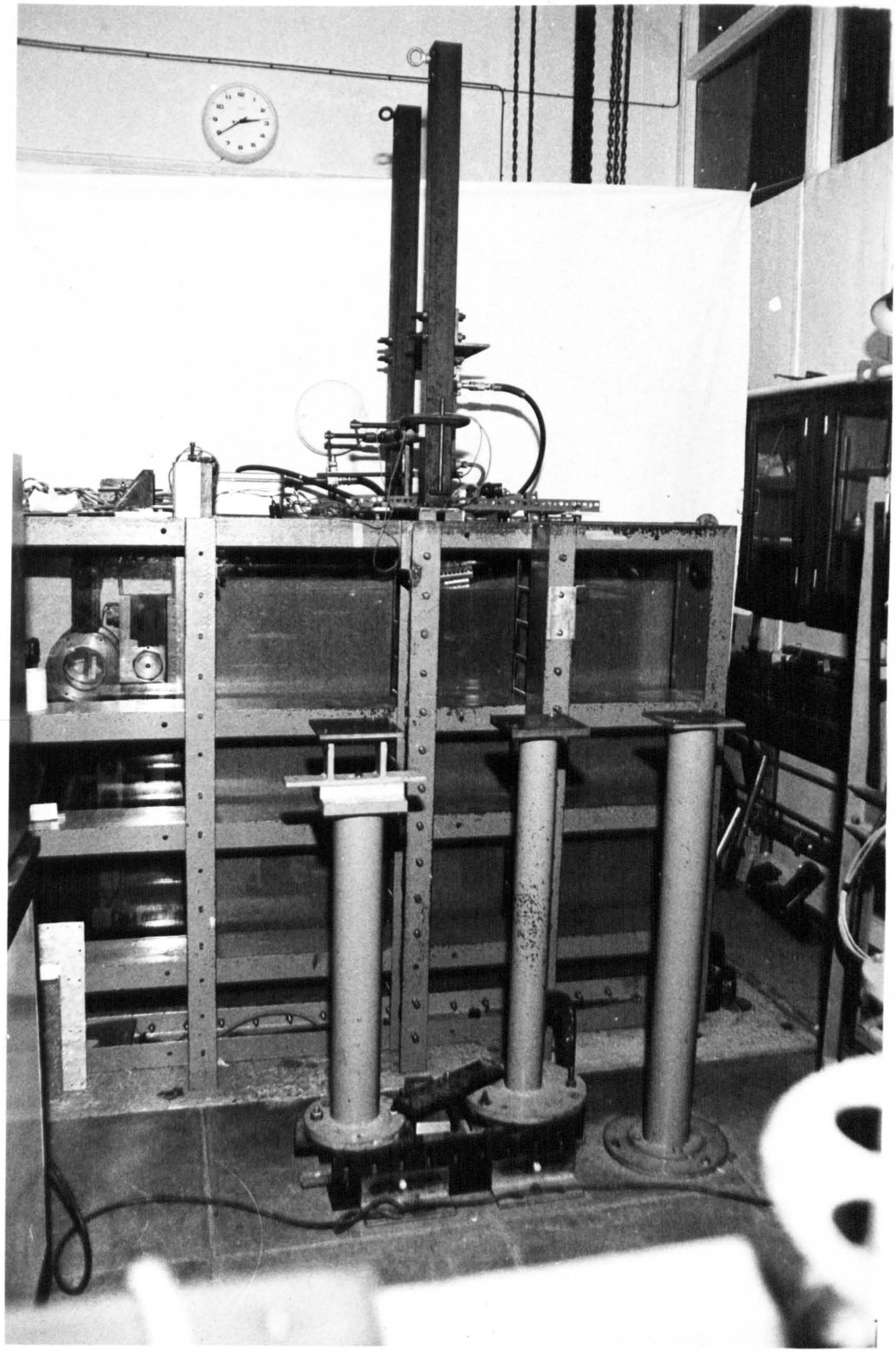

Fig. 3·1 The Footing Apparatus at Cambridge (FAC)

B1

B2

UB

P2

PR

TLC2

TLC1

LB

SLO

BA

ABO

TBP

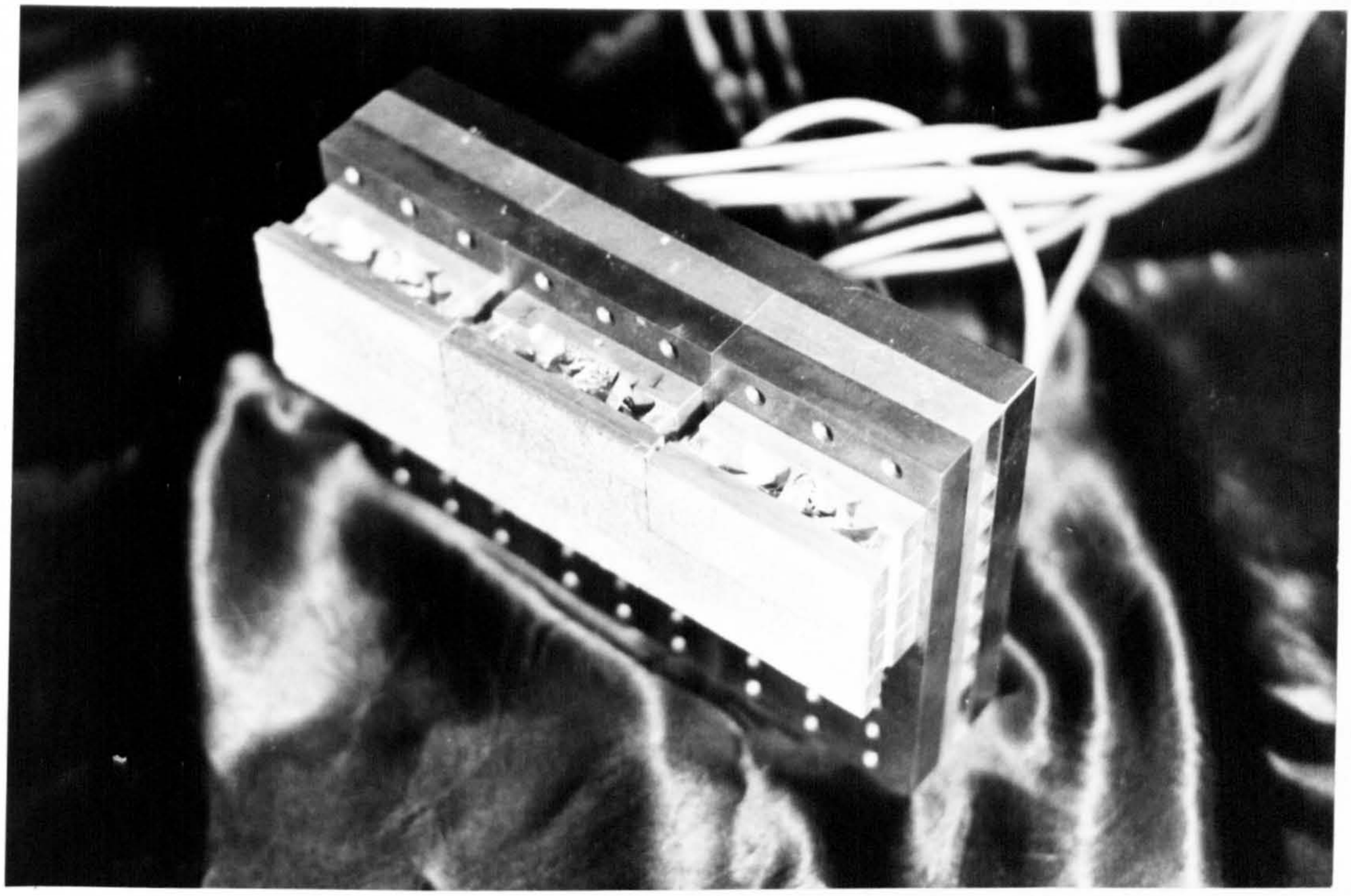

Fig. 3.2 The footing with the load cells.

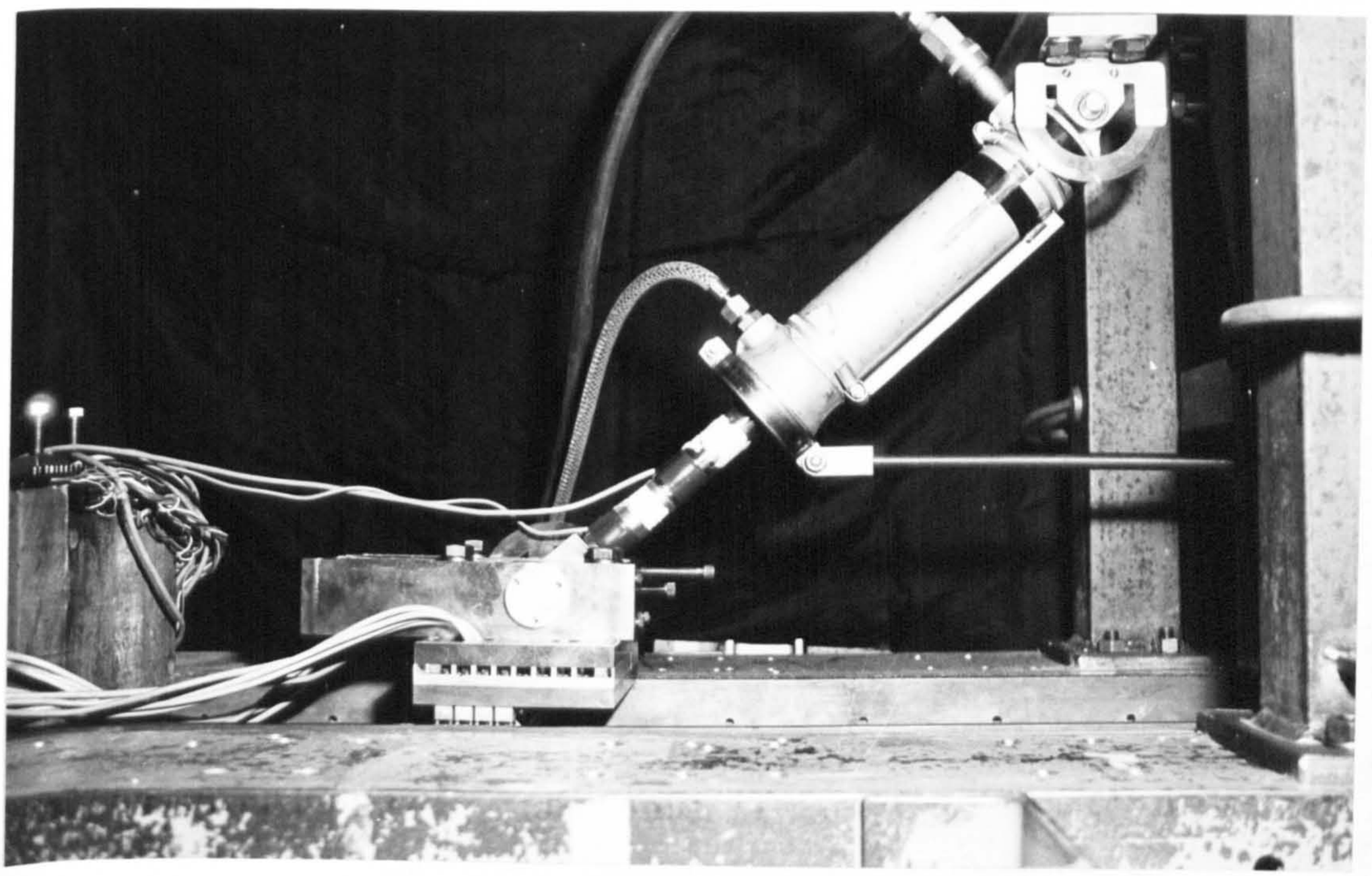

Fig. 3.3 The jack-footing assembly.

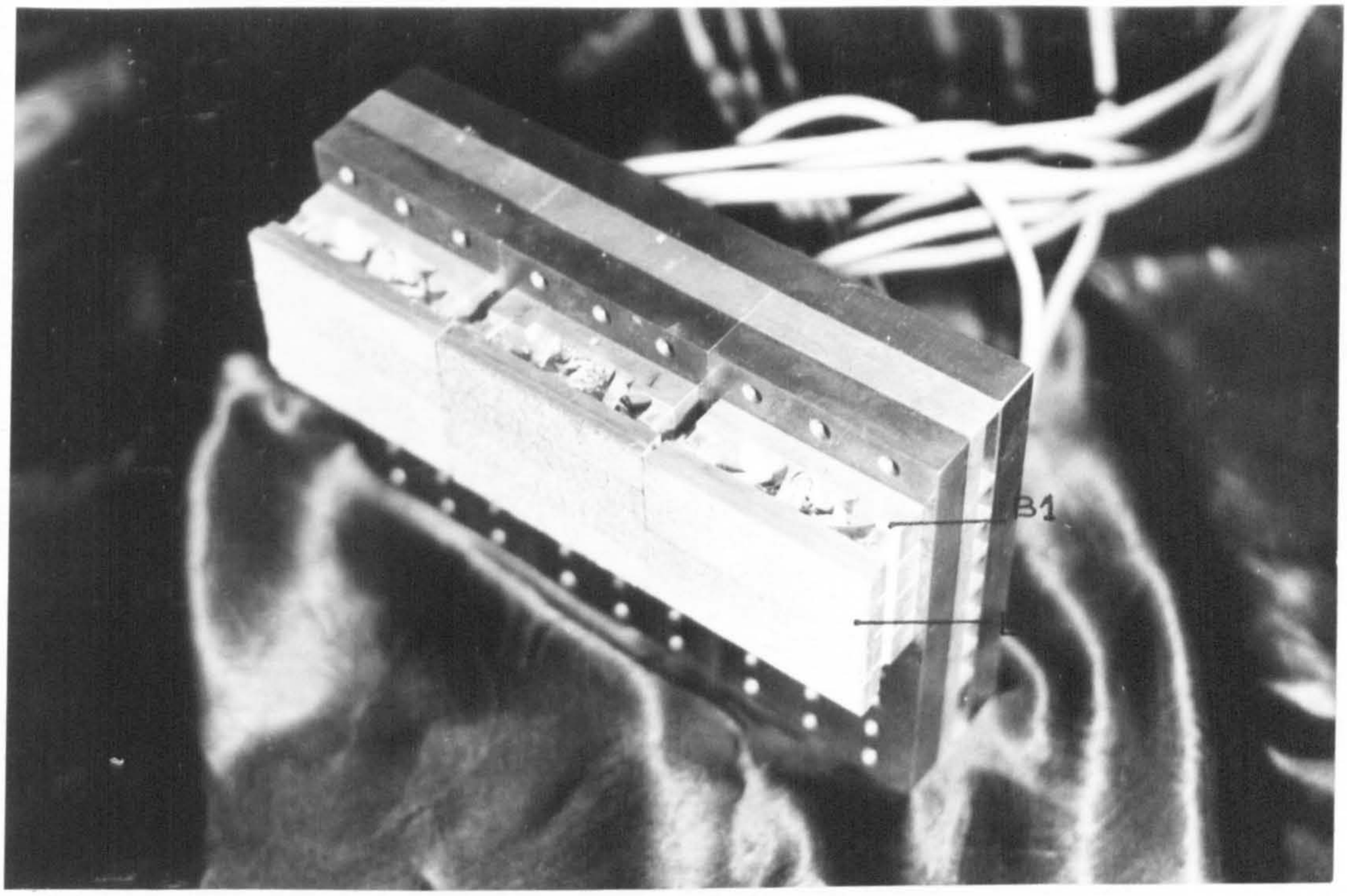

Fig. 3.2 The footing with the load cells.

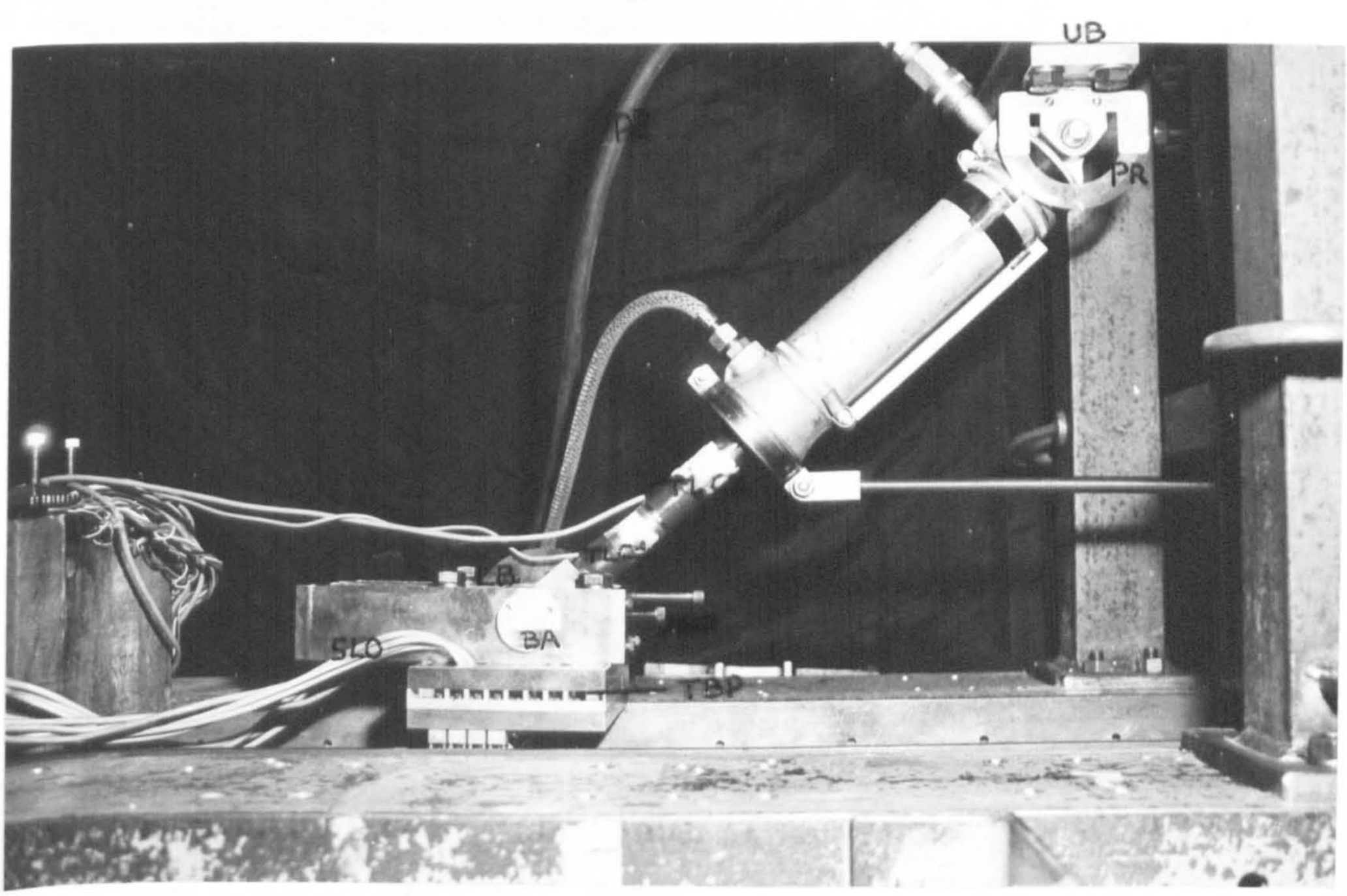

Fig. 3.3 The jack-footing assembly.

P2

J

S

RE

G

VAL3

VAL

V

N

P1

SP

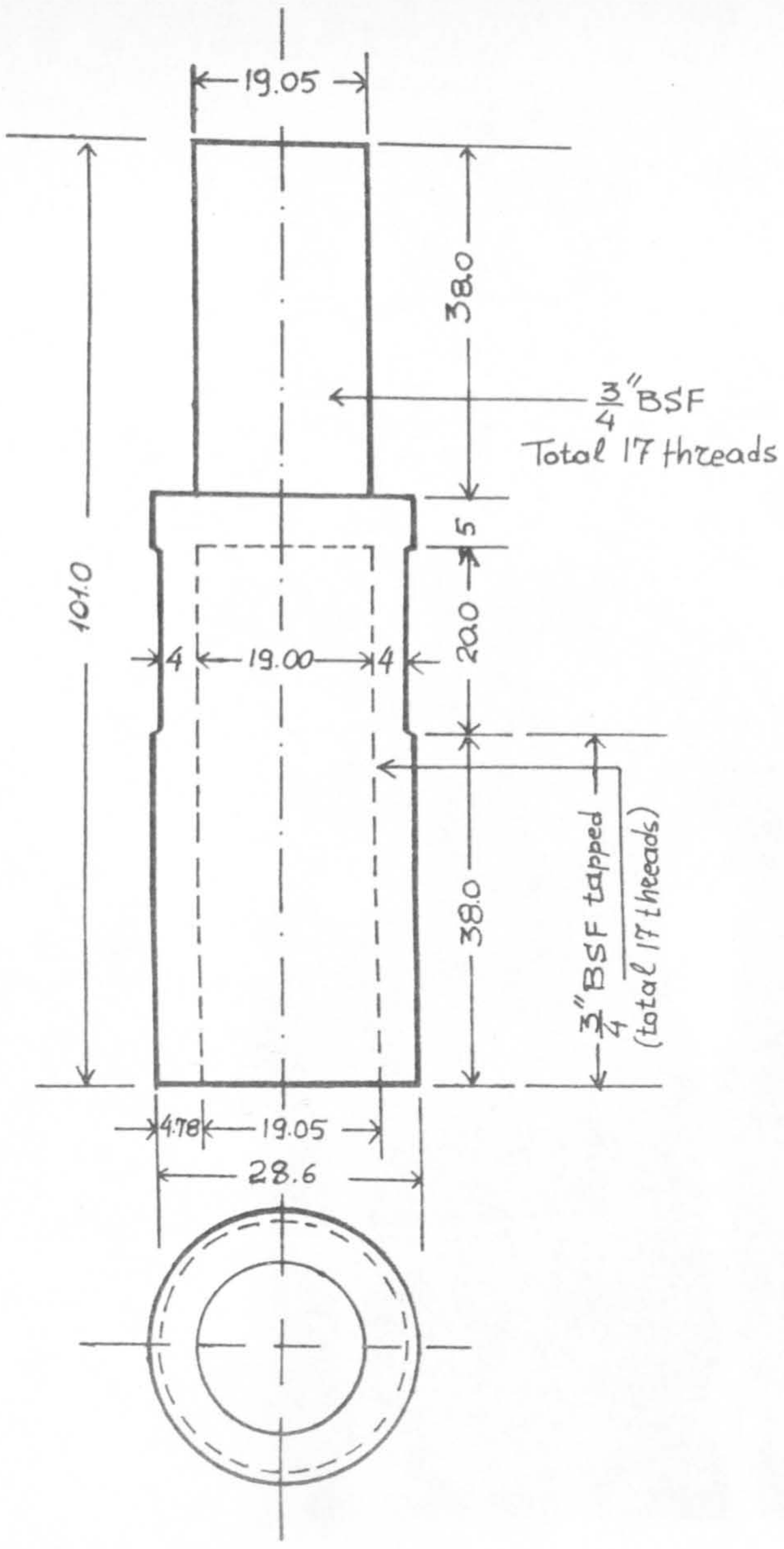

Fig. 3.4 The loading system

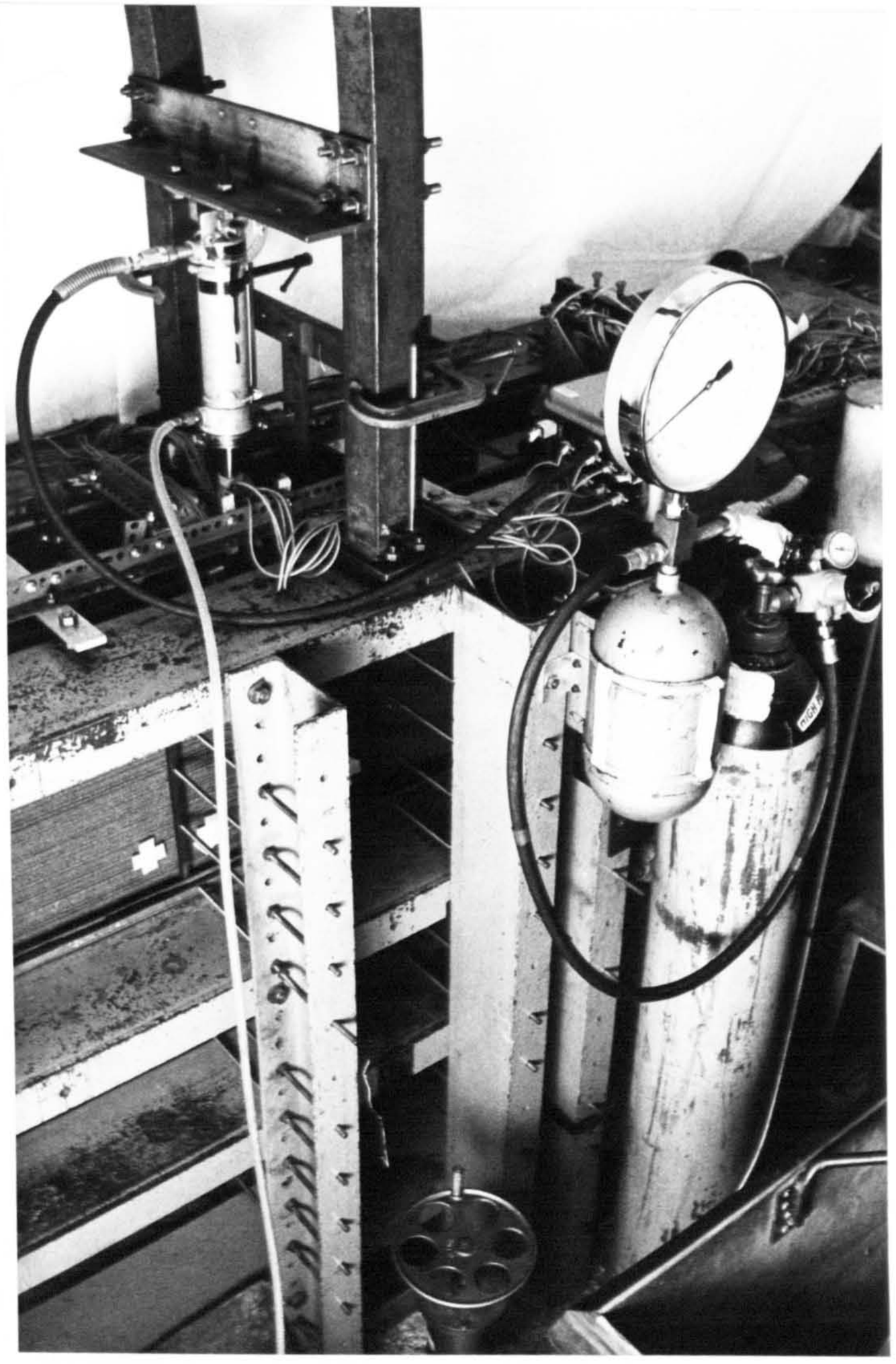

Fig. 3.5 Load cell to record the total load.

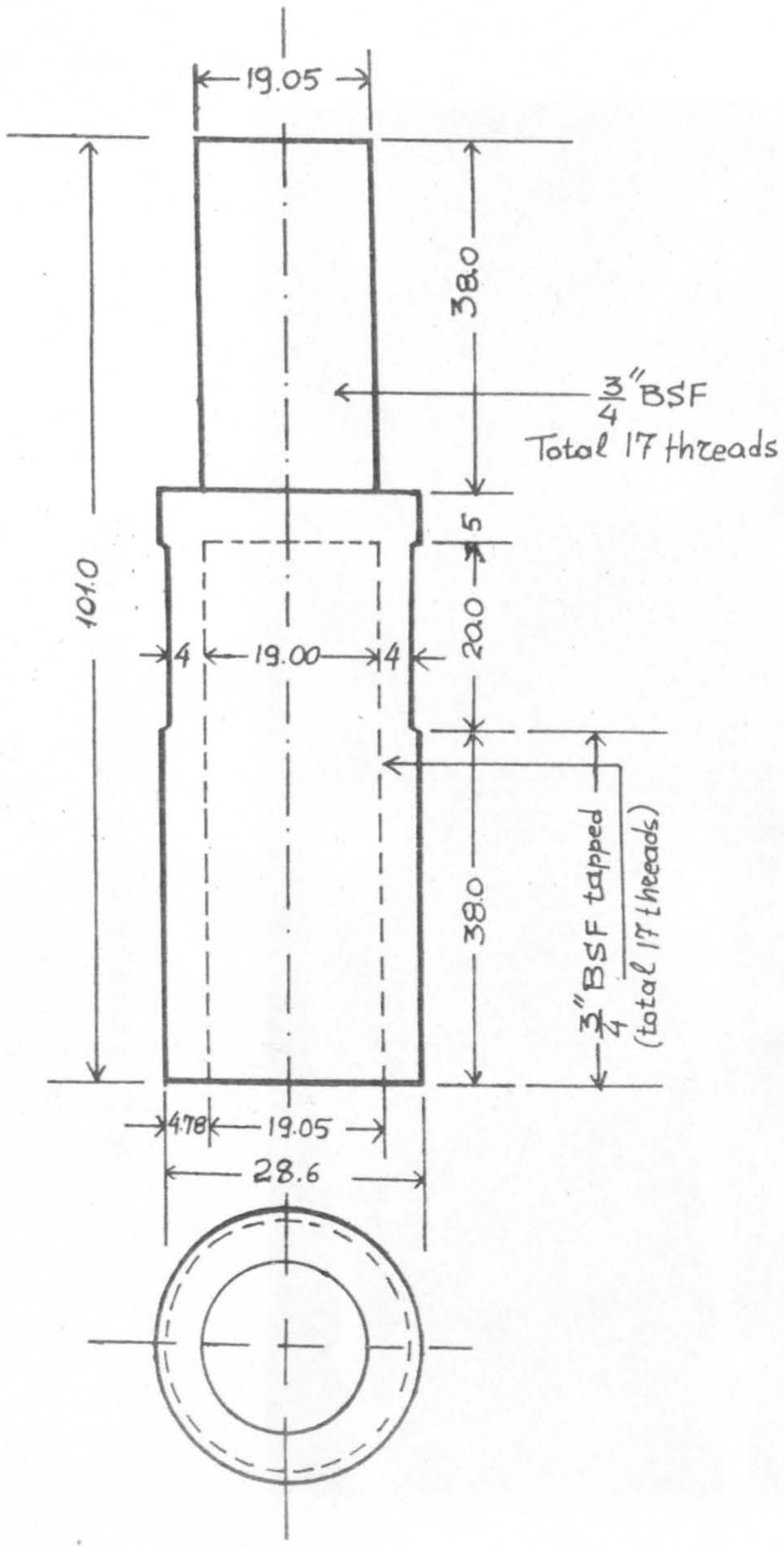

Fig. 3.4 The loading system

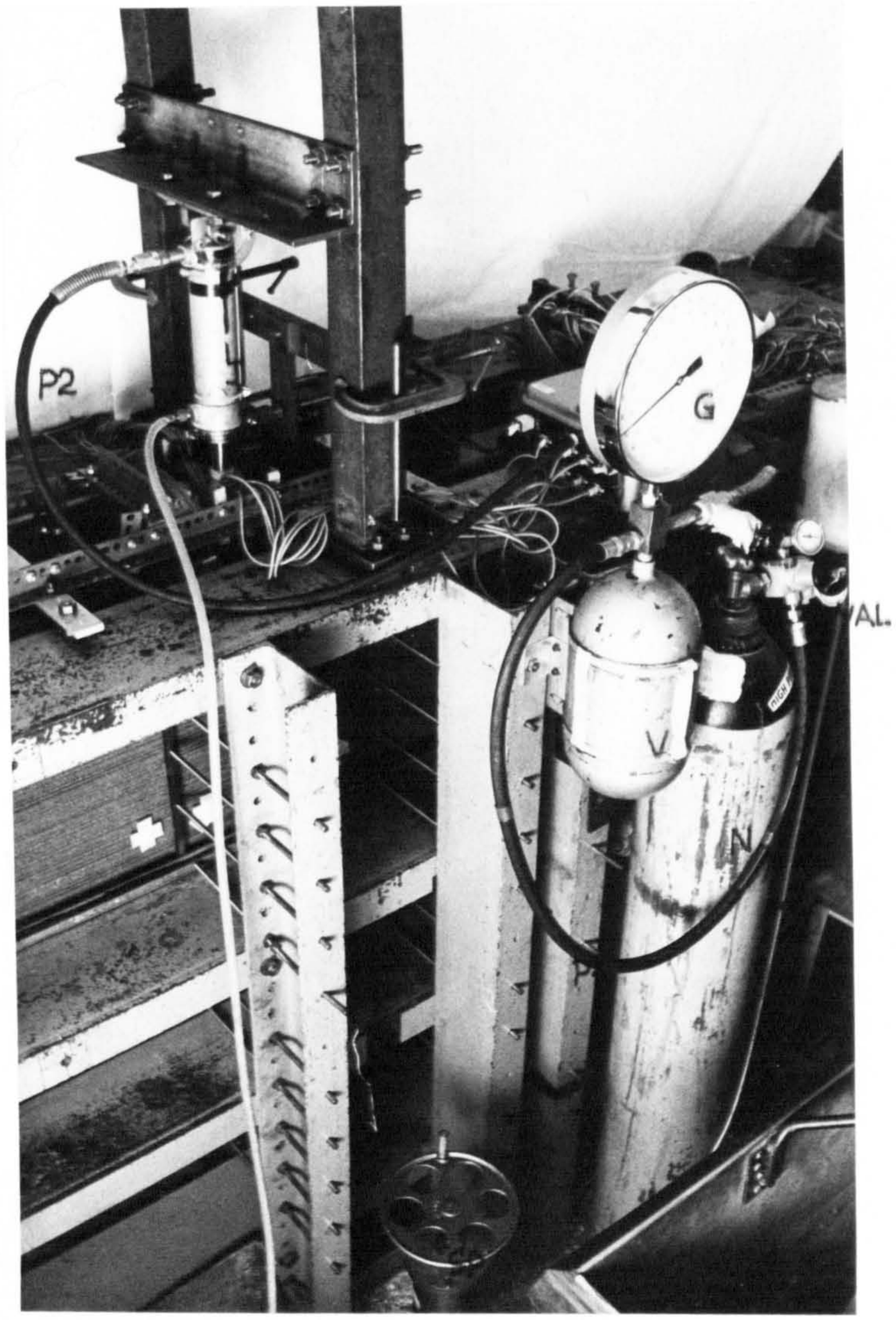

Fig. 3.5 Load cell to record the total load.

PRB

AP STP

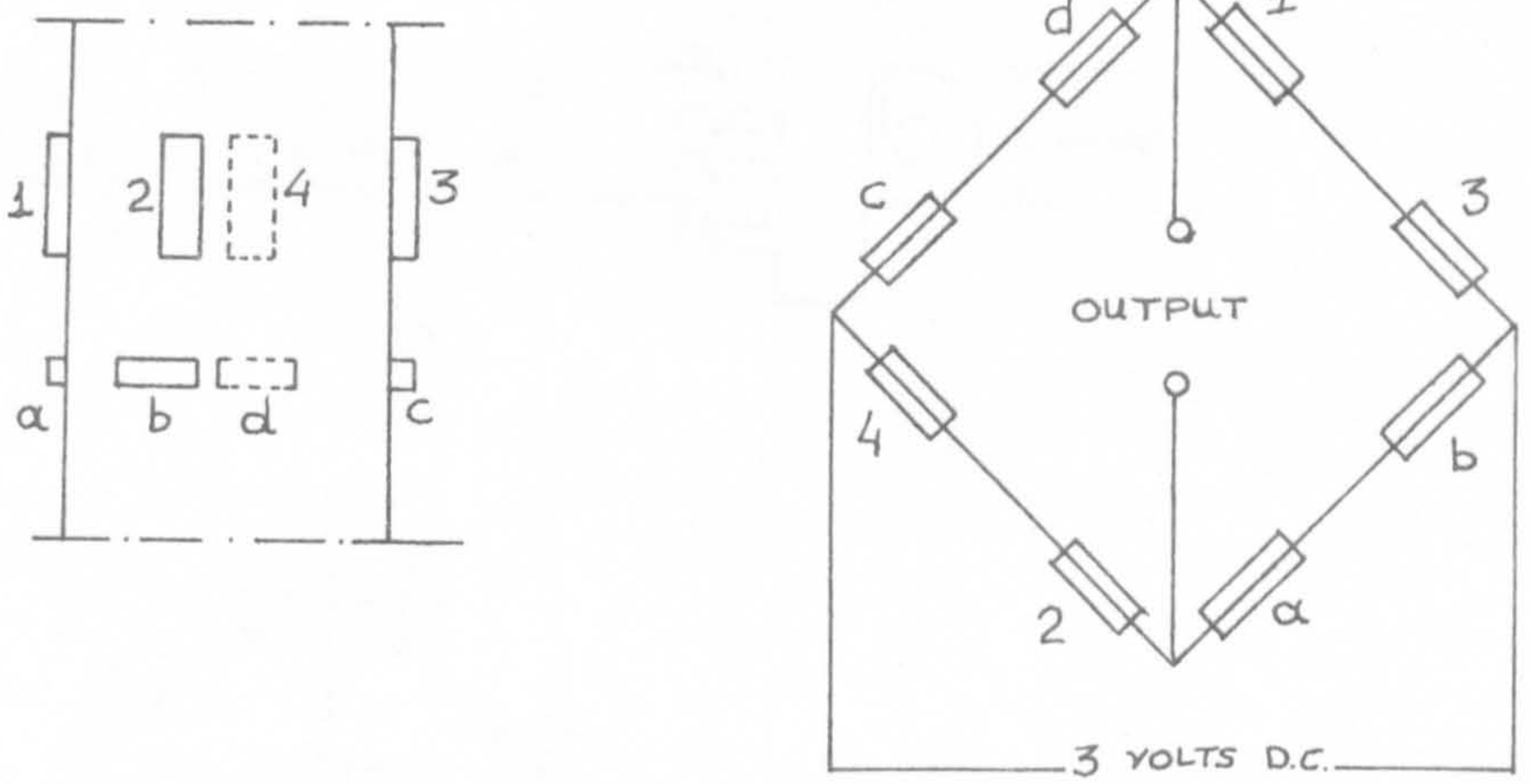

Fig. 3.6 The strain gauges arrangement and the resultant circuit.

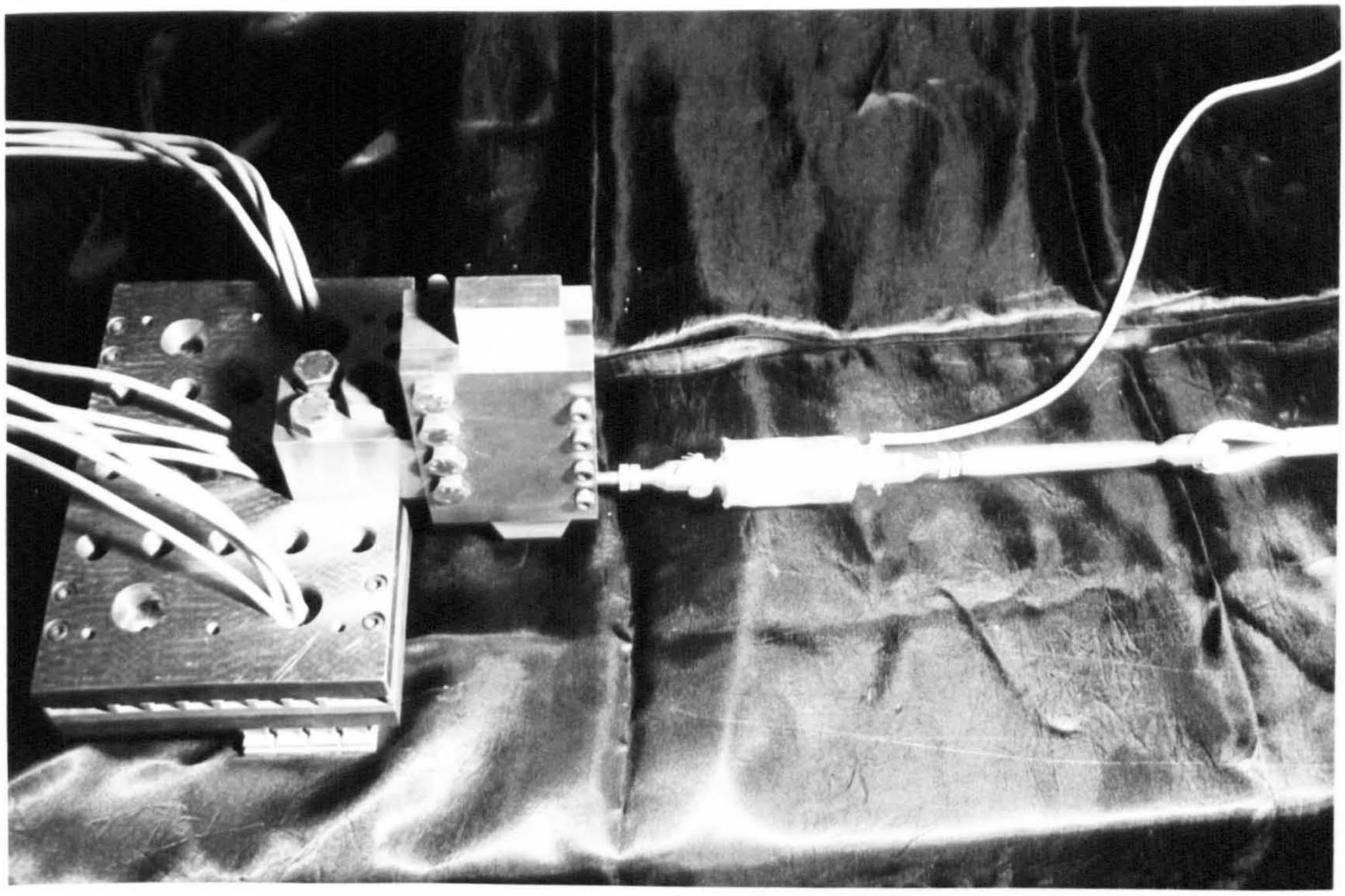

Fig. 3.7 The attachment for horizontal load

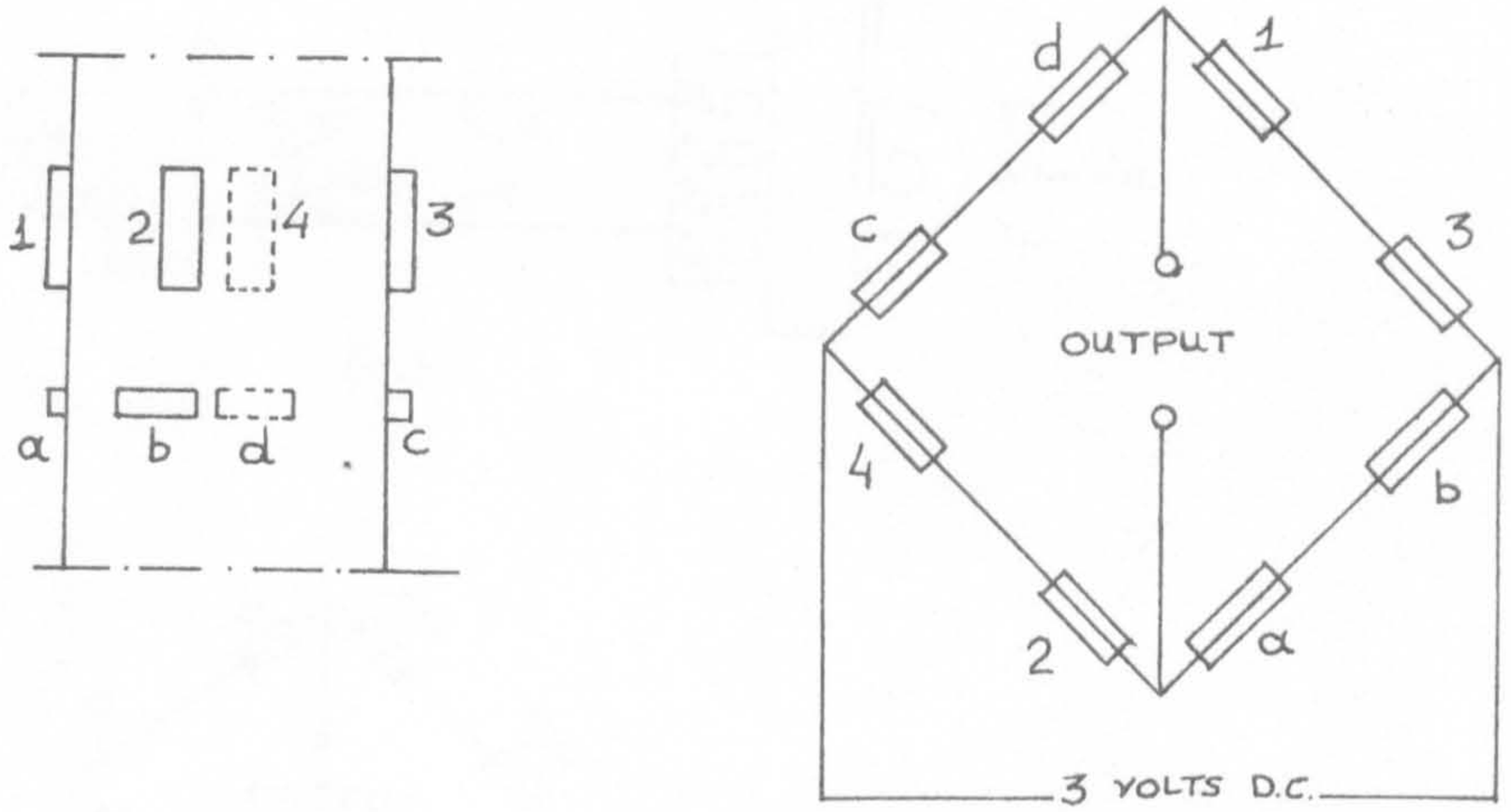

Fig. 3.6 The strain gauges arrangement and the resultant circuit.

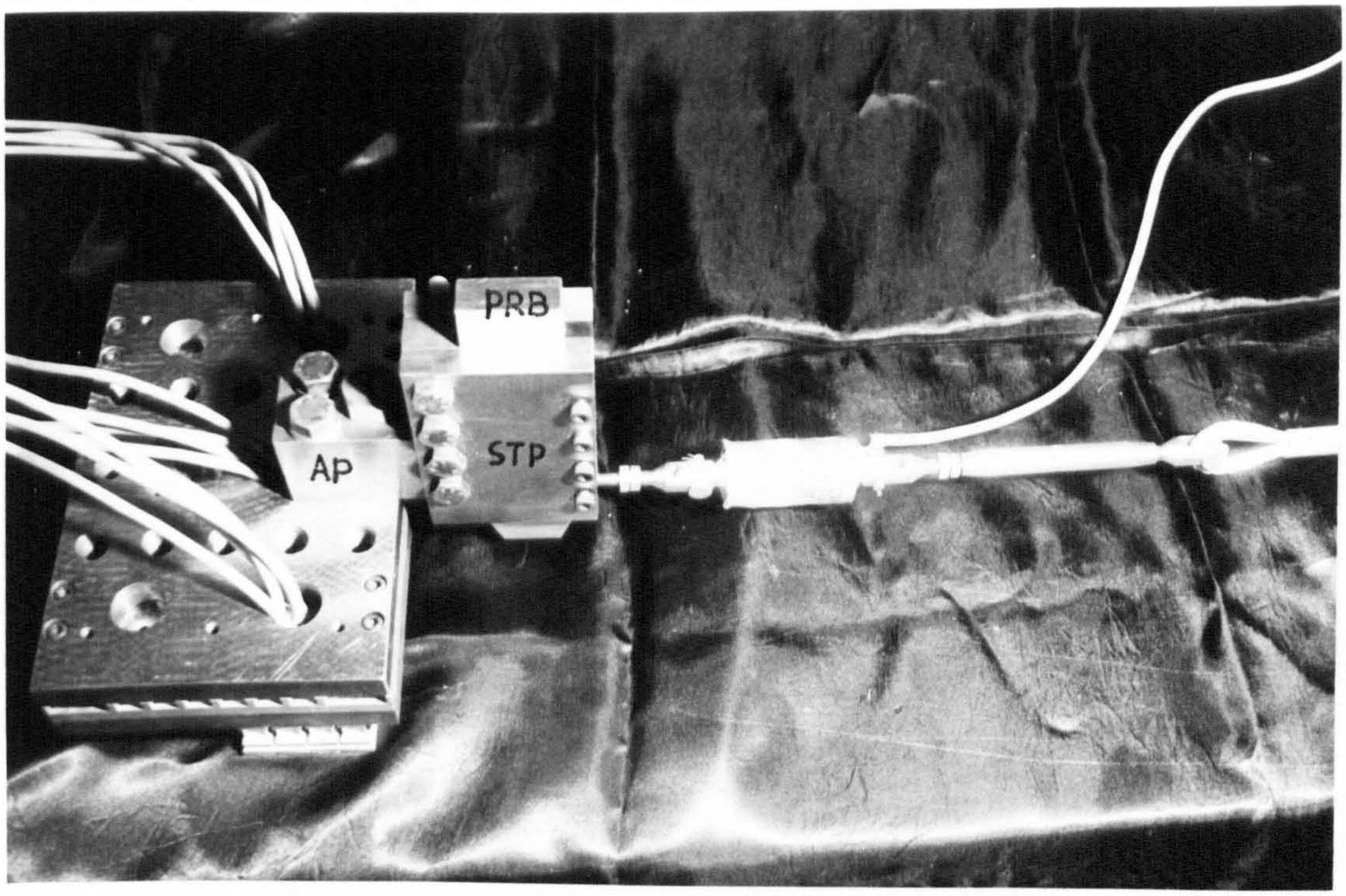

Fig. 3.7 The attachment for horizontal load

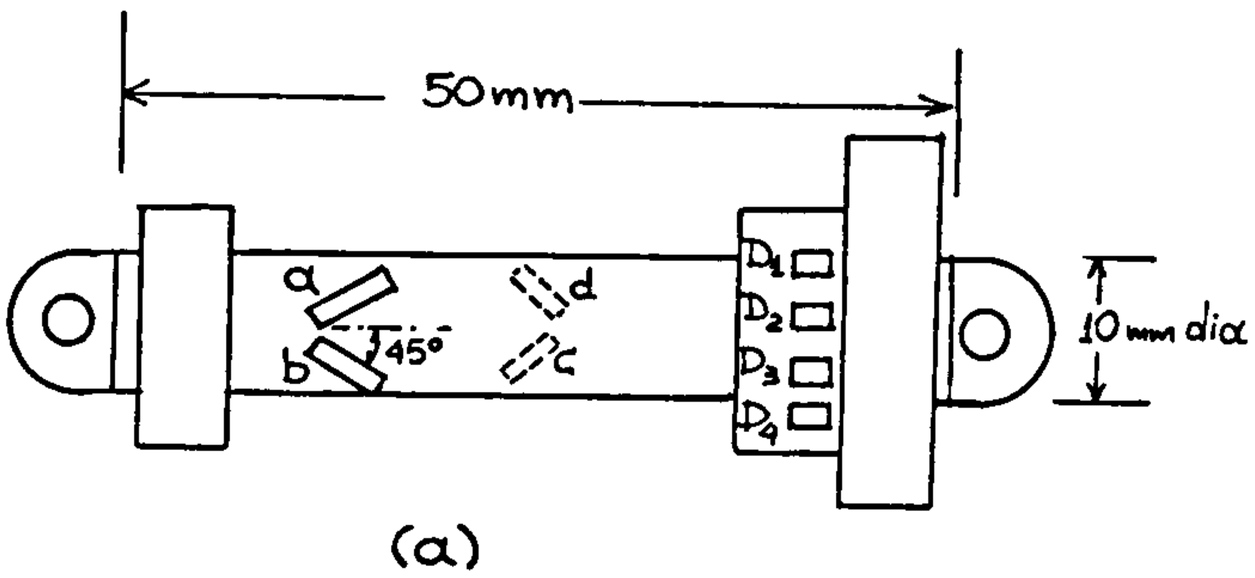

(a)

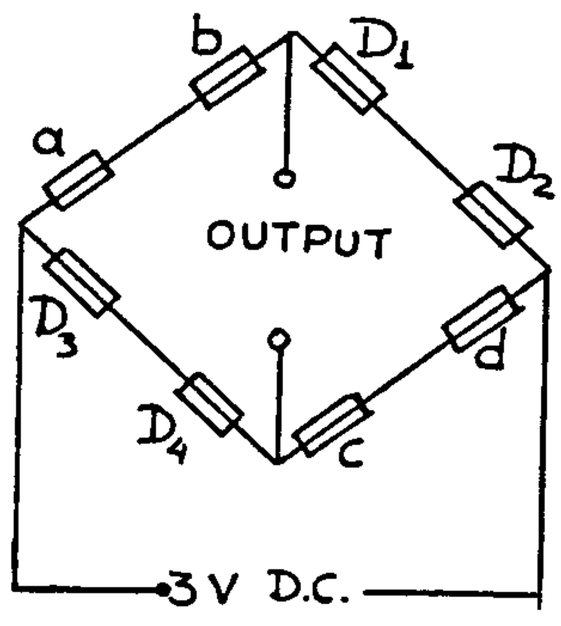

(b)

Fig. 3.8 Load cell to record the horizontal load
(a) Strain gauges arrangement (b) The circuit.

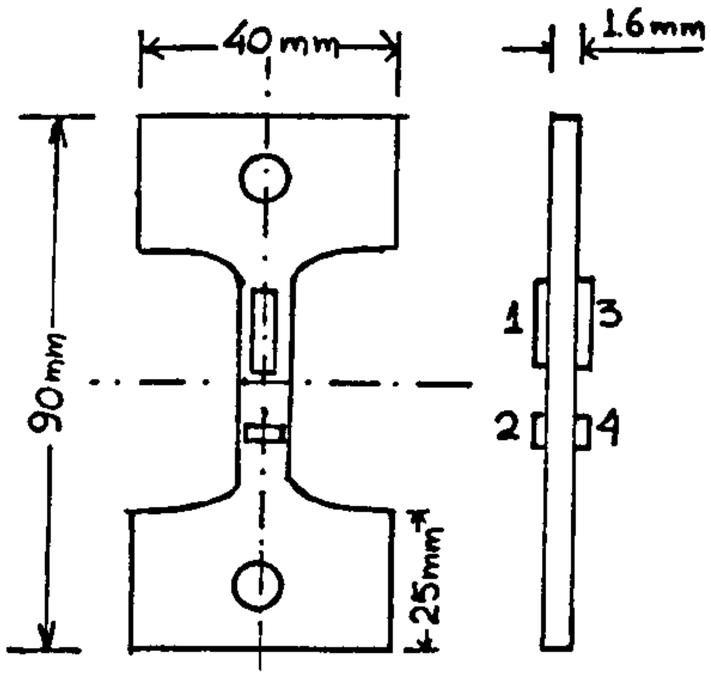

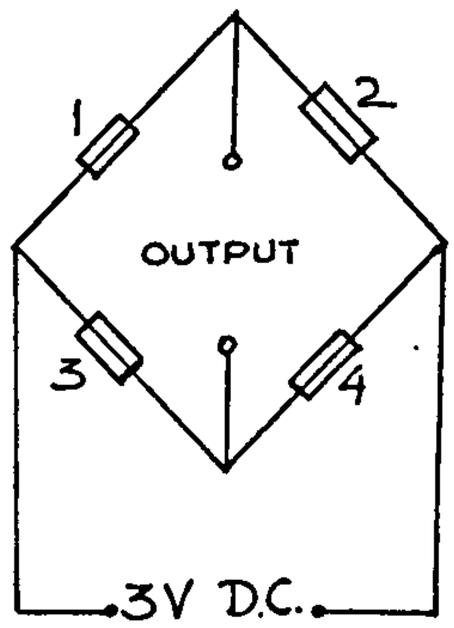

Fig. 3.9 Load cell to record small horizontal loads: Strain gauges arrangement and the resultant circuit.

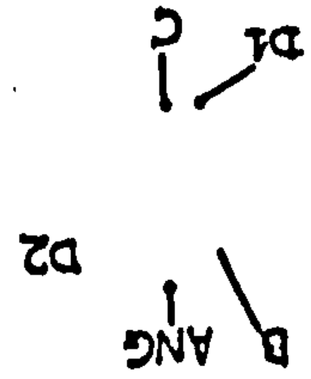
D1
C
B
ANG
D2

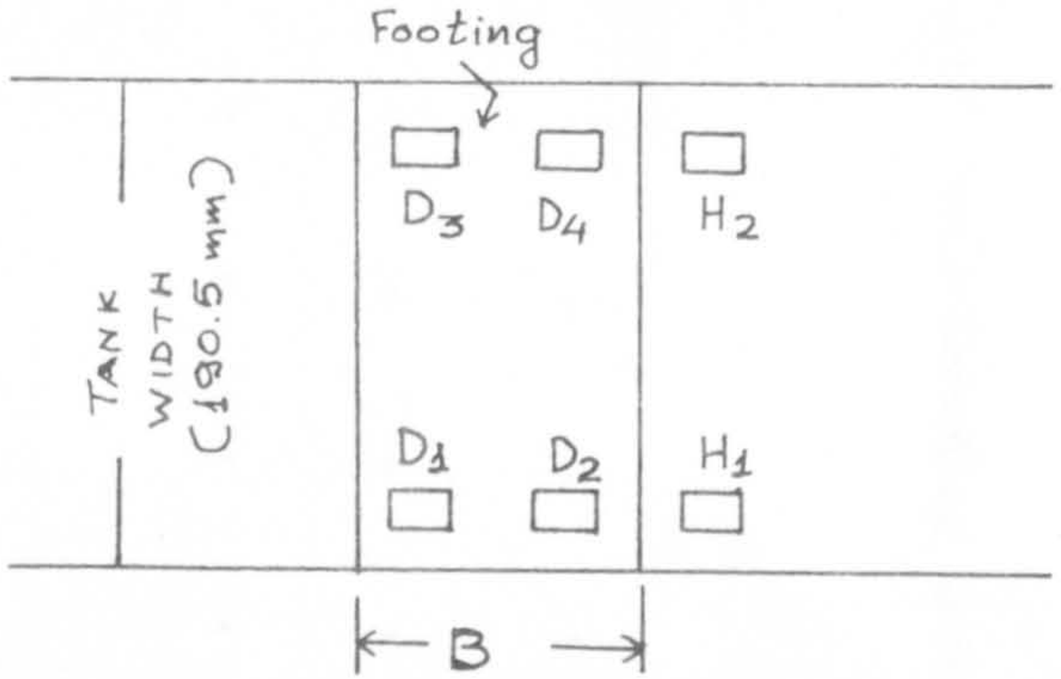

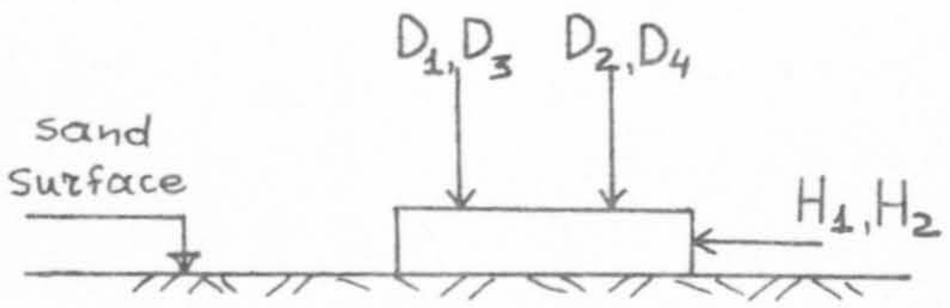

Fig. 3.11 The arrangement of the dial gauges.

←

Fig. 3.10 The FAC with the pulley system →

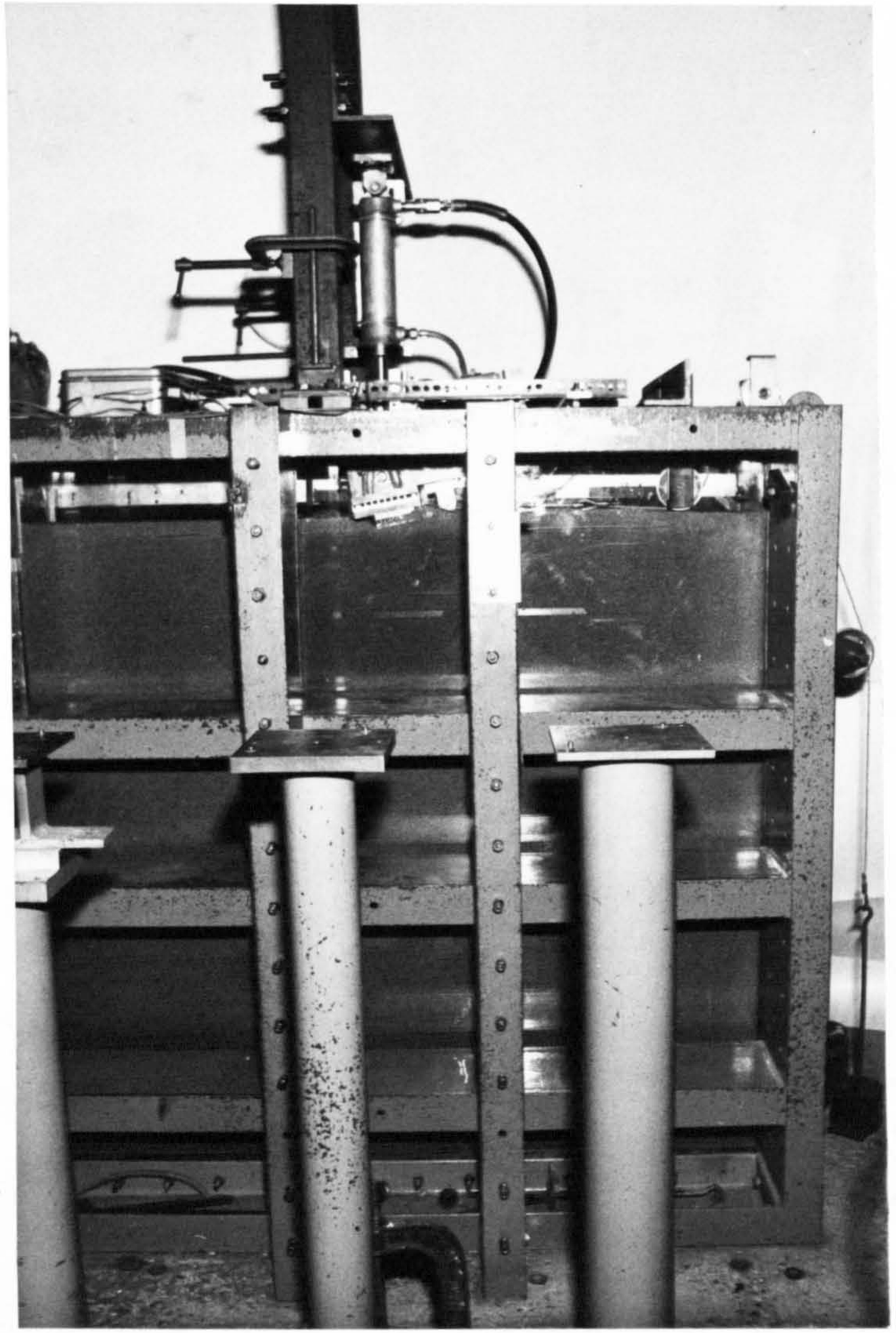

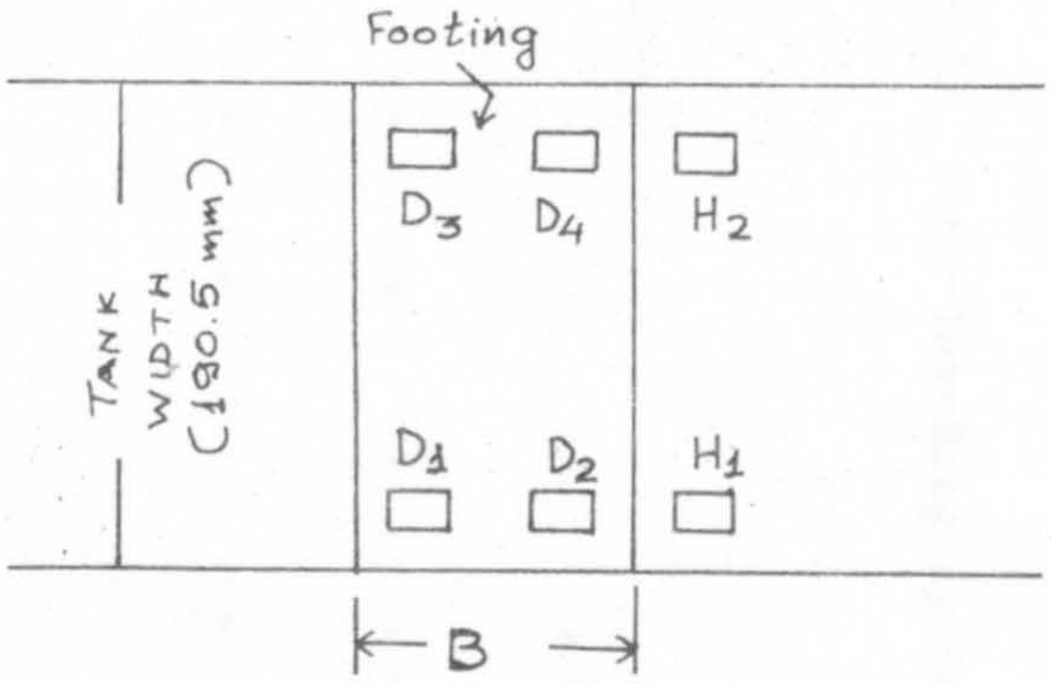

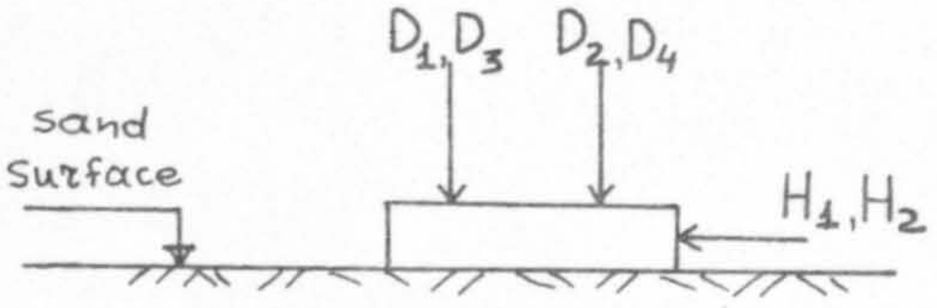

Fig. 3.10 The FAC with the pulley system →

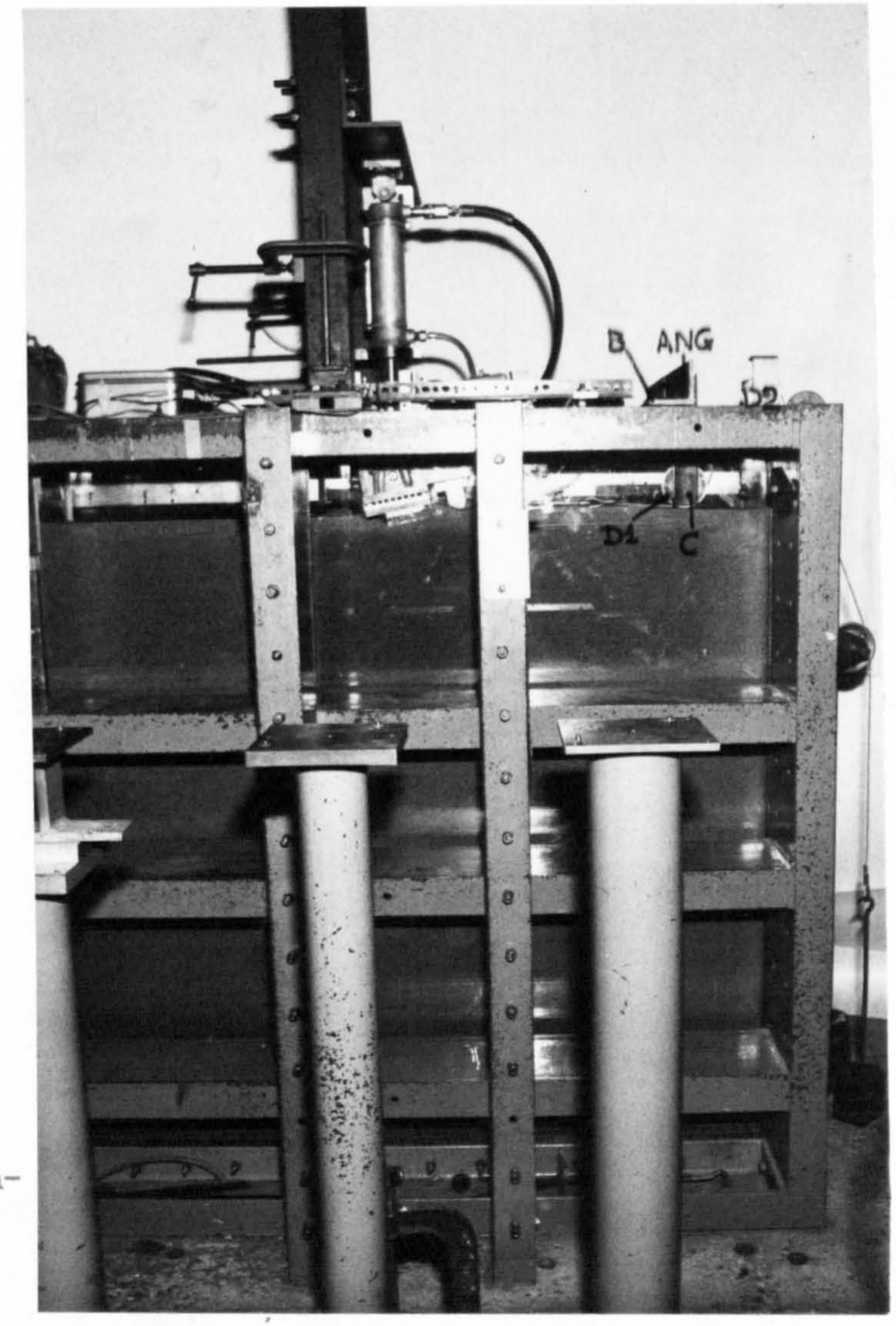

Fig. 3.11 The arrangement of the dial gauges.

←

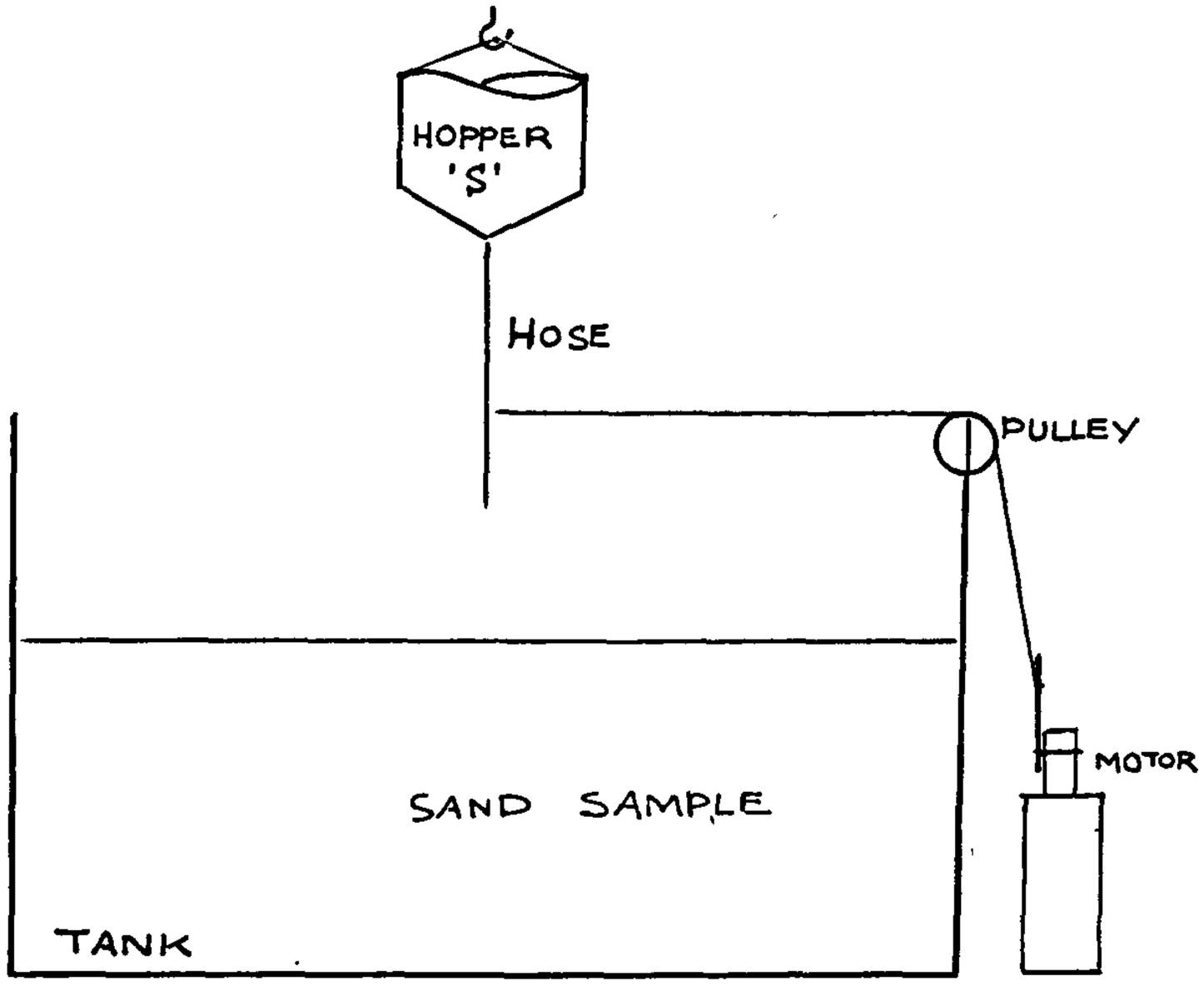

Fig. 3.12 Preparation of the first sand bed(FAC).

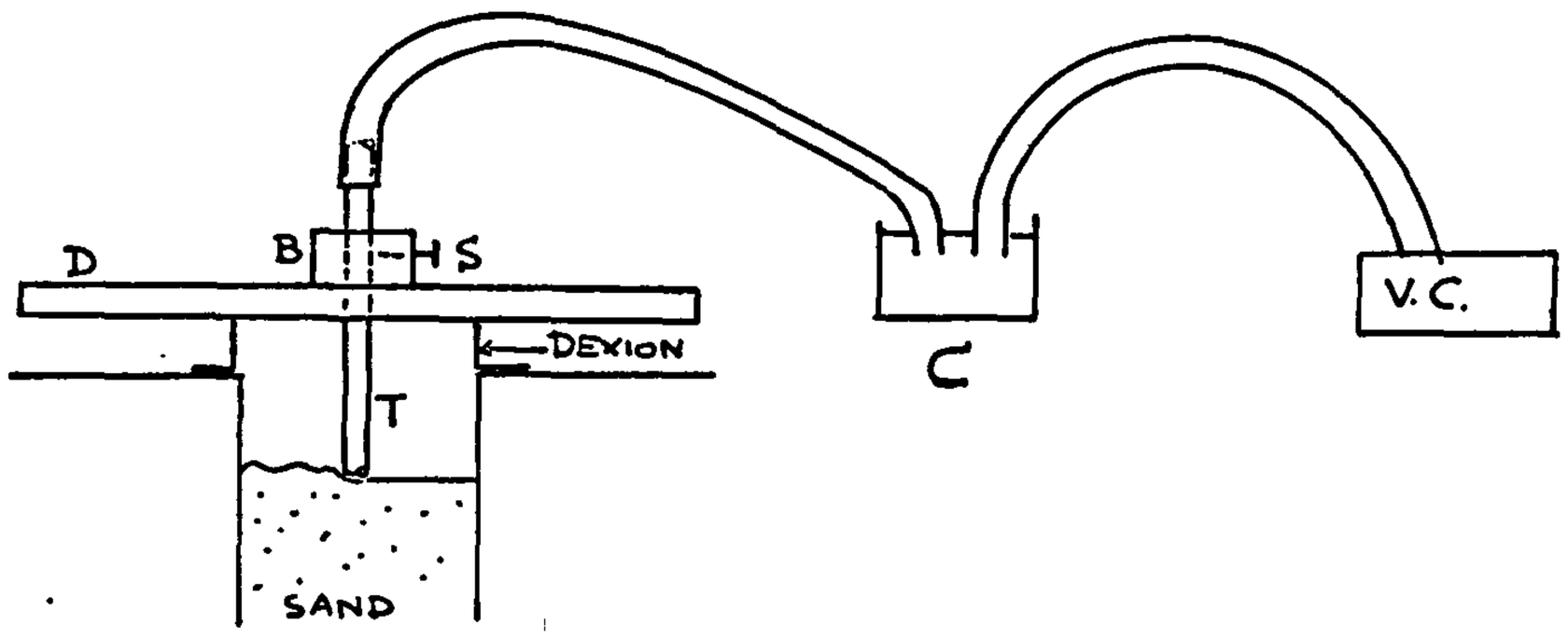

Fig. 3.13 Sand-levelling system.

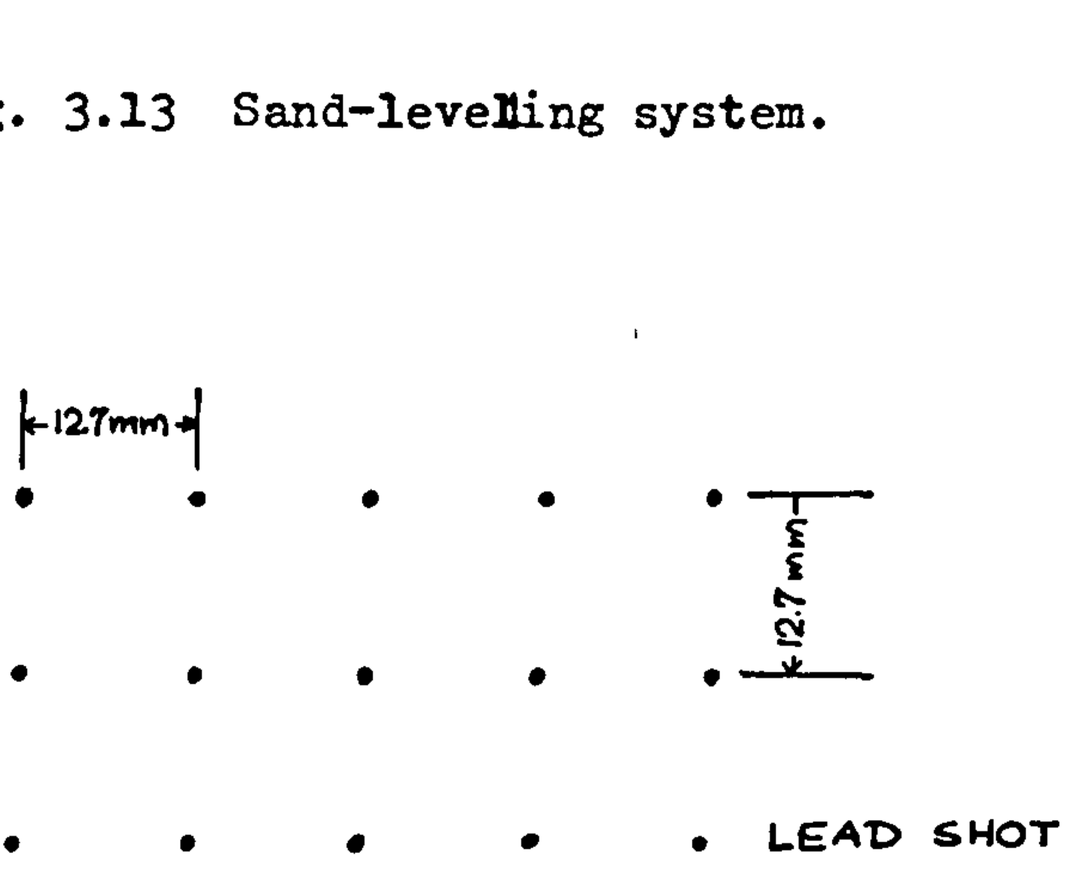

Fig. 3.14 Lead shot network.

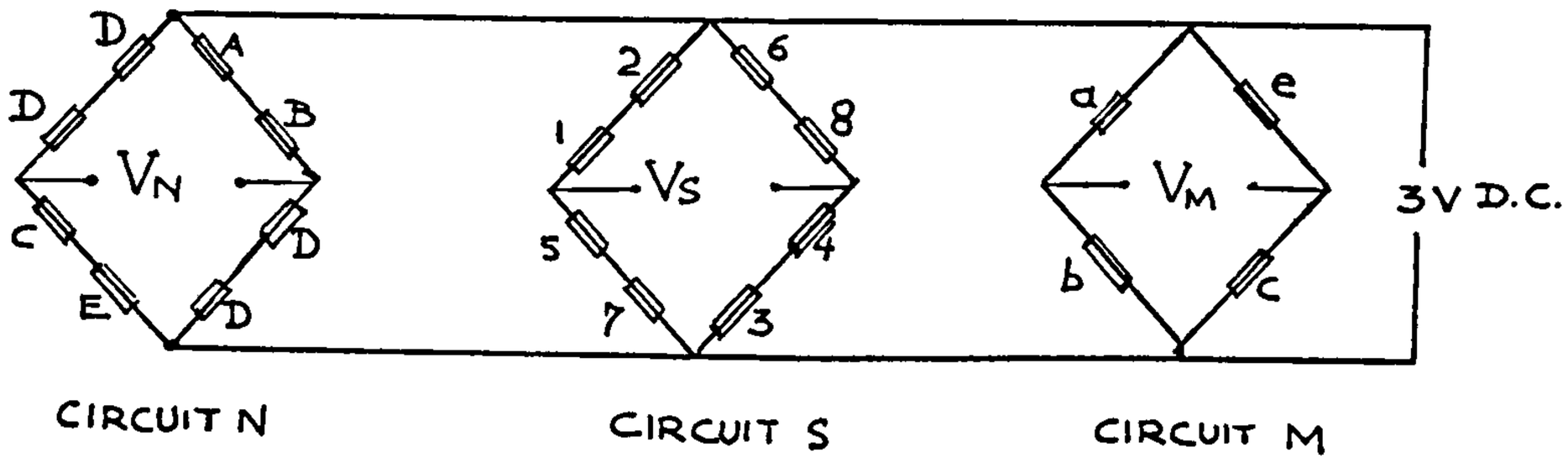

(a)

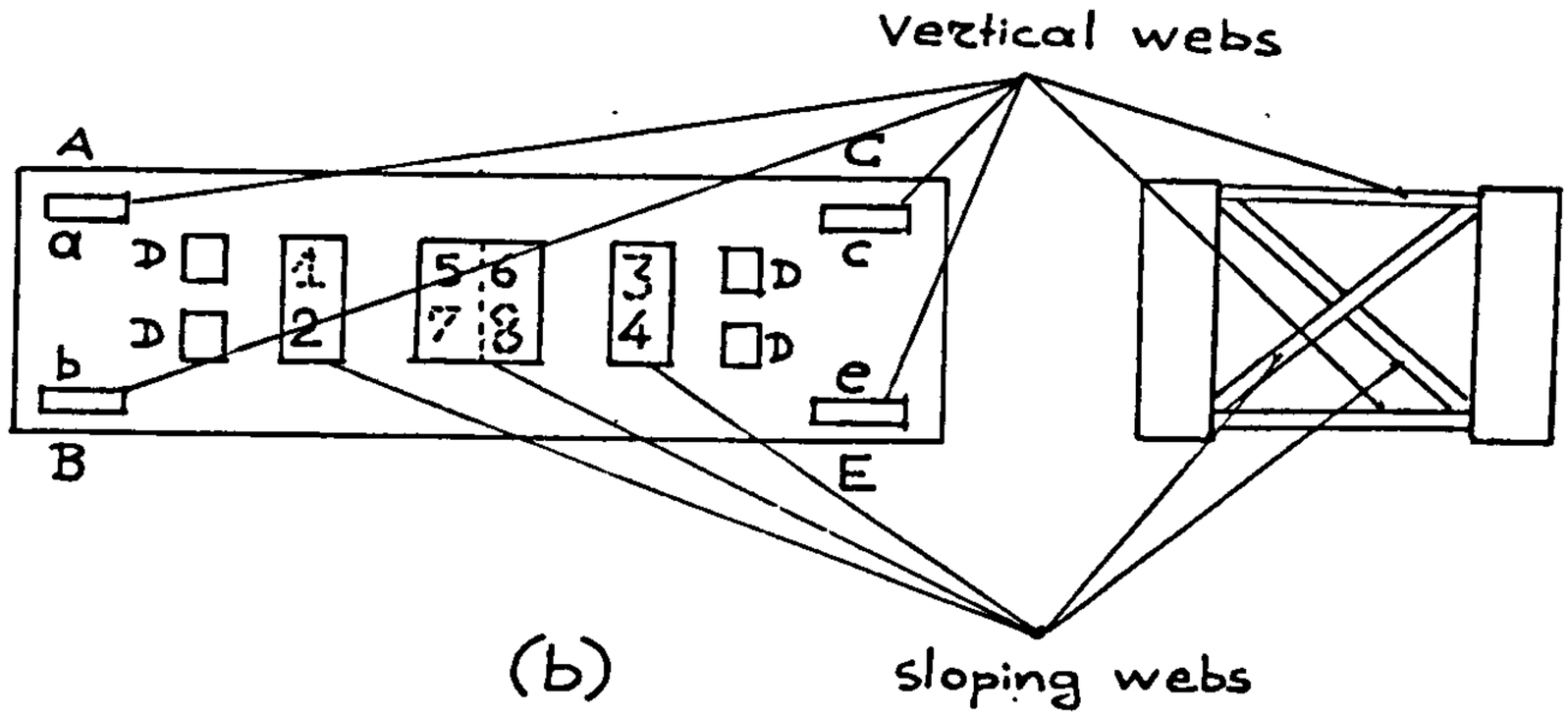

Fig. 3.15 Contact stress load cell
(a) The three circuits (b) The strain gauges arrangement.

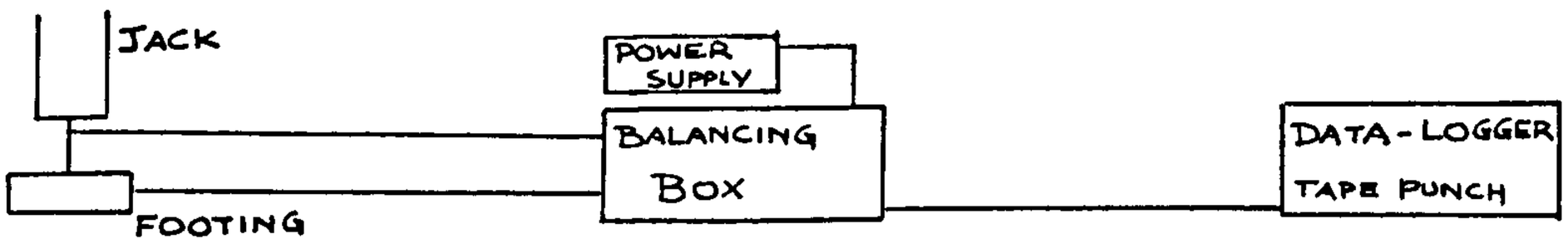

Fig. 3.16 General layout of the electrical connections at the FAC.

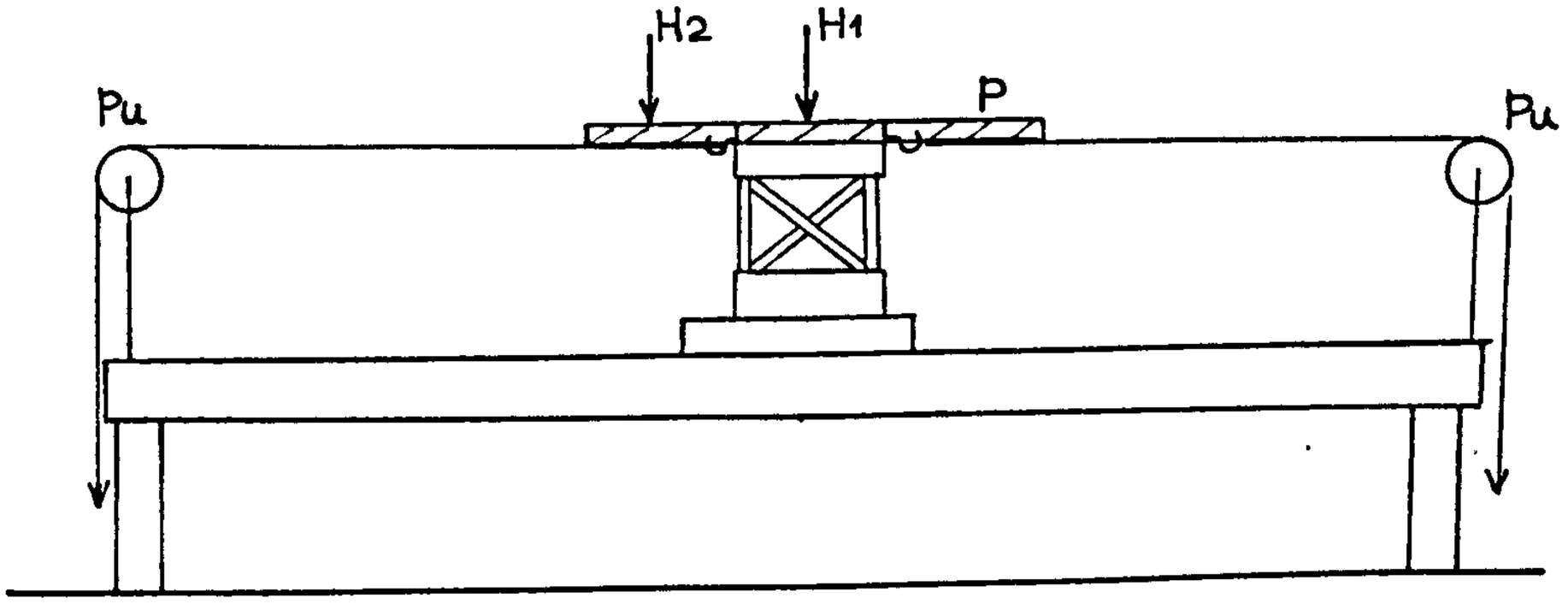

Fig. 3.17 Calibration of the load cell.

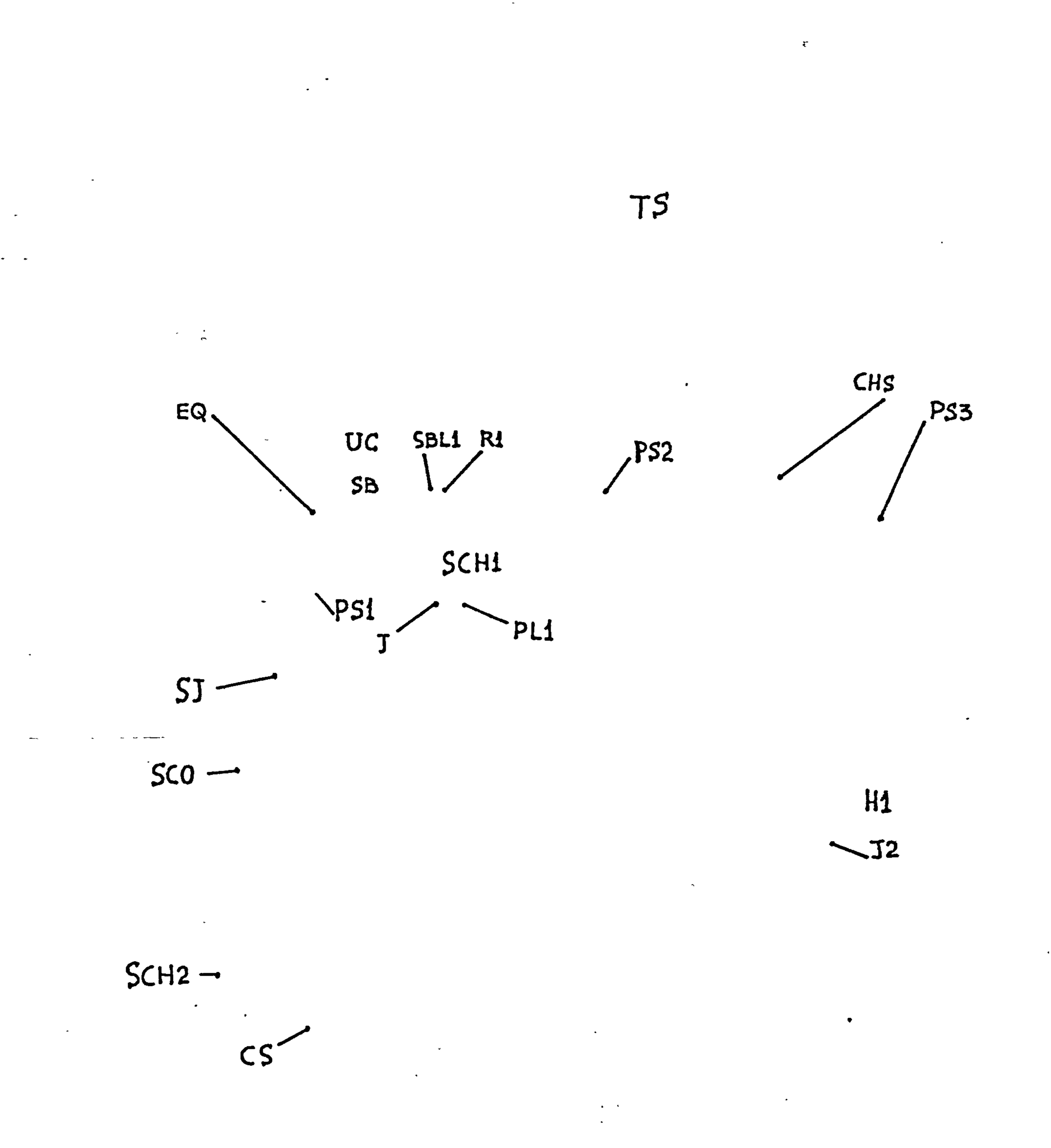

Fig.4.1 The Footing Apparatus at Southampton (FAS)

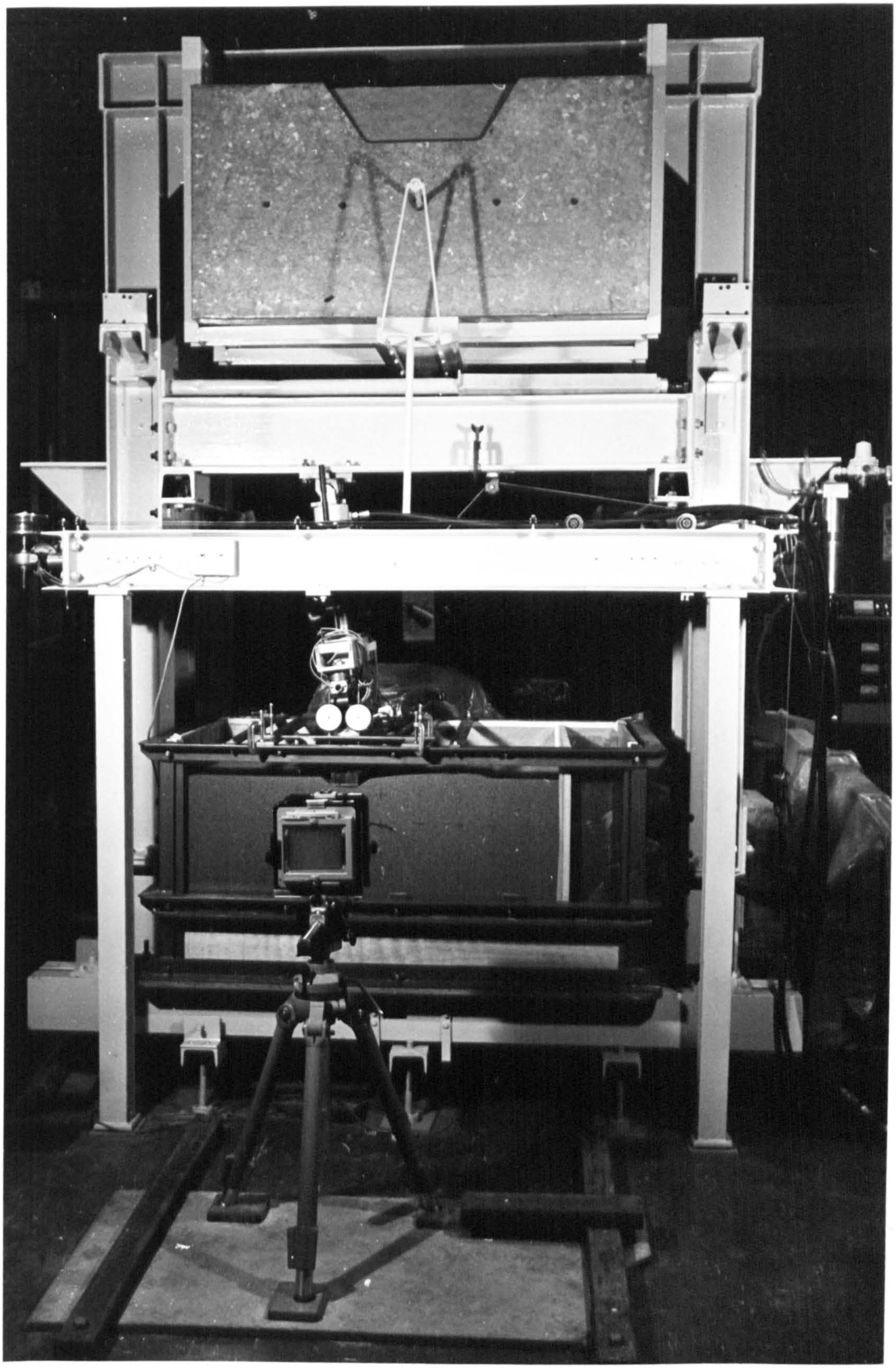

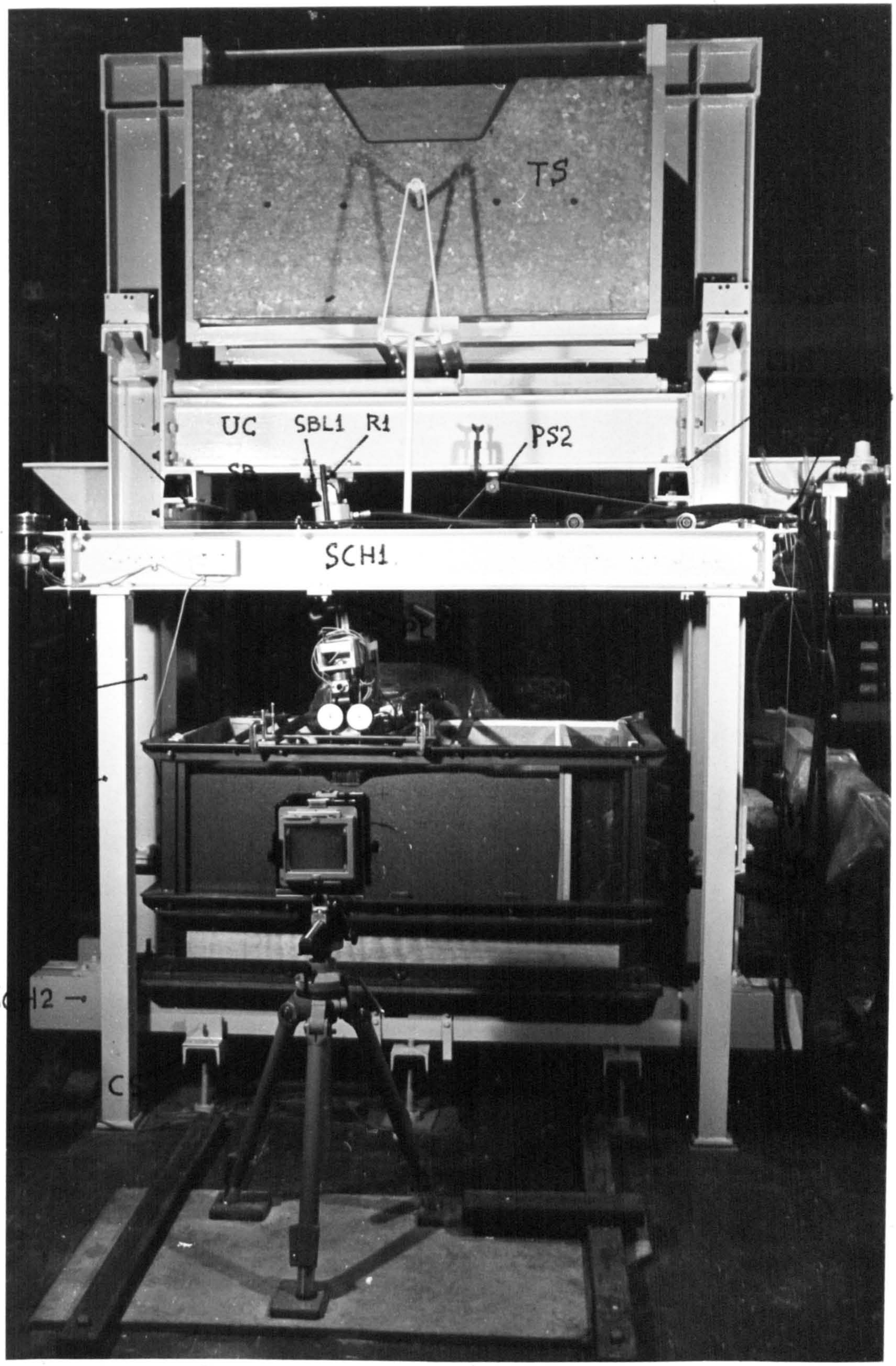

Fig.4.1 The Footing Apparatus at Southampton (FAS)

PL1

CHAN

B

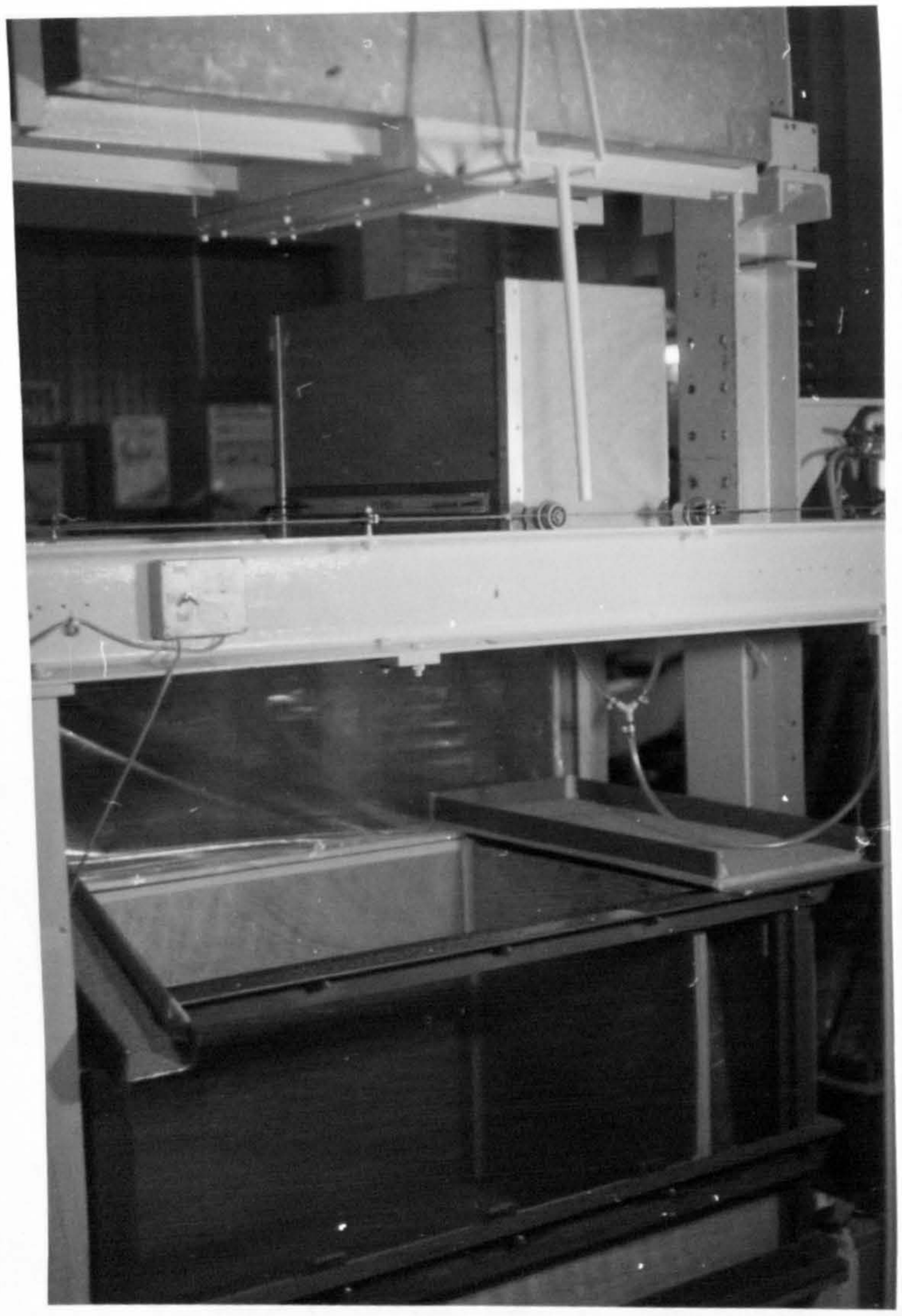

Fig. 4.2a The footing assembly (side view).

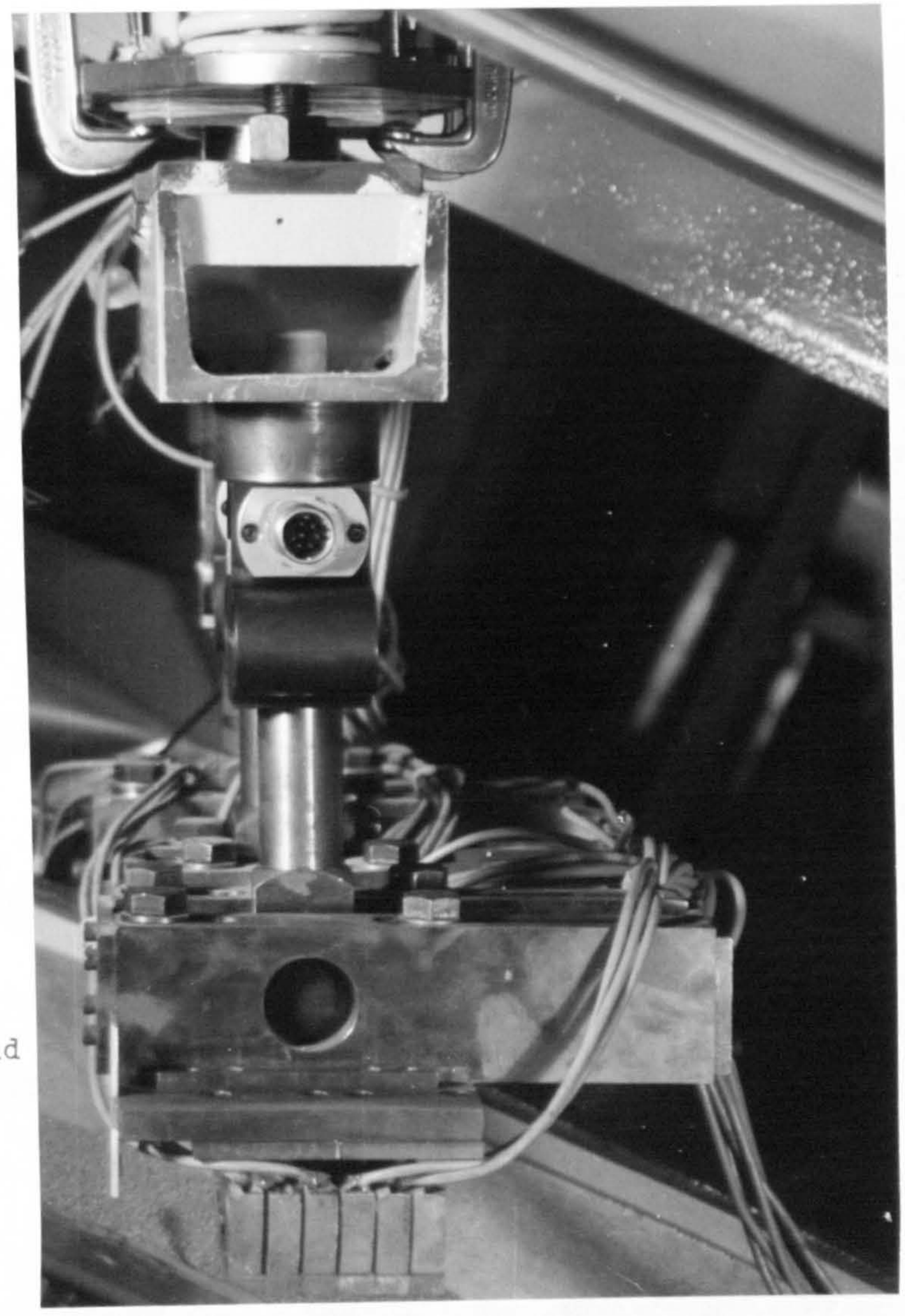

Fig. 4.3 The sand spreader.

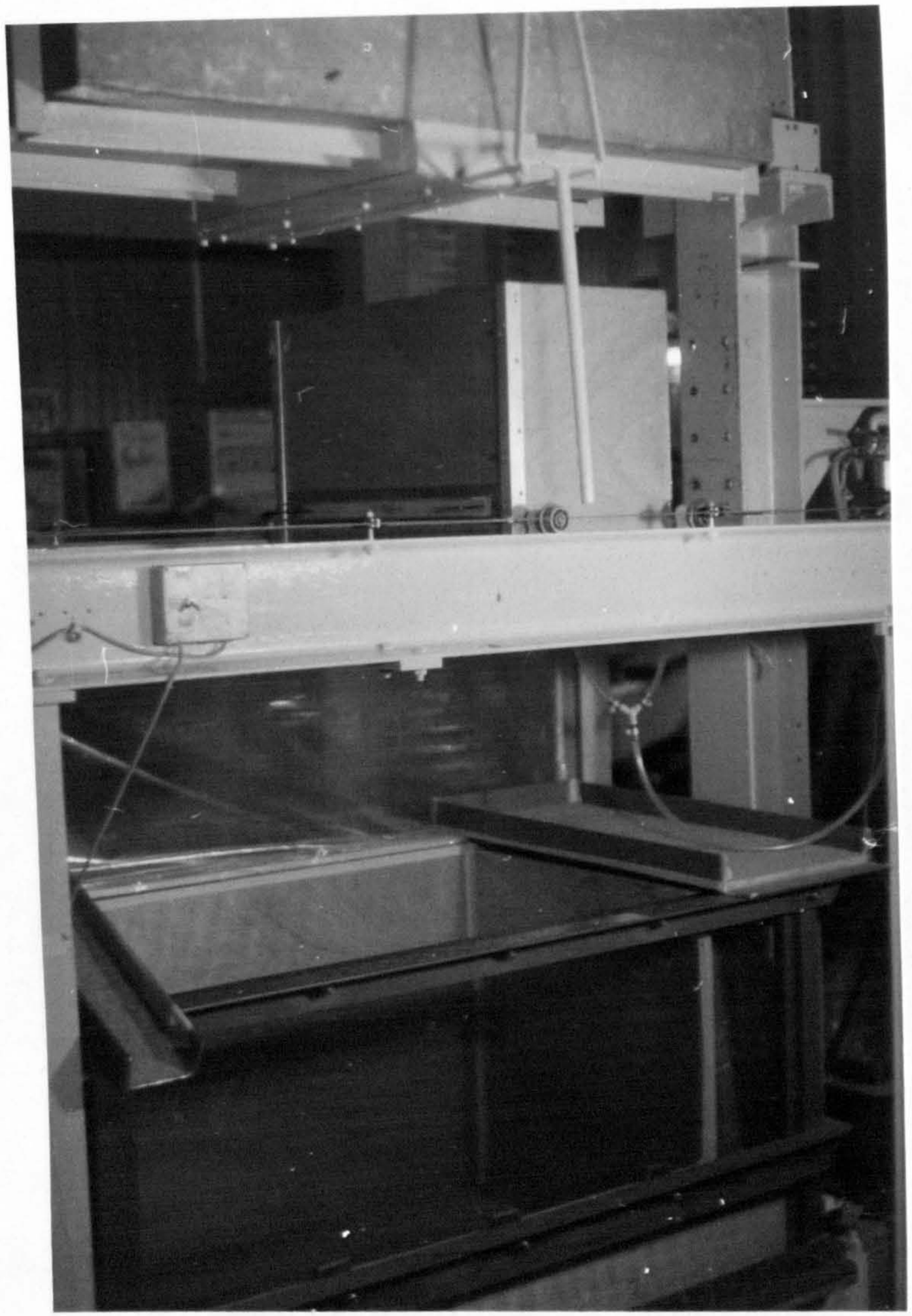

Fig. 4.2a The footing assembly (side view).

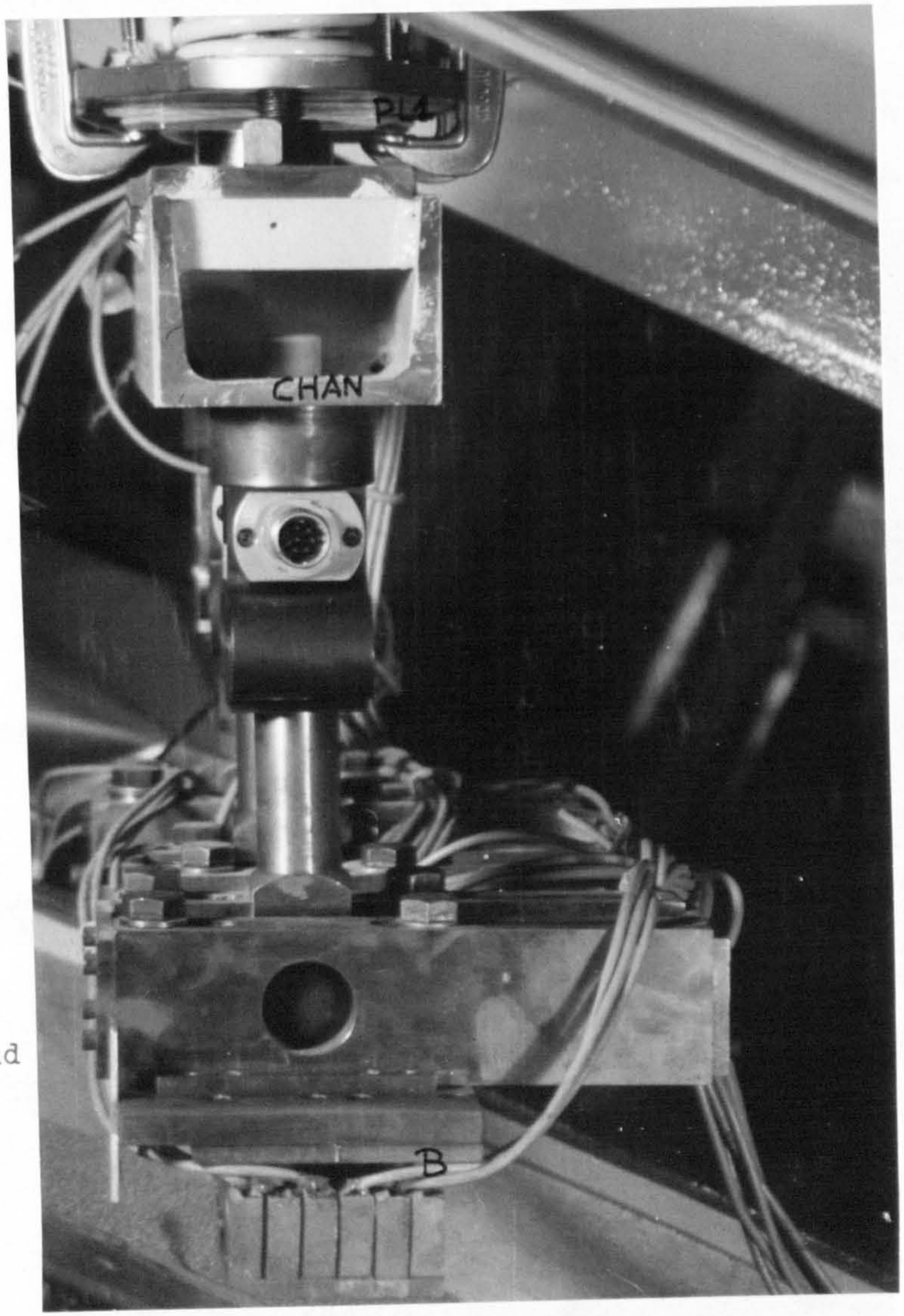

Fig. 4.3 The sand spreader.

CHAN

Shear
Connector

Shear
connector

S.F.

C.F.

D.F.

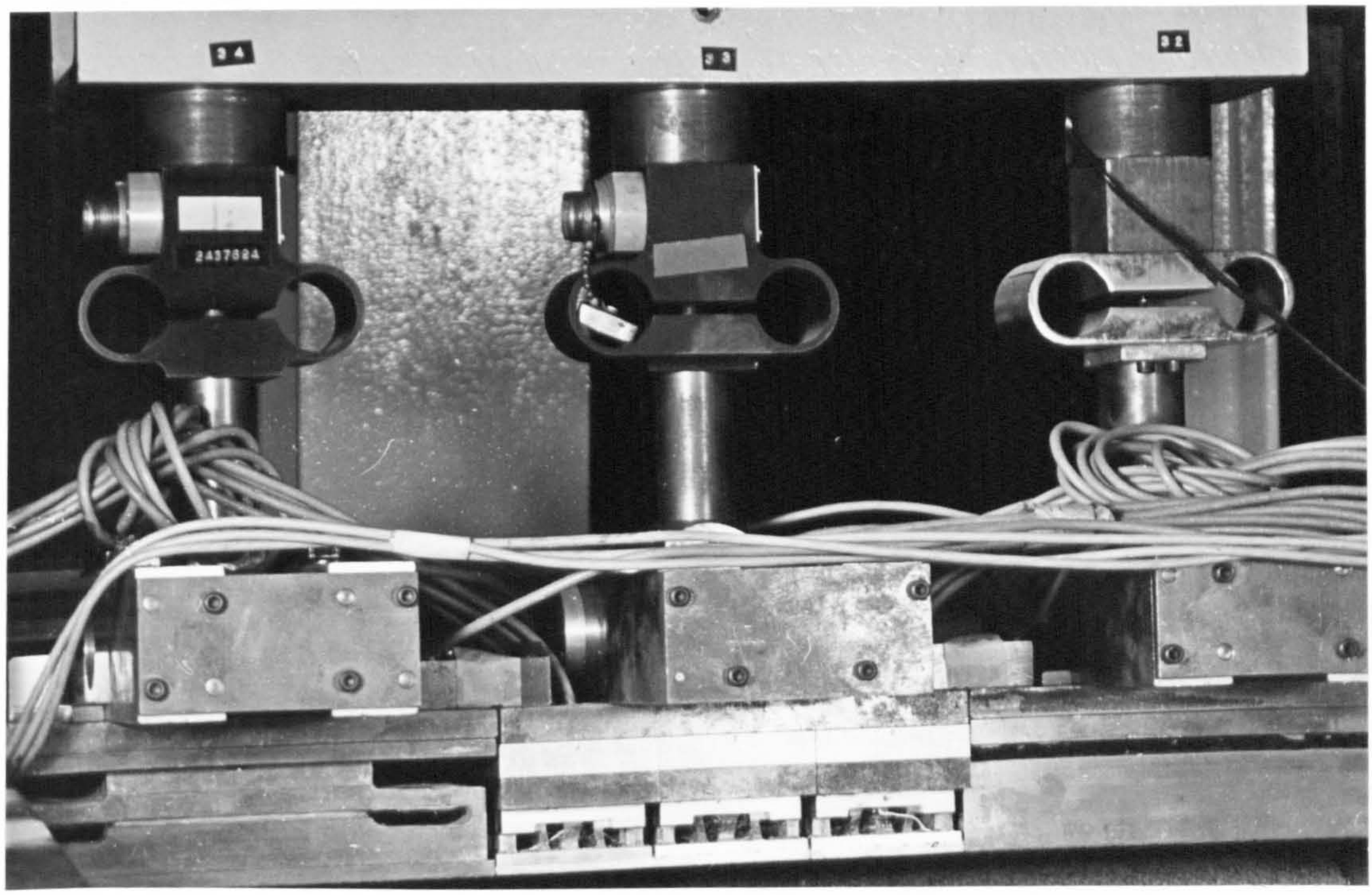

Fig. 4.2b The footing assembly (front view).

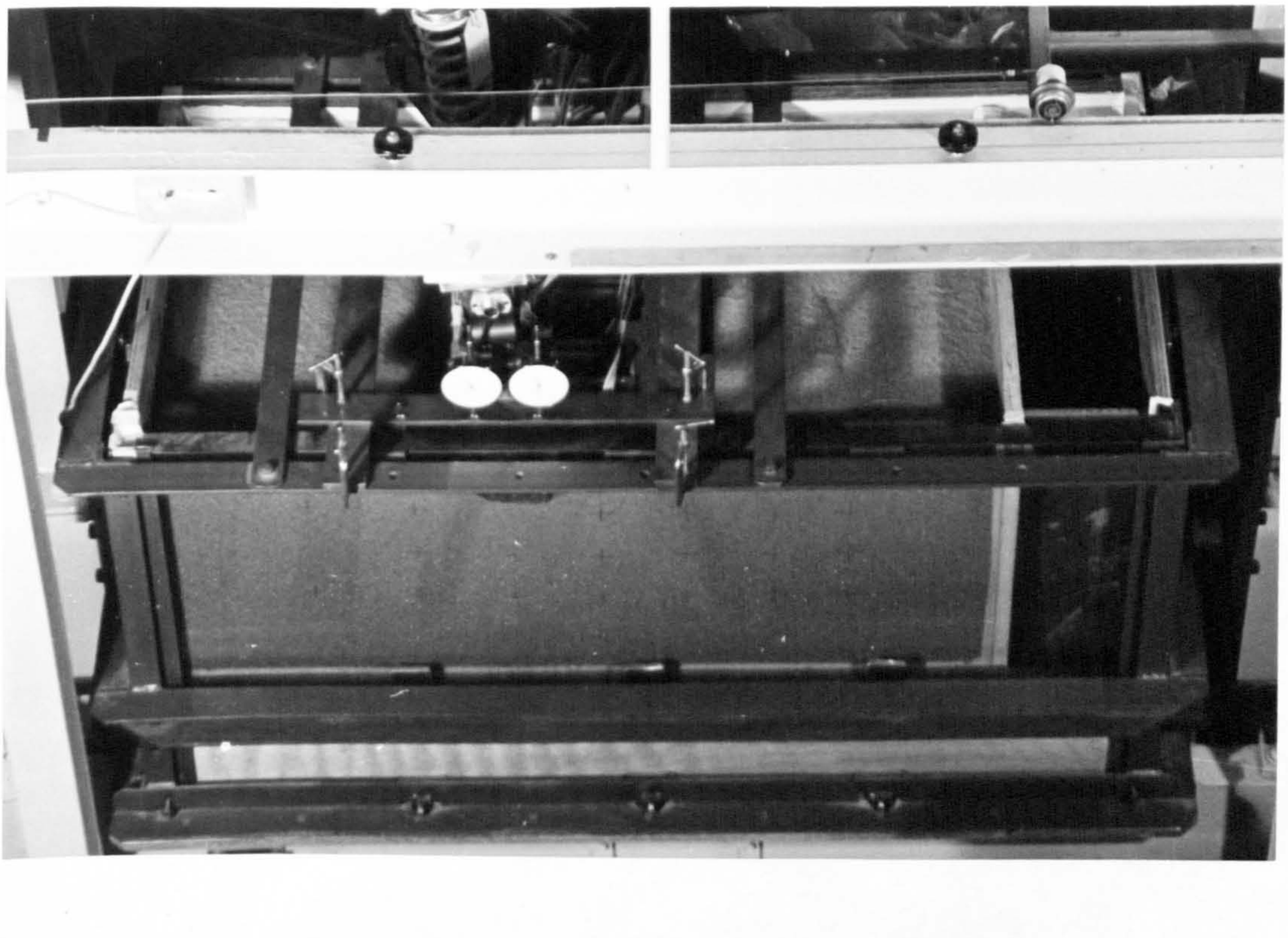

Fig. 4.4 The sand container.

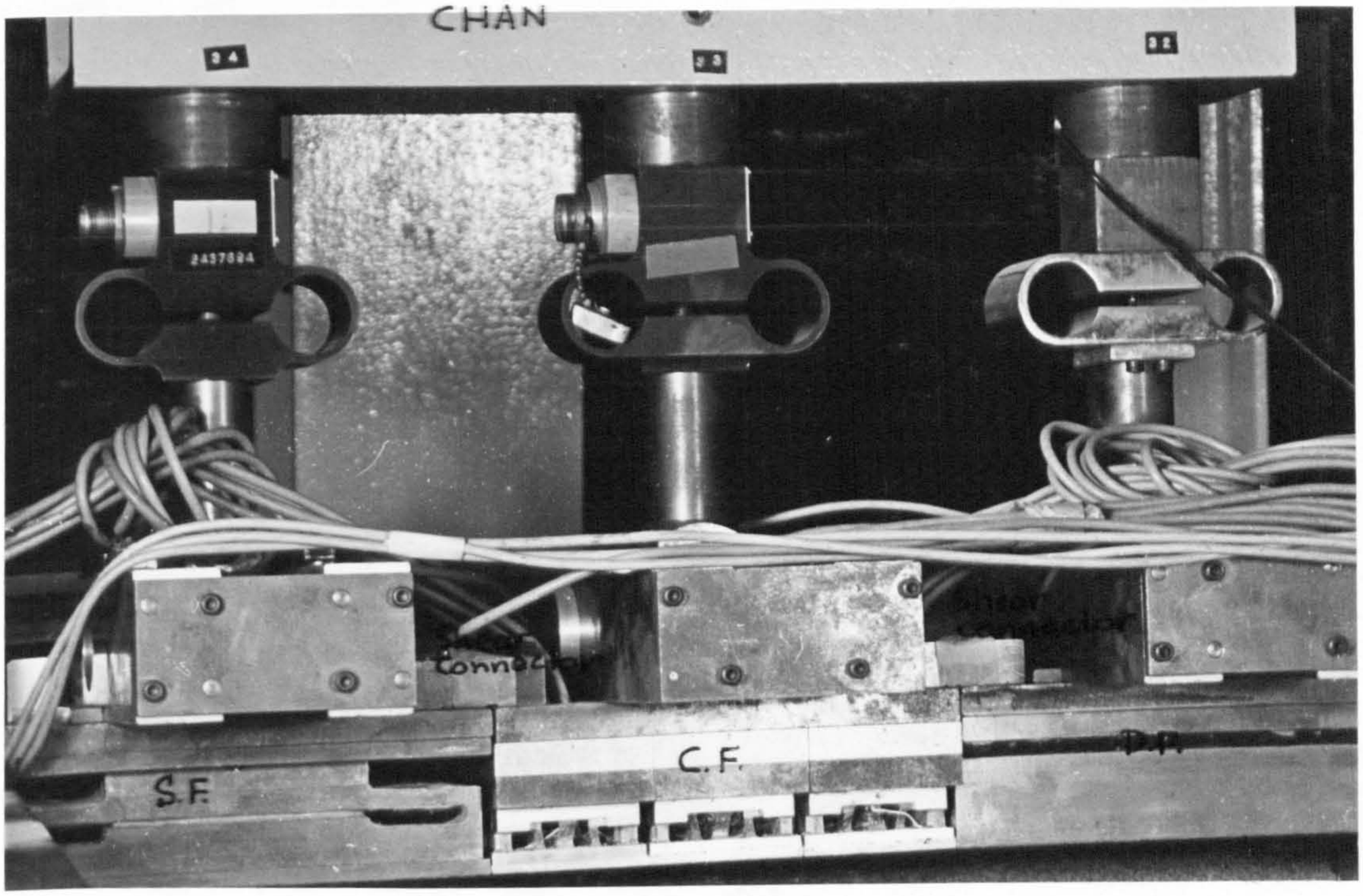

Fig. 4.2b The footing assembly (front view).

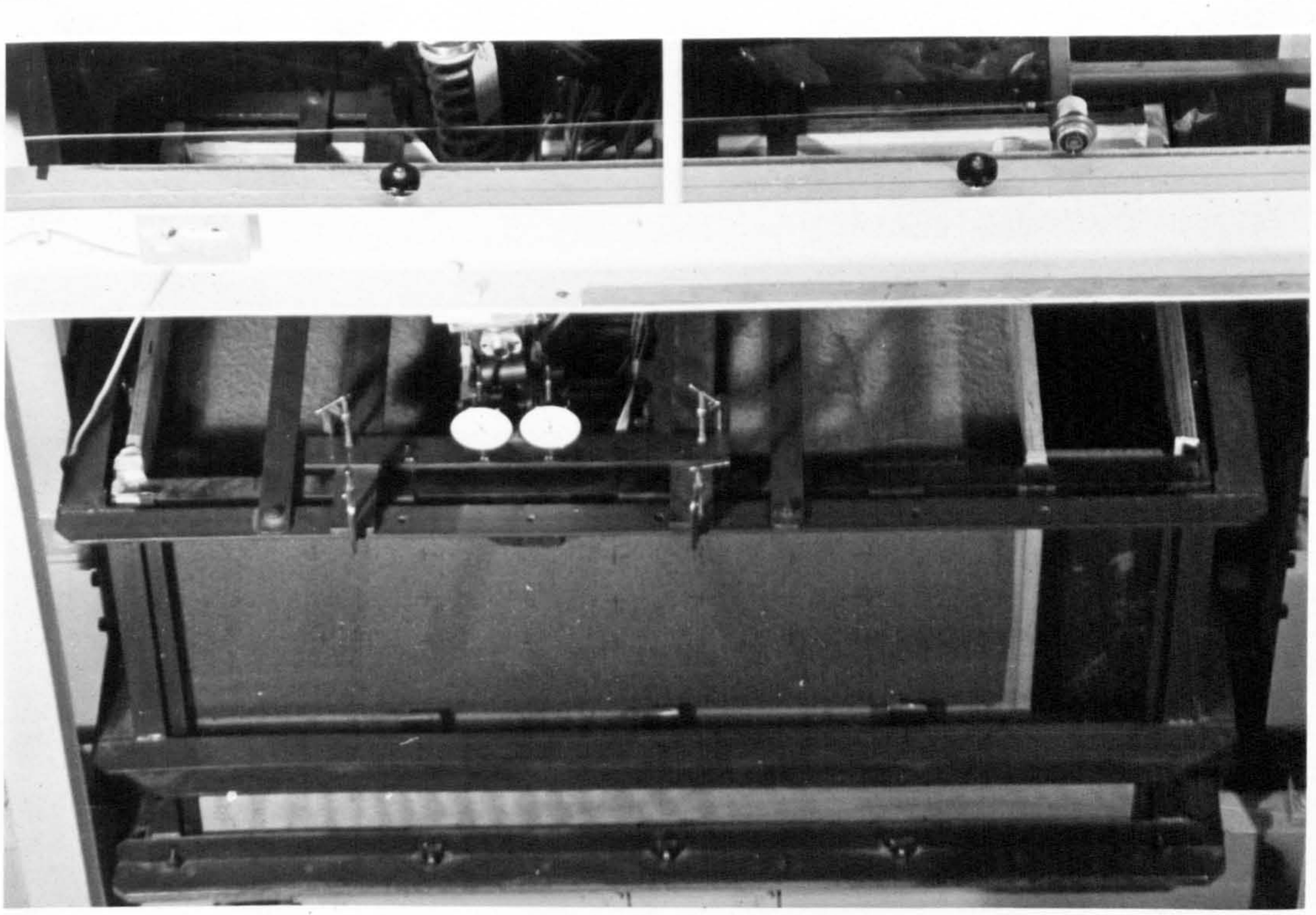

Fig. 4.4 The sand container.

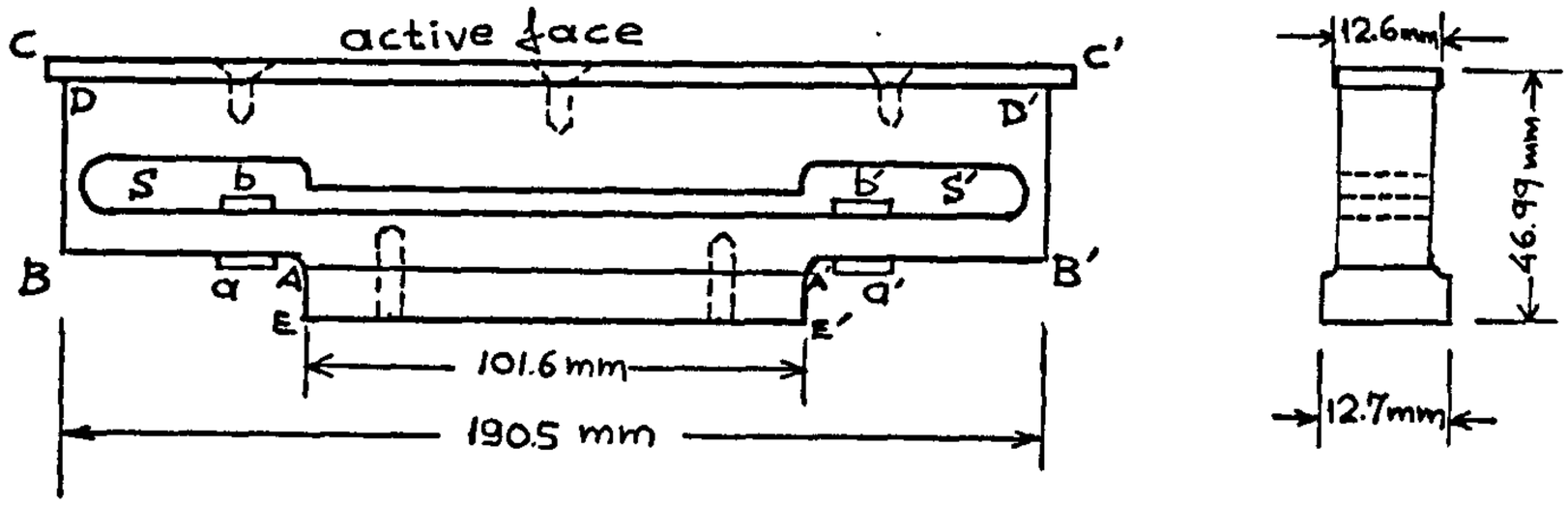

Fig. 4.5 The normal load cell of the Southampton Footing.

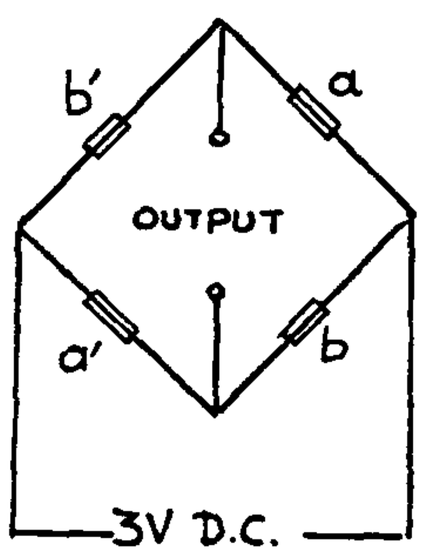

Fig. 4.6 The circuit of the normal load cell.

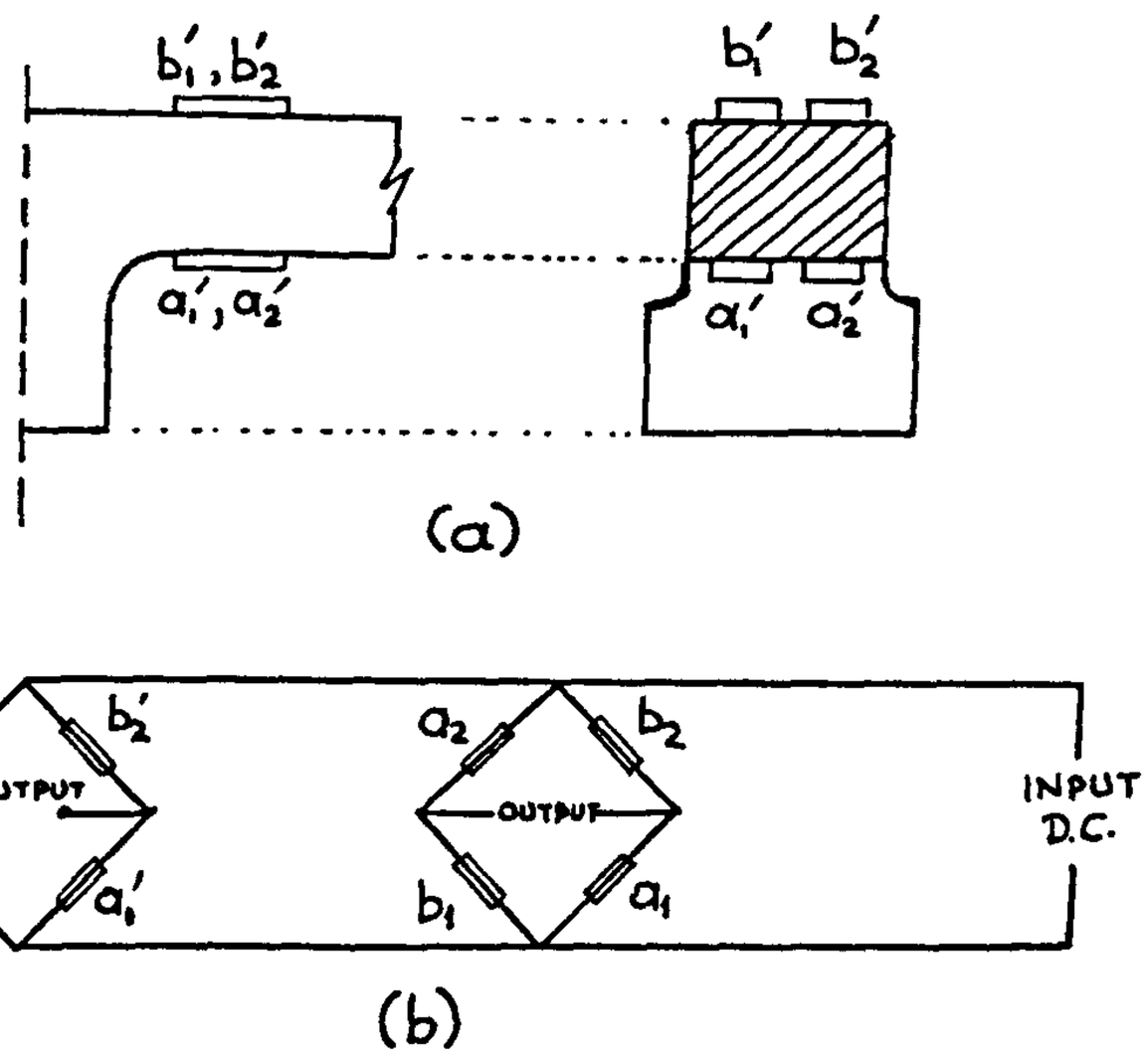

Fig. 4.7 An alternative circuitry for the normal load cell
(a) Strain gauges arrangement (b) Circuit.

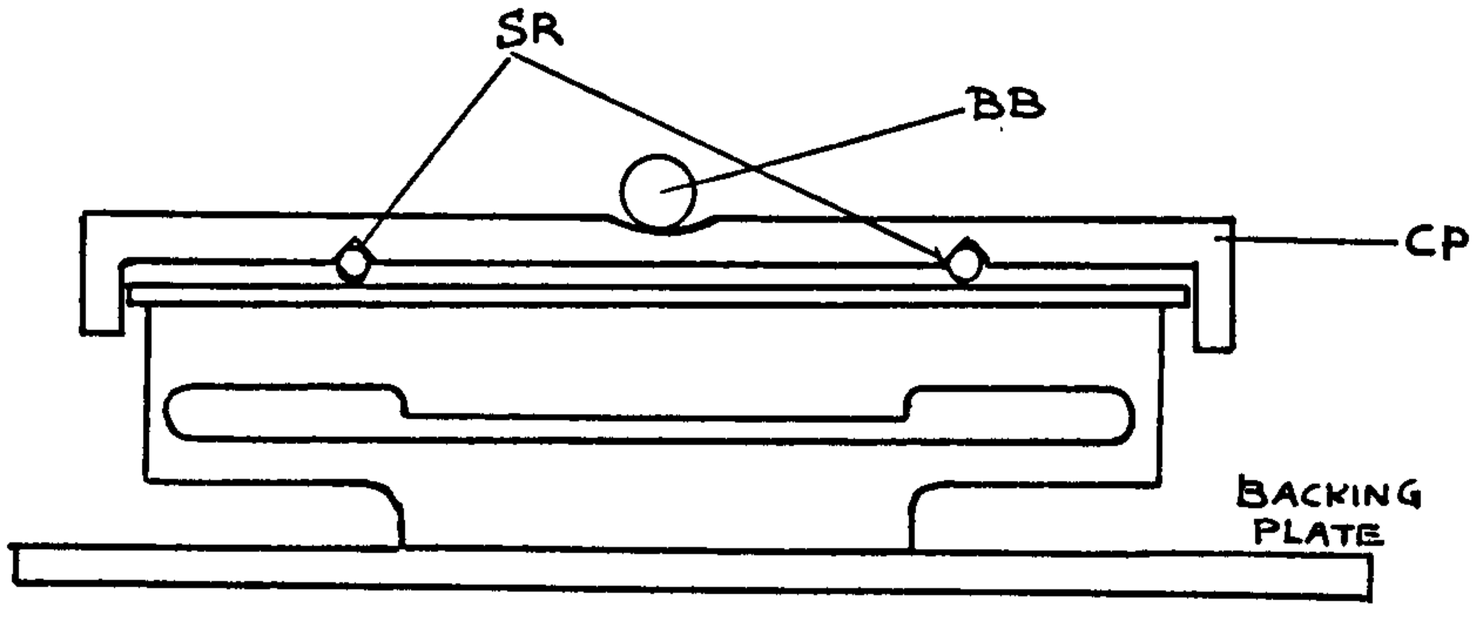

Fig. 4.8 Calibration arrangement for the normal load cell.

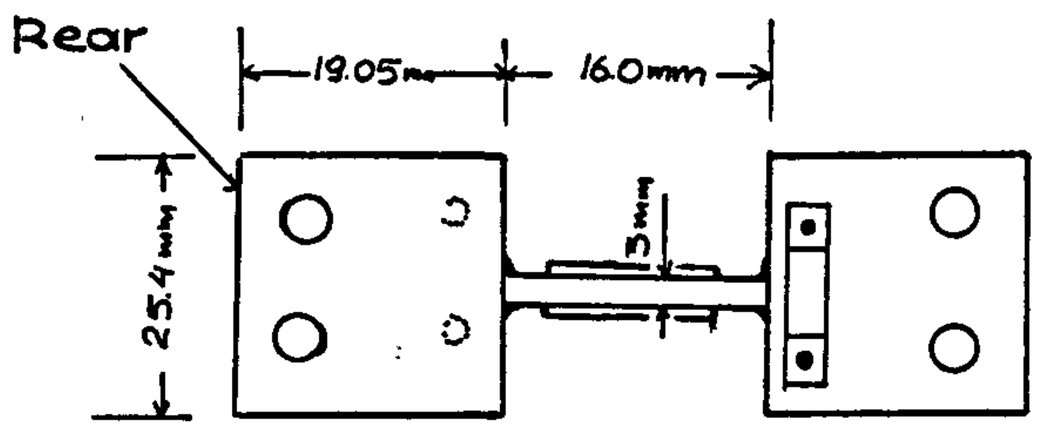

(a)

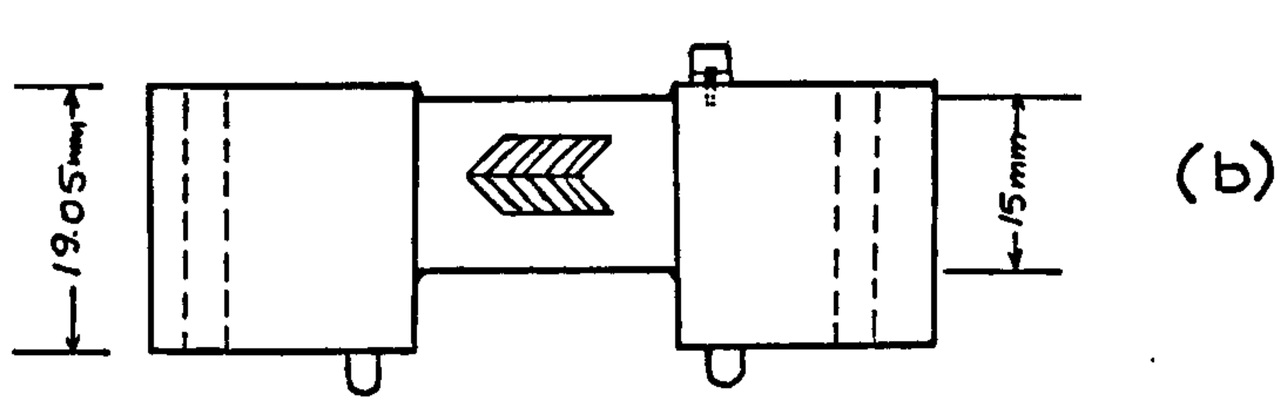

(b)

Fig. 4.9 The 'shear connector'
(a) Plan view (b) Side view.

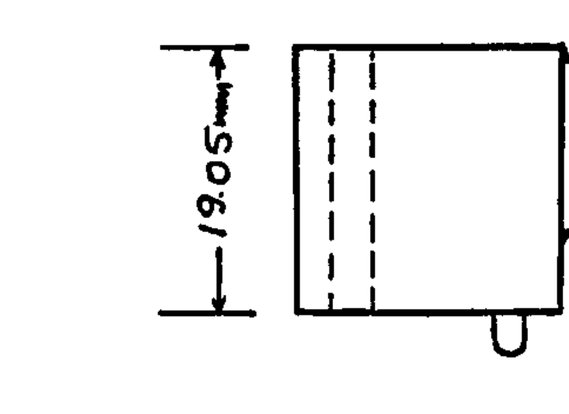

(a)

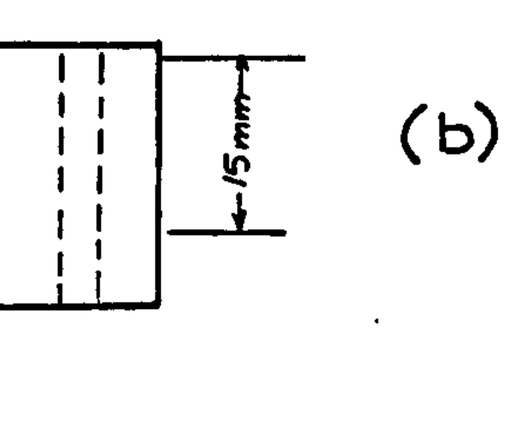

(b)

Fig. 4.10 The 'shear connector'.
(a) Forces on the web and strain gauges arrangement
(b) Circuit.

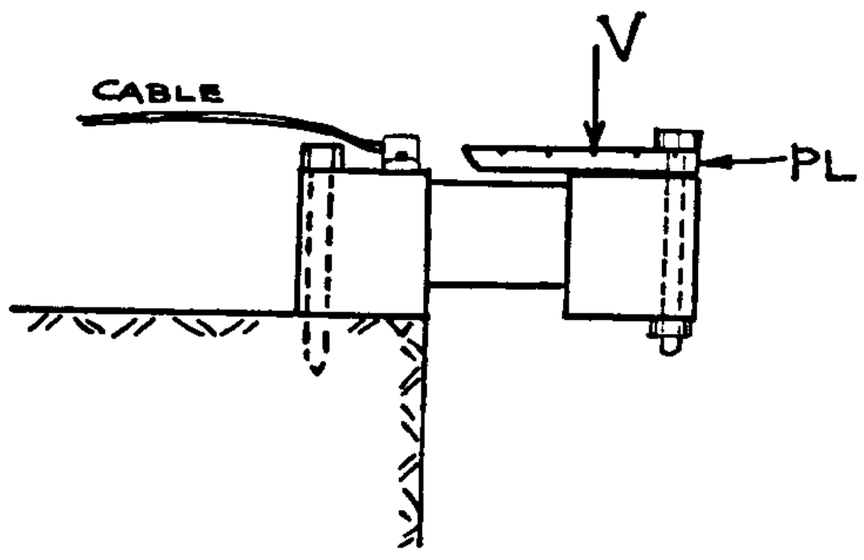

Fig. 4.11 The 'shear connector': Calibration arrangement.

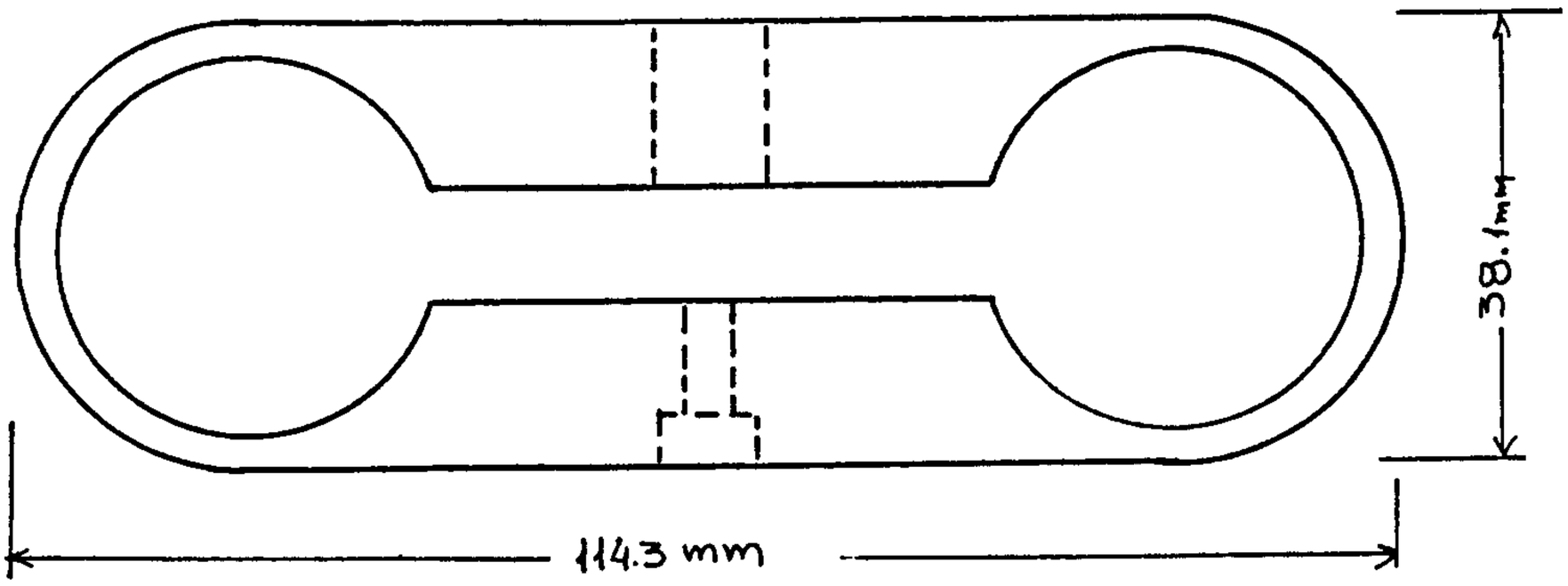

Fig. 4.12 The total load cell.

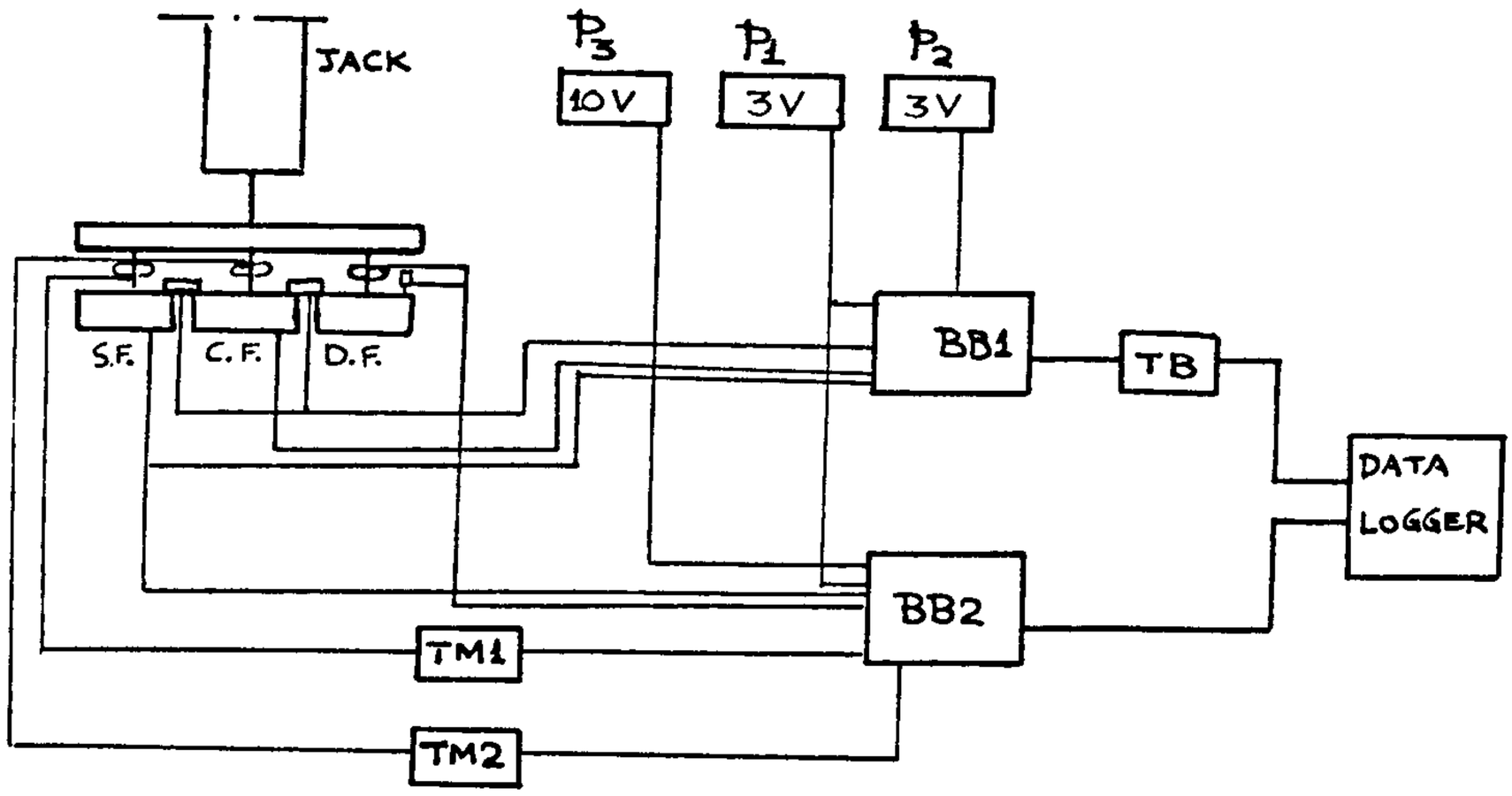

Fig. 4.13 General layout of the electrical connections at the FAS.

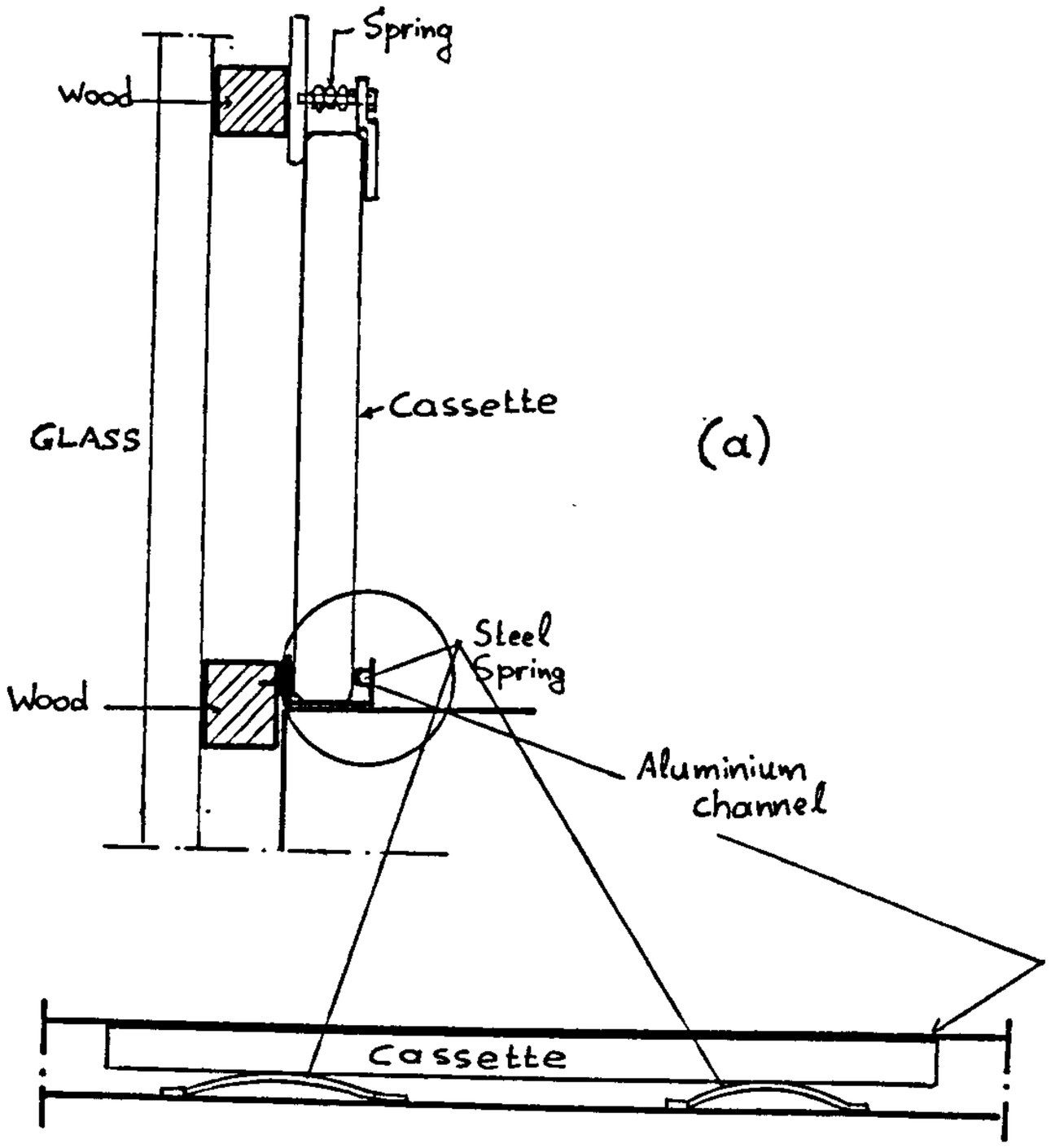

Fig. 5.1 The X-rays cassette holder (a) General arrangement
(b) Detail of the lower aluminium holder

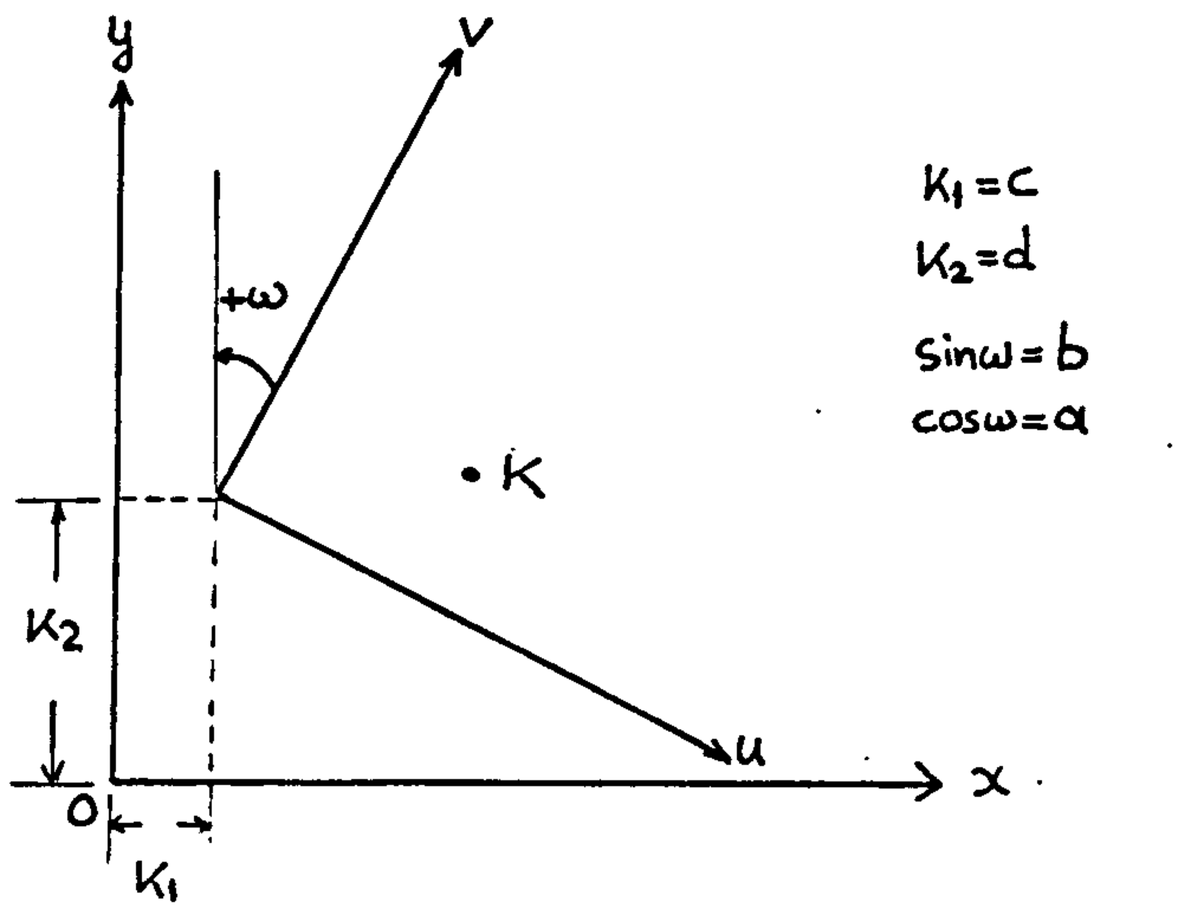

Fig. 5.2 Two normal right handed axis systems.

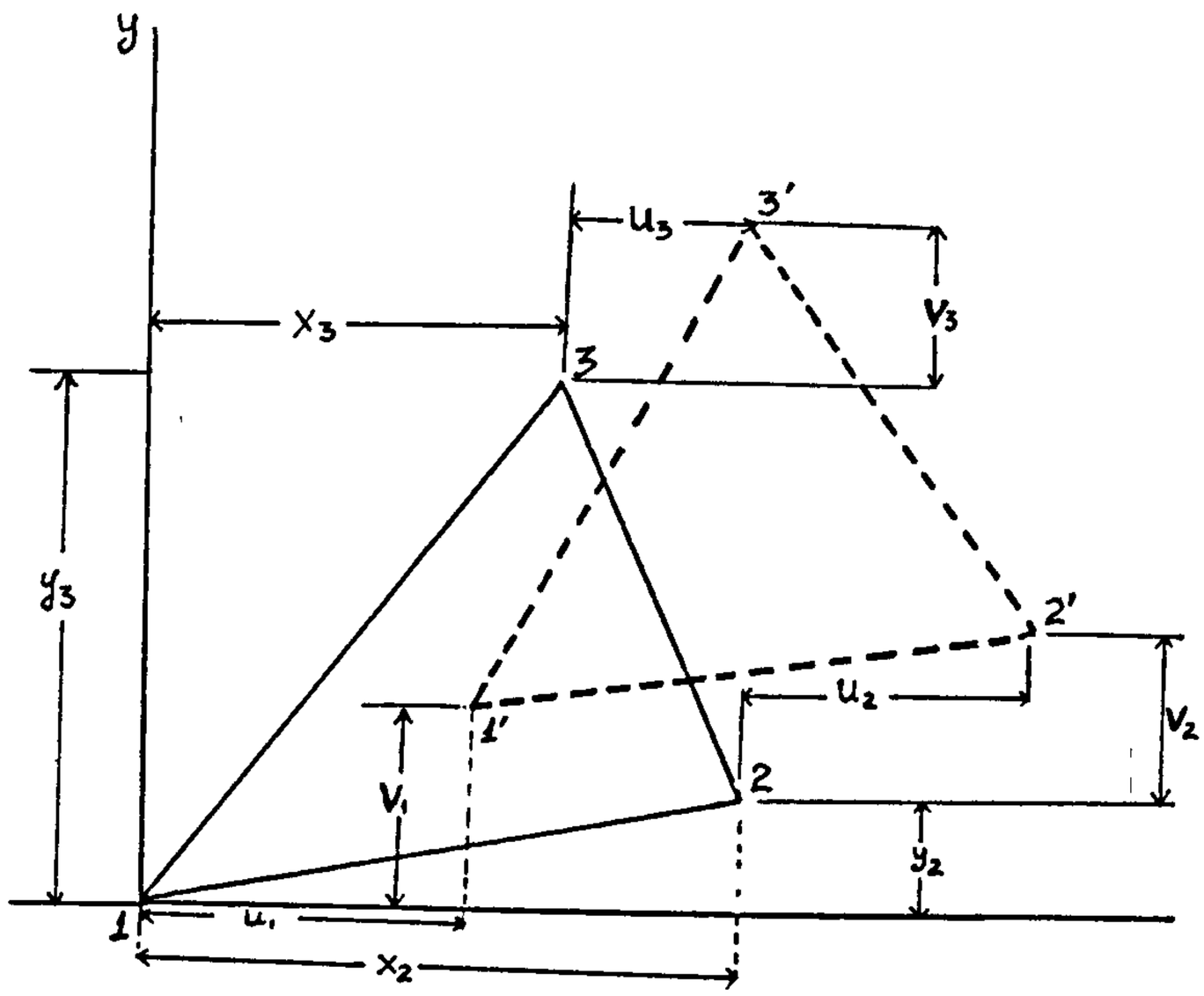

Fig. 5.3 Initial and displaced positions of a triangular element.

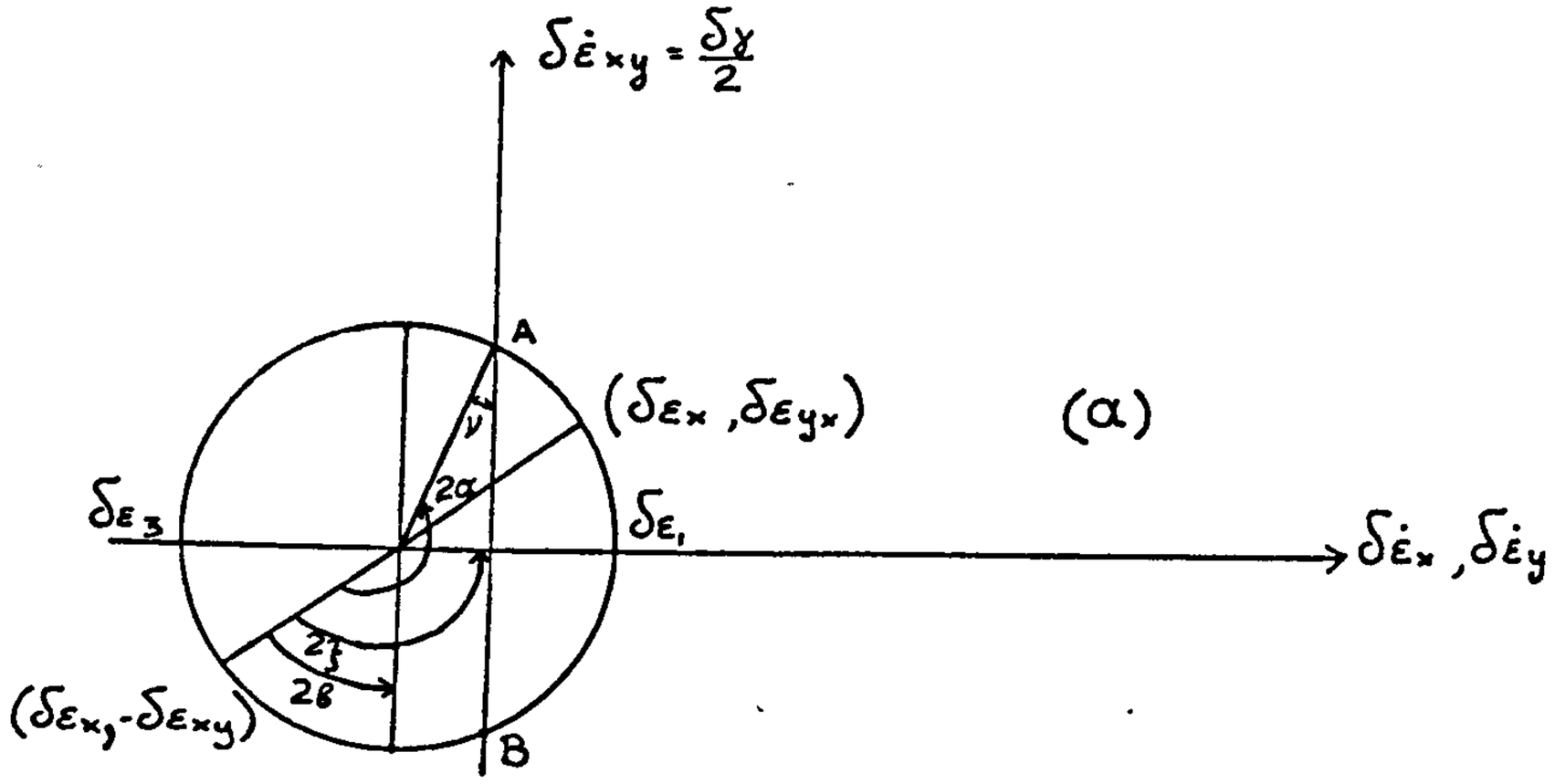

Fig. 5.4 (a) Associated Mohr's circle of strain increment
(b) Zero extension and principal compressive strain increment directions in the soil.

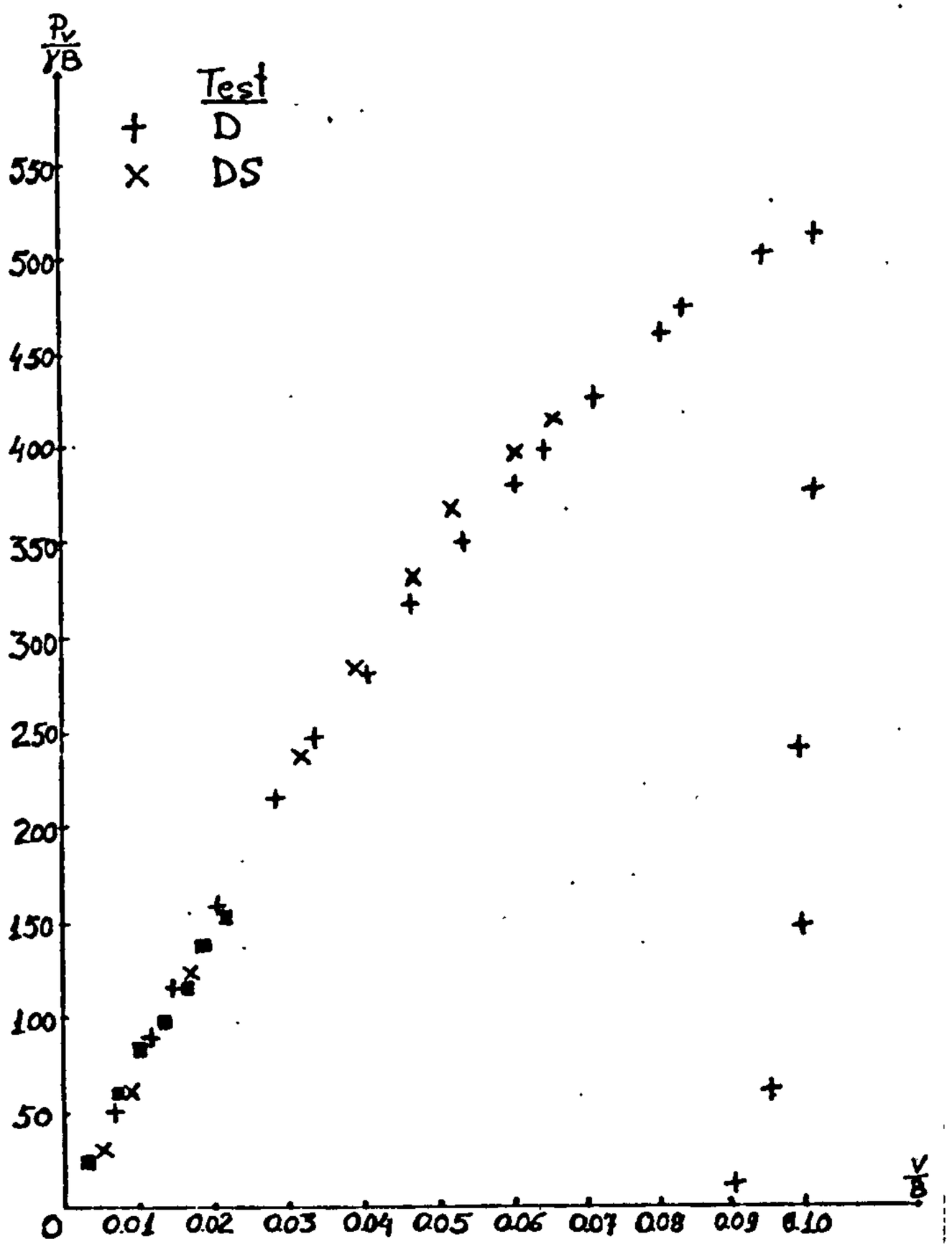

Fig. 6.1 Load displacement relationships for tests
D(e_o=0.52,α_o=0,E_o=0) and
DS(e_o=0.53,α_o=0,E_o=0).

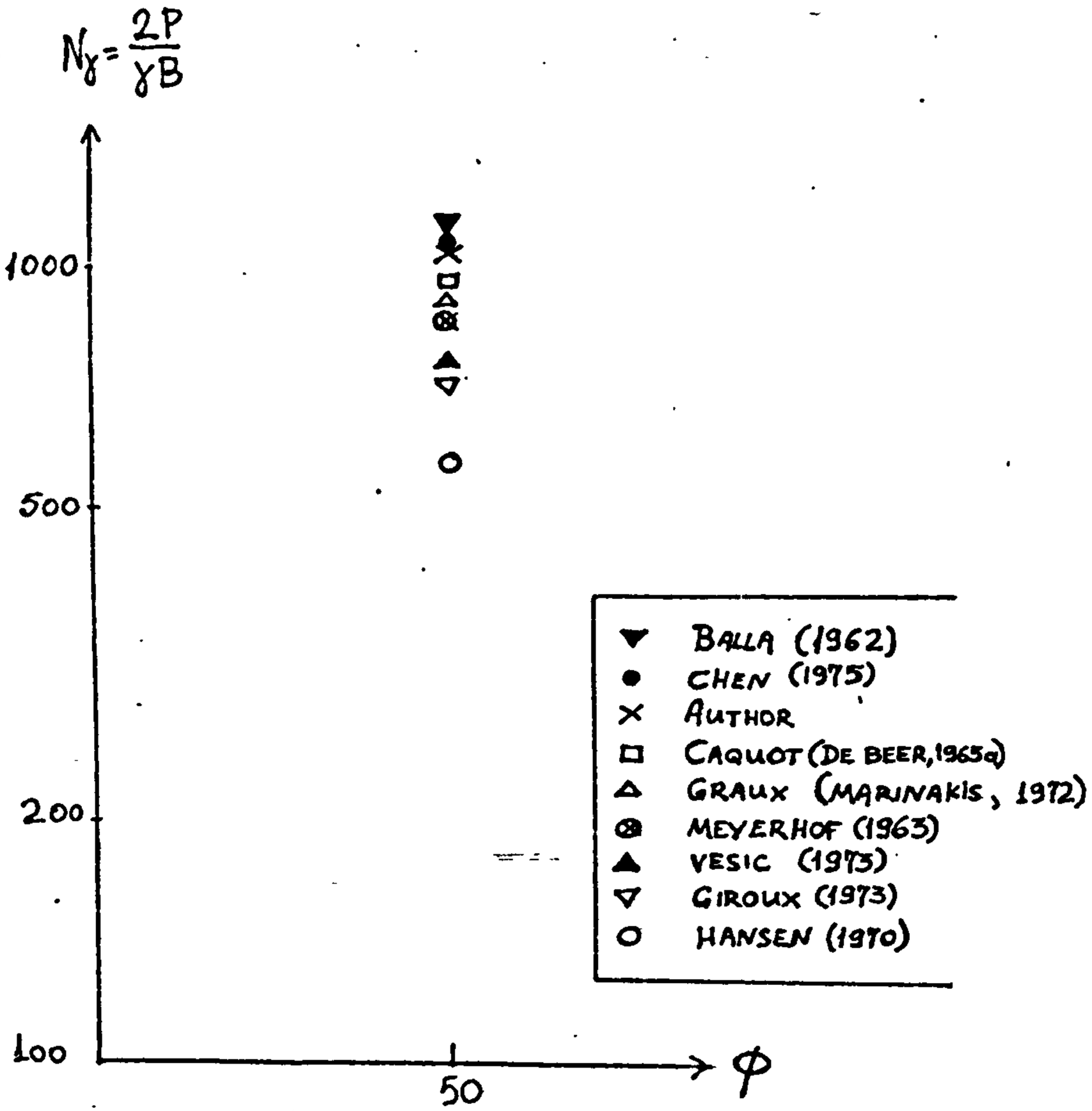

Fig. 6.2 The dimensionless bearing capacity predicted by various formulae suggested, for $\phi = 50^o$.

Fig. 6.3 V/V_{max} versus E=e/B- Author's results.

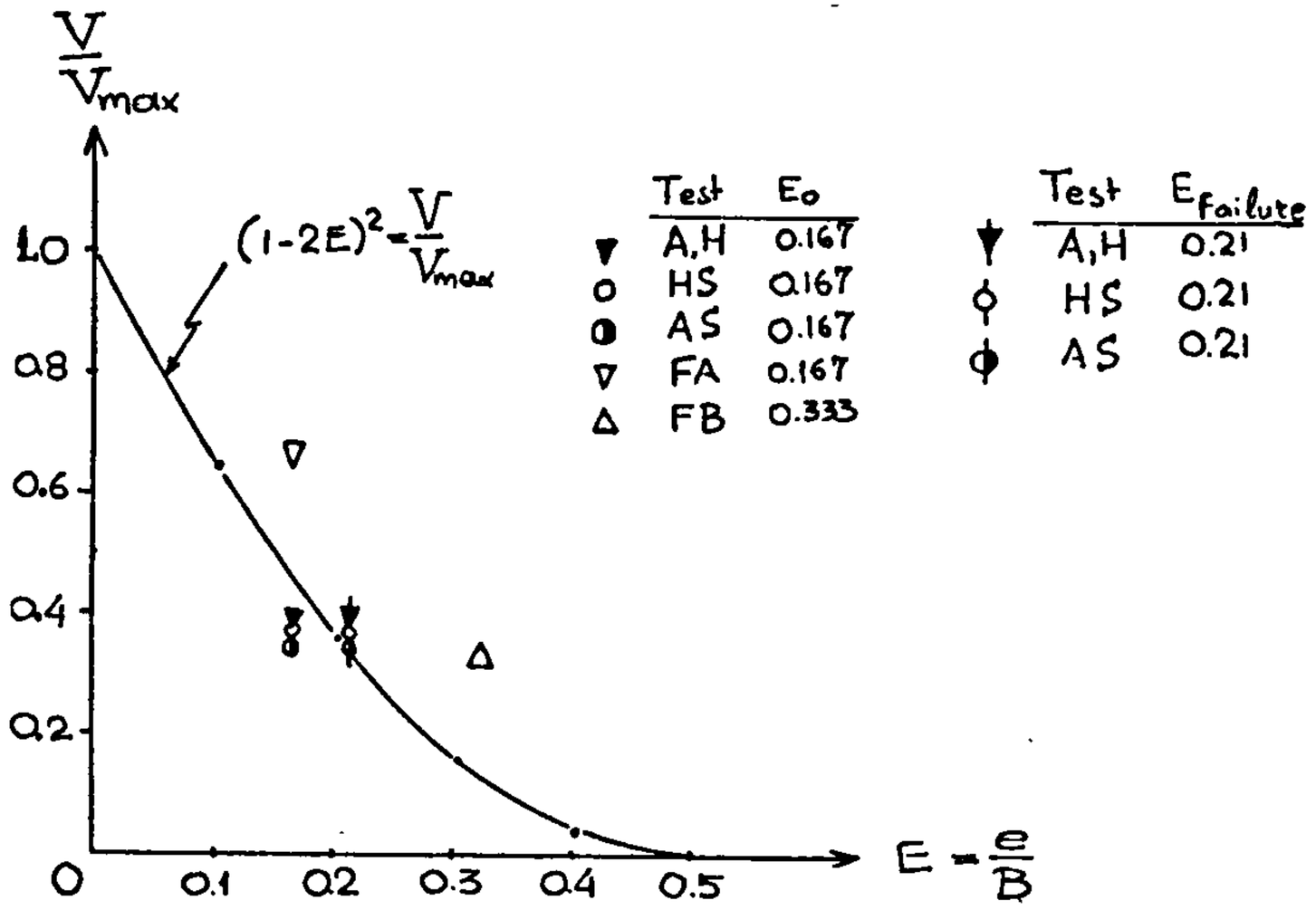

Fig. 6.4 V-H failure envelopes predicted - Comparison with the Author's results from tests in the FAC and FAS.

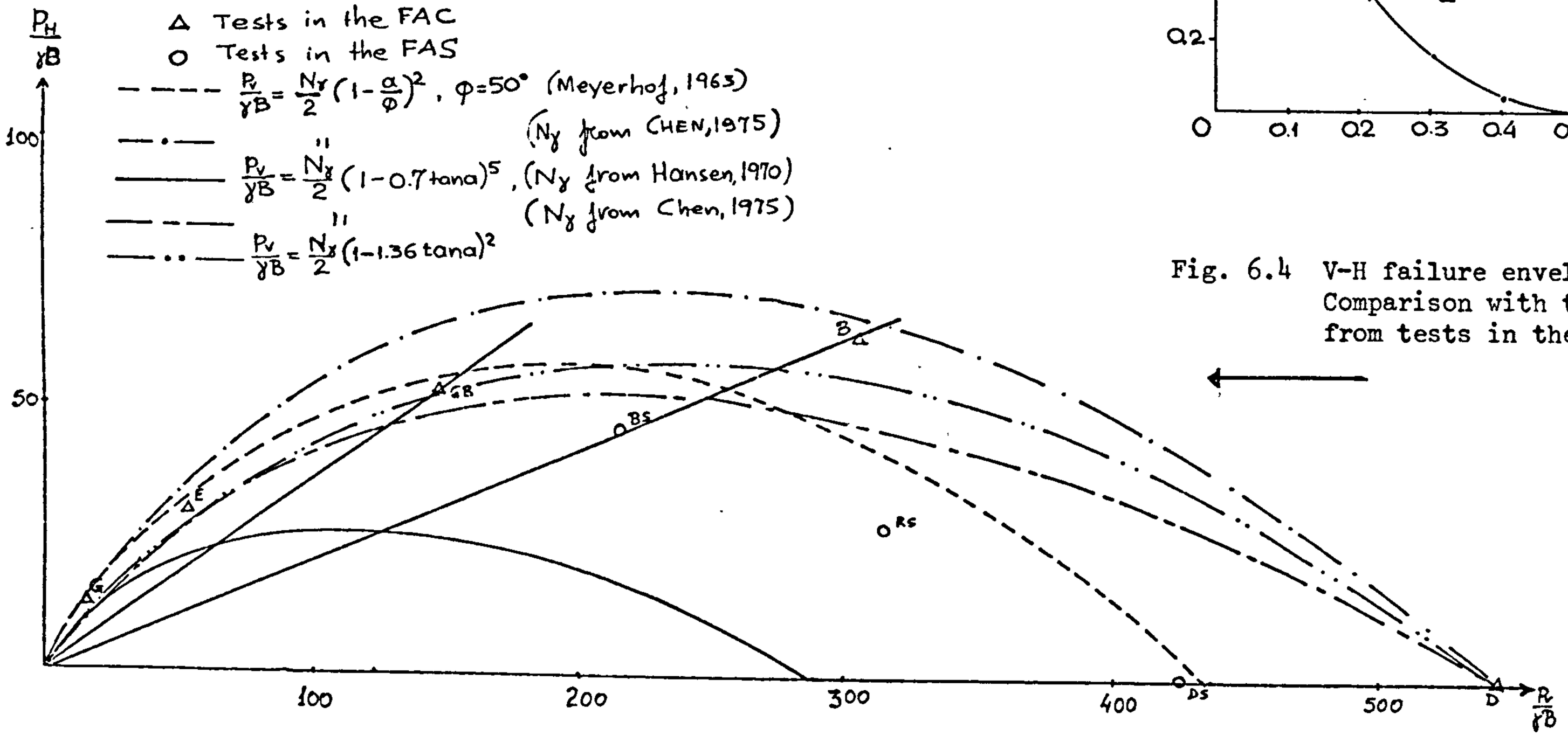

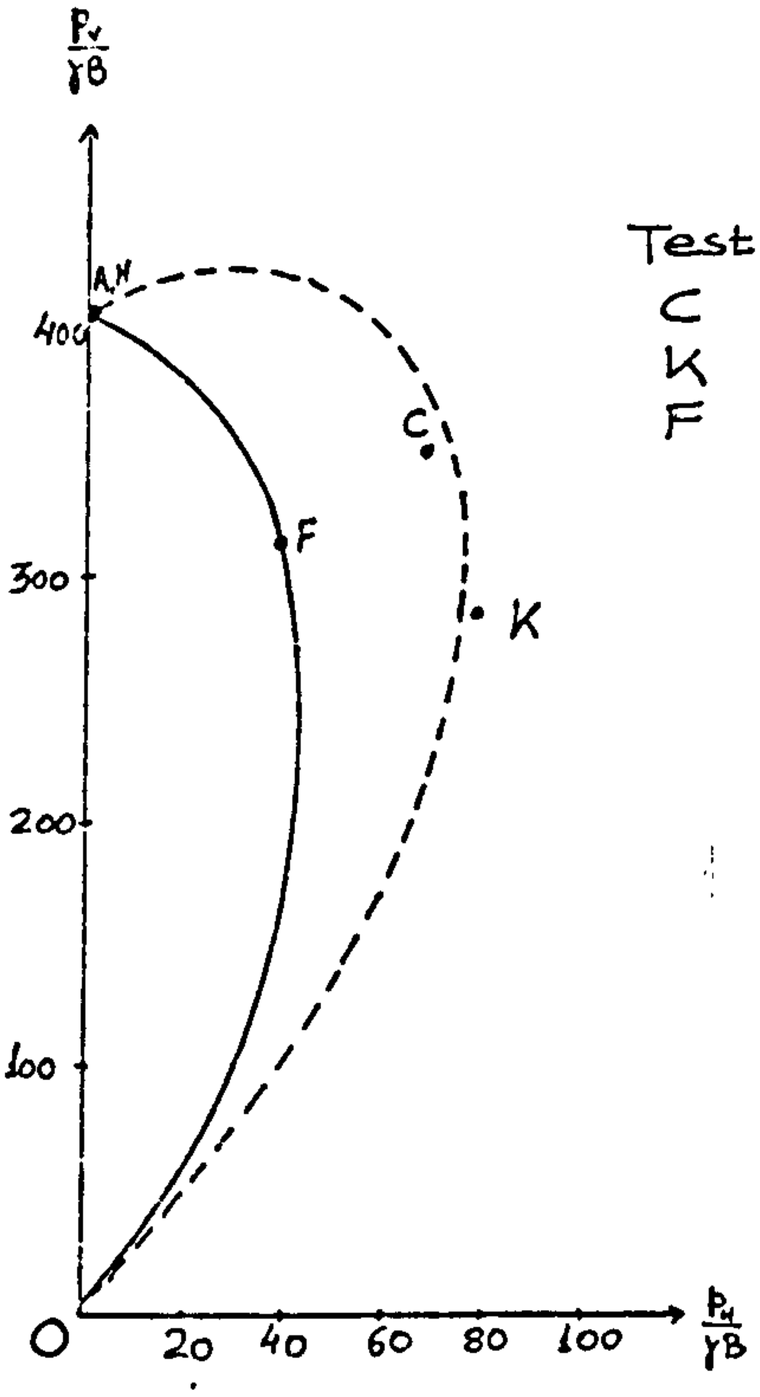

Fig. 6.5 The effect of the 'Negative' eccentricity on the bearing capacity of footings on sand.

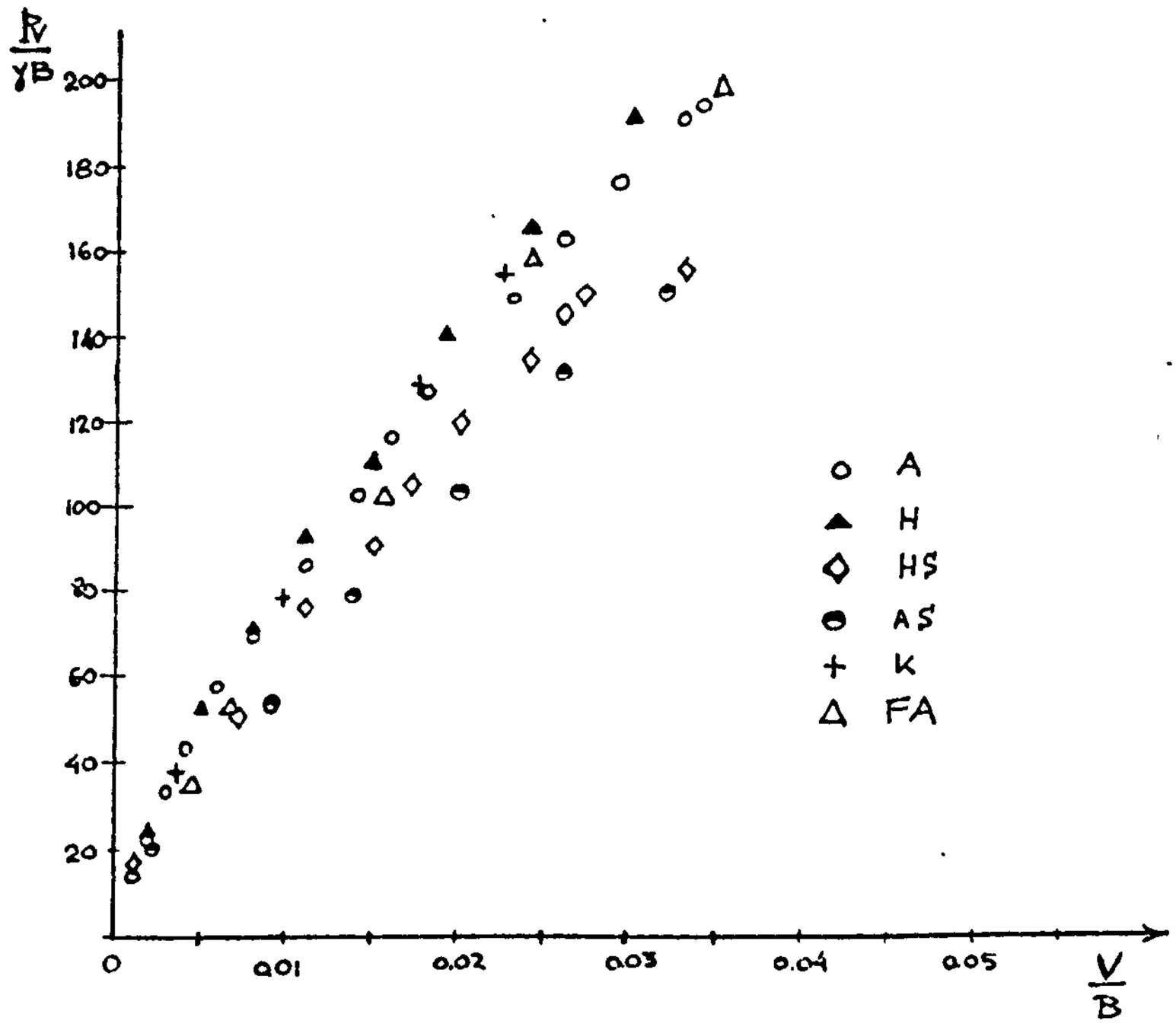

Fig. 6.6 Vertical load-vertical displacement relationships for a footing under a vertical load($E \neq 0$)

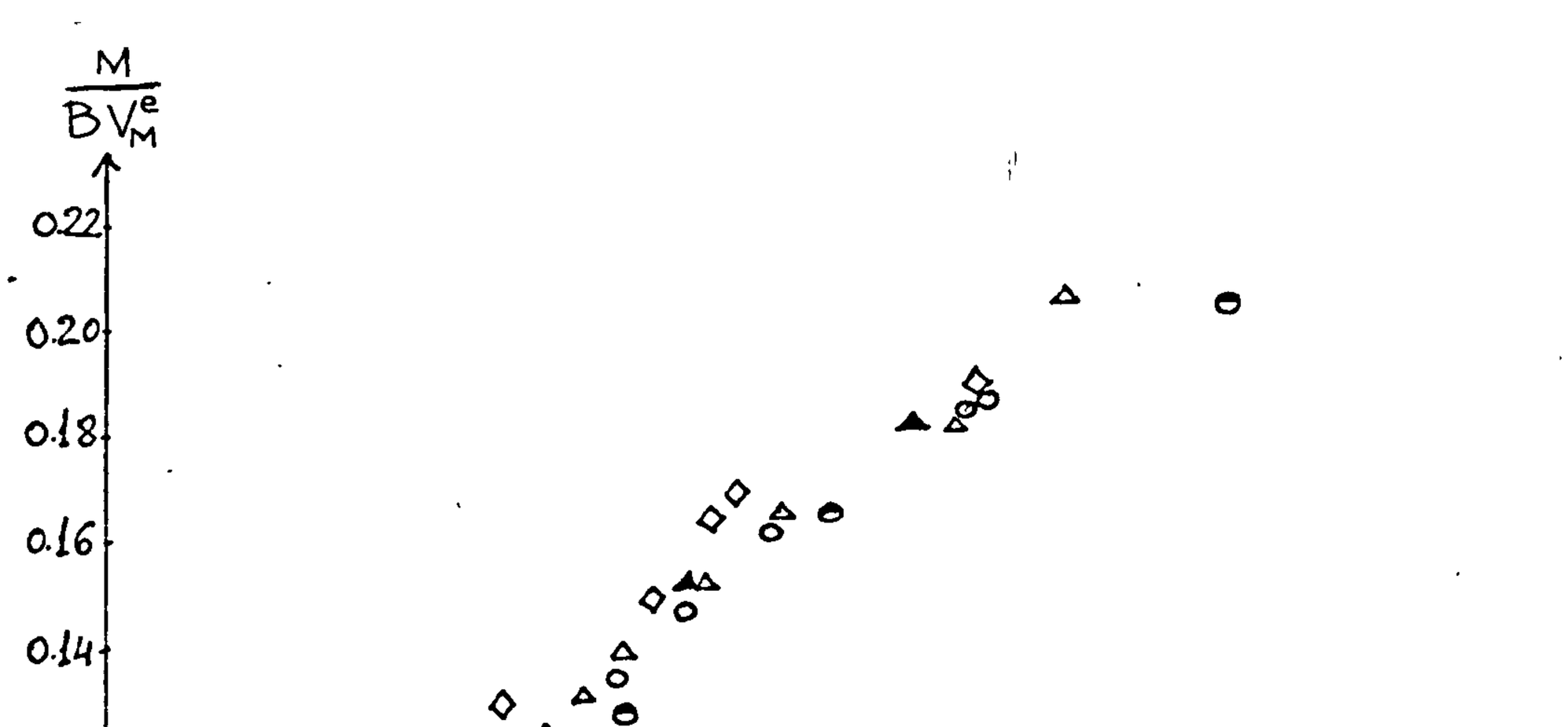

Fig. 6.7 Moment-rotation relationships for a footing under a vertical eccentric load.

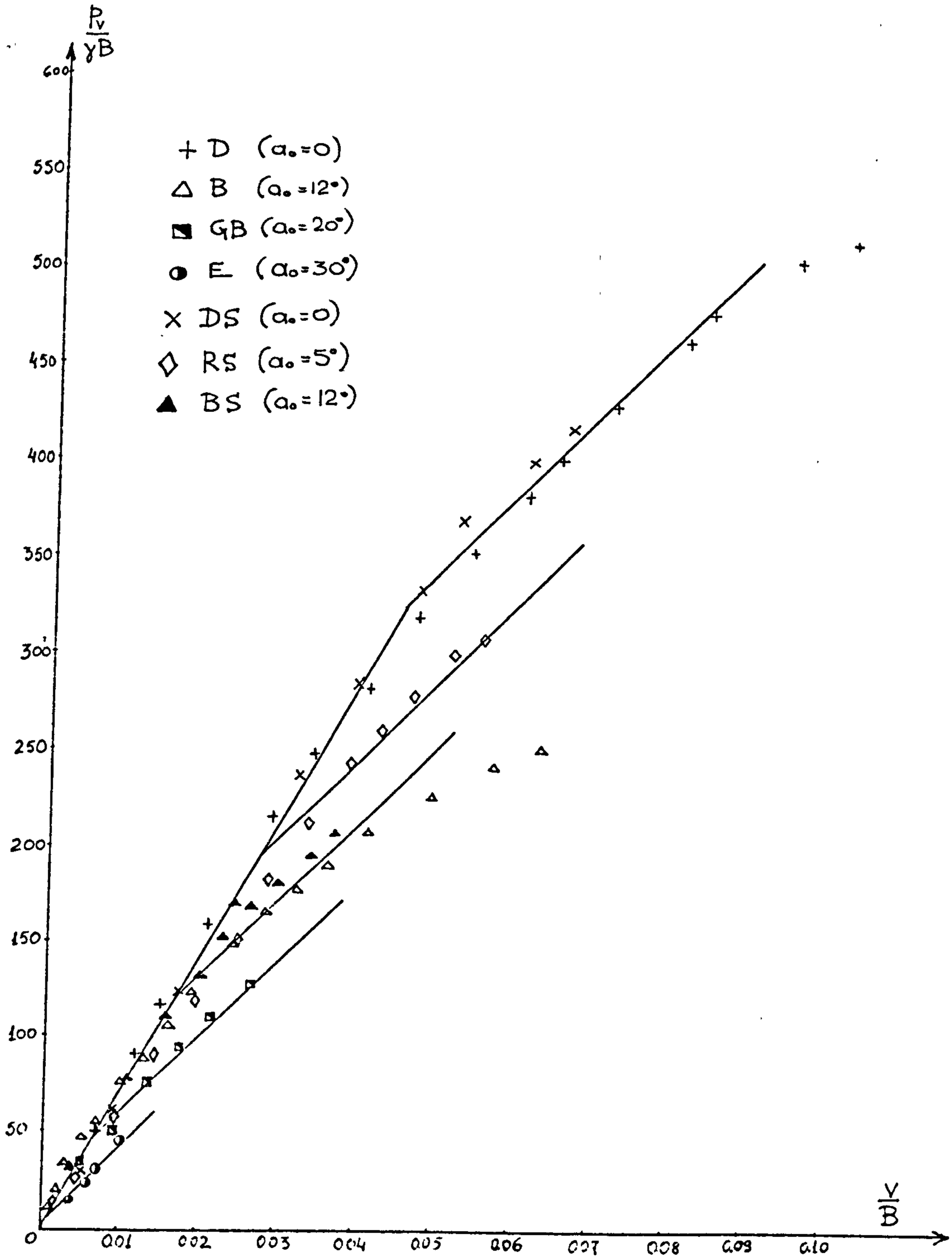

Fig. 6.8 Vertical component of the load-vertical displacement relationships under an inclined central load.

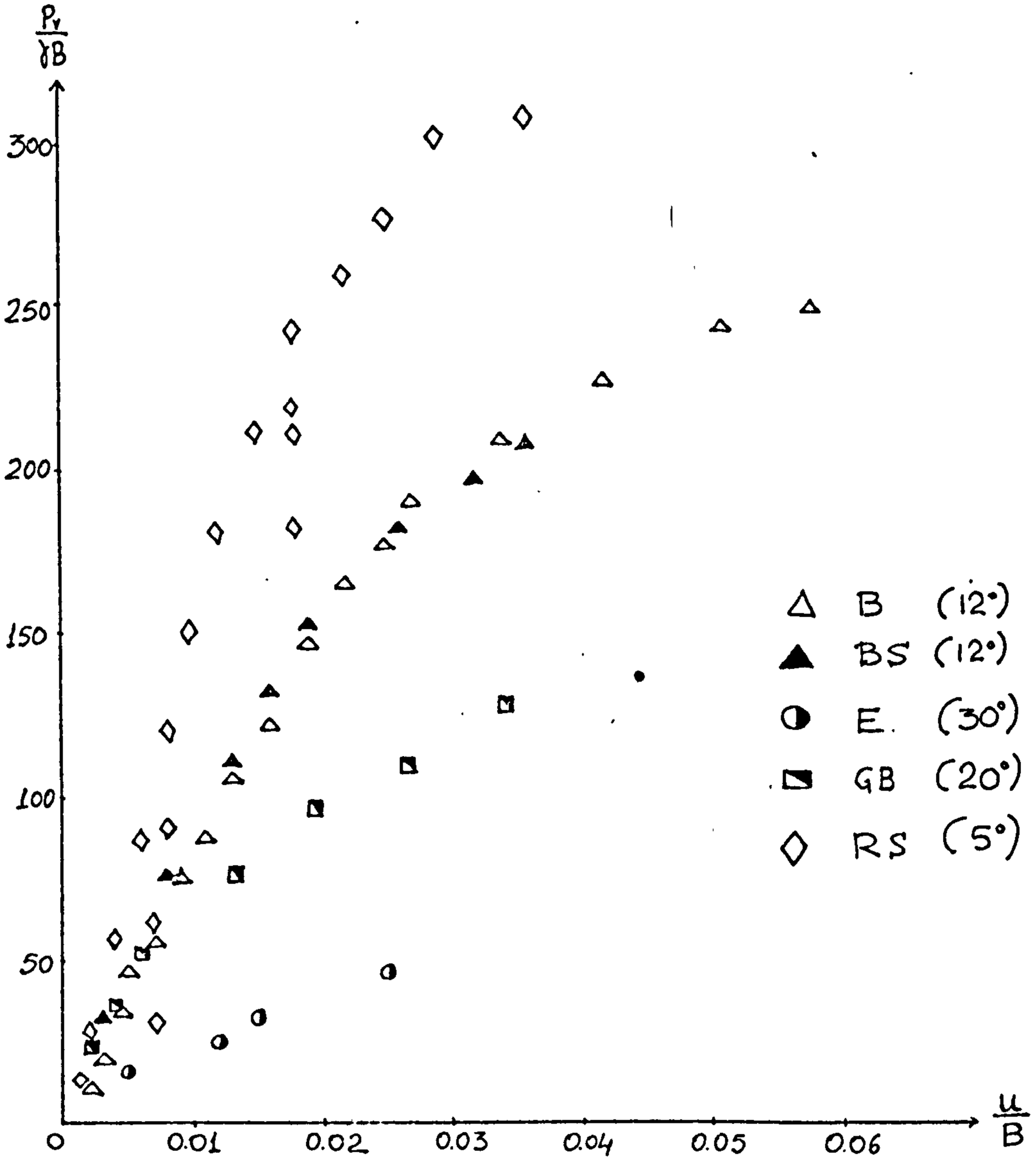

Fig. 6.9 Vertical component of the load-horizontal displacement relationships under an inclined central load.

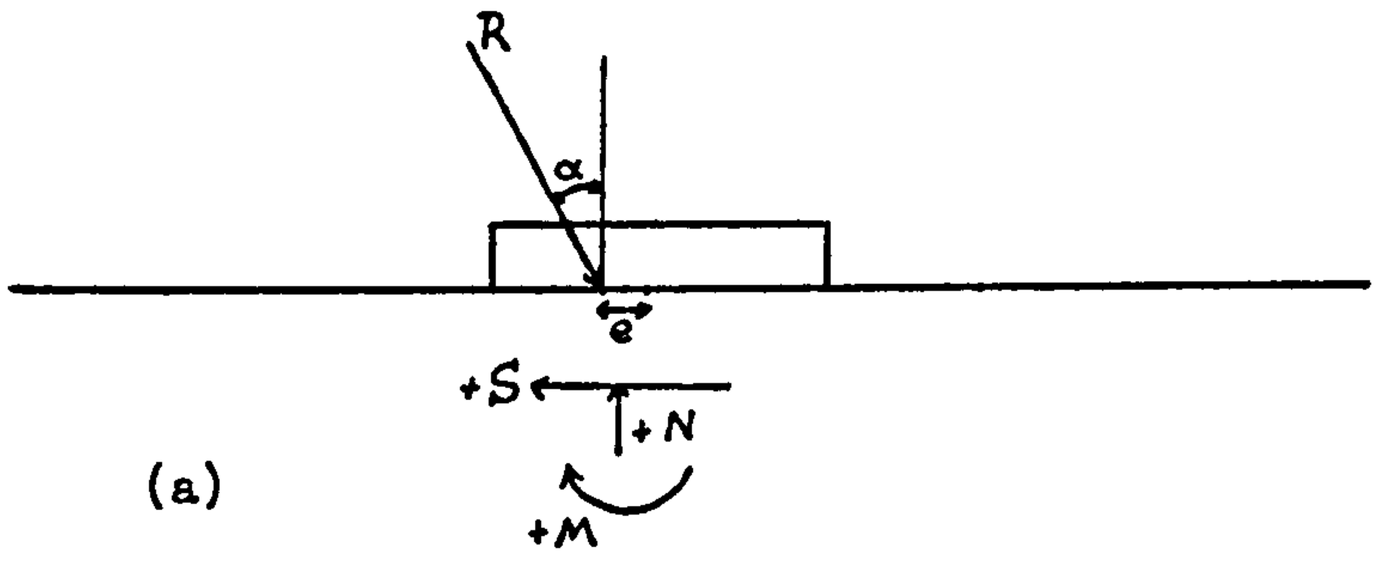

(a)

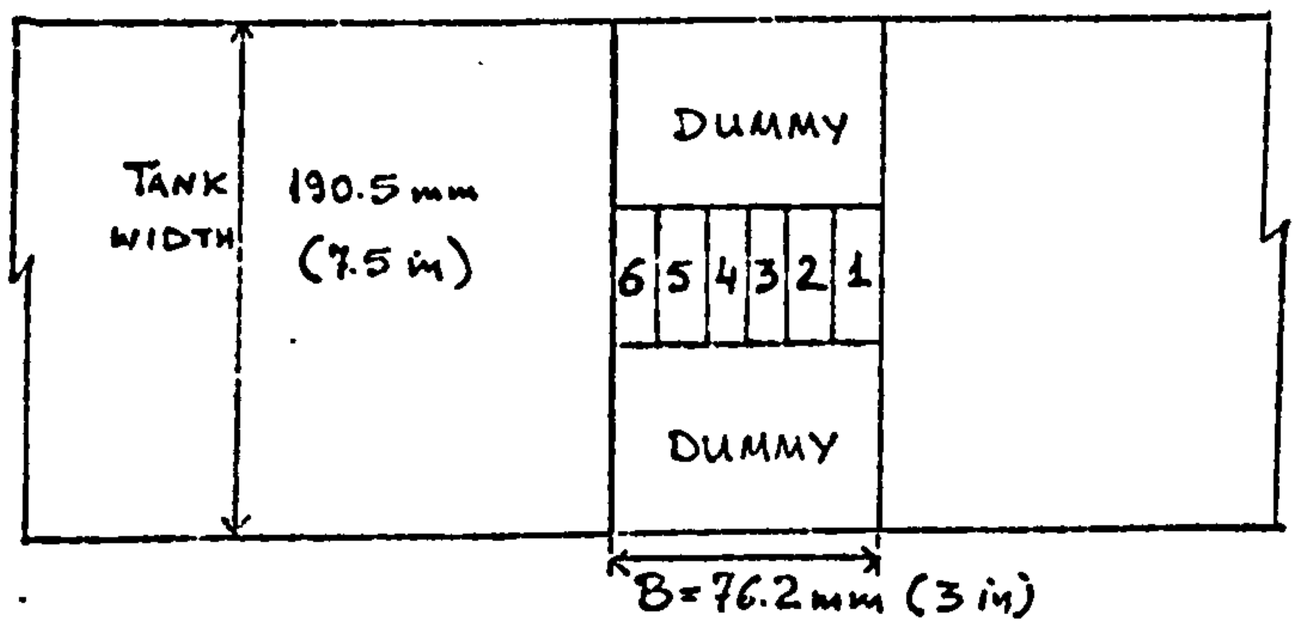

(b)

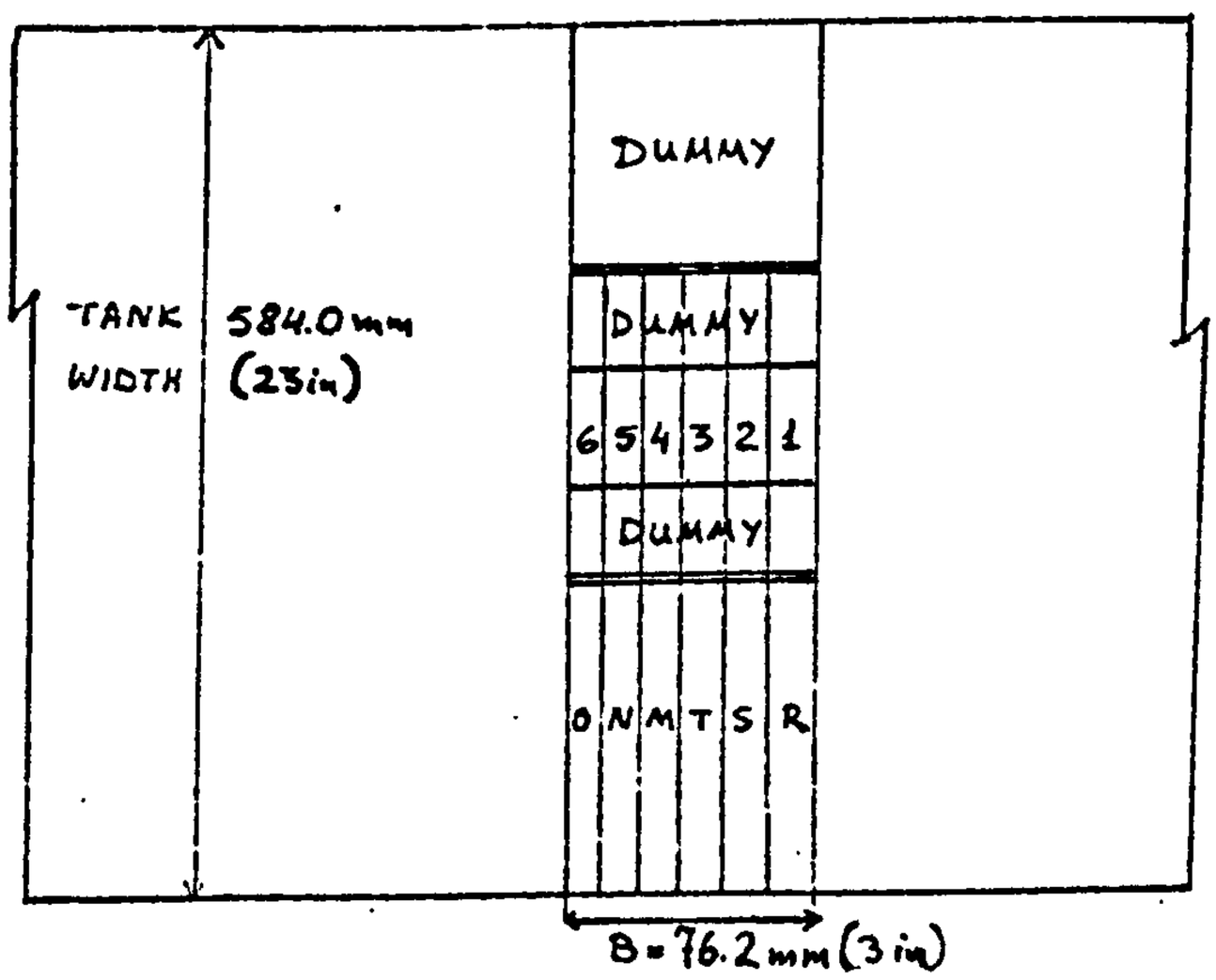

(c)

Fig. 6.10 Contact stress load cells arrangement
(a) Positive contact stresses (b) FAC (c) FAS

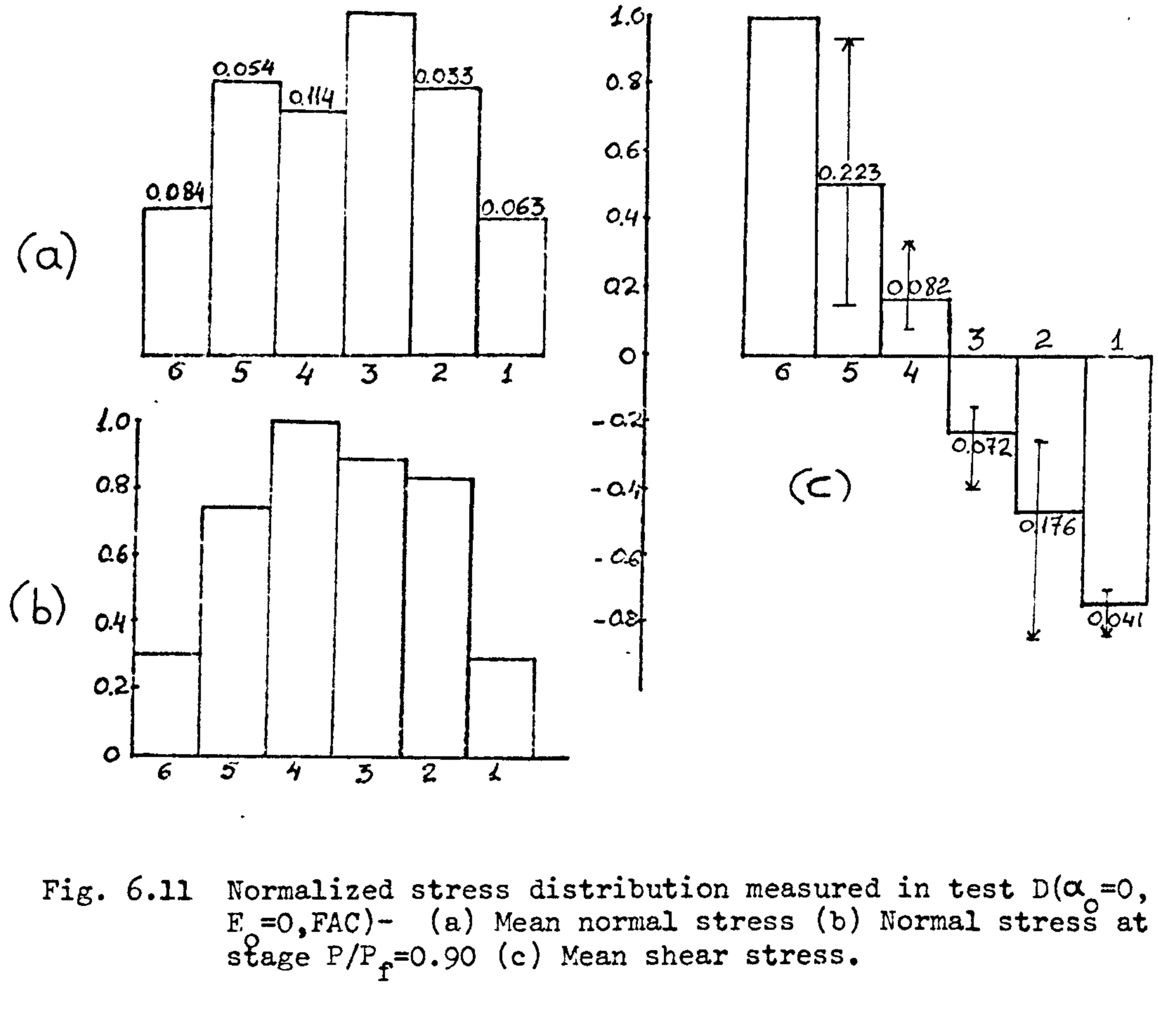

Fig. 6.11 Normalized stress distribution measured in test D(α_o=0, E_o=0,FAC)- (a) Mean normal stress (b) Normal stress at stage P/P_f=0.90 (c) Mean shear stress.

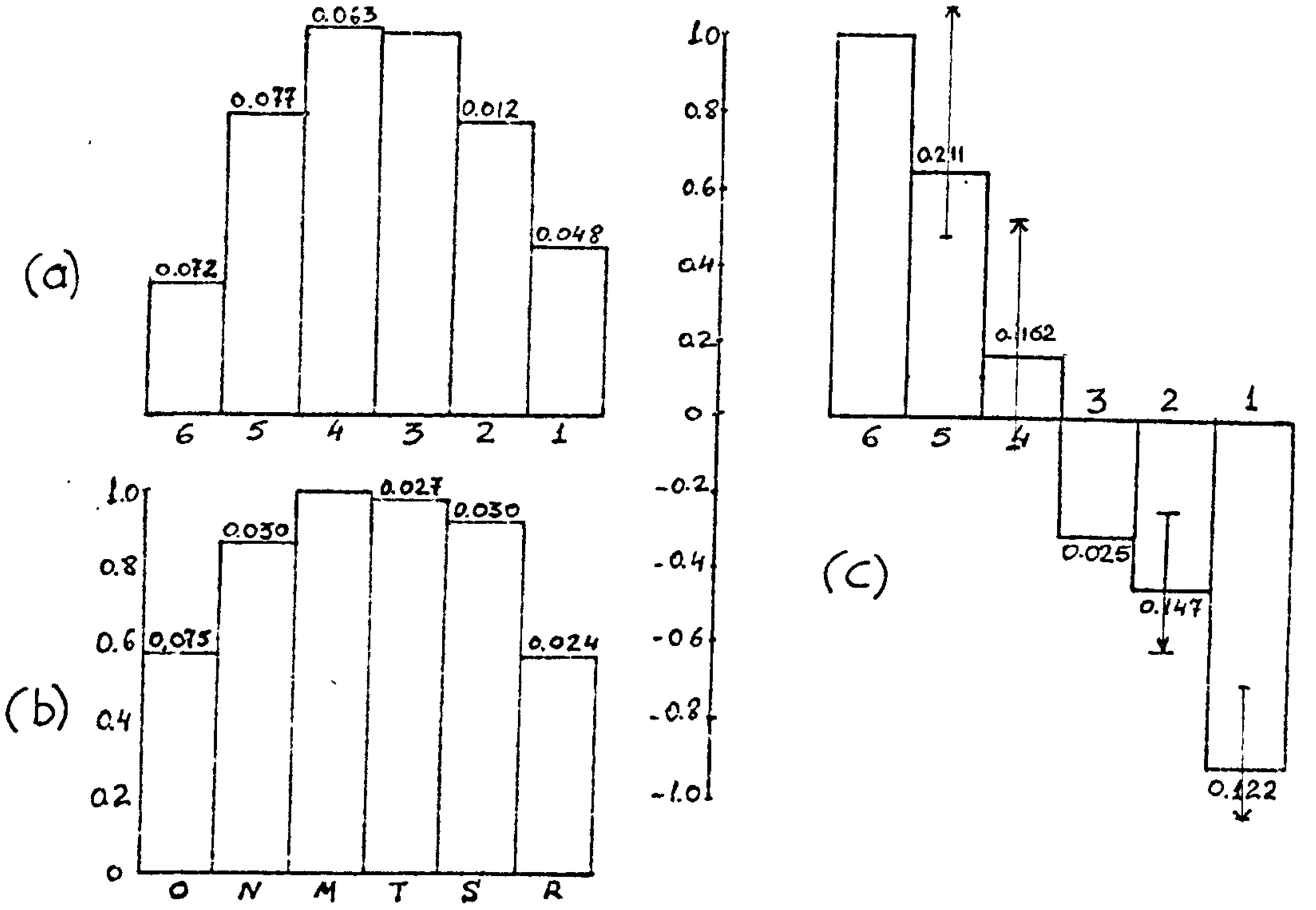

Fig. 6.12 Normalized mean stress distribution measured in test DS(α_o=0,E_o=0,FAS) - (a) Normal stress - Centre section (C.F.) (b) Normal stress - Side section (S.F.) (c) Shear stress.

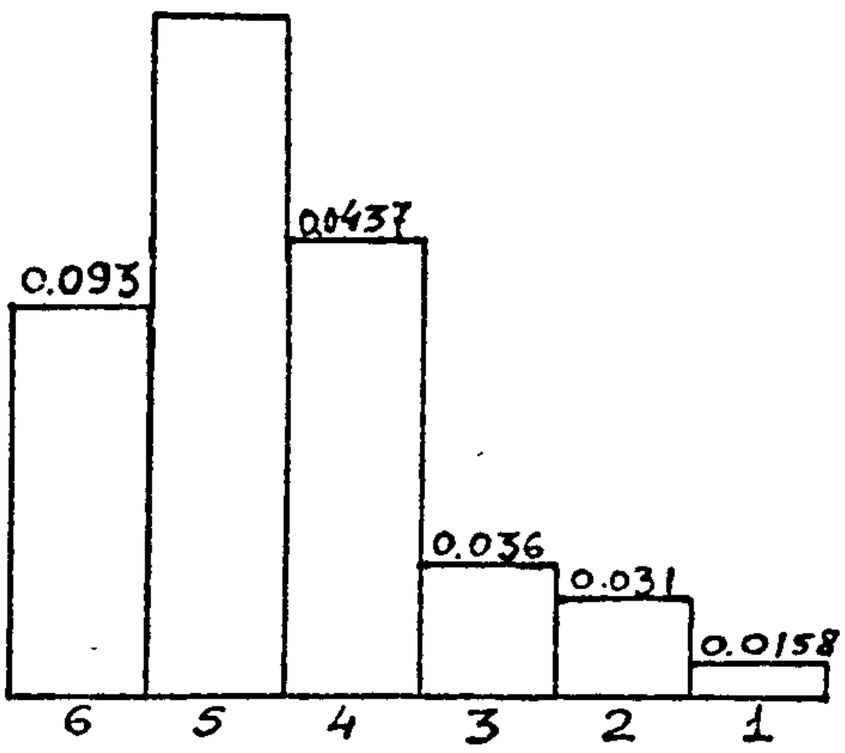

Fig. 6.13 Normalized mean stress distribution measured in test A(α_o=0,E_o=0.167,FAC) - (a) Normal stress (b) Shear stress.

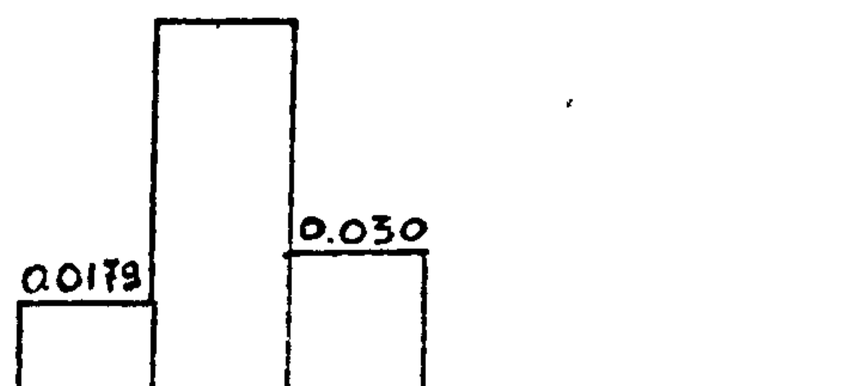

Fig. 6.14 Normalized mean stress distribution measured in test H(α_o=0,E_o=0.167,FAC) - (a) Normal stress (b) Shear stress.

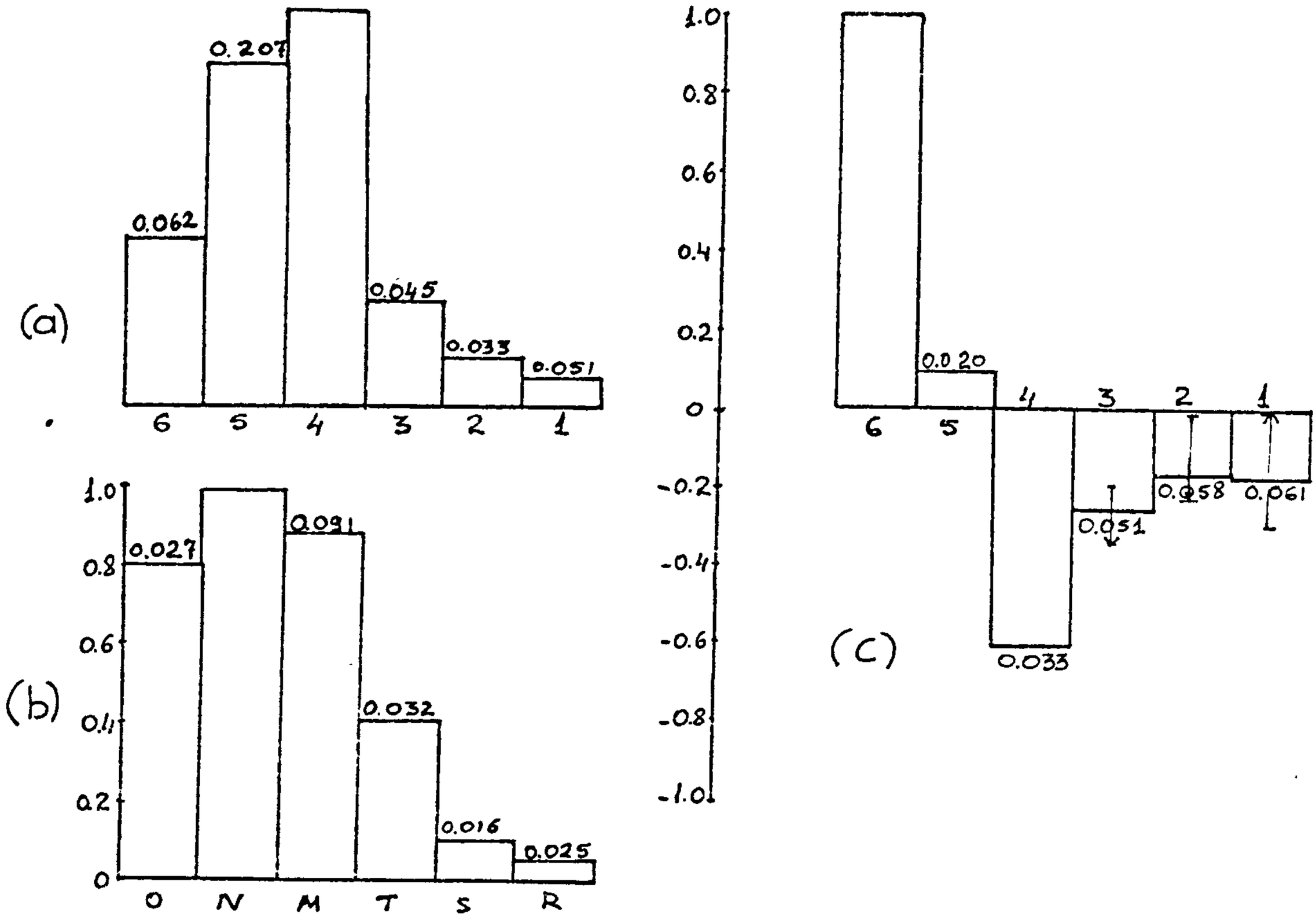

Fig. 6.15 Normalized mean stress distribution measured in test HS(α_o=0,E_o=0.167,FAS) - (a)Normal stress - Central section (C.F.) (b) Normal stress - Side section (S.F.) (c) Shear stress.

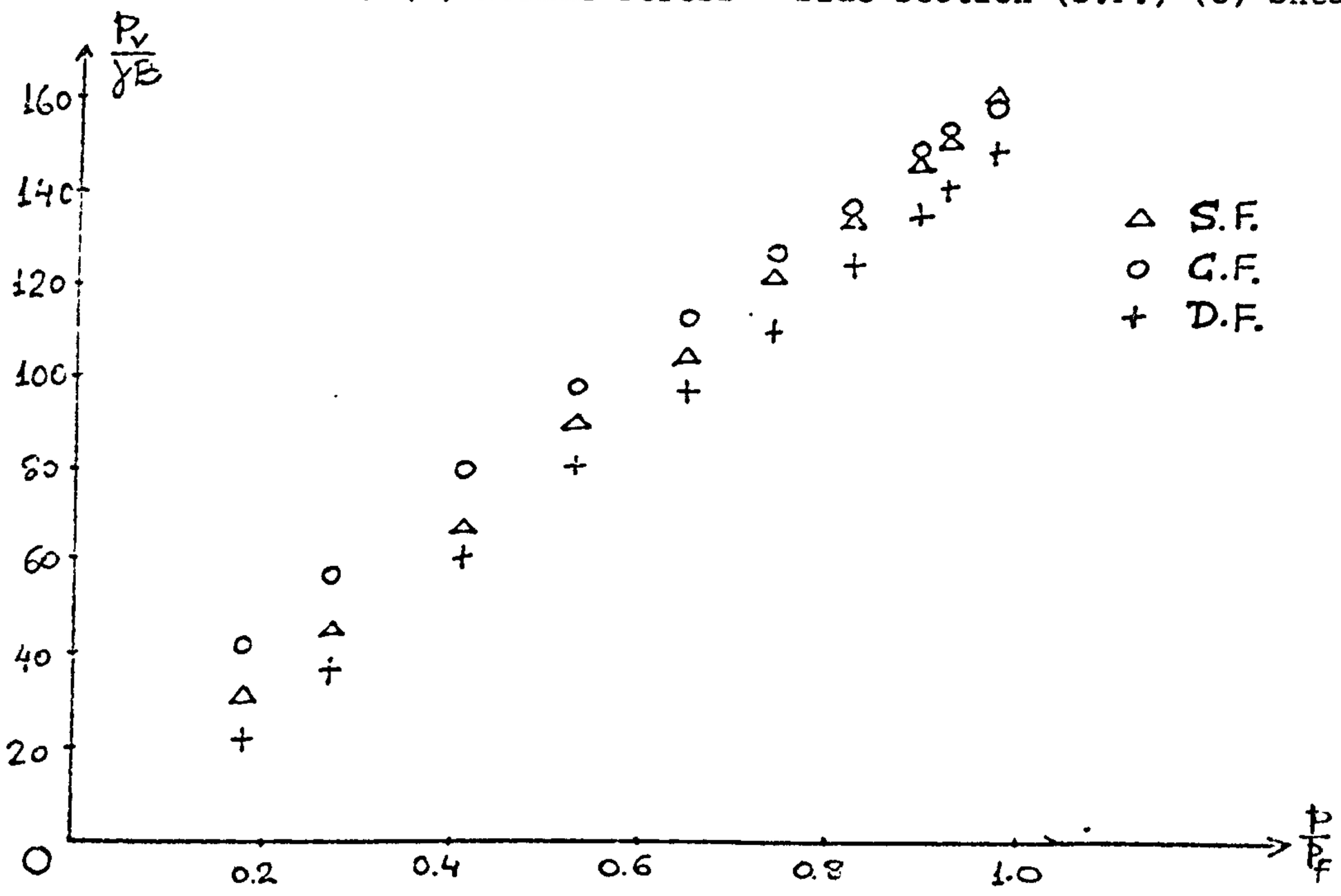

Fig. 6.16 Total load recorded by each section of the footing in test HS(α_o=0,E_o=0.167,FAS).

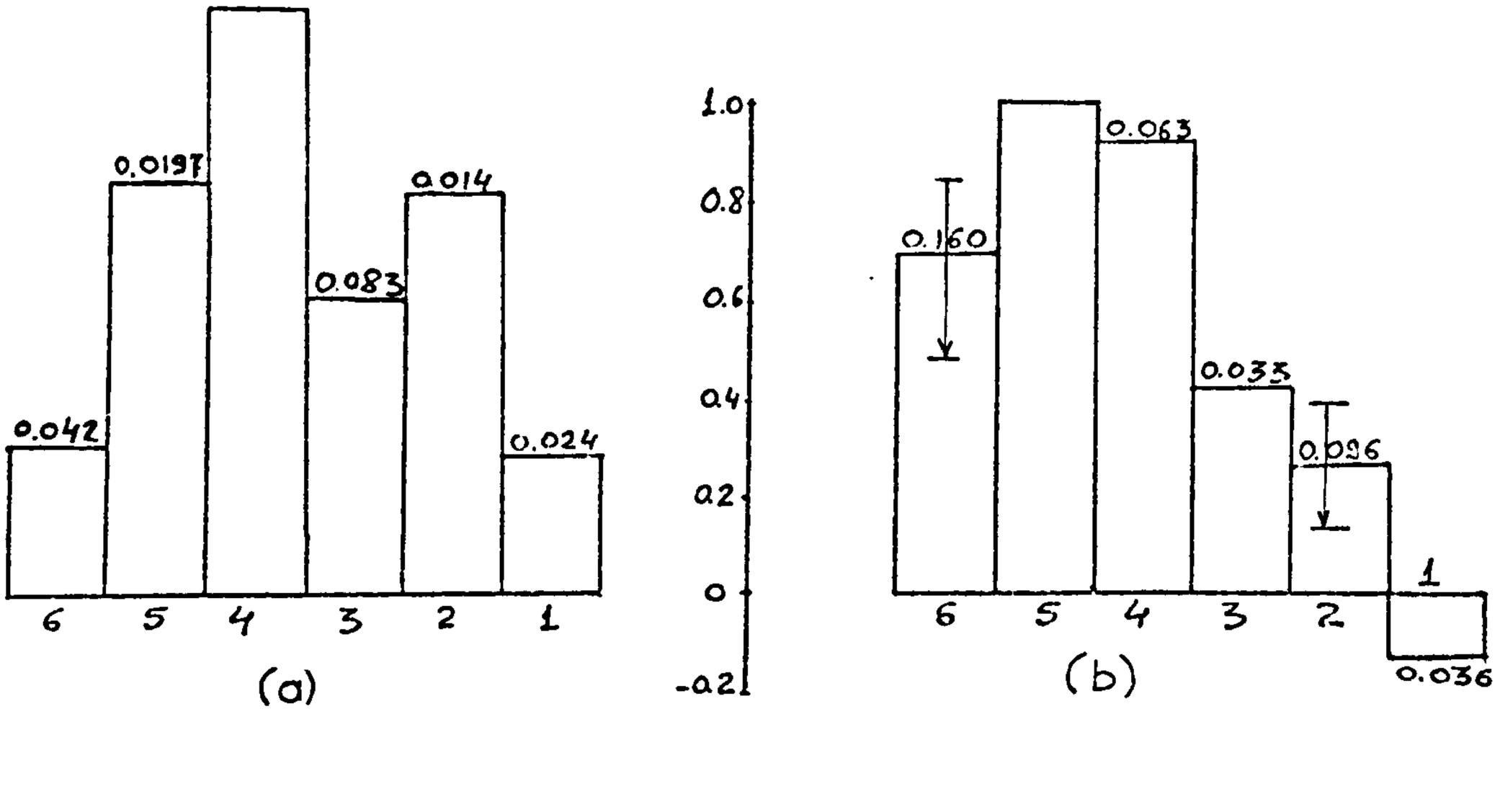

Fig. 6.17 Normalized mean stress distribution measured in the FAC
(a) Normal stress and (b) Shear stress - test B(α_o=12°,E_o=0)
(c) Normal stress and (d) Shear stress - test GB(α_o=20°,E_o=0)
(e) Normal stress and (f) Shear stress - test E(α_o=30°,E_o=0).

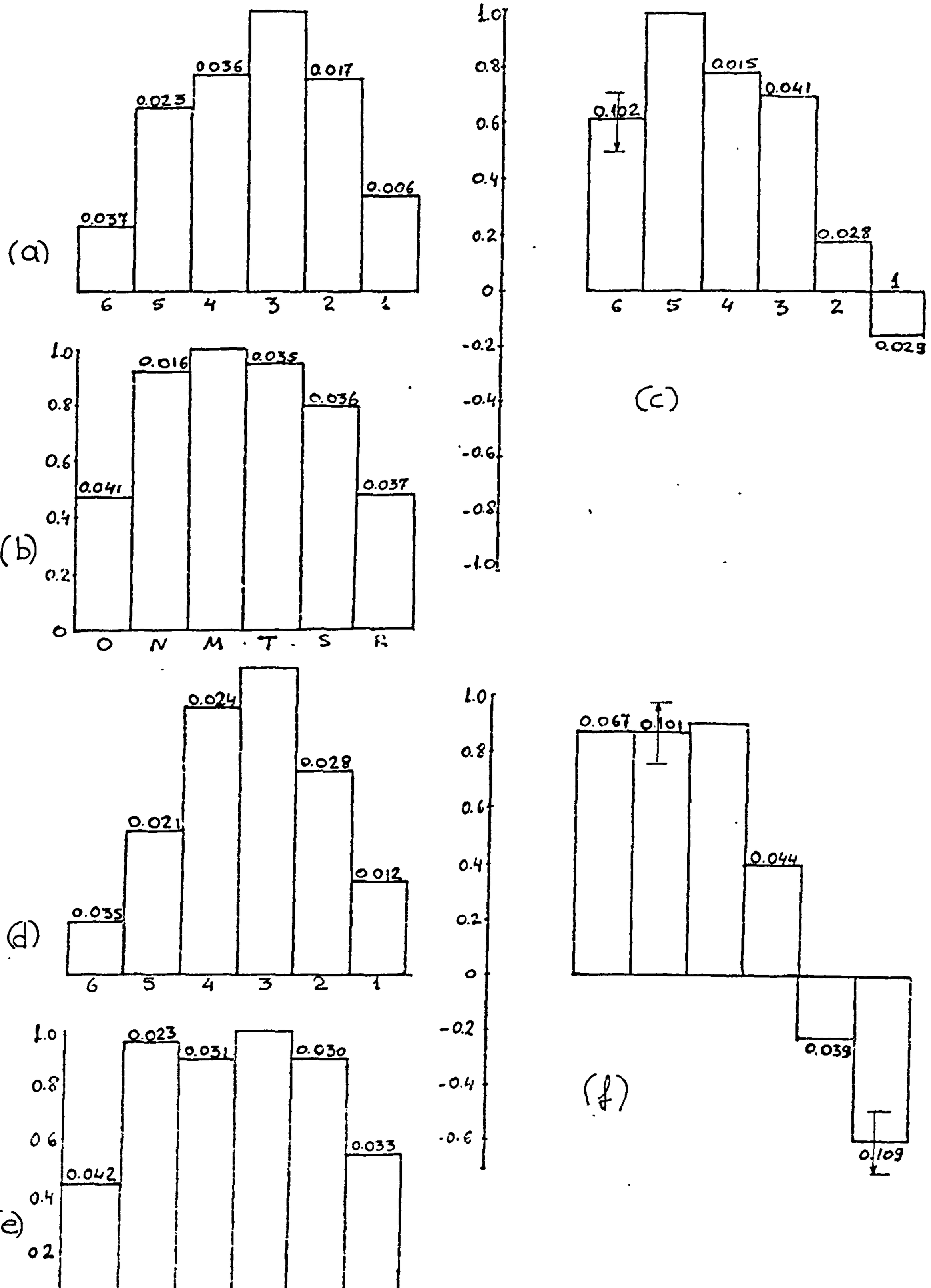

Fig. 6.18 Normalized mean stress distribution measured in the FAS (a) Normal stress - Centre section (b) Normal stress - Side section and (c) Shear stress: Test BS($\alpha_o = 12^o, E_o = 0$) (d) Normal stress - Centre section (e) Normal stress - Side section and (f) Shear stress: Test RS($\alpha_o = 5^o, E_o = 0$).

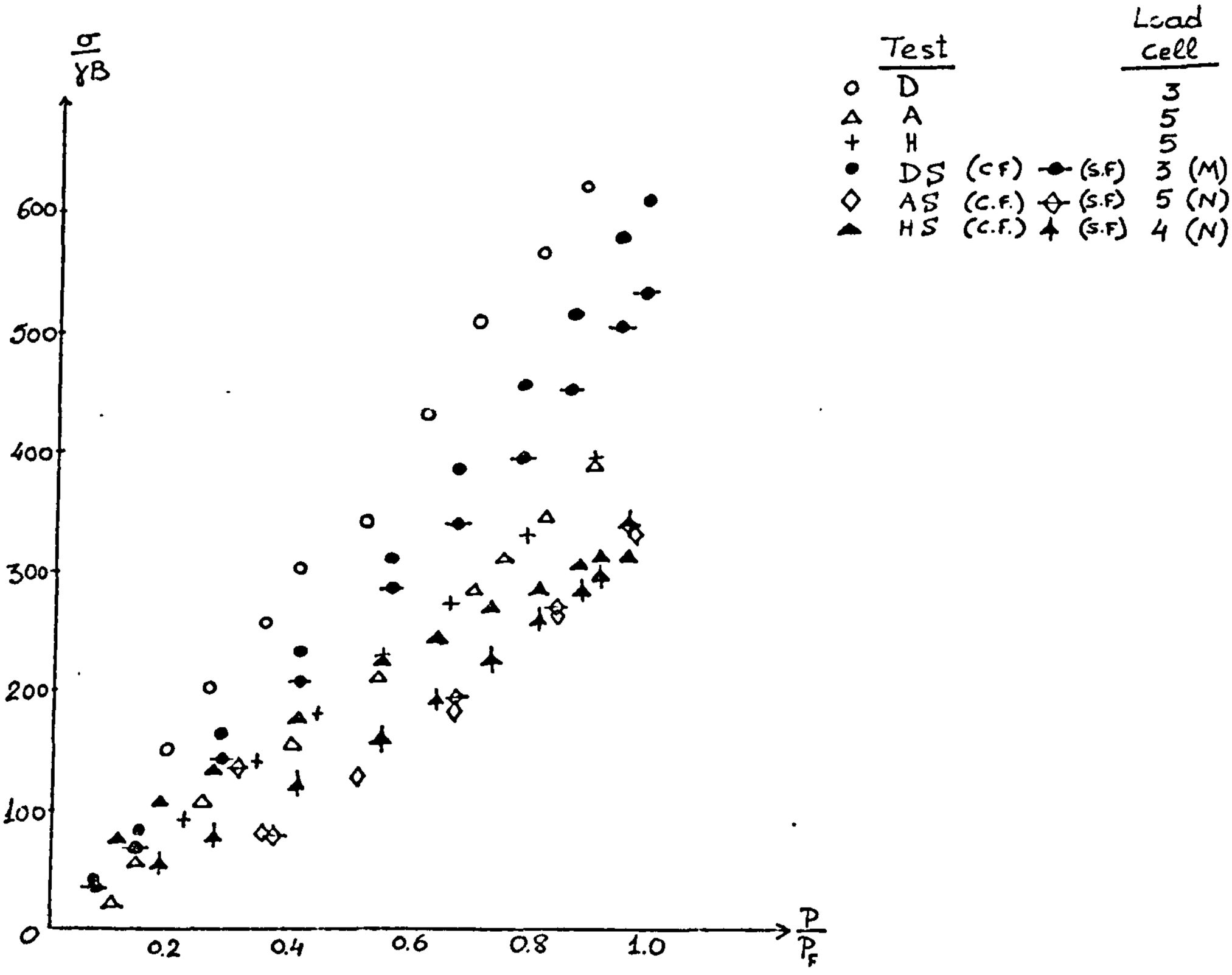

Fig. 6.19 The normal stresses recorded by the 'normalizing' load cell during tests D,A,H,DS,AS,HS.

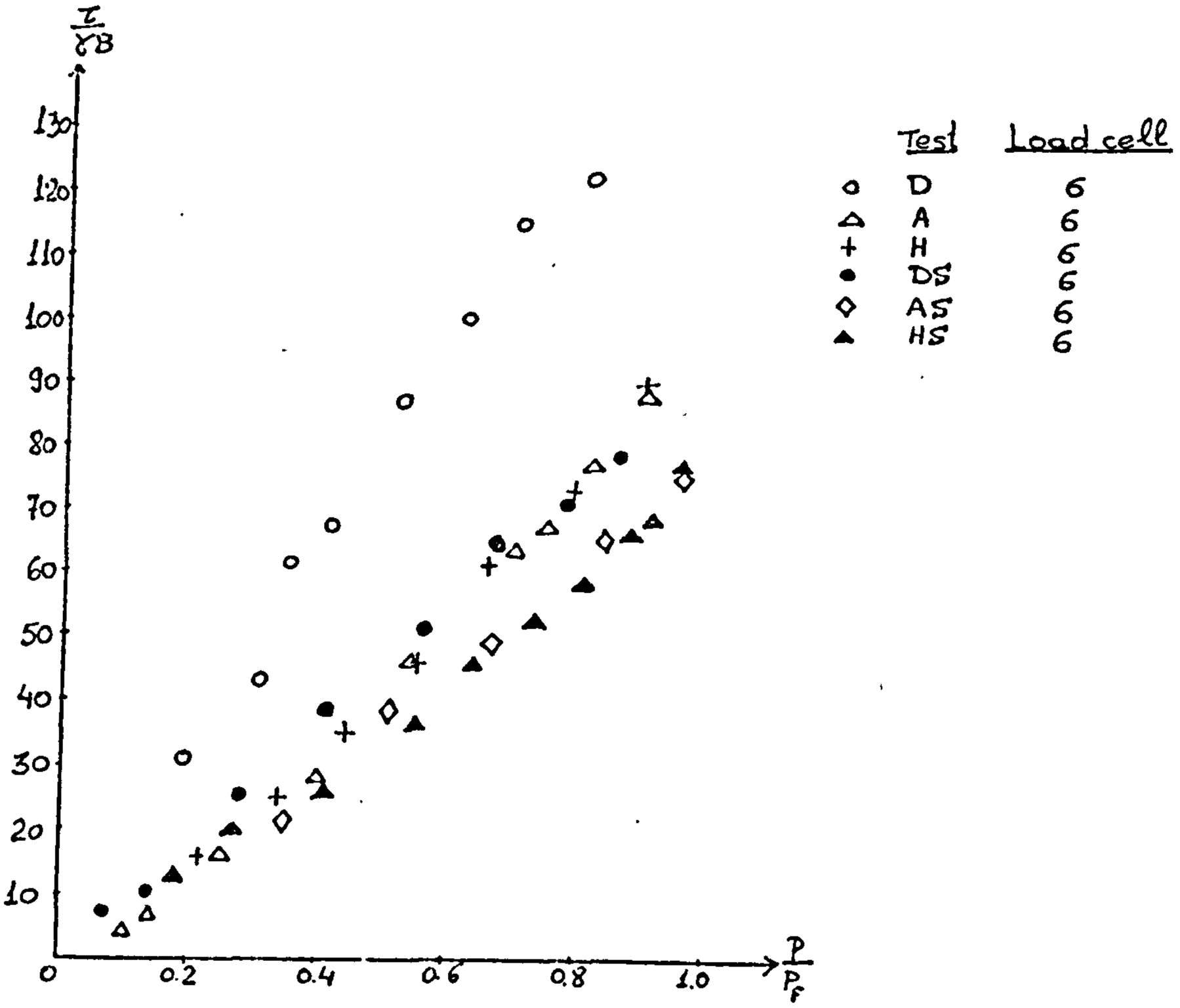

Fig. 6.20 The shear stresses recorded by the 'normalizing' load cell during tests D,A,H,DS,AS,HS.

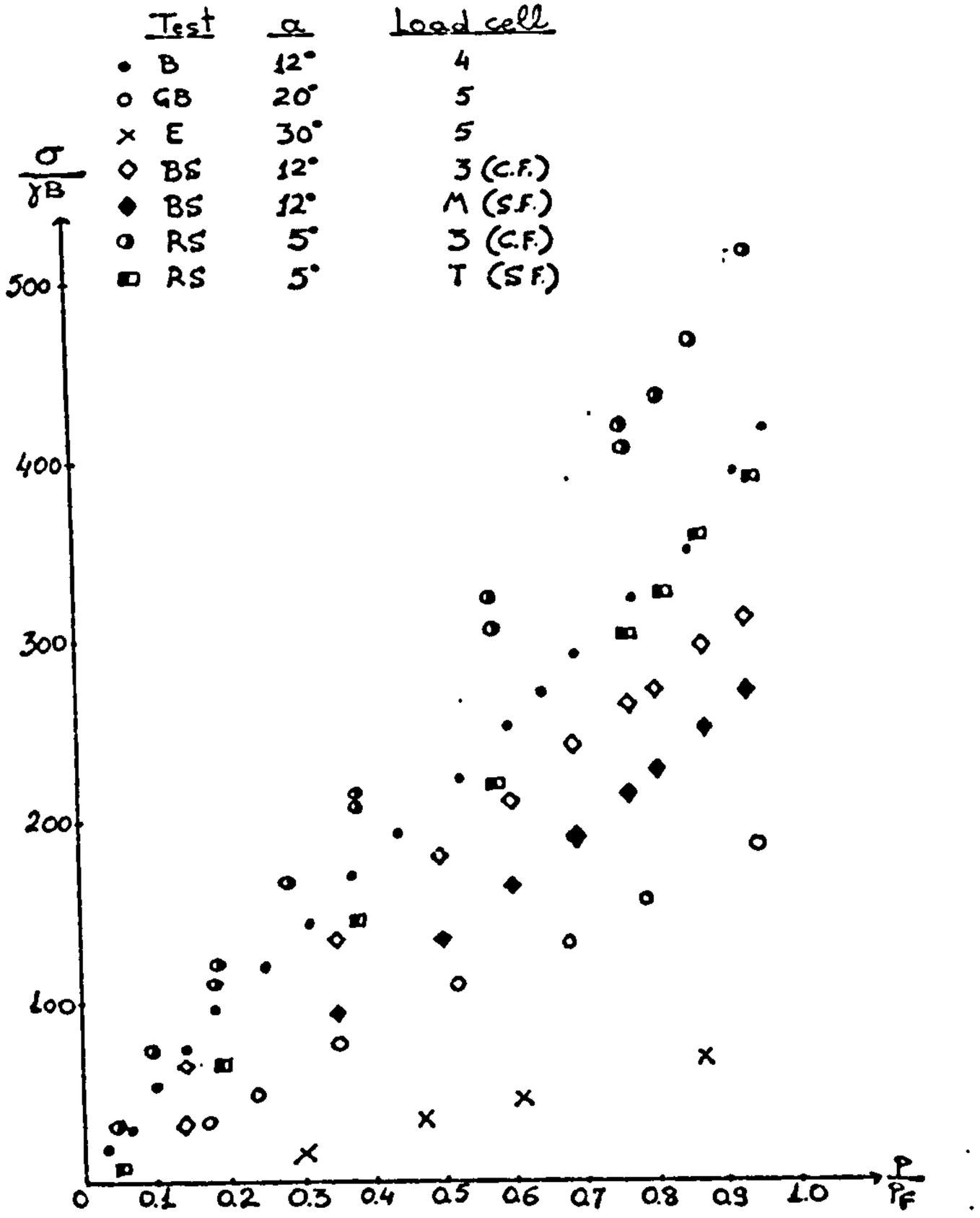

Fig. 6.21 The normal stresses recorded by the 'normalizing' load cell during tests B,GB,E,BS,RS.

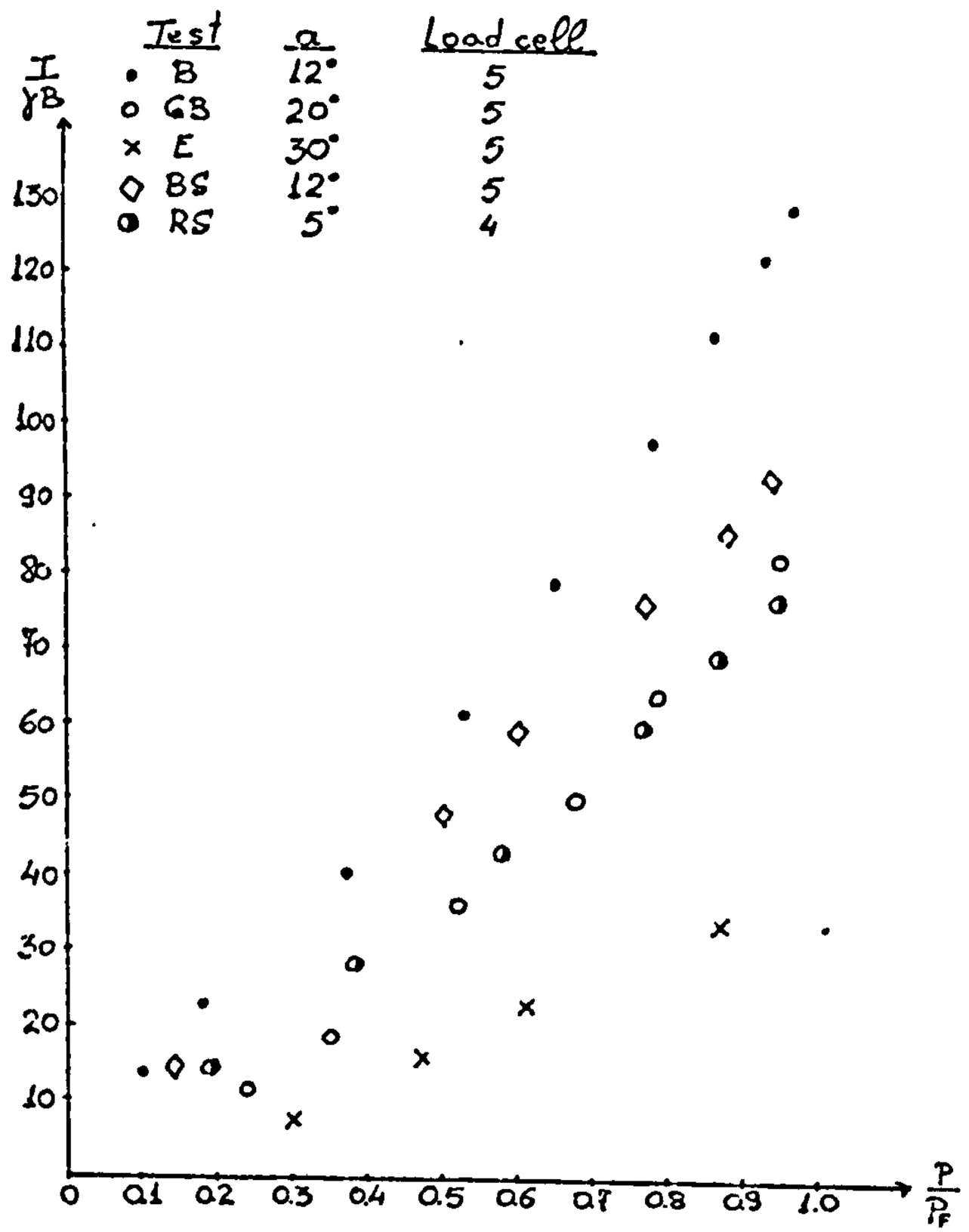

Fig. 6.22 The shear stresses recorded by the 'normalizing' load cell during tests B,GB,E,BS,RS.

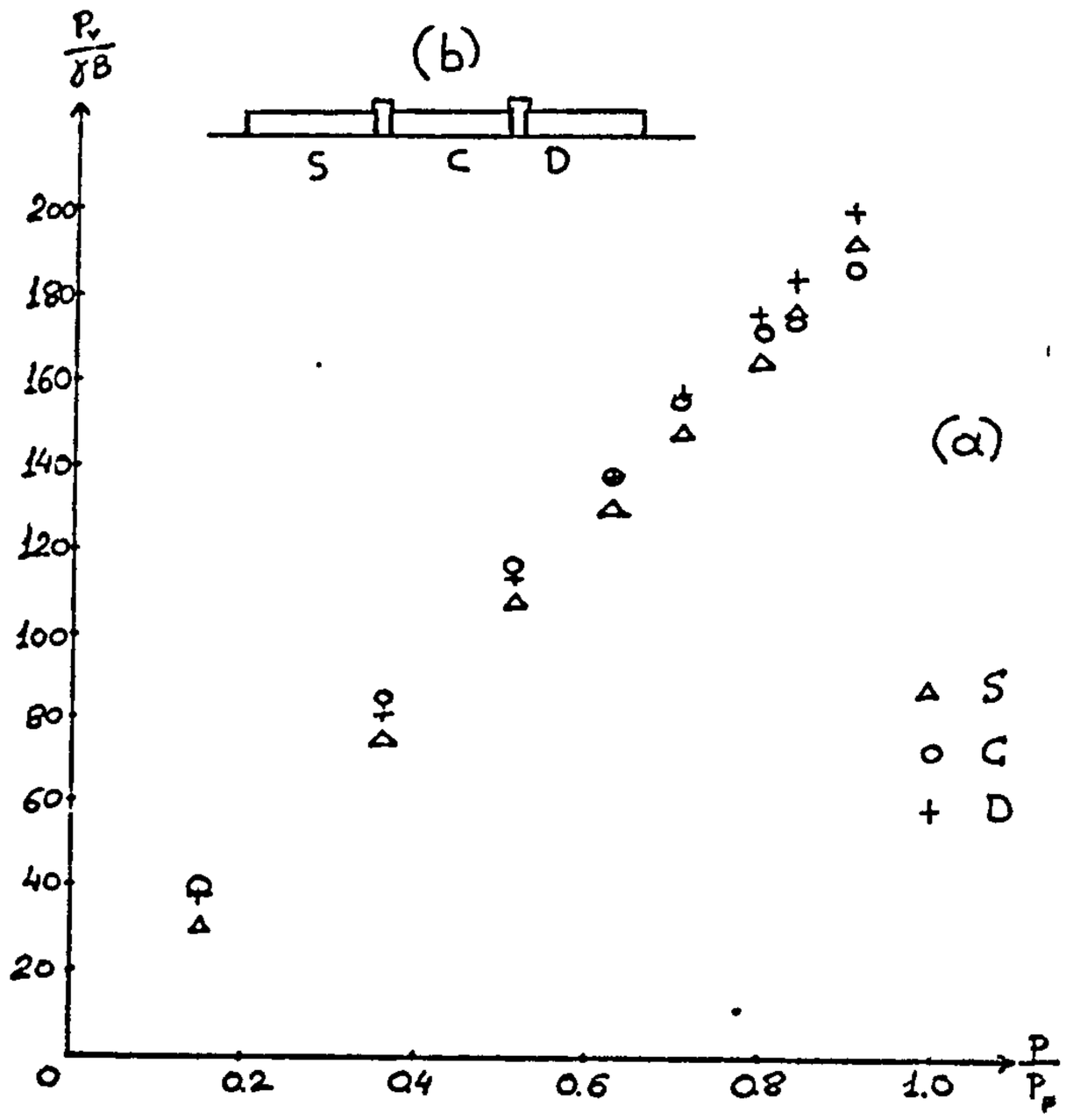

Fig. 6.23 The average pressure underneath each section of the footing during test BS.

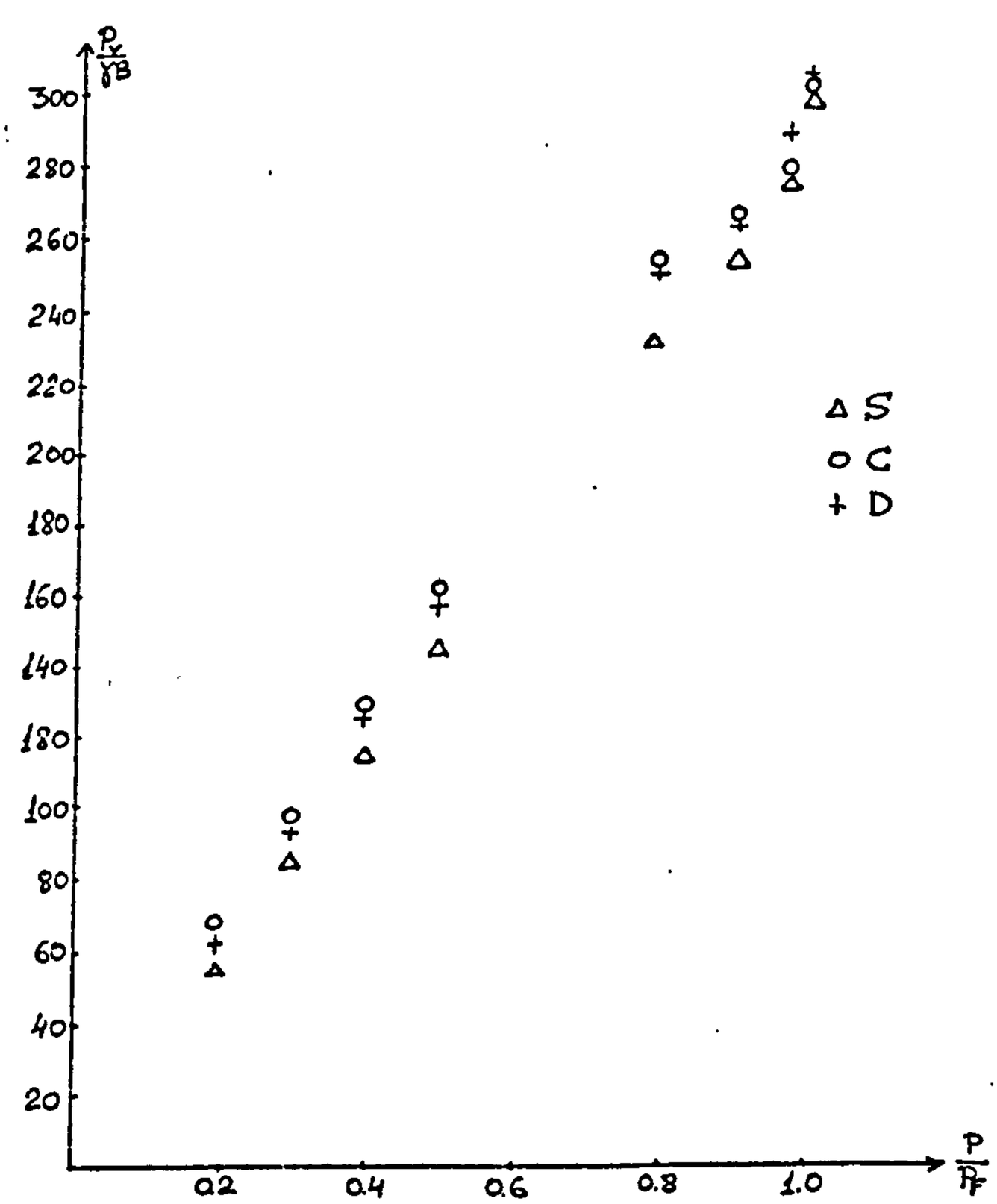

Fig. 6.24 The average pressure underneath each section of the footing during test RS.

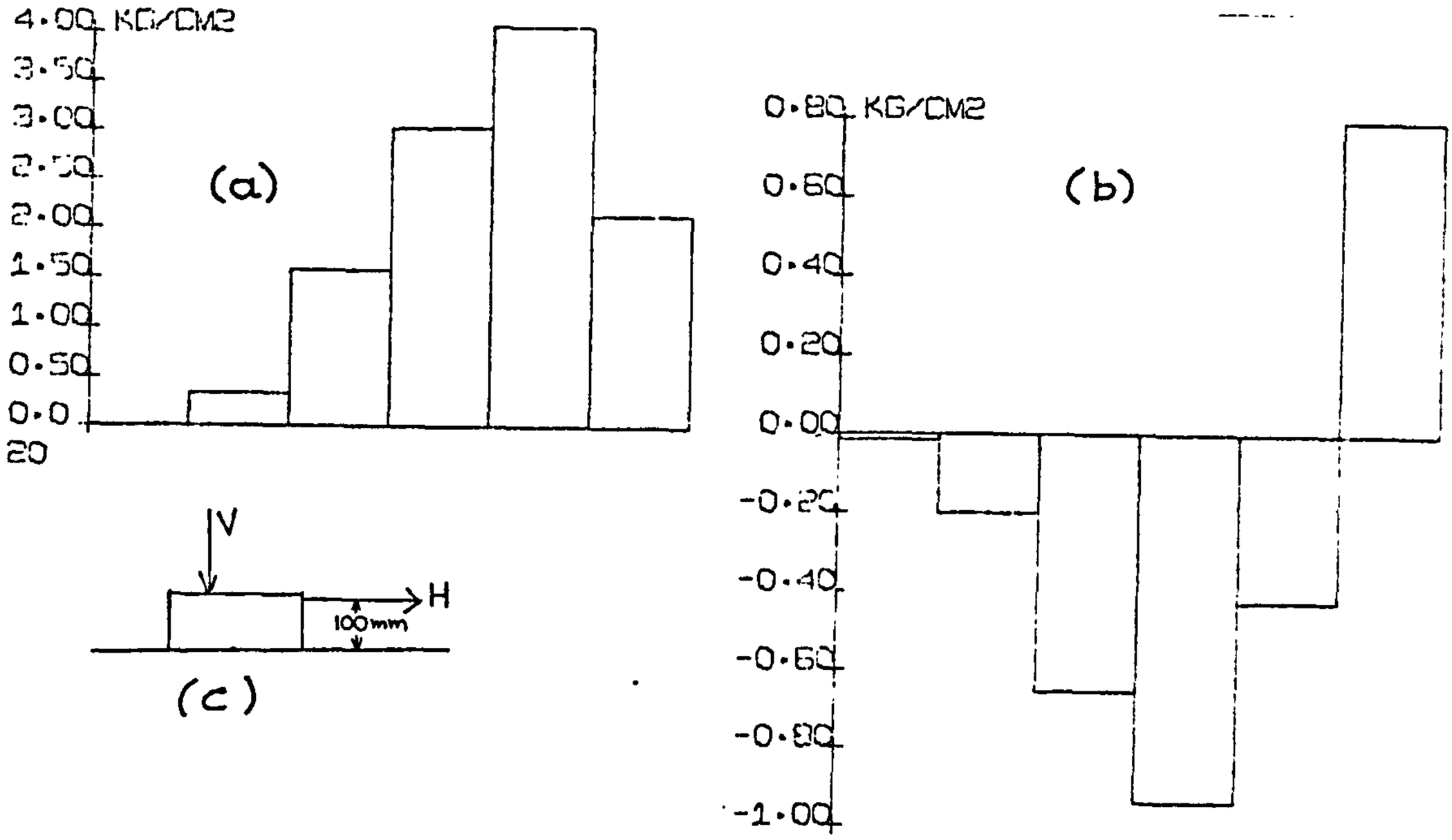

Fig. 6.25 Stress distribution from test F(e_o=0.52) at a stage near failure. (a) Normal stress (b) Shear stress (c) Load combination in test F.

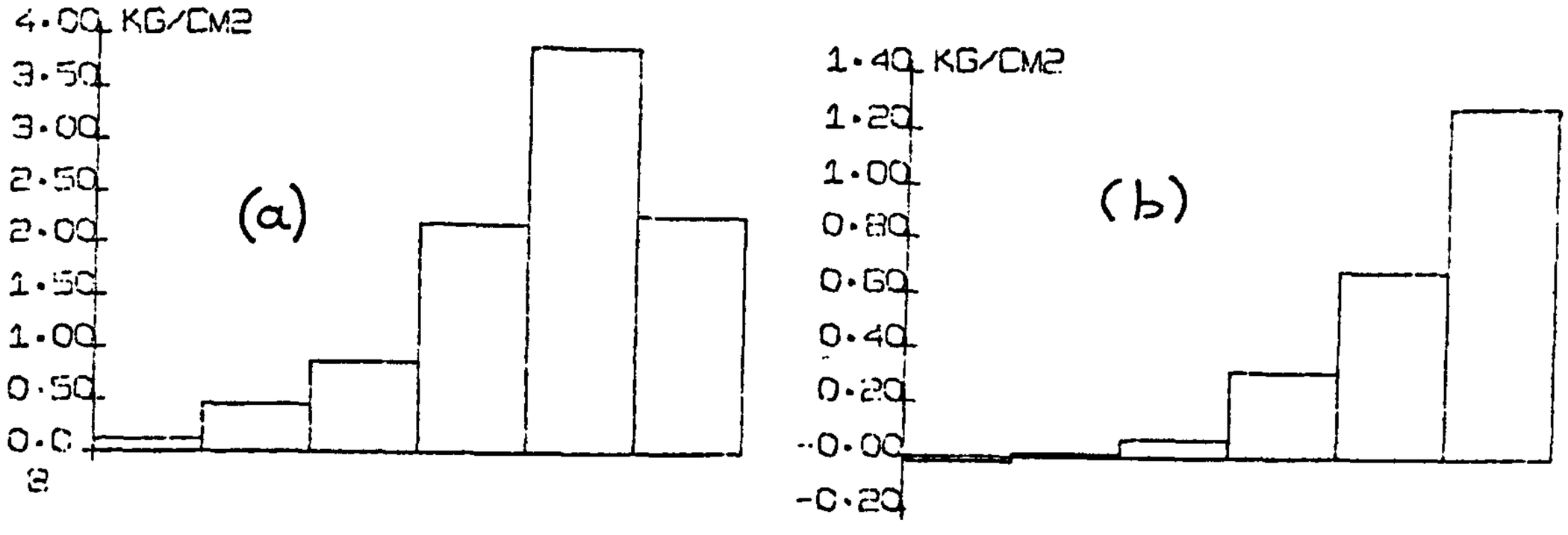

Fig. 6.26 Stress distribution from test C(e_o=0.52) at a stage 0.90 of the failure load. (a) Normal stress (b) Shear stress (c) Load combination in test C.

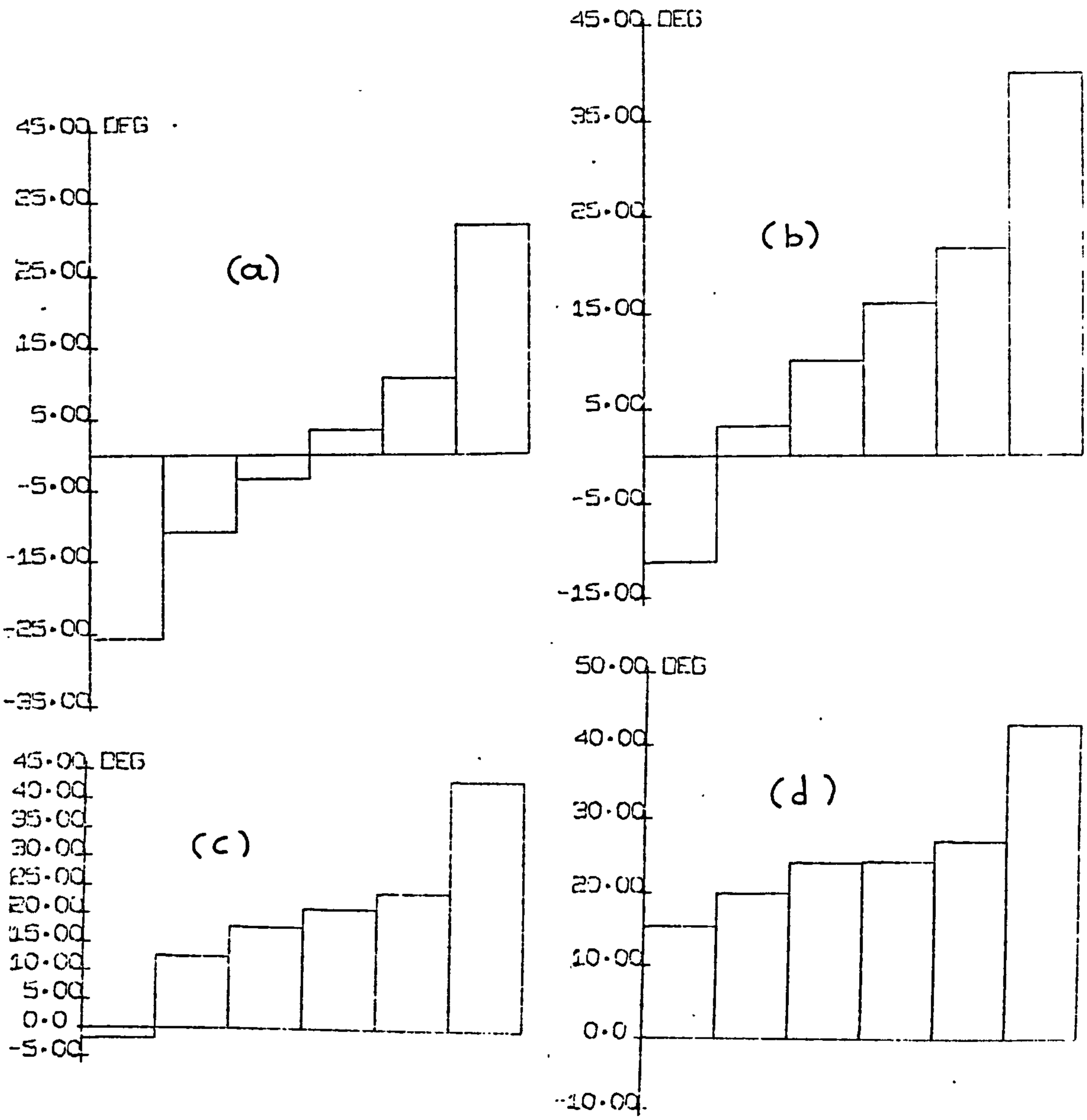

Fig. 6.27 Distribution of the angle of base friction from tests in the FAC (a) Test D(α_o=0) (b) Test B (α_o=12°)(c) Test GB (α_o=20°) (d) Test E (α_o=30°).

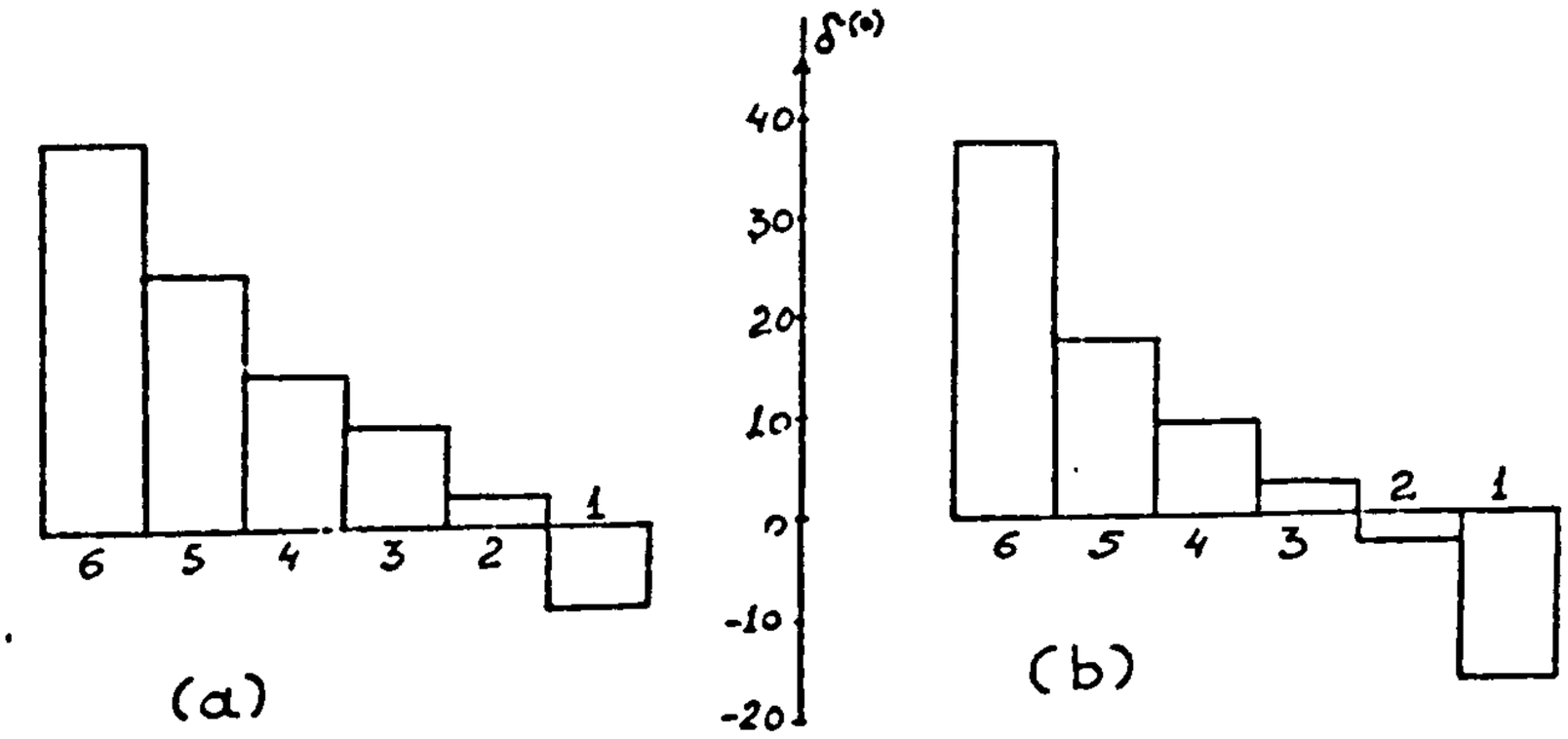

Fig. 6.28 Distribution of the angle of base friction from tests in the FAC (a) Test BS (α_o=12°) (b) Test RS(α_o=5°).

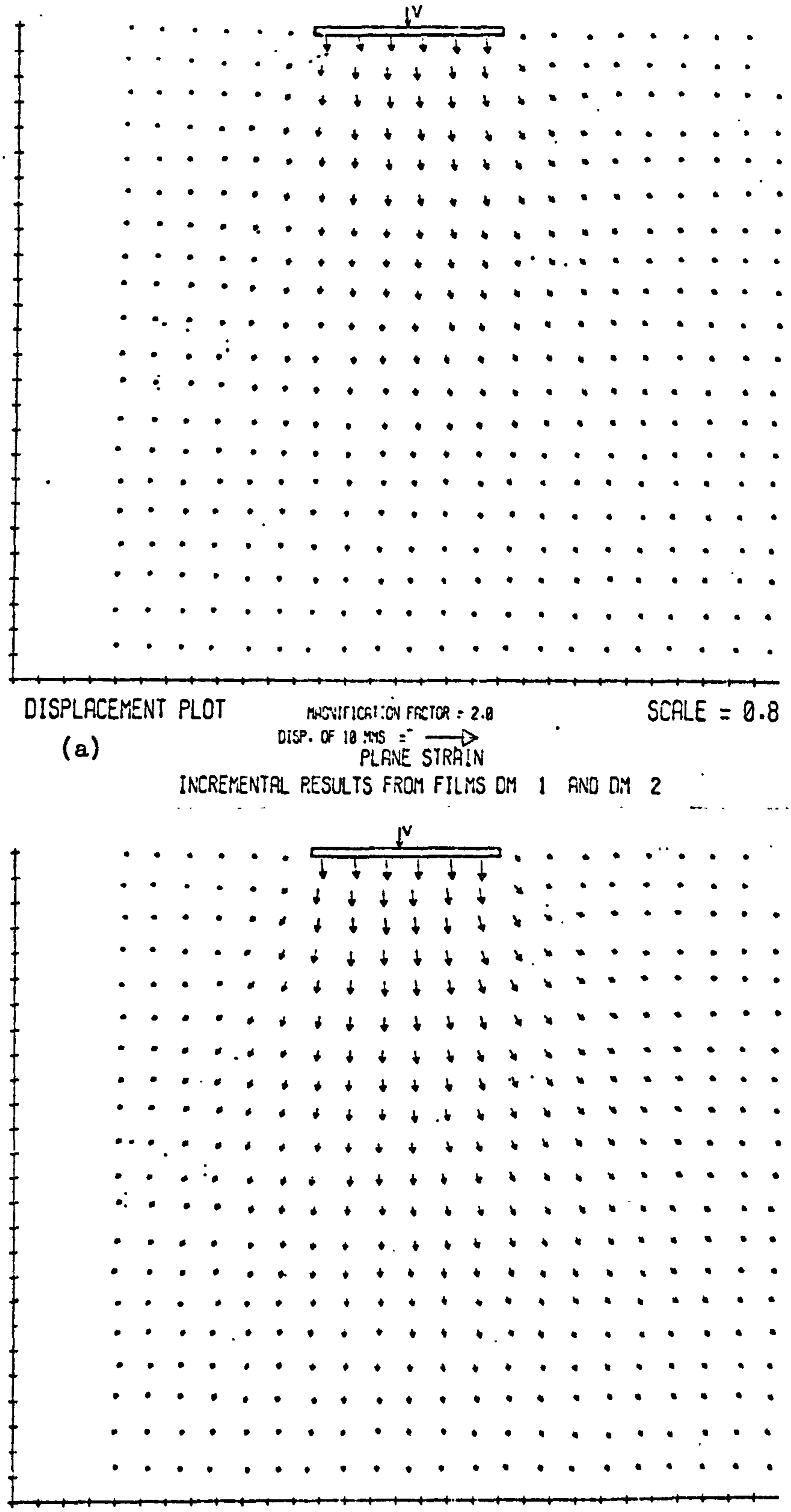

Fig. 7.1 Total displacement fields from test D(e_o=0.52,α_o=0,E_o=0) at stages: (a)0.46 (b) 0.59 of the failure load.

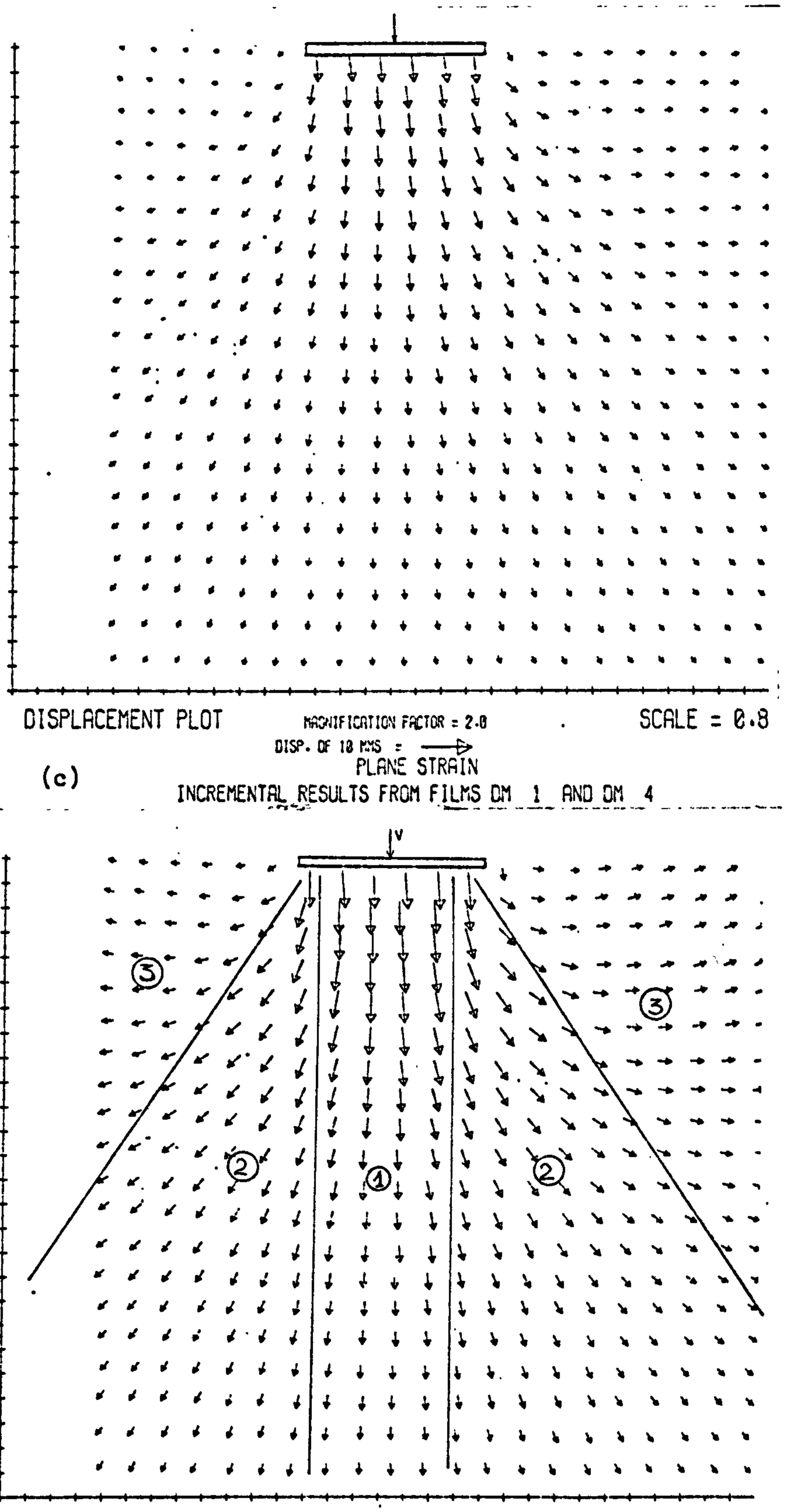

Fig. 7.1 Total displacement fields from test D(e_o=0.52, α_o=0, E_o=0) at stages (c) 0.74 (d) 0.93 of the failure load.

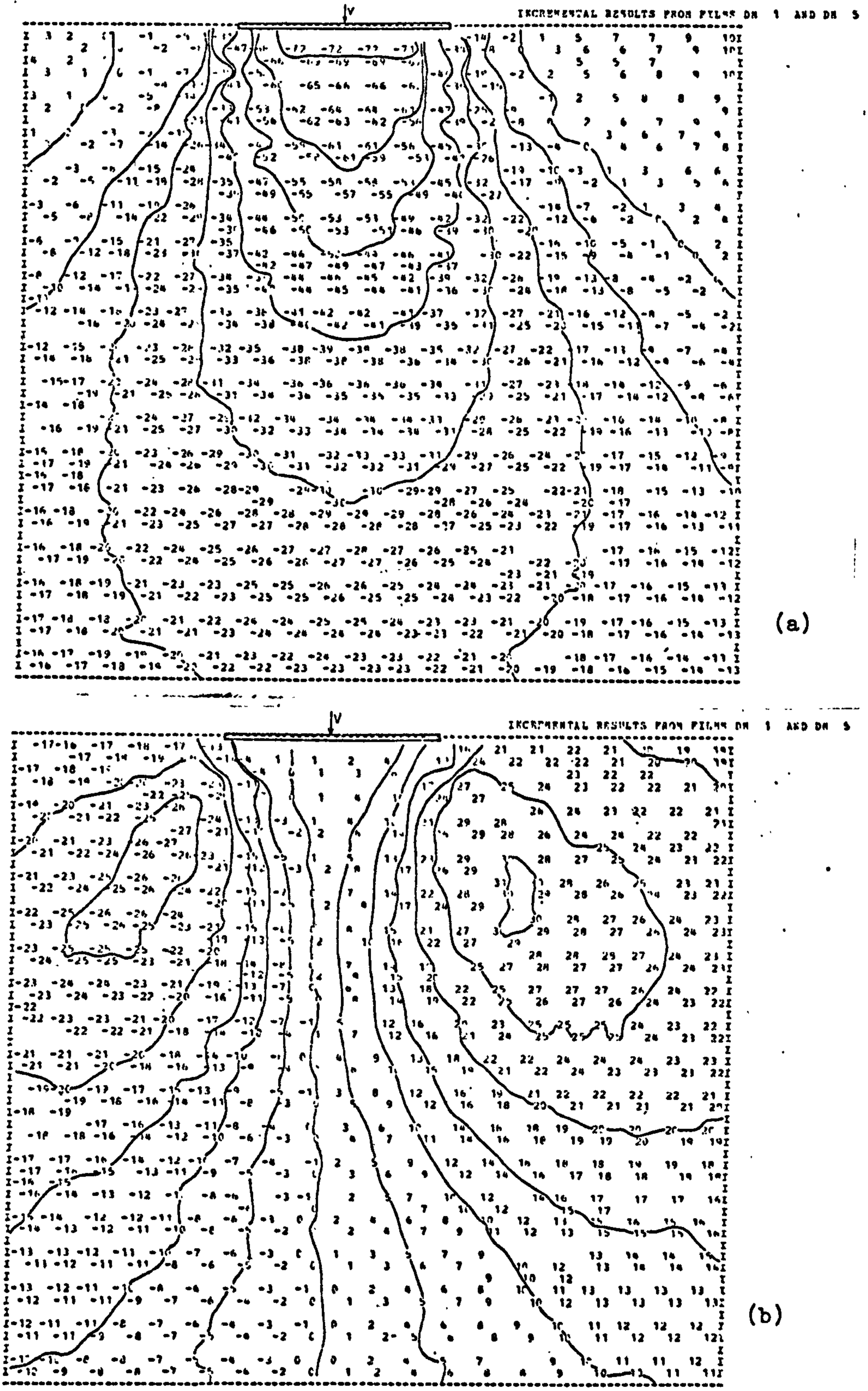

Fig. 7.2 Total displacement fields from test D(e_o=0.52,α_o=0,E_o=0) at stage 0.93 of the failure load (in 0.10mm)
(a) Vertical (b) Horizontal.

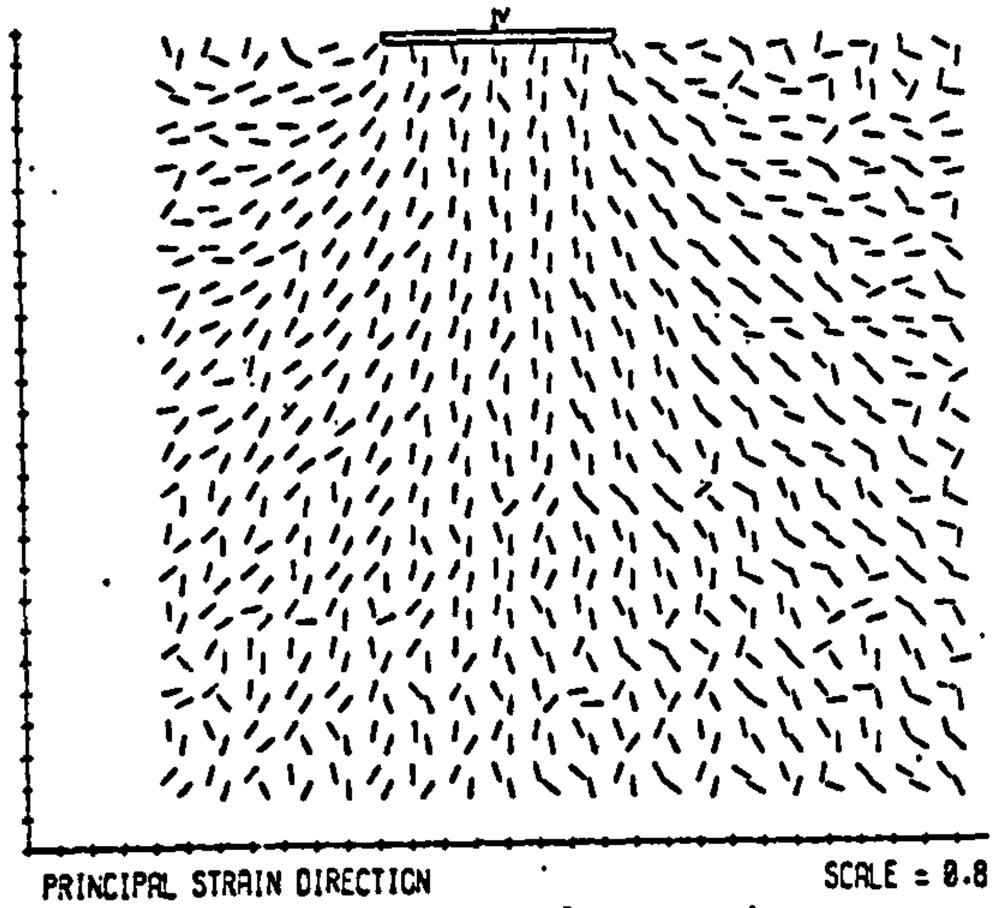

(a)

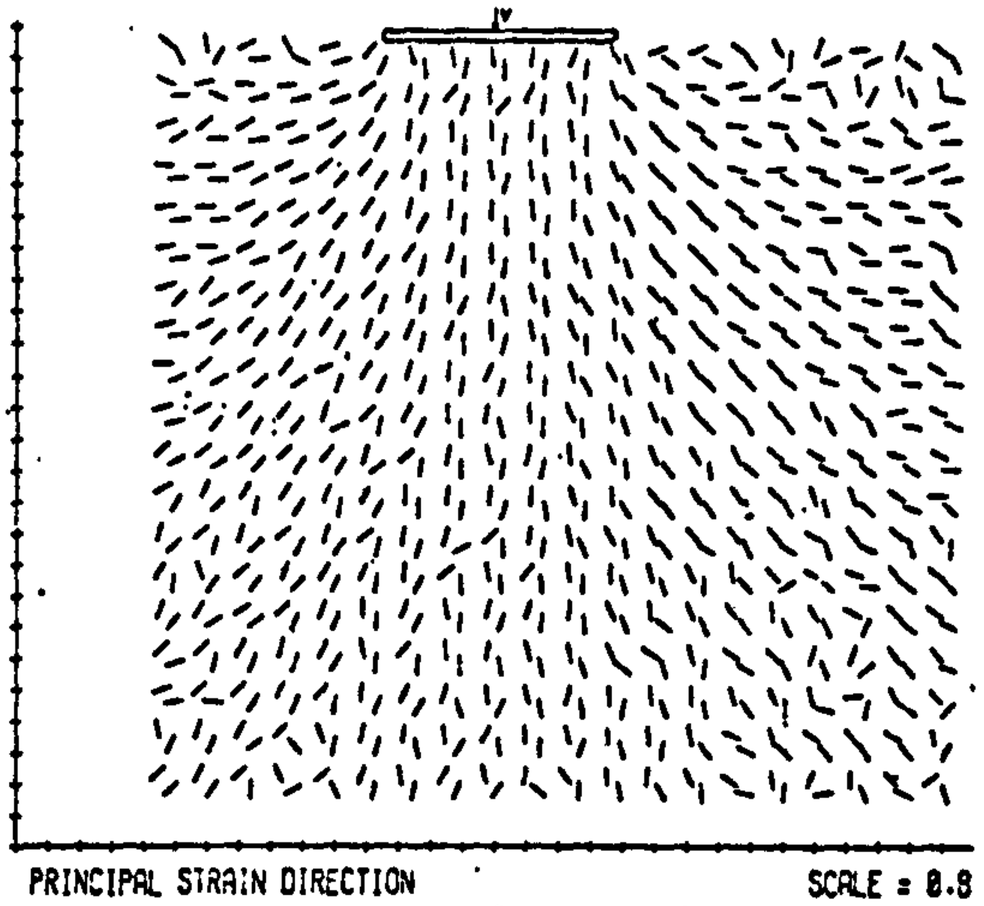

(b)

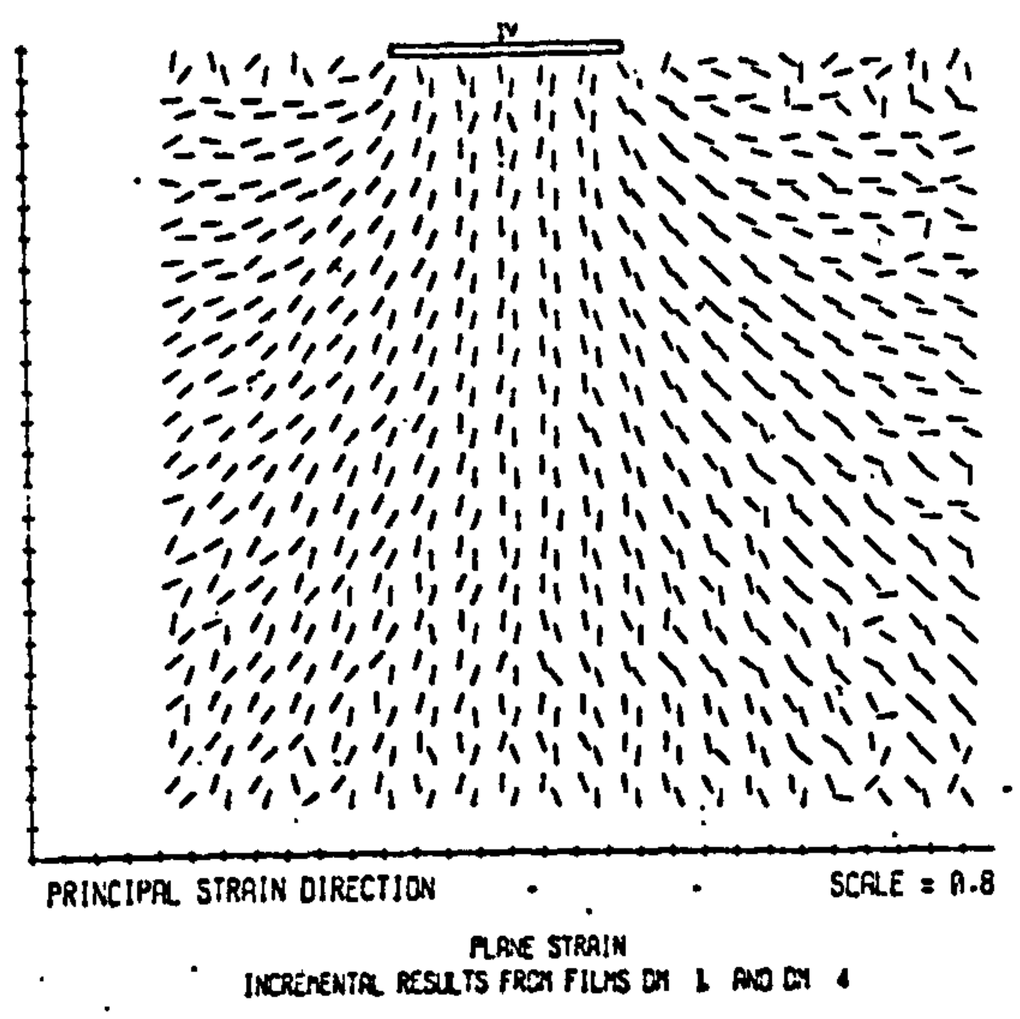

(c)

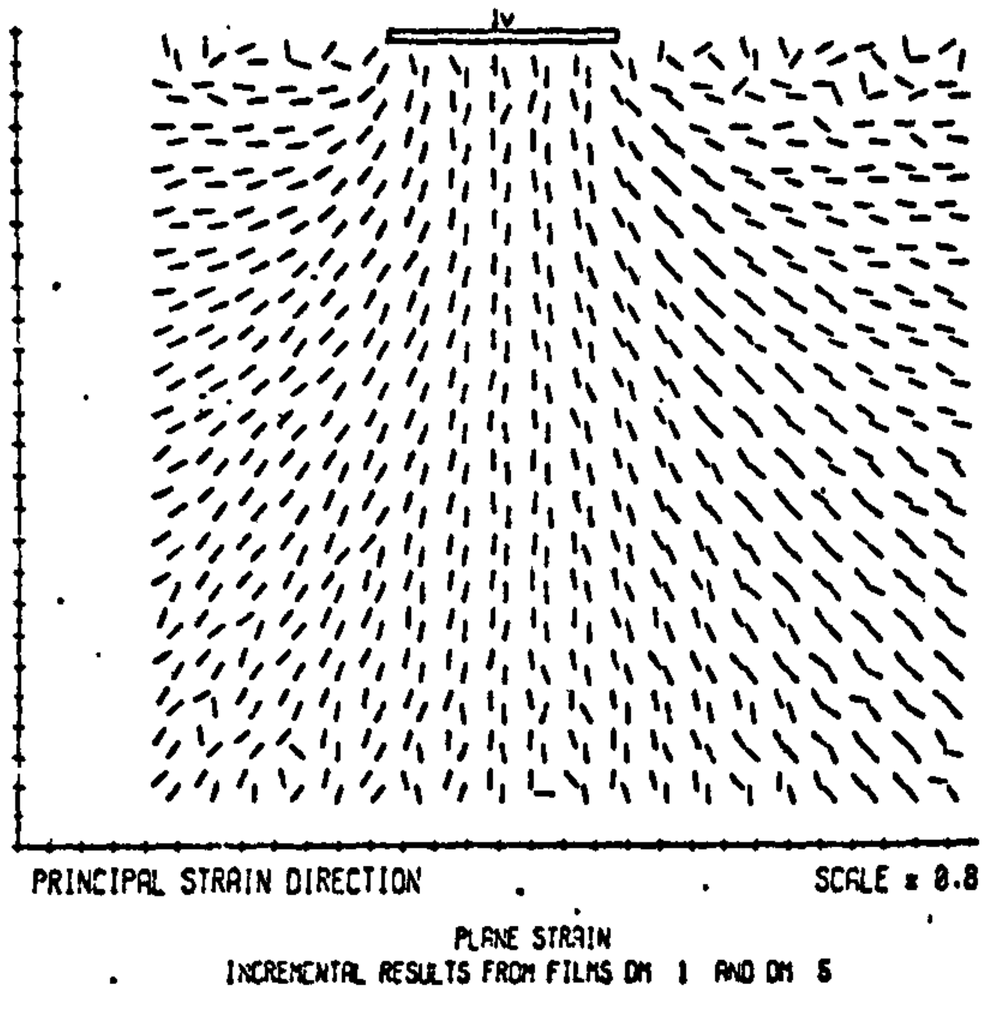

(d)

Fig. 7.3 The major principal compressive strain directions from test D(e_o=0.52,α_o=0,E_o=0) at stages: (a) 0.46 (b) 0.59 (c) 0.74 and (d) 0.93 of the failure load.

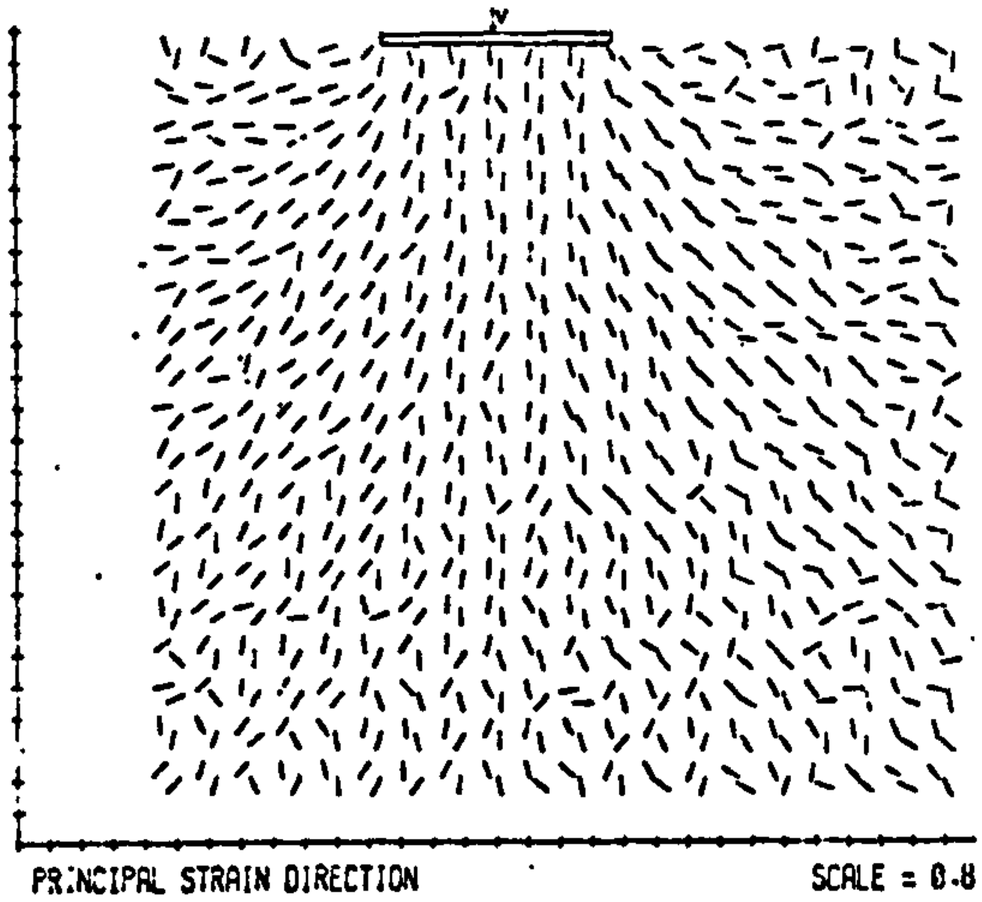

(a)

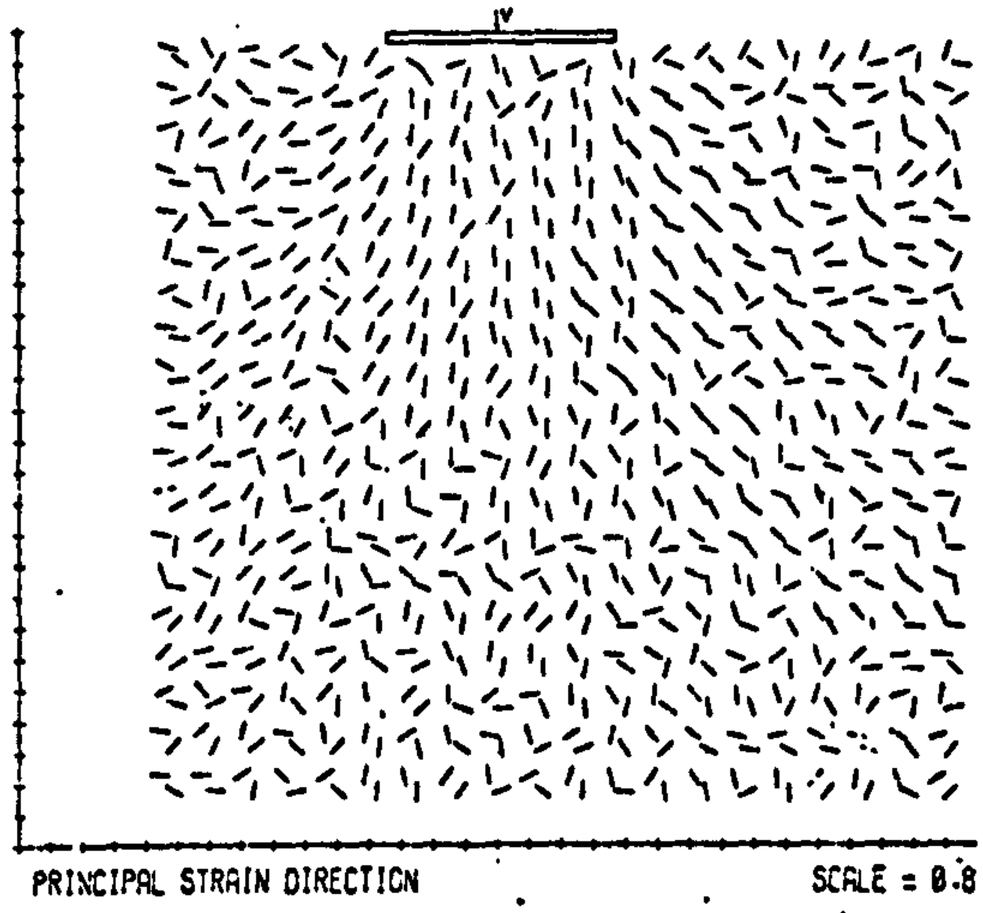

(b)

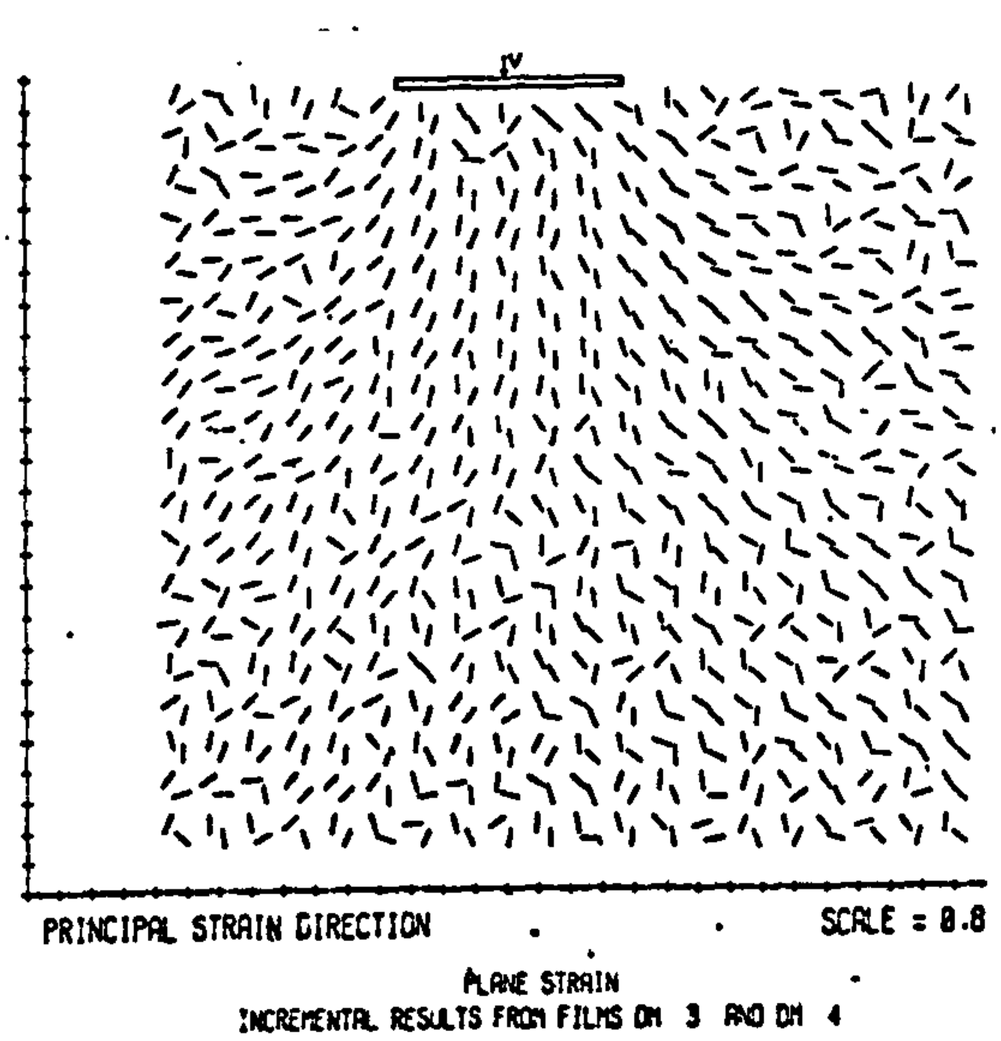

(c)

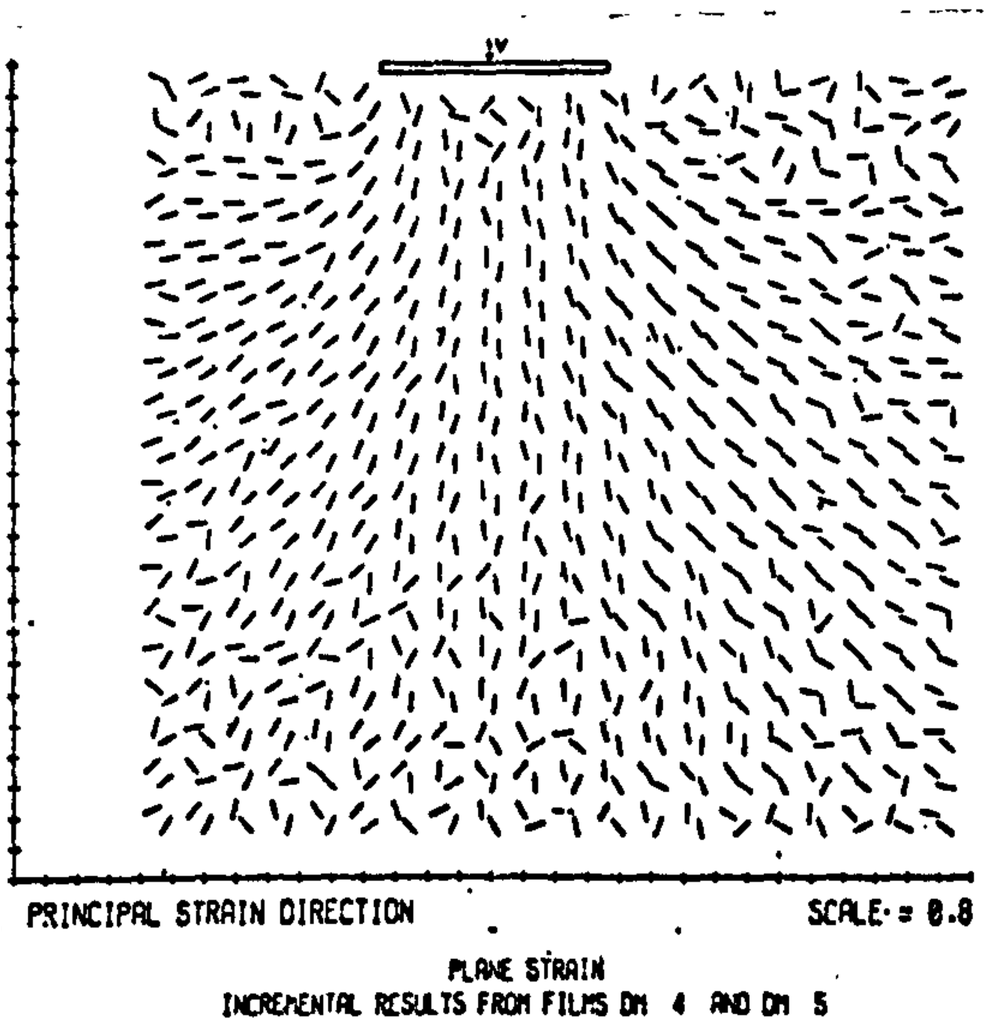

(d)

Fig. 7.4 The major principal compressive strain increment directions from test D(e_o=0.52,α_o=0,E_o=0) for increments: (a) 0.0-0.43 (b) 0.43-0.59 (c) 0.59-0.74 and (d) 0.74-0.93 of the failure load.

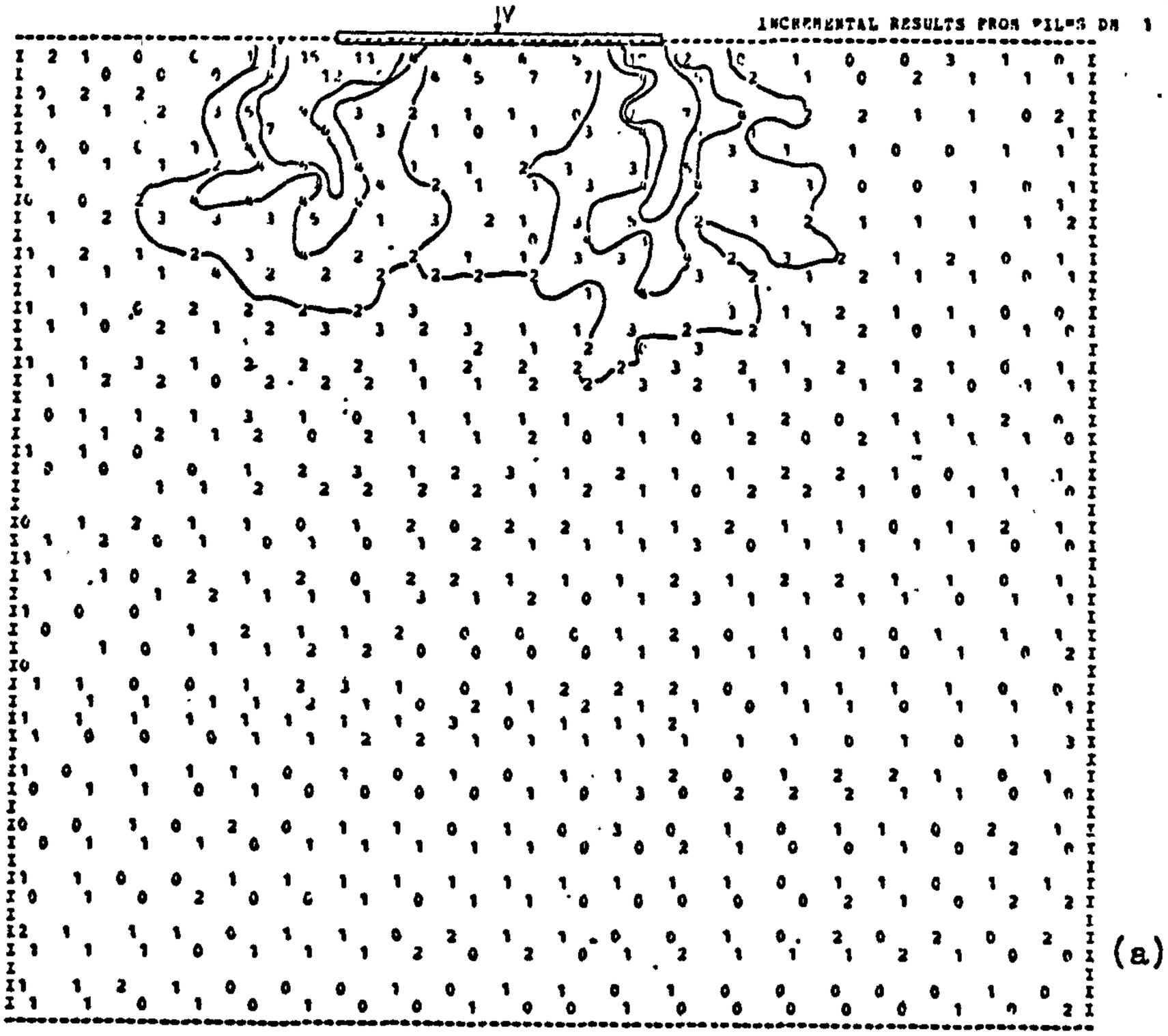

(a)

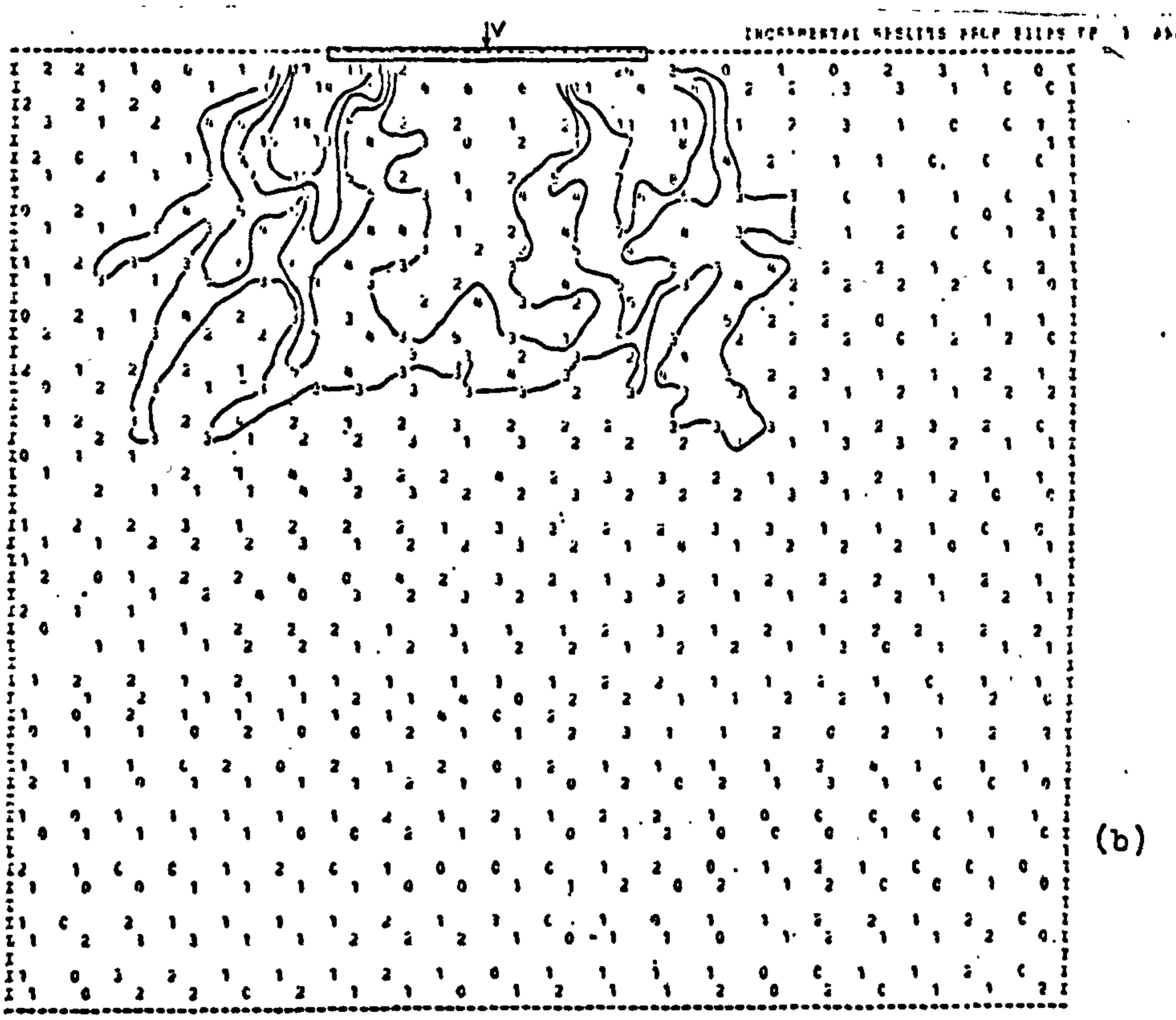

(b)

Fig. 7.5 The total maximum shear strains (in percent) from test $D(e_o=0.52, \alpha_o=0, E_o=0)$ at stages: (a) 0.46 (b) 0.59 of the failure load.

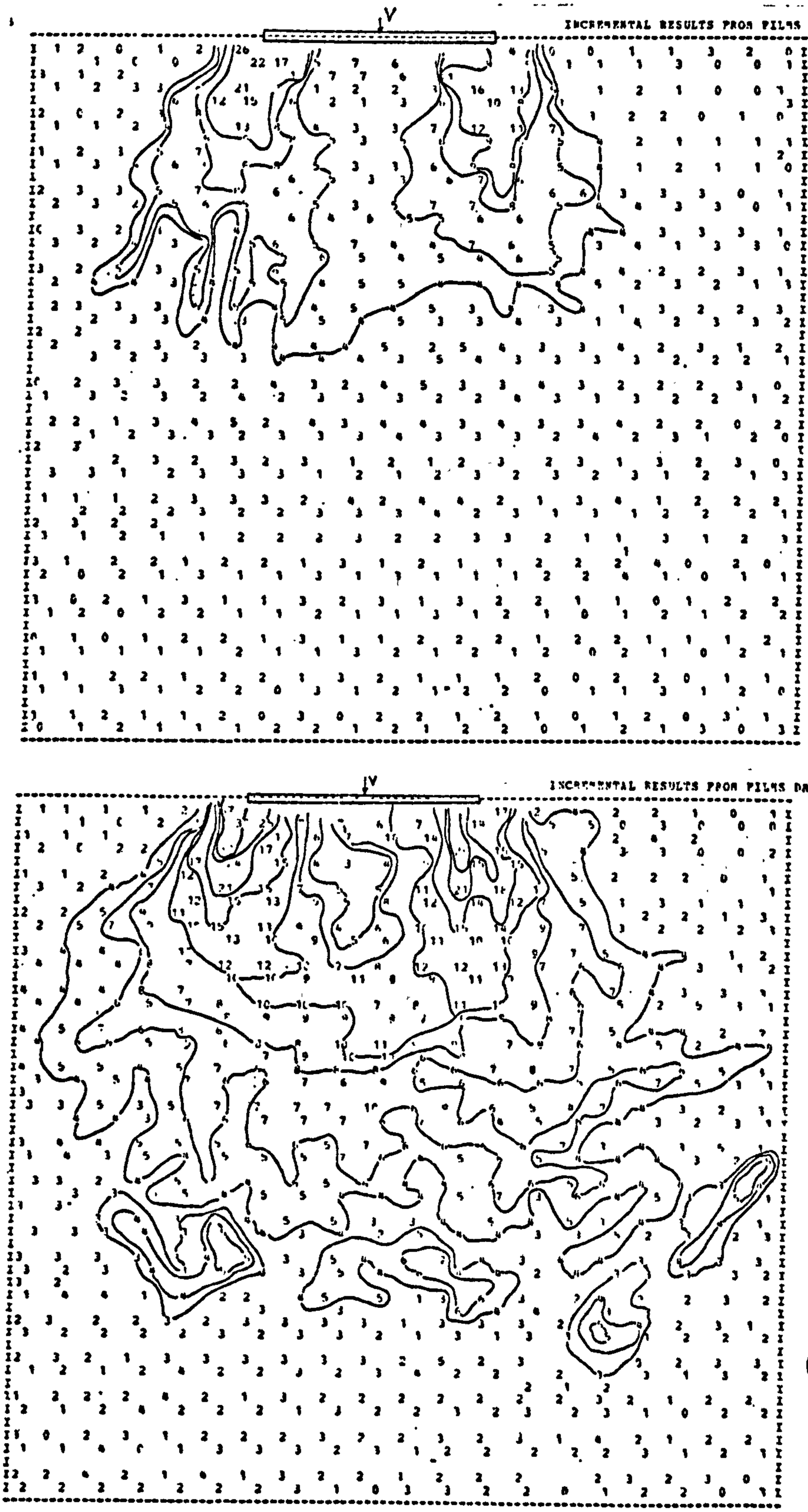

Fig. 7.5 The total maximum shear strains (in percent) from test $D(e_o=0.52, \alpha_o=0, E_o=0)$ at stages: (c) 0.74 and (d) 0.93 of the failure load.

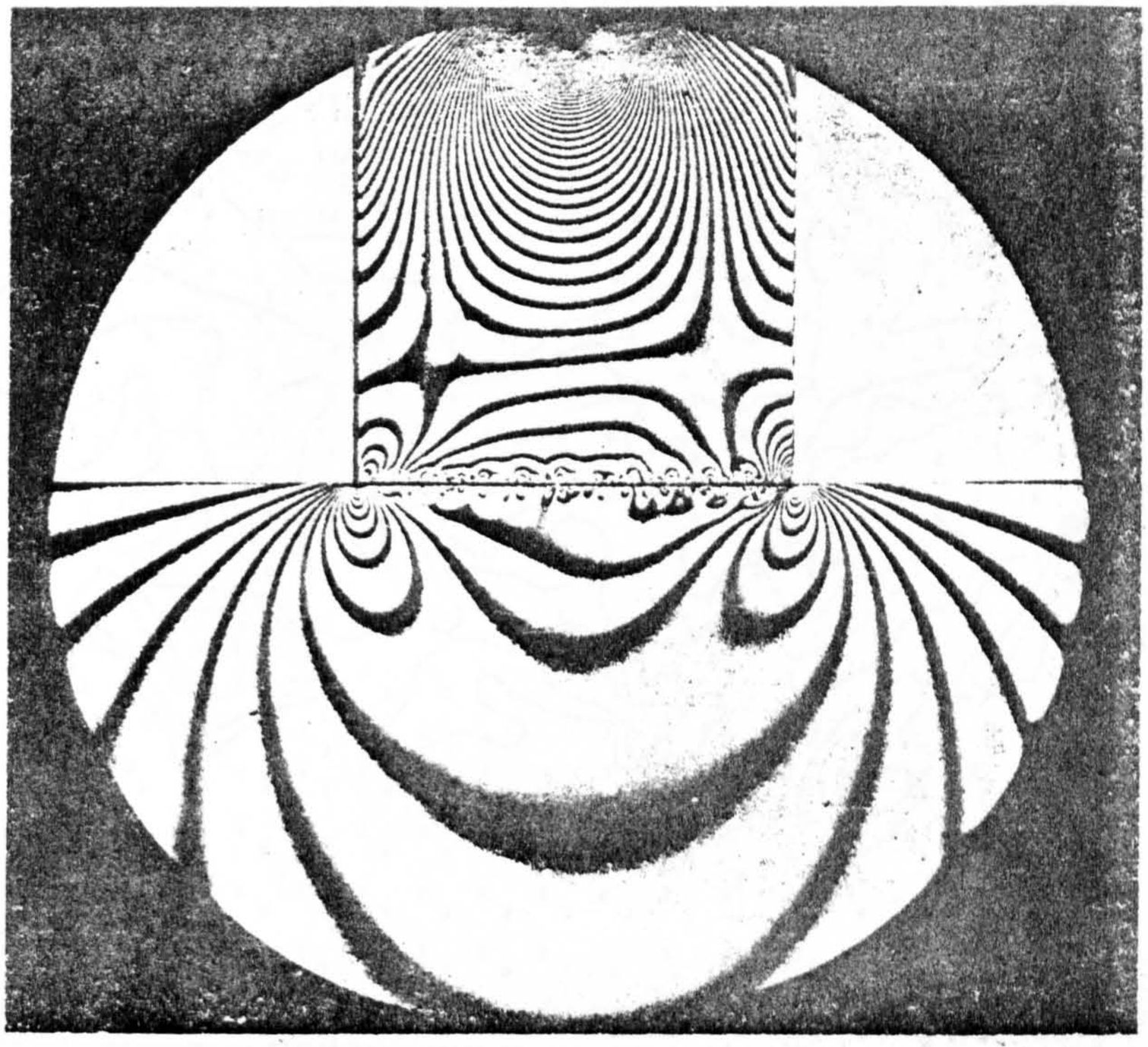

Fig. 7.6 Equal stress contours from a photoelastic pattern of a rigid foundation on an elastic base (Frocht,1948).

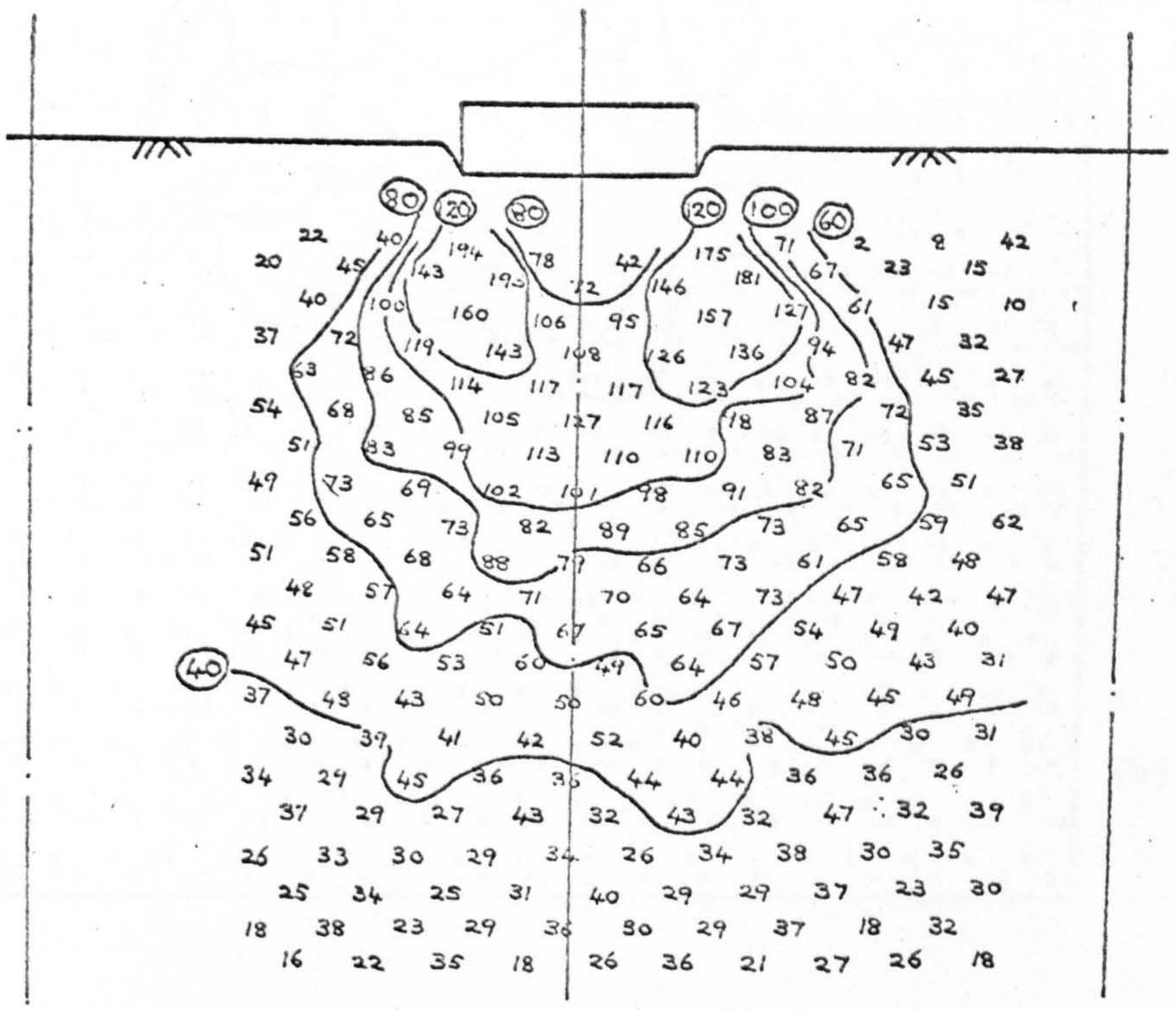

Fig. 7.7 The total maximum shear strains from test H(B=76.2mm,e_o=0.525) at 0.955 of the failure load (Tennekoon,1970).

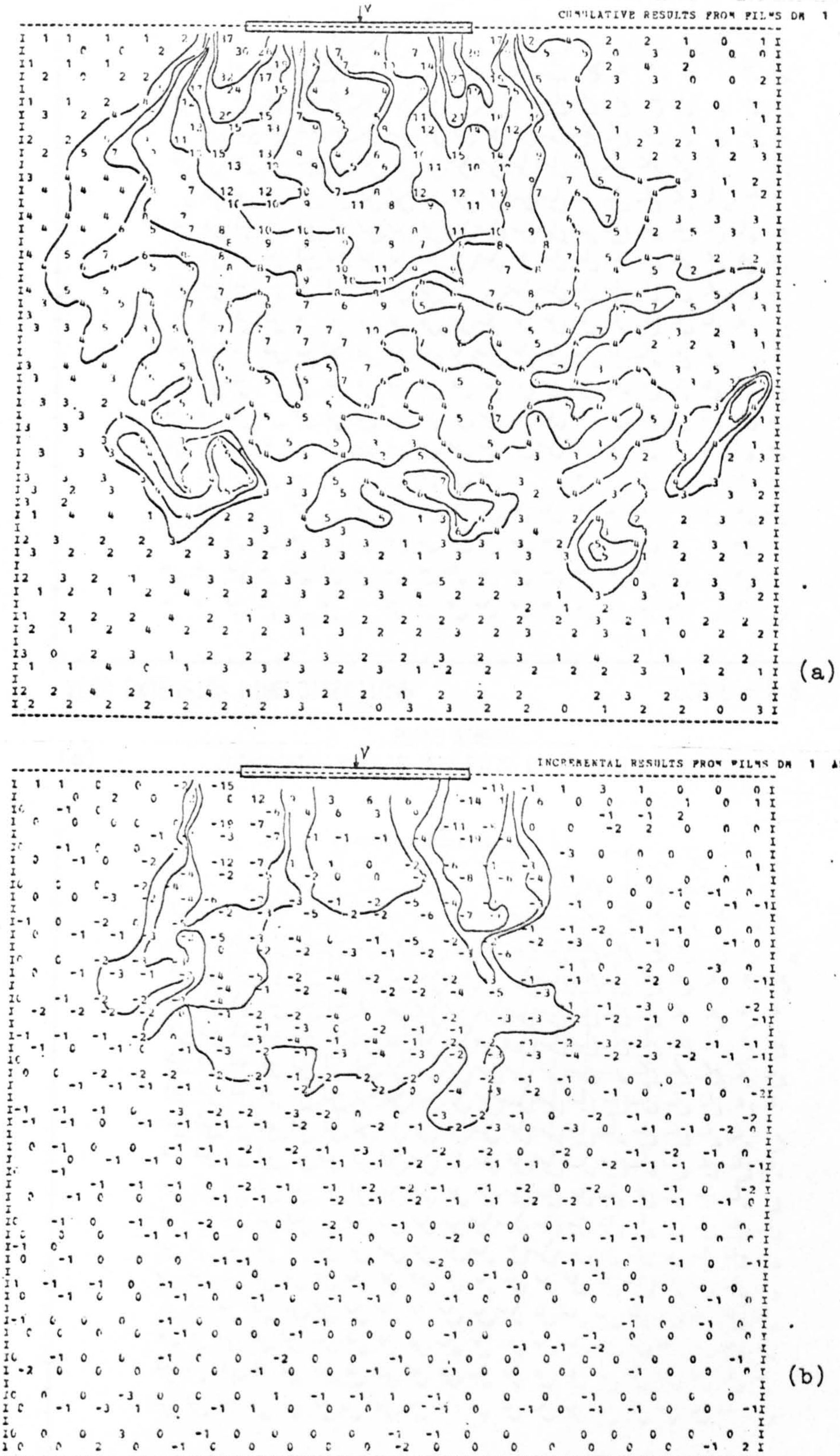

Fig. 7.8(a)The cumulative maximum shear strains (in percent) from test D(e_o=0.52,α_o=0,E_o=0) and (b) the total volumetric strains (in percent) from test D(e_o=0.52,α_o=0,E_o=0) at stage 0.93 of the failure load.

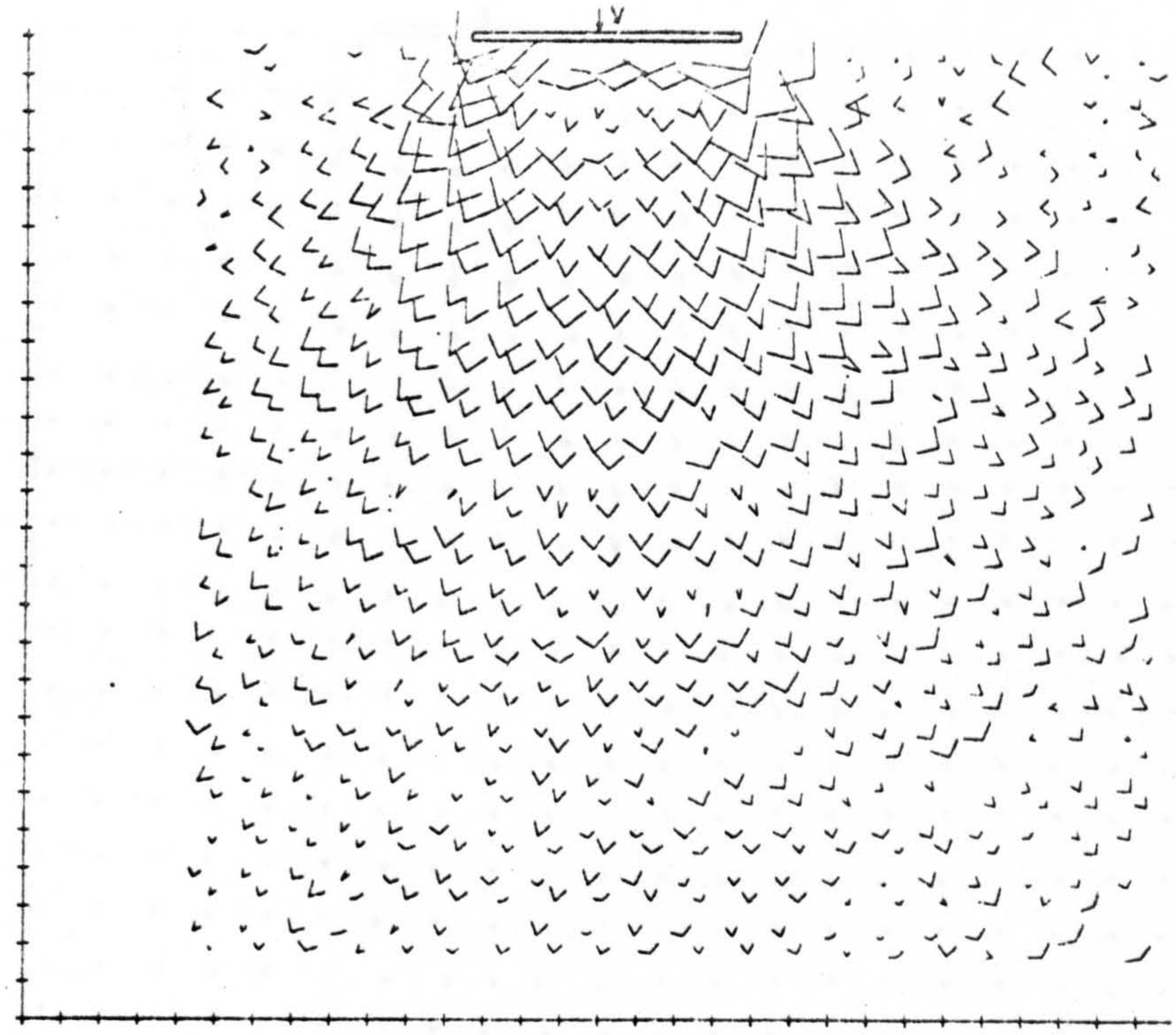

(a)

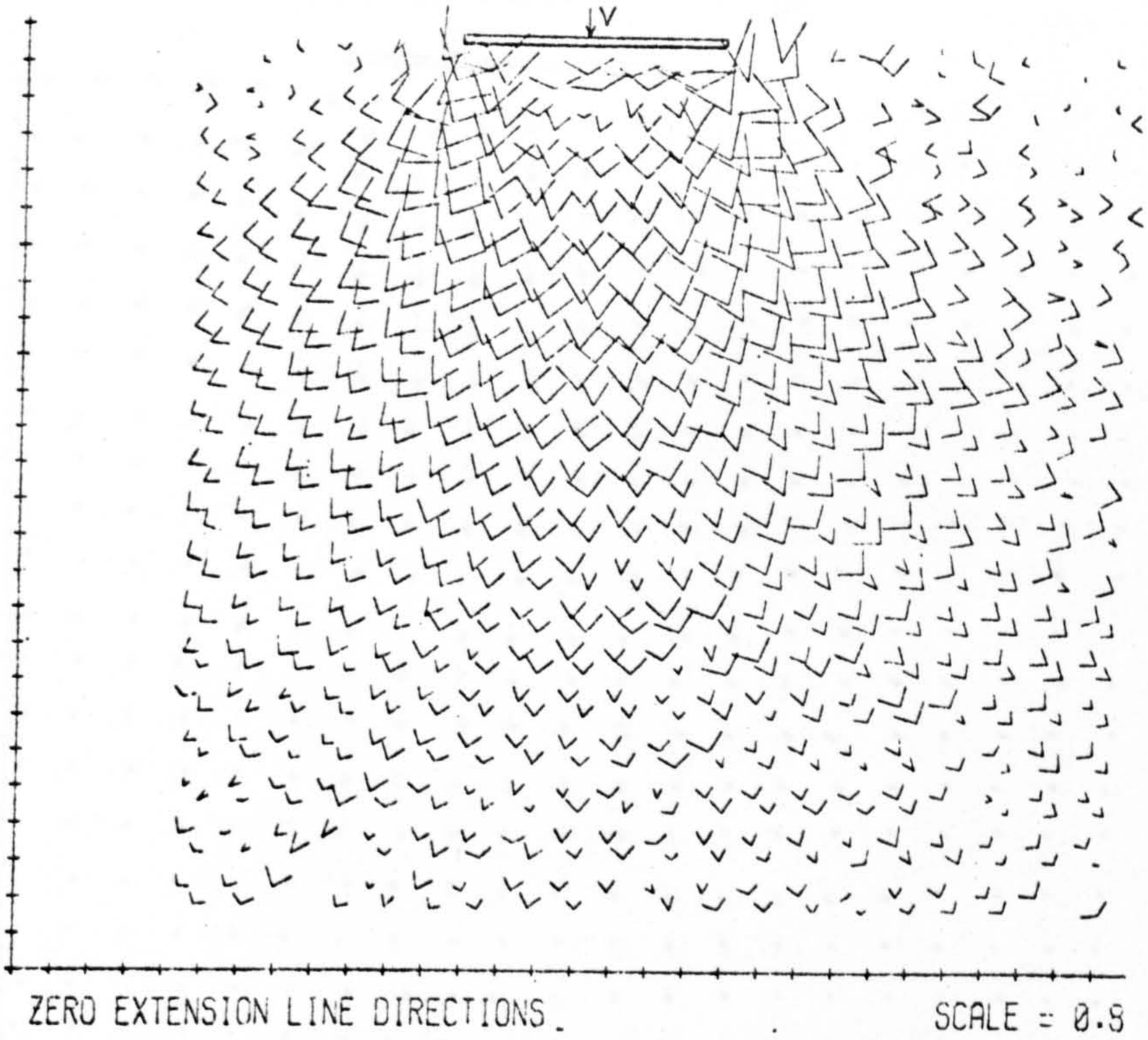

(b)

Fig. 7.9 The zero extension line directions from test D(e_o=0.52, α_o=0, E_o=0) at stages (a) 0.74 and (b) 0.93 of the failure load.

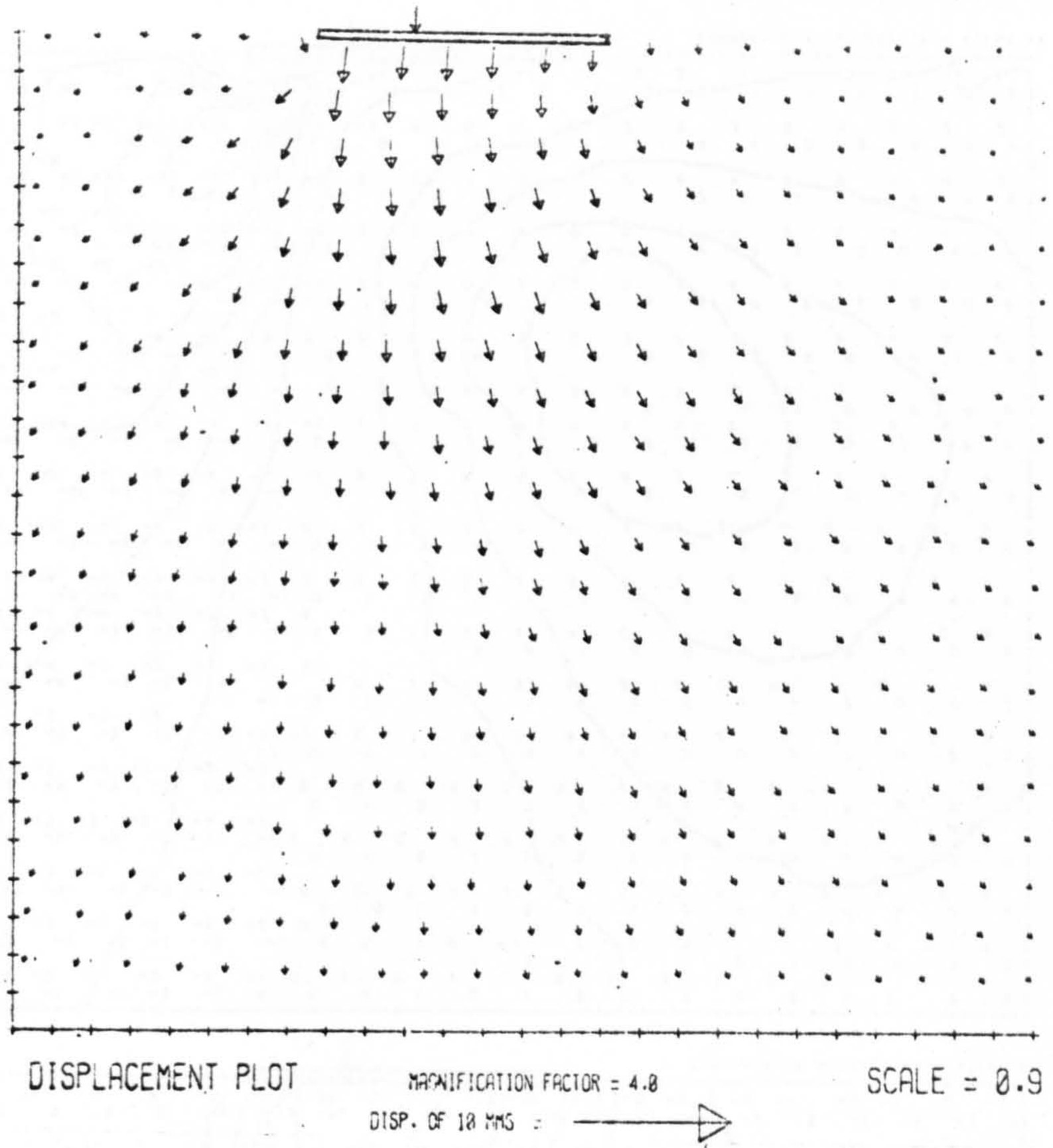

Fig. 7.10 Total displacement fields from test A(e_o=0.52,α_o=0,E_o=0.167) at stages (a) 0.72 and (b) 0.91 Of the failure load.

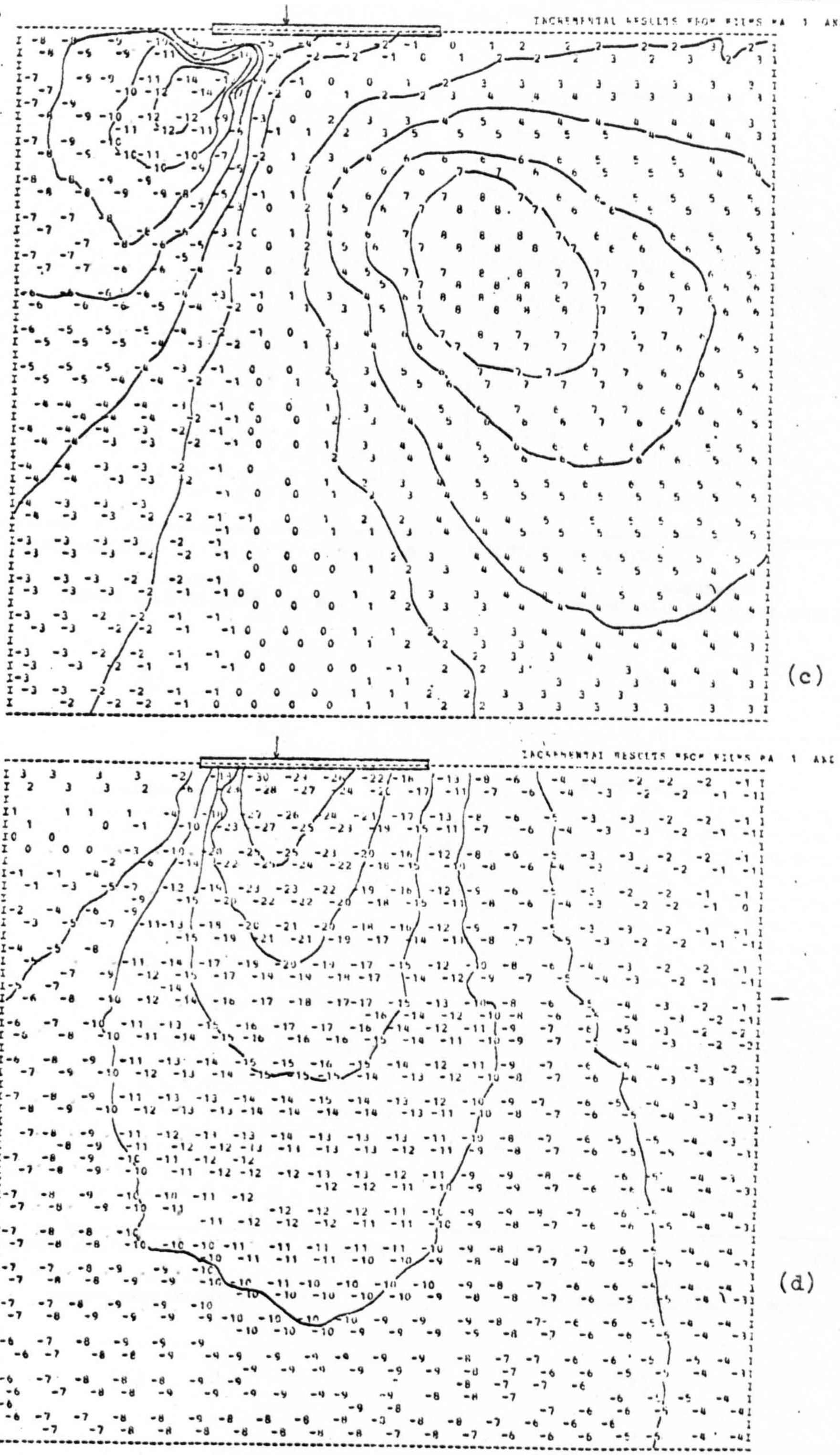

Fig. 7.10 Total displacement fields from test A(e_o=0.52,α_o=0,E_o=0.167) at stages (c) Horizontal and (d) vertical displacements at stage 0.91 of the failure load.

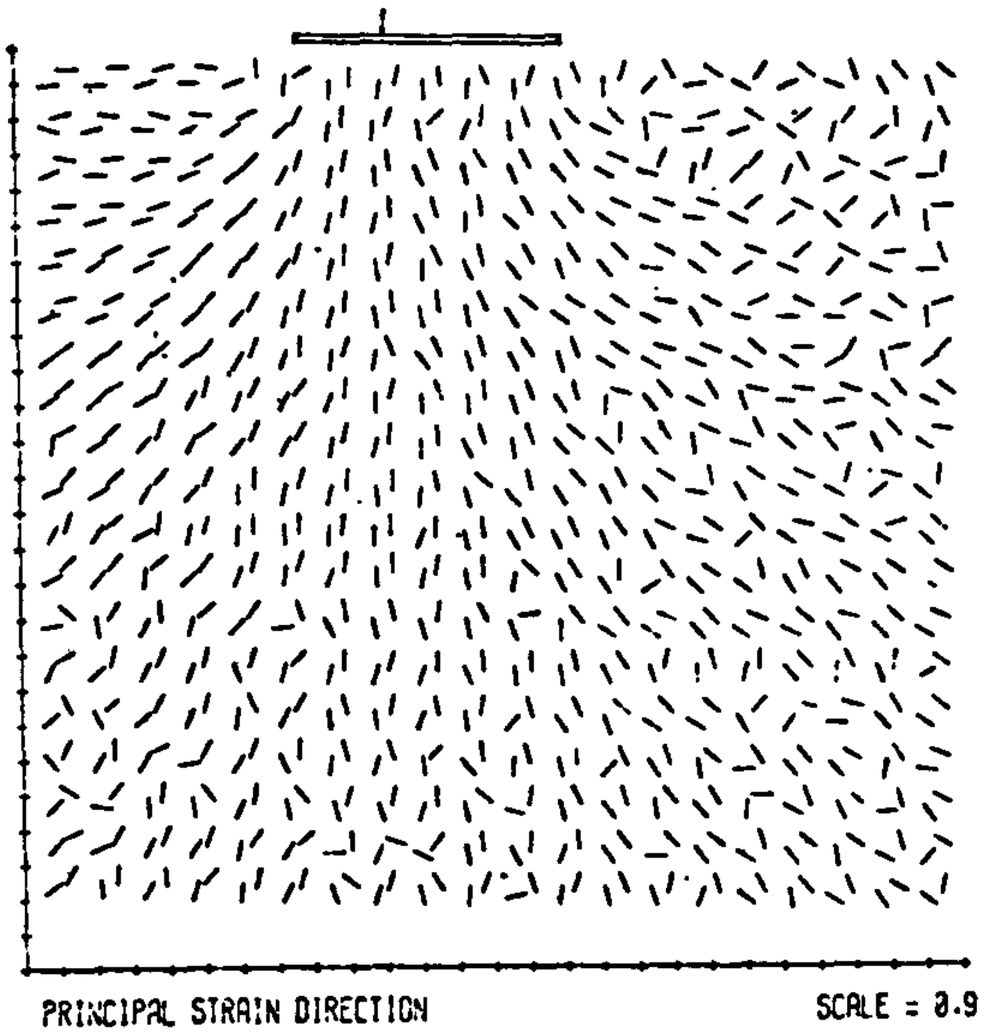

(a)

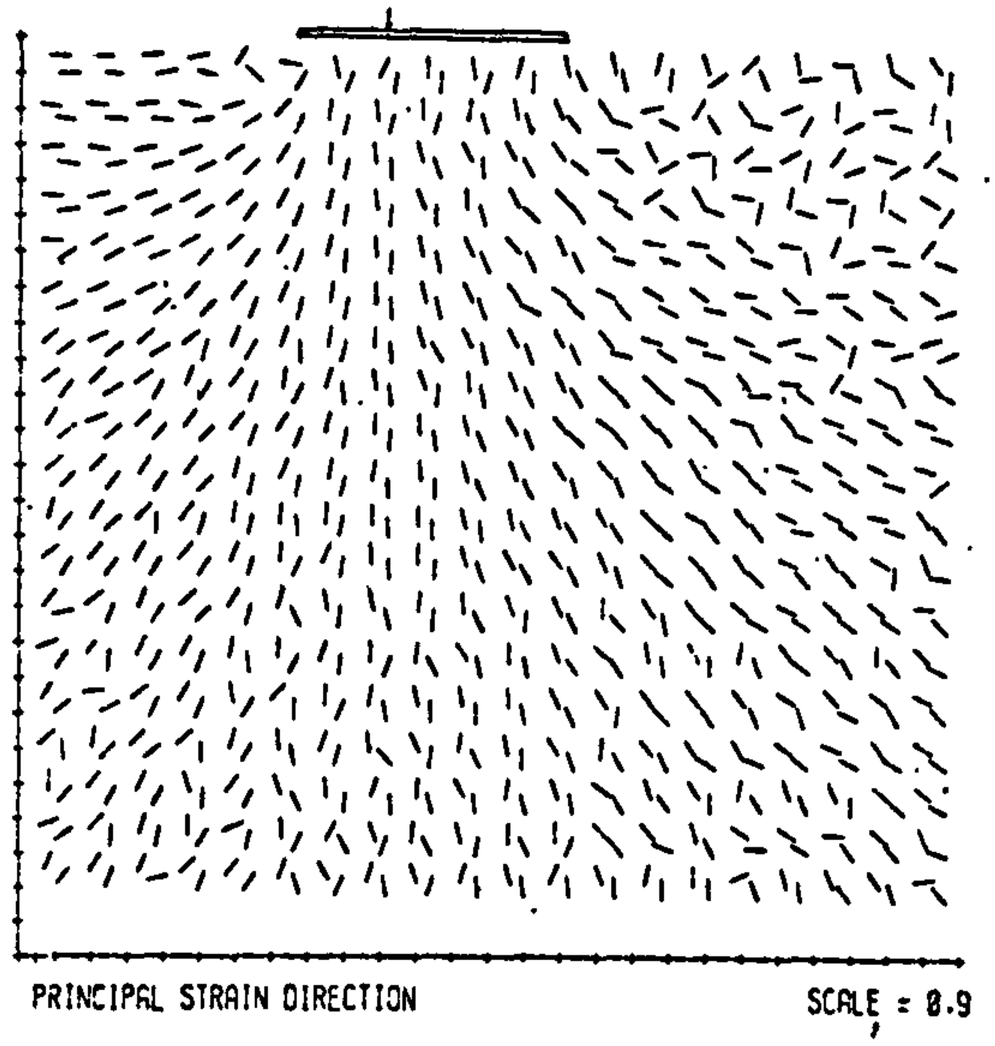

(b)

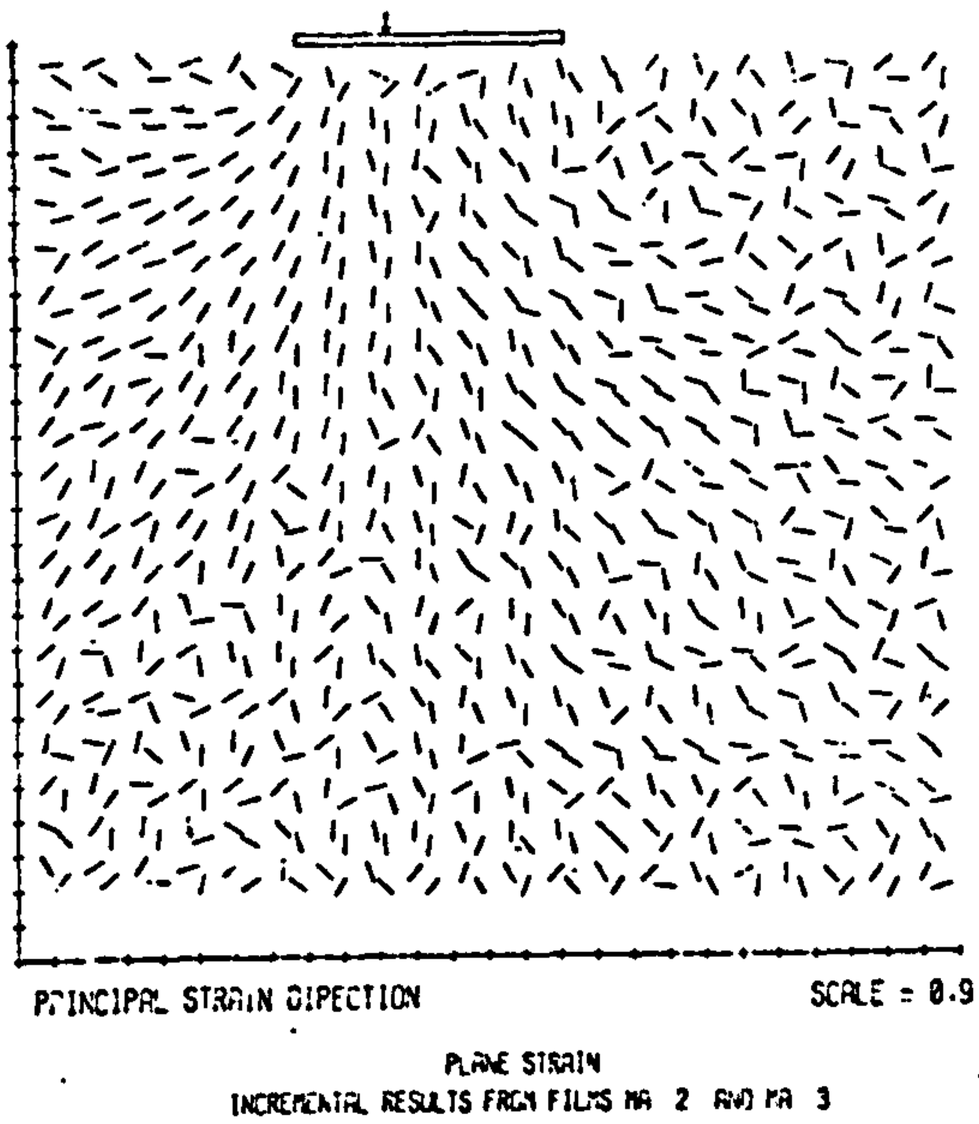

(c)

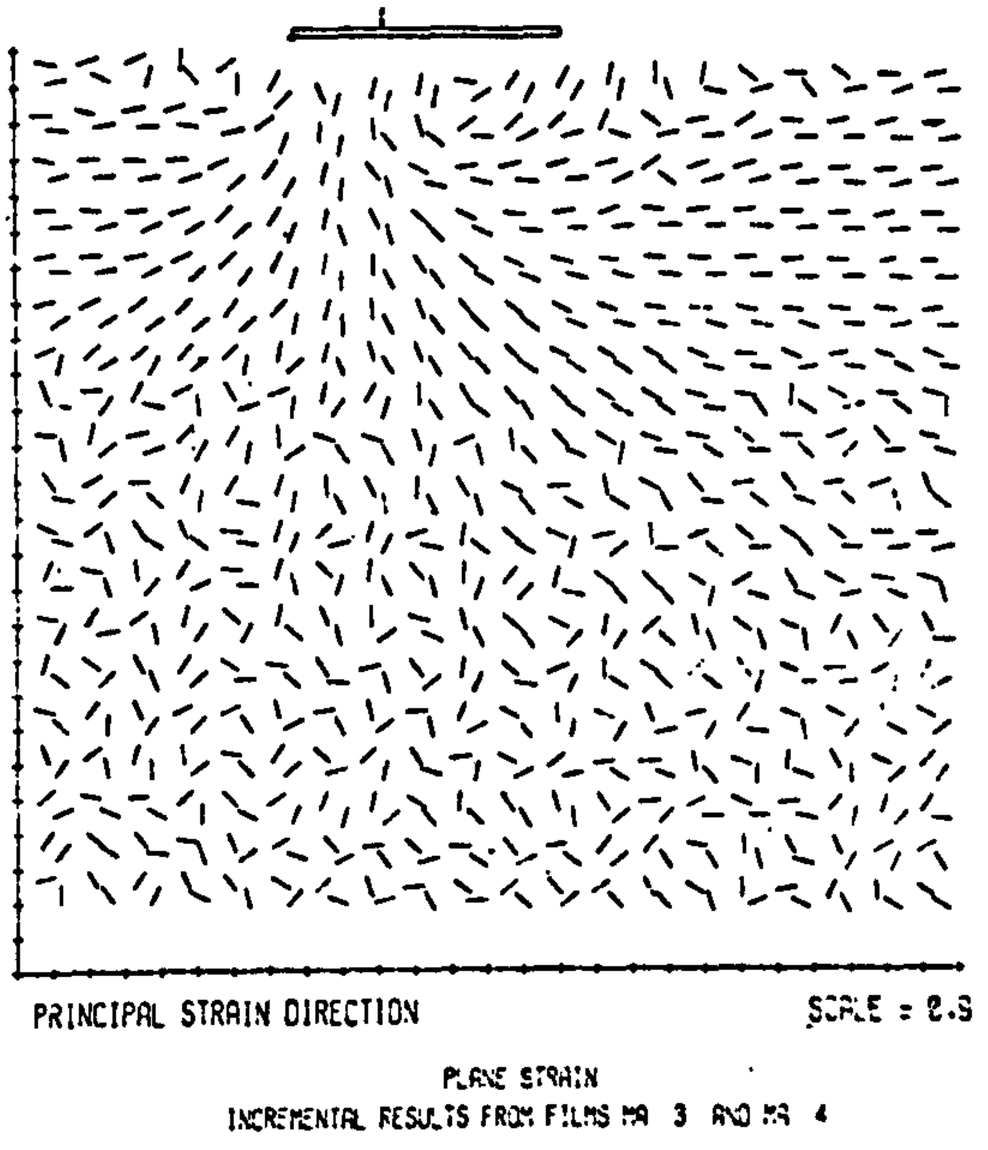

(d)

Fig. 7.11 The major principal compressive strain directions from test A(e_o=0.52,α_o=0,E_o=0.167) at stages (a) 0.72 and (b) 0.91 of the failure load.

The major principal compressive strain rate directions between stages (c) 0.72-0.91 and (d) 0.91-failure.

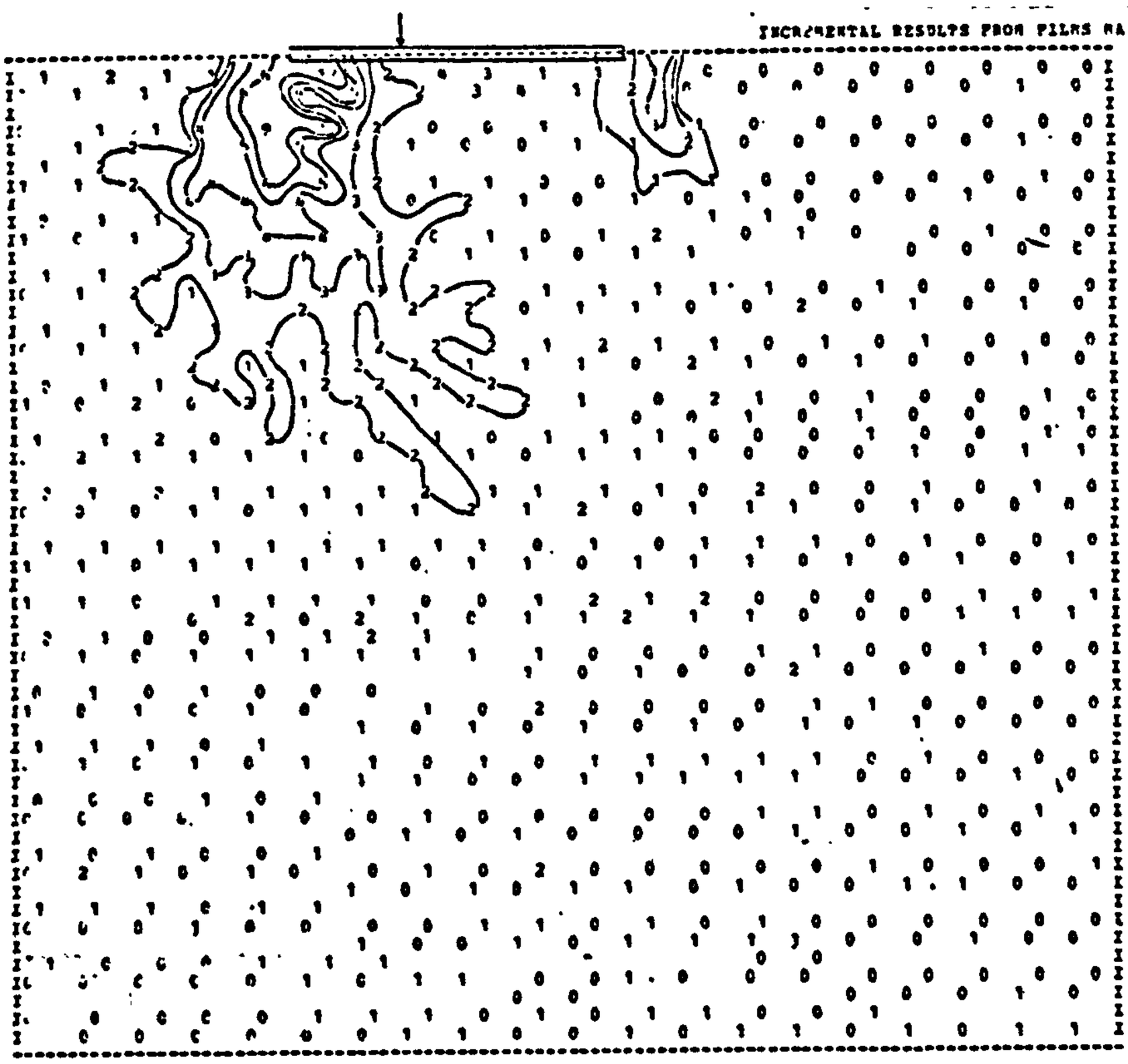

(a)

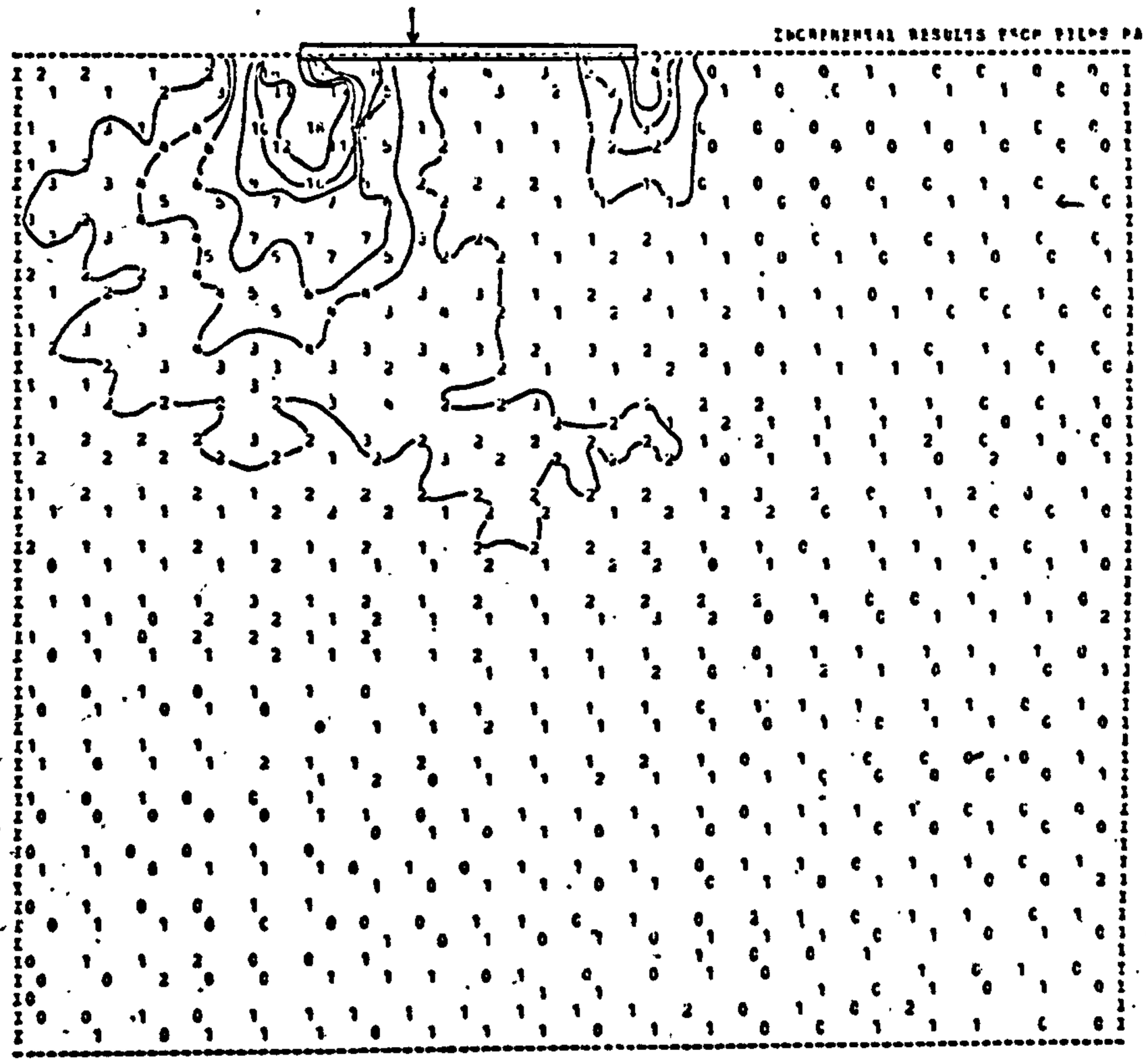

(b)

Fig. 7.12 The total maximum shear strain fields from test A(e_o=0.52, α_o=0, E_o=0.167) at stages (a) 0.72 and (b) 0.91 of the failure load.

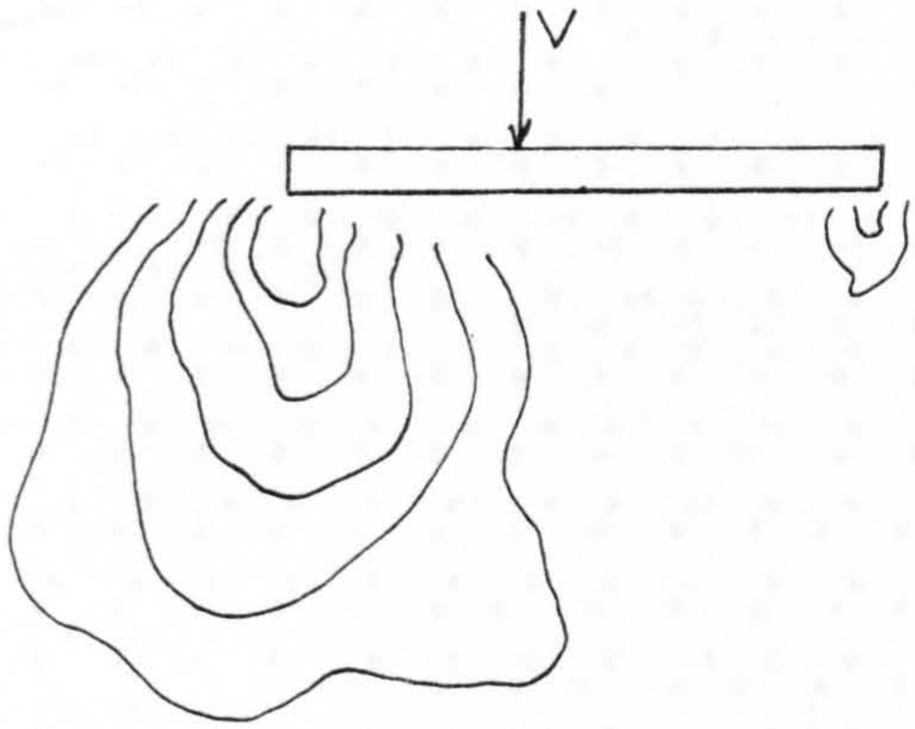

Fig. 7.12c The shear strain pattern from test A.

Fig. 7.13 Maximum shear stress contours in an elastic plate under a normal concentrated load (Frocht,1948).

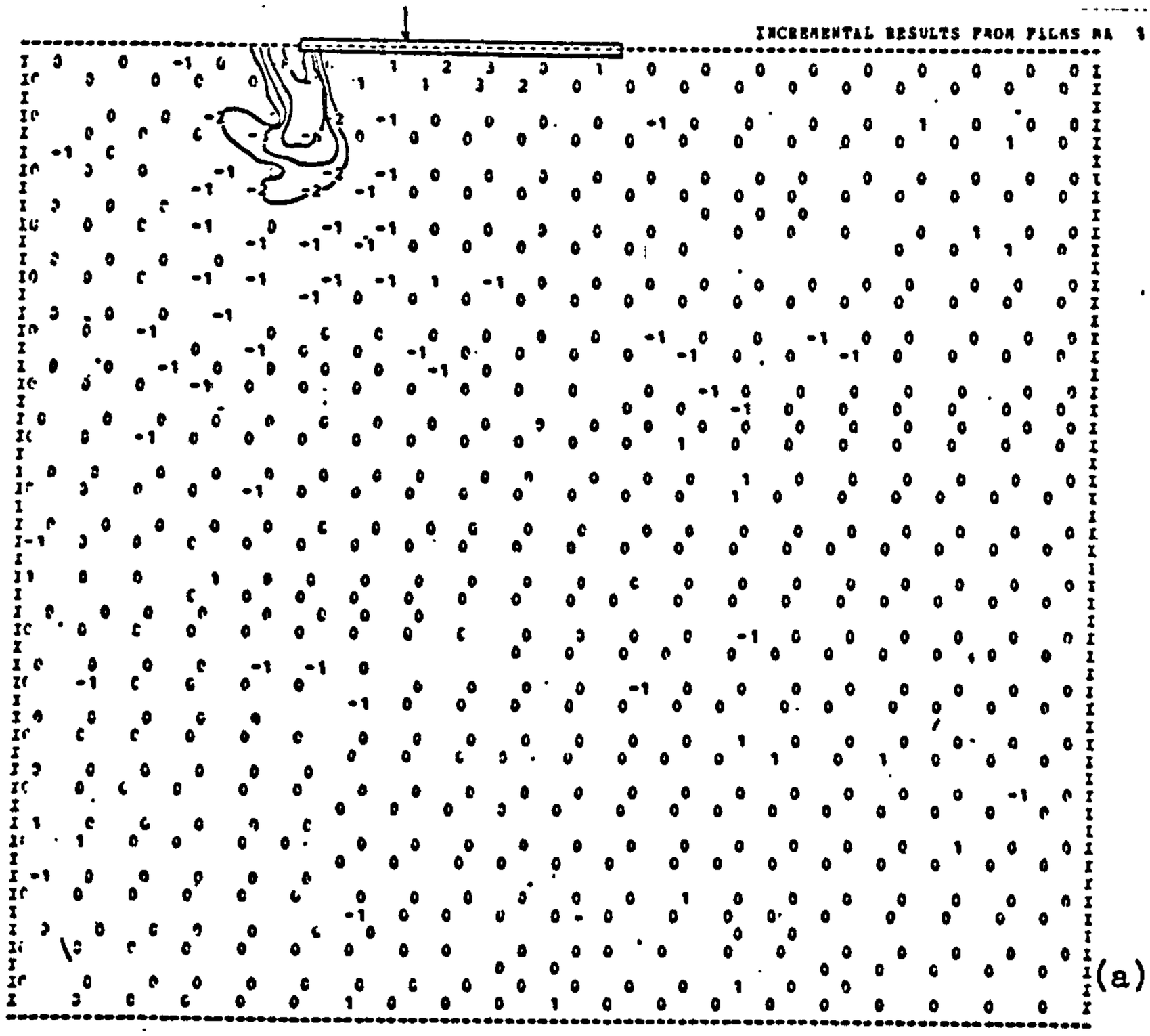

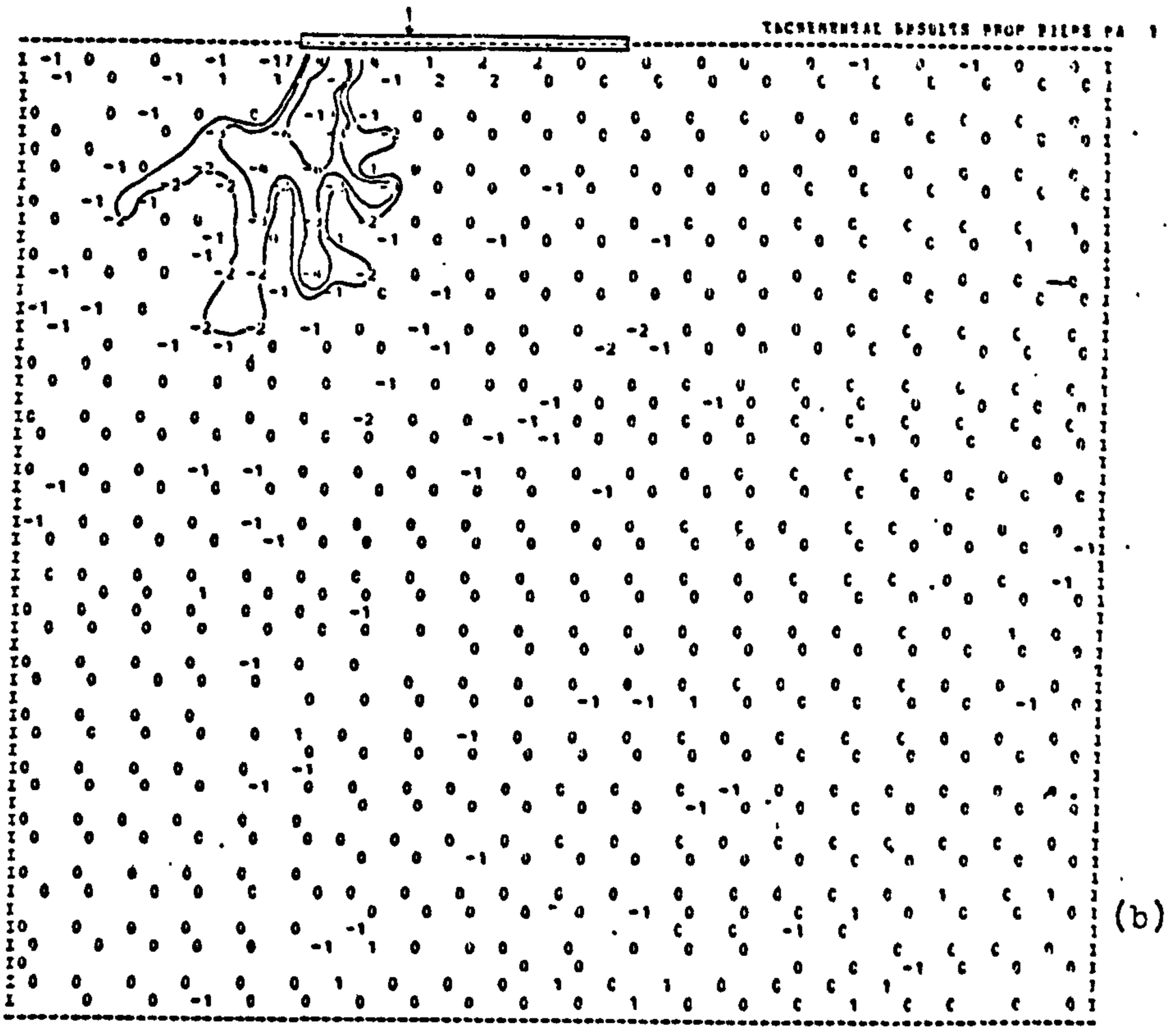

Fig. 7.14 Total volumetric strains from test A(e_o=0.52,α_o=0,E_o=0.167) at stages (a) 0.72 and (b) 0.91 of the failure load.

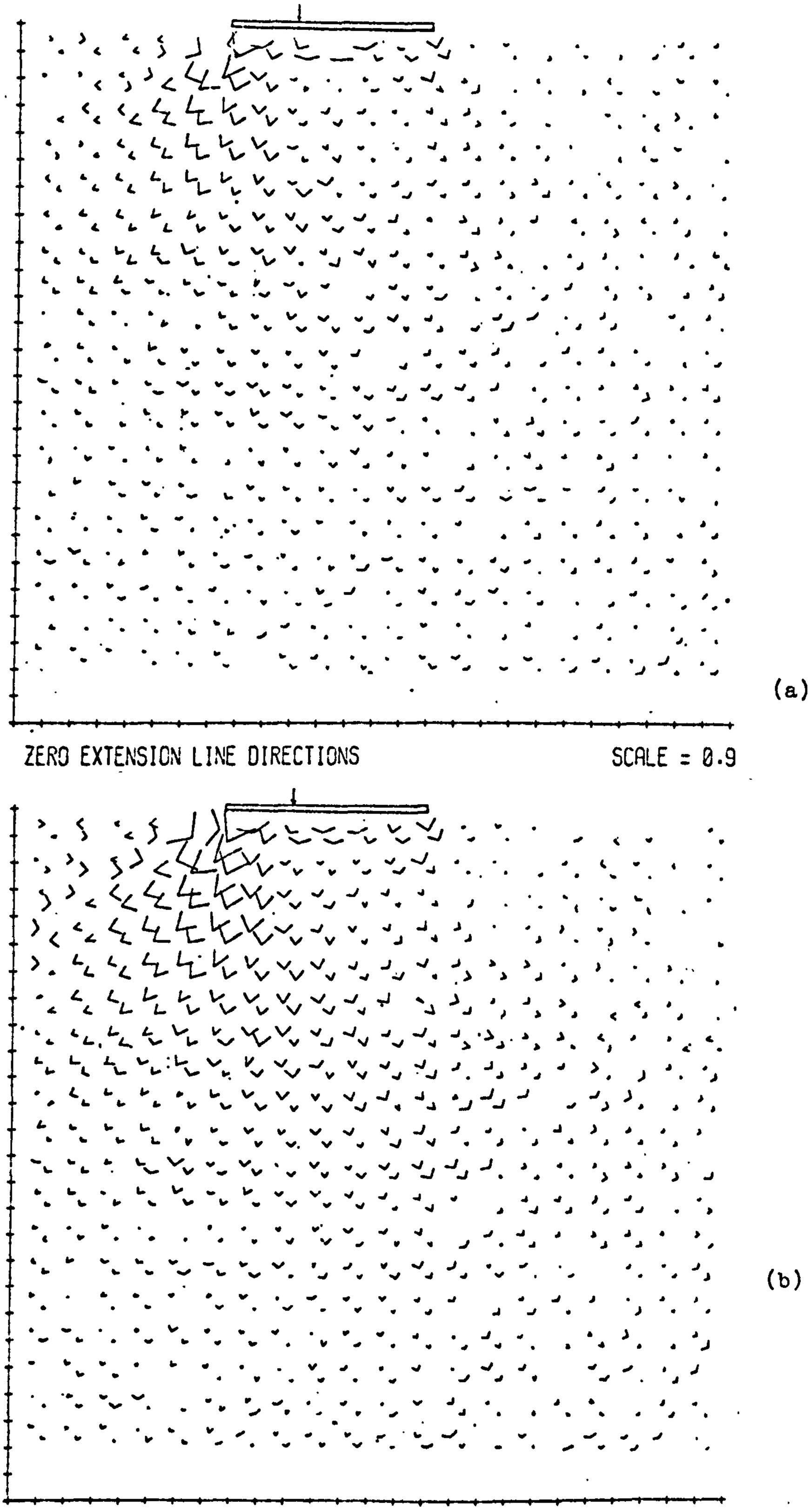

Fig. 7.15 The zero extension line direction from test A(e_o=0.52,α_o=0, E_o=0.167) at stages (a) 0.72 and (b) 0.91 of the failure load.

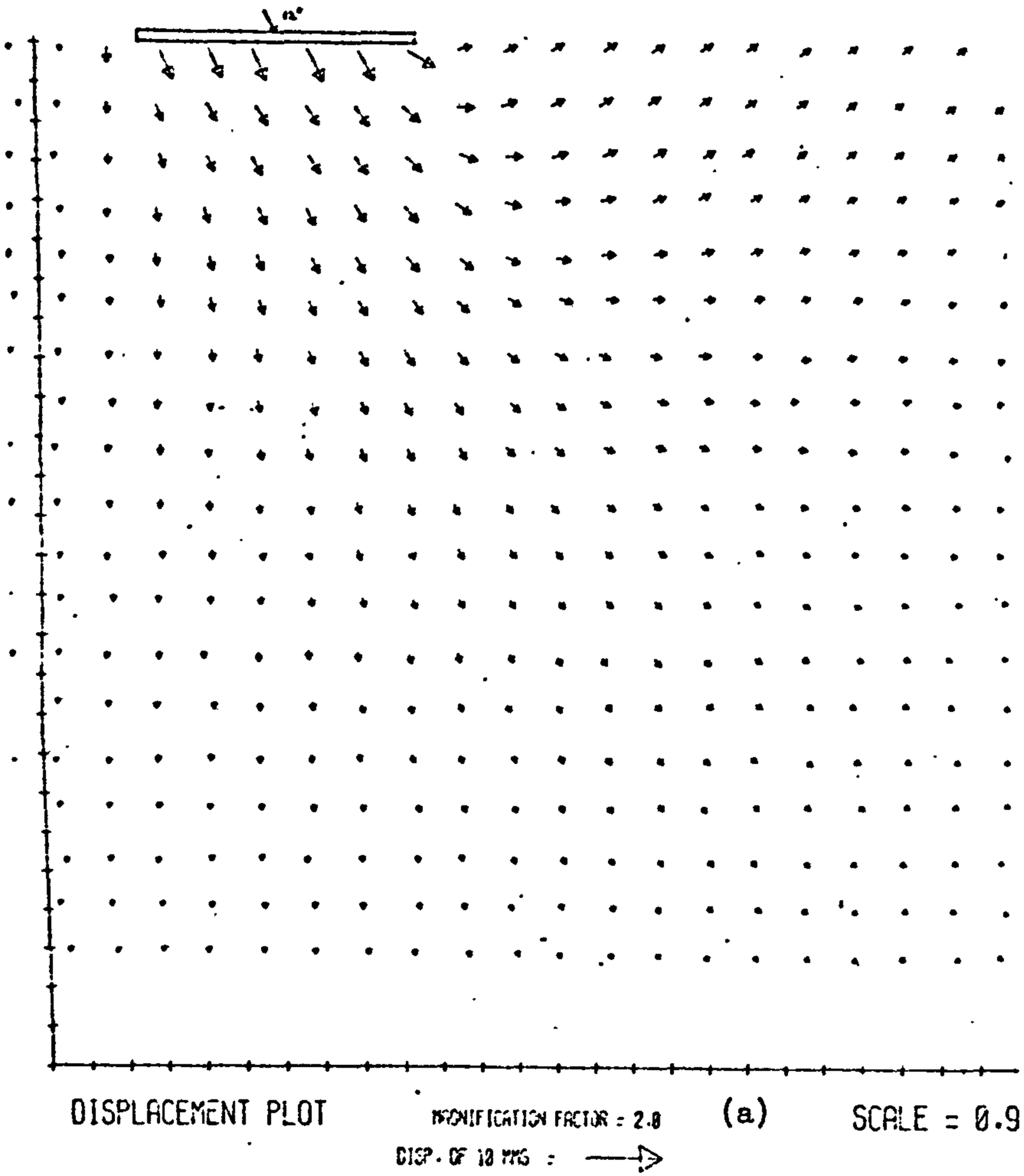

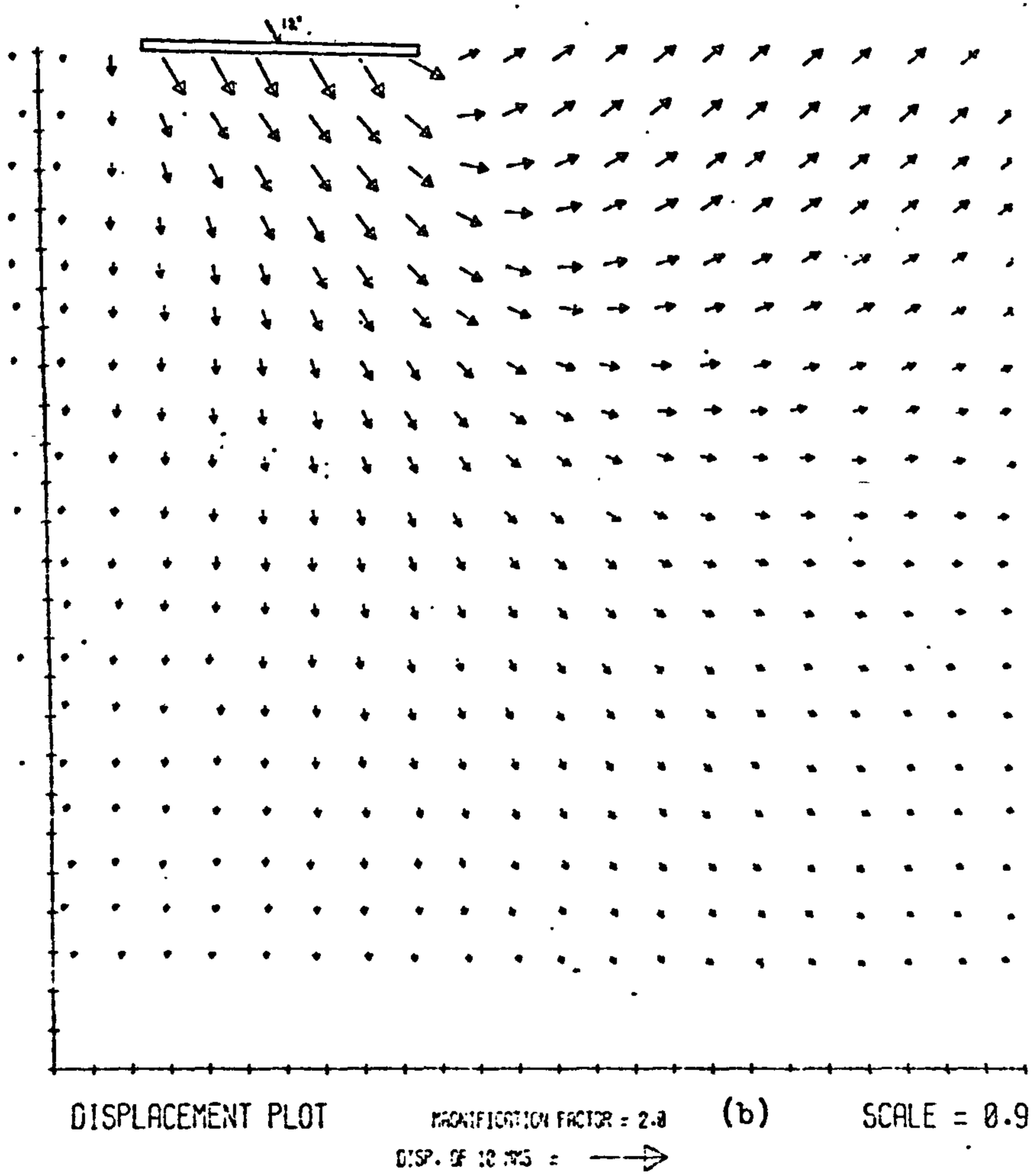

Fig. 7.16 Total displacement fields from test B(e_o=0.52,α_o=12°,E_o=0) at stages (a) 0.70 and (b) 0.86 of the failure load.

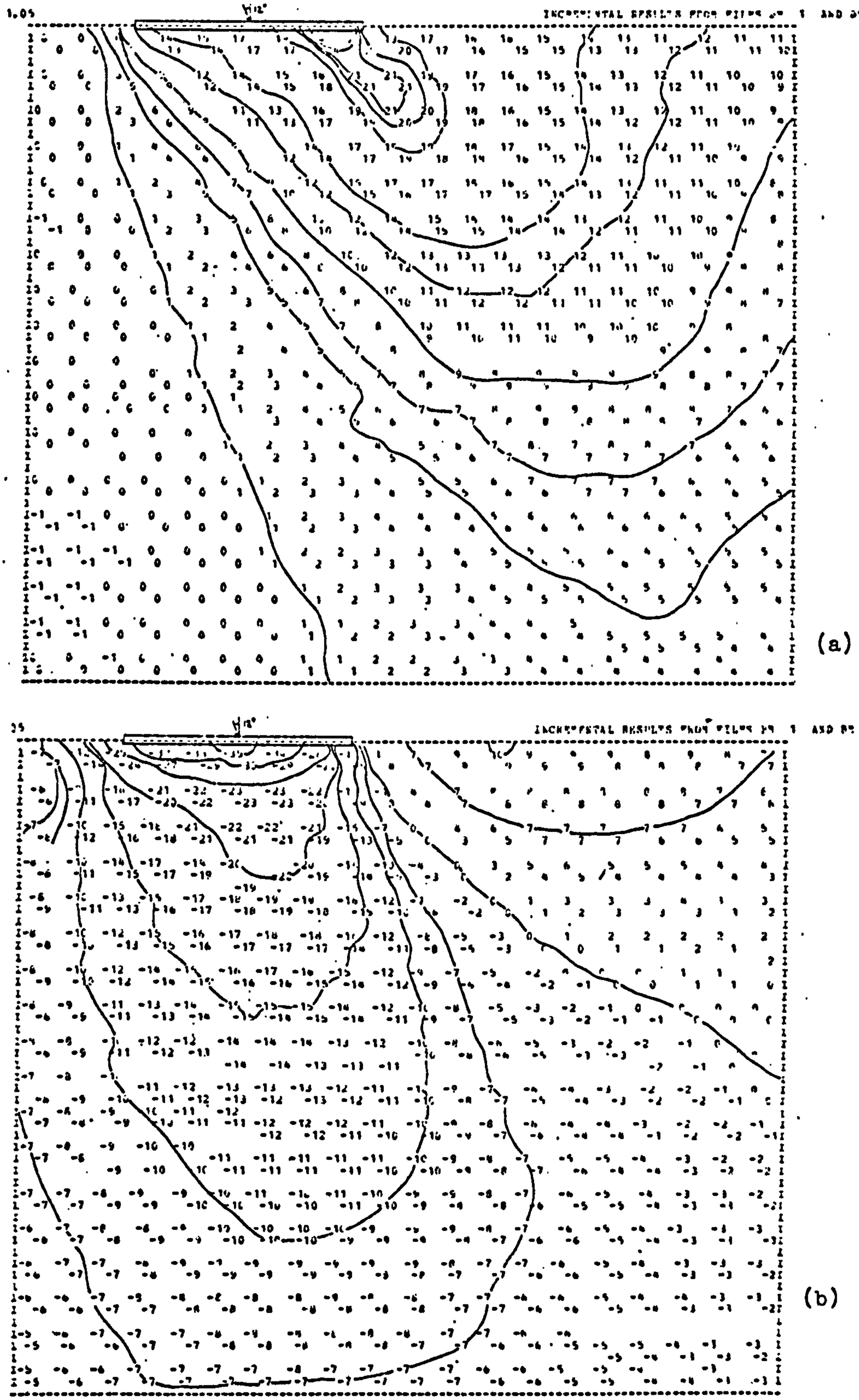

Fig. 7.17 Total displacement fields (units in 0.1mm) from test B(e_o=0.52, α_o=12°, E_o=0) at stage 0.70 of the failure load
(a) Horizontal (b) Vertical displacements

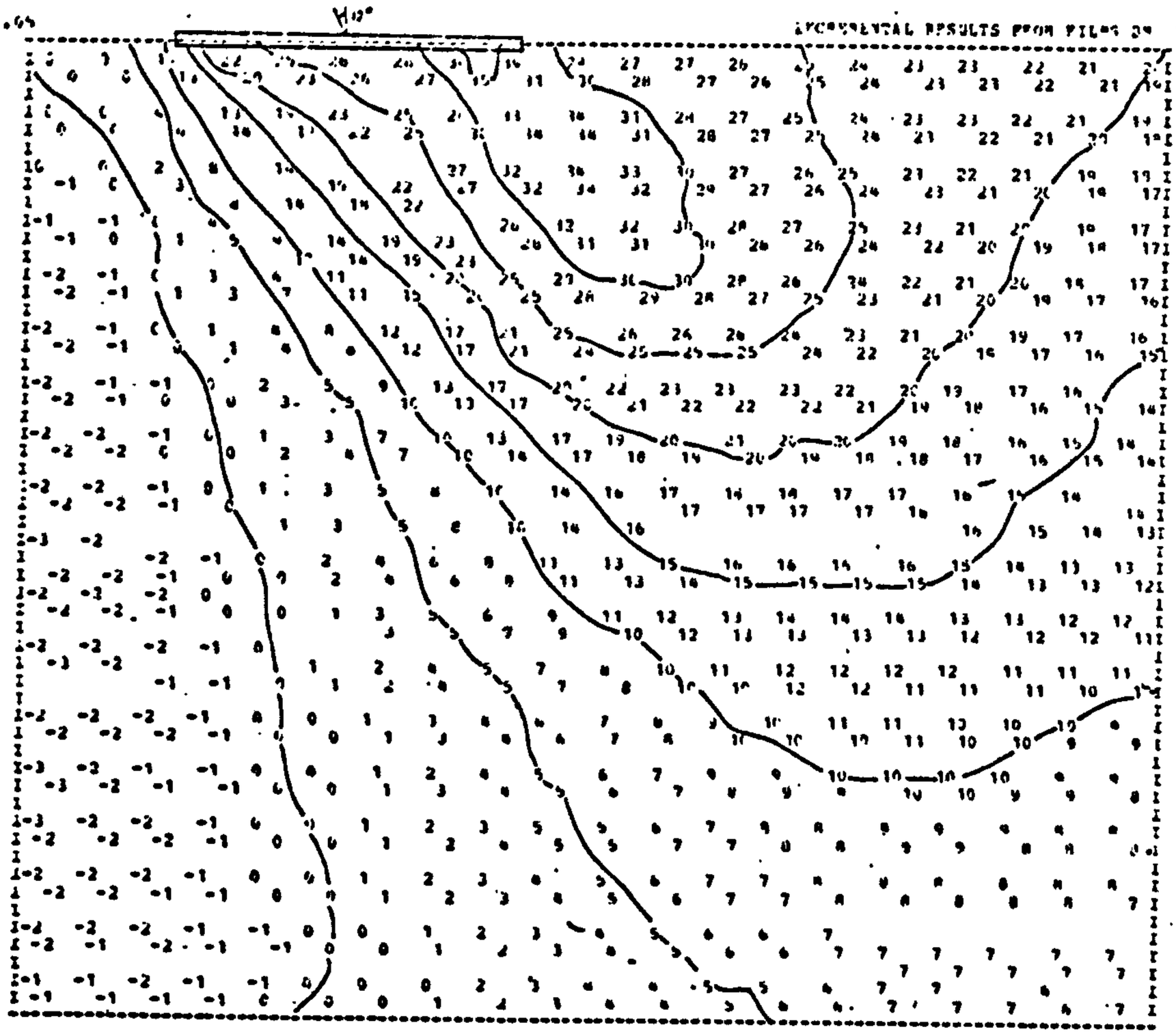

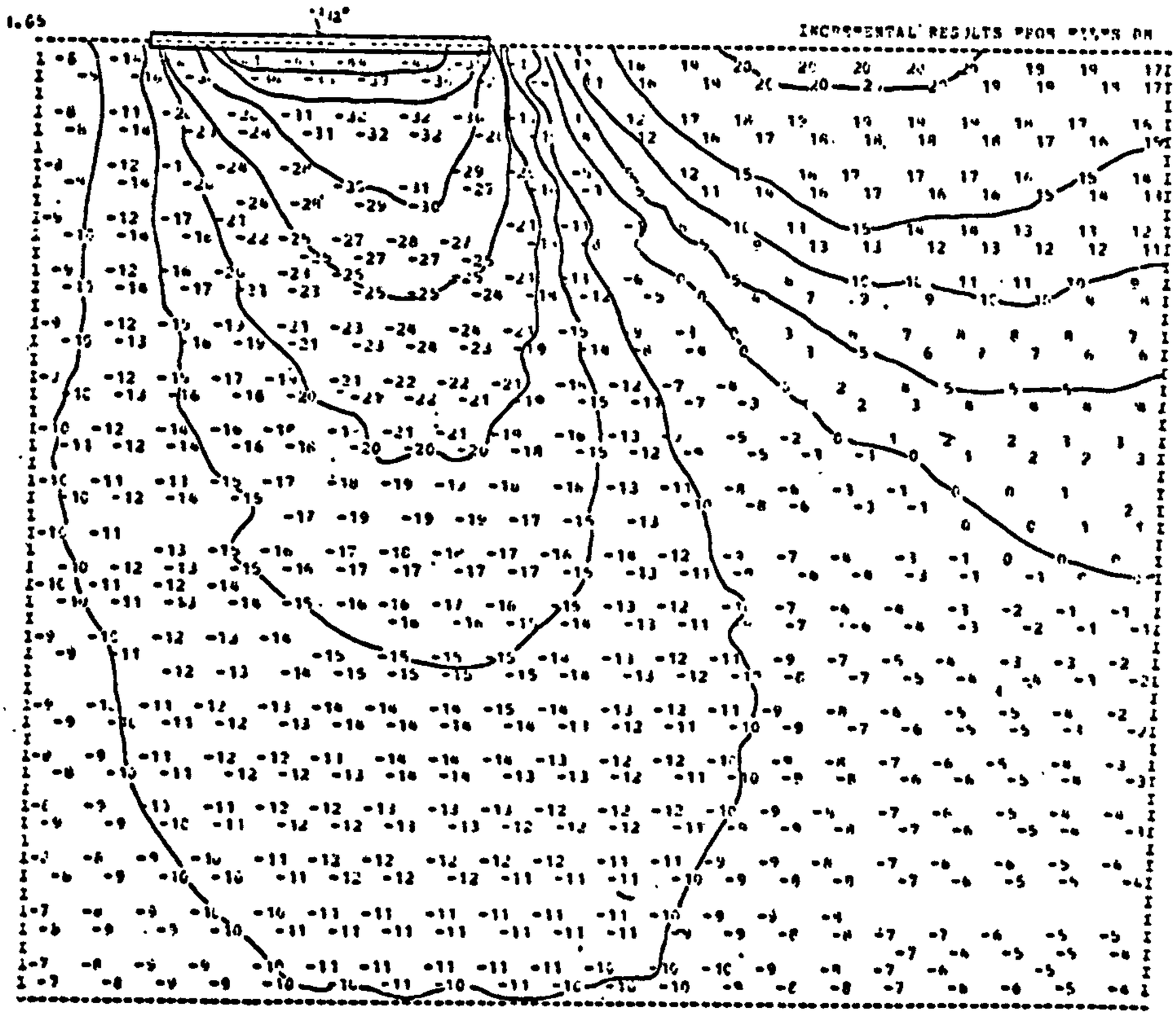

Fig. 7.17 Total displacement fields (units in 0.1mm) from test B(e_o=0.52,α_o=12°,E_o=0) at stage 0.86 of the failure load
(c) Horizontal (d) Vertical.

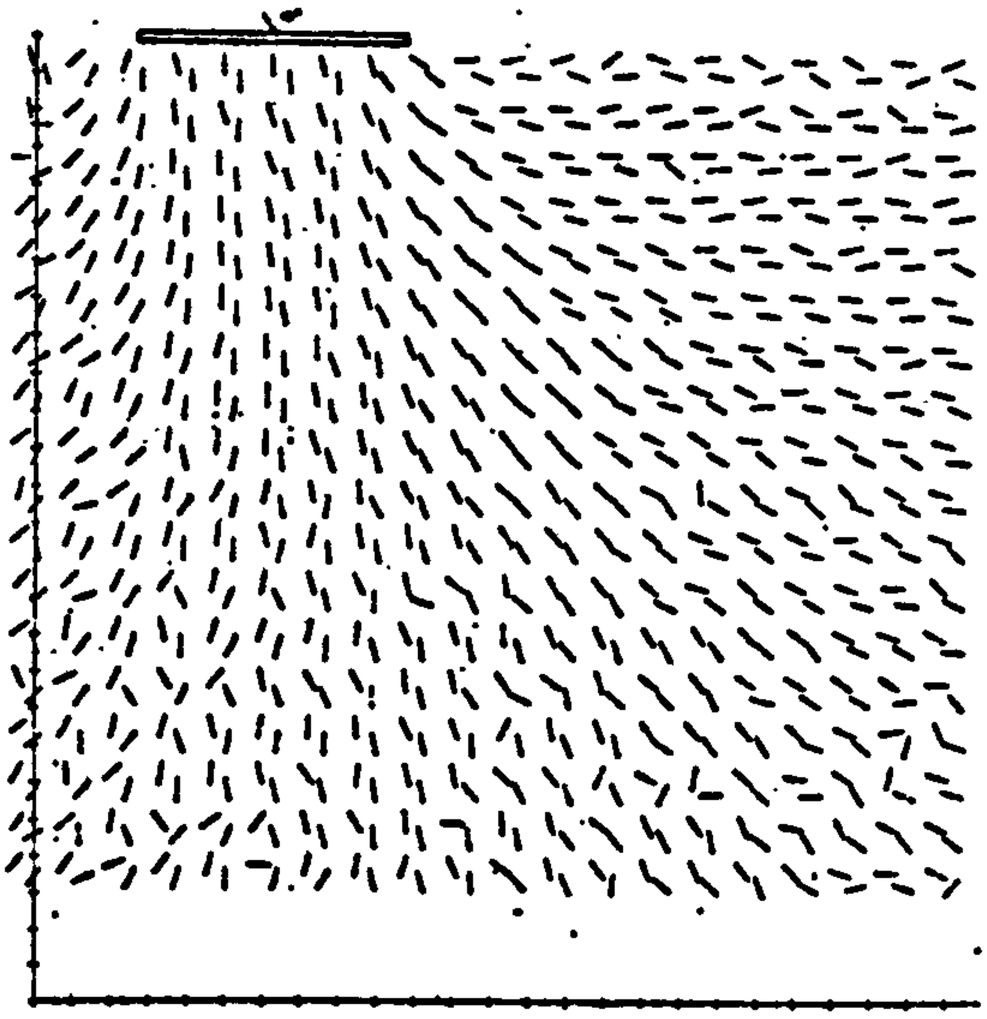

PLANE STRAIN
INCREMENTAL RESULTS FROM FILMS BM 1 AND BM 3

(a)

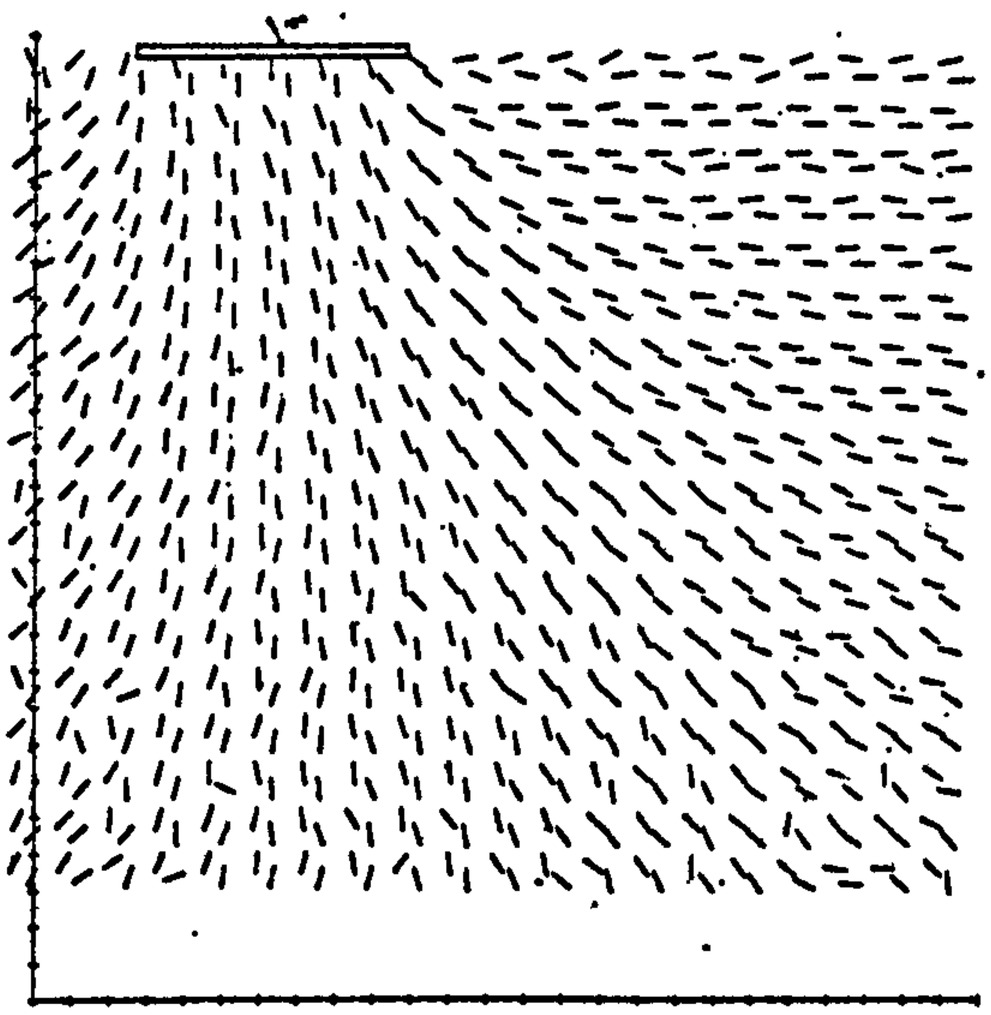

PLANE STRAIN
INCREMENTAL RESULTS FROM FILMS BM 1 AND BM 4

(b)

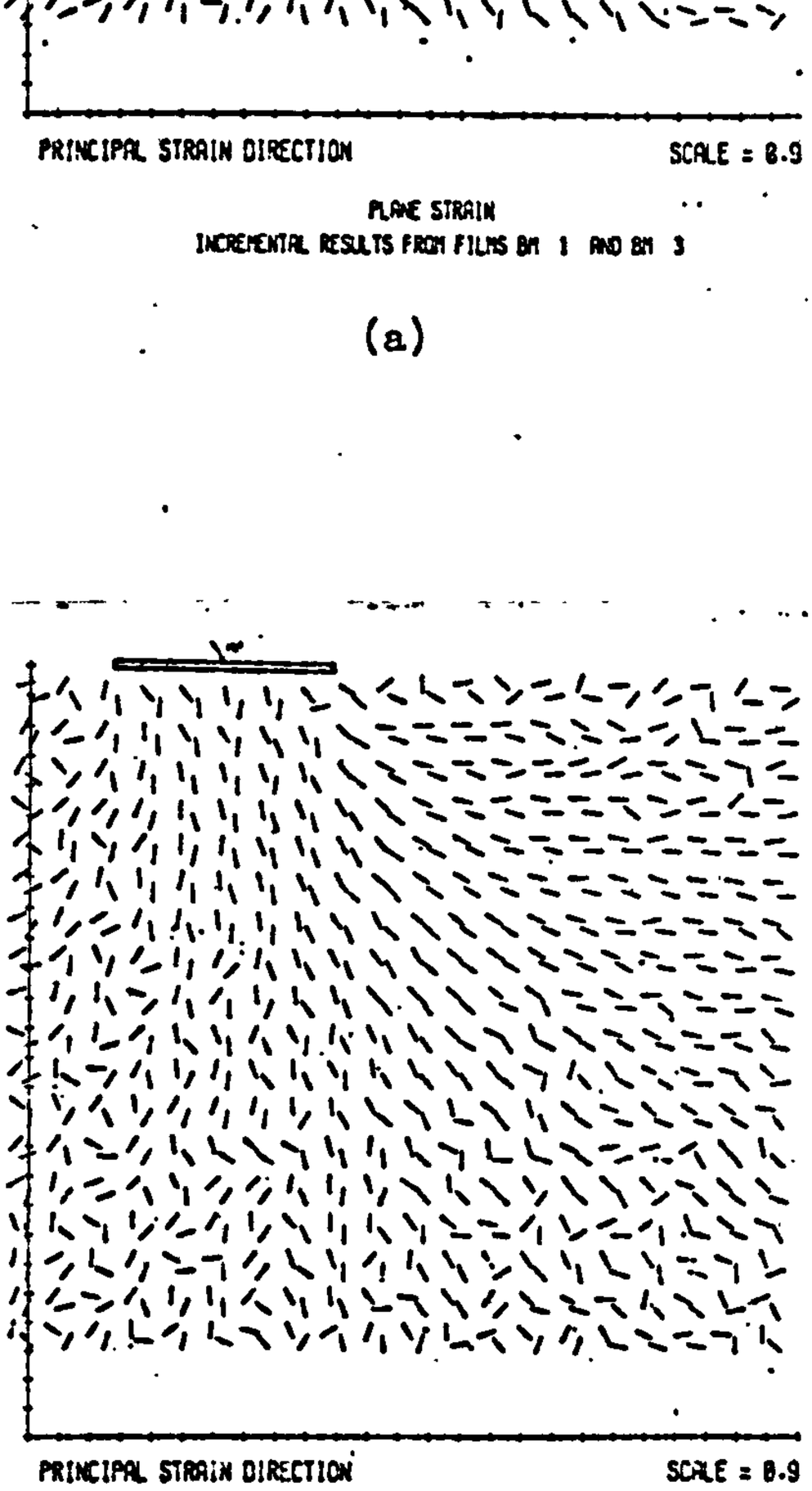

PLANE STRAIN
INCREMENTAL RESULTS FROM FILMS BM 3 AND BM 4

(c)

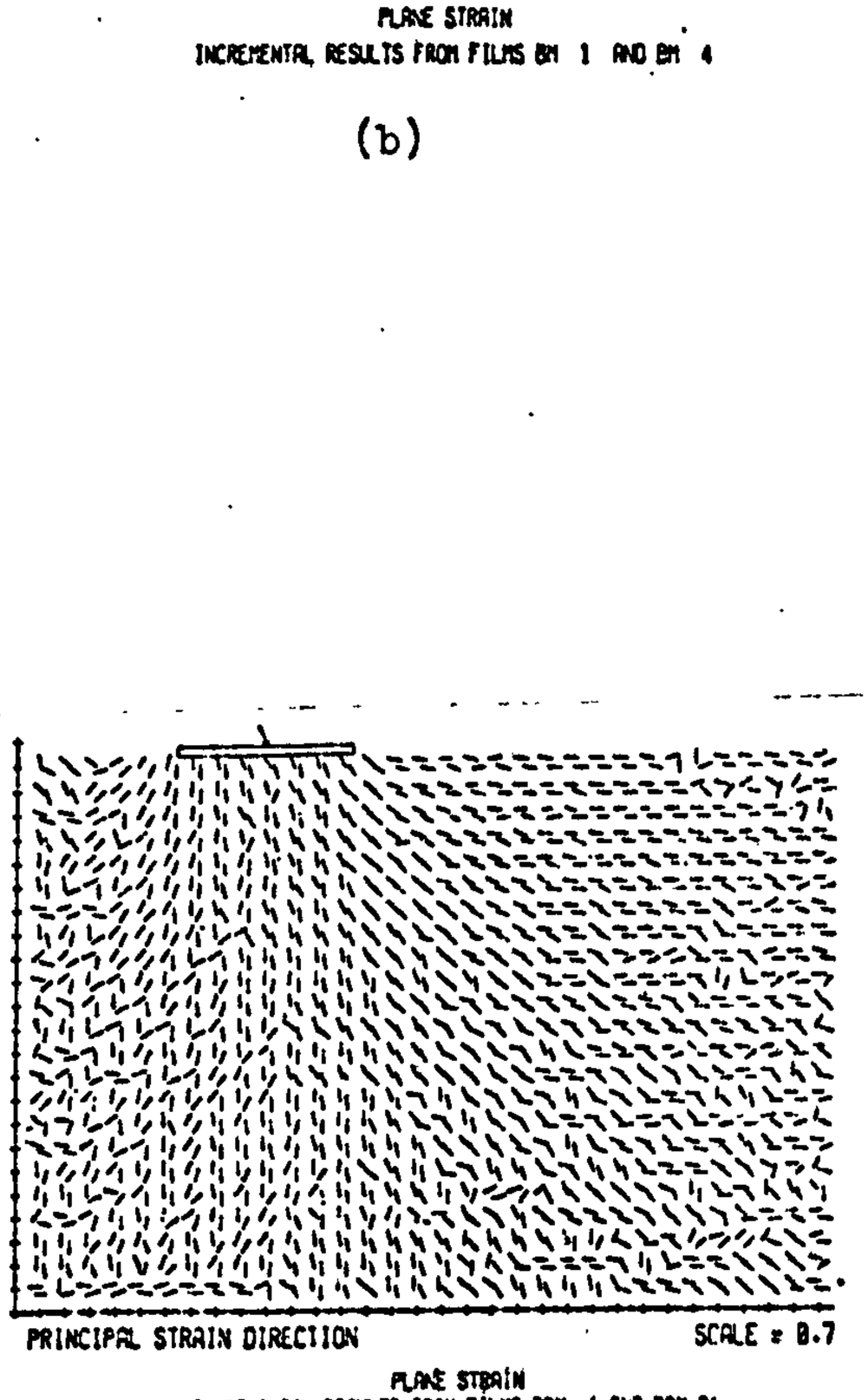

PLANE STRAIN
INCREMENTAL RESULTS FROM FILMS BPM 1 AND BPM 31

(d)

Fig. 7.18 The major principal compressive strain directions from test B(e_o=0.52,α_o=12°,E_o=0) at stages (a) 0.70 and (b) 0.86 of the failure load.
The major principal compressive strain rate directions between stages (c) 0.70-0.86 and (d) 0.0-0.53 of the failure load.

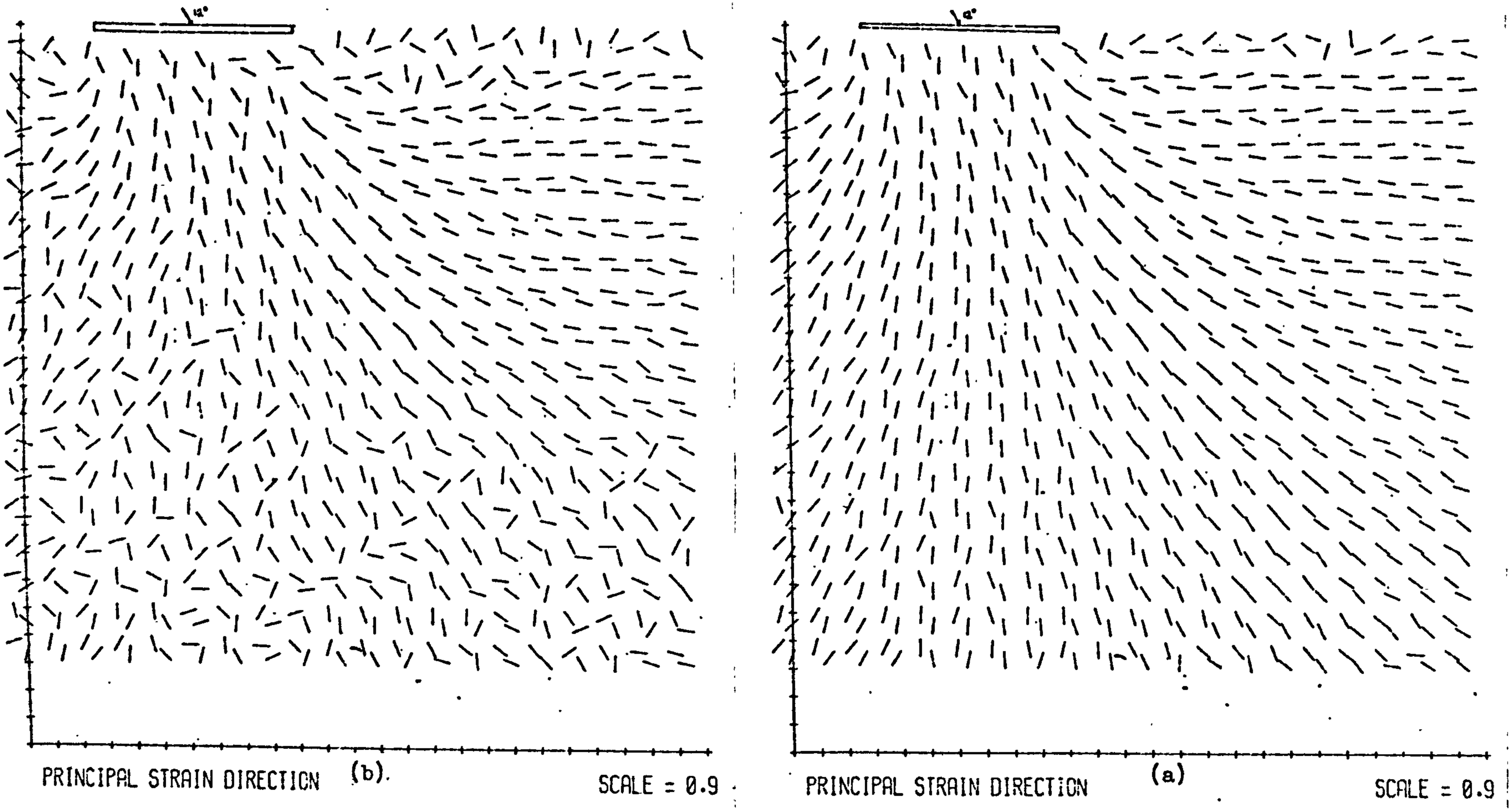

Fig. 7.19 The major principal compressive strain directions from test B(e_o=0.52,α_o=12°,E_o=0) between stages (a) 0.86-failure and (b) 0.0-failure.

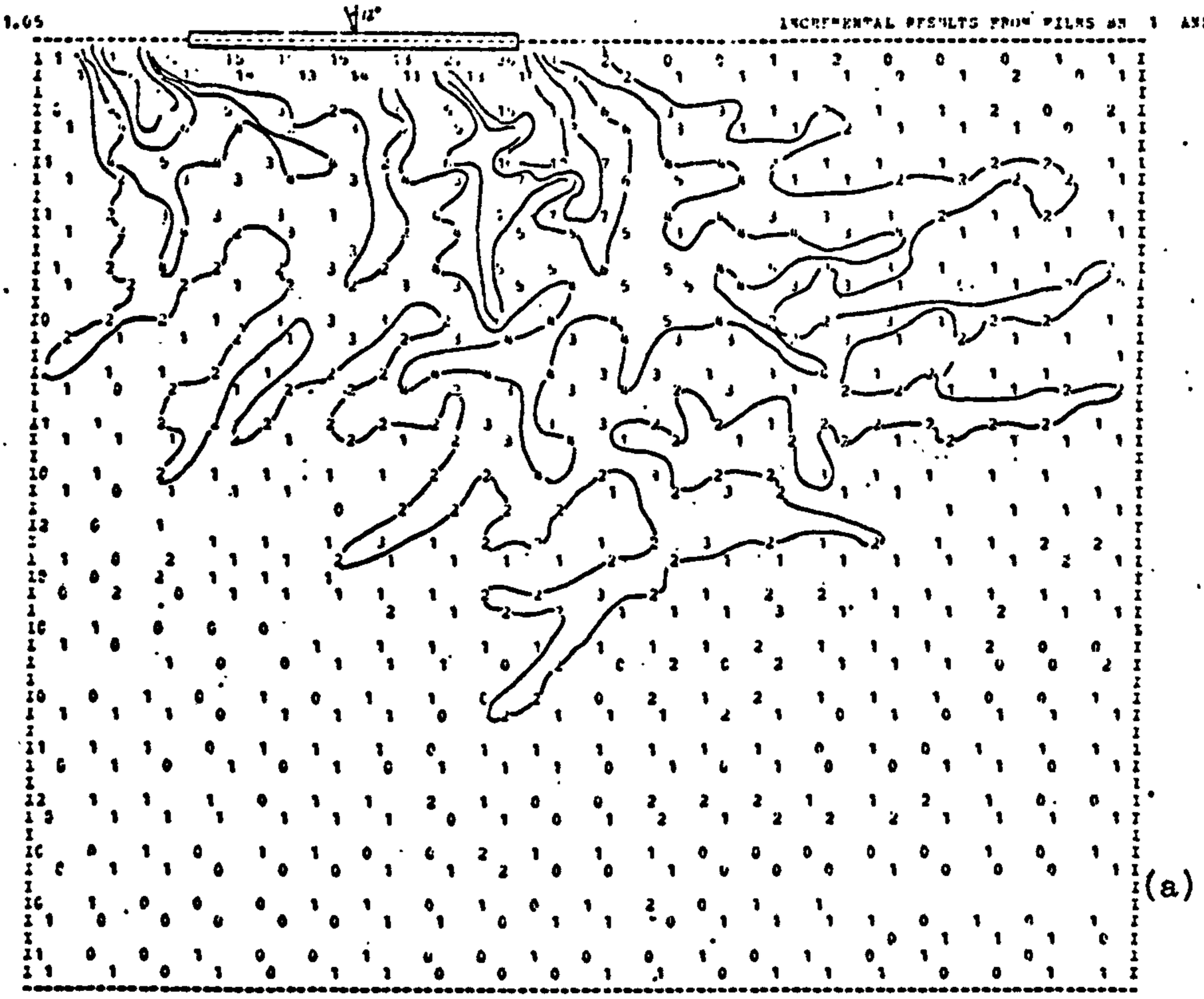

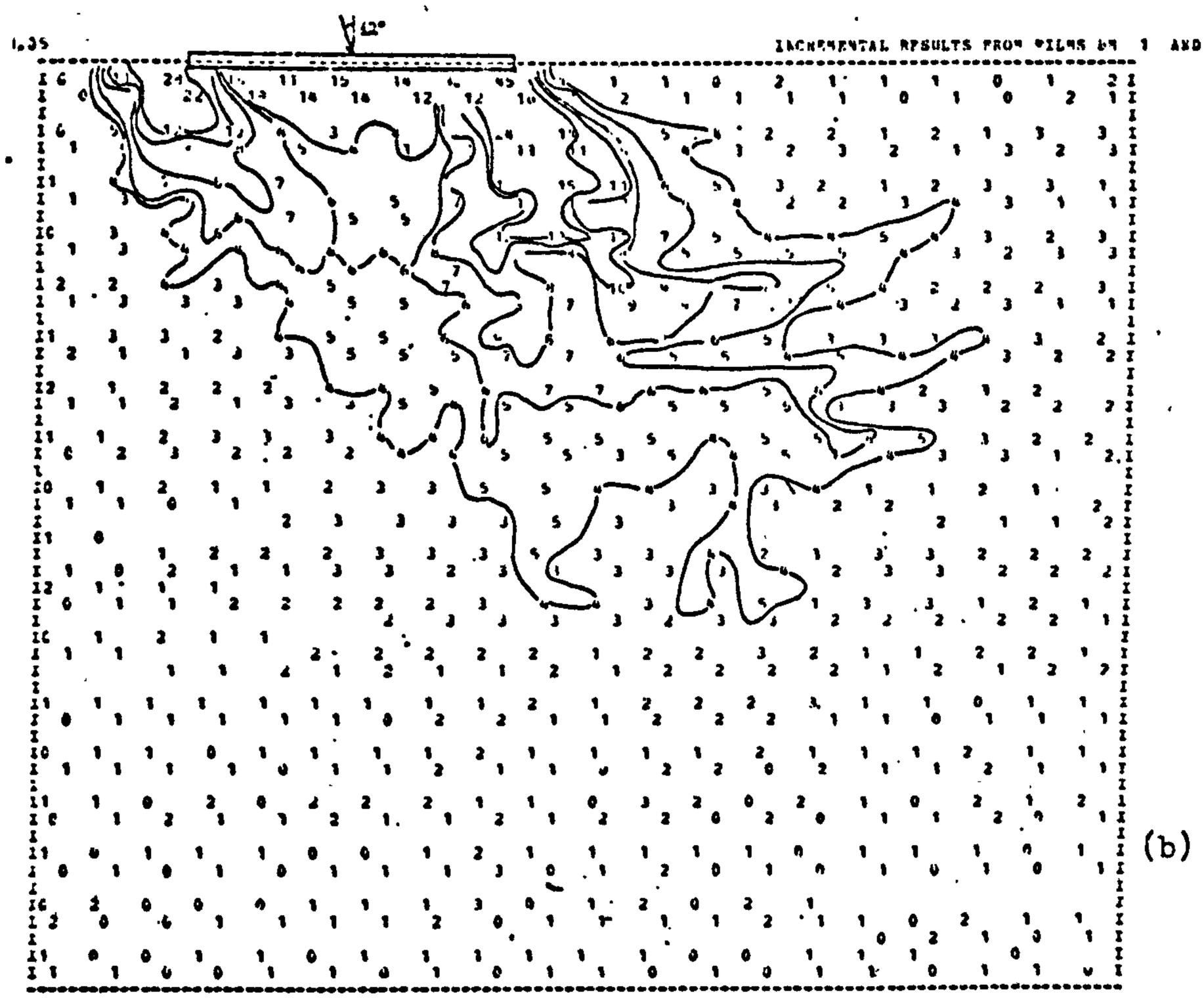

Fig. 7.20 The total maximum shear strain fields from test B(e_o=0.52, α_o=12°, E_o=0) at stages (a) 0.70 and (b) 0.86 of the failure load.

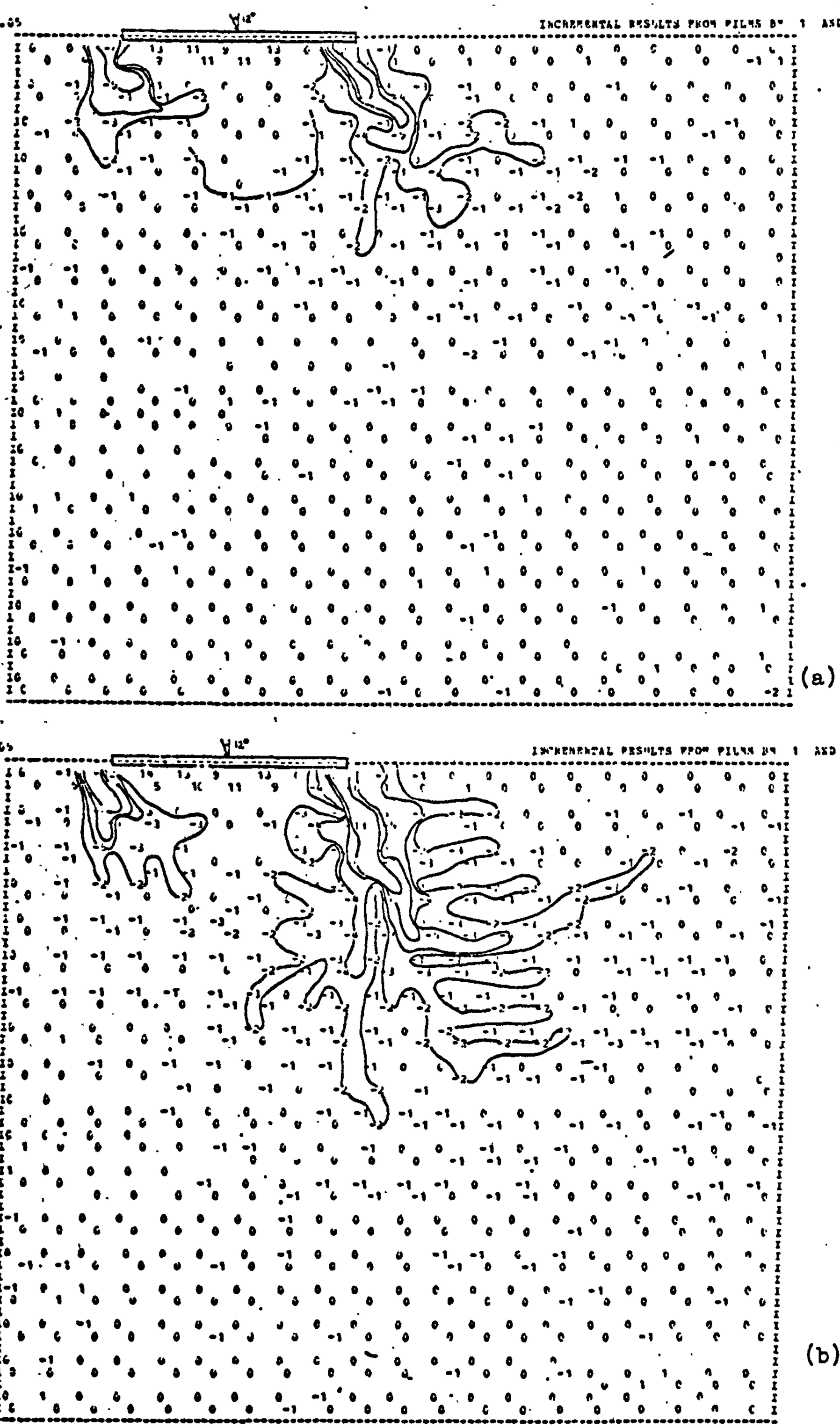

Fig. 7.21 The volumetric strains from test B(e_o=0.52, α_o=12°, E_o=0) at stages (a) 0.70 and (b) 0.86 of the failure load.

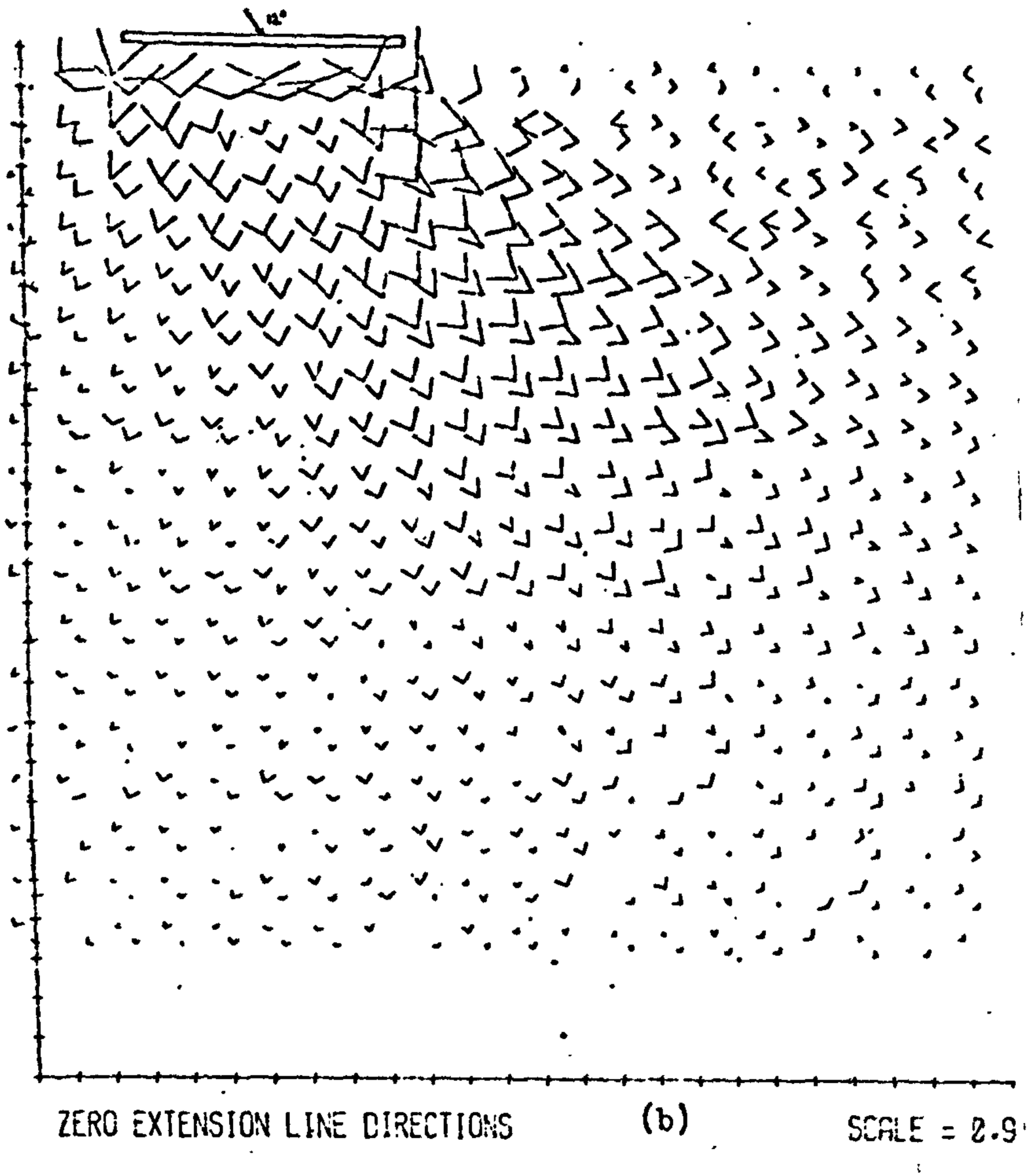

Fig. 7.22 The zero extension line directions from test B(e_o=0.52,α_o=12°,E_o=0) at stages (a) 0.70 and (b) 0.86 of the failure load.

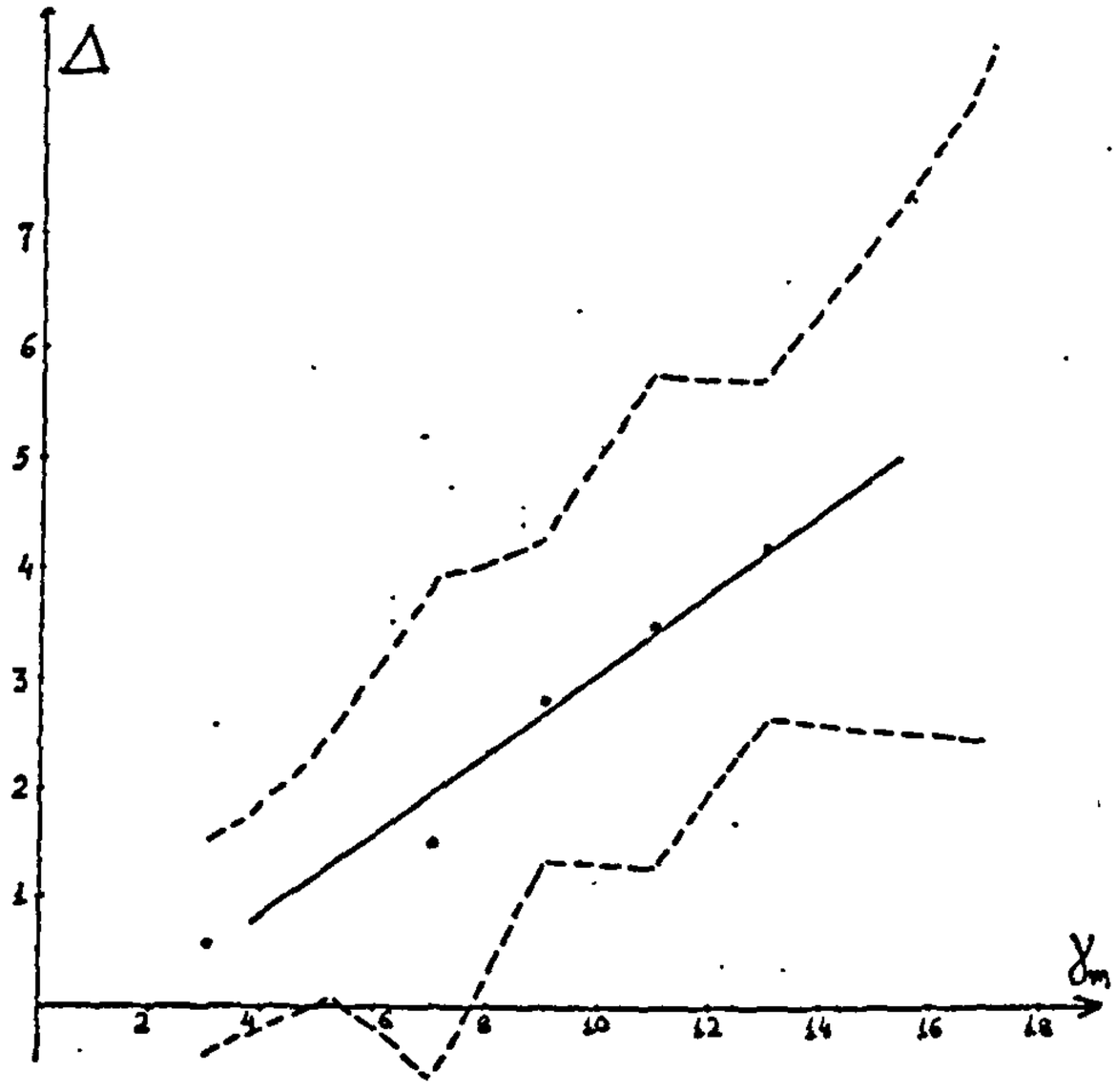

(a)

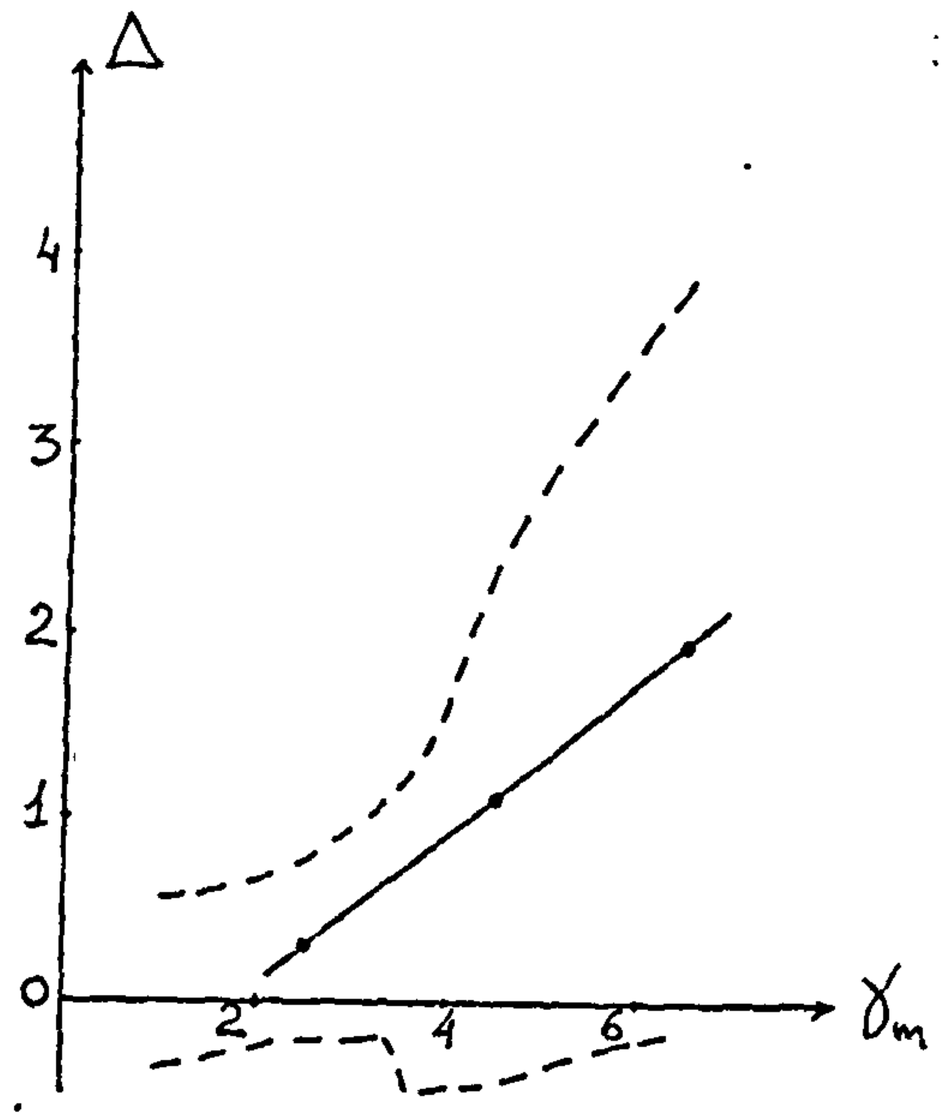

(b)

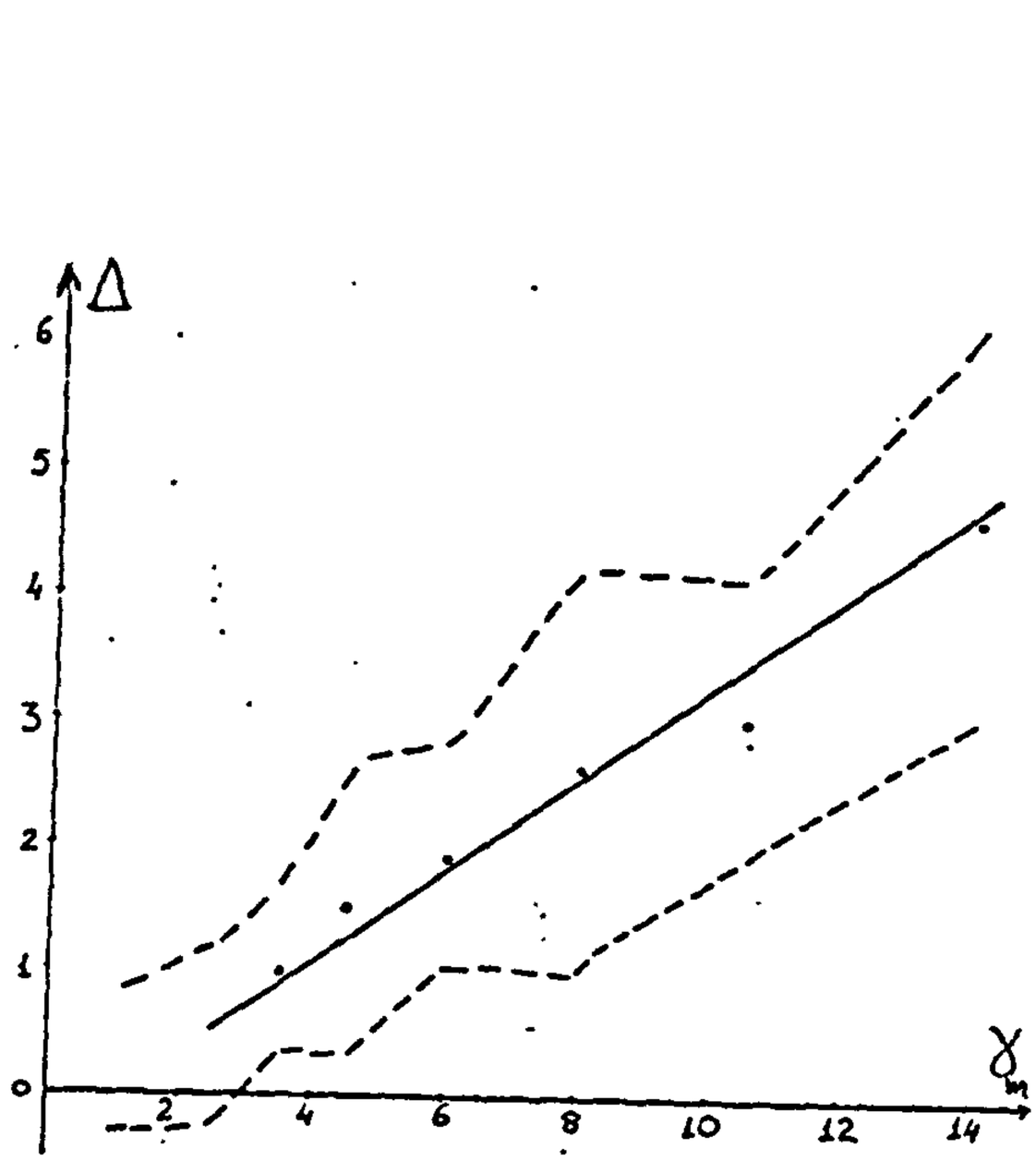

(c)

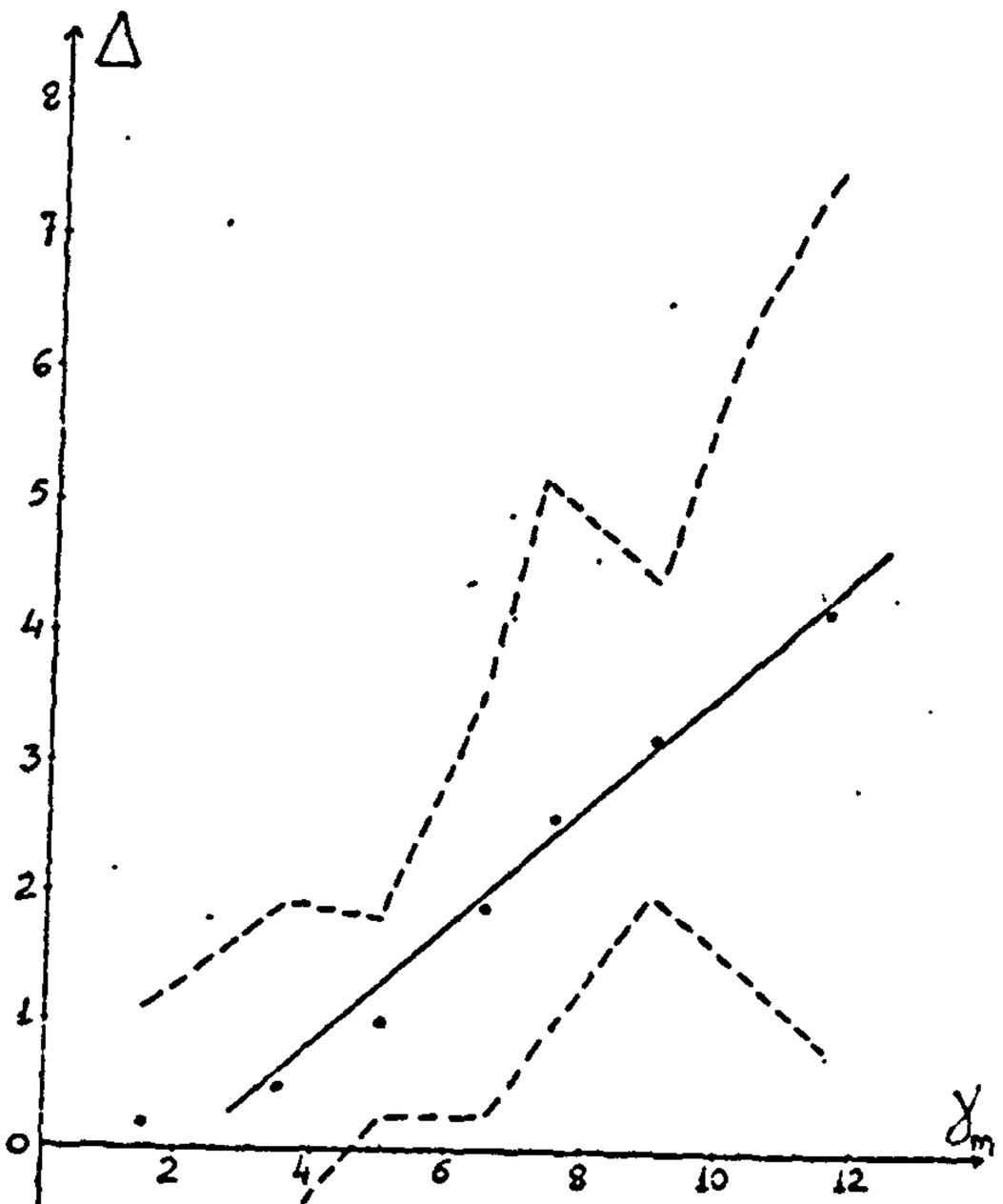

(d)

Fig. 7.23 The average volumetric-maximum shear strain relationships and the standard deviations of the volumetric strains from tests: (a) D(e_o=0.52,α_o=0,E_o=0) (b) A(e_o=0.52,α_o=0,E_o=0.167) (c) B(e_o=0.52,α_o=12°,E_o=0) and (d) C(e_o=0.52,α_o=12°,E_o=-0.167).

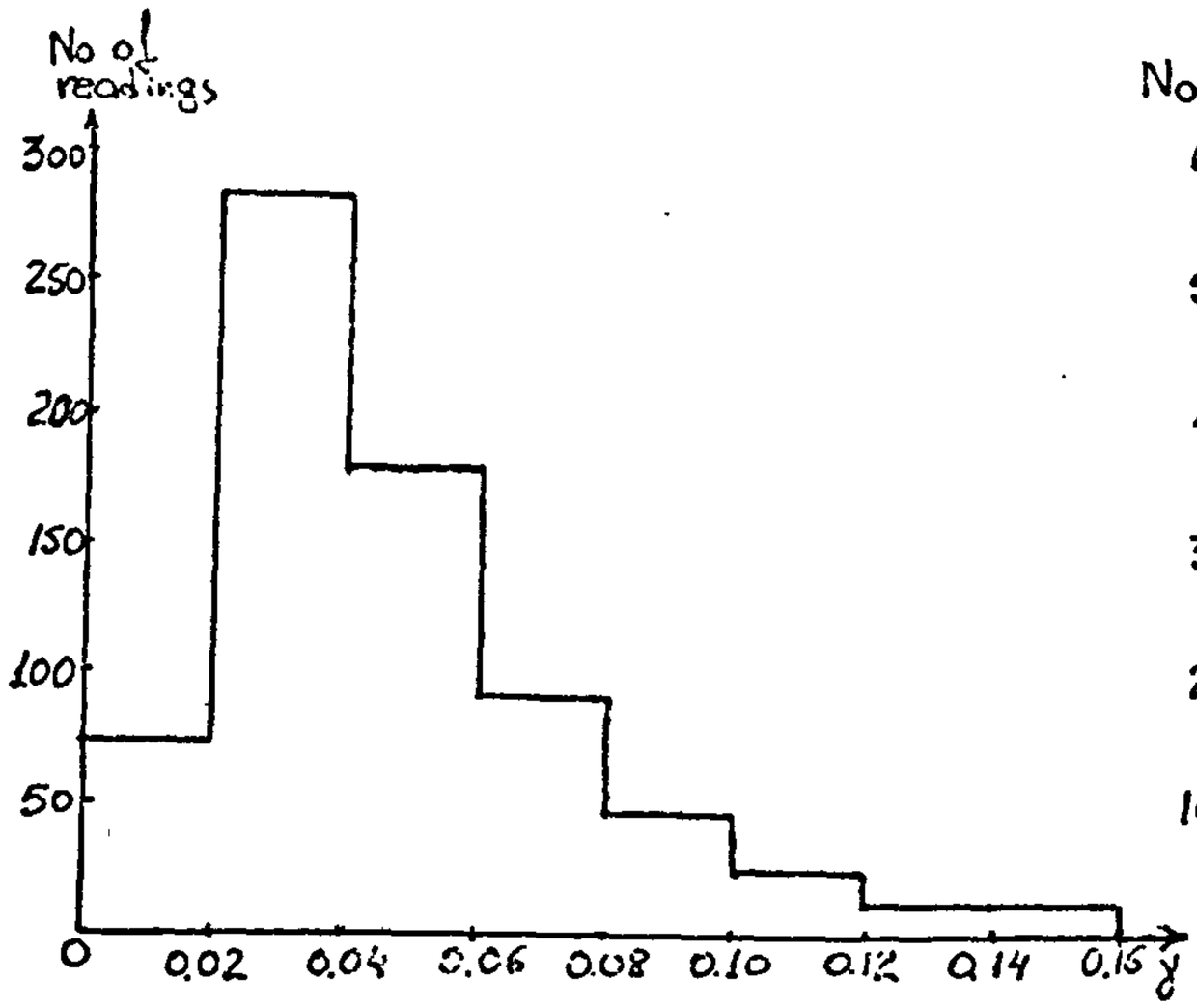

(a)

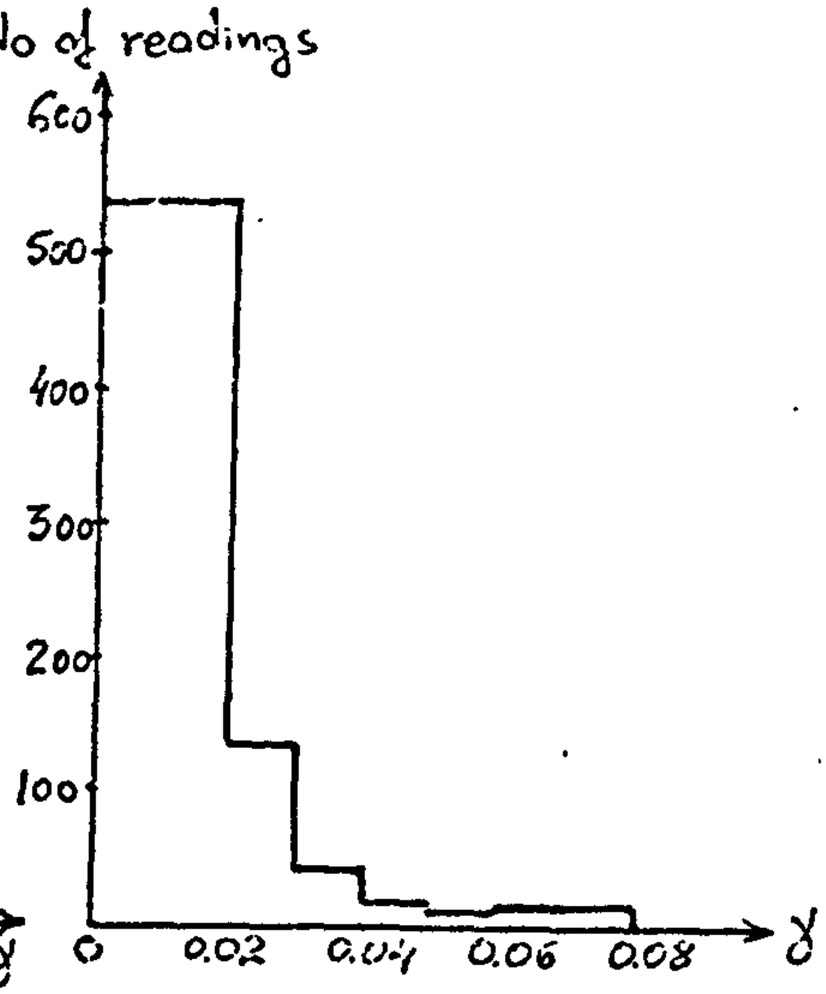

(b)

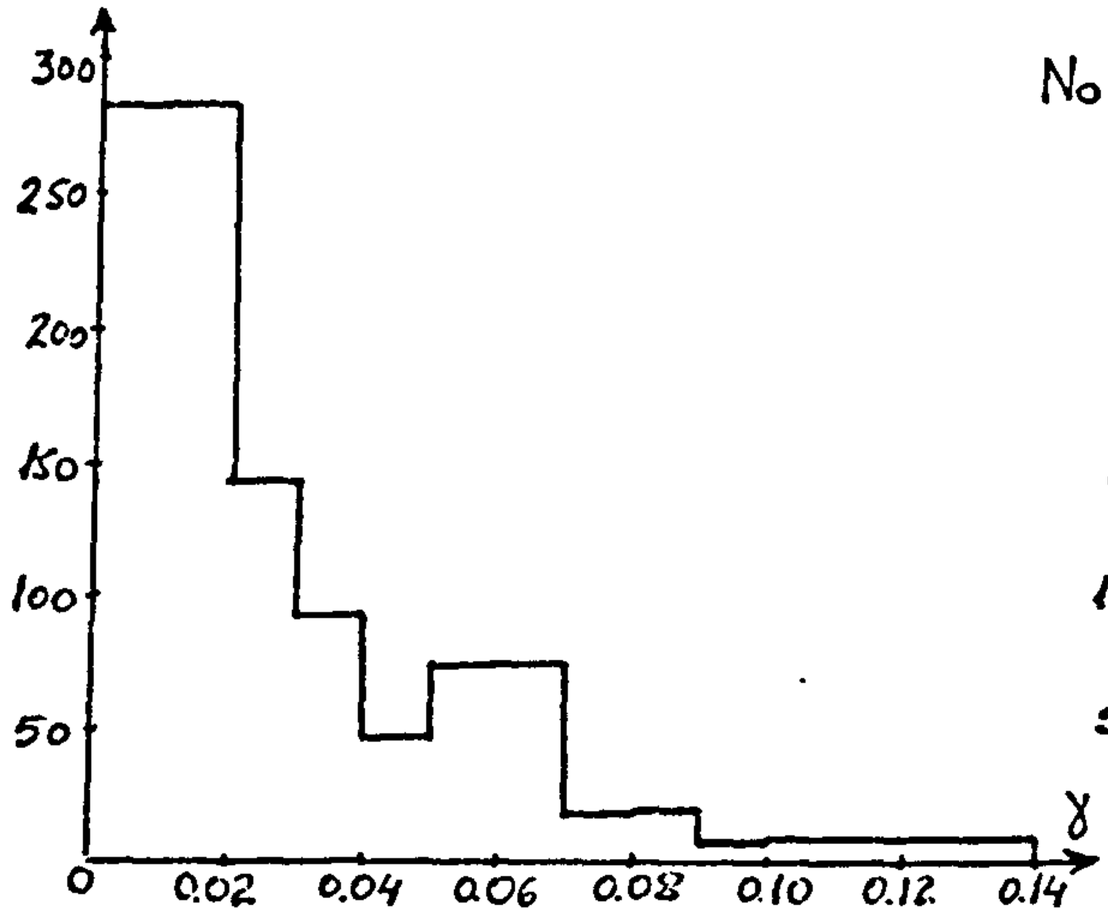

(c)

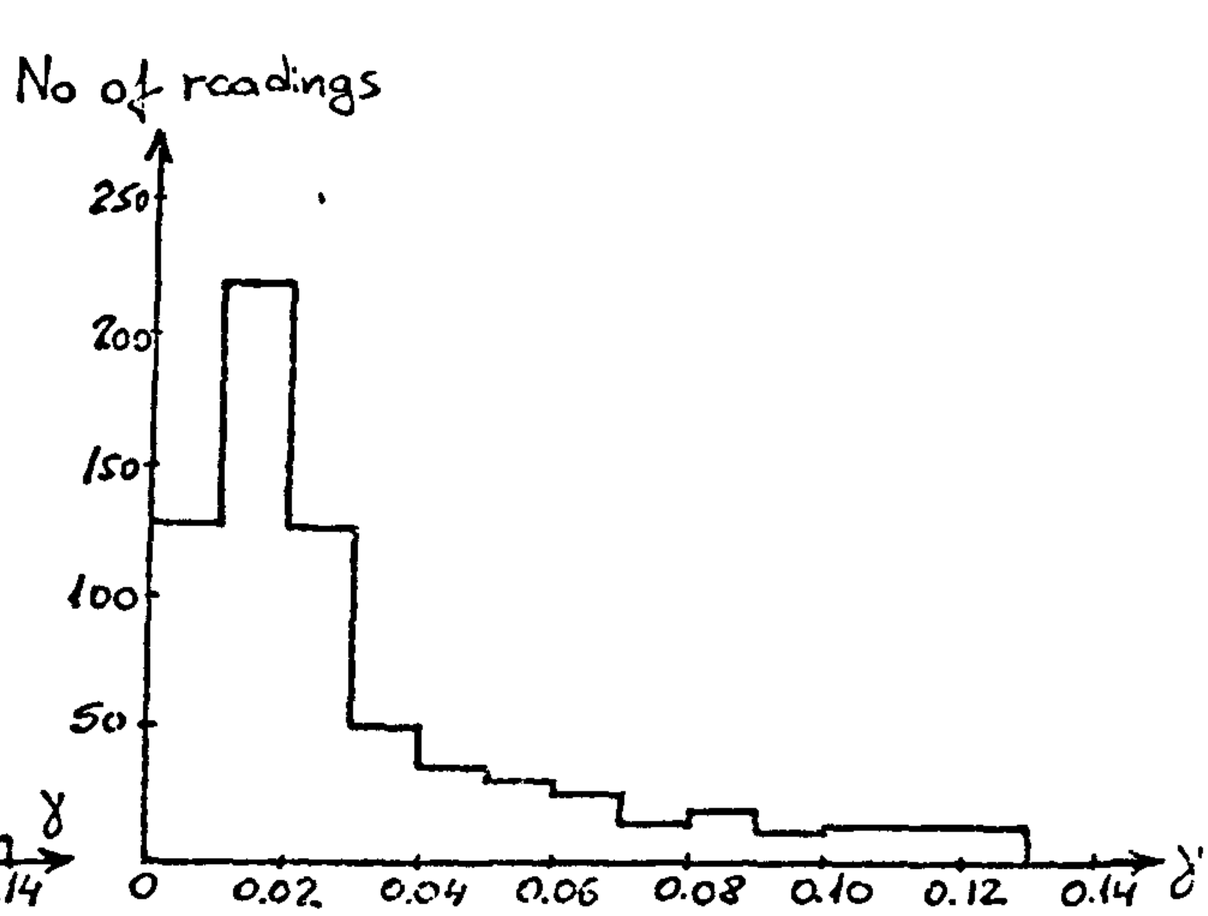

(d)

Fig. 7.24 The distribution of the number of readings used in the calculation of the average Δ-γ_M relationships from tests (a) D (b) A (c) B (d) C, shown in fig. 7.23.

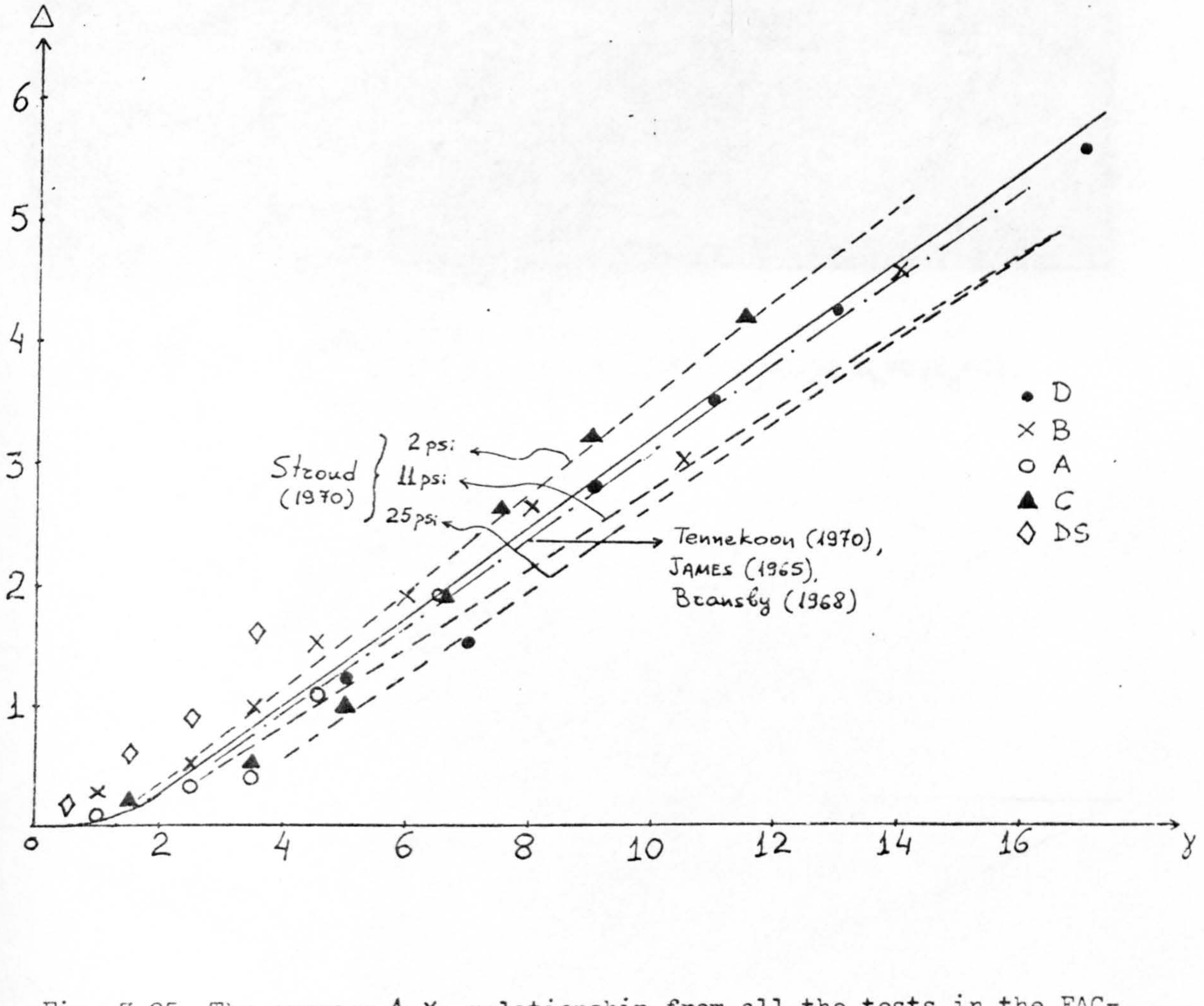

Fig. 7.25 The average Δ-γ_M relationship from all the tests in the FAC-Comparison with results from the SSA (Stroud, 1970).

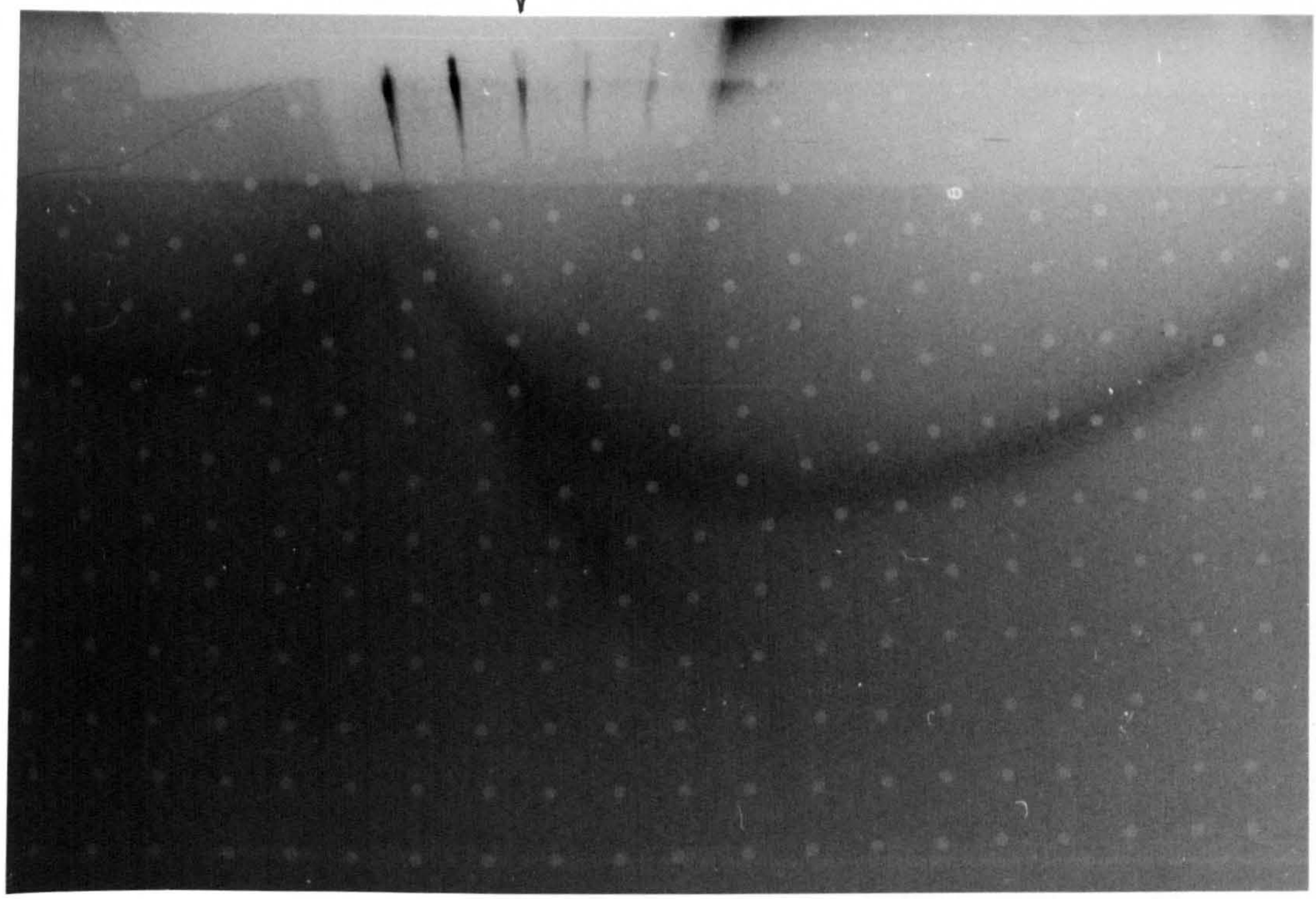

Fig. 7.26 The failure surface in test D(e_o=0.52, α_o=0, E_o=0).

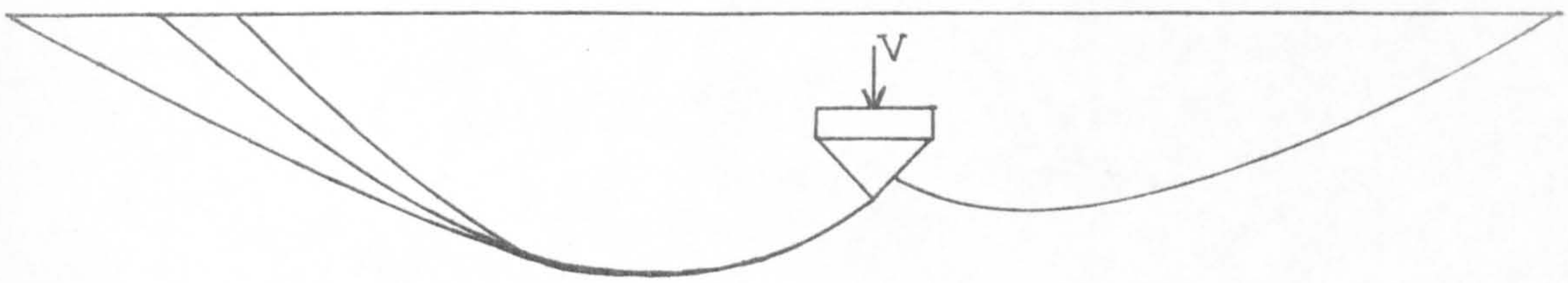

Fig.7.27 The failure surfaces in test H(B=76.2 mm, e_o=0.525, α_o=0°, E_o=0)-From Tennekoon(1970).

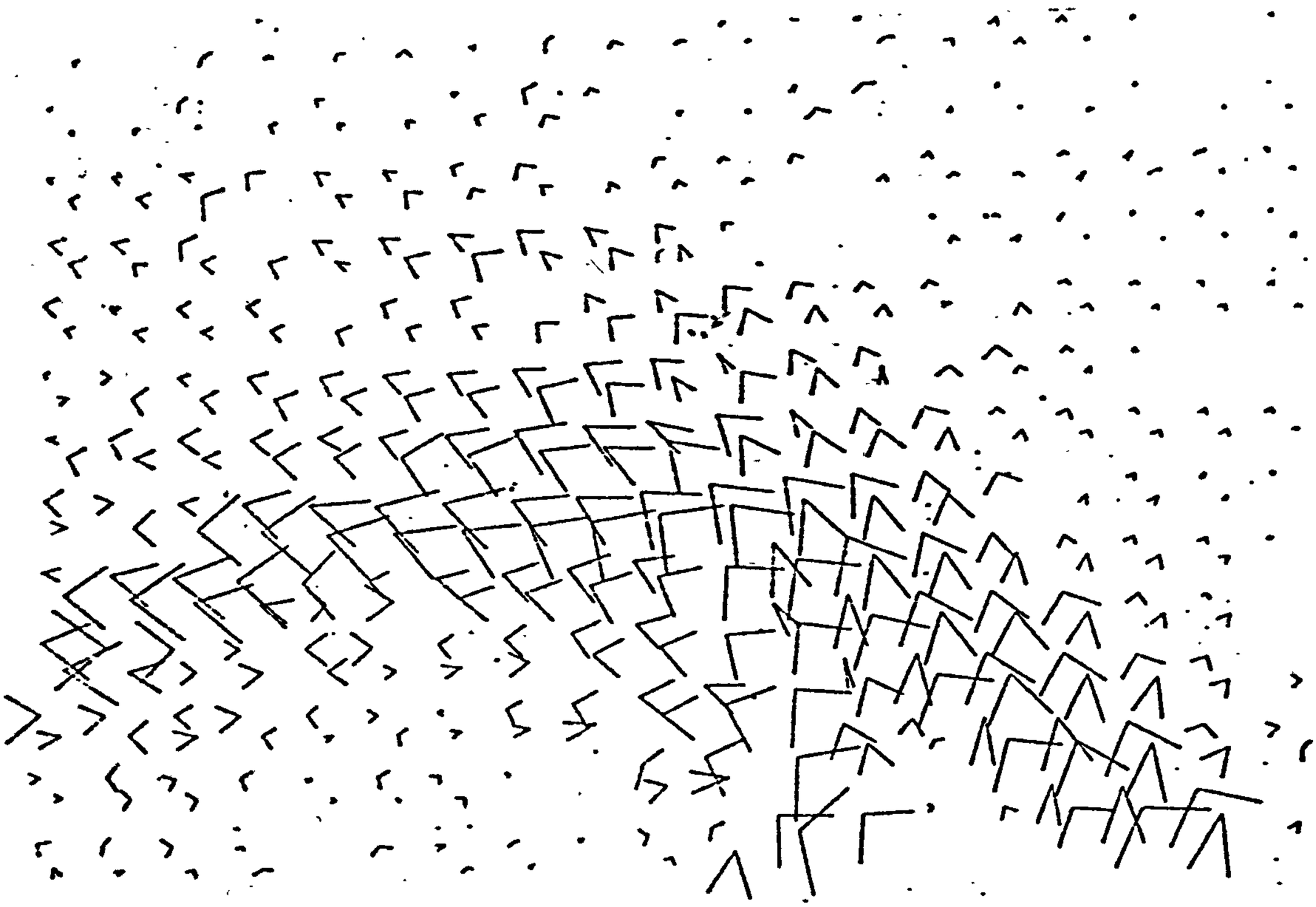

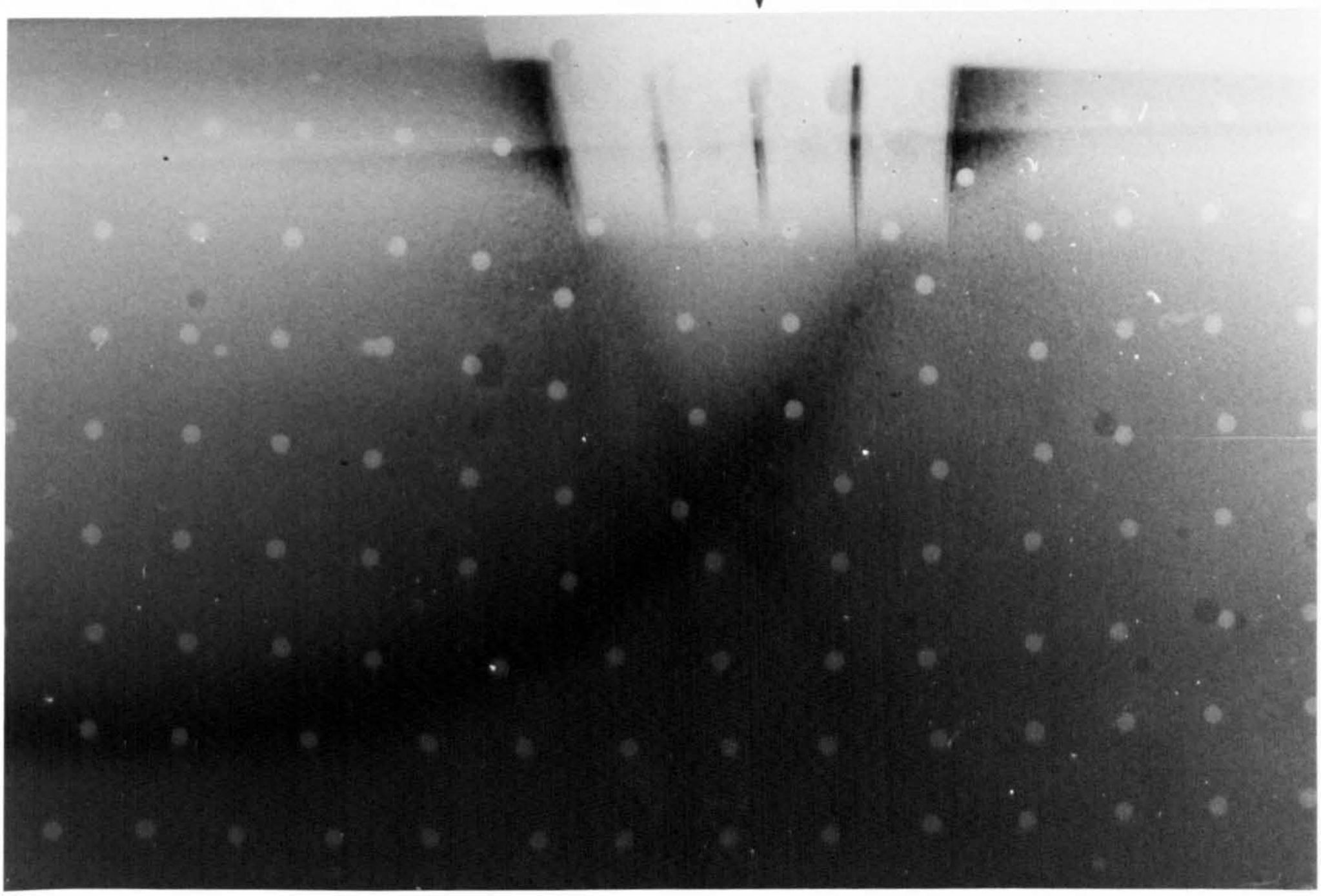

Fig. 7.28 Failure surface under a vertical central load ($B=50.8mm, e_o=0.52$).

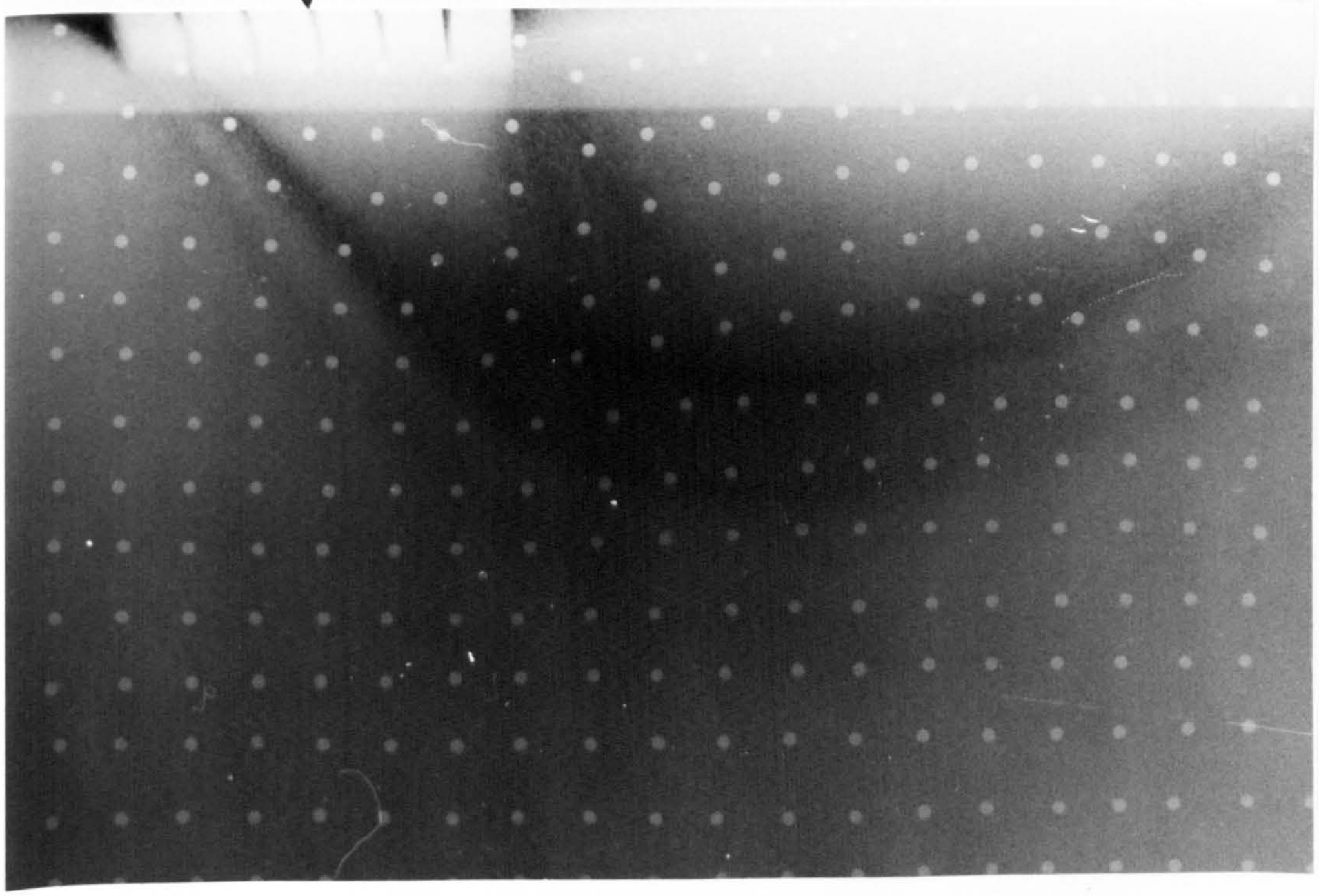

Fig. 7.29 The failure surface in test B($e_o=0.52, \alpha_o=12^o, E_o=0$).

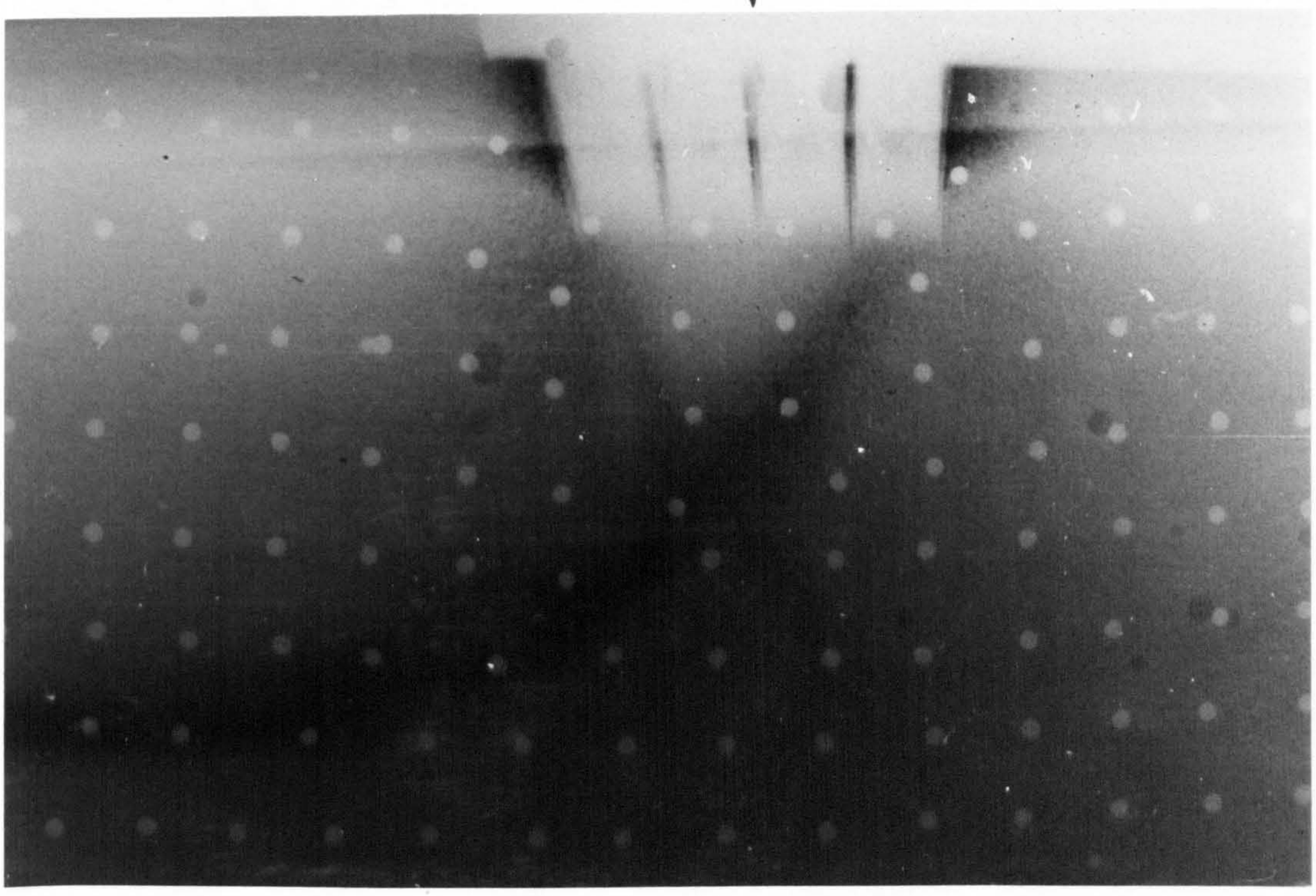

Fig. 7.28 Failure surface under a vertical central load ($B=50.8mm, e_o=0.52$).

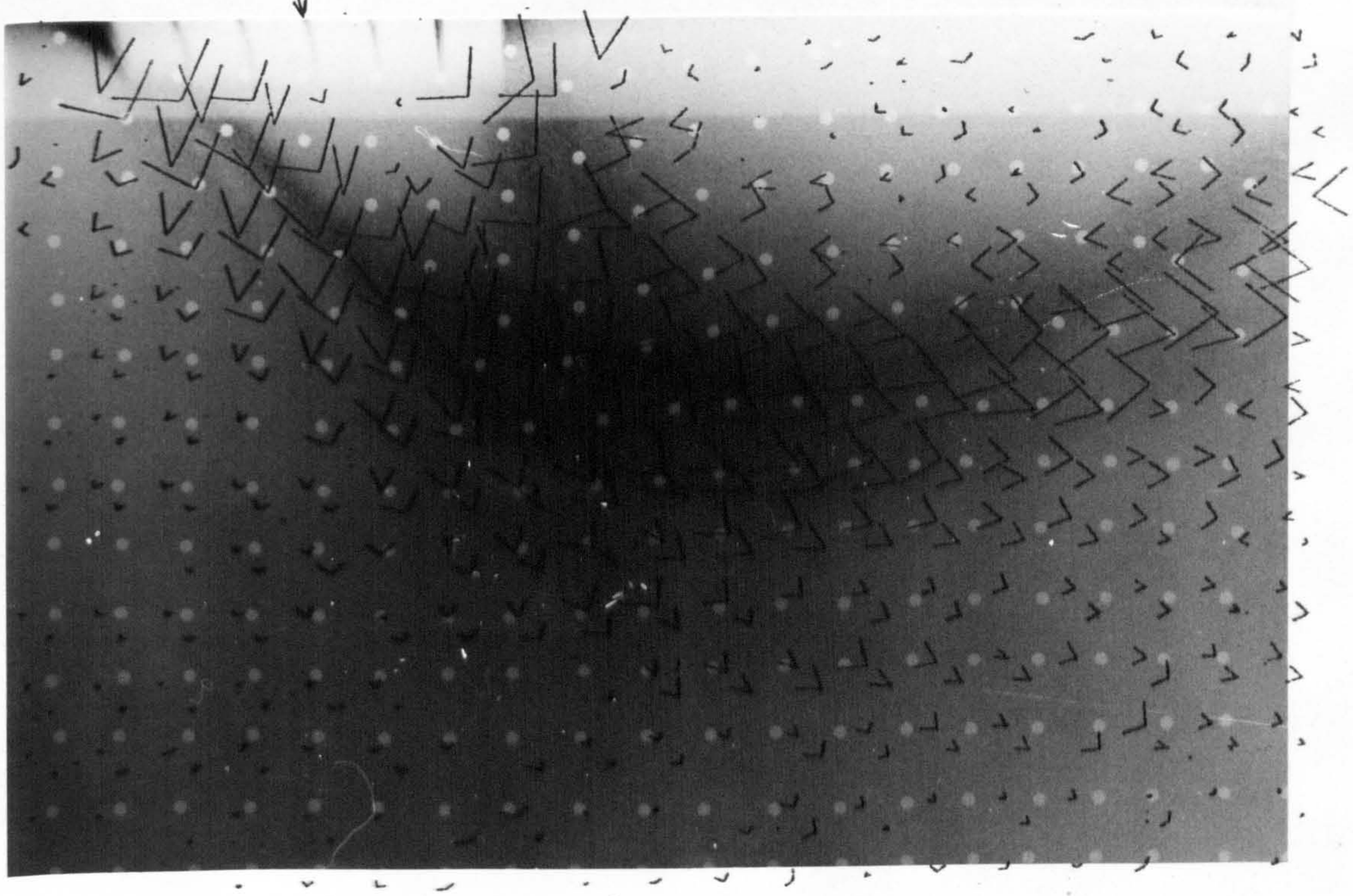

Fig. 7.29 The failure surface in test B($e_o=0.52, \alpha_o=12^o, E_o=0$).

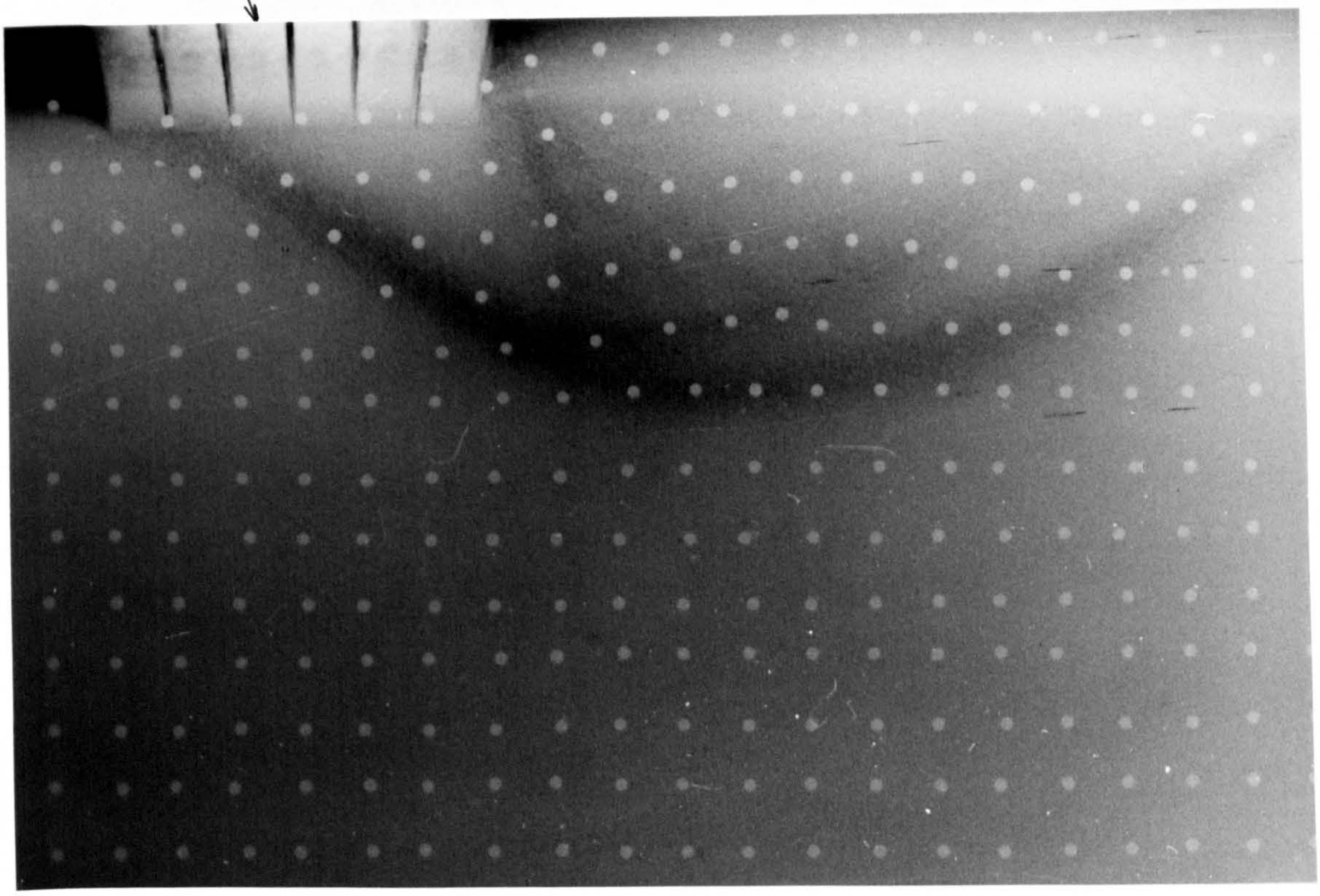

Fig. 7.30 The failure surface in test GB(e_o=0.52, α_o=20°, E_o=0).

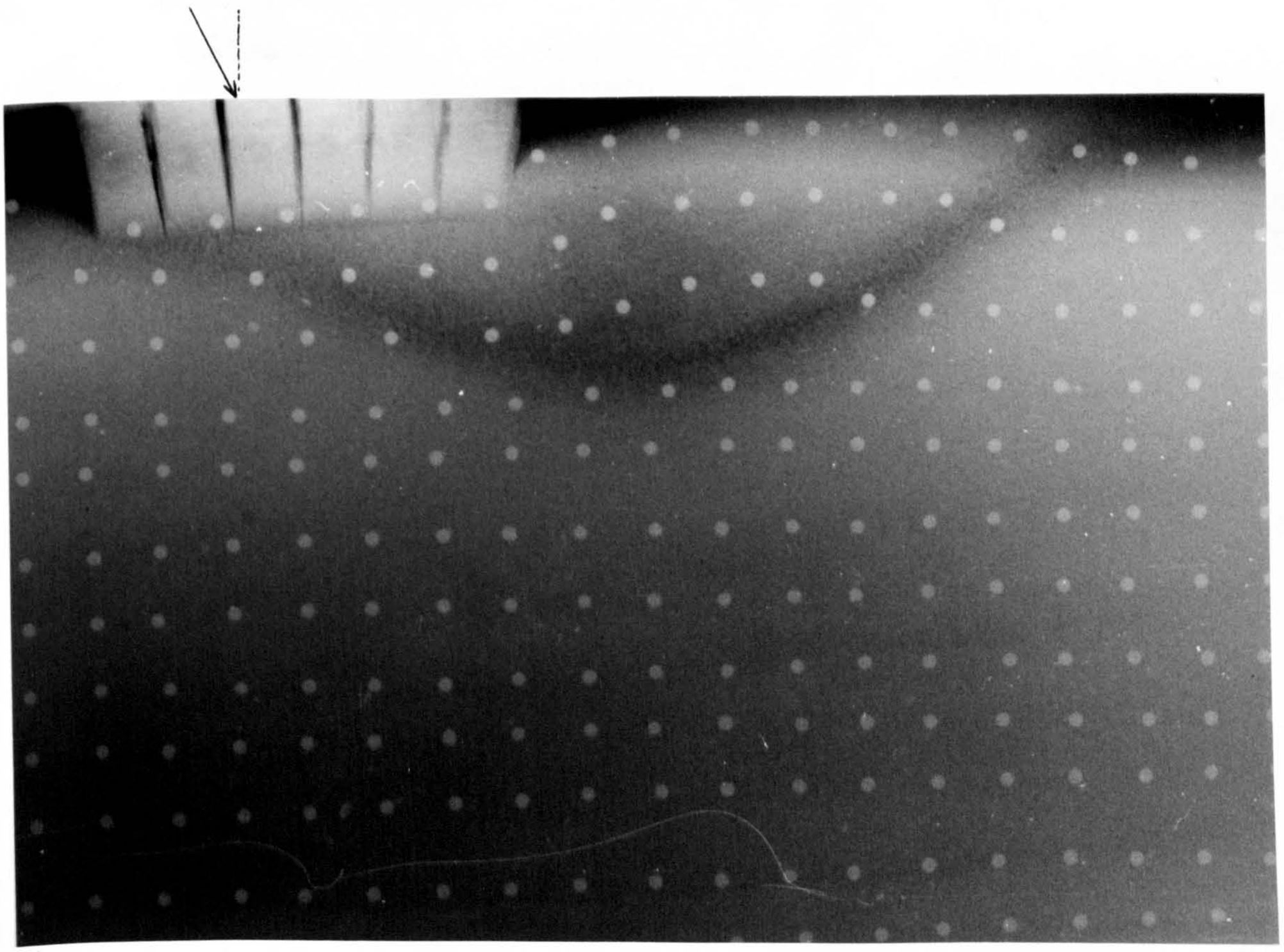

Fig. 7.31 The failure surface in test E(e_o=0.52, α_o=30°, E_o=0).

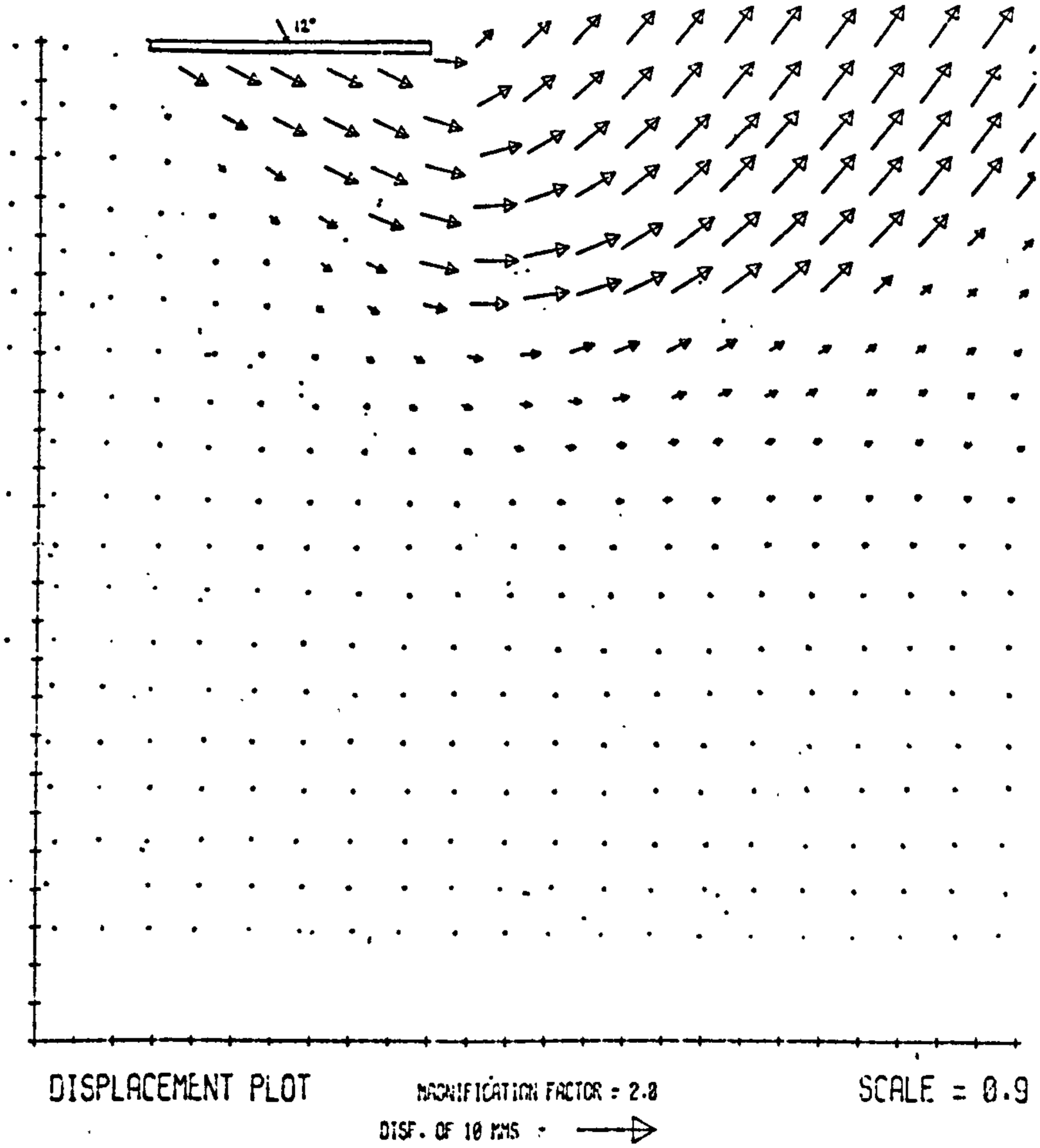

(a)

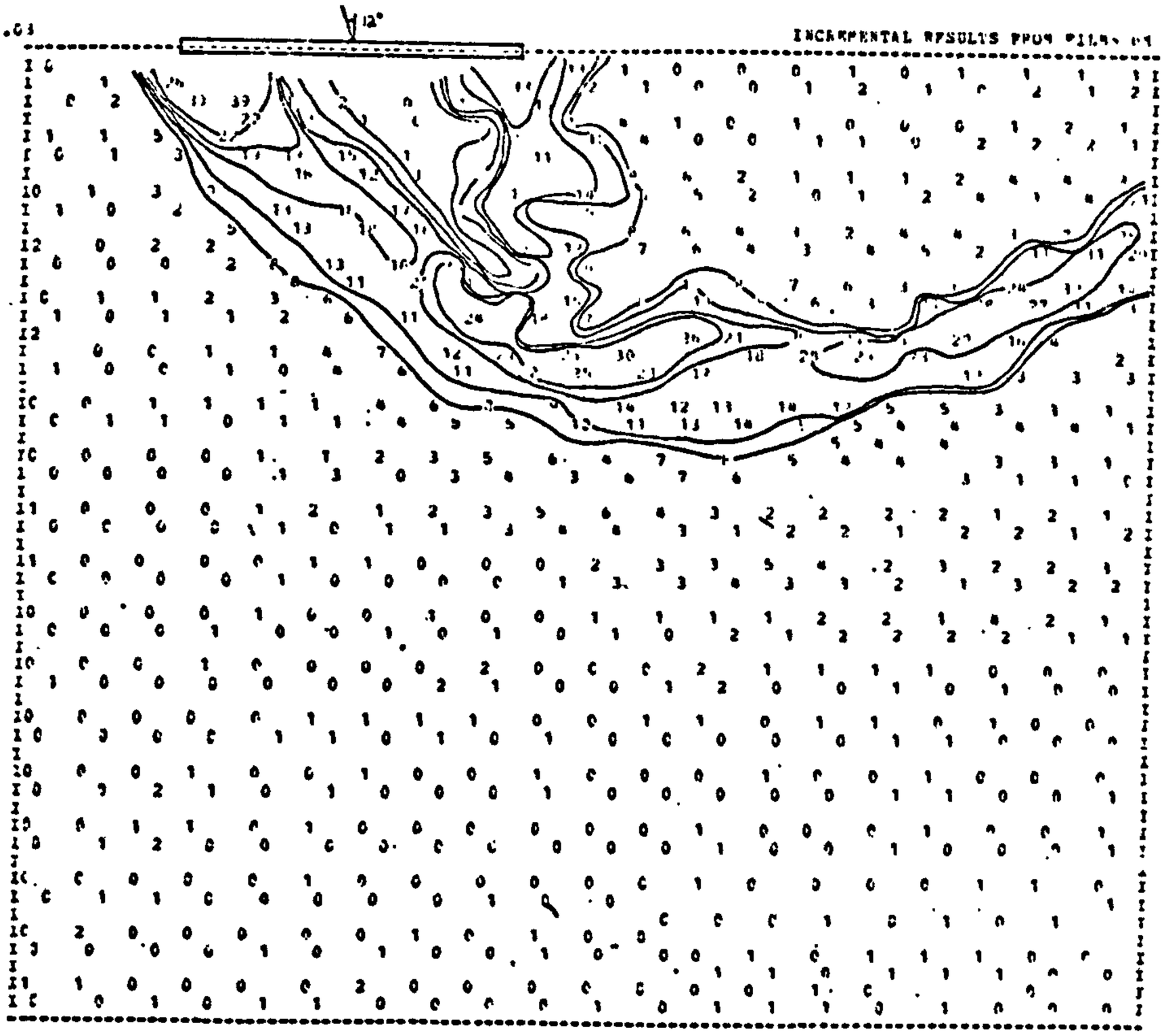

(b)

Fig. 7.32 Incremental results from test B(e_o=0.52,α_o=12°,E_o=0) between stages 0.86-1.00 of the failure load (a) displacement field (b) maximum shear strain field .

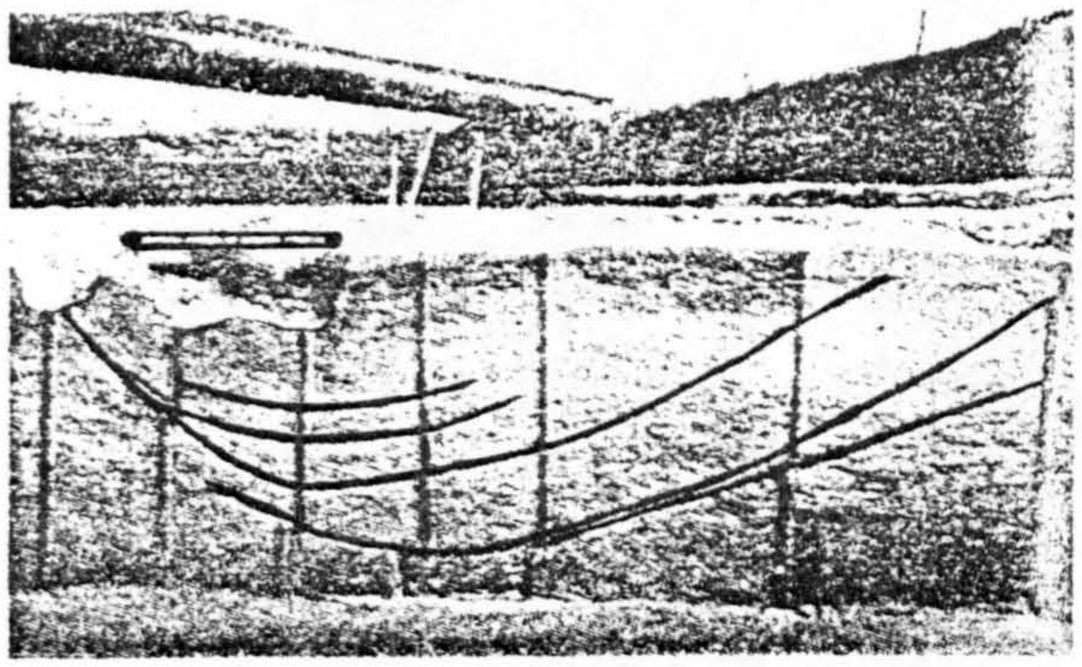

(a)

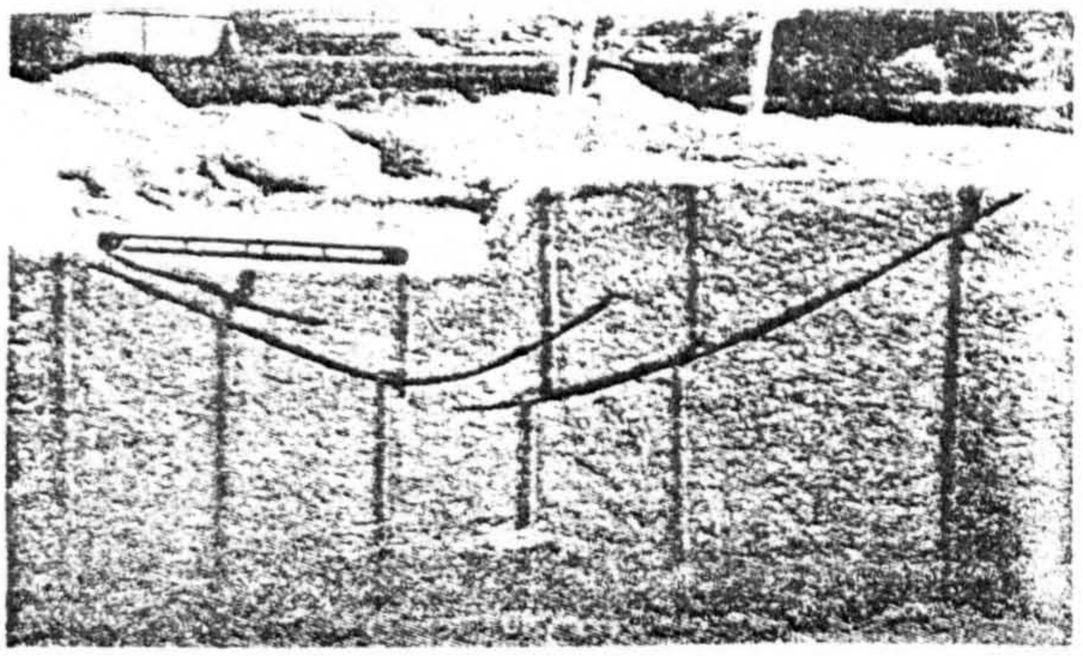

(b)

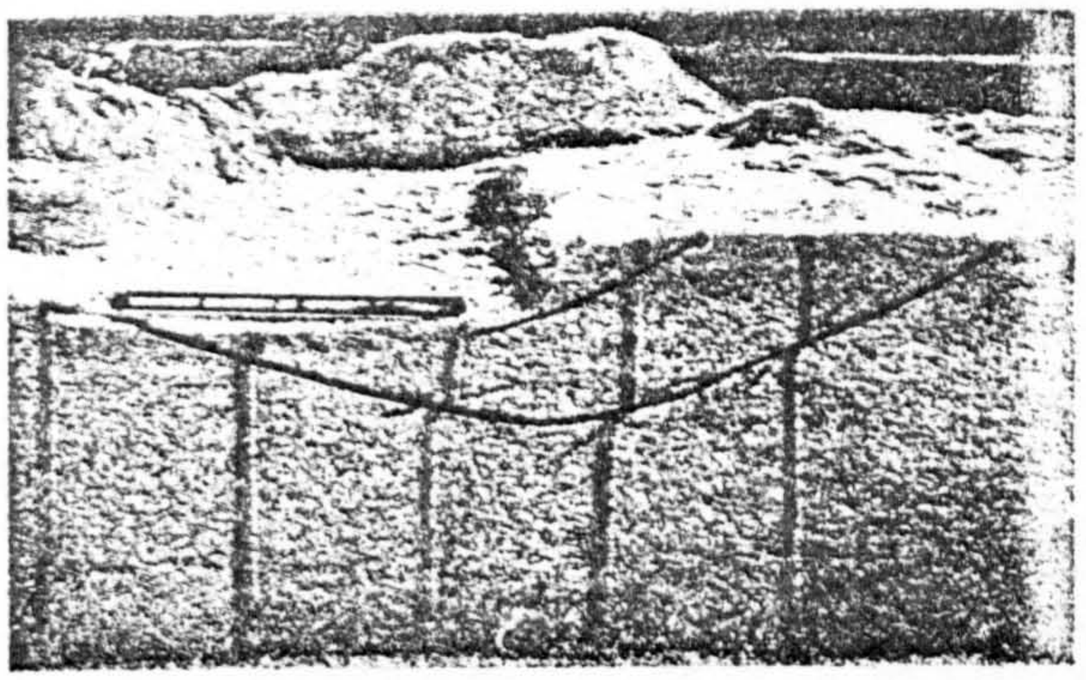

(c)

Fig. 7.33 Failure surfaces from large field tests under inclined central loads (a) $\alpha = 10^{\circ}$ (b) $\alpha = 20^{\circ}$ (c) $\alpha = 30^{\circ}$ (Muhs and Weiss, 1973).

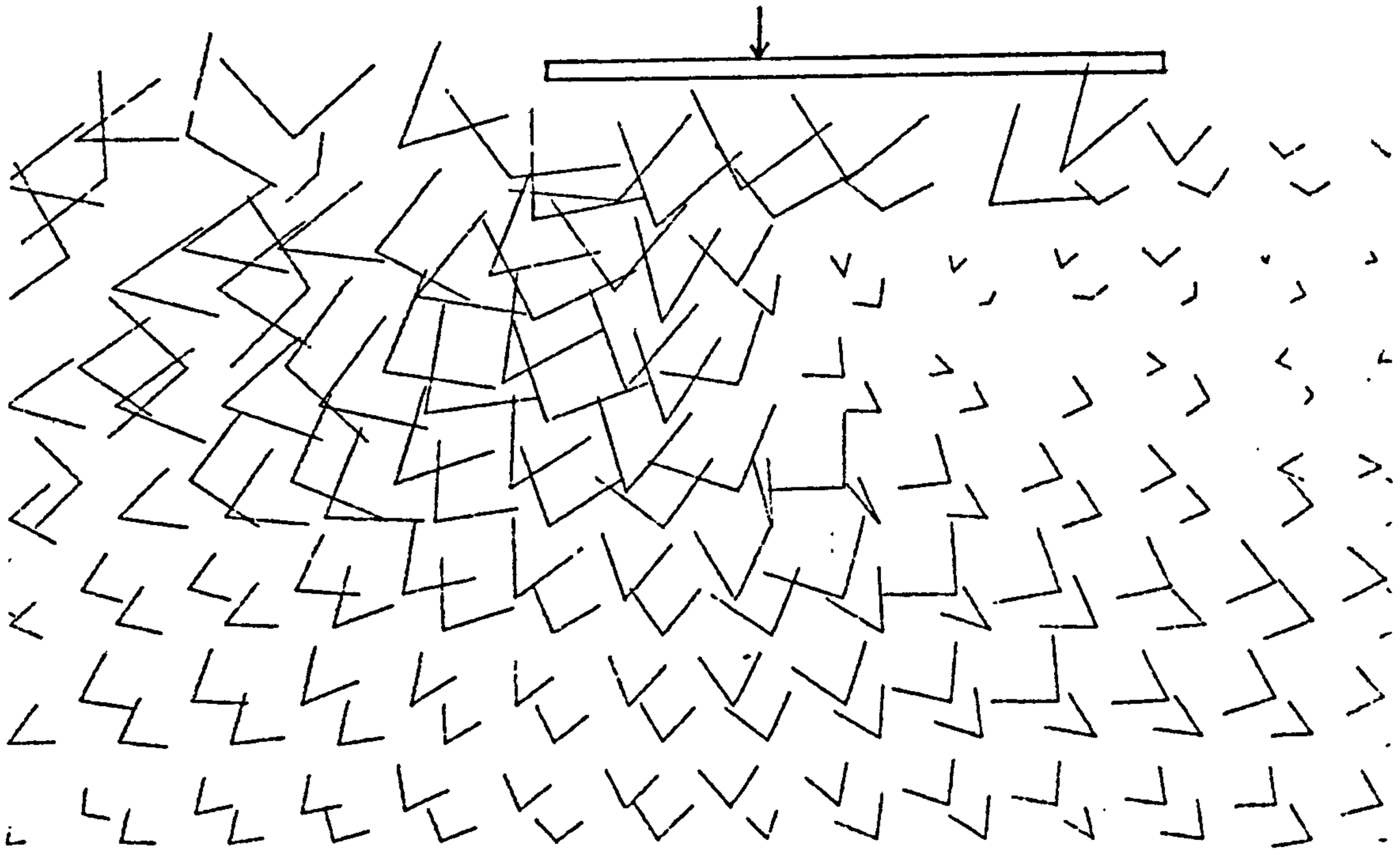

Fig. 7.34 The zero extension line directions from test A(Failure surface shown in next page).

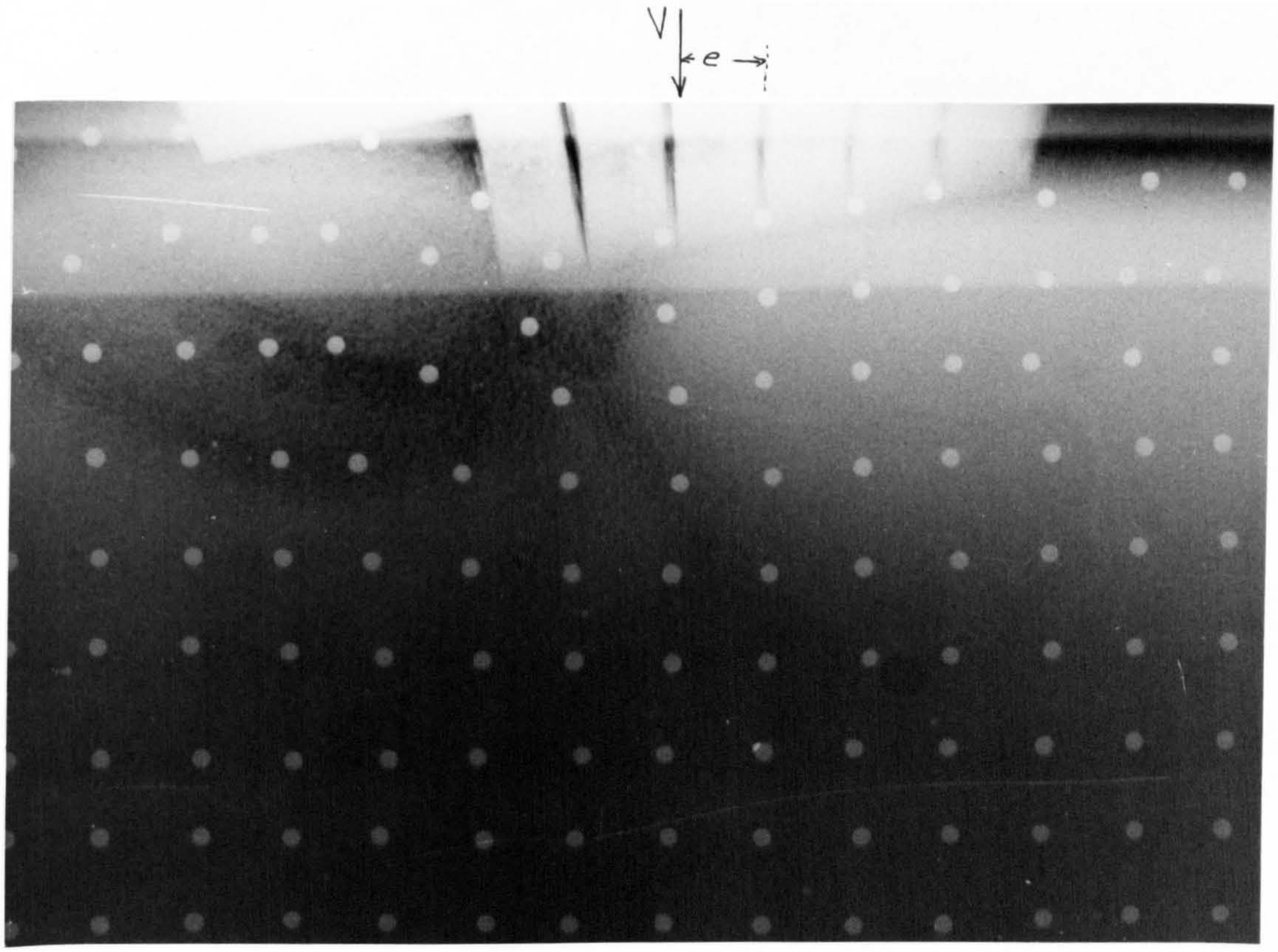

Fig. 7.34 The failure surface in test A(e_o=0.52, α_o=0, E_o=0.167).

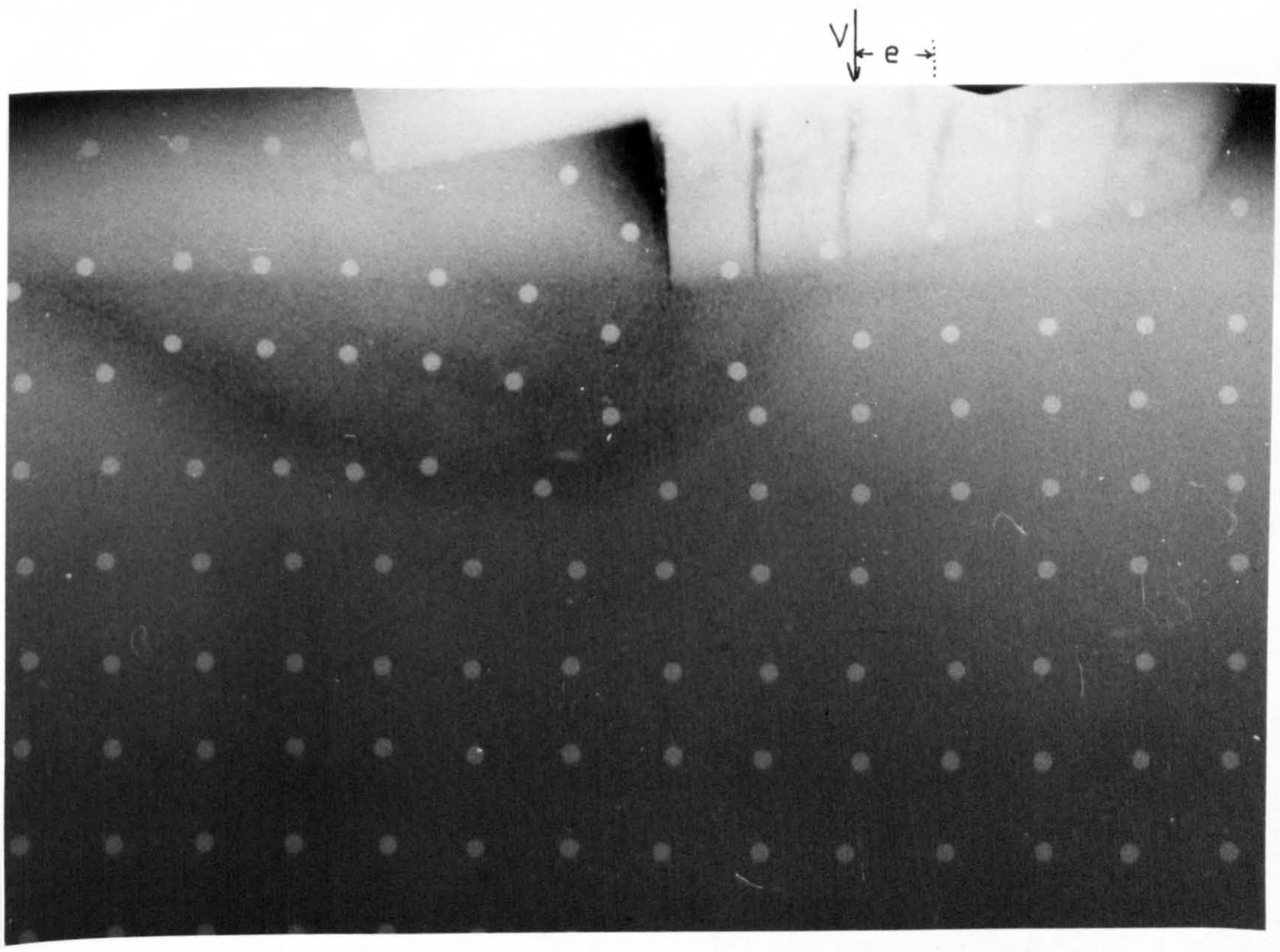

Fig. 7.35 The failure surface in test H(e_o=0.52, α_o=0, E_o=0.167).

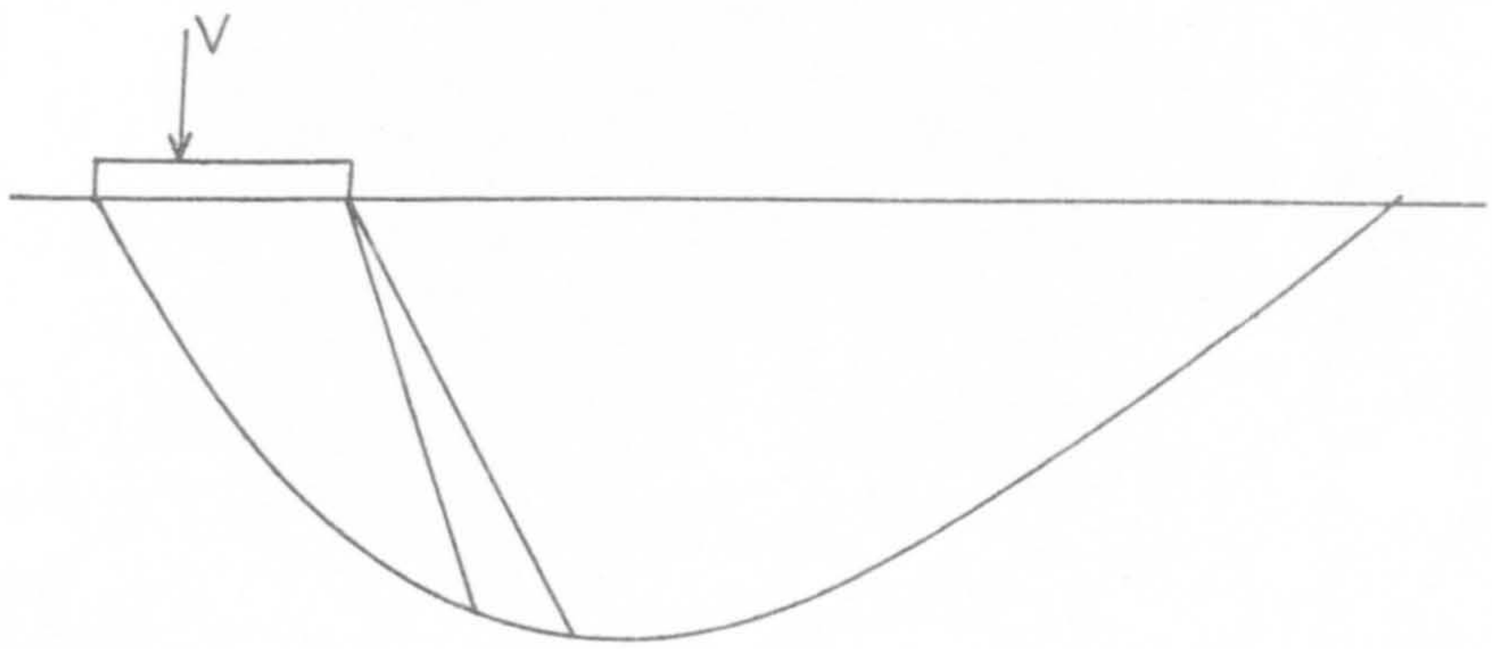

Fig. 7.36 The failure surface in test FA(e_o=0.52,α_o=0,E_o=0.167)

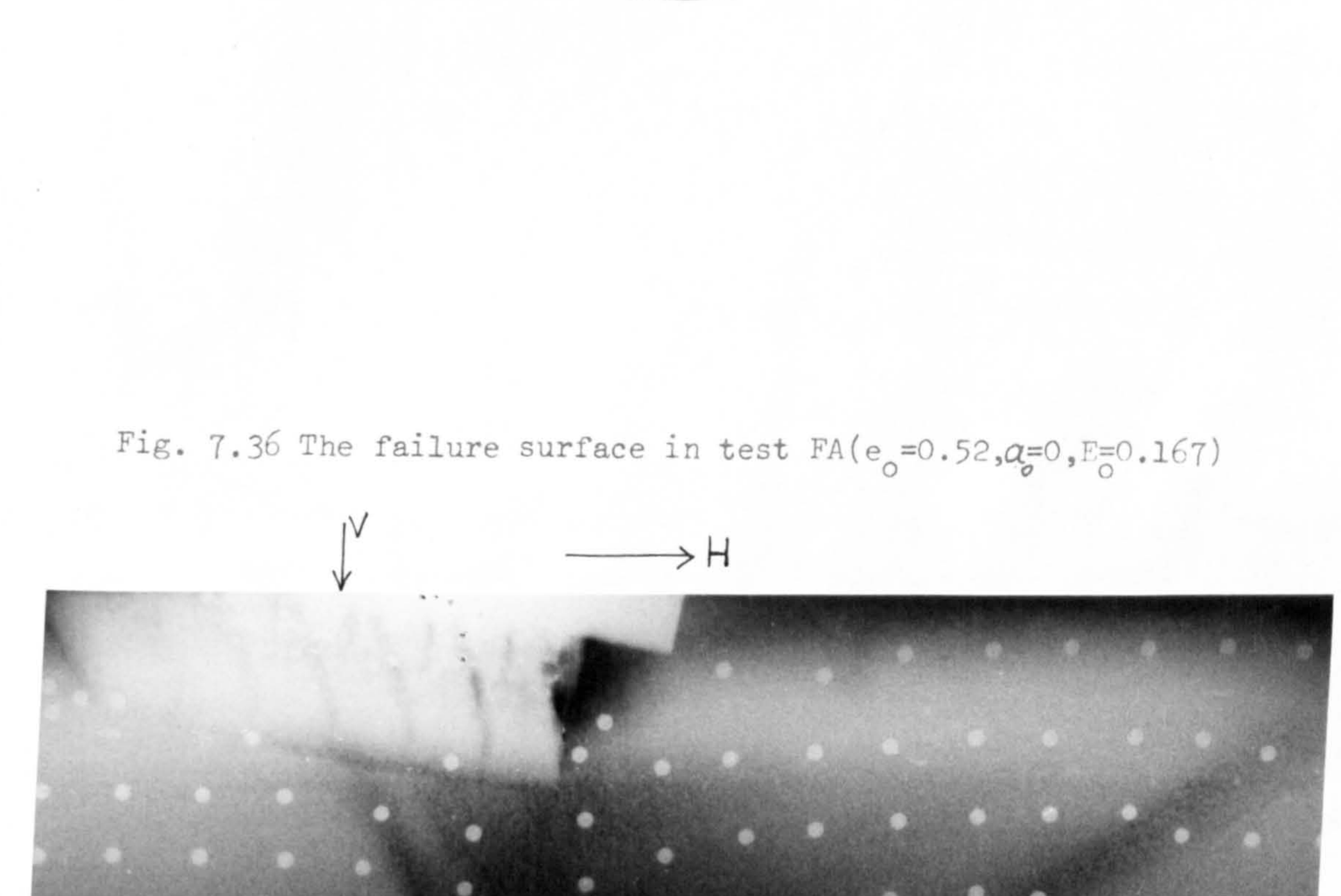

Fig. 7.37 The failure surface in test F(e_o=0.52, independent horizontal load at 100 mm from the footing base).

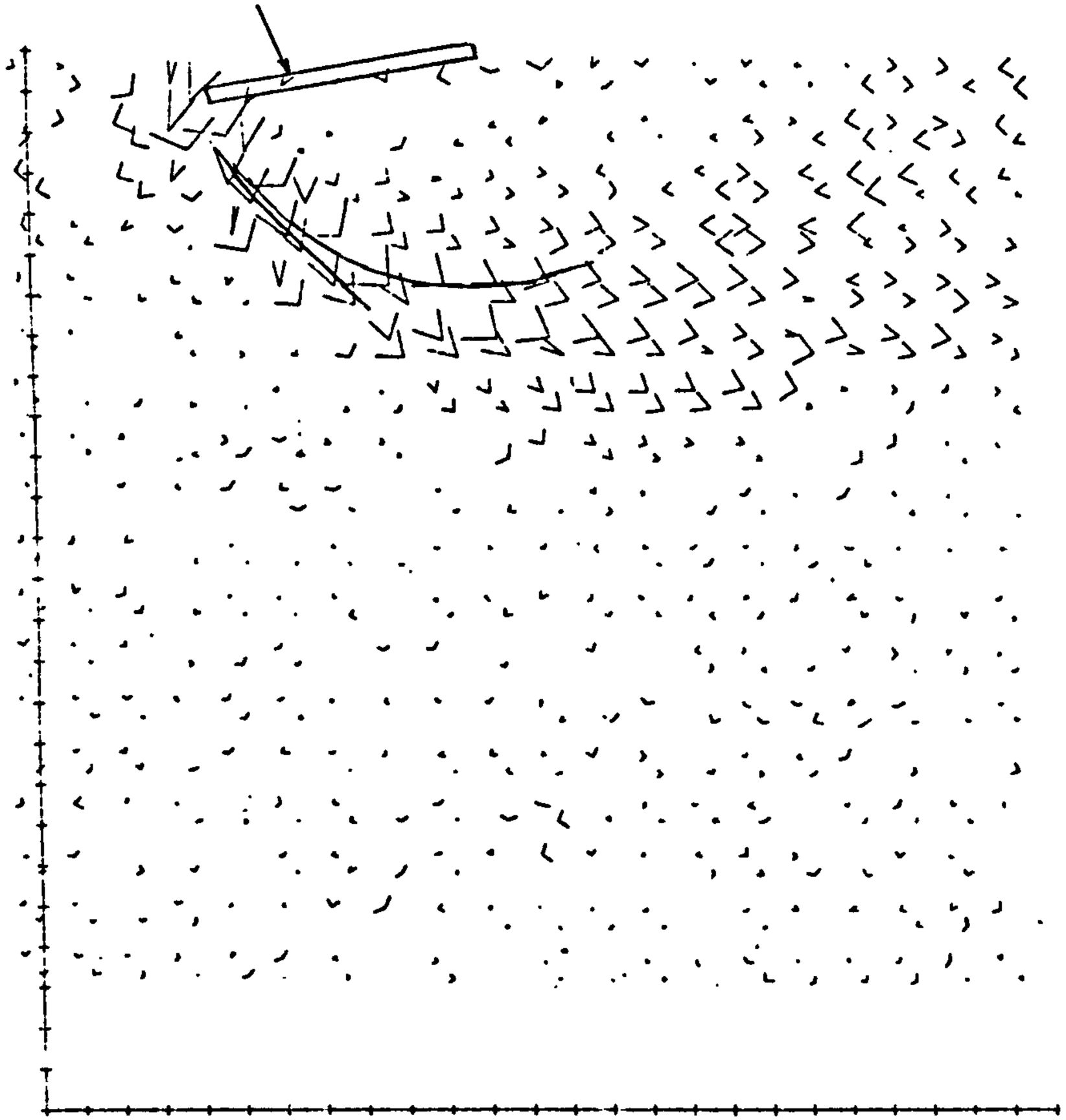

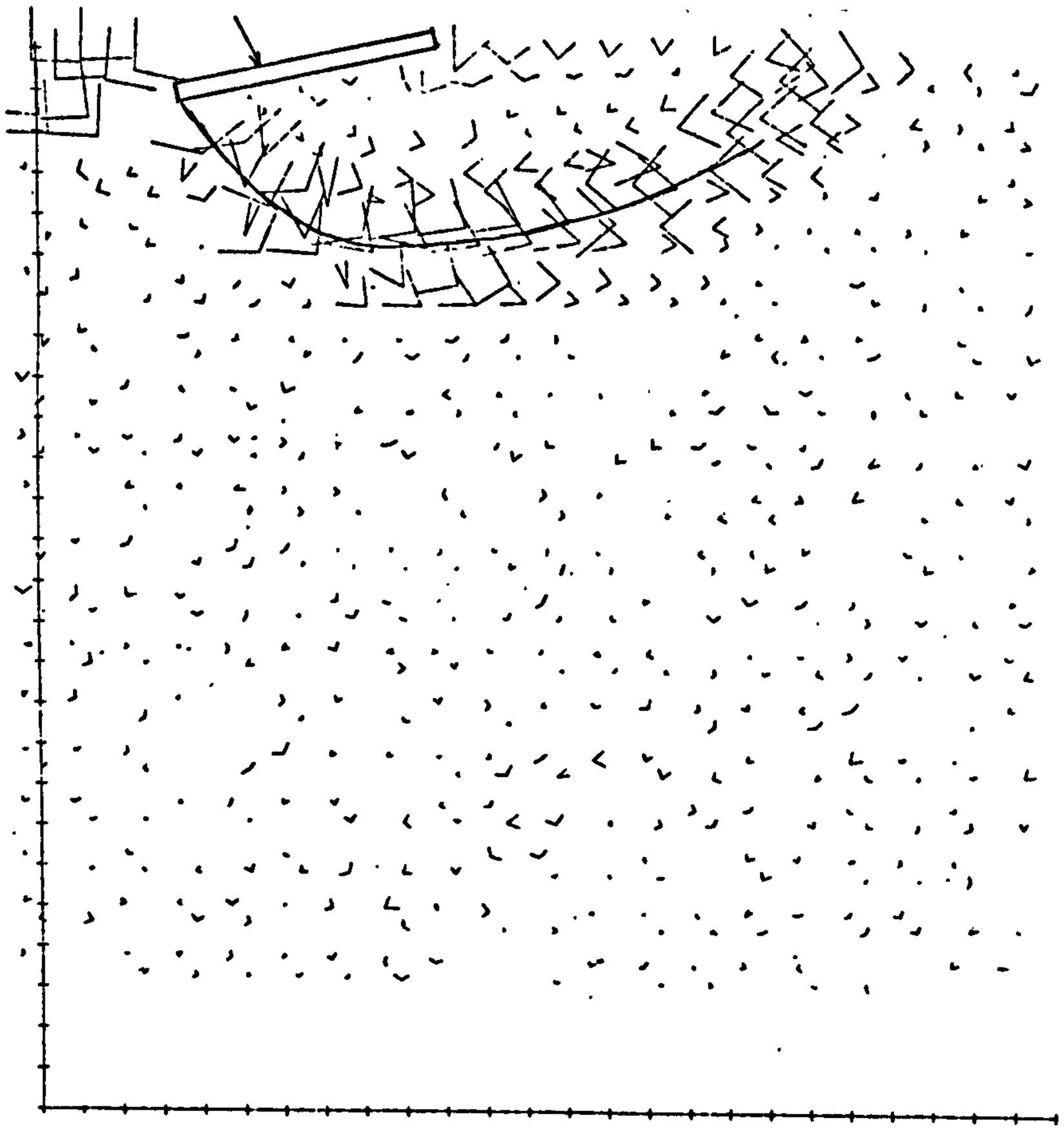

Fig. 7.38 The failure surfaces in test C(e_o=0.52,α_o=12°,E_o=-0.167) and superposed zero extension line direction between stages (a) 0.96-failure (b) just after failure.

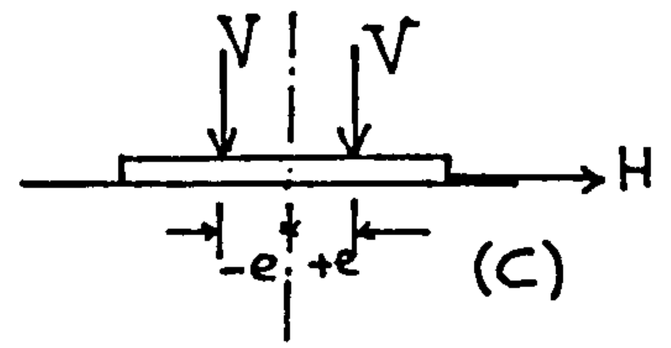

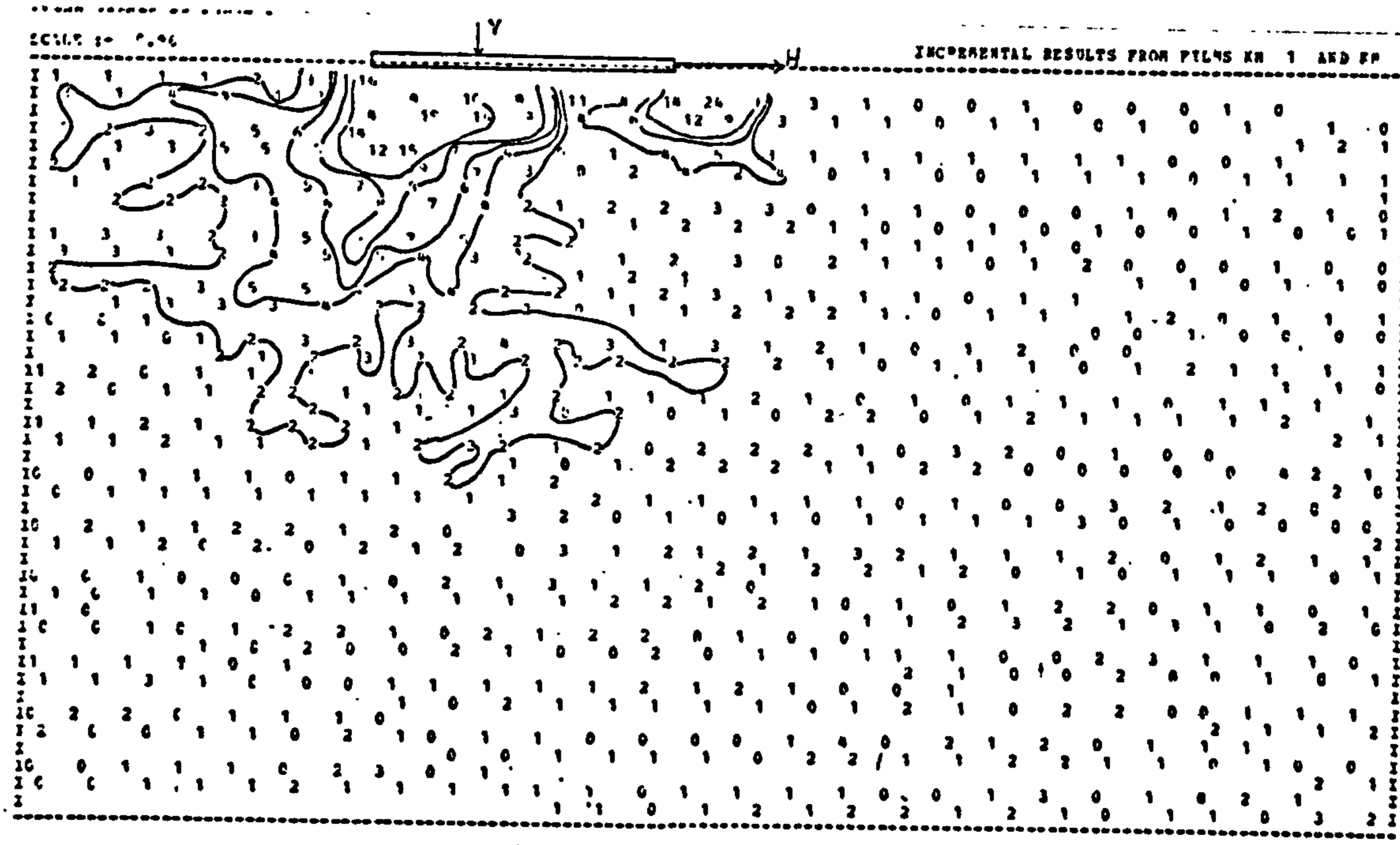

Fig. 7.39a The total maximum shear strains from test K(e_o=0.52,E_o=-0.167 , independent horizontal load along the footing base).

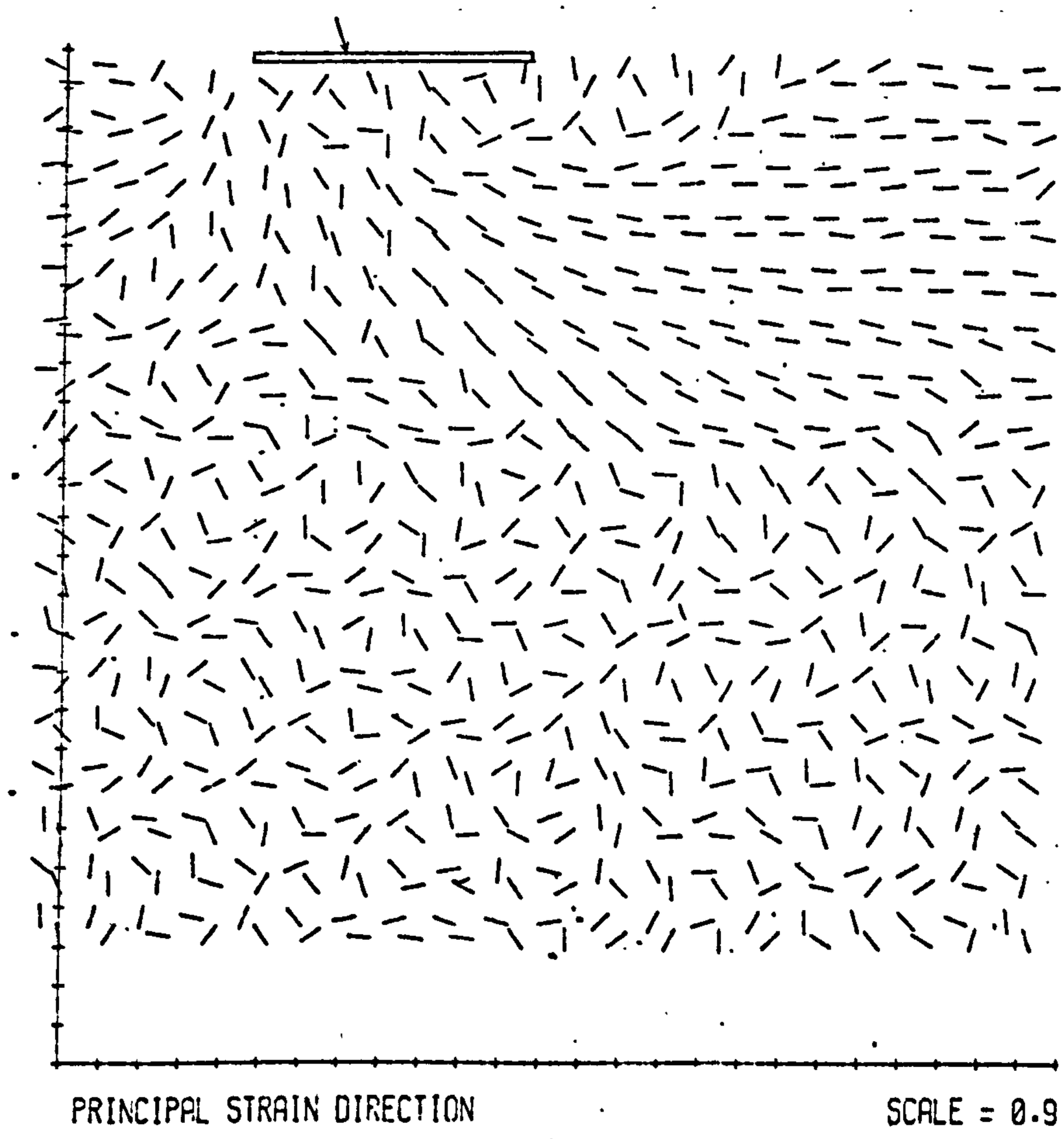

Fig. 7.39b The major principal compressive strain rate directions from test C(e_o=0.52,α_o=12°,E_o=-0.167) between stages 0.96-failure.

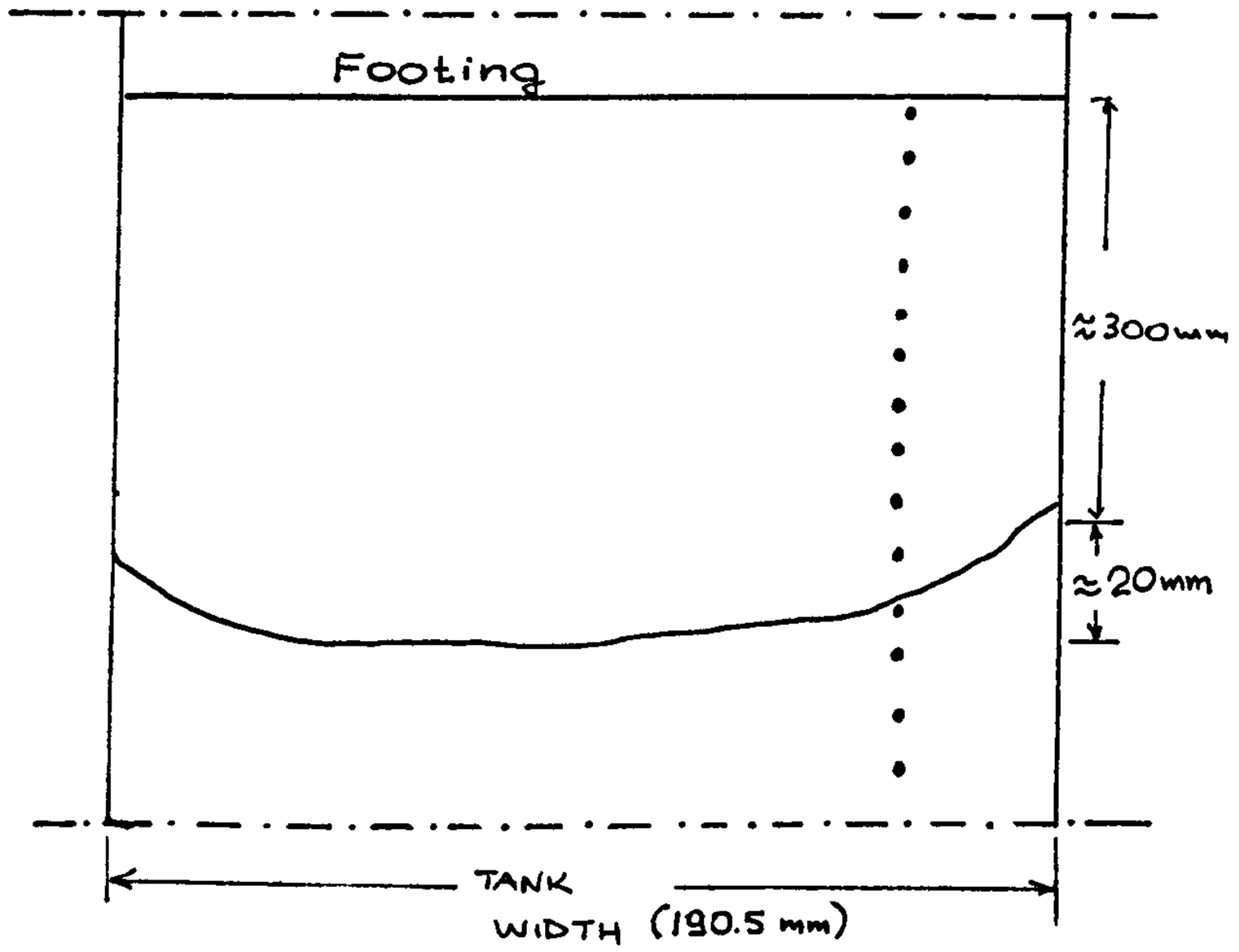

Fig. 7.40 The typical shape of the failure surface outcrop from tests in the FAC.

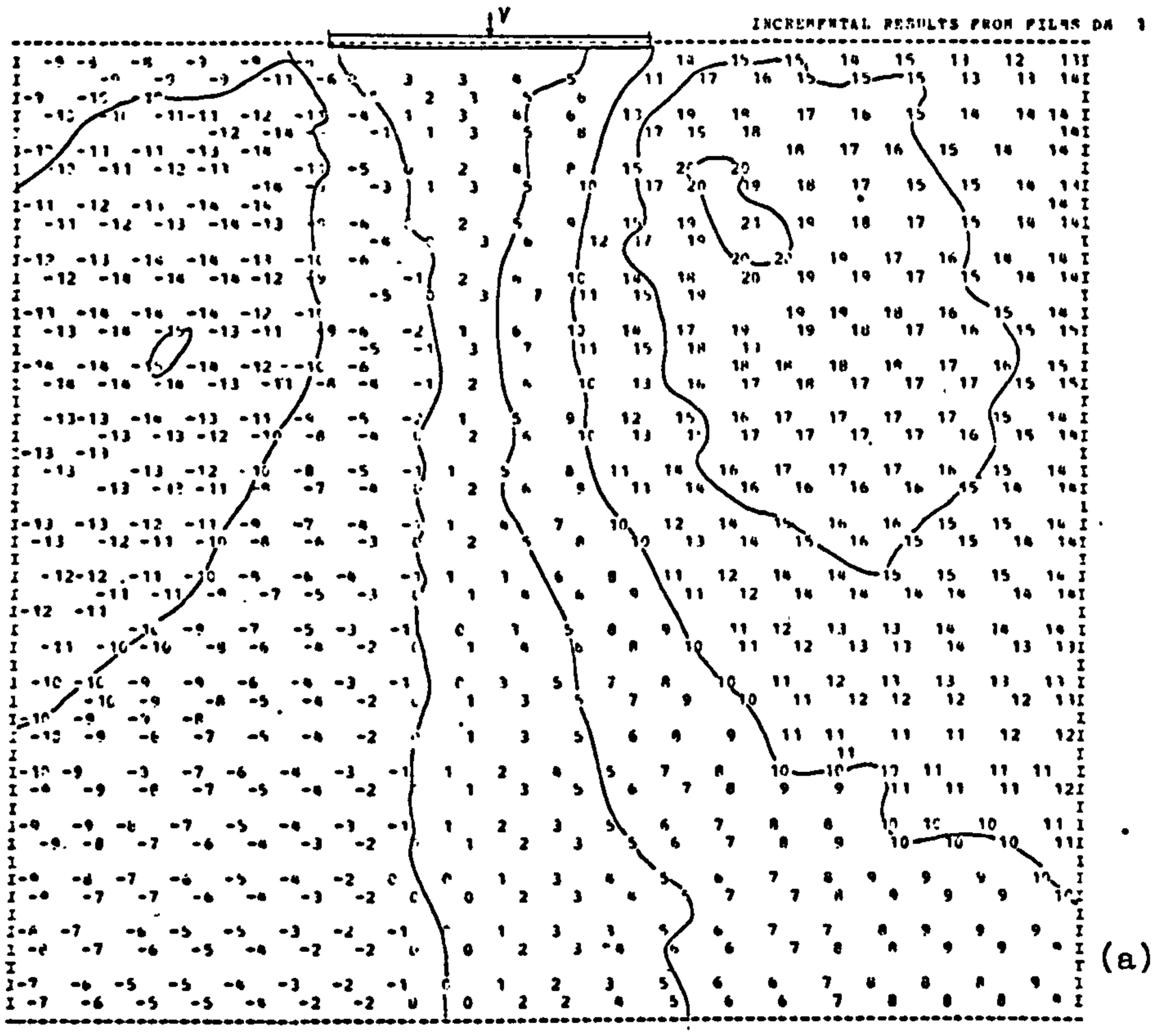

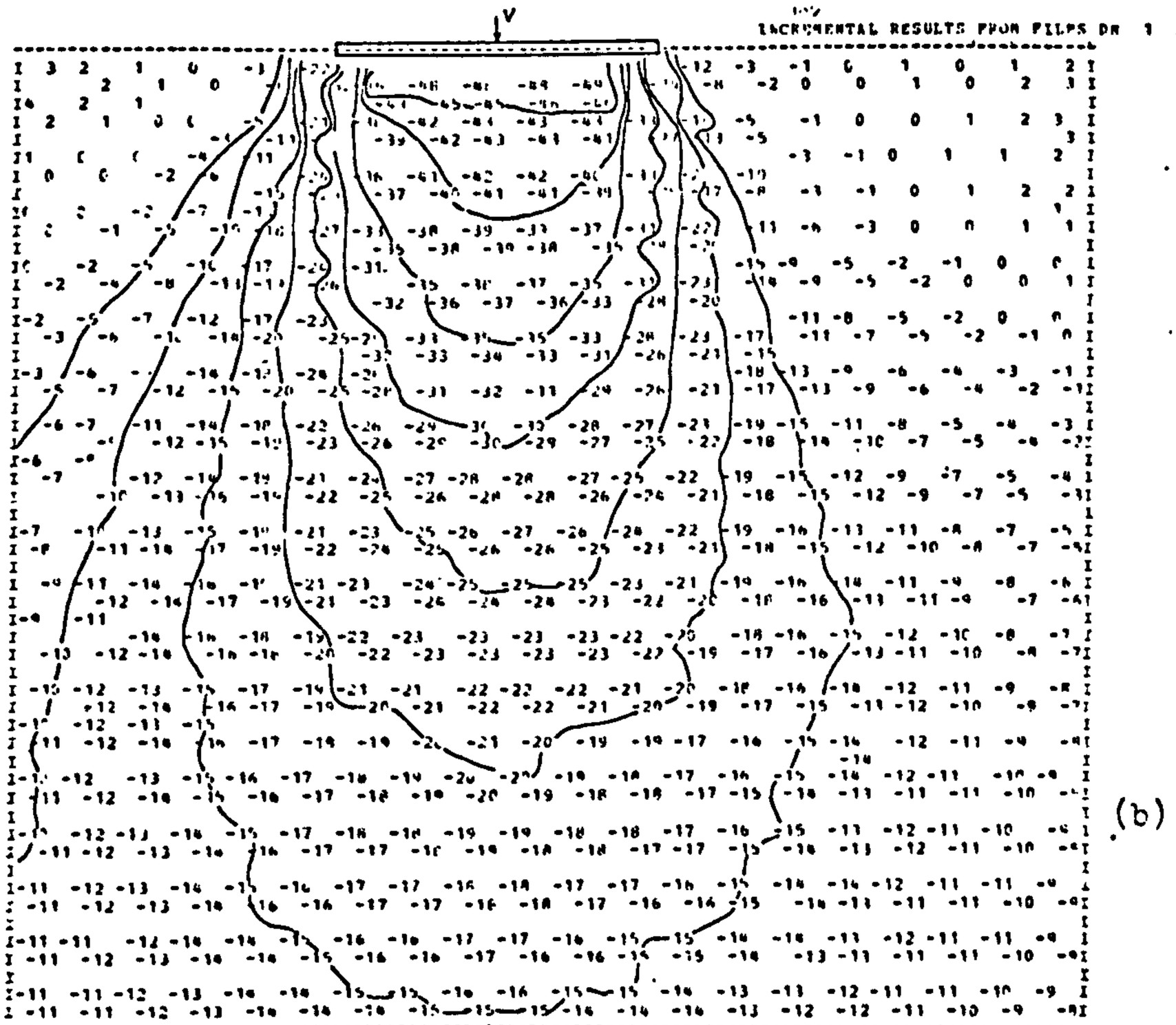

Fig. 7.41 Total displacement fields from test D(e_o=0.52,α_o=0,E_o=0) at stage 0.74 of the failure load

(a) Horizontal (b) Vertical (X-Rays).

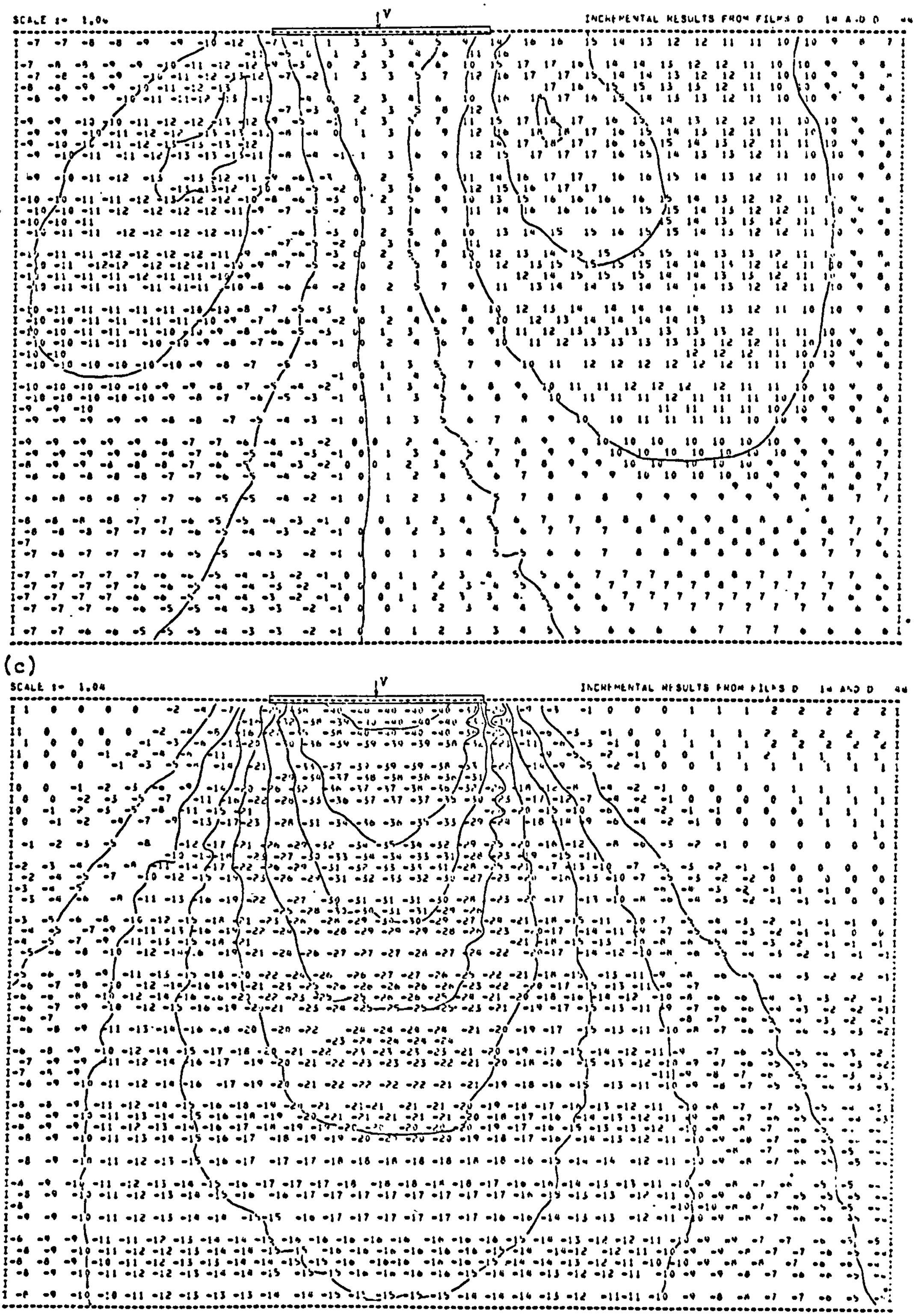

Fig. 7.41 Total displacement fields from test D(e_o=0.52,σ_o=0,E_o=0) at stage 0.74 of the failure load
(c) Horizontal (d) Vertical - Stereophotogrammetry.

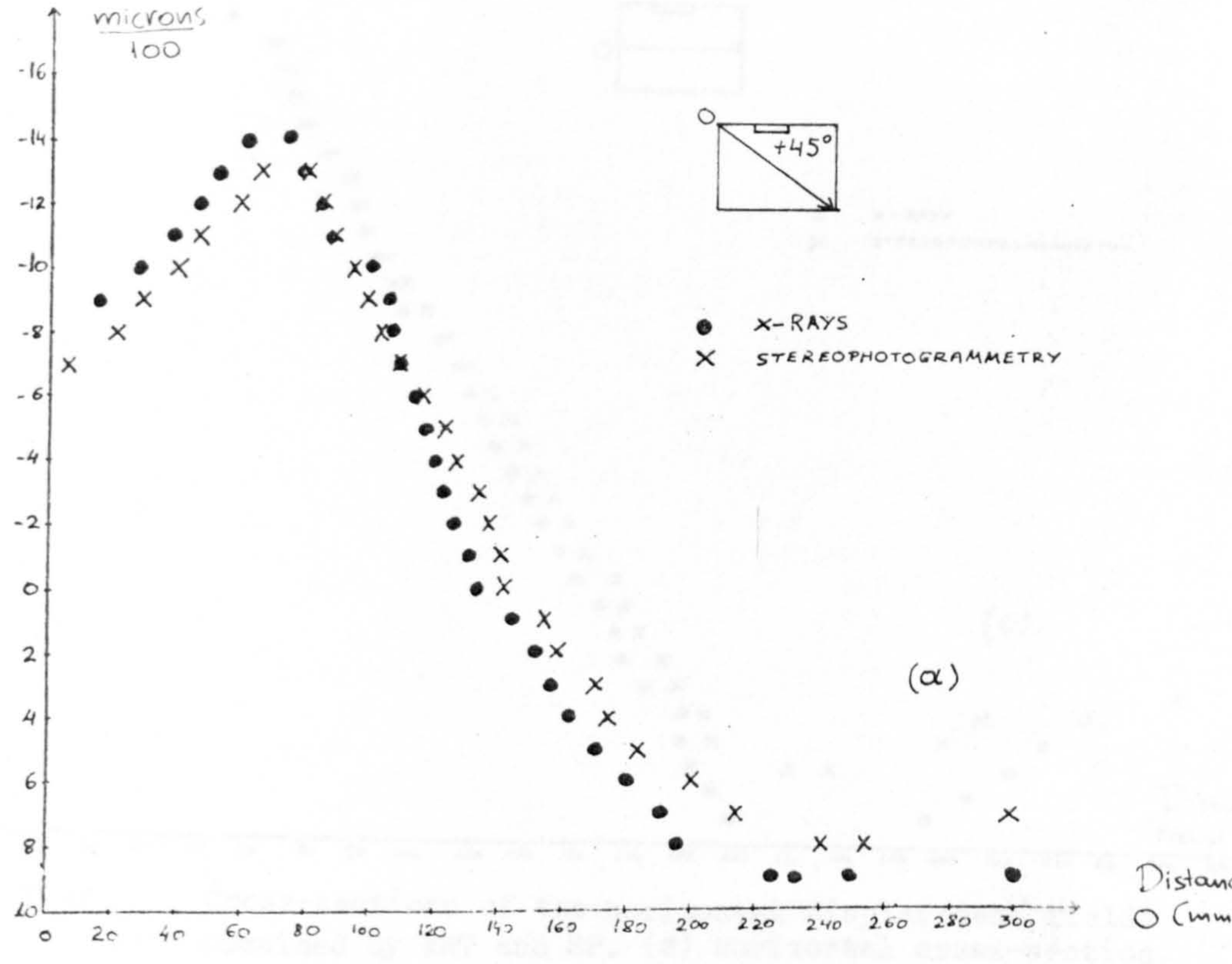

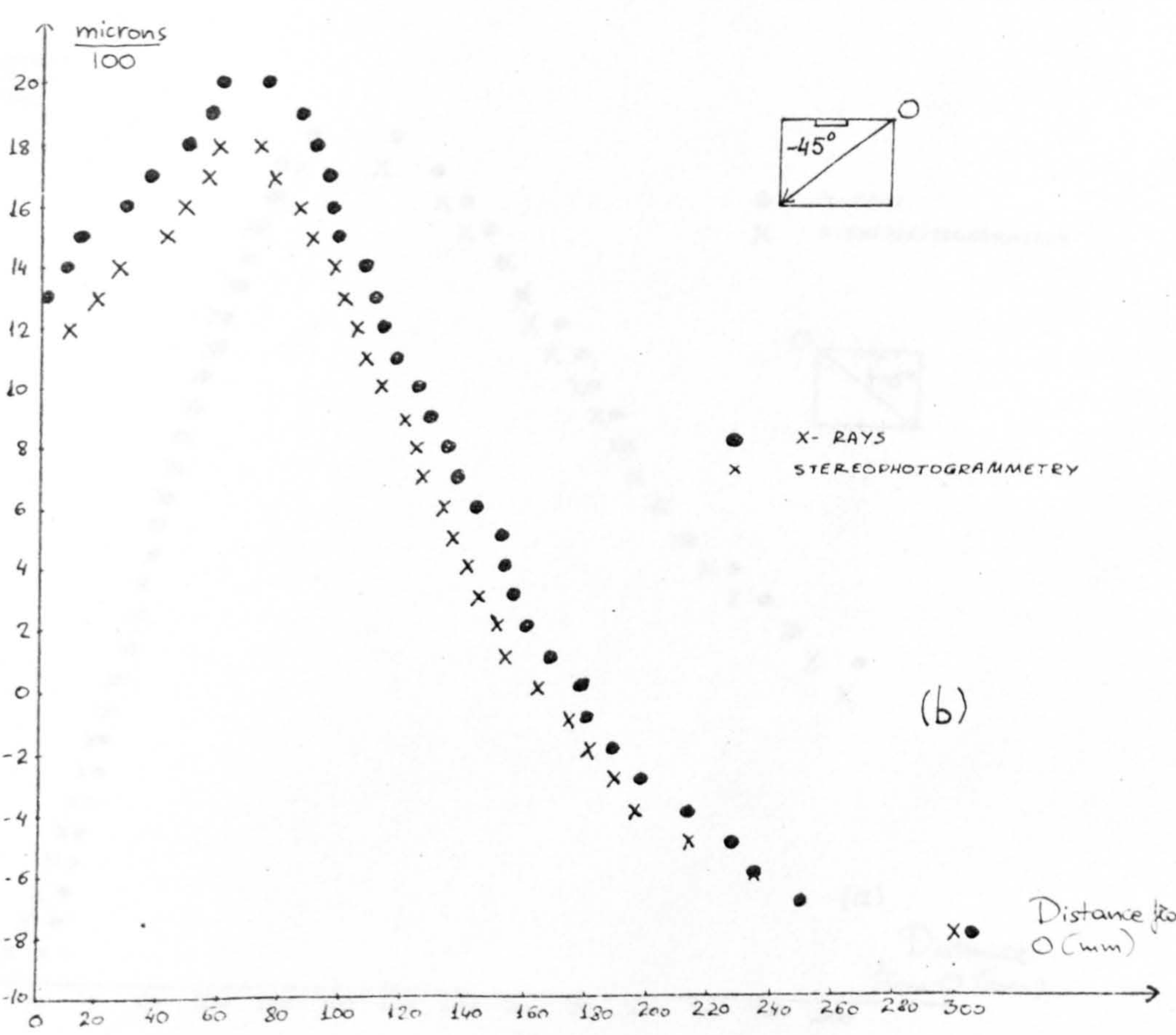

Fig. 7.42 Cross-sections of the horizontal displacement fields obtained by XRT and SP. (a) $+45^{\circ}$ (b) -45° .

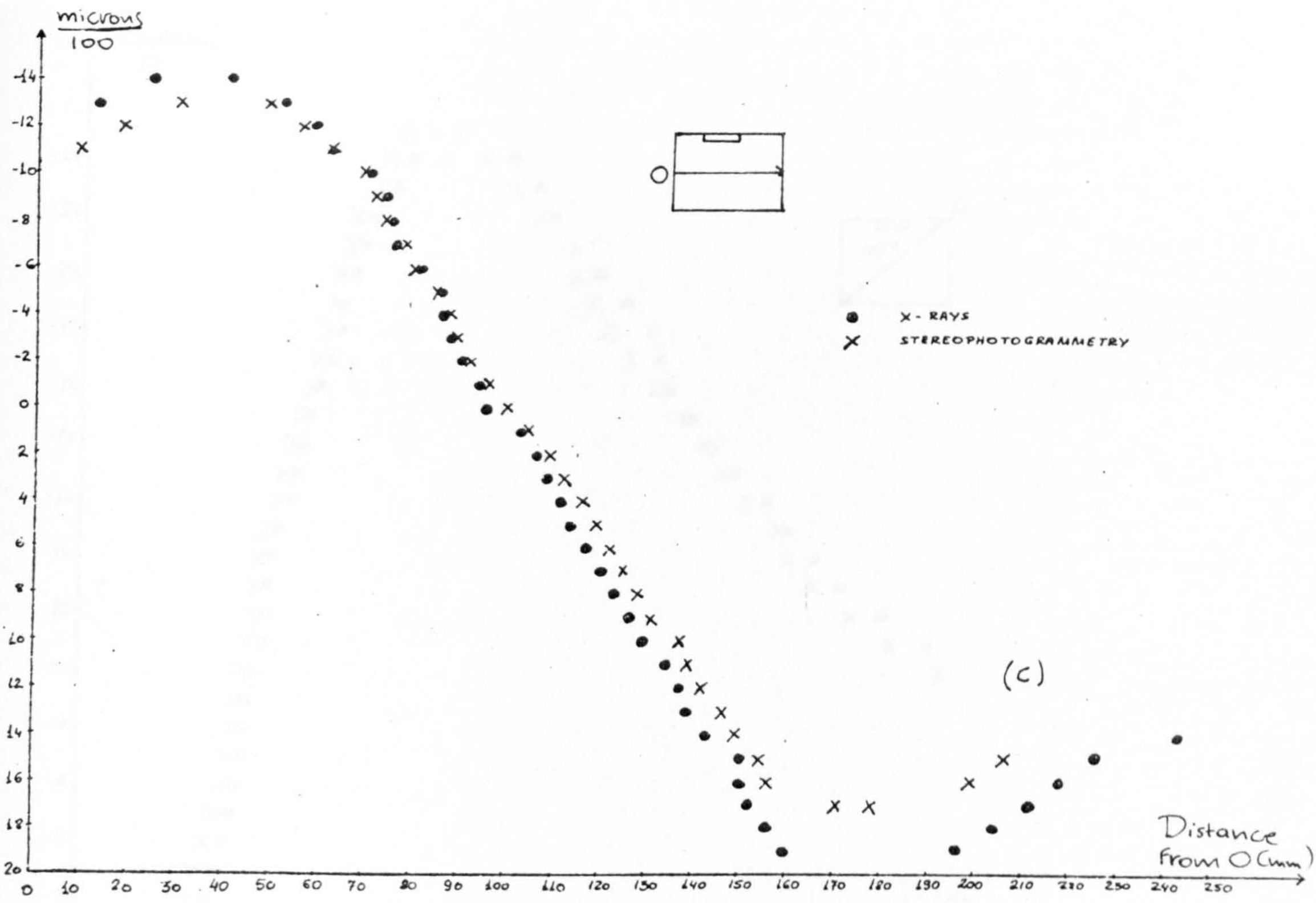

Fig. 7.42 Cross-sections of the horizontal displacement fields obtained by XRT and SP. (c) Horizontal cross-section.

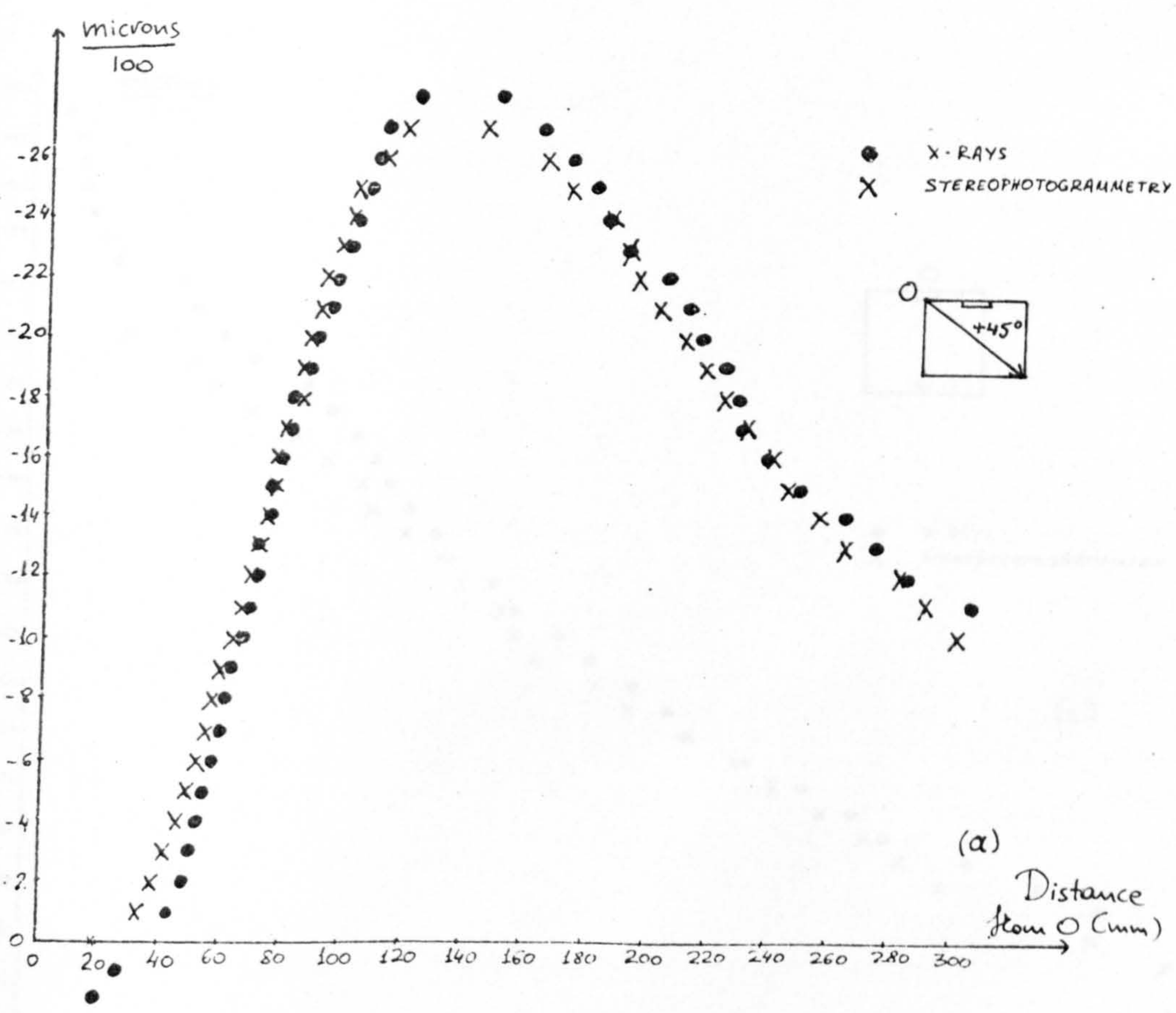

Fig. 7.43 Cross sections of the vertical displacement fields obtained by XRT and SP (a) $+45^{o}$.

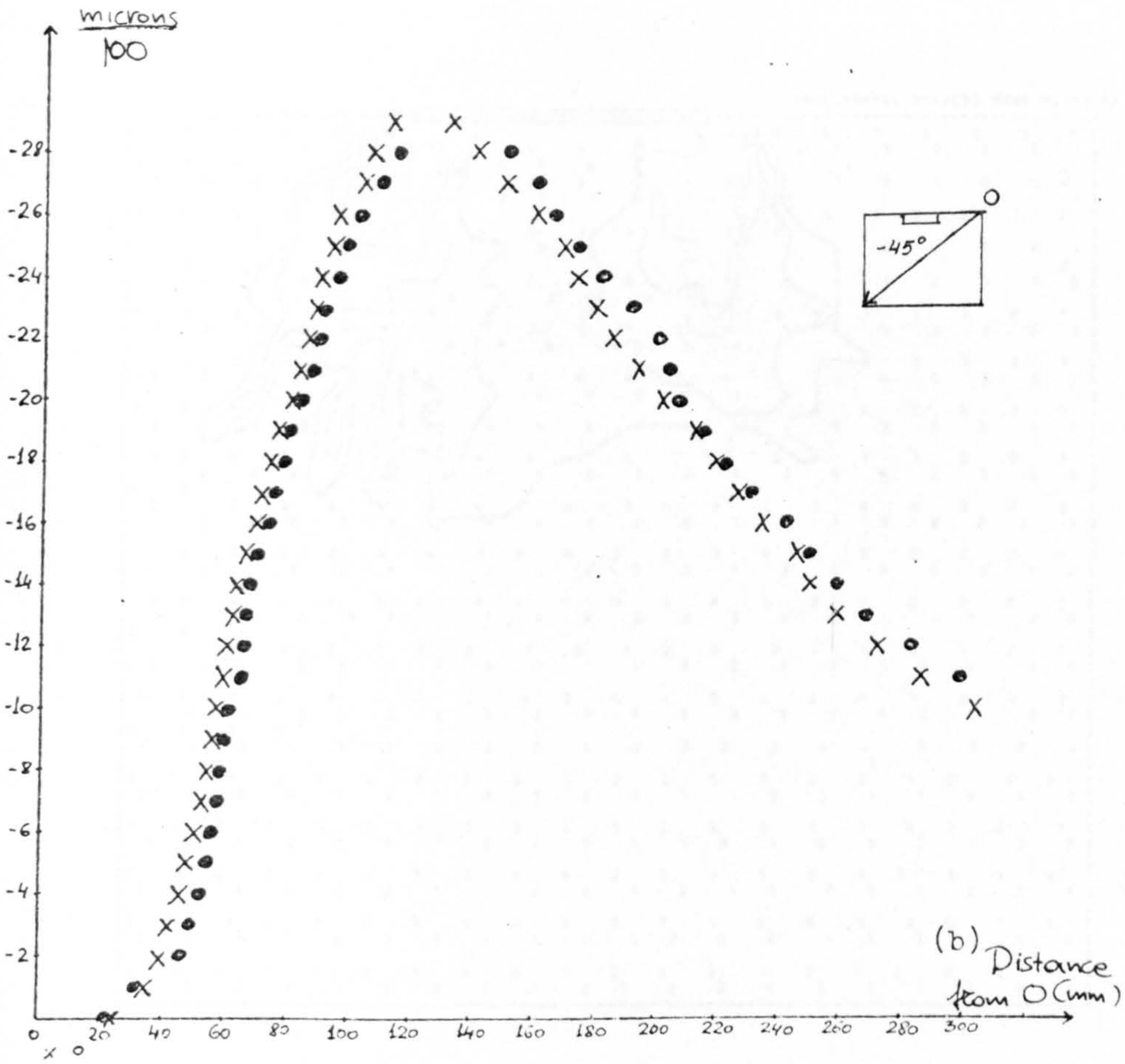

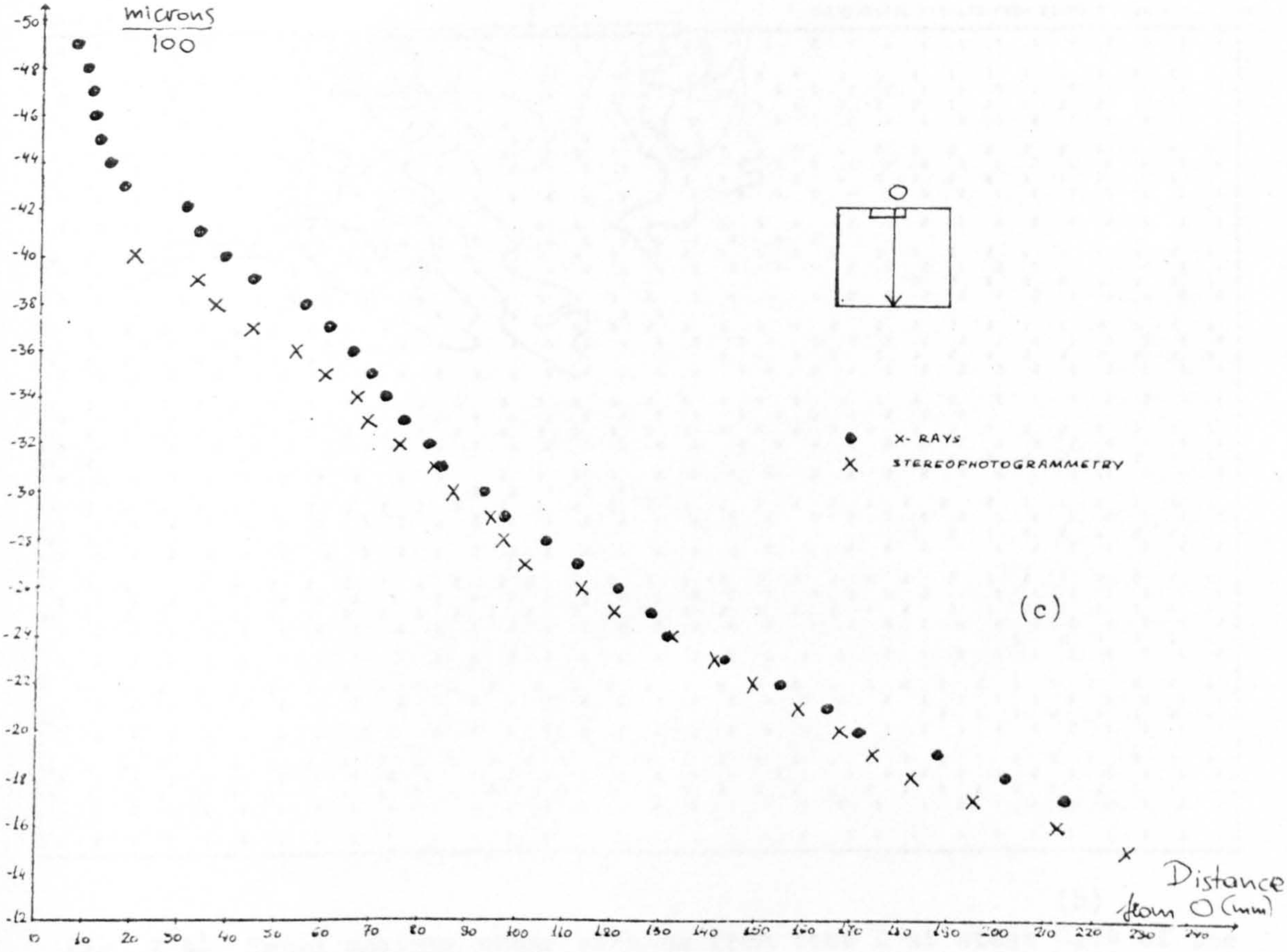

Fig. 7.43 Cross sections of the vertical displacement fields obtained by XRT and SP. (b) -45^{o} (c) vertical-symetrical cross-section.

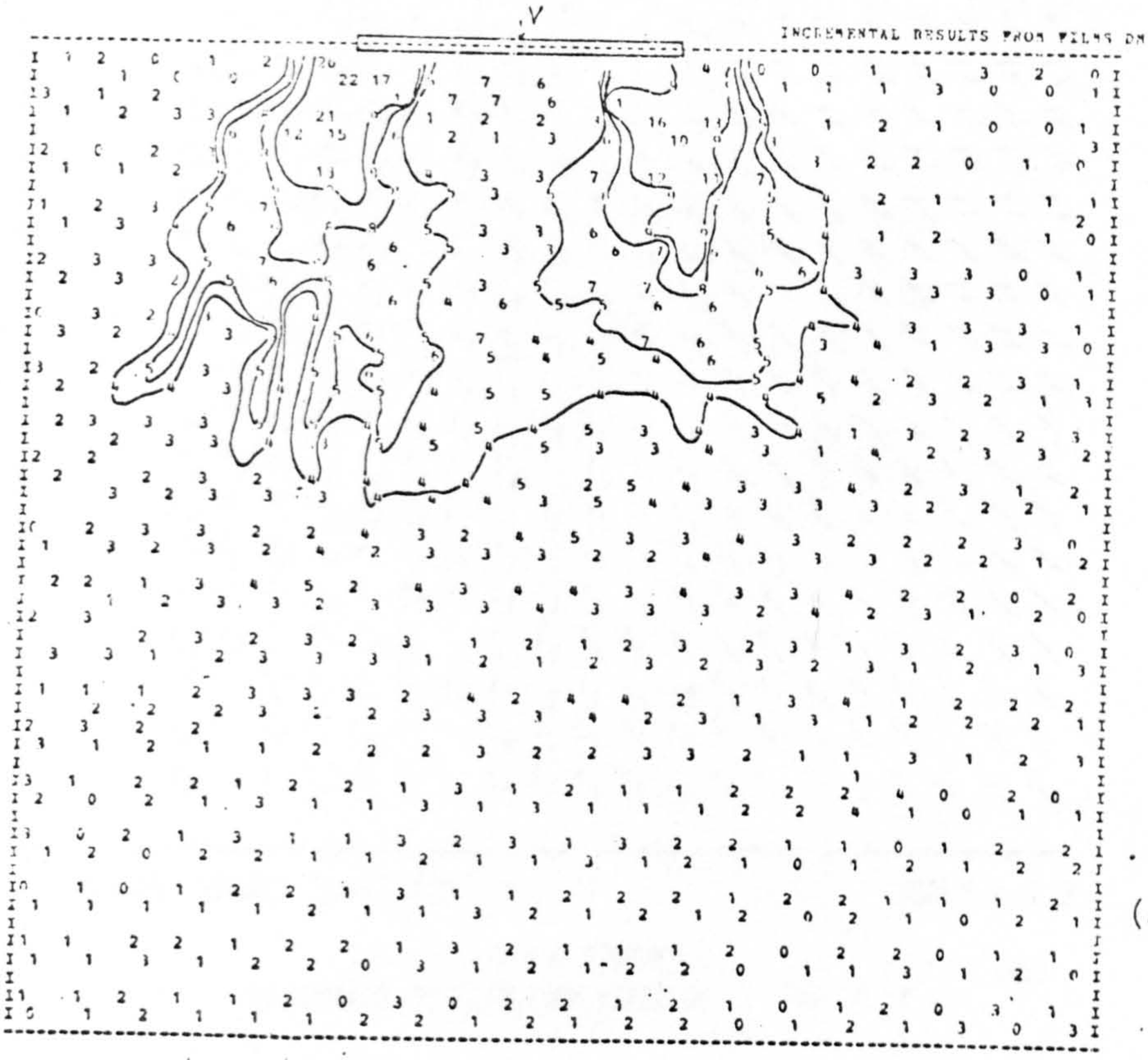

(a)

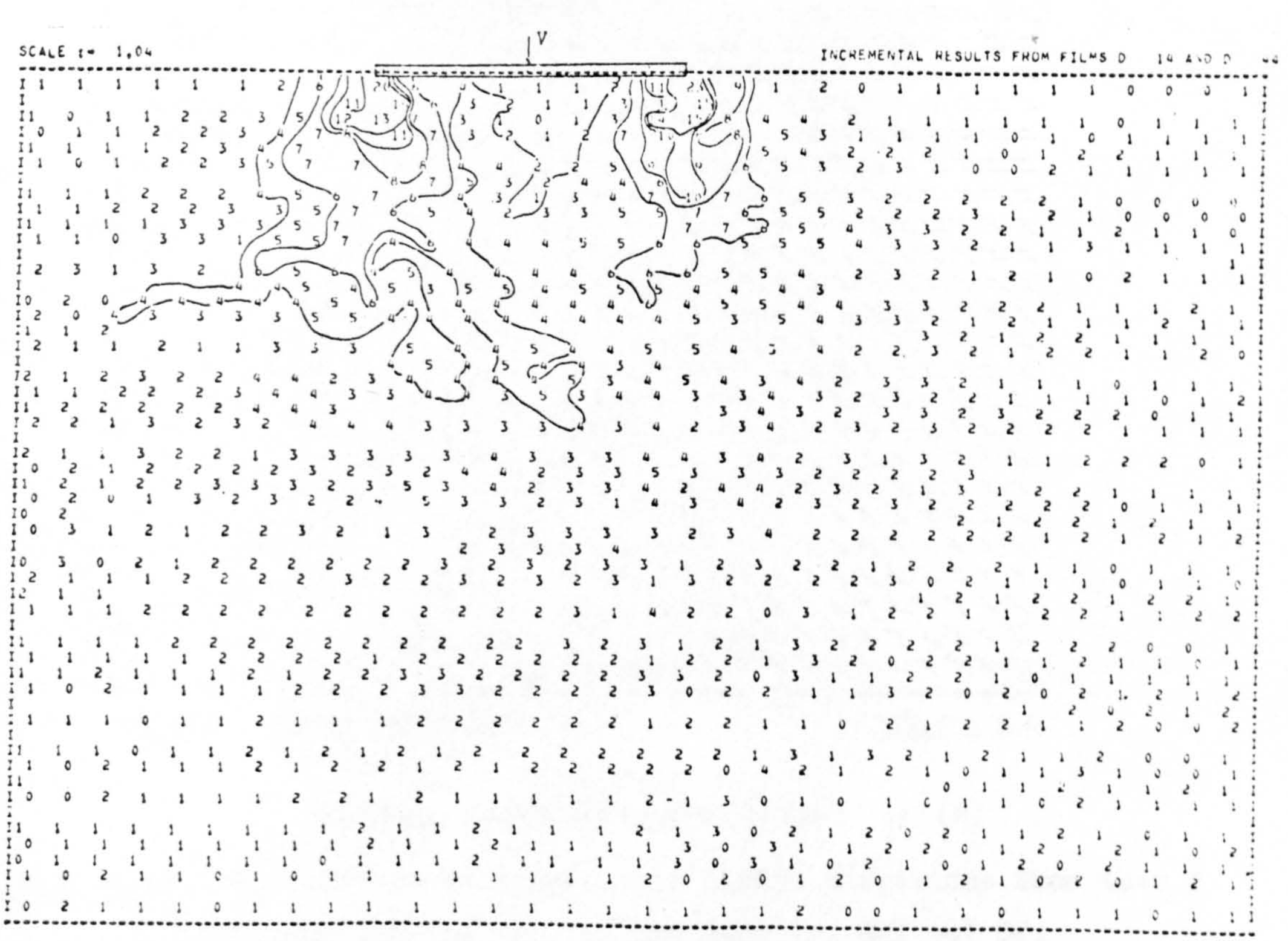

(b)

Fig. 7.44 Total maximum shear strains from test D at stage 0.74 of the failure load (a) x-Rays (b) Stereophotogrammetry.

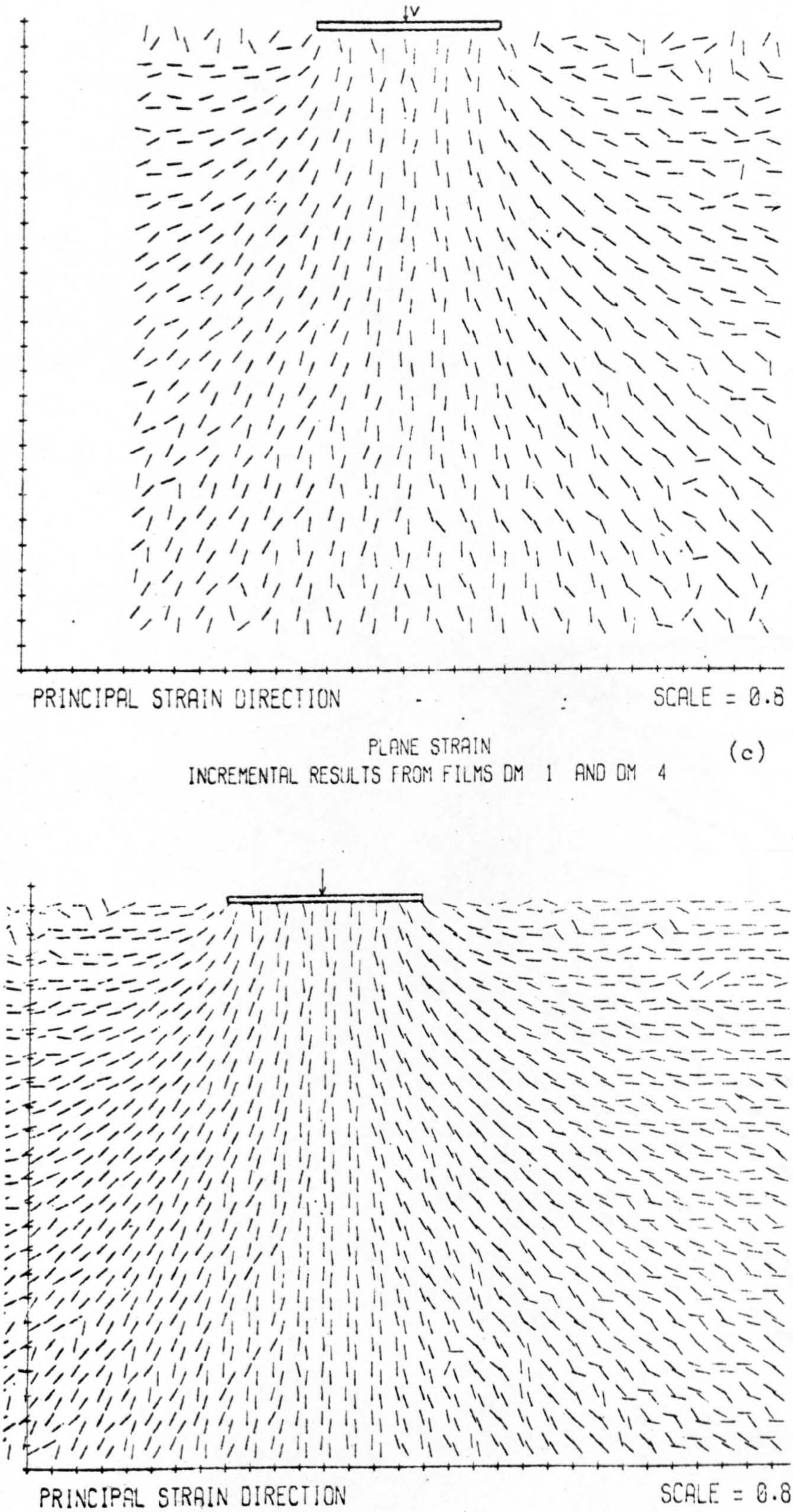

Fig. 7.44 Major principal compressive strain directions from test D at stage 0.74 of the failure load (c) XRT (d) SP.

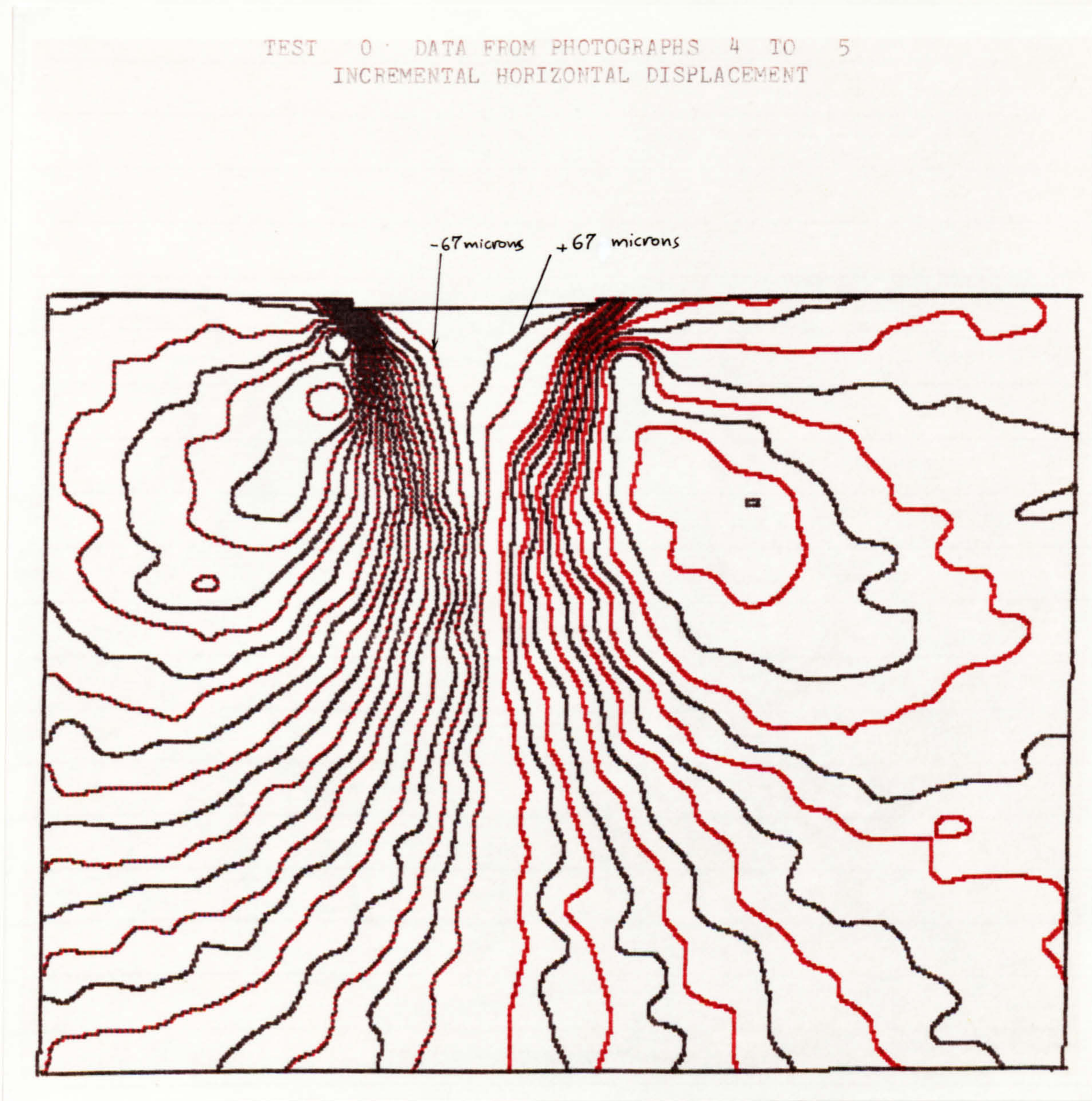

Fig. 7.45 Horizontal displacement field from test D between stages 0.74-0.93 of the failure load (Stereophotogrammetry).

Fig. 7.46 Vertical displacement field from test D between stages 0.74-0.93 of the failure load (Stereophotogrammetry).

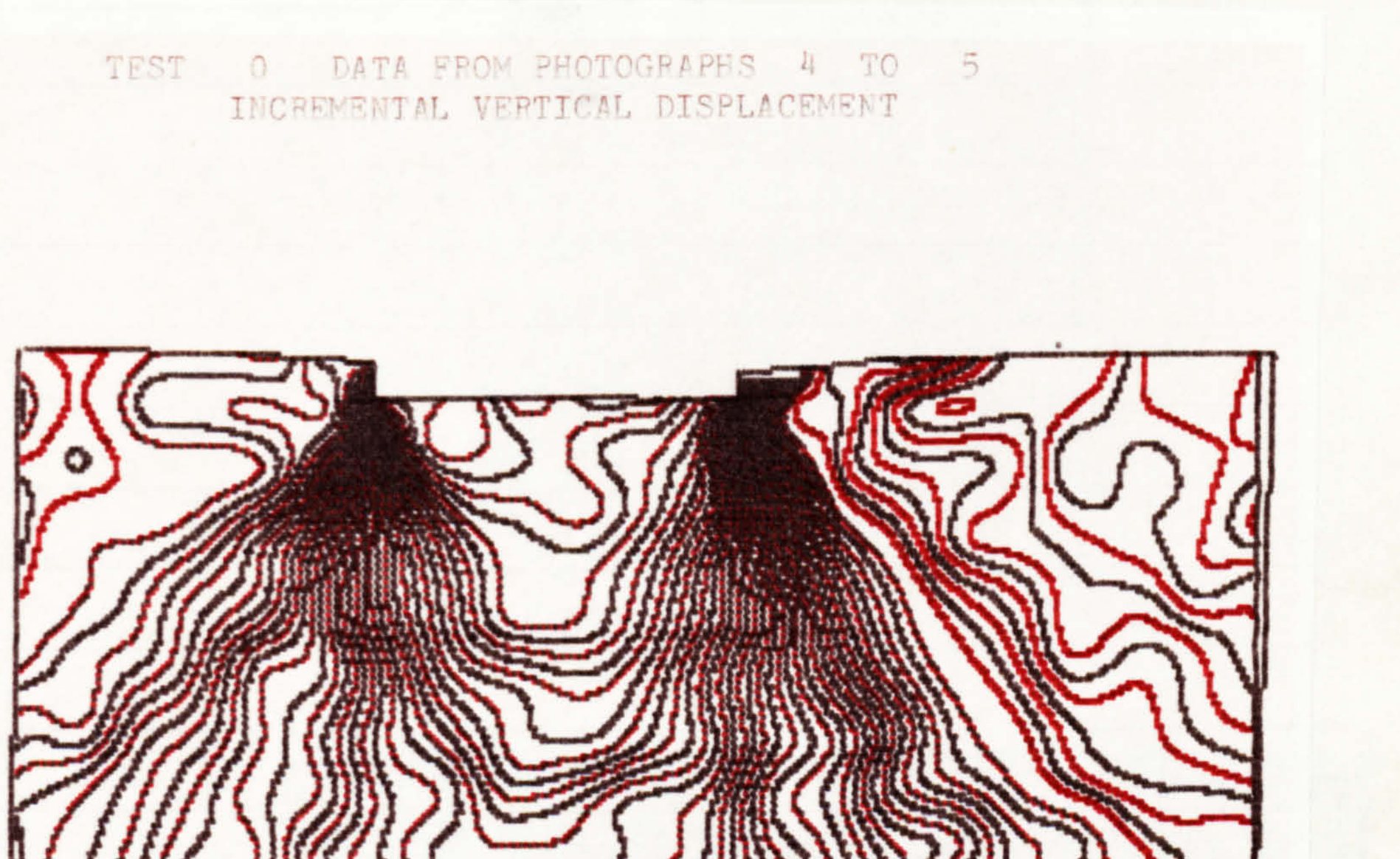

Fig. 7.47 Vertical displacement field from test D between stages 0.74-0.93 of the failure load (x-Rays).

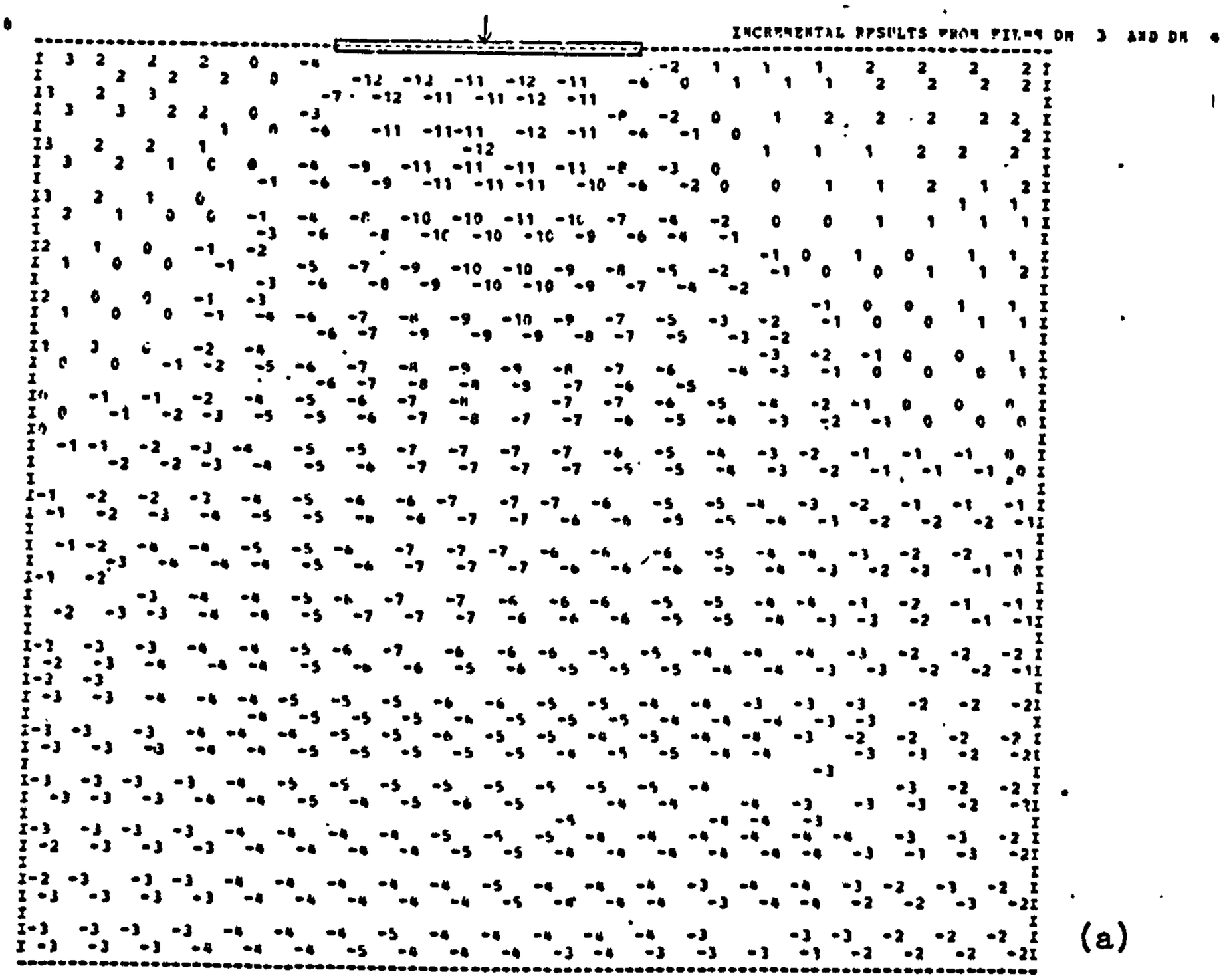

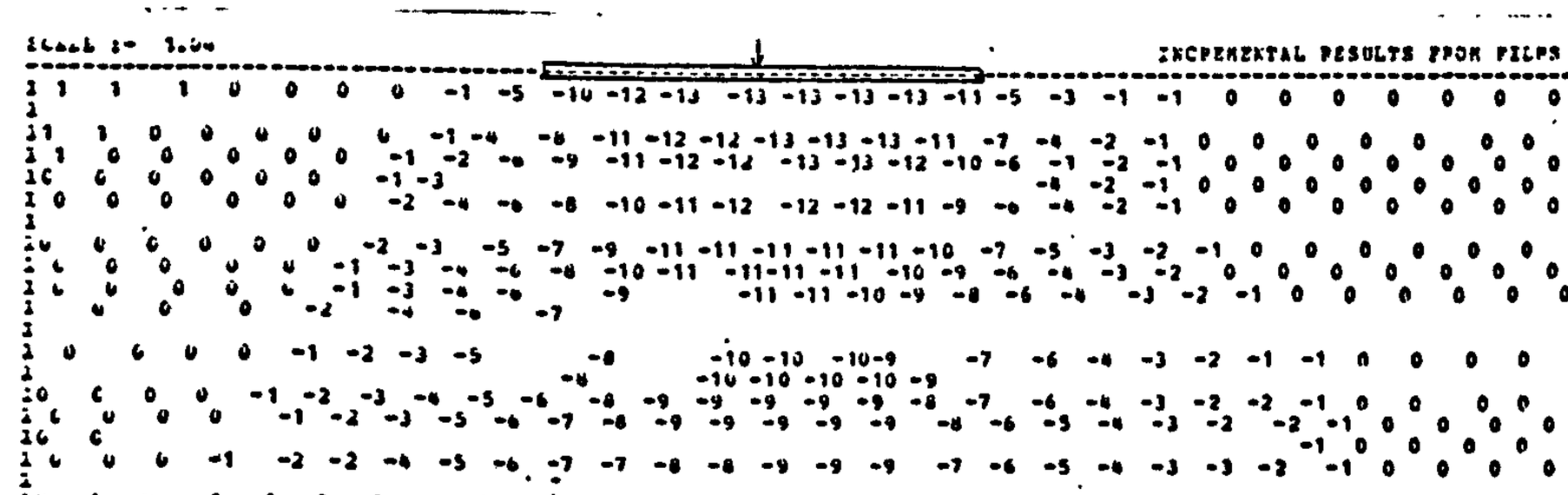

Fig. 7.48 Maximum shear strains from test D between stages 0.59-0.74 of the failure load (a) x-Rays (b) Stereophotogrammetry

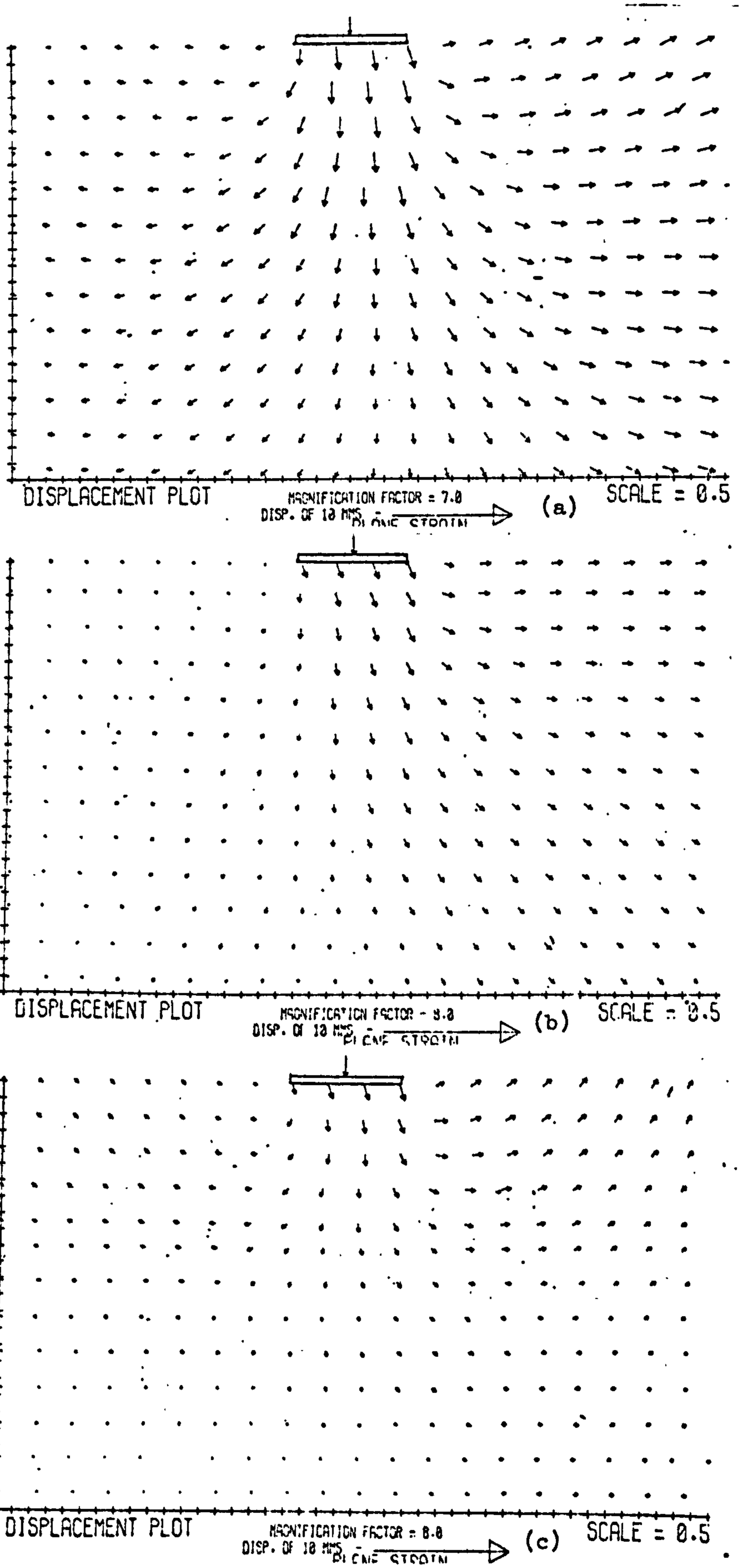

Fig. 7.49 Incremental displacement fields from test DS(e_o=0.53, α_o=0, E_o=0) in the FAS between stages:
(a) 0.0-0.67 (b) 0.67-0.86 (c) 0.86-0.98.

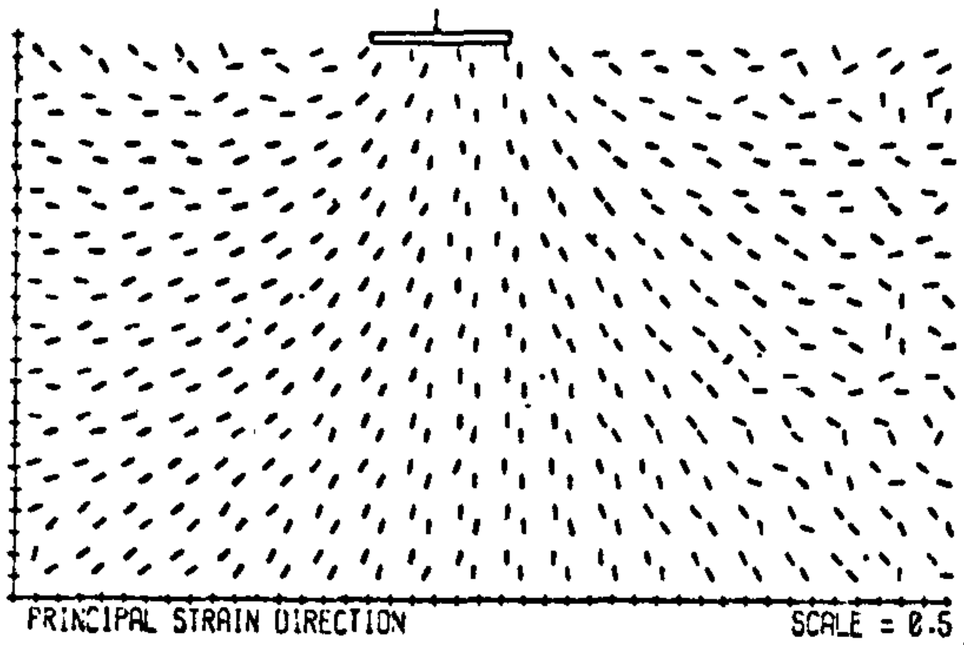

(a)

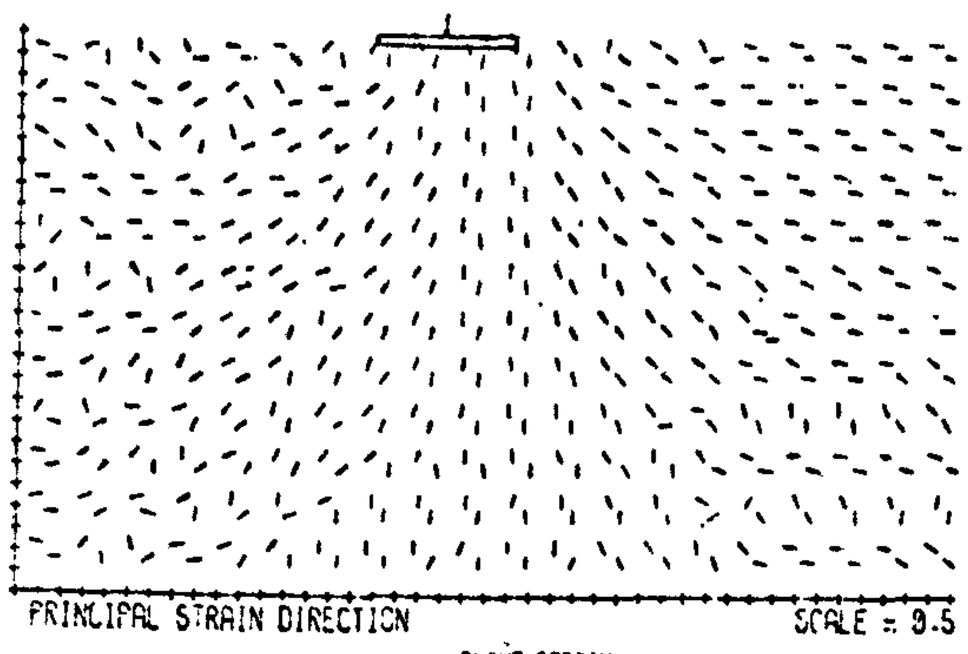

(b)

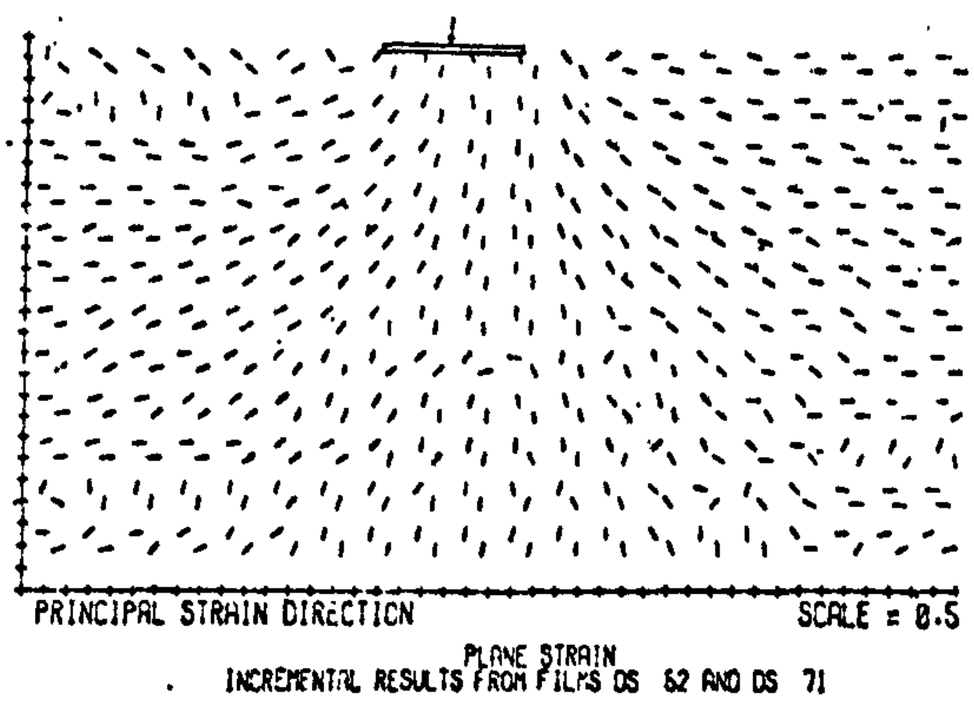

(c)

Fig. 7.50 The major principal compressive strain rate directions from test DS between stages (a) 0.0-0.67 (b) 0.67-0.86 and (c) 0.86-0.98.

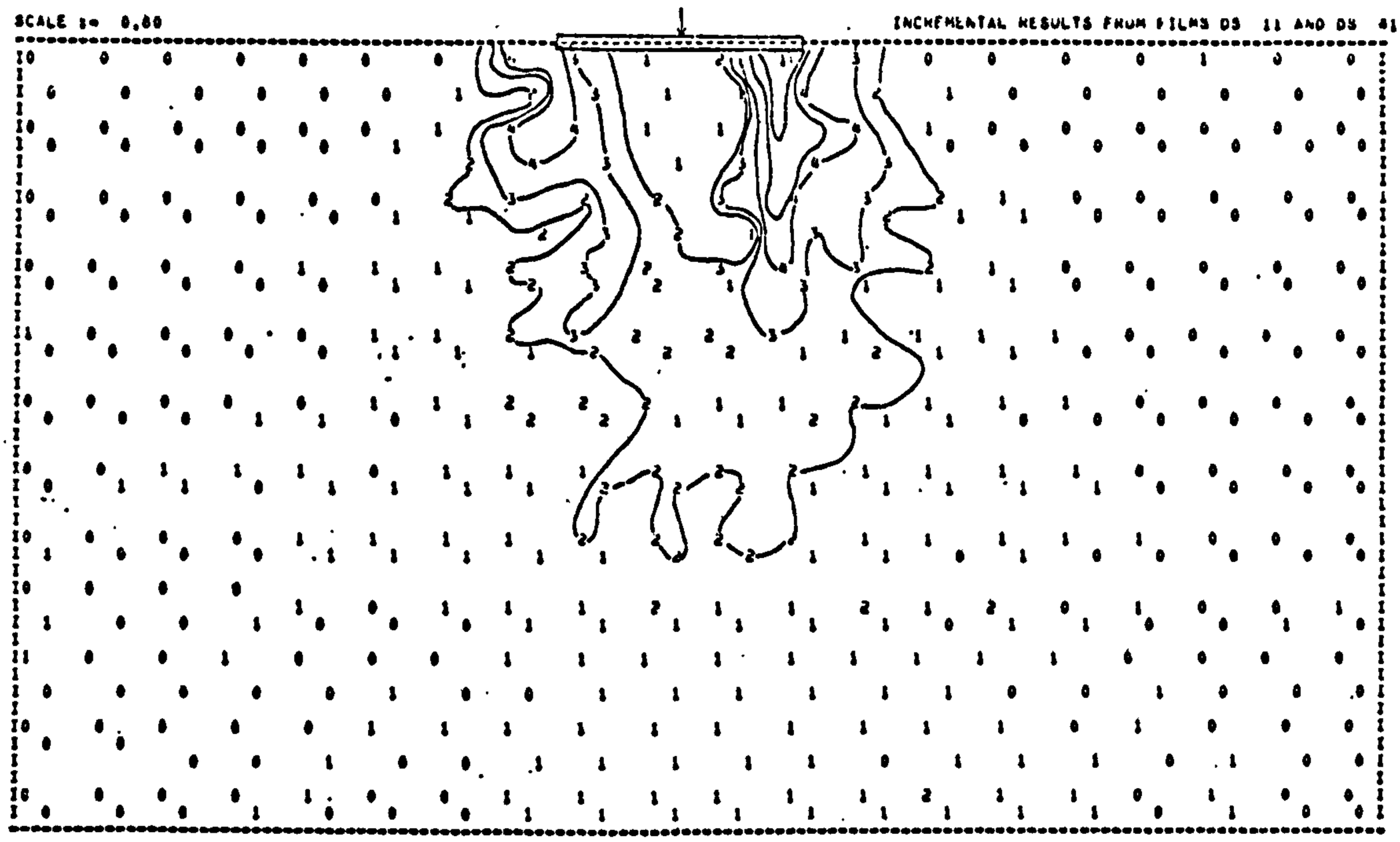

(a)

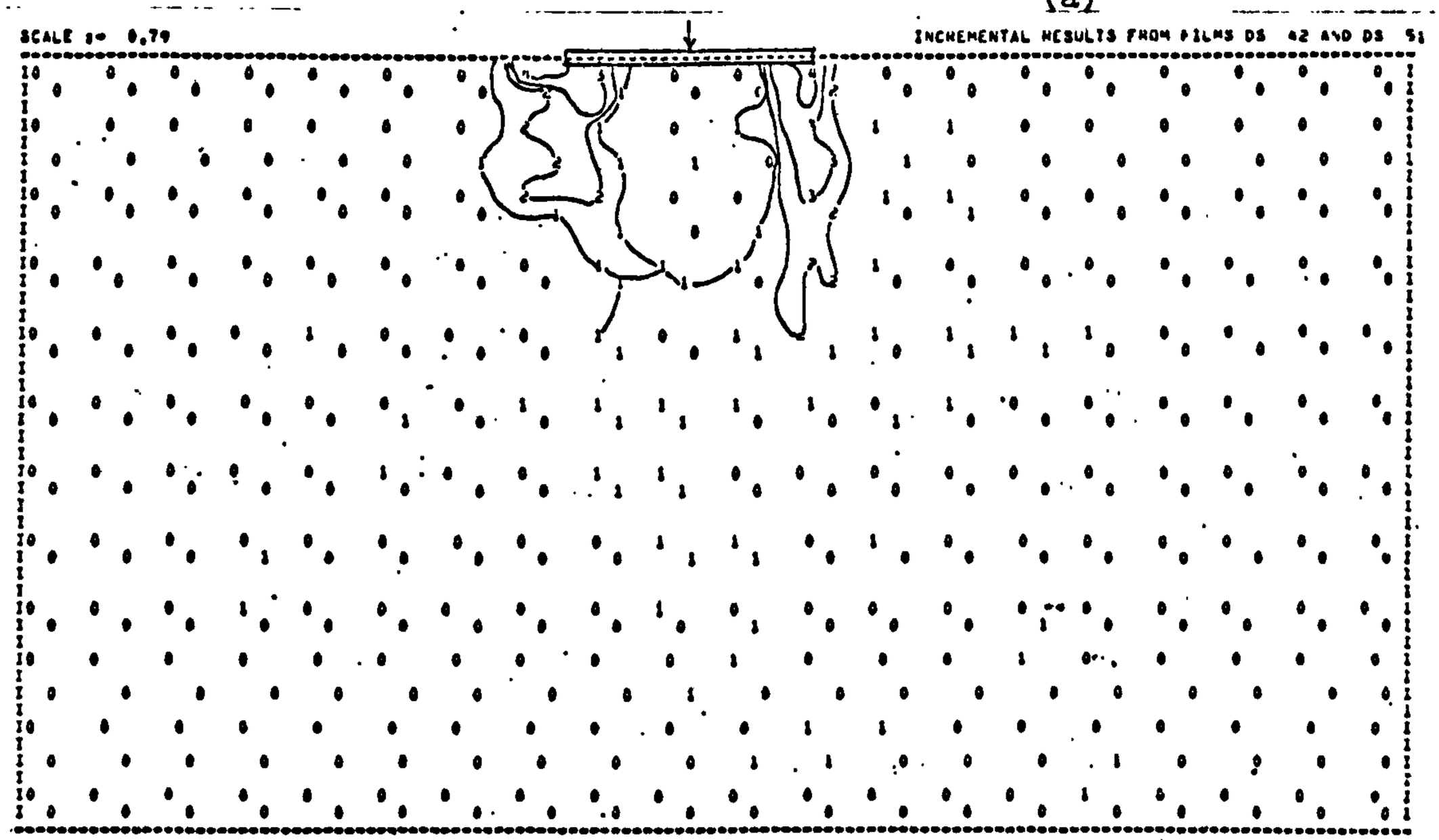

(b)

Fig. 7.51 Maximum shear strains from test DS (FAS) between stages (a) 0.0-0.67 (b) 0.67-0.86.

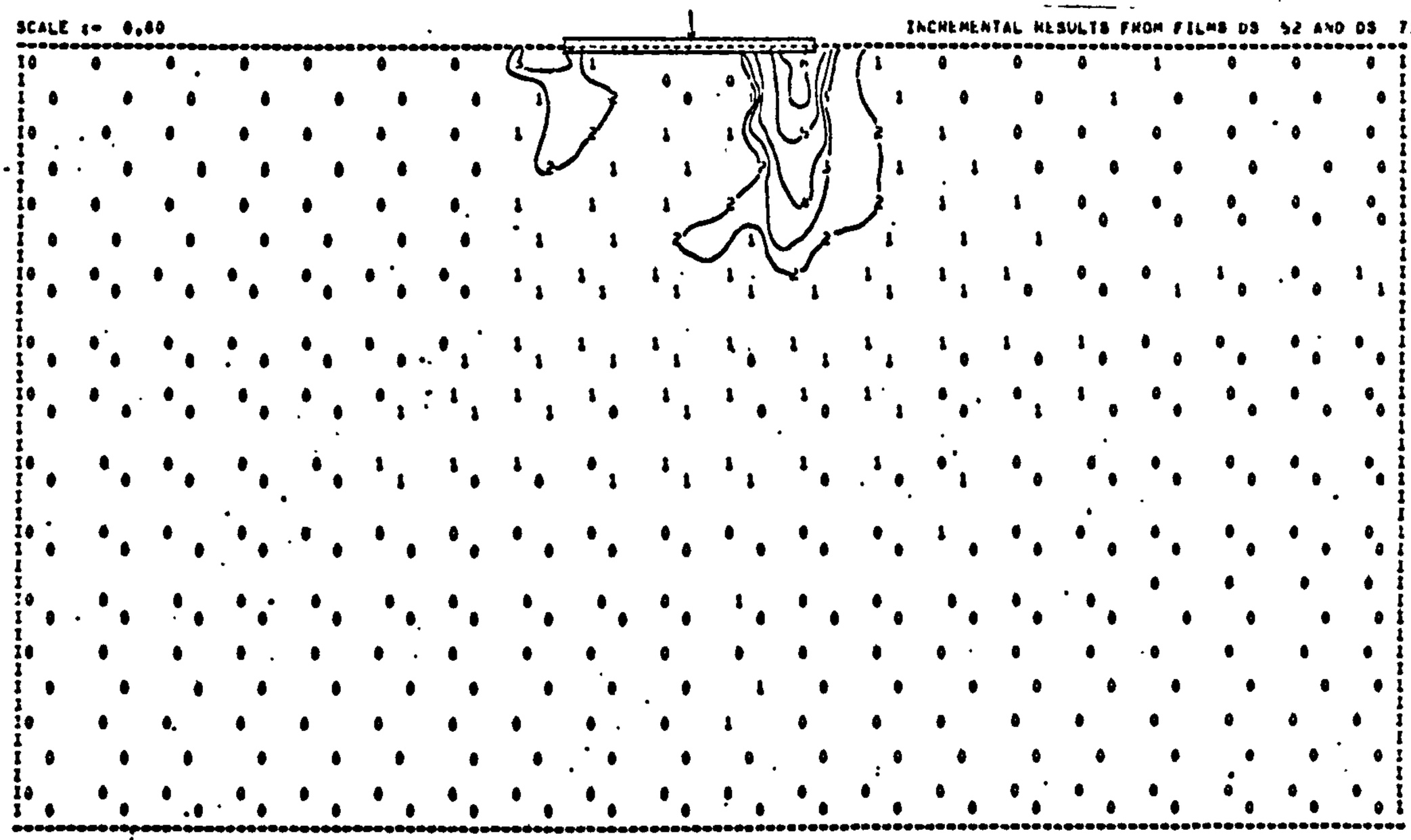

(c)

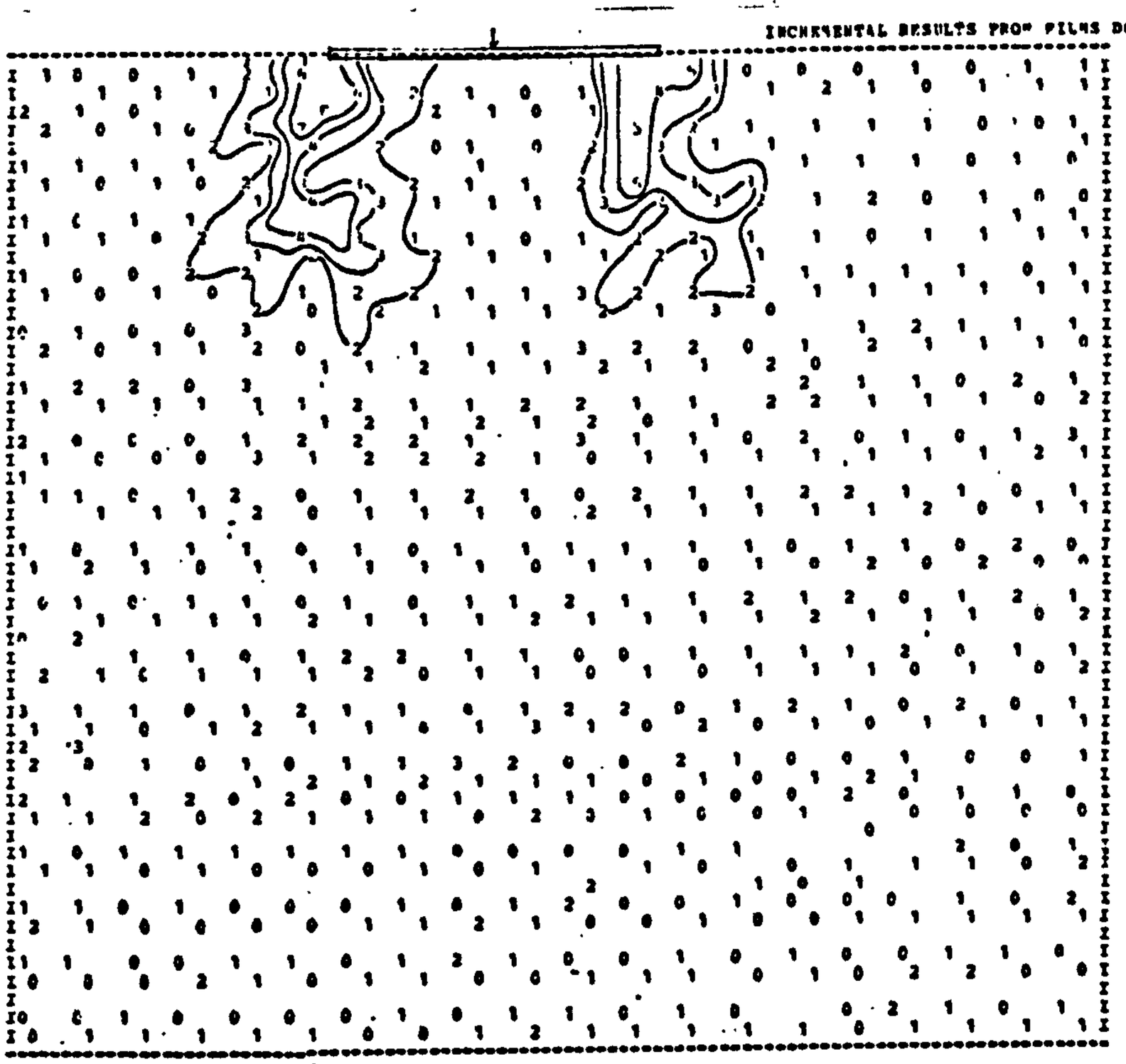

(d)

Fig. 7.51 Maximum shear strains from test DS (FAS) between stages (c) 0.86-0.98 of the failure load (d) maximum shear strains from test D (FAC) between stages 0.59-0.74.

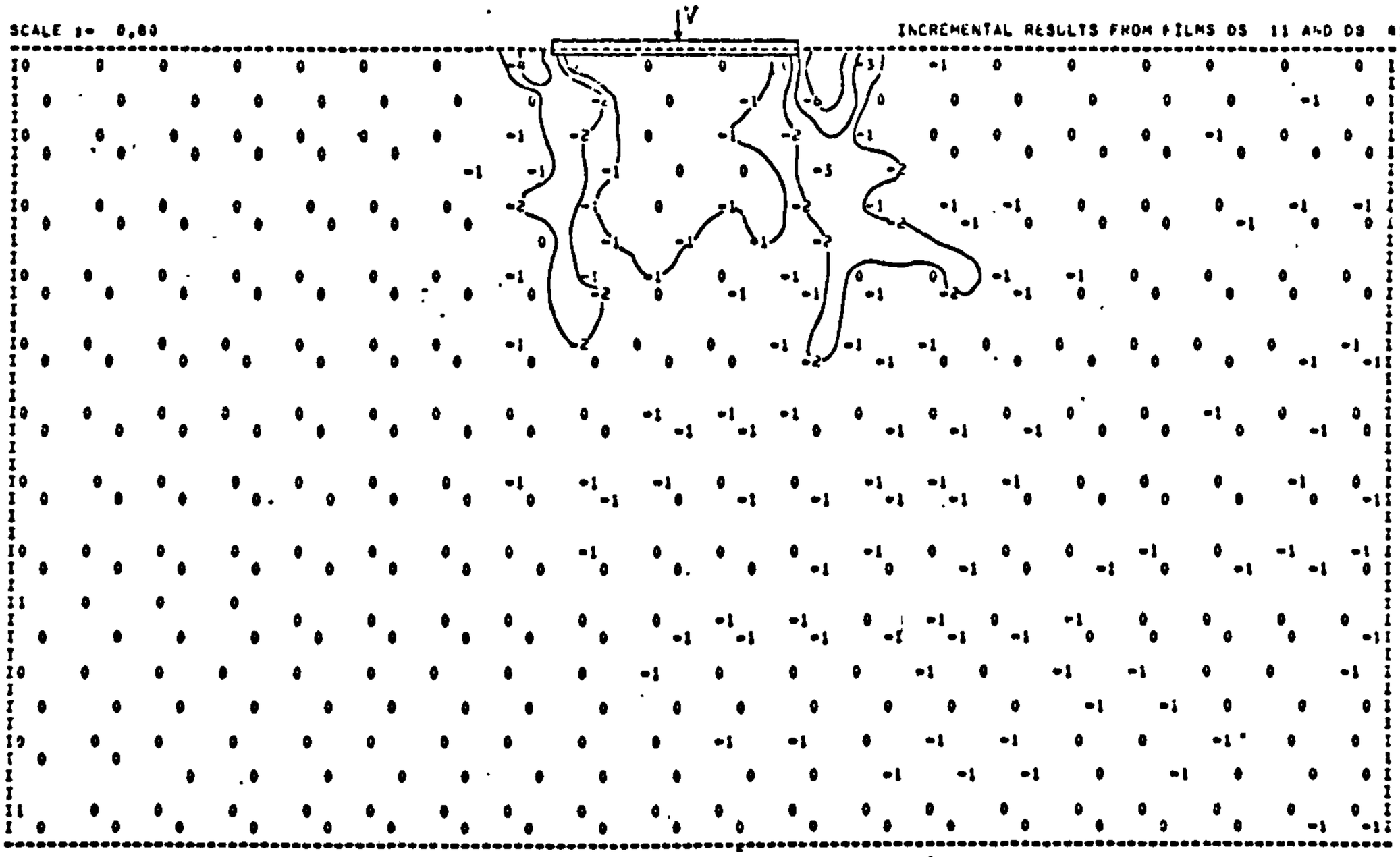

Fig. 7.52 The volumetric strains from test DS(FAS) between stages 0.0-0.67 of the failure load.

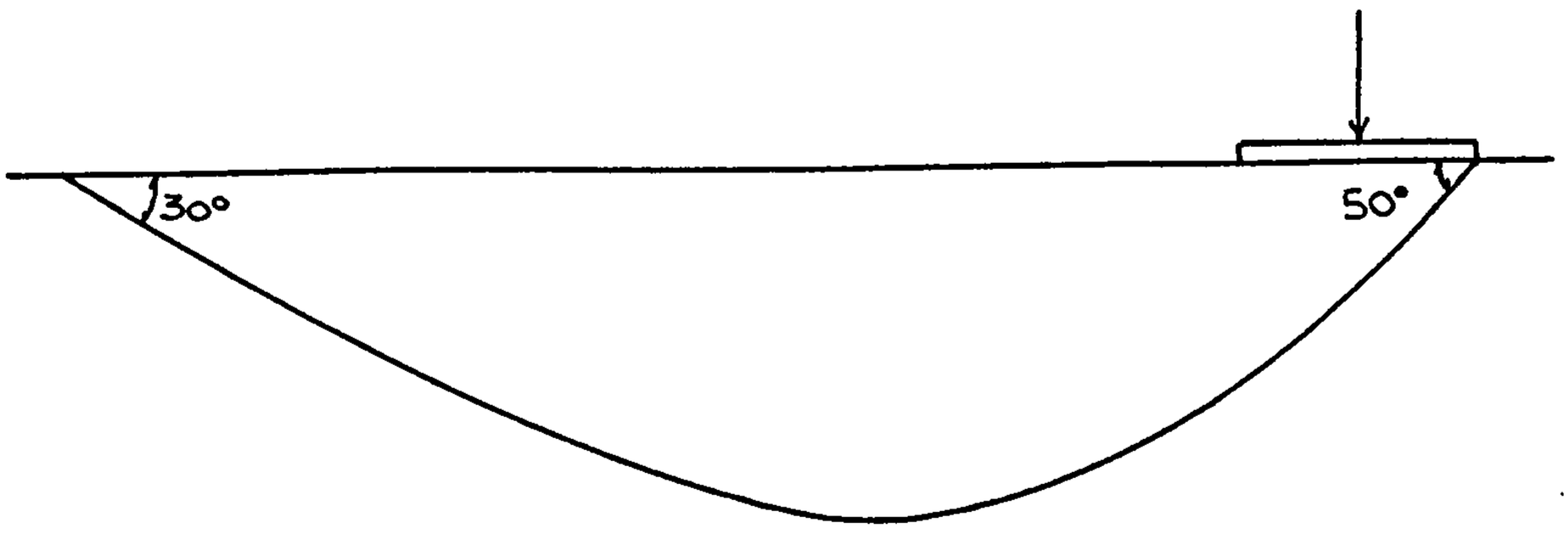

Fig. 7.53 The failure surface in test DS(e_o=0.53,α_o=0,E_o=0).

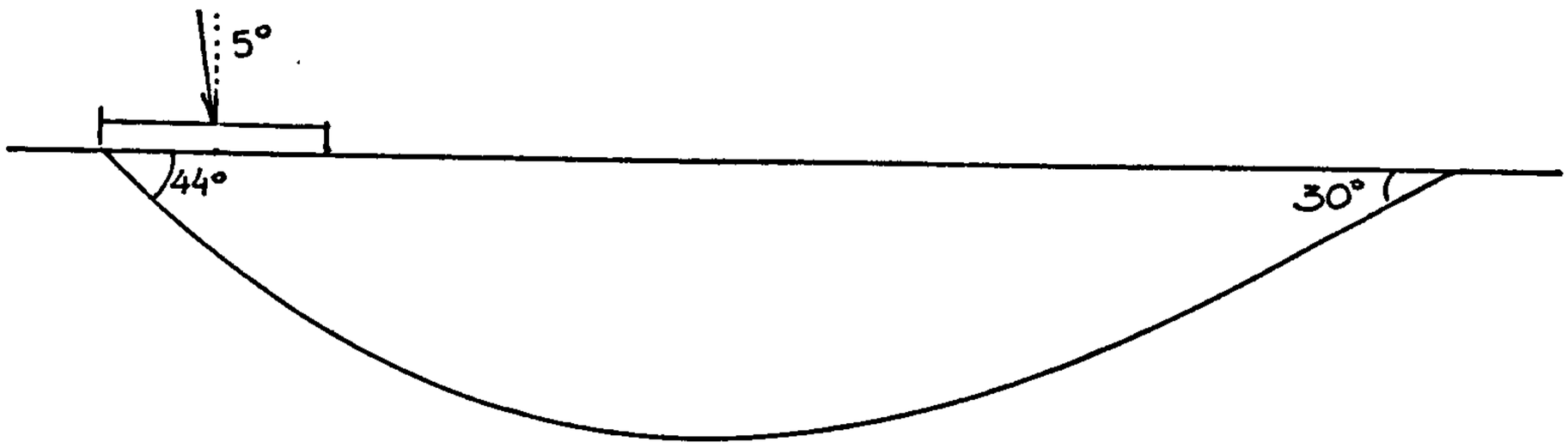

Fig. 7.54 The failure surface in tests RS(e_o=0.54,α_o=5°).

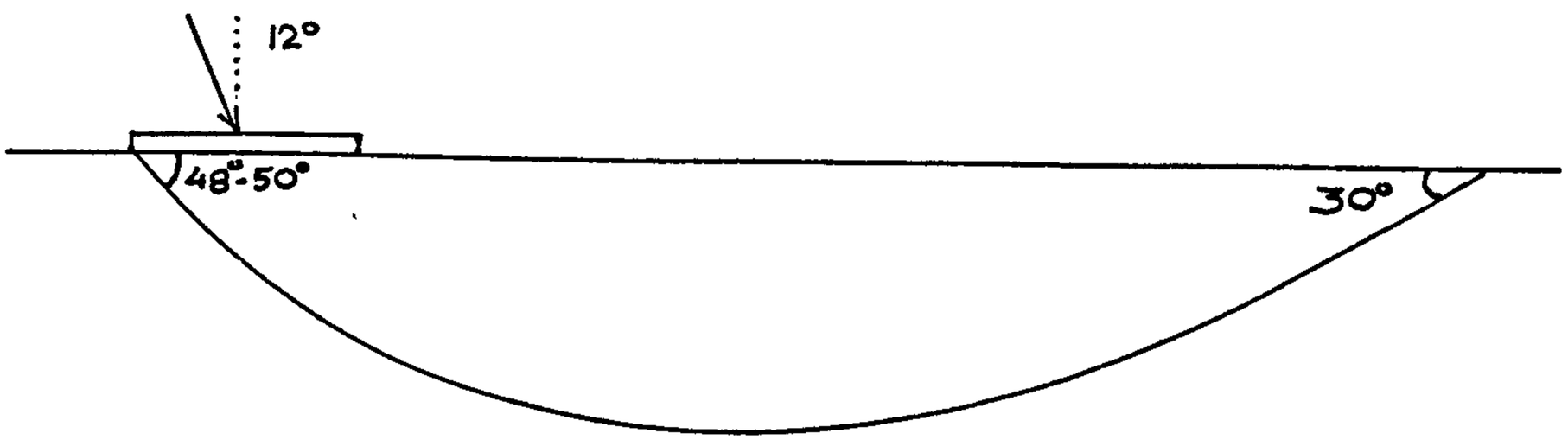

Fig. 7.55 The failure surface in test BS(e_o=0.53,α_o=12°).

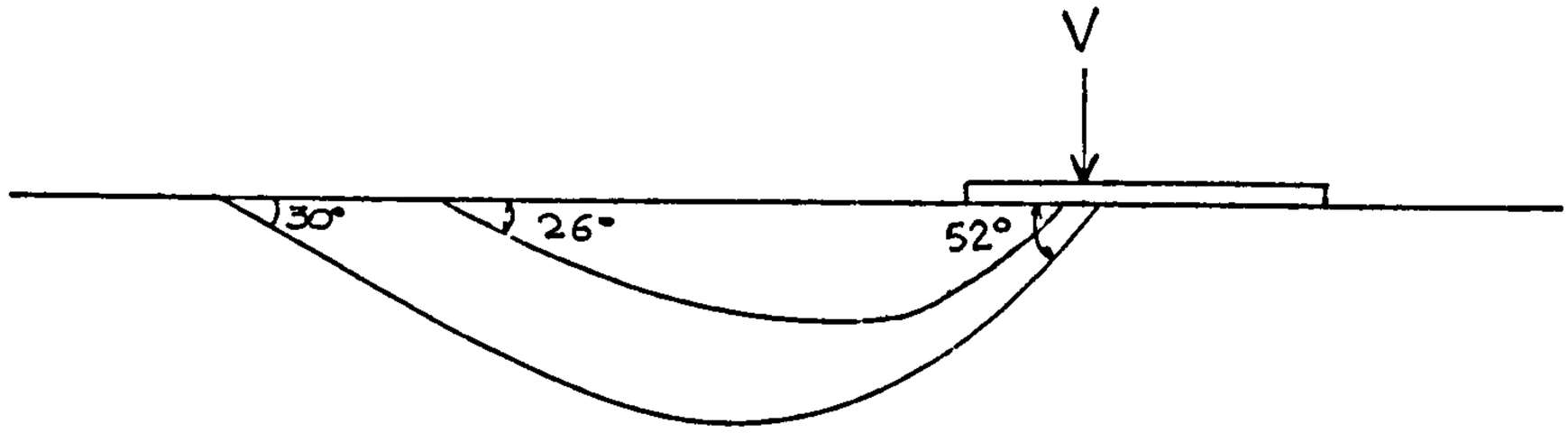

Fig. 7.56 The failure surface in test AS(e_o=0.54,F_o=0.167).

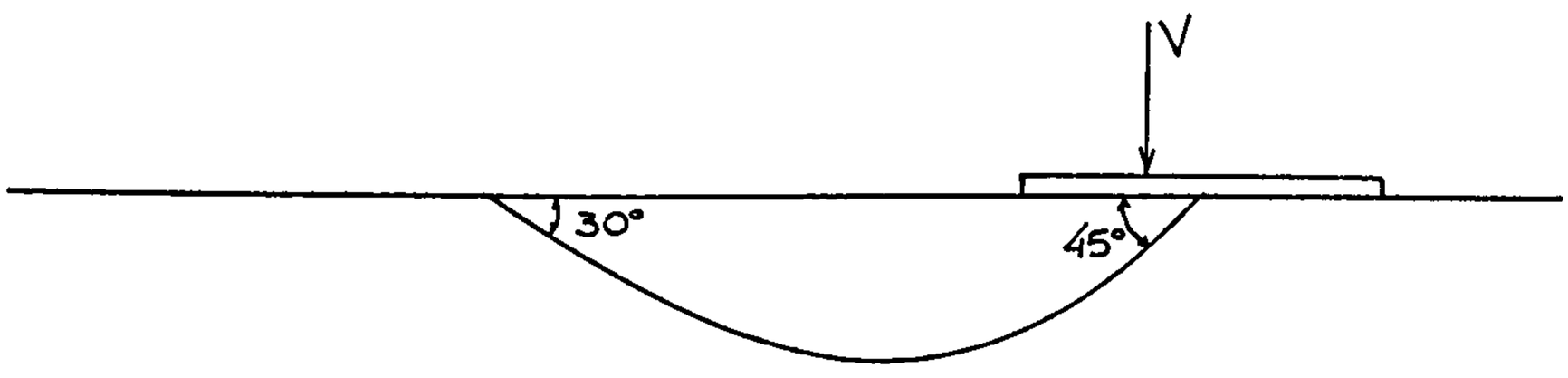

Fig. 7.57 The failure surface in test HS(e_o=0.53,E_o=0.167).

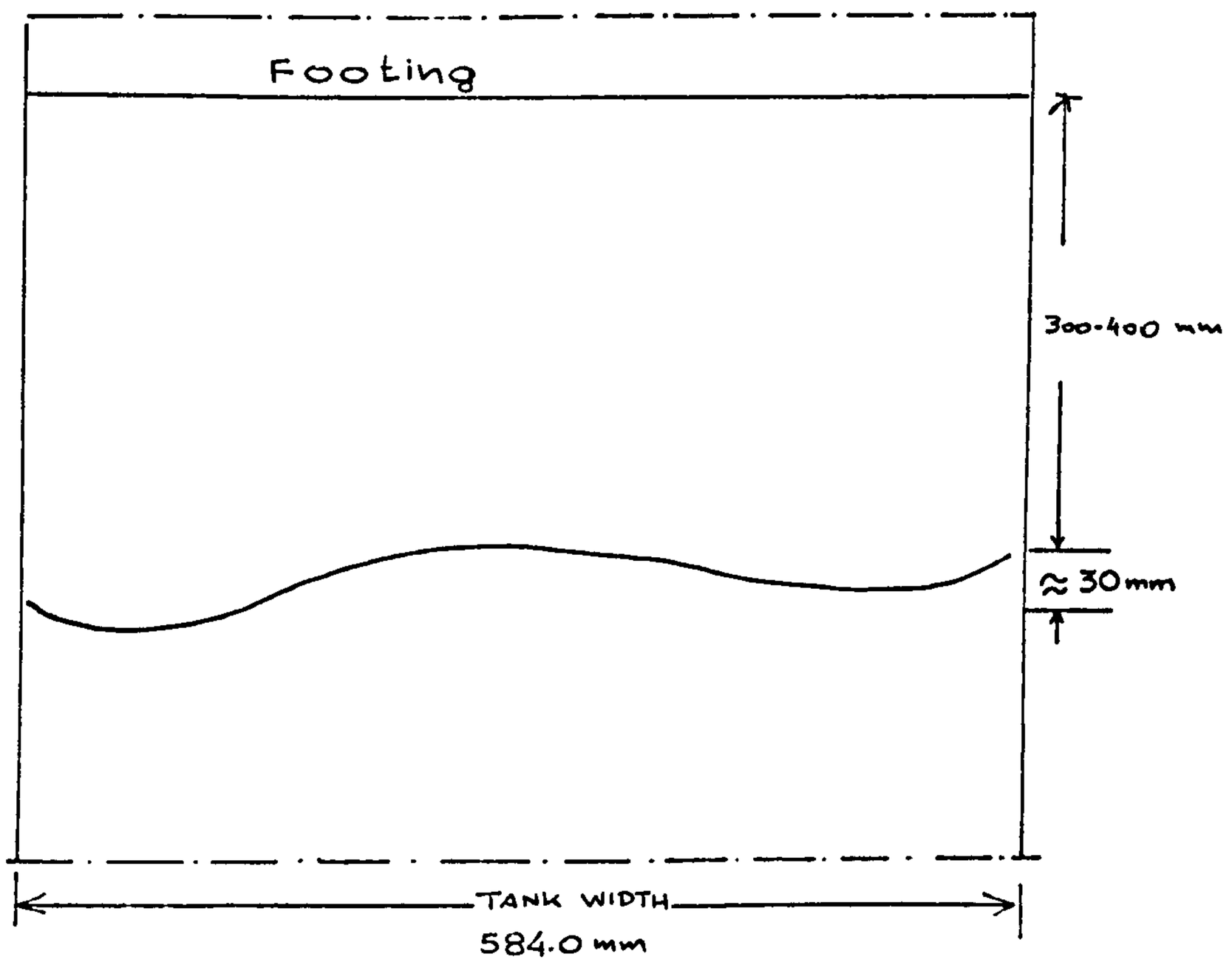

Fig. 7.58 The typical shape of the failure surface outcrop from tests in the FAS.

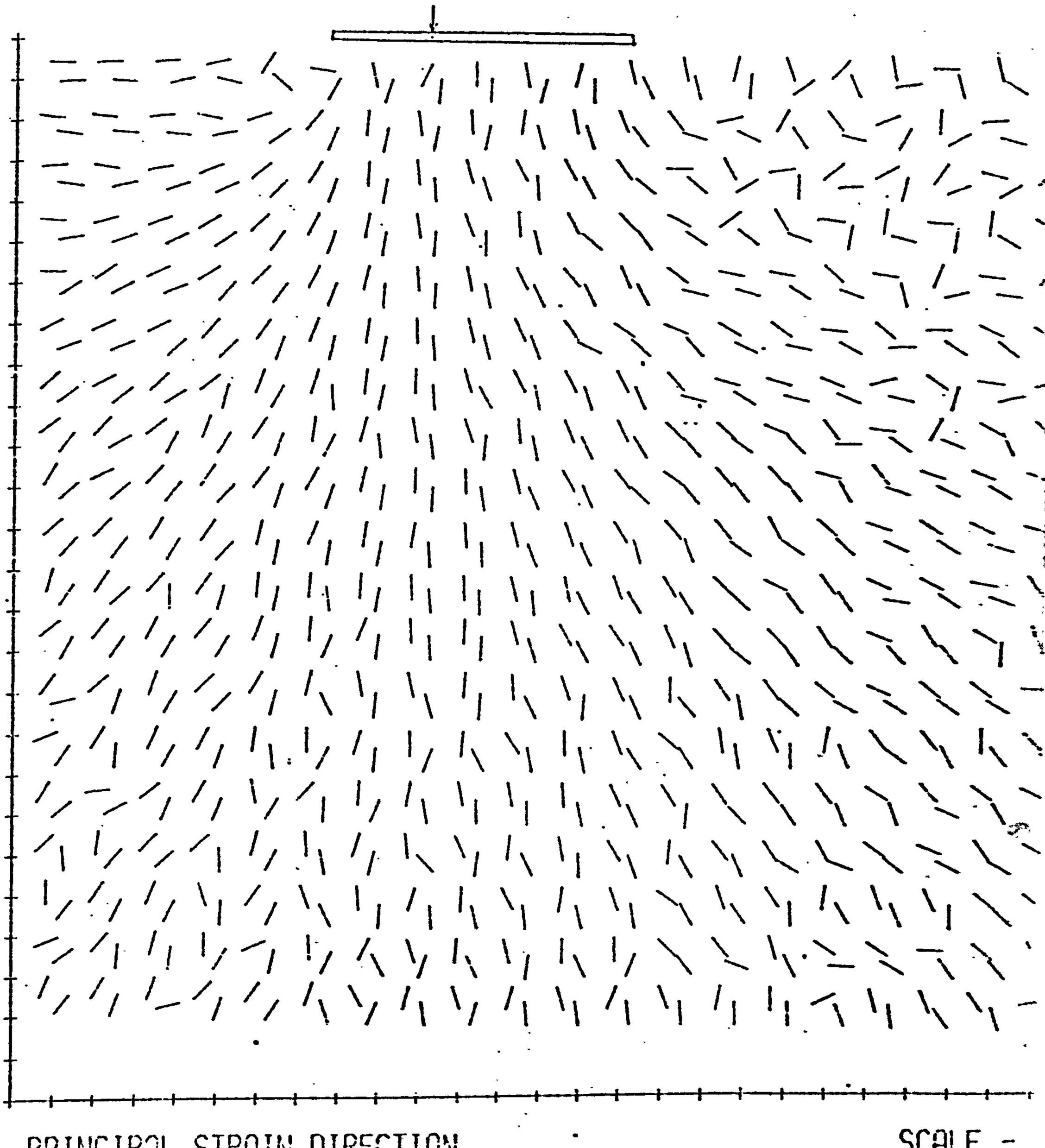

PRINCIPAL STRAIN DIRECTION

SCALE =

PLANE STRAIN

INCREMENTAL RESULTS FROM FILMS MA 1 AND MA 3

TEST A

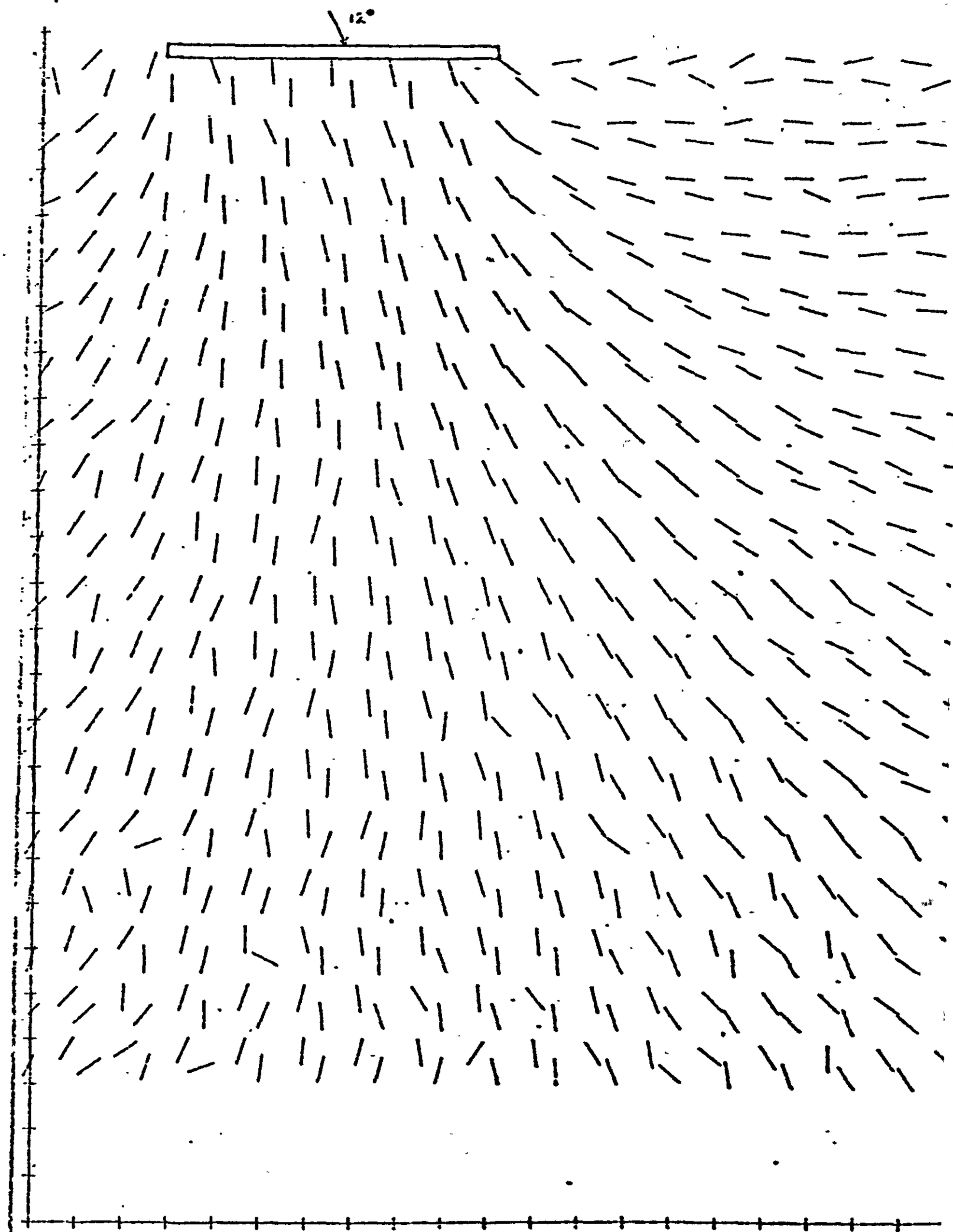

PRINCIPAL STRAIN DIRECTION

PLANE STRAIN

INCREMENTAL RESULTS FROM FILMS BM 1 AND B

TEST B

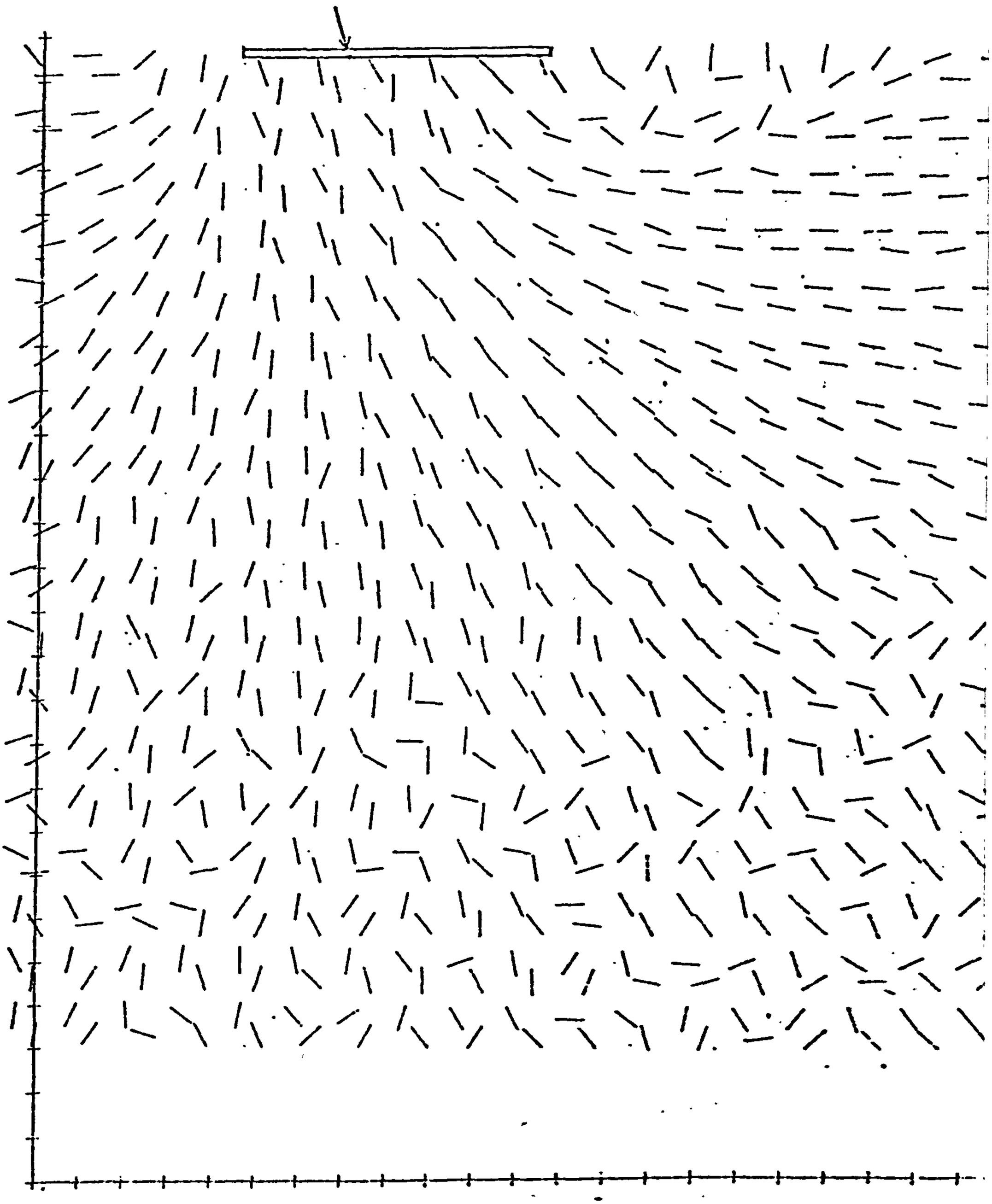

PRINCIPAL STRAIN DIRECTION

SCI

TEST C

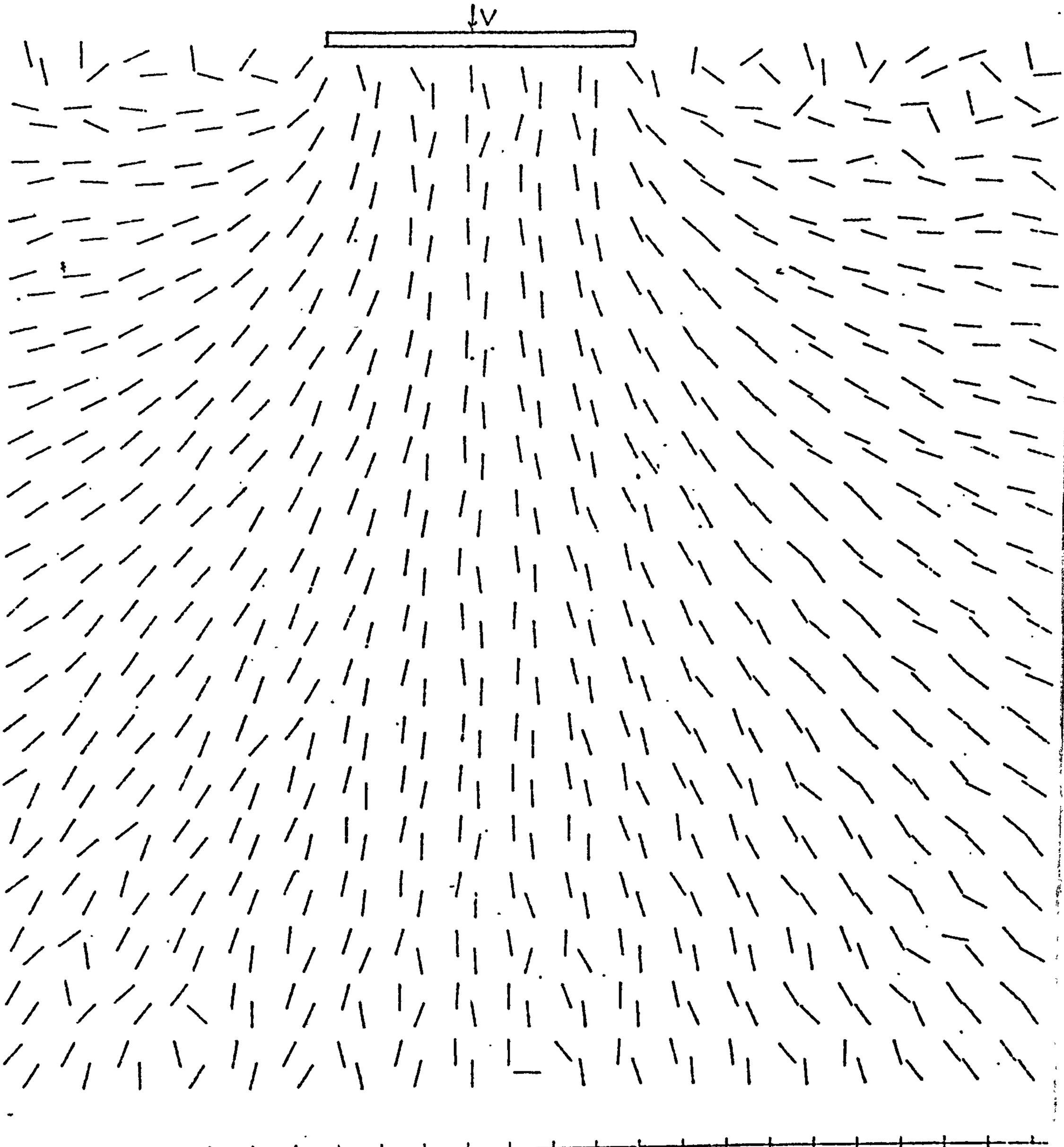

PLANE STRAIN

INCREMENTAL RESULTS FROM FILMS DM 1 AND DM 5

TEST D

Fig. 7.59

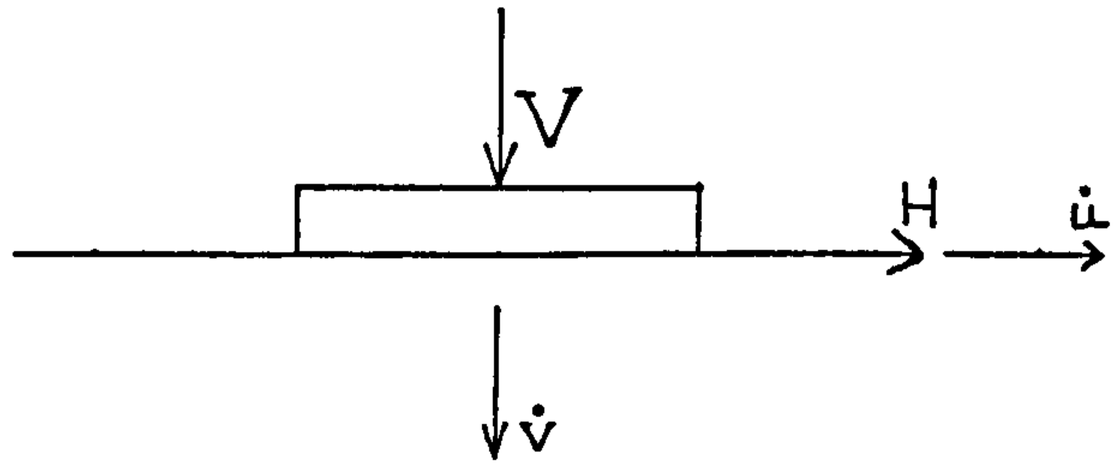

Fig. 8.1 Load and displacement axes.

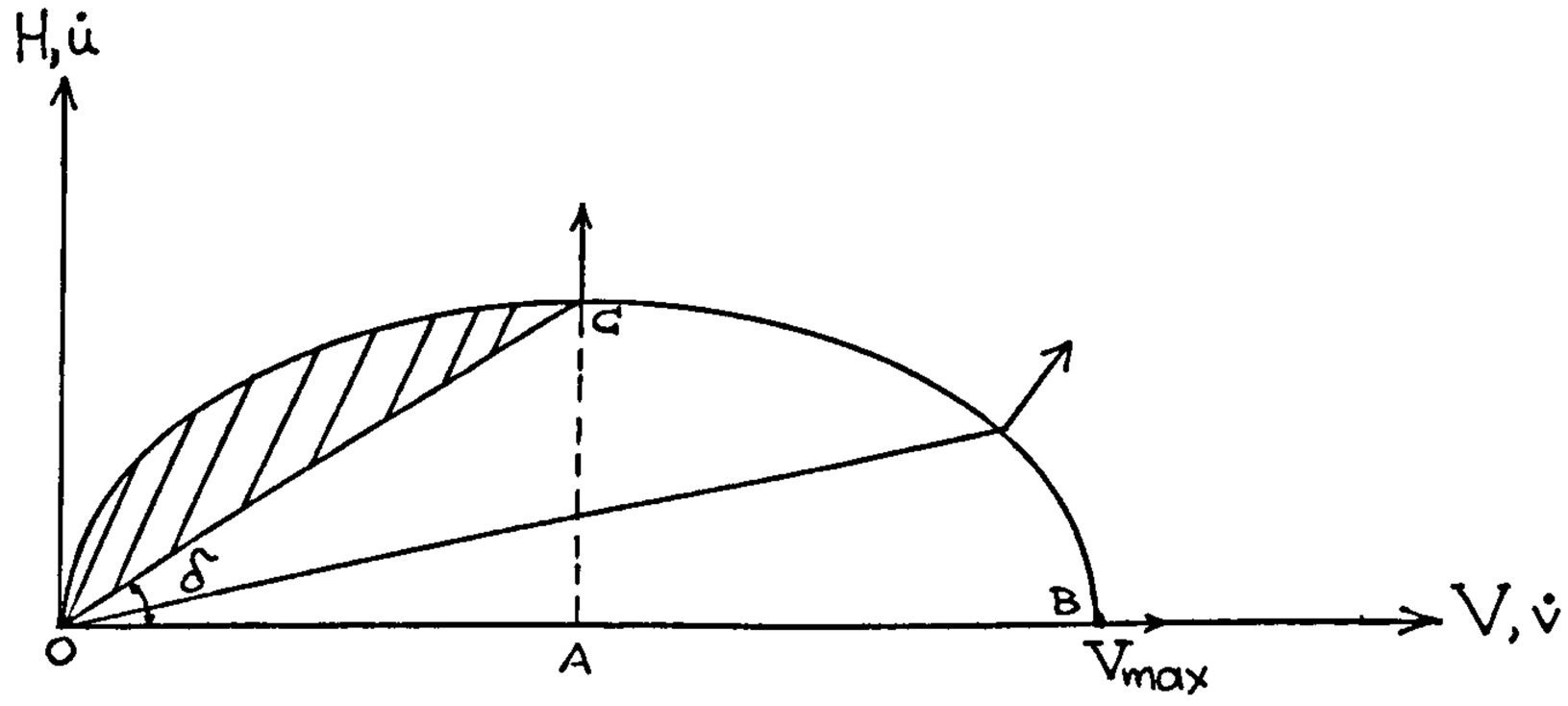

Fig. 8.2 Plastic potential for a footing on sand.

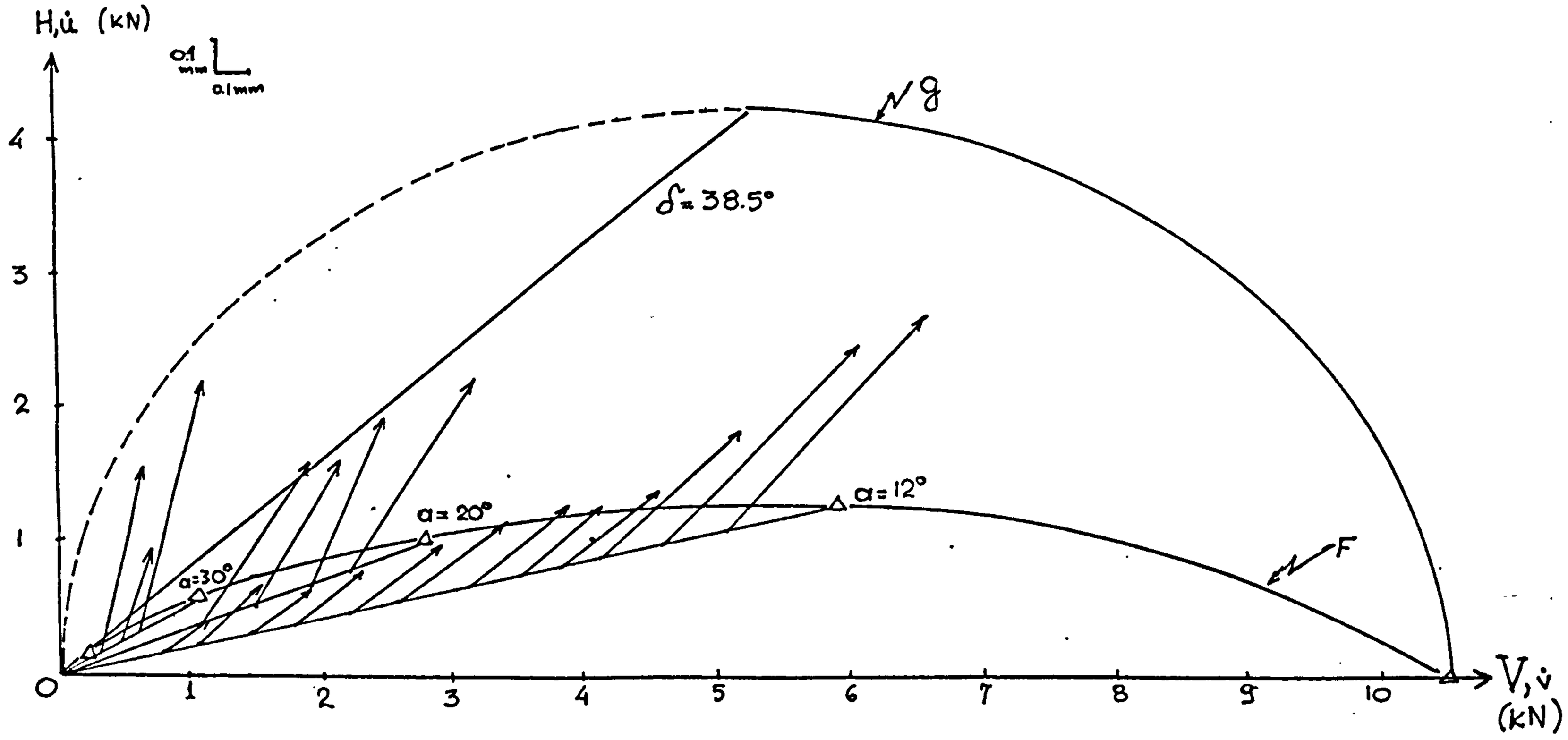

Fig. 8.3 Failure envelope, plastic potential and associated displacements. Tests in the FAC.

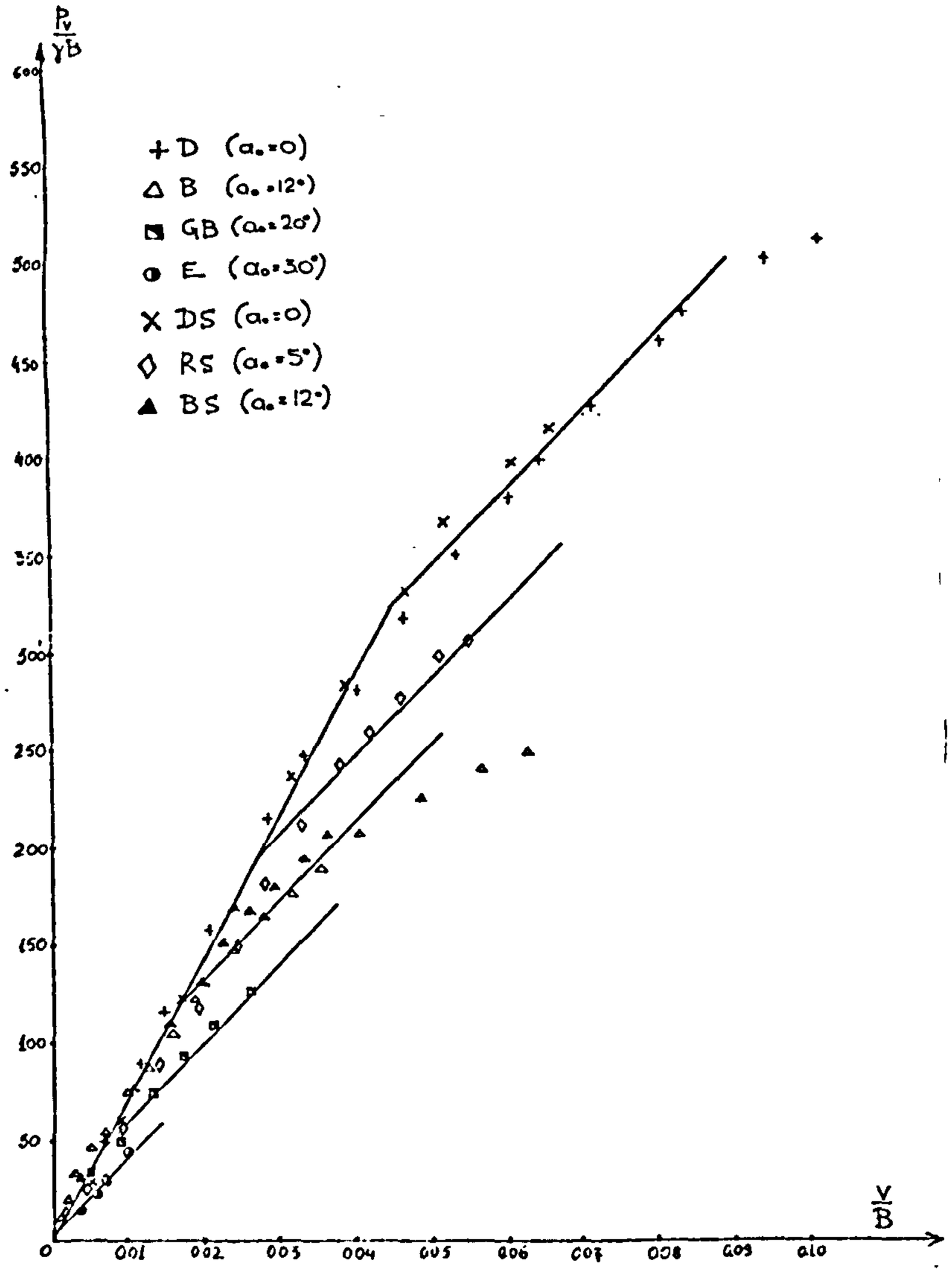

Fig. 8.4 Vertical component of the load versus vertical displacement for various load inclinations.

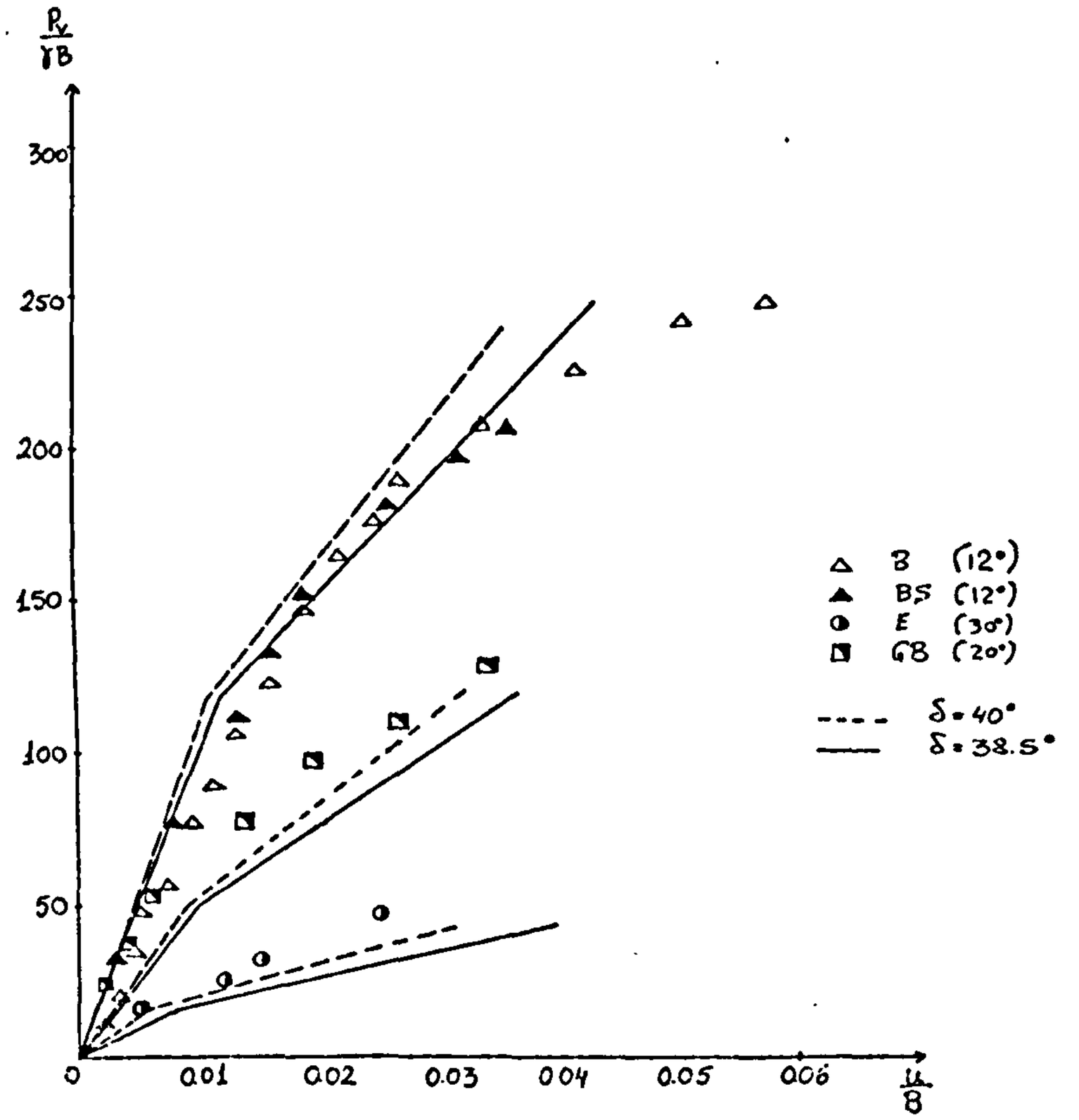

Fig. 8.5 Experimental and predicted vertical component of the load versus horizontal displacement relationship.

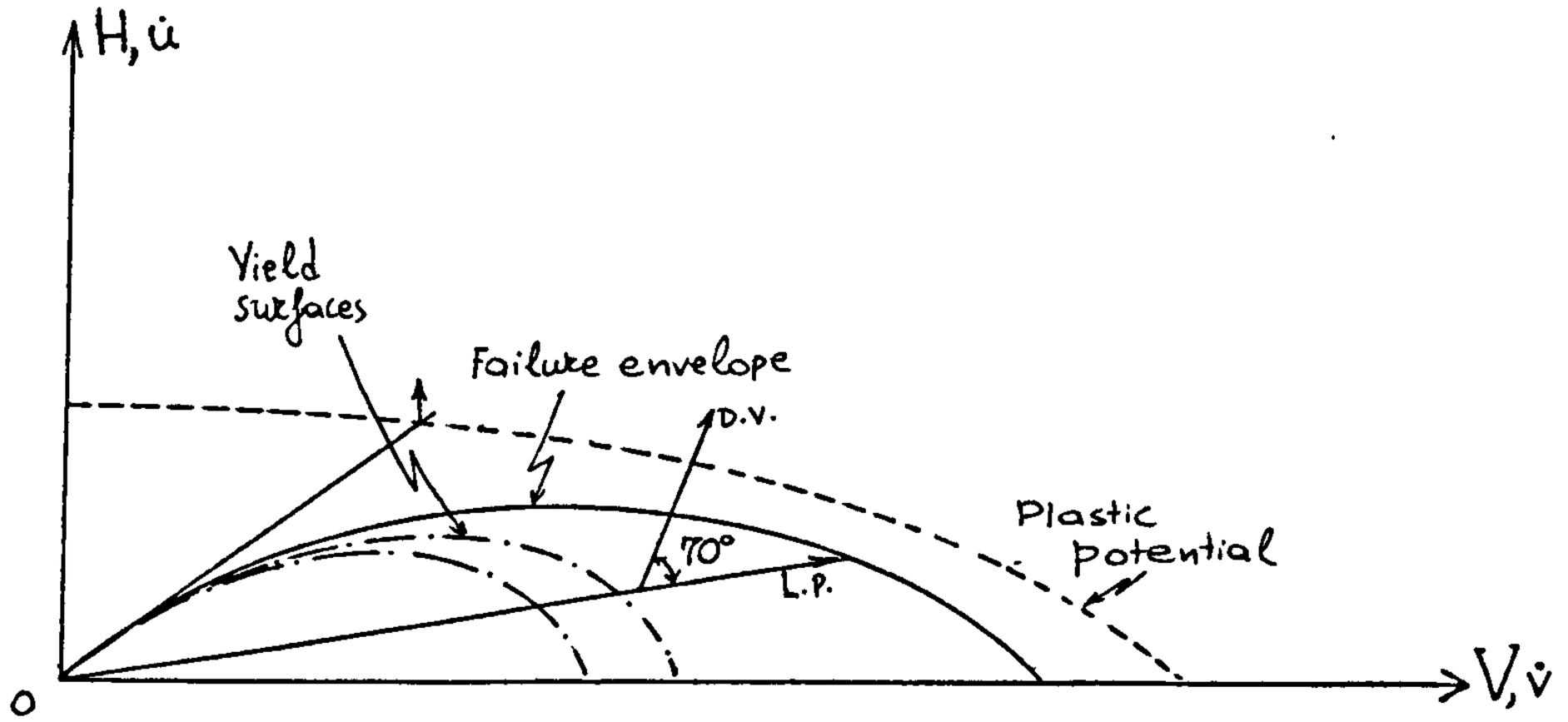

Fig. 8.6 V-H failure envelope and plastic potential (from Yip, 1977).

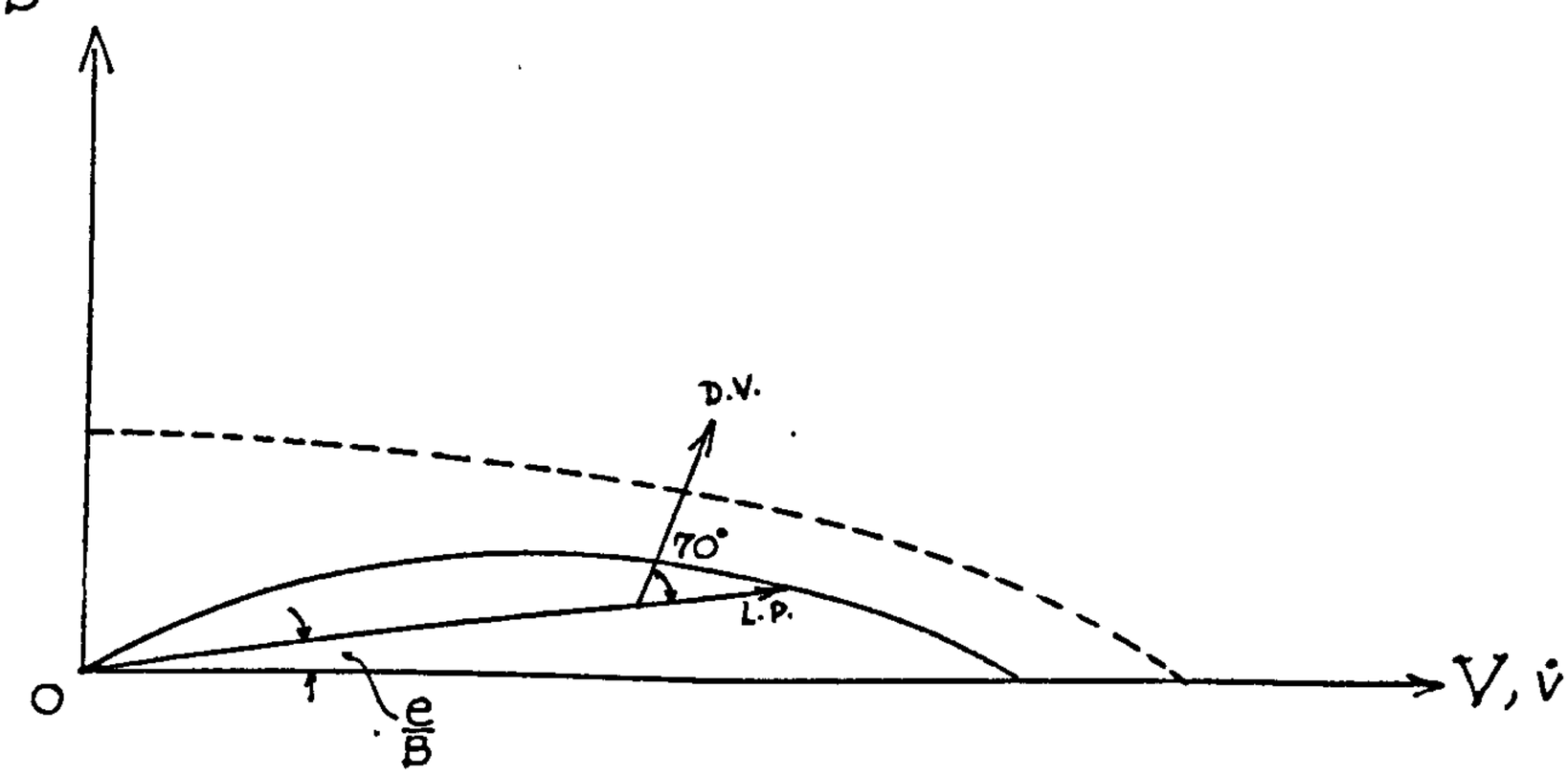

Fig. 8.7 V-M failure envelope and plastic potential (from Yip,1977).

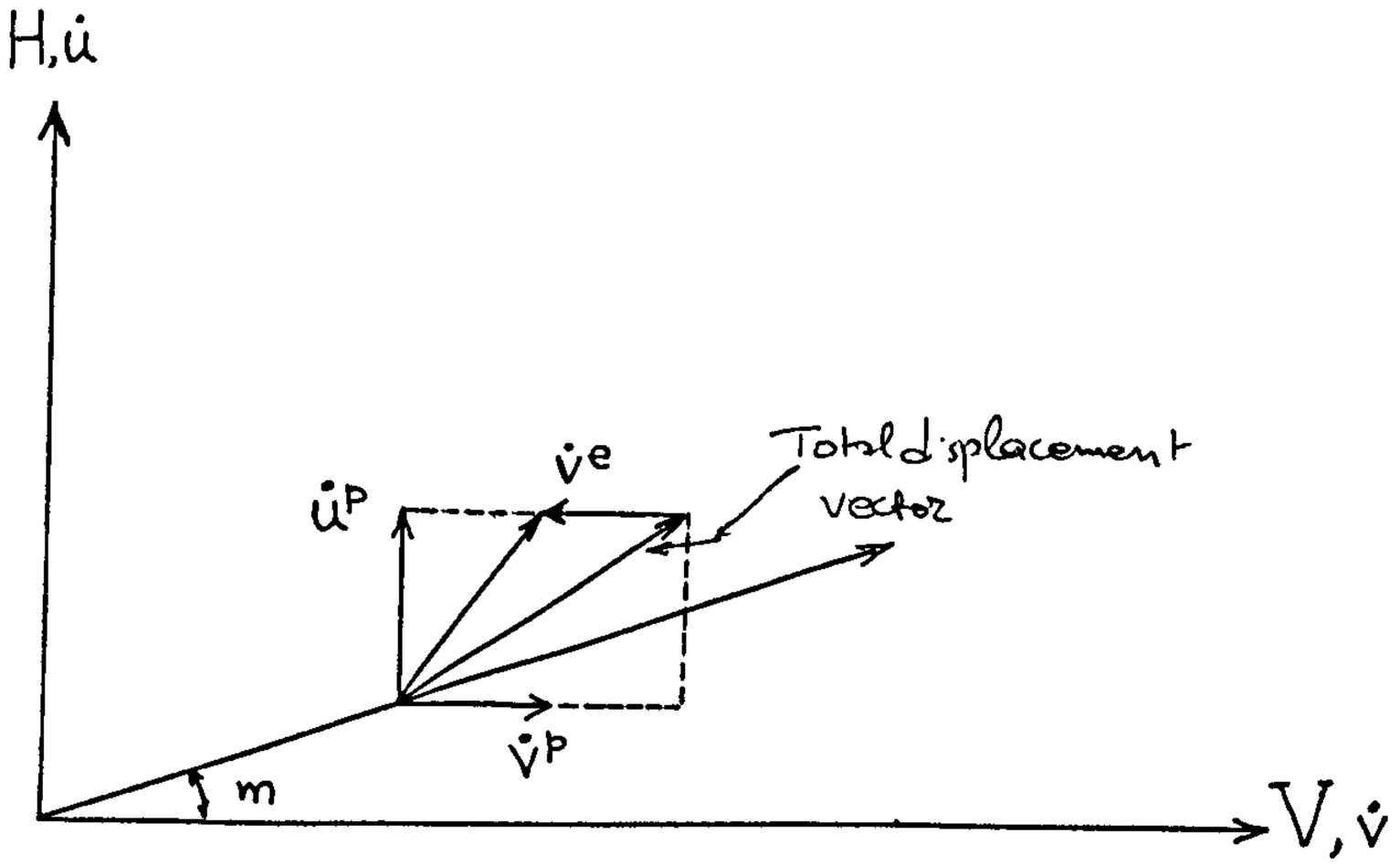

Fig. 8.8 Elastic and plastic displacement increments.

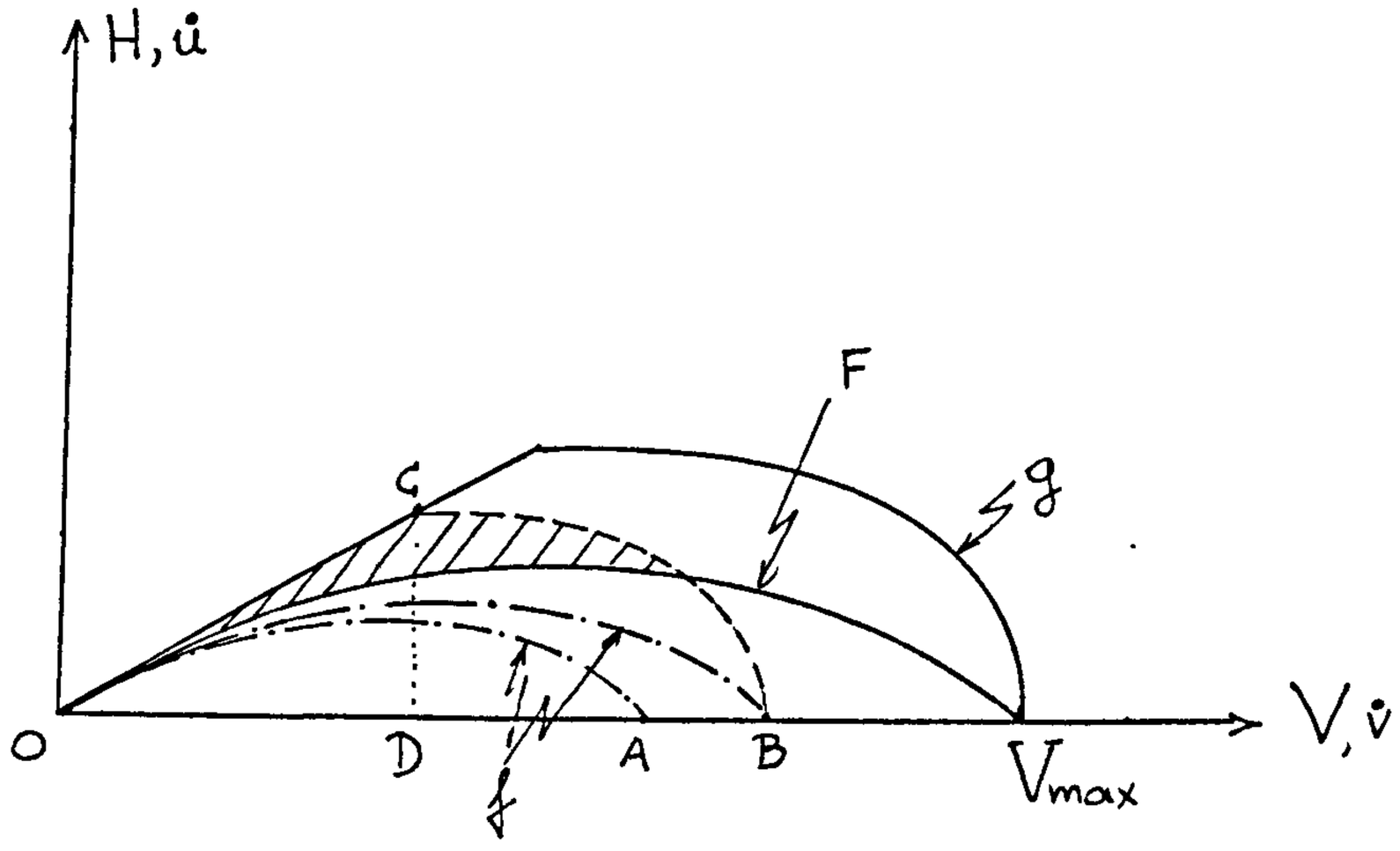

Fig. 8.9 Yield surfaces and plastic potentials for a footing on sand.

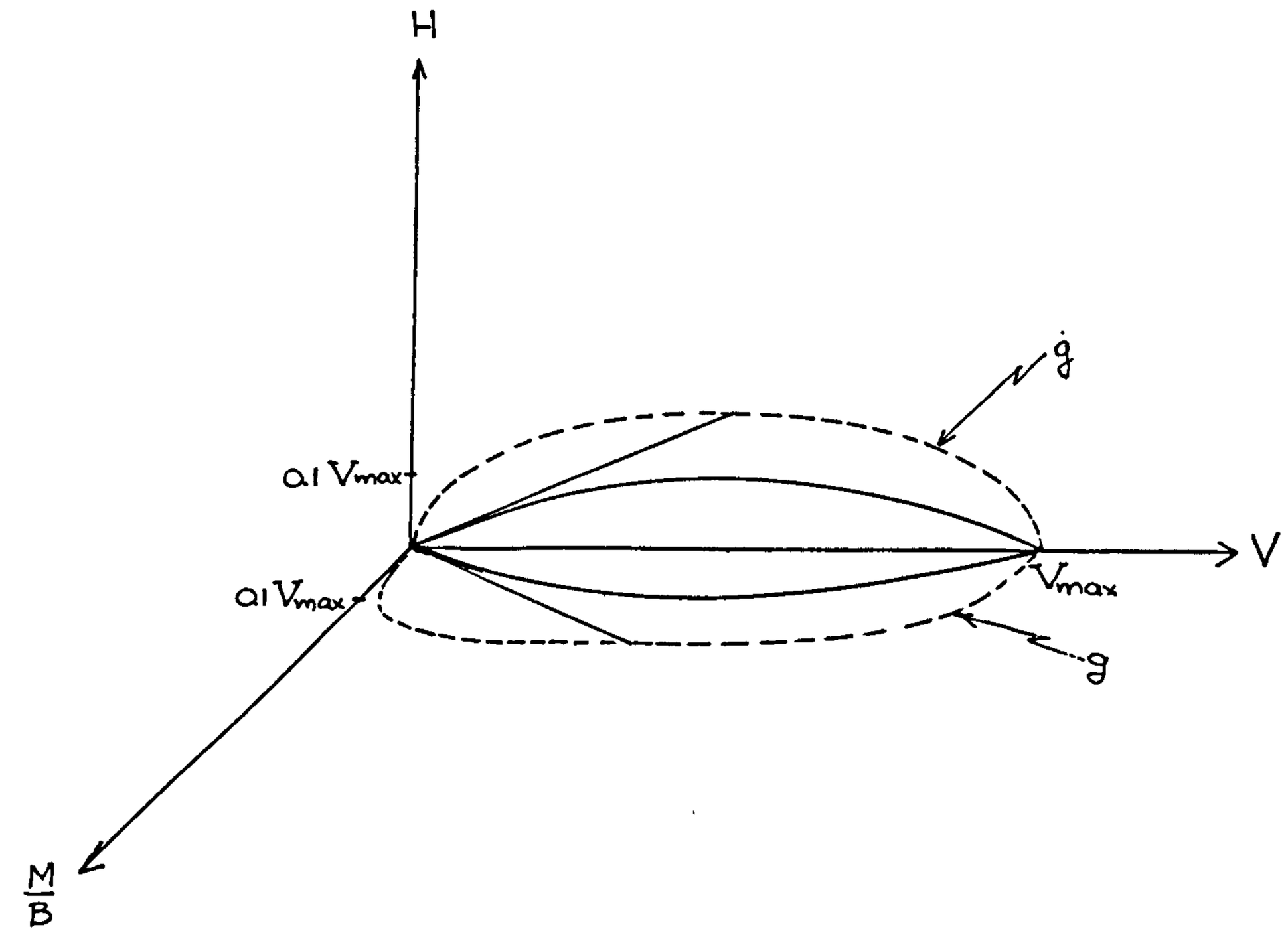

Fig. 9.1 Failure envelope and plastic potential for a footing on sand under V-H-M.

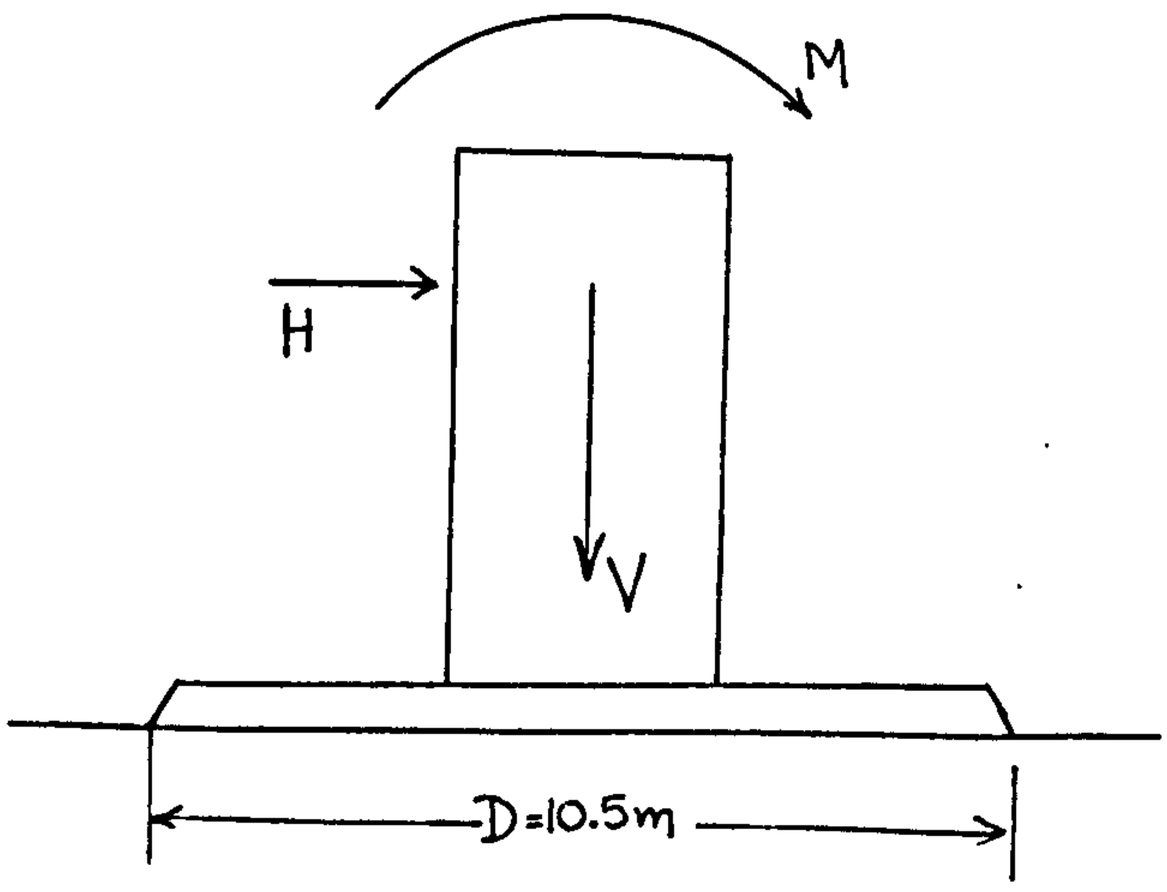

V = 1250 kN
H = 490 kN
M = 3220 kNm
Φ = 38° (drained triaxial).

Fig. 9.2 The tower at the Christchurch bay.